frontiers | Research Topics

Updates on the role of surfactant proteins A and D in innate immune responses

Edited by
Taruna Madan and Nicole Thielens

Published in
Frontiers in Immunology

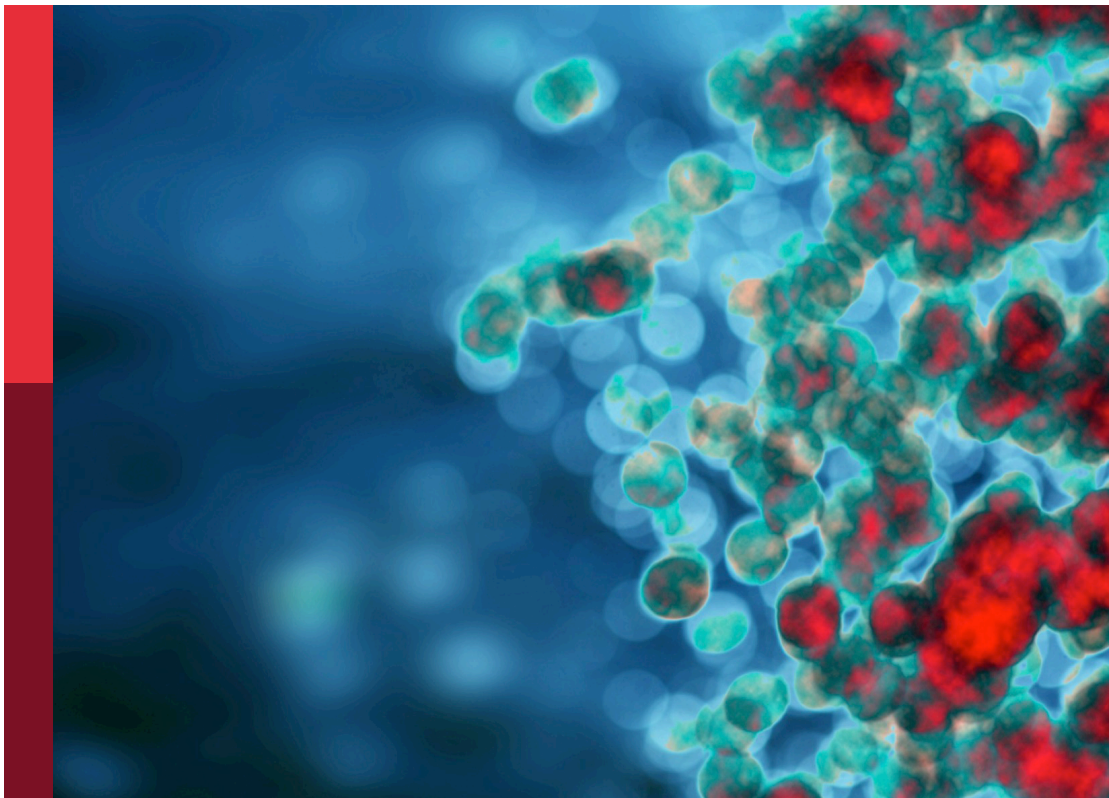

ISSN 1664-8714
ISBN 978-2-83252-020-8
DOI 10.3389/978-2-83252-020-8

About Frontiers

Frontiers is more than just an open access publisher of scholarly articles: it is a pioneering approach to the world of academia, radically improving the way scholarly research is managed. The grand vision of Frontiers is a world where all people have an equal opportunity to seek, share and generate knowledge. Frontiers provides immediate and permanent online open access to all its publications, but this alone is not enough to realize our grand goals.

Frontiers journal series

The Frontiers journal series is a multi-tier and interdisciplinary set of open-access, online journals, promising a paradigm shift from the current review, selection and dissemination processes in academic publishing. All Frontiers journals are driven by researchers for researchers; therefore, they constitute a service to the scholarly community. At the same time, the *Frontiers journal series* operates on a revolutionary invention, the tiered publishing system, initially addressing specific communities of scholars, and gradually climbing up to broader public understanding, thus serving the interests of the lay society, too.

Dedication to quality

Each Frontiers article is a landmark of the highest quality, thanks to genuinely collaborative interactions between authors and review editors, who include some of the world's best academicians. Research must be certified by peers before entering a stream of knowledge that may eventually reach the public - and shape society; therefore, Frontiers only applies the most rigorous and unbiased reviews. Frontiers revolutionizes research publishing by freely delivering the most outstanding research, evaluated with no bias from both the academic and social point of view. By applying the most advanced information technologies, Frontiers is catapulting scholarly publishing into a new generation.

What are Frontiers Research Topics?

Frontiers Research Topics are very popular trademarks of the *Frontiers journals series*: they are collections of at least ten articles, all centered on a particular subject. With their unique mix of varied contributions from Original Research to Review Articles, Frontiers Research Topics unify the most influential researchers, the latest key findings and historical advances in a hot research area.

Find out more on how to host your own Frontiers Research Topic or contribute to one as an author by contacting the Frontiers editorial office: frontiersin.org/about/contact

Updates on the role of surfactant proteins A and D in innate immune responses

Topic editors

Taruna Madan — National Institute for Research in Reproductive Health (ICMR), India

Nicole Thielens — UMR5075 Institut de Biologie Structurale (IBS), France

Citation

Madan, T., Thielens, N., eds. (2023). *Updates on the role of surfactant proteins A and D in innate immune responses*. Lausanne: Frontiers Media SA.

doi: 10.3389/978-2-83252-020-8

Table of contents

frontiers | Frontiers in Immunology

TYPE Editorial
PUBLISHED 13 December 2022
DOI 10.3389/fimmu.2022.1113210

OPEN ACCESS

EDITED AND REVIEWED BY
Francesca Granucci,
University of Milano-Bicocca, Italy

*CORRESPONDENCE
Taruna Madan
taruna_m@hotmail.com
Nicole M. Thielens
nicole.thielens@ibs.fr

SPECIALTY SECTION
This article was submitted to Molecular Innate Immunity, a section of the journal Frontiers in Immunology

RECEIVED 01 December 2022
ACCEPTED 05 December 2022
PUBLISHED 13 December 2022

CITATION
Madan T and Thielens NM (2022) Editorial: Updates on the role of surfactant proteins A and D in innate immune responses. *Front. Immunol.* 13:1113210. doi: 10.3389/fimmu.2022.1113210

Editorial: Updates on the role of surfactant proteins A and D in innate immune responses

Taruna Madan[1]* and Nicole M. Thielens[2]*

[1]Department of Innate Immunity, ICMR-National Institute for Research in Reproductive and Child Health, Mumbai, India, [2]Université Grenoble Alpes, CNRS, CEA, IBS, Grenoble, France

KEYWORDS

SP-A, SP-D, alveolar macrophages, SNP, prostate cancer, SARS-CoV-2, RSV, lung diseases

Editorial on the Research Topic
Updates on the role of surfactant proteins A and D in innate immune responses

Surfactant proteins A (SP-A) and D (SP-D) are collagen-containing calcium-dependent lectins, serving as soluble innate immune molecules. They maintain pulmonary and extrapulmonary homeostasis through their multiple roles as anti-infectious, immunomodulatory, and anti-cancer agents. These proteins bind to target ligands on pathogens, allergens, tumor and apoptotic cells, bringing about the effector functions *via* their interaction with cell surface receptors, enhancing target clearance from mucosal entry points and modulating the inflammatory response. Recombinant molecules of SP-A and SP-D may represent potential therapeutic strategies, with their actions aiding the blockade of viral, bacterial, and fungal infections and their immunomodulatory capacity to prevent excessive inflammatory responses. The eleven original research manuscripts of this themed collection highlight recent achievements regarding the role of SP-A and SP-D in innate immune responses.

Four of the articles relate to lung alveolar cells, including alveolar macrophages (AMs) which are the main cells involved in SP-A/D-mediated immune response in the lung. The first study by Wang et al. demonstrated that intratracheal spraying of engineered nanomaterials (ENMs) of four different types (fullerene, carbon nanotubes, titanium or silicon dioxides) induced inflammation in the rat lung, most of the administered ENMs being phagocytosed by AMs. *In vitro* analyses in the presence of rat bronchoalveolar lavage fluid (BALF) revealed that SP-A/D opsonized all tested ENMs and enhanced their phagocytosis by AMs through CD14 whereas cytokine production was dependent on the type of ENM phagocytosed. SP-A/D, therefore, play an important role by opsonizing inhaled nanoparticles, thereby contributing to decreased lung toxicity.

Two contributions from the group of J. Floros investigated changes in the toponome of AMs and in the miRNome of lung alveolar cells (LACs) of SP-A knockout (KO) mice following Klebsiella pneumoniae exposure. Phelps et al. employed the toponome imaging system (TIS) with serial immunostaining of cells for the localization of multiple markers, allowing characterization of multi-protein clusters, referred to as Combinatorial Molecular Phenotypes

(CMPs). They reported a decrease of CMPs exclusive to infected AMs in KO mice, which may underlie the susceptibility of these mice to infection. In addition, both KO groups (infected and non-infected) exhibited more exclusive CMPs than the corresponding WT groups, suggesting that SP-A may participate directly to CMP formation through interactions with various cell surface molecules. As underlined by the authors, future studies will require exploration of CMP differences by using additional markers and/or by influencing specific markers by exogenous SP-A treatment. Thorenoor and Floros studied the role of exogenous SP-A rescue on the regulation of the LACs miRNome, the targets of miRNA-RNA, and the gene expression in SP-A-KO infected male and female mice. All analyses reveal sex differences and involvement of the miRNA-RNA targets in inflammation, anti-apoptosis and cell cycle pathways. The gene expression profiles identify the TNF, cell cycle, and TP-53 (known to play a role in cancer) signaling nodes under the studied conditions. These findings are relevant to be considered for the potential therapeutic use of SP-A in pulmonary diseases.

The fourth study by Garcia-Fojeda et al. focused on SP-A-dependent signaling pathways that enhanced IL-4 mediated activation of tissue repair program in AMs. They showed that SP-A activated PI3K-Akt dependent signaling pathways and contributed to increased proliferation and alternative activation of AMs. In addition, SP-A and IL-4 synergistically enhanced mitochondrial respiration and glycolysis in AMs. The signaling events that drive the SP-A-dependent amplification of IL-4 effects on AMs may aid in the development of new approaches to control lung diseases caused by exaggerated repair responses.

Understanding on the genetic basis of the role of SPs in lung diseases and infections has been enhanced by three studies. A contribution by Abbasi et al. compared single nucleotide polymorphisms (SNPs) of SP genes in two interstitial lung diseases, Idiopathic Pulmonary Fibrosis (IPF) and Hypersensitivity Pneumonitis (HP), in previously described Mexican study groups. Novel computational models were used to assess the epistatic effects of SNP-SNP interactions in both the diseases. The results show that IPF and HP are associated with some common SP genetic variants, suggesting shared pathophysiological mechanisms. However, one of the SNP interactions involving the *SFTPA1*, *SFTPA2* and *SFTPD* genes is associated with a disease-specific outcome, suggesting that specific interactions may serve as markers to distinguish between epithelial-driven fibrosis (IPF) and inflammatory-driven fibrosis (HP).

To understand if the genetic heterogeneity of SP-A is the reason for its dysfunctionality in asthma, Francisco et al., evaluated the functional significance of a single nucleotide polymorphism within the carbohydrate recognition domain of Surfactant Protein-A2 (SP-A2), which results in an amino acid substitution at position 223 from glutamine (Q) to lysine (K). With strong evidences of higher anti-asthmatic potential of SP-A 223Q in the asthmatics, humanized mice and the primary bronchial epithelial cells from asthmatics, the authors developed 10 and 20 amino acid peptides of SP-A2 spanning position 223Q and the exogenous administration of SP-A 223Q peptides significantly lowered eosinophilic inflammation, mucin production and airways hyperresponsiveness in a house dust mite model of asthma, protect from lung function decline during an IL-13 challenge model in mice, and decrease IL-13-induced MUC5AC gene expression in primary airway epithelial cells from asthmatics.

Depicolzuane et al., tested the hypothesis that RSV severity in infants is associated with single nucleotide polymorphisms (SNPs) of surfactant proteins (SPs) in a prospective cohort of 405 RSV-positive children classified into moderate and severe. Increased risk of severe disease was associated with rs1059047_C of the SFTPA1 whereas the rs17886395_C of the SFTPA2 and rs2243639_A of the SFTPD were associated with protection. Importantly, the risk to severity was not associated with SNPs of hydrophobic SFTPB and SFTPC.

Two studies investigated the role of SP-A and SP-D in host defense against SARS-CoV-2. Hsieh et al., provided *in vitro* evidences for the protective role of rfhSP-D against SARS-CoV-2 infection. With a dose-responsive binding to S1 spike protein of SARS-CoV-2 and its receptor binding domain, rfhSP-D significantly inhibited interaction of S1 protein with the hACE2 overexpressing HEK293T cells. A ~0.5 RLU fold reduction in the entry of pseudotyped lentiviral particles validated the therapeutic potential of rfhSP-D.

Aramyan et al., utilized a hybrid quantum and classical *in silico* modeling technique that utilized protein graph pruning and indicated that SP-A may ligate the S protein with a similar affinity to the ACE2-Spike binding. With the high affinity SP-A binding site localized to the fusion region of the SARS-CoV-2 S protein, responsible for viral entry, the authors speculate that SP-A may not directly compete with ACE2 for the binding site on the S protein, but may interfere with viral entry to the cell by hindering necessary conformational changes or the fusion process.

To explore a novel solution to the growing problem of multidrug-resistant bacteria, Coya et al., investigated the therapeutic impact of human SP-A and a recombinant trimeric fragment (rfhSP-A) together with antibiotics against pathogenic Gram-negative bacteria. SP-A directly interacted with polymyxin B and showed synergistic microbicidal activity with polymyxin B and E against three SP-A-resistant pathogenic bacteria: Klebsiella pneumoniae, non-typable Haemophilus influenzae (NTHi), and Pseudomonas aeruginosa facilitated by the formation of SP-A/PMB aggregates and enhanced bacterial membrane permeabilization. A molecular derivative of PMB lacking the acyl chain (PMBN) with binding ability but no bactericidal activity showed synergistic bactericidal activity against Gram-negative bacteria along with SP-A. The trimeric rfhSP-A fragment had relatively lower but significant direct bactericidal activity against *K. pneumoniae*, NTHi, and *P. aeruginosa*.

Novel anti-tumoral immune mechanisms of SP-D in prostate cancer (PCa) have been elucidated by Ganguly et al.. These are suggestive of transformation of an immunologically "cold tumour" into a "hot tumour", thereby implicating possible synergistic potential of recombinant fragment of human SP-D (rfhSP-D) along with the immune check point inhibitor therapy.

Decreased expression and increased proteolytic degradation of SP-D was observed in early and advanced stages of PCa in the transgenic adenocarcinoma of mouse prostate (TRAMP) model associated with increased serine proteases producing granulocytes and polymorphonuclear myeloid-derived suppressor cells (PMN MDSCs). Importantly, treatment of *ex-vivo* cultured TRAMP tumours with rfhSP-D and elastase inhibitor, Sivelestat led to polarization towards M1 macrophages with downregulation of PMN MDSCs and enhanced immunogenic cell death.

To summarise, this Research Topic provides much enhanced knowledge of the impact of SPs and their genetic heterogeneity on lung immunity and infections and on the immune component of prostate tumour microenvironment strengthening the premise of clinical application of SPs in various pulmonary diseases and cancer.

Author contributions

Both TM and NMT have made a substantial, direct, and intellectual contribution to the Editorial and approved it for publication.

Acknowledgments

IBS acknowledges integration into the Interdisciplinary Research Institute of Grenoble (IRIG, CEA). TM acknowledges support from ICMR-NIRRCH, Mumbai, India.

Conflict of interest

The authors declare that the research was conducted in the absence of any commercial or financial relationships that could be construed as a potential conflict of interest.

Publisher's note

frontiers in Immunology

ORIGINAL RESEARCH
published: 14 May 2021
doi: 10.3389/fimmu.2021.641360

Human Surfactant Protein D Binds Spike Protein and Acts as an Entry Inhibitor of SARS-CoV-2 Pseudotyped Viral Particles

Miao-Hsi Hsieh[1,2,3], Nazar Beirag[4], Valarmathy Murugaiah[4], Yu-Chi Chou[5], Wen-Shuo Kuo[2], Hui-Fang Kao[2,6], Taruna Madan[7], Uday Kishore[4] and Jiu-Yao Wang[2,3,8]**

[1] Institute of Basic Medical Sciences, College of Medicine, National Cheng Kung University, Tainan, Taiwan, [2] Center for Allergy & Clinical Immunology Research (ACIR), National Cheng Kung University Hospital, College of Medicine, National Cheng Kung University, Tainan, Taiwan, [3] Department of Pediatrics, College of Medicine, National Cheng Kung University Hospital, Tainan, Taiwan, [4] Biosciences, College of Health, Medicine and Life Sciences, Brunel University London, Uxbridge, United Kingdom, [5] Biomedical Translation Research Center (BioTReC), Academia Sinica, Taipei, Taiwan, [6] Department of Nursing, National Tainan Junior College of Nursing, Tainan, Taiwan, [7] Department of Innate Immunity, ICMR-National Institute for Research in Reproductive Health, Mumbai, India, [8] Children's Hospital, China Medical University, Taichung, Taiwan

OPEN ACCESS

Edited by:
Nicole Thielens,
UMR5075 Institut de Biologie Structurale (IBS), France

Reviewed by:
Kevan Hartshorn,
Boston University, United States
Howard William Clark,
University of Southampton, United Kingdom

***Correspondence:**
Jiu-Yao Wang
a122@mail.ncku.edu.tw
Uday Kishore
uday.kishore@brunel.ac.uk;
ukishore@hotmail.com

Specialty section:
This article was submitted to Molecular Innate Immunity, a section of the journal Frontiers in Immunology

Received: 14 December 2020
Accepted: 20 April 2021
Published: 14 May 2021

Citation:
Hsieh M-H, Beirag N, Murugaiah V, Chou Y-C, Kuo W-S, Kao H-F, Madan T, Kishore U and Wang J-Y (2021) Human Surfactant Protein D Binds Spike Protein and Acts as an Entry Inhibitor of SARS-CoV-2 Pseudotyped Viral Particles. Front. Immunol. 12:641360. doi: 10.3389/fimmu.2021.641360

Human SP-D is a potent innate immune molecule whose presence at pulmonary mucosal surfaces allows its role in immune surveillance against pathogens. Higher levels of serum SP-D have been reported in the patients with severe acute respiratory syndrome coronavirus (SARS-CoV). Studies have suggested the ability of human SP-D to recognise spike glycoprotein of SARS-CoV; its interaction with HCoV-229E strain leads to viral inhibition in human bronchial epithelial (16HBE) cells. Previous studies have reported that a recombinant fragment of human SP-D (rfhSP-D) composed of 8 Gly-X-Y repeats, neck and CRD region, can act against a range of viral pathogens including influenza A Virus and Respiratory Syncytial Virus *in vitro*, *in vivo* and *ex vivo*. In this context, this study was aimed at examining the likely protective role of rfhSP-D against SARS-CoV-2 infection. rfhSP-D showed a dose-responsive binding to S1 spike protein of SARS-CoV-2 and its receptor binding domain. Importantly, rfhSP-D inhibited interaction of S1 protein with the HEK293T cells overexpressing human angiotensin converting enzyme 2 (hACE2). The protective role of rfhSP-D against SARS-CoV-2 infection as an entry inhibitor was further validated by the use of pseudotyped lentiviral particles expressing SARS-CoV-2 S1 protein; ~0.5 RLU fold reduction in viral entry was seen following treatment with rfhSP-D (10 µg/ml). These results highlight the therapeutic potential of rfhSP-D in SARS-CoV-2 infection and merit pre-clinical studies in animal models.

Keywords: innate immunity, SARS-COV-2, spike protein, human pulmonary collectins, surfactant protein D, angiotensin converting enzyme 2

INTRODUCTION

Human surfactant protein D (SP-D), a collagen-containing C-type lectin and a member of the collectin family, is known to be involved in pulmonary surfactant homeostasis and immunity (1). SP-D is primarily synthesized and secreted into the air space of the lungs by alveolar type II and Clara cells (2, 3). Its primary structure is organized into four regions: a cysteine-rich N-terminus, a triple-helical collagen region composed of Gly-X-Y triplets repeats, an α-helical coiled neck region, and a C-terminal C-type lectin or carbohydrate recognition domain (CRD) (1). As a versatile innate immune molecule, SP-D can interact with a number of pathogens, triggering clearance mechanisms against viruses, bacteria, and fungi, as well as and apoptotic cells (4).

Direct interaction of SP-D with a range of viruses results in viral neutralization, and induction of phagocytosis *in vitro* (5, 6). Anti-viral activity of human SP-D against Influenza A Virus (IAV) infection has been reported. SP-D binds haemagglutinin (HA) and neuraminidase (NA) glycoproteins of IAV, and inhibits hemagglutination at initial stages of the infection (7). A recombinant fragment of human SP-D (rfhSP-D), composed of homotrimeric neck and CRD region, was also shown to bind HA, NA and Matrix 1 (M1) protein of IAV, and act as an entry inhibitor of IAV infection on A549 lung epithelial cells (8). Furthermore, SP-D binds to gp120 and inhibits HIV-1 infectivity and replication (9) in U937 monocytic cells, Jurkat T cells and PBMCs, in addition to suppressing HIV-1 triggered cytokine storm (10). Higher levels of serum SP-D have been detected in patients infected with severe acute respiratory syndrome (SARS) coronavirus (SARS-CoV) (11). SARS-CoV spike glycoprotein is recognized by SP-D (12). Interaction between SP-D and HCoV-229E, another coronavirus strain, leads to inhibition of viral infection in human bronchial epithelial (16HBE) cells (13).

SARS coronavirus 2 (SARS-CoV-2) is an enveloped β-coronavirus, belonging to the Coronaviridae family of viruses, and is genetically close to SARS-CoV (~80% sequence similarity) and bat coronavirus RaTG13 (96.2%) (14, 15). The envelope of SARS-CoV-2 is coated by the spike (S) glycoprotein, a small envelope (E) glycoprotein, membrane (M) glycoprotein, nucleocapsid (N) protein, and several putative accessory proteins (15–17). The SARS-CoV-2 mediates its entry into the host cell using the S1 sub-unit of the S glycoprotein by binding to angiotensin-converting enzyme 2 (ACE2) receptor (18). However, viral entry into the host cells requires not only binding to the ACE2 receptor, but also priming of the S protein by a transmembrane protease serine 2 (TMPRSS2) *via* cleavage of the S protein at S1/S2 sites (19). This cleavage is very crucial for the virus-host cell membrane fusion and cell entry (20). Following viral replication, assembly, and release, the infected host cells undergo pyroptosis, thus, releasing Damage-Associated Molecular Patterns (DAMPs) (21). DAMPs are then recognised by surrounding macrophages and monocytes that respond to viral infection by inducing cytokine storm (22). However, in some cases, an impaired or dysregulated immune response can also occur, causing an Acute Respiratory Distress Syndrome (ARDS) (23, 24).

Designing and developing new anti-viral therapeutic strategies are crucial for treating SARS-CoV-2. The likely anti-viral effects of immune-surveillance molecules like SP-D have not been well investigated in SARS-CoV-2 infection. Since rfhSP-D has been shown to inhibit viral infection and replication of IAV and HIV-1, this study was aimed at investigating whether rfhSP-D can interfere with the binding of SARS-CoV-2 S1, and receptor binding domain (RBD) of SARS-CoV-2 with ACE-2. The ability of rfhSP-D to inhibit infection of SARS-CoV-2 was examined using pseudotyped lentiviral particles expressing SARS-CoV-2 S1 protein.

MATERIAL AND METHODS

Expression and Purification of rfhSP-D

DNA sequences coding for 8 Gly-X-Y repeats of collagen region, α-helical neck and CRD region of human SP-D were cloned under T7 promoter and expressed in *Escherichia coli* BL21 (λDE3) pLysS using construct pUK-D1 (25, 26). Primary bacterial inoculum (25 ml) was grown in Luria-Bertani (LB) medium (500 ml) with 34 μg/ml chloramphenicol and 100 μg/ml ampicillin (Sigma-Aldrich) at 37°C until an OD_{600} of 0.6 was reached. Following isopropyl β-D-thiogalactoside (IPTG) (0.5mM) induction, the transformed *E. coli* cells were grown further for another 3 h at 37°C on a shaker. The bacterial cells were harvested by centrifugation (5000 rpm, 4°C, 10 min), and the cell pellet was re-suspended in lysis buffer containing 50 mM Tris–HCl, pH 7.5, 200 mM NaCl, 5 mM EDTA, 0.1% v/v Triton X-100, 0.1 mM phenylmethane sulfonyl fluoride (PMSF) (Sigma-Aldrich), and 50 μg lysozyme/ml (Sigma-Aldrich) at 4°C for 1 h. The lysed cell lysate was then sonicated at 60 Hz for 30 sec with an interval of 2 min (12 cycles) using a Soniprep 150 (MSE, London, UK), followed by centrifugation (12,000 rpm, 15 min). The inclusion bodies were denatured using buffer (50 ml) containing 0.5 M Tris–HCl, 0.1 M NaCl, pH7.5 and 8 M urea for 1 h at 4°C. The soluble fraction was dialysed against the same buffer containing varied concentration of urea (4 M, 2 M, 1 M, 0 M) for 2 h each. The refolded material was then dialysed against affinity buffer (50 mM Tris–HCl, pH7.5, 100 mM NaCl, 10 mM $CaCl_2$) for 2 h at 4°C. The affinity buffer dialysed supernatant was then loaded on to a maltose-agarose column (5 ml) (Sigma-Aldrich); the bound rfhSP-D was eluted using elution buffer containing 50 mM Tris–HCl, 100 mM NaCl, and 10 mM EDTA. Purified rfhSP-D was run on SDS-PAGE to assess its purity. LPS was removed using Endotoxin Removal Resin (Sigma-Aldrich). LPS level was determined using QCL-1000 Limulus amebocyte lysate system (Lonza) and found to be < 5 pg/μg of rfhSP-D.

ELISA

Polystyrene microtiter plates (Sigma-Aldrich) were coated with SARS-CoV-2 spike S1 protein (NativeAntigen S1. NCBI accession number YP_009724390.1 AA1-674, produced in HEK 293 cells; Acro, AA Val 16 - Arg 685, accession #

QHD43416.1, produced in HEK 293 cells) or RBD (Acro, Arg319-Phe541, accession #QHD43416.1, produced in HEK 293 cells) (27) (5 μg/ml, 100 μl/well) at 4°C overnight using carbonate/bicarbonate (CBC) buffer, pH 9.6 (Sigma-Aldrich). The following day, the microtiter wells were washed three times with Tris Buffered Saline-Tween (TBST, pH 7.2-7.4) containing 0.05% v/v Tween 20 (Sigma-Aldrich) and 5mM $CaCl_2$ (Thermo Fisher Scientific). The wells were then blocked by TBS containing 1% w/v BSA and 5mM $CaCl_2$, for 1 h. After washing three times with TBST, the wells were incubated with two-fold dilutions of rfhSP-D or recombinant human full-length SP-D (hFL-SP-D, R&D, 1920-SP, produced in HEK 293 cells) protein (100μl/well) in the blocking buffer at 4°C overnight. Next day, the wells were washed and then incubated with biotinylated mouse anti-Human SP-D detection antibody (1:180) (R&D Systems) for 2 h at room temperature. After washing, the wells were incubated with Streptavidin horseradish peroxidase (HRP)-conjugate (1:40; R&D System) for 20 min, followed by washing three times. TMB substrate (100 μl/well; Thermo Fisher Scientific) was added to each well and the reaction was stopped using 1M H_2SO_4 (50 μl/well; Sigma-Aldrich). Absorbance at 450nm were measured by VersaMax™ ELISA Microplate Reader.

Competition ELISA

Polystyrene microtiter plates were coated with 2 μg/ml rfhSP-D (100 μl/well) at 4°C overnight using CBC buffer and washed three times with TBS buffer containing 0.05% v/v Tween 20 and 5mM $CaCl_2$. The wells were blocked with TBS containing 1% BSA and 5mM $CaCl_2$ for 1h. The wells were then washed three times and incubated with SARS-CoV-2 spike S1 protein (sheep-IgG tag) or RBD (His-tag) (2.5 or 5 μg/ml, 100 μl/well) separately in blocking buffer containing 10mM maltose and 10mM EDTA at 4°C overnight. Next day, the wells were washed and then incubated with anti-sheep IgG-HRP antibodies (Genetex, GTX27111, 0.5 μg/ml, 100 μl/well) (1:2000) or anti-His antibodies (Genetex, GTX628914, 0.5 μg/ml, 100 μl/well) (1:2000) for 2 h. For the detection of RBD binding, the wells were further incubated with anti-mouse IgG antibody (Abcam, ab6728, 0.5 μg/ml, 100 μl/well) (1:2000) for 2 h. After washing, the plates were incubated with TMB substrate (100 μl/well) and then quenched with 1M H_2SO_4 (50 μl/well). Absorbance at 450nm was recorded by VersaMax™ ELISA Microplate Reader.

Western Blotting

HEK293T and HEK293T-ACE2 cells (0.5×10^5) were lysed by RIPA buffer (Thermo Fisher Scientific) containing protease inhibitor (AMRESCO VWR life sciences) on ice for 15 minutes and then centrifugation (13000 rpm, 4°C, 15 min). 30 μg samples resuspended in Laemmli sample buffer (10 μl) and heated at 100°C for 10 minutes. The samples were loaded into an SDS-PAGE (8% v/v) gel and then electrophoretically transferred onto the PVDF membrane (320mA for 2h) (Sigma-Aldrich) in transfer buffer [25mM Tris–HCl pH 7.5, 190 mM glycine (Sigma-Aldrich), and 20% v/v methanol (Thermo Fisher Scientific)]. The membranes were blocked by 5% w/v dried milk powder (Sigma-Aldrich) diluted in TBS+ 0.05% v/v Tween 20 (TBST) for 1h at room temperature and incubated with anti-SARS-CoV-2 (COVID-19) Spike antibody (GeneTex, GTX135356; 1:1000) or anti-ACE2 antibody [SN0754] (GeneTex, GTX01160; 1:1000) at 4°C overnight. The membranes were washed three times and probed with secondary Goat anti-rabbit IgG horseradish peroxidase (HRP)-conjugate (1:10000; Fisher Scientific) for 1h at room temperature. Following TBST washes, the protein expression was measured by Western Lightning Plus ECL (PerkinElmer) and chemiluminescent detection was performed using FluorChem R system (ProteinSimple, San Jose, CA, USA).

Cell Culture and Treatments

Human embryonic kidney (HEK) 293T or HEK293T cells overexpressing ACE2 receptor (HEK293T-ACE2) were cultured in complete Gibco Dulbecco's Modified Eagle Medium (DMEM), supplemented with 10% v/v fetal bovine serum (FBS), 100 U/ml penicillin (Sigma-Aldrich) and 100 μg/ml streptomycin (Sigma-Aldrich), and left to grow at 37°C in the presence of 5% v/v CO_2 for approximately 48 h before passaging. ACE2-stably expressing HEK-293T cells were selected by Blasticidin S HCl (Thermo Fisher Scientific). Since HEK293T cells were adherent, they were detached using 2× Trypsin-EDTA (0.5%) (Thermo Fisher Scientific) for 10 min at 37°C. Cells were then centrifuged at 1,500 rpm for 5 min, followed by re-suspension in complete DMEM medium. To determine the cell count and viability, an equal volume of the cell suspension and Trypan Blue (0.4% w/v) (Thermo Fisher Scientific) solution were vortexed, followed by cell count using a hemocytometer with Neubauer rulings (Sigma-Aldrich). Cells were then re-suspended in complete DMEM for further use.

Generation of ACE2-Stably Expressing HEK-293T Cells

Human ACE2 gene was amplified from MGC library (cDNA clone MGC:47598) by using Kapa HiFi PCR kit (Kapa Biosystems), and sub-cloned into NheI and EcoRI sites of pLAS2w.Pbsd (a lentiviral transfer vector from RNA core, Academia Sinica, Taiwan) by using GenBuilderTM Cloning kit (GeneScript®). For generation of VSV-G pseudotyped lentivirus carrying human ACE2 gene, three plasmids (pCMV-DR8.91, pLAS2w.ACE2.Pbsd and pMD.G) were transiently transfected into HEK-293T cells by using TransIT®-LT1 transfection reagent (Mirus). The culture medium was harvested to infect HEK-293T cells, and then the infected cells were selected with 5 μg/ml blasticidin for one week to generate HEK-293T-ACE2 stable cells.

Flow Cytometry

ACE2 expression was assessed between HEK293T cells overexpressing ACE2 receptor (HEK293T-ACE2) and HEK293T cells alone using flow cytometry. Briefly, both ACE2-transfected and non-transfected HEK293T cells ($1x10^5$ cells) were incubated with ACE2 antibody [N1N2, N-term (GeneTex, GTX101395), (1:250)] for 1 h at room temperature. Following PBS washes, the cells were probed with Goat anti-Rabbit IgG (H+L) Cross-Adsorbed Secondary Antibody linked to Alexa Fluor 647 (Thermo Fisher Scientific) (0.6 μl/100 μl per tube) for 1 h at room temperature in dark. After washing with PBS, the cells were resuspended in FACS buffer (PBS containing 2% FBS) and subjected to flow cytometry.

For binding experiment using rfhSP-D (27), SARS-CoV-2 S1 protein containing a C-terminal His-tag (Acro; S1N-C52H3) (5 μg/ml) was tagged with anti-His antibody (Genetex; GT359) (1:100) at 4°C for 1 h, followed by pre-incubation with a series of two-fold dilutions of rfhSP-D (10 μg/ml) or mock (medium only) at 4°C for 1 h. HEK293T-ACE2 cells ($1x10^5$ cells) were incubated in DMEM incomplete medium with the mixture of SARS-CoV-2 S1 protein, anti-His antibodies and rfhSP-D at 37°C for 2 h. The cells were collected and washed with FACS buffer twice and incubated with anti-mouse IgG-PE conjugate (Genetex, GTX25881) (1:100) for 30 min and washed three times. The live cells were gated from FSC vs. SSC dot plot in order to determine the PE positive cells containing S1 on their surface by CytoFLEX.

Fluorescence Microscopy

HEK293T and HEK293T-ACE2 cells (0.5×10^5) were grown on coverslips in complete DMEM medium overnight under standard culture conditions, as mentioned above. Next day, cells were washed with PBS three times, the coverslips were fixed with 4% v/v paraformaldehyde (Sigma-Aldrich) for 15 minutes, and then washed twice. The coverslips were permeabilized with 0.25% v/v Triton-100 (Sigma-Aldrich) for 15 min. After washing, coverslips were blocked with 2% w/v BSA for 1h and incubated with ACE2 antibody [SN0754 (1:250) (GeneTex, GTX01160)], followed by Goat anti-rabbit IgG (H+L) cross-adsorbed secondary antibody (1:500) (Thermo Fisher Scientific) for 1 h at room temperature in dark. After incubation with secondary antibody, the cells were washed twice with PBS and mounted in the medium with DAPI (Abcam) on the slides to visualize under an upright fluorescence microscope (BX51; Olympus).

Production of SARS-CoV-2 Pseudotyped Lentivirus

The pseudotyped lentivirus carrying SARS-CoV-2 spike protein was generated by transiently transfecting HEK293T cells with pCMV-DR8.91, pLAS2w.Fluc.Ppuro and pcDNA3.1-nCoV-SD18 (SARS-CoV-2 spike gene with 54 nucleotides deletion at its C-terminus was synthesized and cloned into pcDNA3.1 expression vector). HEK293T cells were seeded one day before, and then transfected with the indicated plasmids using TransIT®-LT1 transfection reagent (Mirus). The culture medium was replenished at 16 h and harvested at 48 h and 72 h post-transfection. Cell debris was removed by centrifugation at 4,000 x g for 10 min, and the supernatant was passed through 0.45-mm syringe filter (Pall Corporation). The pseudotyped lentivirus was aliquoted and stored at -80°C until further use. The transduction unit (TU) of SARS-CoV-2 pseudotyped lentivirus was estimated using cell viability assay in response to the limited dilution of lentivirus. In brief, HEK293T cells, stably expressing human ACE2, were plated on 96-well plate one day before lentivirus transduction. For titrating, different amounts of lentivirus particles were added to the culture medium containing polybrene (final concentration 8 mg/ml). Spin infection was carried out at 1,100 x g in 96-well plate for 30 min at 37°C. After Incubating cells at 37°C for 16 h, the culture medium containing virus particles and polybrene was removed and replaced with fresh complete DMEM containing 2.5 μg/ml puromycin. After treating with puromycin for 48 h, the culture media was removed, and the cell viability was assessed using 10% AlarmaBlue reagents, according to manufacturer's instruction. The survival of uninfected cells (without puromycin treatment) was set as 100%. The virus particle titer (TU) was determined by plotting the survival of cells versus diluted viral dose.

Pseudotyped Virus Neutralization Assay

HEK293T cells in 10 cm petridishes were transfected with pCMVΔR8.91, pcDNA nCoV-SD18 and pLAS2w.FLuc.Ppuro plasmids (5, 2, 8 μg, respectively). Next day, cells were washed with PBS gently, and replaced with 10 ml of fresh medium (RPMI containing 10% FBS). The medium at 48 and 72 h were collected and stored in -80°C for future use. HEK293T-ACE2 cells (HEK293T cells overexpressing ACE2 receptor) ($0.5x10^5$ cells) were pre-incubated with rfhSP-D (0, 5, 10 and 20 μg/ml) for 24 h and then washed twice with PBS. The SARS-CoV-2 pseudotyped lentiviral particle containing medium (500μl/well) was added on to the cells, followed by incubation at 37°C under standard culture conditions. After 2 h, fresh complete DMEM medium (500 μl) was added on to the cells and incubated at 37°C. Following 72 h incubation, the cells were washed with PBS twice, and incubated with lysis buffer at 37°C for 10 min. Firefly luciferase activity (RLU) was measured using ONE-Glo™ Luciferase Assay System (Promega) and FlexStation.

Statistical Analysis

GraphPad Prism 6.0 software was used to generate all the graphs. Unpaired t test was used for the statistical analysis. The significance values were considered between rfhSP-D treated and untreated conditions, based on *$p<0.05$. Error bars show the SEM (figure legends).

RESULTS

Interaction of rfhSP-D and Recombinant Human Full-Length SP-D (hFL-SP-D) With S1 Protein and Its RBD

In SARS-CoV, S-protein is the predominant surface glycoprotein recognized by the host innate immune system. The S protein of SARS-CoV-2 has almost 76% identity to SARS-CoV. Previous studies indicated that SP-D bound S protein of SARS-CoV which required Ca^{2+}; the binding was inhibited by maltose. Therefore, the first part of this study was aimed at examining the interaction of LPS-free rfhSP-D and hFL-SP-D with spike protein (S1) using direct binding ELISA. It was found that rfhSP-D/hFL-SP-D bound SARS-CoV-2 S1 protein in a dose-dependent manner (**Figure 1A**); this interaction was inhibited by maltose and EDTA (**Figure 2A**). Among varied concentrations of rfhSP-D tested, a strong and maximum binding of rfhSP-D with SARS-CoV-2 S1 (5 μg/ml) was observed at 10 μg/ml.

The binding of SARS-CoV-2 to its cellular receptor, ACE2, is mediated by the RBD region of the S protein. A higher binding

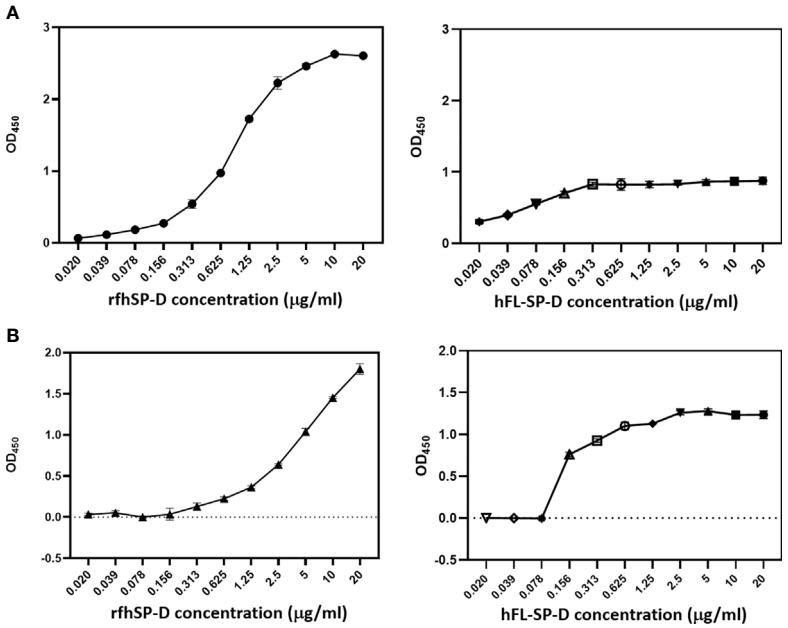

FIGURE 1 | rfhSP-D and recombinant human full-length SP-D (hFL-SP-D) binding with the spike (S1) **(A)** and its RBD **(B)** of the SARS-CoV-2 was determined *via* direct ELISA. Microtiter wells were coated with SARS-CoV-2 spike S1 protein (5 μg/ml) (HEK 293 cells) or RBD (5 μg/ml) (HEK 293 cells) in carbonate-bicarbonate buffer, pH 9.6 overnight at 4°C. The following day, the wells were blocked with Tris Buffered Saline (TBS) buffer containing 1% BSA and 5mM $CaCl_2$, pH 7.2-7.4. After washing the wells with TBS, the wells were incubated with a series of two-fold dilutions of rfhSP-D or hFL-SP-D protein in blocking buffer at 4°C overnight. The binding between S1 protein and rfhSP-D was detected using biotinylated mouse anti-Human SP-D detection antibody (1:180), followed by probing with Streptavidin horseradish peroxidase (HRP)-conjugate 1:40. The data were expressed as mean of three independent experiments done in triplicates ± SEM. Significance was determined using the unpaired t test statistical analysis. The error bars show SEM. Control, maltose and EDTA groups compared to 2.5 μg or 5 μg S1 (RBD) in $CaCl_2$.

affinity has been reported for RBD of SARS-COV-2 to ACE2 receptor compared to SARS-CoV (28). Furthermore, RBD of SARS-CoV-2 has been suggested to have a crucial role in spike protein-induced viral attachment, fusion, and entry into the host cells (29). In this context, this study was also aimed at determining the ability of rfhSP-D/hFL-SP-D to bind RBD of SARS-CoV-2 (**Figure 1B**) *via* direct ELISA (RBD coated, incubated with two-fold dilutions of rfhSP-D (100 μg/ml), and probed with anti-SP-D antibody; R&D Systems). rfhSP-D bound RBD in a dose-dependent manner. It reduced the binding affinity by maltose, but chelation of Ca^{2+} by EDTA did not significantly affect the interaction between rfhSP-D and RBD region (**Figure 2B**). No rfhSP-D binding was observed in the absence of RBD, indicating a lack of non-specific interaction in this assay. To further evaluate the dose response of Maltose and EDTA (5, 10 and 20mM), rfhSP-D was coated and probed with S1 and RBD (at 2.5 and 5 μg/ml) (**Figure 2B**). These results suggest that the protein-protein interaction may occur between the CRD region of rfhSP-D and the RBD region of S protein in a calcium-independent manner.

rfhSP-D Inhibits Interaction of SARS-CoV-2 S1 With Membrane Expressed ACE2 on HEK293T Cells

The S1 spike protein of the SARS-CoV-2 contains RBD that can recognise and interact with its cellular receptor, angiotensin-converting enzyme 2 (ACE2) (30, 31), thus mediating viral entry into the host cells. Since rfhSP-D was found to interact with the spike protein and its RBD at the protein level, we also tested the ability of rfhSP-D to interact with HEK293T cells overexpressing ACE2 receptor. Successful transfection of the ACE2 receptor gene into HEK293T cells was verified by measuring the expression levels of ACE2 receptor *via* immunofluorescence microscopy (**Figure 3A**), flow cytometry (**Figure 3B**) and western blotting (**Figure 3C**). Quantitative and qualitative analysis of the ACE2 receptor using ACE2 antibody (SN0754) revealed a higher signal for ACE2 on HEK293T-ACE2 cells when compared to HEK293T cells alone (**Figures 3A, B**). This study also focused on examining whether rfhSP-D treatment can inhibit the interaction between SARS-CoV-2 S1 and ACE2 receptor on HEK293T cells (**Figure 4**). Pre-incubation of SARS-CoV-2 S1 protein (2 μg/ml) with a varied concentration of rfhSP-D (0.625 -10 μg/ml) was found to reduce S1 binding to HEK293T cells overexpressing ACE2 receptor in a dose-dependent manner (**Figure 4**). The rfhSP-D at 10 μg/ml was found to reduce the binding of S1 to ACE2 receptor on HEK293T cells by approximately 7.95% when compared to the control (S1 + 0 μg/ml rfhSP-D) (**Figure 4**).

rfhSP-D Acts as an Entry Inhibitor of SARS-CoV-2 Infection

After confirming the ability of rfhSP-D to prevent the interaction between SARS-CoV-2 S1 protein and HEK293T cells

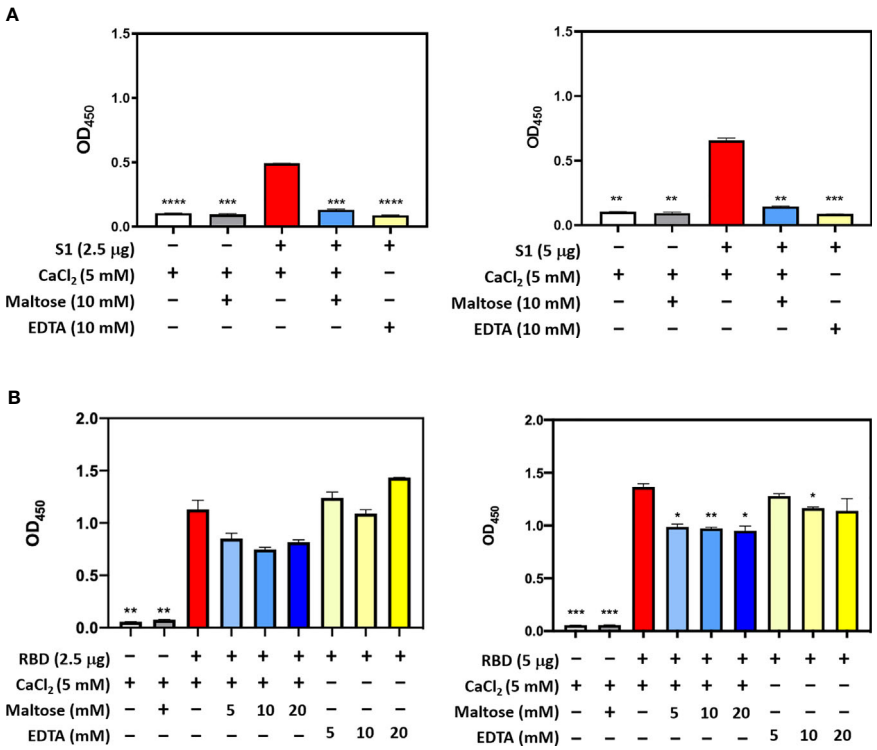

FIGURE 2 | Competitive ELISA to show the impact of Maltose and EDTA on rfhSP-D binding to S1 **(A)** and its RBD **(B)**. Polystyrene microtiter plates were coated with 2μg/ml rfhSP-D, and incubated with SARS-CoV-2 spike S1 protein (2.5 and 5 μg/ml) (sheep-IgG tag) or RBD (His-tag) (2.5 and 5 μg/ml). The binding was detected using anti-sheep IgG HRP antibodies (1:2000) or anti-His antibodies (1:2000). Absorbance at 450nm were recorded by VersaMax™ ELISA Microplate Reader. Significance was determined using the unpaired t test statistical analysis. The error bars show SEM. All group compared to RBD in $CaCl_2$ (*$p < 0.05$; **$p < 0.01$; ***$p < 0.001$; ****$p < 0.0001$).

overexpressing ACE2 receptor, we investigated whether rfhSP-D modulated viral entry using a luciferase reporter assay with pseudotyped lentiviral particles expressing SARS-CoV-2 S1 protein (**Figure 5**). SARS-CoV-2 pseudotyped lentiviral particles were produced as a safe strategy to study the involvement of S1 glycoprotein in the recognition and neutralization of the virus by a varied concentration of rfhSP-D. The production of lentiviral particles pseudotyped with envelope protein S1 was carried out by co-transfecting HEK293T cells with plasmid containing the coding sequence of the indicated pcDNA3.1-nCoV-SD18 (SARS-CoV-2 spike gene), pLAS2w.Fluc.Ppuro, and pCMV-DR8.91. Purified pseudotyped particles and cell lysate harvested at 48 and 72 h were analyzed *via* western blotting, and the expression level of SARS-CoV-2 spike protein was determined using anti-SARS-CoV-2 (COVID-19) Spike polyclonal antibody (**Figure 5A**). Cells pre-incubated rfhSP-D (5 and 10 μg/ml) showed a significant ~ 0.5 RLU fold reduction in luciferase activity (1.0×10^5 RLU) compared to the cells+SARS-CoV-2 (1.5×10^5 RLU) (**Figure 5B**). The reduced luciferase activity, following treatment with rfhSP-D, indicated that the interaction between rfhSP-D and SARS-CoV-2 S1 protein interfered with S1-containing viral particle binding to ACE2, and hence, prevented the entry of the virus into the HEK323T-ACE2 cells (**Figure 5**).

DISCUSSION

The innate immune system has evolved cellular and molecular defense mechanisms critical for the recognition and restriction of SARS-CoV-2-mediated respiratory tract infections, and for the activation of subsequent adaptive immune responses (32). SARS-CoV-2 infection is responsible for a higher transmissibility, mortality and morbidity rates that has caused the current global pandemic (33–35). Given that the SARS-CoV-2 is a newly emerged pandemic infection, it is fundamentally crucial to understand the role of host innate and adaptive immune response, which in turn, is likely to have profound impact on designing and developing effective anti-SARS-CoV-2 therapies.

The primary target for SARS-CoV-2 is the alveolar epithelial type II cells (36), and the viral entry to the host cell is mediated by the ACE2 receptor (37). Furthermore, viral entry into the host cells also depends on the activity of TMPRSS2 protease as it facilitates S protein cleavage into S1 and S2 portions. This enables S-mediated targeting and receptor-mediated early fusion pathway driven by the S2 subunit (19). The present study confirmed the ability of rfhSP-D to act as an entry inhibitor of pseudotyped lentiviral particles expressing SARS-CoV-2 S1 protein in hACE-2 overexpressing HEK293T cells mimicking the human SARS-CoV-2 infection.

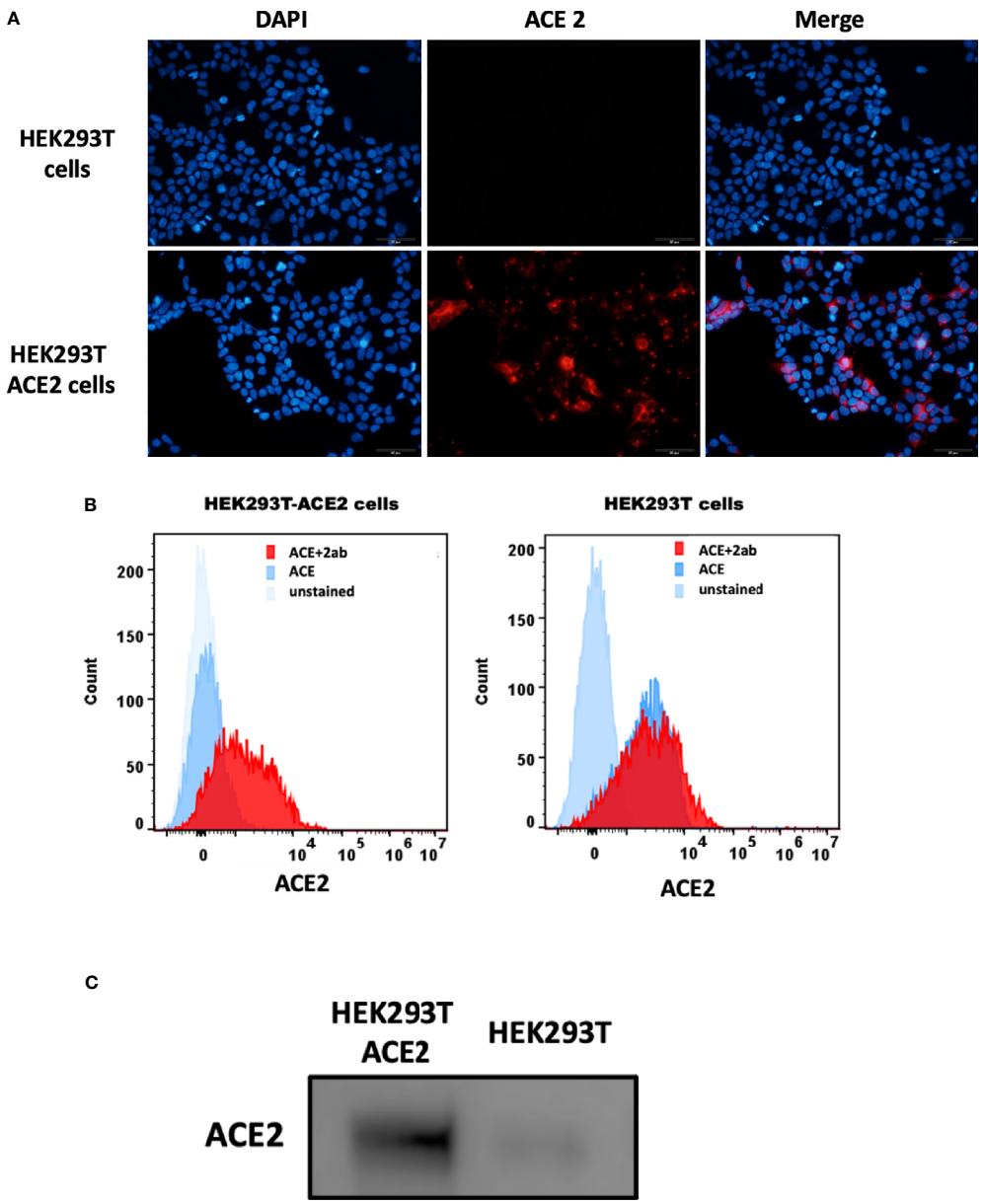

FIGURE 3 | Expression of ACE2 receptor on HEK293T cells by immunofluorescence microscopy **(A)**, flow cytometry **(B)** and western blotting **(C)**. **(A)** HEK293T ($0.5x10^5$ cells) and HEK293T-ACE2 cells ($0.5x10^5$ cells) were seeded on coverslips, followed by incubation at 37°C under standard culture conditions. After wasing the cells with PBS twice, the ACE2 expression was detected in both cell lines using the ACE2 antibody [SN0754](1:250), followed byincubation for 1 h at room temperature. Following PBS washes, Goat anti-rabbit IgG (H+L) cross-adsorbed secondary antibody (1:500) was added. Following PBS washes, the coverslips were mounted in medium with DAPI on a microscopy slide and viewed under a fluorescence microscope (Olympus). **(B)** Flow cytometric analysis of ACE2 expression was determined by the shift in the fluorescence intensity using ACE2 antibody [N1N2], N-term (GeneTex) (1:250). The ACE2 expression was detected by CytoFLEX. **(C)** The ACE2 expression was examined by western blotting using ACE2 antibody [SN0754] (GeneTex) (1:1000).

Human SP-D is a lung collectin, synthesized by Clara cells (38) and alveolar type-II cells (1). Anti-viral role of SP-D has been reported against HIV-1 and IAV infection (5, 6, 8, 39, 40). In addition, increased serum SP-D has been observed in SARS-CoV and SARS-CoV-2 patients (11, 41). Interaction between SP-D and the S protein of SARS-CoV leads to enhanced phagocytosis (11, 12). Furthermore, SP-D can also inhibit viral infection of 16HBE cells infected with HCoV-229E (13). However, SP-D-mediated inhibition of SARS-CoV infection and its subsequent immune response is not fully studied. Therefore, this study was aimed at examining the ability of rfhSP-D to act as an entry inhibitor of SARS-CoV-2 infection using pseudotyped lentiviral particles expressing SARS-CoV-2 S1 protein. Being a potent innate immune molecule present in

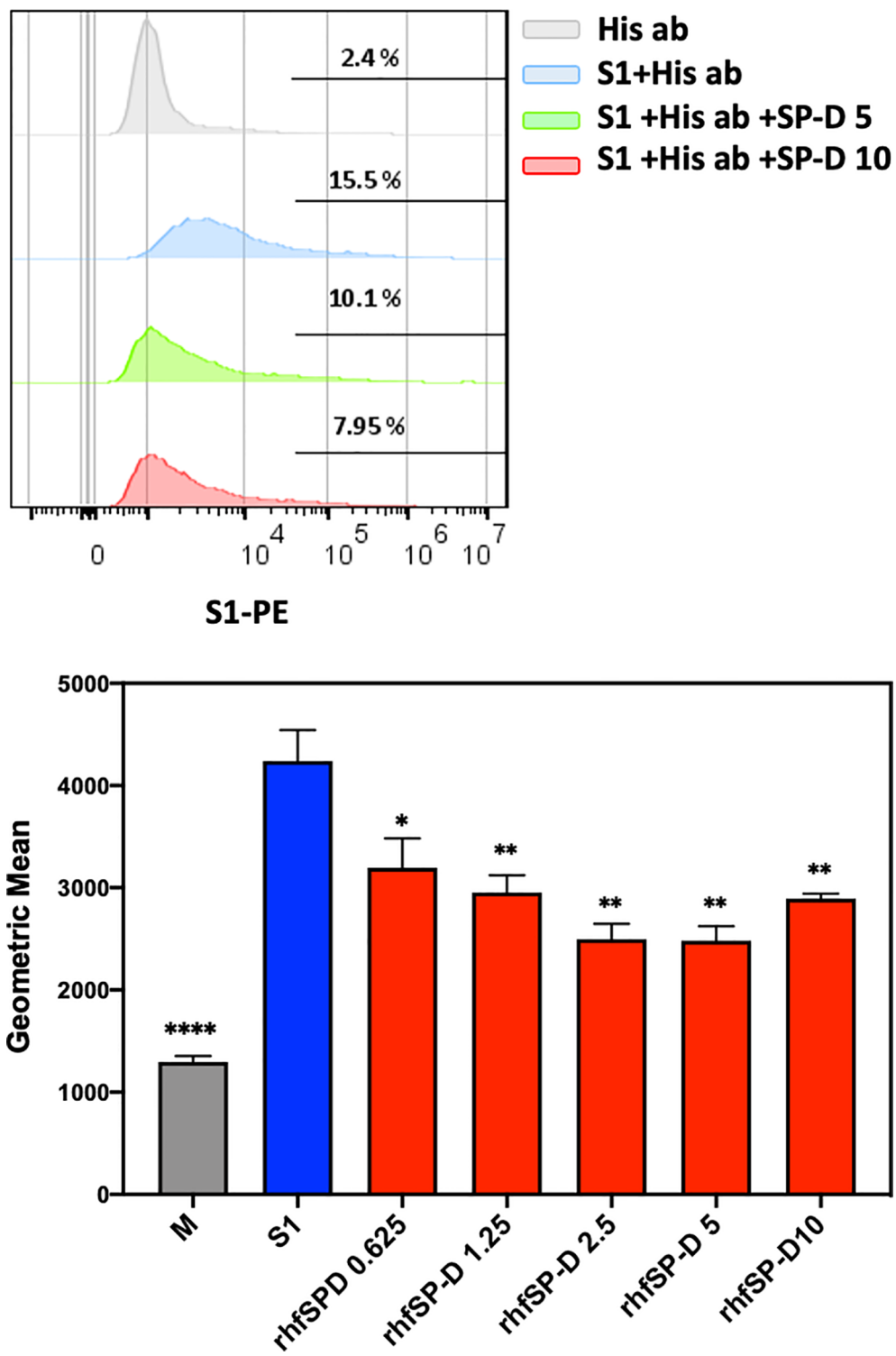

FIGURE 4 | rfhSP-D treatment inhibits the interaction between SARS-CoV-2 S1 and ACE2 receptor on HEK293T cells. Protein complex was made by tagging SARS-CoV-2 S1 protein (5 ug/ml) with anti-His antibody (10ug/ml), followed by incubation with rfhSP-D (0.625, 1.25, 2.5, 5 or 10 µg/ml) for 2h at room temperature. This complex (S1+ anti-His+rfhSP-D) was added on to HEK293T-ACE2 cells ($1x10^5$ cells) at 37°C for 2 h. The cells were collected and washed with FACS buffer twice and incubated with anti-mouse IgG PE conjugate (Genetex, GTX25881) (1:100) for 30 min and washed three times. The cells stained with S1 were detected by CytoFLEX. Significance was determined using the unpaired t test statistical analysis. All groups compared to S1. The error bars show SEM. M=mock (*$p < 0.05$; **$p < 0.01$; ****$p < 0.0001$) (n = 3).

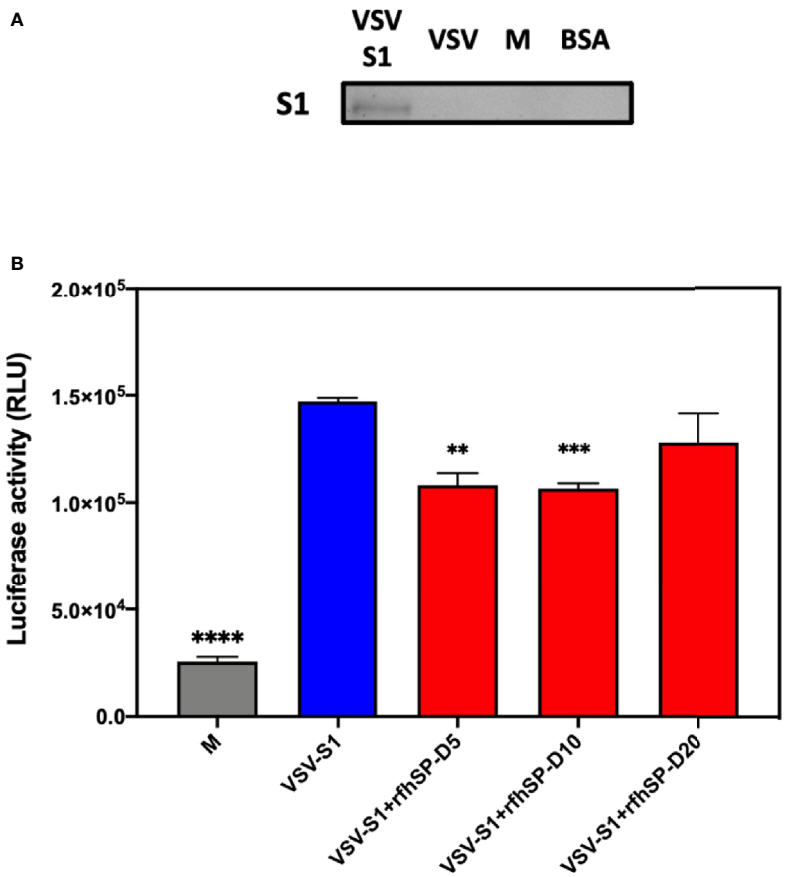

FIGURE 5 | rfhSP-D acts as an entry inhibitor of SARS-CoV-2 infection. **(A)** The SARS-CoV-2 pseudotyped lentiviral particle and pseudotyped lentiviral particle containing medium were determined the S1 expression by western blotting. **(B)** Luciferase reporter activity of rfhSP-D treated HEK293T cells (overexpressing ACE2 receptor) transduced with of SARS-CoV-2 S1 pseudotyped lentiviral particles. Significance was determined using the unpaired t test statistical analysis. All groups compared to VSV-S1. The error bars show SEM. M=medium (**p<0.01; ***p<0.001; ****p<0.0001) (n = 3).

the lung surfactant, SP-D is expected to play an important protective role in the pathogenesis of COVID-19.

Owing to a significant similarity in the S proteins of SARS-CoV and SARS-CoV-2, it was hypothesized that SP-D may interact with S protein of SARS-CoV-2. The results confirmed that affinity purified, and LPS-free rfhSP-D interacted with S1 protein of SARS-CoV-2 and its RBD in a dose-dependent manner akin to the recombinant hFLSP-D. Inhibition of rfhSP-D binding to S protein by EDTA or maltose suggested that rfhSP-D bound to the carbohydrate moieties on S protein of SARS-CoV-2 (12). We also examined whether rfhSP-D treatment can inhibit the interaction of SARS-CoV-2 S1 with ACE2 receptor on HEK293T cells. SARS-CoV-2 S1 protein (5 μg/ml), pre-incubated with a varied concentration of rfhSP-D (0.625 -10 μg/ml), showed reduced binding to HEK293T cells overexpressing ACE2 receptor in a dose-dependent manner.

Targeting viral entry into a host cell is an emerging approach for designing and developing anti-viral therapies as viral propagation can be either restricted or blocked at an early stage of viral cycle, diminishing drug resistance by released viral particles. In this study, we examined the entry inhibitor role of rfhSP-D against SARS-CoV-2 by luciferase reporter assay. Pseudotyped lentiviral particles were generated as a safe alternative method to mimic the structural surface of SARS-CoV-2, and to test whether rfhSP-D treatment can promote or prevent viral entry into the host cells. Approximately 0.5 RLU fold reduction was seen with rfhSP-D (5 or 10 μg/ml) treatment when compared to untreated sample (1 RLU fold; Cells + SARS-CoV-2). A significantly reduced luminescent signal following rfhSP-D treatment indicated that the interaction of rfhSP-D with SARS-CoV-2-S1 restricted the binding and entry of the virus, suggestive of an entry inhibitory role of rfhSP-D against SARS-CoV-2 infection.

SARS-CoV-2 mediated lung injury is correlated with diffuse alveolar damage and air space oedema, thus, accompanied by interstitial infiltration of inflammatory cells, triggering of coagulation, and fibrin deposition (42–45). Potential biomarkers to be considered during SARS infection include increased levels of inflammatory plasma makers, coagulation, and fibrinolysis (46, 47). Damage to the alveolar epithelial barrier

is a characteristic feature of an acute respiratory distress syndrome (ARDS) and acute lung injury (ALI); levels of plasma surfactant proteins such as SP-A and SP-D may have a prognostic value (48–50). Thus, this study prompts further investigation into the role of pulmonary surfactant in COVID-19.

In summary, rfhSP-D, containing homotrimeric neck and CRD regions, acts as an entry inhibitor of SARS-CoV-2 infection by restricting the viral entry into HEK293T cells overexpressing ACE2 receptor. Time is ripe for taking the knowledge about the involvement of rfhSP-D and its associated anti-viral effects forward to develop a novel therapeutic approach to target multiple cellular signaling pathways. The mechanisms which enable rfhSP-D to trigger anti-viral effect are virus-specific due to the differential effect and variation in terms of the cell types and putative receptors. There is a clear therapeutic potential of rfhSP-D against SARS-CoV-2; although increased glycosylation of spike protein leads to evasion of antibody susceptibility, it is expected to enhance the susceptibility of the virus to soluble pattern recognition receptors (PRRs) such as SP-D. Having established the specific nature of interactions between rfhSP-D and SARS-CoV-2, we hope to examine host response in the murine models of infection using wild type and SP-D knock-out mice.

DATA AVAILABILITY STATEMENT

The raw data supporting the conclusions of this article will be made available by the authors, without undue reservation.

AUTHOR CONTRIBUTIONS

M-HH and NB carried out crucial experiments that were validated by Y-CC, W-SK and H-FK. M-HH, VM, UK, and J-YW analysed the data. VM, TM, UK, and J-YW prepared the manuscript. All authors contributed to the article and approved the submitted version.

FUNDING

J-YW is supported by the Ministry of Science and Technology (MOST) in Taiwan under grant nos. MOST 107-2314-B-006 -046 –MY1-3, and received funding in part from the Headquarters of University Advancement at the National Cheng Kung University, which is sponsored by the Ministry of Education in Taiwan.

REFERENCES

1. Kishore U, Greenhough TJ, Waters P, Shrive AK, Ghai R, Kamran MF, et al. And SP-D: Structure, Function and Receptors. *Mol Immunol* (2006) 43 (9):1293–315. doi: 10.1016/j.molimm.2005.08.004
2. Crouch E, Parghi D, Kuan S, Persson A. Surfactant Protein D: Subcellular Localization in Nonciliated Bronchiolar Epithelial Cells. *Am J Physiol-Lung Cell Mol Physiol* (1992) 263(1):L60–6. doi: 10.1152/ajplung.1992.263.1.L60
3. Voorhout W, Veenendaal T, Kuroki Y, Ogasawara Y, Van Golde L, Geuze H. Immunocytochemical Localization of Surfactant Protein D (Sp-D) in Type II Cells, Clara Cells, and Alveolar Macrophages of Rat Lung. *J Histochem Cytochem* (1992) 40(10):1589–97. doi: 10.1177/40.10.1527377
4. Nayak A, Dodagatta-Marri E, Tsolaki AG, Kishore U. An Insight Into the Diverse Roles of Surfactant Proteins, SP-A and SP-D in Innate and Adaptive Immunity. *Front Immunol* (2012) 3:131. doi: 10.3389/fimmu.2012.00131
5. Hartshorn KL, Crouch EC, White MR, Eggleton P, Tauber AI, Chang D, et al. Evidence for a Protective Role of Pulmonary Surfactant Protein D (Sp-D) Against Influenza A Viruses. *J Clin Invest* (1994) 94(1):311–9. doi: 10.1172/JCI117323
6. Hartshorn KL, White MR, Voelker DR, Coburn J, Zaner K, Crouch EC. Mechanism of Binding of Surfactant Protein D to Influenza A Viruses: Importance of Binding to Haemagglutinin to Antiviral Activity. *Biochem J* (2000) 351(Pt 2):449–58. doi: 10.1042/bj3510449
7. Hillaire ML, Haagsman HP, Osterhaus AD, Rimmelzwaan GF, van Eijk M. Pulmonary Surfactant Protein D in First-Line Innate Defence Against Influenza A Virus Infections. *J Innate Immun* (2013) 5(3):197–208. doi: 10.1159/000346374
8. Al-Ahdal MN, Murugaiah V, Varghese PM, Abozaid SM, Saba I, Al-Qahtani AA, et al. Entry Inhibition and Modulation of Pro-Inflammatory Immune Response Against Influenza A Virus by a Recombinant Truncated Surfactant Protein D. *Front Immunol* (2018) 9:1586. doi: 10.3389/fimmu.2018.01586
9. Meschi J, Crouch EC, Skolnik P, Yahya K, Holmskov U, Leth-Larsen R, et al. Surfactant Protein D Binds to Human Immunodeficiency Virus (HIV) Envelope Protein gp120 and Inhibits HIV Replication. *J Gen Virol* (2005) 86(11):3097–107. doi: 10.1099/vir.0.80764-0
10. Pandit H, Gopal S, Sonawani A, Yadav AK, Qaseem AS, Warke H, et al. Surfactant Protein D Inhibits HIV-1 Infection of Target Cells Via Interference With Gp120-CD4 Interaction and Modulates Pro-Inflammatory Cytokine Production. *PLoS One* (2014) 9(7):e102395. doi: 10.1371/journal.pone.0102395
11. Wu YP, Liu ZH, Wei R, Pan SD, Mao NY, Chen B, et al. Elevated Plasma Surfactant Protein D (Sp-D) Levels and a Direct Correlation With Anti-Severe Acute Respiratory Syndrome Coronavirus-Specific IgG Antibody in SARS Patients. *Scand J Immunol* (2009) 69(6):508–15. doi: 10.1111/j.1365-3083.2009.02245.x
12. Leth-Larsen R, Zhong F, Chow VT, Holmskov U, Lu J. The SARS Coronavirus Spike Glycoprotein is Selectively Recognized by Lung Surfactant Protein D and Activates Macrophages. *Immunobiology* (2007) 212(3):201–11. doi: 10.1016/j.imbio.2006.12.001
13. Funk CJ, Wang J, Ito Y, Travanty EA, Voelker DR, Holmes KV, et al. Infection of Human Alveolar Macrophages by Human Coronavirus Strain 229E. *J Gen Virol* (2012) 93(Pt 3):494–503. doi: 10.1099/vir.0.038414-0
14. Yan R, Zhang Y, Li Y, Xia L, Guo Y, Zhou Q. Structural Basis for the Recognition of SARS-CoV-2 by Full-Length Human ACE2. *Science* (2020) 367(6485):1444–8. doi: 10.1126/science.abb2762
15. Ludwig S and Zarbock A. Coronaviruses and SARS-Cov-2: A Brief Overview. *Anesth Analg* (2020) 131(1):93–6. doi: 10.1213/ANE.0000000000004845
16. Kim JM, Chung YS, Jo HJ, Lee NJ, Kim MS, Woo SH, et al. Identification of Coronavirus Isolated From a Patient in Korea With COVID-19. *Osong Public Health Res Perspect* (2020) 11(1):3–7. doi: 10.24171/j.phrp.2020.11.1.02
17. Varghese PM, Tsolaki AG, Yasmin H, Shastri A, Ferluga J, Vatish M, et al. Host-Pathogen Interaction in COVID-19: Pathogenesis, Potential Therapeutics and Vaccination Strategies. *Immunobiology* (2020) 225 (6):152008. doi: 10.1016/j.imbio.2020.152008
18. Astuti I. And Ysrafil, Severe Acute Respiratory Syndrome Coronavirus 2 (SARS-Cov-2): An Overview of Viral Structure and Host Response. *Diabetes Metab Syndr* (2020) 14(4):407–12. doi: 10.1016/j.dsx.2020.04.020
19. Hoffmann M, Kleine-Weber H, Schroeder S, Kruger N, Herrler T, Erichsen S, et al. SARS-Cov-2 Cell Entry Depends on ACE2 and TMPRSS2 and Is Blocked by a Clinically Proven Protease Inhibitor. *Cell* (2020) 181(2):271–80.e8. doi: 10.1016/j.cell.2020.02.052
20. Matsuyama S, Nao N, Shirato K, Kawase M, Saito S, Takayama I, et al. Enhanced Isolation of SARS-CoV-2 by TMPRSS2-expressing Cells. *Proc Natl Acad Sci* (2020) 117(13):7001–3. doi: 10.1073/pnas.2002589117
21. Gubernatorova EO, Gorshkova EA, Polinova AI, Drutskaya MS. Il-6: Relevance for Immunopathology of SARS-Cov-2. *Cytokine Growth Factor Rev* (2020) 53:13–24. doi: 10.1016/j.cytogfr.2020.05.009

22. Ratajczak MZ and Kucia M. Sars-CoV-2 Infection and Overactivation of Nlrp3 Inflammasome as a Trigger of Cytokine "Storm" and Risk Factor for Damage of Hematopoietic Stem Cells. *Leukemia* (2020) 34(7):1726–9. doi: 10.1038/s41375-020-0887-9
23. Torres Acosta MA, Singer BD. Pathogenesis of COVID-19-induced ARDS: Implications for an Ageing Population. *Eur Respir J* (2020) 56(3):1–12. doi: 10.1183/13993003.02049-2020
24. D'Abramo A, Lepore L, Palazzolo C, Barreca F, Liuzzi G, Lalle E, et al. Acute Respiratory Distress Syndrome Due to SARS-CoV-2 and Influenza A Co-Infection in an Italian Patient: Mini-review of the Literature. *Int J Infect Dis* (2020) 97:236–9. doi: 10.1016/j.ijid.2020.06.056
25. Kaur A, Riaz MS, Murugaiah V, Varghese PM, Singh SK, Kishore U. A Recombinant Fragment of Human Surfactant Protein D Induces Apoptosis in Pancreatic Cancer Cell Lines Via Fas-Mediated Pathway. *Front Immunol* (2018) 9:1126. doi: 10.3389/fimmu.2018.01126
26. Murugaiah V, Agostinis C, Vargheses P, Belmonte B, Vieni S, Alaql F, et al. Hyaluronic Acid Present in the Tumour Microenvironment can Negate the Pro-Apoptotic Effect of a Recombinant Fragment of Human Surfactant Protein-D on Breast Cancer Cells. *Front Immunol* (2020) 11(1171):1–17. doi: 10.3389/fimmu.2020.01171
27. Wang C, Li W, Drabek D, Okba NMA, van Haperen R, Osterhaus A, et al. A Human Monoclonal Antibody Blocking SARS-CoV-2 Infection. *Nat Commun* (2020) 11(1):2251. doi: 10.1038/s41467-020-16256-y
28. Shang J, Ye G, Shi K, Wan Y, Luo C, Aihara H, et al. Structural Basis of Receptor Recognition by SARS-Cov-2. *Nature* (2020) 581(7807):221–4. doi: 10.1038/s41586-020-2179-y
29. Ortega JT, Serrano ML, Pujol FH, Rangel HR. Role of Changes in SARS-CoV-2 Spike Protein in the Interaction With the Human ACE2 Receptor: An in Silico Analysis. *EXCLI J* (2020) 19:410–7. doi: 10.17179/excli2020-1167
30. Wan Y, Shang J, Graham R, Baric RS, Li F. Receptor Recognition by the Novel Coronavirus From Wuhan: An Analysis Based on Decade-Long Structural Studies of SARS Coronavirus. *J Virol* (2020) 94(7):1–9. doi: 10.1128/JVI.00127-20
31. Li F. Receptor Recognition Mechanisms of Coronaviruses: A Decade of Structural Studies. *J Virol* (2015) 89(4):1954–64. doi: 10.1128/JVI.02615-14
32. Fung TS and Liu DX. Human Coronavirus: Host-Pathogen Interaction. *Annu Rev Microbiol* (2019) 73:529–57. doi: 10.1146/annurev-micro-020518-115759
33. Zhong N, Zheng B, Li Y, Poon L, Xie Z, Chan K, et al. Epidemiology and Cause of Severe Acute Respiratory Syndrome (SARS) in Guangdong, People's Republic of China, in February, 2003. *Lancet* (2003) 362(9393):1353–8. doi: 10.1016/S0140-6736(03)14630-2
34. Anderson RM, Fraser C, Ghani AC, Donnelly CA, Riley S, Ferguson NM, et al. Epidemiology, Transmission Dynamics and Control of SARS: The 2002–2003 Epidemic. *Philos Trans R Soc London Ser B: Biol Sci* (2004) 359(1447):1091–105. doi: 10.1098/rstb.2004.1490
35. Heymann DL. The International Response to the Outbreak of SARS in 2003. Philosophical Transactions of the Royal Society of London. *Ser B: Biol Sci* (2004) 359(1447):1127–9. doi: 10.1098/rstb.2004.1484
36. Xu J, Xu X, Jiang L, Dua K, Hansbro PM, Liu G. Sars-CoV-2 Induces Transcriptional Signatures in Human Lung Epithelial Cells That Promote Lung Fibrosis. *Respir Res* (2020) 21(1):182. doi: 10.1186/s12931-020-01445-6
37. Perrotta F, Matera MG, Cazzola M, Bianco A. Severe Respiratory SARS-CoV2 Infection: Does ACE2 Receptor Matter? *Respir Med* (2020) 168:105996. doi: 10.1016/j.rmed.2020.105996
38. Crouch E, Hartshorn K, Horlacher T, McDonald B, Smith K, Cafarella T, et al. Recognition of Mannosylated Ligands and Influenza A Virus by Human Surfactant Protein D: Contributions of an Extended Site and Residue 343. *Biochemistry* (2009) 48(15):3335–45. doi: 10.1021/bi8022703
39. Ng WC, Tate MD, Brooks AG, Reading PC. Soluble Host Defense Lectins in Innate Immunity to Influenza Virus. *J BioMed Biotechnol* (2012) 2012:732191. doi: 10.1155/2012/732191
40. Hartshorn KL, Webby R, White MR, Tecle T, Pan C, Boucher S, et al. Role of Viral Hemagglutinin Glycosylation in Anti-Influenza Activities of Recombinant Surfactant Protein D. *Respir Res* (2008) 9:65. doi: 10.1186/1465-9921-9-65
41. Kerget B, Kerget F, Kocak AO, Kiziltunc A, Araz O, Ucar EY, et al. Are Serum Interleukin 6 and Surfactant Protein D Levels Associated With the Clinical Course of COVID-19? *Lung* (2020) 198(5):777–84. doi: 10.1007/s00408-020-00393-8
42. Chen J and Subbarao K. The Immunobiology of SARS. *Annu Rev Immunol* (2007) 25:443–72. doi: 10.1146/annurev.immunol.25.022106.141706
43. Lee N, Hui D, Wu A, Chan P, Cameron P, Joynt GM, et al. A Major Outbreak of Severe Acute Respiratory Syndrome in Hong Kong. *N Engl J Med* (2003) 348(20):1986–94. doi: 10.1056/NEJMoa030685
44. Wu YP, Wei R, De Groot PG. SARS in Hong Kong. *N Engl J Med* (2003) 349 (7):708–9. doi: 10.1056/NEJMc031468
45. Ng K, Wu A, Cheng V, Tang B, Chan C, Yung C, et al. Pulmonary Artery Thrombosis in a Patient With Severe Acute Respiratory Syndrome. *Postgrad Med J* (2005) 81(956):e3–3. doi: 10.1136/pgmj.2004.030049
46. Chen B, Lisman T, Ren D. Analysis of Thrombotic Factors in Severe Acute Respiratory Syndrome (SARS) Patients. *Thromb Haemost* (2006) 96(07):100–1. doi: 10.1160/TH05-12-0827
47. Liu Z-H, Wei R, Wu Y-P, Lisman T, Wang Z-X, Han J-J, et al. Elevated Plasma Tissue-Type Plasminogen Activator (t-PA) and Soluble Throm-Bomodulin in Patients Suffering From Severe Acute Respiratory Syndrome (SARS) as a Possible Index for Prognosis and Treatment Strategy. *Biomed Environ Sci* (2005) 18(4):260–4.
48. Matthay MA and Zemans RL. The Acute Respiratory Distress Syndrome: Pathogenesis and Treatment. *Annu Rev Pathol: Mech Dis* (2011) 6:147–63. doi: 10.1146/annurev-pathol-011110-130158
49. Greene KE, Wright JR, Steinberg KP, Ruzinski JT, Caldwell E, WB W, et al. Serial Changes in Surfactant-Associated Proteins in Lung and Serum Before and After Onset of ARDS. *Am J Respir Crit Care Med* (1999) 160(6):1843–50. doi: 10.1164/ajrccm.160.6.9901117
50. Endo S, Sato N, Nakae H, Yamada Y, Makabe H, Abe H, et al. Surfactant Protein A and D (Sp-a, AP-D) Levels in Patients With Septic ARDS. *Res Commun Mol Pathol Pharmacol* (2002) 111(5-6):245.

Conflict of Interest: The authors declare that the research was conducted in the absence of any commercial or financial relationships that could be construed as a potential conflict of interest.

frontiers in Immunology

ORIGINAL RESEARCH
published: 27 October 2021
doi: 10.3389/fimmu.2021.758941

Surfactant Proteins A/D–CD14 on Alveolar Macrophages Is a Common Pathway Associated With Phagocytosis of Nanomaterials and Cytokine Production

Qiqi Wang[1,2†], Qiong Wang[1†], Ziyue Zhao[1], Jingbo Fan[3], Linghan Qin[1], David B. Alexander[4], Hiroyuki Tsuda[4], Dahai Zhao[3*] and Jiegou Xu[1,4*]*

[1] Department of Immunology, School of Basic Medical Sciences, Anhui Medical University, Hefei, China, [2] Department of Clinical Laboratory, Anhui General Hospital of Chinese People's Armed Police Forces, Hefei, China, [3] Department of Respiratory and Critical Care Medicine, The Second Affiliated Hospital, Anhui Medical University, Hefei, China, [4] Laboratory of Nanotoxicology Project, Nagoya City University, Nagoya, Japan

Alveolar macrophages are responsible for clearance of airborne dust and pathogens. How they recognize and phagocytose a variety of engineered nanomaterials (ENMs) with different properties is an important issue for safety assessment of ENMs. Surfactant-associated proteins, specifically existing in the pulmonary surfactant, are important opsonins for phagocytosis of airborne microorganisms. The purposes of the current study are to understand whether opsonization of ENMs by surfactant-associated proteins promotes phagocytosis of ENMs and cytokine production, and to determine whether a common pathway for phagocytosis of ENMs with different properties exists. For these purposes, four ENMs, MWCNT-7, TiO_2, SiO_2, and fullerene C60, with different shapes, sizes, chemical compositions, and surface reactivities, were chosen for this study. Short-term pulmonary exposure to MWCNT-7, TiO_2, SiO_2, and C60 induced inflammation in the rat lung, and most of the administered ENMs were phagocytosed by alveolar macrophages. The ENMs were phagocytosed by isolated primary alveolar macrophages (PAMs) *in vitro*, and phagocytosis was enhanced by rat bronchioalveolar lavage fluid (BALF), suggesting that proteins in the BALF were associated with phagocytosis. Analysis of proteins bound to the 4 ENMs by LC/MS indicated that surfactant-associated proteins A and D (SP-A, SP-D) were common binding proteins for all the 4 ENMs. Both BALF and SP-A, but not SP-D, enhanced TNF-α production by MWCNT-7 treated PAMs; BALF, SP-A, and SP-D increased IL-1β production in TiO_2 and SiO_2 treated PAMs; and BALF, SP-A, and SP-D enhanced IL-6 production in C60 treated PAMs. Knockdown of CD14, a receptor for SP-A/D, significantly reduced phagocytosis of ENMs and SP-A-enhanced cytokine production by PAMs. These results indicate that SP-A/D can opsonize all the test ENMs and enhance phagocytosis of the ENMs by alveolar macrophages through CD14, suggesting that SP-A/D-CD14 is a common pathway mediating phagocytosis of ENMs. Cytokine production induced by ENMs, however,

OPEN ACCESS

Edited by:
Taruna Madan, National Institute for Research in Reproductive Health (ICMR), India

Reviewed by:
Hrishikesh Pandit, National Cancer Institute at Frederick, United States
Guirong Wang, Upstate Medical University, United States

***Correspondence:**
Jiegou Xu
xujiegou@ahmu.edu.cn
Dahai Zhao
zhaodahai@ahmu.edu.cn
Hiroyuki Tsuda
htsuda@phar.nagoya-cu.ac.jp

[†]These authors have contributed equally to this work and share first authorship

Specialty section:
This article was submitted to Molecular Innate Immunity, a section of the journal Frontiers in Immunology

Received: *15 August 2021*
Accepted: *07 October 2021*
Published: *27 October 2021*

Citation:
Wang Q, Wang Q, Zhao Z, Fan J, Qin L, Alexander DB, Tsuda H, Zhao D and Xu J (2021) Surfactant Proteins A/D–CD14 on Alveolar Macrophages Is a Common Pathway Associated With Phagocytosis of Nanomaterials and Cytokine Production. Front. Immunol. 12:758941. doi: 10.3389/fimmu.2021.758941

is dependent on the type of ENM that is phagocytosed. Our results demonstrate a dual role for surfactant proteins as opsonins for both microbes and for inhaled dusts and fibers, including ENMs, allowing macrophages to recognize and remove the vast majority of these particles, thereby, greatly lessening their toxicity in the lung.

Keywords: engineered nanomaterials, alveolar macrophage, surfactant-associated protein A, surfactant-associated protein D, CD14, opsonization

INTRODUCTION

The respiratory tract is the major exposure routine for airborne dusts and pathogens. Alveolar macrophages (AMs) reside in the airway and alveoli, and account for 95% of leukocytes in the lower respiratory tract (1). AMs function mainly in host defense and alveolar homeostasis. Phagocytosis by AMs is a major mechanism for clearance of dusts and microorganisms encountered in the lung (2). AMs have many types of pattern-recognition receptors (PRRs) on the plasma membrane, and recognize a variety of pathogen-associated molecular patterns (PAMPs) in microorganisms (3, 4). AMs also express receptors for the Fc portions of IgG antibodies (Fc receptors) and receptors for complement (complement receptors) that specifically bind IgG- or complement-coated pathogens (5, 6). The process of coating pathogens to promote phagocytosis is called opsonization. The direct binding of PRRs to their corresponding PAMPs and the binding of Fc receptors and complement receptors to opsonized pathogens induce a number of responses in AMs, including production of cytokines, inflammatory mediators and microbicidal enzymes, and mobilization of the cytoskeleton leading to phagocytosis, cell migration, and granule exocytosis. Secreted cytokines and inflammatory mediators then exert regulatory functions on inflammation and immune responses (7, 8). AMs are also involved in the clearance of apoptotic and necrotic cells and the subsequent resolution of pulmonary inflammation (9).

With advances in nanotechnology, engineered nanomaterials (ENMs) are increasingly being developed. The unique physicochemical features of ENMs including size effect, surface effect and quantum effect are very different from their bulk counterparts and make ENMs to be applied in almost every field such as material industry, semiconductor industry, daily life products and biomedical field. Increased production and application of ENMs may lead to increased respiratory exposure to ENMs during their production, consumption, and disposal. Understanding their pro-inflammatory and clearance mechanisms in the lung is critical for safety assessment of ENMs. Numerous studies in animals indicate that inhaled ENMs are taken up and cleared by AMs (10, 11). ENMs have little antigenicity and do not possess molecular structural regions like the PAMPs of microbes. How AMs recognize different ENMs with different sizes, chemical compositions, physical morphologies, and surface reactivity is currently an open question. It is widely accepted that ENMs are bound by proteins from various biological fluids, forming tiers of proteins coating the surface of the ENM. In turn, this protein corona may promote phagocytosis through interaction of bound complement proteins or IgG with complement receptors and Fc receptors (12, 13). The composition of the protein corona depends upon both the biological fluid in which the ENM is present and the physiochemical characteristics of the ENM (14). Most studies on the interaction between ENMs and proteins are based on protein coronas that form in serum/plasma. Pulmonary surfactant is a complex mixture composed of more than 90% lipids and 5-10% proteins that covers the inner face of the alveoli and reduces surface tension at the air-water interface in the alveoli to prevent alveolar collapse at the end of expiration (15). Surfactant-associated proteins (SP-A, SP-B, SP-C and SP-D) differ from one another in their synthesis, oligomerization, and function (16). SP-B and SP-C are hydrophobic and reduce the surface tension of the lung, while SP-A and SP-D are more hydrophilic and have important roles in the regulation of innate immune responses (17). SP-A and SP-D can bind to many different microbial pathogens and act as opsonins to enhance phagocytosis of microbial pathogens by AMs (18, 19). Coating of MWCNTs with pulmonary surfactant and bronchoalveolar lavage fluids (BALF)-derived protein corona on diesel exhaust nanoparticles enhance the nanoparticle uptake and pro-inflammatory responses in macrophages *in vitro* (20, 21), and SP-A and SP-D are found to bind the nanoparticles (21). Furthermore, SP-D can opsonize carbon nanotubes and augment their phagocytosis and pro-inflammatory responses *in vitro* (22). It is likely that surfactant proteins mediate phagocytosis of nanoparticles and subsequent cytokine production.

In the current study, we addressed two main questions: 1) whether a common spectrum of surfactant proteins was bound to different ENMs? 2) what proteins on AMs were responsible for recognizing the bound surfactant proteins and subsequent phagocytosis and cytokine secretion? For these purposes, 4 types of ENMs (fullerene C60, TiO_2, SiO_2, and MWCNT), differing in size, shape, surface reactivity, and chemical composition, were chosen for analysis of their binding proteins in rat bronchoalveolar lavage fluid (BALF) and cytokine productions. SP-A and SP-D were identified as common binding proteins for all 4 ENMs, and enhanced phagocytosis of the ENMs and cytokine production by AMs *in vitro*. Notably, the enhancing effects were dependent on CD14.

MATERIALS AND METHODS

Preparation of Nanomaterial Suspensions

MWCNTs (MWCNT-7) were obtained from Mitsui Chemicals Co., Ltd. Tokyo, Japan; TiO_2 (rutile type, with a mean primary

size of 20 nm) was provided by Japan Cosmetic Association, Tokyo, Japan; SiO_2 (with a primary size of 10-20 nm) was purchased from Sigma-Aldrich, USA; and Fullerene C60 (with a mean primary size of 1 nm) was provided by Frontier Carbon Corporation, Japan. 10 mg of the 4 types of ENMs was suspended in saline containing 0.5% (w/v) Pluronic® F-68 (PF-68, a non-ionic detergent from Sigma-Aldrich, USA) to a final concentration of 500 μg/ml. The MWCNT-7 suspension was homogenized for 1 minute four times (total of 4 min) using a Polytron PT1600E bench-top homogenizer (Kinematica, Switzerland) at a speed of 3000 rpm. The prepared four nanomaterial suspensions were sonicated at 600W for 5 minutes 6 times with 2-minute rest intervals using a JY92-2 sonicator (Scientz Co., Ltd, Ningbo, China). To ensure the dispersion and suspension of the nanomaterials, the suspensions were further sonicated for 5 minutes 4 times before use. Characterization of the suspended 4 nanomaterials, including shape, element analysis, and size distribution are shown in **Supplementary Figures S1**–**S3**.

Animals

Eight weeks-old female wild-type Sprague-Dawley (SD) rats were obtained from the Animal Center of Anhui Medical University. The rats were housed in the Animal Center and received Oriental MF basal diet and water *ad libitum*. The animal experiment protocols were approved by the Animal Ethics Committee of Anhui Medical University.

Intratracheal Spraying of Nanomaterial Suspensions

Twenty-five female SD rats were divided in to 5 groups and about 0.5 ml of the vehicle or 500 μg/ml MWCNT-7, TiO_2, SiO2, or C60 suspensions were administered by intratracheally spraying using an intratracheal aerosolizer (series IA-1B, Penncentury, Philadelphia, USA), as previously described (23), 2 times per week for 2 weeks. The total amount of the administered nanomaterials was 4 mg per kilogram of body weight for each rat. Three days after the last spraying, the animals were sacrificed under isoflurane anesthesia, and the lung was excised, fixed in 4% paraformaldehyde solution in phosphate-buffered saline (PBS) adjusted to pH 7.3, and processed for light microscopic examination and transmission electron microscopy (TEM) or scanning electron microscopy (SEM).

Light Microscopy and Electron Microscopy

Hematoxylin-eosin (HE) stained sections of the lung tissues treated with the 4 ENM suspensions were used to observe lung inflammation and localization of the nanomaterials. For transmission electron microscopic (TEM) observation of TiO_2, SiO_2 and C60, paraffin blocks were deparaffinized and small pieces of the lung tissues were embedded in epon resin and processed for nanomaterial observation using a JEM-2100 transmission electron microscope (JEOL Co. Ltd, Tokyo, Japan). Since MWCNT-7 is difficult to be cut by an electronic microtome, scanning electron microscopy (SEM) was used to observe the MWCNT-7-treated lung tissues. Briefly, the HE-stained slides of the lung tissues were immersed in xylene for 3 days to remove the cover glass, immersed in 100% ethanol for 10 min to remove the xylene, and then air-dried for 2 hours at room temperature. The slides were then coated with platinum for observation using a Model S-4700 Field Emission SEM (Hitachi High Technologies Corporation, Tokyo, Japan) at 5–10 kV.

Preparation of BALF and Isolation of Rat Alveolar Macrophages

Eight weeks-old female wild-type SD rats were placed under deep anesthesia with intraperitoneally injected sodium pentobarbital and sacrificed by exsanguination from the inferior vena cava. The lung was excised under aseptic conditions and injected with 5 ml of saline through the trachea. After gentle shaking, the fluid in the lung was collected. This was repeated 2 more times. The collected fluid was centrifuged at 1800g for 5min at 4°C, and the supernatant (BALF) was concentrated with a concentrator tube (Millipore) and stored at -80°C until use. The cell pellet was resuspended in RPMI 1640 medium containing 10% fetal bovine serum (Gibco, USA), seeded in a six-well plate and cultured at 37°C for 90 minutes. The cells were washed with PBS three times to remove red blood cells, other cells, and cell debris. The remaining adherent cells were stained with anti-CD68, a macrophage marker, to confirm their identity. Briefly, the adherent cells were fixed in 4% paraformaldehyde and treated with 0.2% Triton X-100 containing 10% fetal bovine serum (Gibco)/1% bovine serum albumin in PBS at room temperature for 15 minutes, and then incubated with rabbit anti-CD68 (1:50 dilution, Bioss, Beijing, China) overnight at 4°C, and visualized with Cy3 labelled anti-rabbit IgG (1:100 dilution, Proteintech, Wuhan, China). After washing, the cells were counter-stanning with DAPI (Sigma-Aldrich). Images were captured with a florescence microscope (ZEISS LSM880 +Airyscan, Germany). As shown in **Supplementary Figure S4**, more than 95% of the adherent cells were positive for CD68. About 5×10^5-$1x10^6$ alveolar macrophages per rat were isolated.

Binding of Nanomaterials to BALF Proteins, SDS-PAGE, and LC-MS

1.6 ml of the four ENM suspensions (equal to 800 μg of each ENM) were incubated with 1 ml of the 20-fold concentrated rat BALF at 37°C in a shaker at 200 rpm for 4-6 hours, and then centrifuged at 20000×g for 30 minutes to separate the nanomaterials from the supernatants. The precipitates were re-suspended in PBS, and the suspensions were centrifuged at 20000×g for 10 minutes and the supernatants were discarded. The washing steps were repeated 2 more times. The final ENM precipitates with their bound proteins were resuspended in 50 μl of sodium dodecyl sulfate polyacrylamide gel electrophoresis (SDS-PAGE) buffer (10% glycerol, 62.5 mM Tris-HCl [pH 6.8], 2% 2-mercaptoethanol, 2% SDS), heated for 5 minutes at 95°C, and then centrifuged at 20000×g for 30 minutes to dissociate the bound proteins from the nanomaterial precipitates. After protein quantification with BCA (BestBio, Shanghai, China), 10 μl of the final suspensions was subjected

for SDS-PAGE and the gels was silver-stained with a silver staining kit (BestBio). DTT was added to 20 μl of the remaining SDS-PAGE buffer-dissociated protein solution to a final concentration of 100 mM DTT and boiled 5 minutes. The samples were analyzed by Liquid Chromatography with Tandem Mass Spectrometry (LC-MS) (Shanghai Applied Protein Technology Company, Ltd, Shanghai, China).

Exposure of ENMs to Primary Alveolar Macrophages

In vitro 1×10^6 rat primary alveolar macrophages (PAMs) were cultured at 37°C overnight in a 6-well plate in RPMI 1640 culture medium containing 10% fetal bovine serum (Gibco). The PAMs were then washed 3 times with PBS and cultured in X-VIVO™ serum-free medium (Lonza, Belgium) The cells were then treated with saline containing 0.5% (w/v) Pluronic® F-68, 1 μg/ml MWCNT-7, TiO_2, SiO2, or C60 suspended in saline containing 0.5% (w/v) Pluronic® F-68, or 1 μg/ml of MWCNT-7, TiO_2, SiO2, or C60, pre-incubated for 4 hours with 1 μg/ml of recombinant human SP-A, SP-D or 10% concentrated BALF, and continued culture for 12 hours. The cells were harvested for RNA isolation and quantitative polymerase chain reaction (qPCR) analysis of cytokine expression, and the culture supernatants were collected for ELISA detection of cytokines.

qPCR and ELISA Analyses of IL-1β, IL-6, and TNF-α Production

Total RNA from rat PAMs was extracted with Trizol (Magen, Guangzhou, China) according to the manufacturer's instructions. 500 ng of the RNA samples was reverse transcribed using a HiScript® II RT SuperMix kit (Vazyme Biotech, Nanjing, China), and qPCR analyses of IL-1β, IL-6, and TNF-α were then performed using the AceQqPCR SYBR Green Master Mix (Vazyme). GAPDH was used as an internal reference, and the relative expression of each gene was analyzed by the $2^{-\triangle\triangle CT}$ method. The primer pairs (forward/backward) used were the following: CAGCAGCATCTCGACAAGAG/CATCATCCCAC GAGTCACAG for IL-1β; AGTT- GCCTTCTTGGGACTGA/ TCCAAGATCTCCCTGAGAACA for IL-6; ACTCCCAGA-AAAGCAAGCAA/CGAGCAGGAATGAGAAGAGG for TNF-α; and GACATGCCG- CCTGGAGAAAC/AGCCCAGGATGC CCTTTAGT for GAPDH. Detection of IL-1β, IL-6, and TNF-α in the supernatants of rat primary alveolar macrophage cultures was performed with rat ELISA kits (MLBio, Shanghai, China) according to the manufacturer's instructions.

Analysis of ENM Phagocytosis by Polarized Light Microscopy

1×10^6 rat PAMs were seeded in 6-cm culture dishes with pre-placed microscope cover glass (NEST, China) and cultured in X-VIVO™ serum-free medium (Lonza) and cultured overnight. The cells were treated with saline containing 0.5% (w/v) Pluronic® F-68; 1 μg/ml MWCNT-7, TiO_2, SiO2, or C60 suspended in saline containing 0.5% (w/v) Pluronic® F-68; or 1 μg/ml of MWCNT-7, TiO_2, SiO2, or C60, pre-incubated for 4 hours with 1 μg/ml of recombinant human SP-A, SP-D or 10% concentrated BALF, and continued culture for 12 hours. The cells were then fixed with 4% paraformaldehyde and stained with HE. The Cells with phagocytosed ENMs were identified using an ECLIPSE polarizing microscope (LV100NPOL, Nikon, Japan). Total cell number and the number of the cells with phagocytosed ENMs in 10 fields (40x magnification) were counted, and the percent of the cells with phagocytosed ENMs (number of cells with phagocytosed ENMs/total number of cells) was determined.

Knockdown of LRP1, CD14, and SIRPα and Its Effect on Cytokine Production and Phagocytosis

Small interfering RNAs (siRNA) were used to knock-down the expression of LDL receptor related protein 1 (LRP1), CD14, and signal regulatory protein alpha (SIRPα). 3 pairs of siRNAs for each of the genes were provided by GenePharma Co. Ltd., Shanghai, China. The pair of siRNAs with the best silencing efficacy was determined by preliminary experiments. The siRNA sequences used for further experiments were as follows: GCUAAACUCGCUCAAUCUATT/UAGAUUGAGCGAG UUUAGCTT for CD14; CCAUCAAACGGGCAUUCAUTT/ AUGAAUGCCCGUUUGAUGGTT for LRP1; and GCUC UAUGUACUCGCCAAATT/UUUGGCGAGUACA UAGAGCTT for SIRPα. 1×10^6 rat PAMs were seeded in each well of a 6-well plate and cultured at 37°C overnight. Negative control RNA or siRNAs for LRP1, CD14, and SIRPα were transfected into the cells using Lipofectamine 2000 (Thermo Fisher, USA). 6 hours later, the culture media was changed to X-VIVO™ serum-free medium (Lonza), and then treated with 1 μg/ml MWCNT-7, TiO_2, SiO2, or C60 suspended in saline containing 0.5% (w/v) PF-68; or 1 μg/ml of MWCNT-7, TiO_2, SiO2, or C60, pre-incubated for 4 hours with 1 μg/ml of recombinant human SP-A, SP-D or 10% concentrated BALF, and continued culture for 12 hours. The cells were harvested for RNA isolation, qPCR analysis of silencing efficacy and cytokine expression, and western blotting; the culture supernatants were collected for ELISA. The silencing efficacy of LRP1, CD14, and SIRPα was analyzed by qPCR, as described above, and confirmed by western blotting. The specific primers used were CCAGGAACTTTGGCTTTGCTC/ACCGATGGA CAACTTTCAGG for CD14; CCAATTGTGCATTTTTGCAG/ GAATCAGGGGCATAGGTGAA for LRP1; and GTGTCTGT TGCTGCTGGAGA/GCATCTTCTGGGGTGACATT for SIRPα. The expression of LRP1, CD14, and SIRPα proteins was detected by western blotting. The cells were lysed in RIPA buffer (150mM NaCl, 50mM Tris pH 7.4, 1% sodium deoxycholate, 0.1% SDS, 1% Triton X-100, and 1mM PMSF) for 5 minutes and centrifuged at 4°C 12000 rpm for 20min. After protein quantification with a BCA kit (Bestbio), aliquots of the supernatants (20 μg protein) were separated by 10% sodium dodecyl sulfate polyacrylamide gel electrophoresis (SDS-PAGE) and then transferred to a PVDF membrane (Millipore, Boston, USA). After blocking in 5% nonfat milk, the PVDF membranes were incubated with primary antibodies (anti-GAPDH from Peprotech, USA, 1:500 dilution, as an internal control; anti-CD14 from Bioss, Beijing, China, 1:500 dilution; anti-SIRPα from Cell Signaling Technology, Danvers, USA, 1:1000 dilution;

anti-LRP1 from Abcam, USA, 1:10000 dilution) at 4°C overnight. After three washings, the PVDF membrane was incubated with peroxidase conjugated anti-mouse or anti-rabbit secondary antibodies (1:10,000) for 60 minutes. The protein was visualized with ECL (Thermo Fisher) detection solution in a GEL Imaging System (Tanon, Shanghai, China). The effect of LRP1, CD1, and SIRPα knockdown on IL-1β, IL-6, and TNF-α production was analyzed by qPCR and ELISA, and its effect on ENM phagocytosis was assessed by polarized light microscopy, as described above.

Statistical Analysis

Statistical analysis was performed using SSPS17 software. The statistical significance was analyzed using two tailed Student's t test. A p value of <0.05 was considered to be significant.

RESULTS

Most Intratracheally Administered Nanomaterials Were Taken up By Alveolar Macrophages

Four types of ENMs with different shapes, chemical compositions, sizes, and surface properties were chosen for this study. MWCNT-7 is a carbon-based nanotube with a hydrophobic surface; TiO_2 is a rod-like particle with a hydrophilic surface; SiO_2 and C60 are round nanoparticles with a hydrophilic and hydrophobic surface, respectively. They form aggregates with different sizes in suspensions. Characterization of their shape and chemical composition is shown in **Supplementary Figures S1, S2**. Their size distribution of the suspensions in 0.5% PF-68 saline was comparable to that of the suspensions in 0.5% PF-68 saline supplemented with the concentrated BALF (**Supplementary Figure S3**).

Intratracheal spraying is a simple method for delivery of agents into the lung. In our preliminary experiment, black ink administered into the lung by intratracheal spraying was delivered evenly to each lobe and found to be taken up by AMs (**Supplementary Figure S4**). Intratracheal administration of MWCNT-7, TiO_2, SiO_2, and C60 suspensions to the rat lung induced pulmonary inflammation to different extents. Compared with 0.5% PF-68 saline (NC, **Figure 1A**), MWCNT-7 elicited a strong inflammatory response, with increased number of AMs and thickening of the alveolar epithelium (**Figure 1B**); while TiO_2 and SiO_2 (**Figures 1C, D**) had little effect on the alveolar epithelium, although particle-burdened alveolar macrophages were often observed. Similar to MWCNT-7, C60 caused a strong inflammatory response (**Figure 1E**). The number of AMs per 200◊sight field in the MWCNT-7, TiO_2, SiO_2, or C60 treated lung tissues was significantly increased compared with that of the NC (**Figure 1F**). Most of the induced AMs were found with burden ENM aggregates (**Figures 1B–E**). Further observation with SEM for MWCNT-7 (since MWCNT-7 is difficult to be cut by an electronic microtome) and TEM for TiO_2, SiO_2, and C60 revealed that the ENM aggregates were in the cytoplasm of the AMs and likely to exist in the phagosomes (**Figures 1G–J** correspondingly for MWCNT-7, TiO_2, SiO_2, and C60). These results indicate that uptake by AMs is a main mechanism for clearance of the deposited particles.

BALF Enhanced the Uptake of Nanomaterials by Alveolar Macrophages

Previous studies have demonstrated that ENMs are bound by proteins biological fluids, forming tiers of proteins surrounding the nanomaterials (14). This protein corona affects the biological behavior of the nanomaterial, including phagocytosis by macrophages (24). To determine whether secretory fluid in the respiratory tract and alveoli influences phagocytosis by alveolar macrophages of the 4 ENMs being studied, we prepared BALF and primary alveolar macrophages (PAMs). Immunofluorescence staining indicated that more than 95% of isolated cells were positive for CD68, a macrophage marker (**Supplementary Figure S5**). The 4 ENMs, with or without pre-incubation of BALF, were then exposed *in vitro* to the isolated PAMs. The number of PAMs with internalized ENMs with or without pre-incubation of BALF were compared under polarized light microscopy. The results indicated that pre-incubation with BALF increased the uptake of MWCNT-7, TiO_2, and SiO_2 by PAMs (**Figure 2**). The percent of PAMs with particles without pre-incubation of BALF (31.7%, 22.7%, and 18.2% for MWCNT-7, TiO_2, and SiO_2, respectively) was significantly lower than with pre-incubation of BALF (61.0%, 43.3%, and 53.7% for MWCNT-7, TiO_2, and SiO_2, respectively) (**Figure 2I**). Because C60 is isotropic and cannot be specifically visualized using polarized light microscopy, therefore, phagocytosis of C60 was not quantified (**Figures 2G, H**). The results obtained from MWCNT-7, TiO_2, and SiO_2 suggest that proteins in the BALF are likely to adsorb to ENMs and promote their uptake by PAMs.

Usually, there are two ways for internalization of ENMs into a cell: clathrin-dependent endocytosis and actin-dependent phagocytosis. For determining whether the 4 ENMs were taken up *via* phagocytosis, PAMs were treated with cytochalasin B (an inhibitor of actin polymerization, thus inhibiting phagocytosis) and exposed with MWCNT-7, TiO_2, and SiO_2 pre-incubated with BALF. Pre-treatment of cytochalasin B significantly reduced the percentage of the PAMs with burden-particles (**Supplementary Figure S6**), indicating that uptake of the ENMs by AMs is mainly *via* phagocytosis.

SP-A, SP-D, and SP-B Are Common Proteins Associated With ENMs

For understanding possible interactions of the proteins present in the BALF with the 4 ENMs, the ENMs were incubated in 20-fold concentrated BALF, precipitated by centrifugation, washed with PBS, and resuspended in SDS-PAGE buffer. The ENM associated proteins were then subjected to SDS-PAGE. SDS-PAGE and silver staining revealed that proteins with different molecular weights and abundance absorbed to the surfaces of the 4 ENMs (**Figure 3A**). Further analysis with LC-MS identified a total of 854 proteins associated with the 4 ENMs. 332 of these proteins were found to be associated with each of the 4 ENMs (**Figure 3B**). The 120 most abundant proteins associated with each of the 4 ENMs are shown in **Supplementary Table S1**. Most of these proteins were serum-derived proteins commonly found in BALF, including albumin,

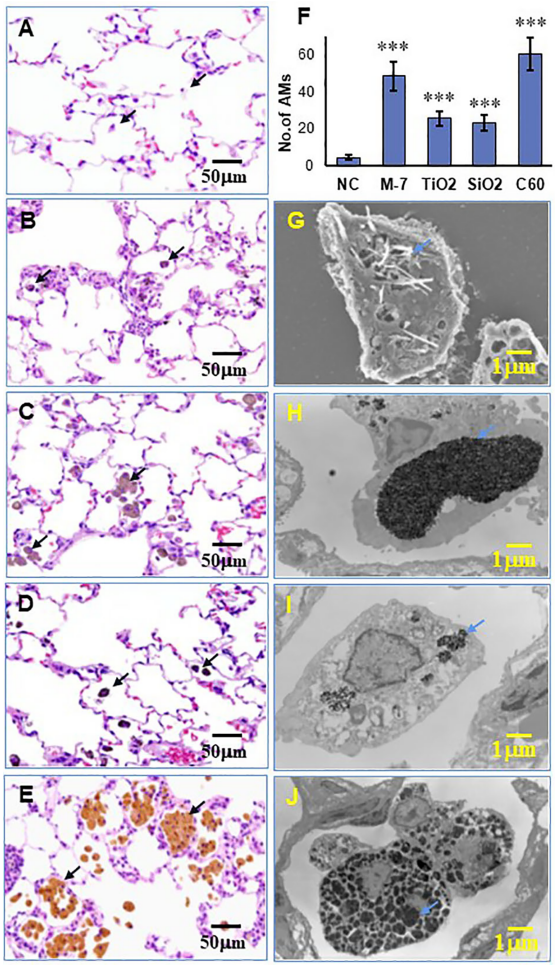

FIGURE 1 | Lung inflammation and phagocytosis of ENMs by alveolar macrophages. Female SD rats were intratracheally sprayed with 0.5 ml of 500 μg/ml MWCNT-7, TiO_2, SiO_2, or C60 suspensions. Lung inflammation in HE-stained slides was examined under light microscopy, and alveolar macrophages with phagocytosed ENMs were indicated with black arrows in the left panel. Representative HE images treated with the control, MWCNT-7, TiO2, SiO2, or C60 were shown in **(A–E)**, respectively. The number of alveolar macrophages per 200x sight field in the treated lung tissues was presented in **(F)**. Phagocytosis of MWCNT-7 in **(G)** was observed under scanning electron microscopy, while the phagocytosed TiO2, SiO2, or C60 in **(H–J)**, respectively, were observed under transmission electron microscopy. The blue arrows in the right panel indicated the phagocytosed ENMs, and *** represents p values less than 0.001.

complement proteins, immunoglobulins, and apolipoproteins. Lung/respiratory tract derived proteins were also common.

Pulmonary surfactant is a complex mixture containing 4 surfactant-associated proteins (SP-A, SP-B, SP-C and SP-D). Notably, SP-A, SP-B, and SP-D were found to be associated with all 4 ENMs (**Figure 3C**). SP-D was among the most abundant proteins associated with MWCNT-7, TiO_2, SiO_2, and C60, while SP-B was among the most abundant proteins associated with MWCNT-7, SiO_2, and C60 (**Supplementary Table S1**).

For further confirming that SP-A and SP-D were bound proteins, the 4 ENMs were incubated with 10-fold concentrated BALF and then separated by centrifugation. Immunofluorescence showed that the large aggregates in the precipitates were stained with anti-SP-A and anti-SP-D (**Supplementary Figure S7A**) and ELISA detection revealed that concentrations of SP-A and SP-D in the supernatants were decreased by the incubation with the 4 ENMs (**Supplementary Figure S7B**), demonstrating that SP-A and SP-D were bound to the 4 ENMs.

SP-A and SP-D Enhanced Nanomaterial-Induced Macrophage Activation and Cytokine Production

We initially investigated the effect of SP-A, SP-B, and SP-D on macrophage activation, using TNF-α, IL-1β and IL-6, the main pro-inflammatory cytokines produced upon macrophage activation, as markers of macrophage activation. Preliminary experiments showed that SP-B-coated ENMs had little effect on the production of these cytokines (data not shown). Similarly, SP-A, SP-D, or BALF alone in the absence of the ENMs (**Supplementary Figure S8A**), or each of the 4 ENMs alone

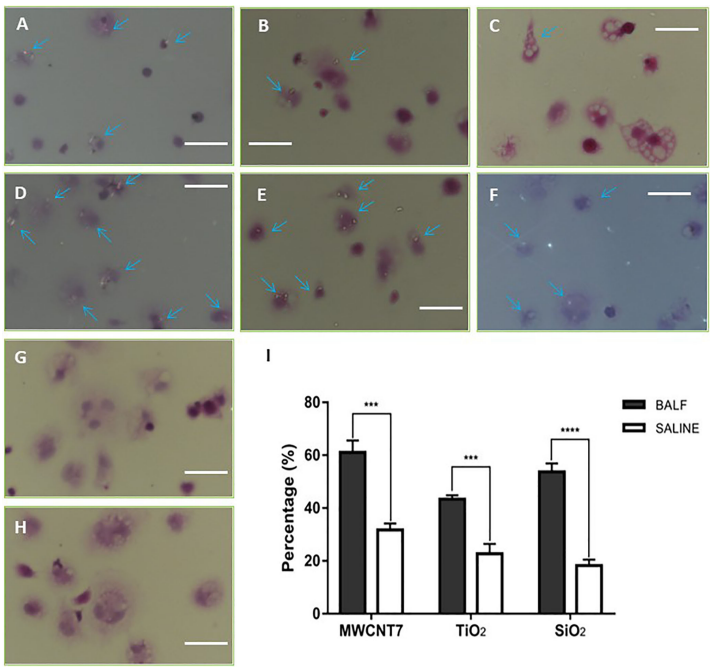

FIGURE 2 | Influence of BALF on phagocytosis of ENMs by primary alveolar macrophages. Primary alveolar macrophages were exposed *in vitro* to 4 types of ENMs (MWCNT-7, TiO_2, SiO_2, and C60) in the absence **(A–C, G)** or presence **(D–F, H)** of BALF. Phagocytosis of ENMs was examined by polarized light microscopy under 40×manification. **(A, D)**, specimens from an MWCNT-7 treated rat, **(B, E)**, specimens from a TiO_2 treated rat. **(C, F)**, specimens from an SiO_2 treated rat. **(G, H)** specimens from a C60 treated rat. Arrows indicate alveolar macrophages with phagocytosed ENMs; bars = 50 μm. C60 is isotropic, and therefore, C60 cannot be specifically identified by polarized microscopy. Consequently, only percentages of alveolar macrophages with phagocytosed MWCNT-7, TiO_2, and SiO_2 were calculated **(I)**. *** and **** represent p values less than 0.001 and 0.0001, respectively.

without SP-A or SP-D coating (**Supplementary Figure S8B**) did not significantly affect cytokine production as detected by qPCR. In contrast, MWCNT-7, pre-incubated with 1μg/ml human recombinant SP-A or SP-D, stimulated a significant increase in TNF-α mRNA expression of PAMs, but not IL-1β or IL-6 mRNA expression (**Figure 4A**). Similar results were also observed when MWCNT-7 was pre-incubated with BALF (**Figure 4A**). Examination of the culture media by ELISA indicated that pre-incubation with SP-A, SP-D, and BALF enhanced MWCNT-7-induced TNF-α secretion (**Figure 4E**).

In TiO_2 treated PAMS, pre-incubation with SP-A or BALF enhanced IL-1β expression, while pre-incubation with SP-D enhanced both IL-1β and IL-6 expression (**Figure 4B**). Similarly, ELISA showed increased IL-1β secretion in the PAMs treated with TiO_2 that was pre-incubated with SP-A, SP-D, or BALF (**Figure 4F**). The response of SiO_2 treated PAMS was similar to that of TiO_2 treated PAMS: SP-A and BALF enhanced IL-1β expression and SP-D enhanced both IL-1β and IL-6 expression (**Figure 4C**). ELISA showed increased IL-1β secretion in the presence of SP-A, SP-D, and BALF (**Figure 4G**). Treatment withC60 pre-incubated with SP-A, SP-D, or BALF upregulated IL-6 expression at both the mRNA and protein secretion, as detected by qPCR and ELISA (**Figures 4H, D**).

In brief, the effect of SP-A and SP-D on macrophage activation as assessed by TNF-α, IL-1β, and IL-6 expression was similar to that of BALF. However, the specific effect on cytokine expression depended on the ENM to which the PAMs were exposed.

Knockdown of CD14 Expression in Alveolar Macrophages Reduced Cytokine Production

It has been reported that LRP1, CD14, and SIRPα are potential receptors for SP-A and SP-D (25–27). Thus, we used siRNA to knock-down the expression of these receptors (**Supplementary Figures S9A, B**). Knockdown of LRP1, CD14, or SIRPα did not significantly change mRNA expression of the cytokines in PAMs (**Figure S10A**). Similarly, neither addition of SP-A or SP-D into the culture medium, nor stimulation with each of the ENMs, affected the cytokine expression at the mRNA level in the receptors-knocked down PAMs (**Supplementary Figures S10B, C**). However, Knockdown of CD14 significantly reduced SP-A-enhanced TNF-α expression in MWCNT-7 stimulated PAMs (**Figures 5A, E**), while SP-D-enhanced TNF-α expression was increased by CD14 silencing (**Figure 5A**). TNF-α expression was also elevated by knockdown of LRP1 and SIRPα (**Figure 5A**). The marked increase in SP-A and SP-D enhanced TNF-α expression by knockdown of LRP1 suggests that LRP1 may be inhibitory to TNF-α production by PAMs.

Knockdown of CD14 decreased SP-A- or SP-D-enhanced IL-1β expression in TiO_2- and SiO_2-stimulated PAMs (**Figures 5B, C, F, G**). Silencing of CD14 expression also decreased

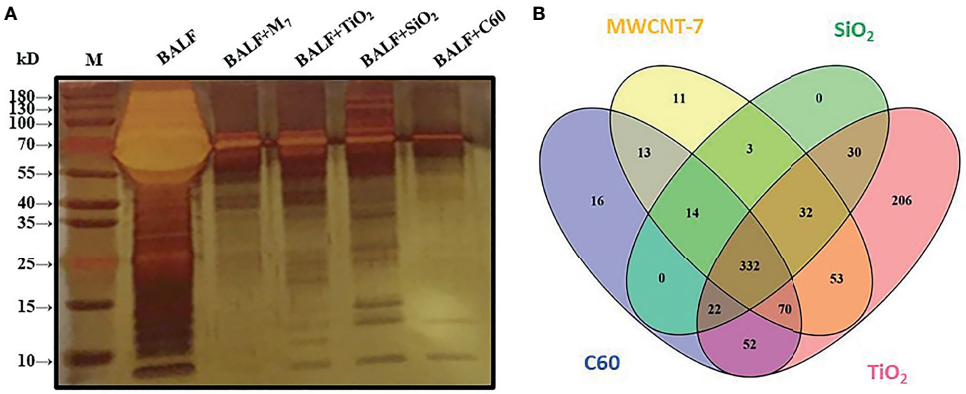

C

Abundance of bound surfactant proteins

	BALF	BALF+MWCNT-7	BALF+TiO_2	BALF+SiO_2	BALF+C60
SP-A	924390	1607000	2182700	93036	4013800
SP-D	12622000	14750000	39184000	622200	62532000
SP-B	17668000	4311200	18976000	365940	4878100

FIGURE 3 | *Analysis of ENM-bound proteins.* 800 μg of MWCNT-7, TiO_2, SiO_2, or C60 was incubated with 1 ml of 20-fold concentrated rat BALF at 37°C for 4-6 hr. The bound proteins were then disassociated from the ENMs and analyzed by SDS-PAGE and LC/MS. **(A)** imagine of SDS-PAGE; **(B)** Venn diagram showing the distribution of the proteins bound to the 4 ENMs; and **(C)** abundance of SP-A, SP-D, and SP-B bound to each type of ENM.

SP-A-enhanced IL-6 expression by C60 stimulated PAMs (**Figures 5D, H**). Knockdown of LRP1 also markedly decreased IL-6 mRNA expression in C60 stimulated PAMs (**Figure 5D**). However, in contrast to mRNA expression, CD14 and LRP1 knockdown increased IL-6 protein secretion by C60 stimulated PAMS. Overall, knockdown of CD14 consistently downregulated SP-A enhanced cytokine mRNA expression, suggesting a common SP-A-CD14 axis for ENM-induced cytokine production.

Knockdown of CD14 Expression in Alveolar Macrophages Reduced ENM Uptake

Finally, we determined the effect of CD14 knockdown on the phagocytosis of ENMs by PAMs. CD14 knockdown reduced phagocytosis of MWCNT-7 pre-incubated with SP-A by PAMs: With pre-incubation of SP-A, 65.3% of the observed PAMS contained MWCNT-7 fibers while only 12.9% of CD14 knockdown PAMs contained MWCNT-7 fibers (**Figures 6A, B, K**). CD14 knockdown also reduced phagocytosis of TiO_2 and SiO_2: In the presence of SP-A, 47.3% of the PAMs contained TiO_2 particles while only 19.5% of CD14 knockdown PAMs contained TiO_2 particles (**Figures 6C, D, K**); in the presence of SP-D, 66.1% of PAMs contained TiO_2 particles while only 16.6% of CD14 knockdown PAMs contained TiO_2 particles (**Figures 6E, F, K**); in the presence of SP-A, 46.0% of the PAMs contained SiO_2 particles while only 16.7% of CD14 knockdown PAMs contained TiO_2 particles (**Figures 6G, H, K**); in the presence of SP-D, 55.5% of PAMs contained SiO_2 particles while only 11.2% of CD14 knockdown PAMs contained TiO_2 particles (**Figures 6I, J, K**). As noted above, because C60 is isotropic, phagocytosis of C60 could not be evaluated using polarized light microscopy.

DISCUSSIONS

Pulmonary inflammation is a common lesion by inhaled ENMs and other airborne dusts. The extent and type of pulmonary inflammation depend on the amount and type of inhaled ENMs deposited in the lung particular in the alveolar region, since mucociliary movement in the upper respiratory tract rapidly and effectively clears large particles deposited in the upper airways. Because of their tiny size, ENMs tend to deposit in the alveolar region. ENMs deposited in the alveolar region are gradually eliminated over time by various clearance mechanisms. If ENMs cannot be effectively cleared, persistent chronic inflammation may lead to chronic obstructive pulmonary disease, emphysema and lung fibrosis. In this study, we chose 4 types of ENMs (MWCNT, TiO_2, SiO_2 and C60), each with different shapes, chemical compositions, sizes, and surface properties, and tried to find out a common clearance mechanism and different cytokine production by alveolar macrophages (AMs). The results may contribute to their toxicological safety assessment and provide instruction for production of safe ENMs.

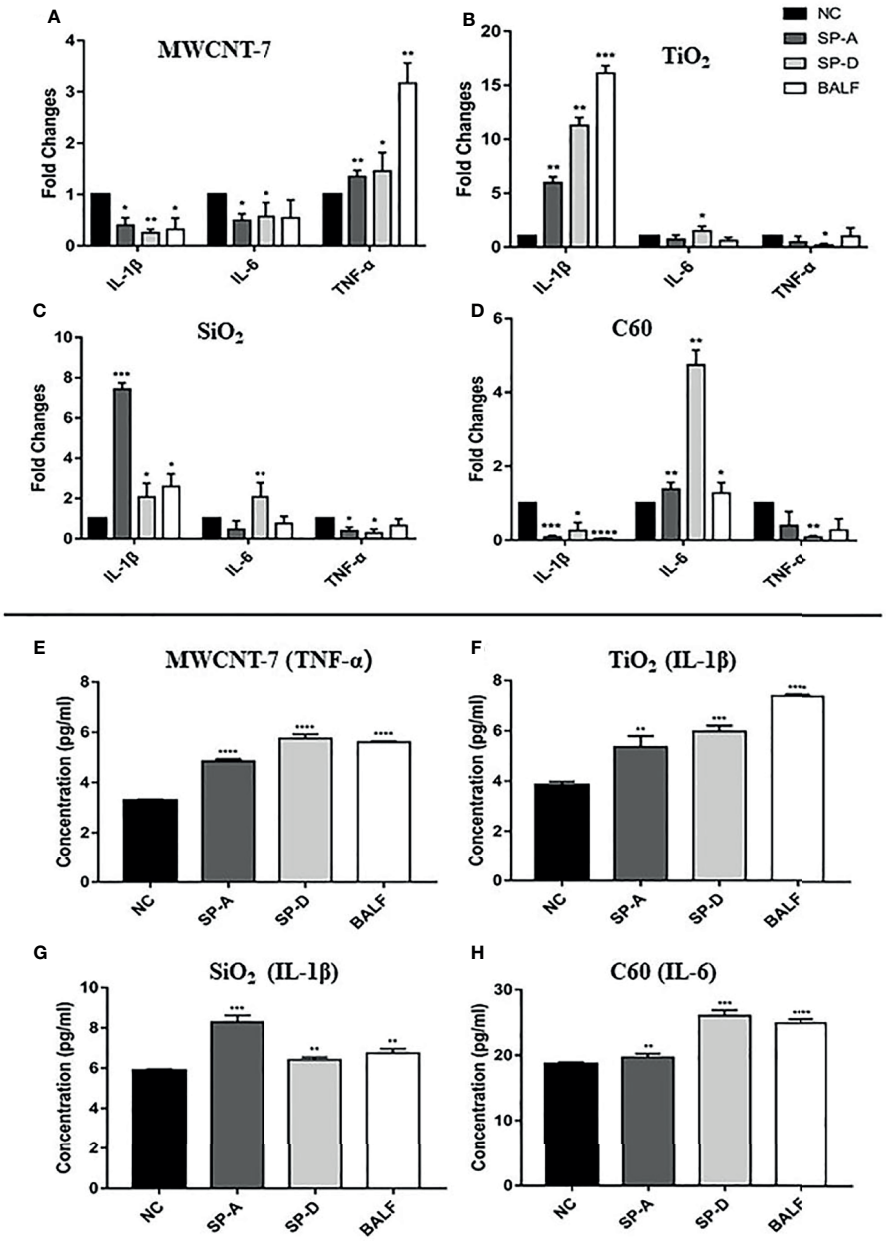

FIGURE 4 | Effects of SP-A and SP-D on cytokine production. Rat primary alveolar macrophages in X-VIVO™ serum-free medium were treated with the vehicle; or 1 μg/ml MWCNT-7, TiO_2, SiO_2, or C60; or 1 μg/ml MWCNT-7, TiO_2, SiO_2, or C60 pre-incubated with 1 μg/ml of recombinant human SP-A, SP-D, or 10% concentrated BALF, and cultured for 12 hours. The RNAs isolated from the treated cells were analyzed by qPCR for expression of TNF-α, IL-1β and IL-6 **(A–D)**. The culture media was collected and used for ELISA detection of TNF-α, IL-1β, and IL-6 **(E–H)**. **(A, E)** treatment with MWCNT-7. **(B, F)**, treatment with TiO_2. **(C, G)**, treatment with SiO_2.D and H, treatment with C60. *, **, *** and **** p values less than 0.05, 0.01, 0.001, and 0.0001, respectively, compared with the negative control (NC).

AMs phagocytose and clear airborne dusts and microbial pathogens encountered in the lung. Inhaled ENMs are also cleared from the lung by macrophages. ENMs have relatively simple chemical compositions. Thus, unlike microorganisms composed of biological macromolecules, most types of ENMs do not have structures that are recognized by receptors, such as PRRs expressed on macrophages. Opsonization of ENMs by proteins that are recognized by macrophages is a likely mechanism by which macrophages recognize and phagocytose ENMs. However, while it is known that SP-A and SP-D are found in the corona of PEG-, PLGA-, or Lipid-modified nanoparticles (28) and that SP-A increases cellular binding and uptake of nanoparticles coated with different polymers by AMs (29), the process by which alveolar macrophages recognize and phagocytose uncoated ENMs has not yet been characterized. The present study was undertaken to investigate this question.

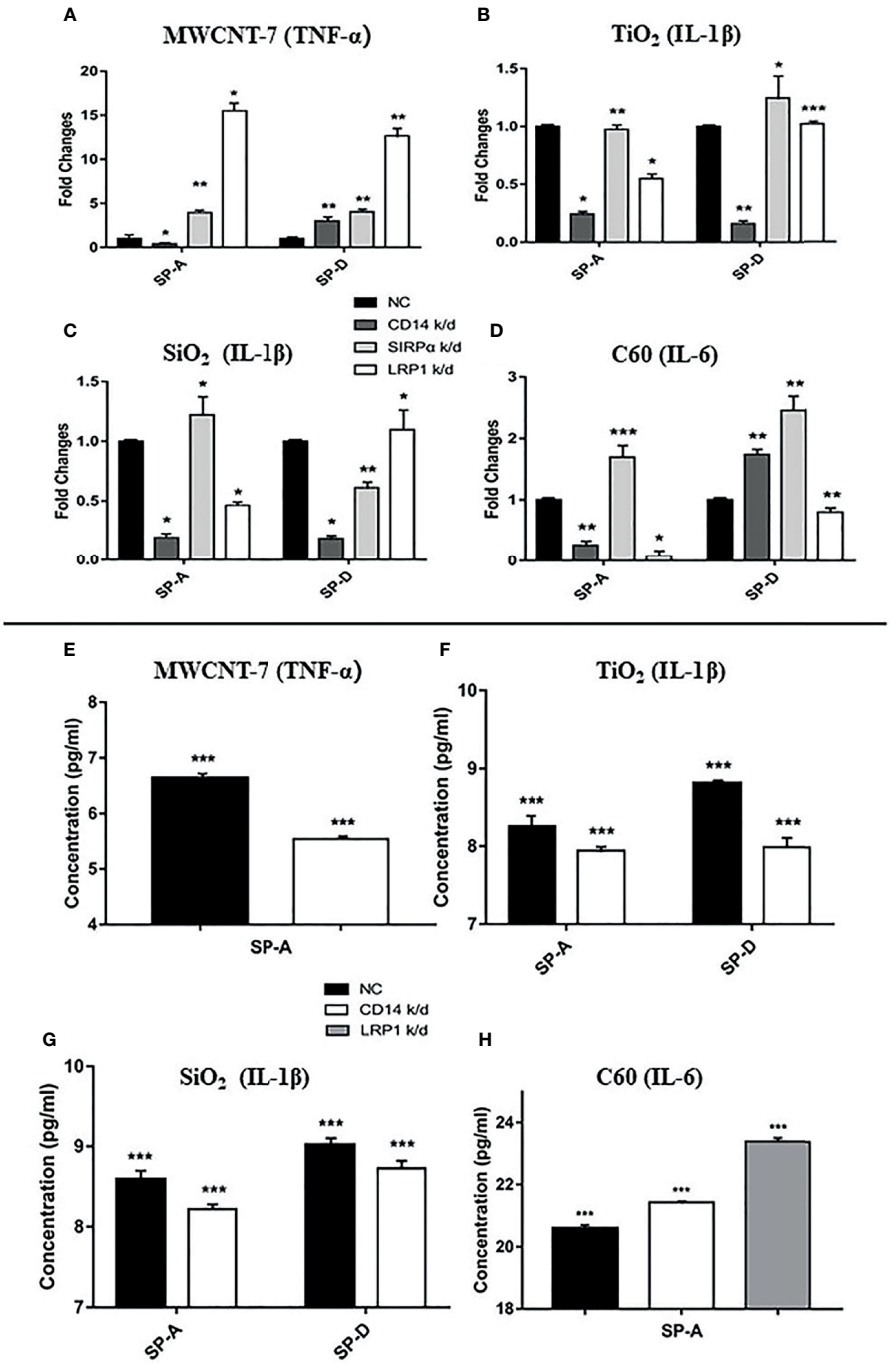

FIGURE 5 | Effect of LRP1, CD14, and SIRPα knockdown on cytokine production. Expression of LRP1, CD14, and SIRPα in rat primary alveolar macrophages was knocked down (k/d) by gene-specific siRNAs. Macrophages were then treated with the vehicle; or 1 μg/ml MWCNT-7, TiO_2, SiO_2, or C60; or 1 μg/ml MWCNT-7, TiO_2, SiO_2, or C60 pre-incubated with 1 μg/ml of recombinant human SP-A, SP-D, or 10% concentrated BALF, and cultured for 12 hours. The cells were harvested for RNA isolation and qPCR analysis **(A–D)** and the culture supernatants were collected for ELISA **(E–H)**. **(A, E)** detection of TNF-α in MWCNT treated cells; **(B, F)** detection of IL-1β in TiO_2 treated cells; **(C, G)** detection of IL-1β in SiO_2 treated cells; and **(D, H)** detection of IL-6 in C60-treated cells. *, ** and *** p values less than 0.05, 0.01, and 0.001, respectively, compared with the negative control (NC).

We initially examined the effect of bronchioalveolar lavage fluid (BALF) on the phagocytosis of 3 different types of ENMs (MWCNT-7, TiO_2, and SiO_2) and found that BALF enhanced phagocytosis of these ENMs by primary rat AMs: C60, the fourth type of ENM used in our study, is isotropic and therefore specific phagocytosis of C60 could not be observed by polarized light microscopy. Next, we examined the proteins associated with the ENMs that could be involved in phagocytosis of these particles.

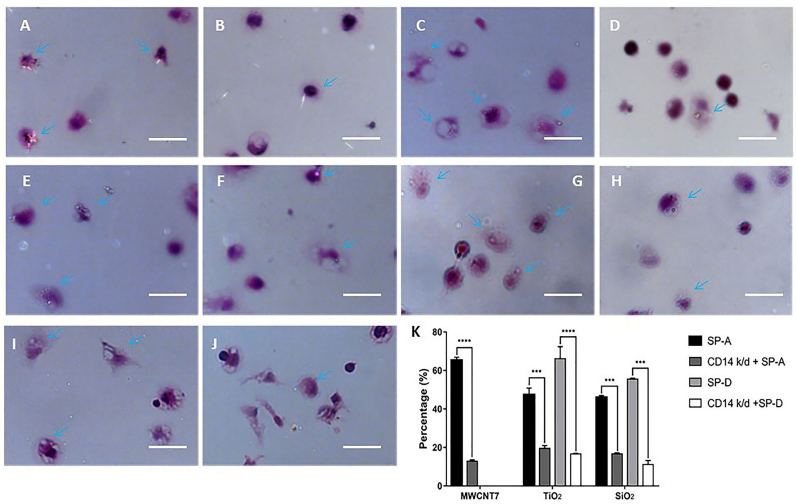

FIGURE 6 | Effect of CD14 knockdown on phagocytosis of MWCNT-7, TiO_2, and SiO_2. Polarized light microscope images of primary alveolar macrophages treated with MWCNT-7 pre-incubated with SP-A **(A)**; CD14-knockdown primary alveolar macrophages treated MWCNT-7 pre-incubated with SP-A **(B)**; primary alveolar macrophages treated with TiO_2 pre-incubated with SP-A **(C)**; CD14-knockdown primary alveolar macrophages treated with TiO_2 pre-incubated with SP-A **(D)**; primary alveolar macrophages treated with TiO_2 pre-incubated with SP-D **(E)**; CD14-knockdown primary alveolar macrophages treated with TiO_2 pre-incubated with SP-A **(F)**; primary alveolar macrophages treated with SiO_2 pre-incubated with SP-A **(G)**; CD14-knockdown primary alveolar macrophages treated with SiO_2 pre-incubated with SP-A **(H)**; primary alveolar macrophages treated with SiO_2 pre-incubated with SP-D **(I)**; and CD14-knockdown primary alveolar macrophages treated with SiO_2 pre-incubated with SP-D **(J)**. Percentages of alveolar macrophages with phagocytosed MWCNT-7, TiO_2, and SiO_2 were shown **(K)**. Arrows indicate alveolar macrophages with phagocytosed ENMs; bars = 50 μm. *** and **** represent p values less than 0.001 and 0.0001, respectively.

We identified 854 proteins that co-precipitated with the 4 different types of ENMs. Of the 854 proteins associated with these ENMs, 332 proteins were associated with all 4 ENMs. Notably, the lung surfactant proteins SP-A, SP-B, and SP-D were associated with all 4 ENMs, and SP-B and SP-D were among the most abundant proteins associated with MWCNT-7, SiO2, and C60. We therefore tested the effect of SP-B, SP-D, and SP-A on macrophage activation by MWCNT-7, TiO_2, SiO_2, and C60. SP-B did not affect macrophage activation by any of the 4 test ENMs. In contrast, SP-A and SP-D enhanced macrophage activation by all 4 test ENMs. These results are in agreement with the known functions of these proteins: SP-B and SP-C are hydrophobic and reduce the surface tension of the lung, while SP-A and SP-D are more hydrophilic and act as opsonins to enhance phagocytosis of microbial pathogens by AMs (18, 19).

Next, we determined the effect of LRP1, CD14, and SIRPα knockdown on the production of cytokines by AMs exposed to the test ENMs in the presence of SP-A or SP-D. While our experiments were performed using primary rat AMs rather than cell lines, allowing variation in CD14 expression levels to exist between cells, downregulation of CD14 in populations of AMs markedly reduced SP-A/ENM-induction of TNF-α mRNA expression by MWCNT-7 treated AMs, IL-1β mRNA expression by TiO_2 and SiO_2 treated AMs, and IL-6 expression by C60 treated AMs, and to a lesser extent, CD14 knockdown decreased protein expression of these cytokines in MWCNT-7, TiO_2, and SiO_2 treated cells. Importantly, downregulation of CD14 also markedly reduced phagocytosis. These results indicate the involvement of the SP-A-CD14 pathway in the phagocytosis of ENMs and subsequent activation of AMs. In the presence of SP-D, downregulation of CD14 also reduced L-1β mRNA expression by TiO_2 and SiO_2 treated AMs, but did not reduce TNF-α mRNA expression by MWCNT-7 treated AMs or IL-6 expression by C60 treated AMs. This result suggests that the SP-D-CD14 pathway differs from the SP-A-CD14 pathway. Since both SP-A and SP-D were associated with all 4 ENMs and CD14 is a receptor for both SP-A and SP-D, the result with SP-D appears to conflict with the result with SP-A. However, the difference is likely related to the fact that CD14 binds to SP-A and SP-D *via* different mechanisms [22], and that the protein corona surrounding the different ENMs is highly complex [14], making it is likely that the interaction and orientation of SP-A and SP-D with ENMs are dependent on the type of ENM to which they attach (summarized in **Supplementary Figure S11**).

SP-A and SP-D are lung-specific proteins existing in the pulmonary surfactant. In addition to their functions in the homeostasis of the pulmonary surfactant (30, 31), they are also involved in the host defense against various pulmonary pathogens, such as respiratory syncytial virus, mycobacterium tuberculosis, bacteria, viruses and fungi (32, 33). Structurally, SP-A and SP-D belong to the collectin family with a C-terminal carbohydrate recognition domain (CRD) and an N-terminal collagen like domain (34) and act as opsonins by interaction *via* the CRD with various microorganisms and their derived components to enhance phagocytic function of AMs through CD14, Toll-like receptors and other receptors expressing on the surface of AMs (22, 35). Our results, indicate that opsonization by SP-A and/or SP-D is an important defense mechanism not only in the elimination of invading microbes, but also in the clearance of inhaled ENMs and is likely to be important in the

clearance of other dusts as well. Our results also suggest that other proteins found in pulmonary surfactant, such as IgG and complement proteins, may also be involved in the clearance of ENMs from the lung, since they were also found to bind to MWCNT-7, TiO_2, SiO_2 and C60 (**Supplementary Table S1**).

Another finding of the current study is that different ENMs induced the expression of different cytokines: increased expression of TNF-α by MWCNT-7; increased expression of IL-1β by TiO_2 and SiO_2; and increased expression of IL-6 by C60. The difference in the induction of these cytokines, and other cytokines, likely contributed to the difference and extent of the pulmonary inflammation in ENM treated rats (see **Figure 1**). For example, MWCNT-7 and C60, which enhance expression of TNF-α and IL-6, respectively, by activated macrophages, are much more inflammatory than TiO_2 and SiO_2, which enhance expression of IL-1β: while IL-1β is a well know inflammatory cytokine, it can also contribute to the resolution of inflammation (36). However, in chronic inflammatory conditions, IL-1β can promote carcinogenesis (37). Thus, while the primary factor in the lung toxicity of an ENM is bio-persistence in the lung, the type of cytokines expressed by activated macrophages also affects the lung toxicity of inhaled ENMs.

In conclusion, SP-A and SP-D opsonized all four of the studied ENMs. SP-A enhanced phagocytosis of the 3 ENMs (MWCNT-7, TiO_2, SiO_2) that could be observed by polarized light microscopy, and SP-A enhanced macrophage activation by all 4 ENMs, indicating that SP-A also enhanced phagocytosis of C60. SP-D also enhanced phagocytosis and macrophage activation by TiO_2 and SiO_2. Interaction of SP-A and SP-D opsonized ENMs with macrophages was *via* interaction with CD14. Our results demonstrate a role for SP-A and SP-D as opsonins for all the test ENMs, allowing macrophages to recognize and remove the vast majority of these particles, thereby, greatly lessening their toxicity in the lung. Our results also show that expression of cytokines by ENM-activated macrophages can differ depending on the type of ENM that comes into contact with the macrophage. However, detailed molecular mechanisms for ENM-specific cytokine induction need further investigation. Importantly, such studies need to include ENMs treated with the biological fluids, such as BALF, present in the tissue in which interactions with the test ENMs occur.

DATA AVAILABILITY STATEMENT

The original contributions presented in the study are included in the article/**Supplementary Material**. Further inquiries can be directed to the corresponding authors.

ETHICS STATEMENT

The animal study was reviewed and approved by Animal Ethics Committee of Anhui Medical University.

AUTHOR CONTRIBUTIONS

QQW, QW, ZZ, JF, and LQ were responsible for the experiments. QQW and QW analyzed the data. QW wrote the initial manuscript, and DA and JX revised the manuscript. HT, DZ, and JX designed the study and provided the funding. All authors contributed to the article and approved the submitted version.

FUNDING

This study was supported by the Key Research and Development Project of Anhui Province (201904b11020024 and 201904a07020064), Health and Labor Sciences Research Grants of Japan (Research on Risk of Chemical Substance 21340601, H25-kagaku-ippan-004 and H24-kagaku-sitei-009), Foundation of Education Bureau of Anhui Province China (KJ2016SD29), and Hefei Municipal Natural Science Foundation (2021037).

SUPPLEMENTARY MATERIAL

The Supplementary Material for this article can be found online at: https://www.frontiersin.org/articles/10.3389/fimmu.2021.758941/full#supplementary-material

REFERENCES

1. Taylor PR, Martinez-Pomares L, Stacey M, Lin HH, Brown GD, Gordon S. Macrophage Receptors and Immune Recognition. *Annu Rev Immunol* (2005) 23:901–44. doi: 10.1146/annurev.immunol.23.021704.115816
2. Gibbings SL, Goyal R, Desch AN, Leach SM, Prabagar M, Atif SM, et al. Transcriptome Analysis Highlights the Conserved Difference Between Embryonic and Postnatal-Derived Alveolar Macrophages. *Blood* (2015) 126 (11):1357–66. doi: 10.1182/blood-2015-01-624809
3. Dey B, Bishai WR. Crosstalk Between Mycobacterium Tuberculosis and the Host Cell. *Semin Immunol* (2014) 26(6):486–96. doi: 10.1016/j.smim.2014.09.002
4. Eddens T, Kolls JK. Host Defenses Against Bacterial Lower Respiratory Tract Infection. *Curr Opin Immunol* (2012) 24(4):424–30. doi: 10.1016/j.coi.2012.07.005
5. Holers VM. Complement and its Receptors: New Insights Into Human Disease. *Annu Rev Immunol* (2014) 32:433–59. doi: 10.1146/annurev-immunol-032713-120154
6. Nimmerjahn F, Ravetch JV. Fc Gamma Receptors as Regulators of Immune Responses. *Nat Rev Immunol* (2008) 8(1):34–47. doi: 10.1038/nri2206
7. Holt PG. Down-Regulation of Immune Responses in the Lower Respiratory Tract: The Role of Alveolar Macrophages. *Clin Exp Immunol* (1986) 63 (2):261–70. doi: 10.1111/j.1365-2249.1995.tb03797.x
8. Thepen T, Van Rooijen N, Kraal G. Alveolar Macrophage Elimination *In Vivo* Is Associated an Increase Pulm Immune Response Mice. *J Exp Med* (1989) 170(2):499–509. doi: 10.1084/jem.170.2.499
9. Tenzer S, Docter D, Kuharev J, Musyanovych A, Fetz V, Hecht R, et al. Rapid Formation of Plasma Protein Corona Critically Affects Nanoparticle Pathophysiology. *Nat Nanotechnol* (2013) 8(10):772–U1000. doi: 10.1038/nnano.2013.181
10. Morfeld P, Treumann S, Ma-Hock L, Bruch J, Landsiedel R. Deposition Behavior of Inhaled Nanostructured TiO2 in Rats: Fractions of Particle Diameter Below 100 Nm (Nanoscale) and the Slicing Bias of Transmission Electron Microscopy. *Inhalation Toxicol* (2012) 24(14):939–51. doi: 10.3109/08958378.2012.738256

11. Semmler-Behnke M, Takenaka S, Fertsch S, Wenk A, Seitz J, Mayer P, et al. Efficient Elimination of Inhaled Nanoparticles From the Alveolar Region: Evidence for Interstitial Uptake and Subsequent Reentrainment Onto Airway Epithelium. *Environ Health Perspect* (2007) 115(5):728–33. doi: 10.1289/ehp.9685
12. Ashby J, Pan S, Zhong W. Size and Surface Functionalization of Iron Oxide Nanoparticles Influence the Composition and Dynamic Nature of Their Protein Corona. *ACS Appl Mater Interfaces* (2014) 6(17):15412–9. doi: 10.1021/am503909q
13. Wan S, Kelly PM, Mahon E, Stockmann H, Rudd PM, Caruso F, et al. The "Sweet" Side of the Protein Corona: Effects of Glycosylation on Nanoparticle-Cell Interactions. *ACS Nano* (2015) 9(2):2157–66. doi: 10.1021/nn506060q
14. Hamad-Schifferli K. How can We Exploit the Protein Corona? *Nanomed (Lond)* (2013) 8(1):1–3. doi: 10.2217/nnm.12.179
15. Han S, Mallampalli RK. The Role of Surfactant in Lung Disease and Host Defense Against Pulmonary Infections. *Ann Am Thorac Soc* (2015) 12(5):765–74. doi: 10.1513/AnnalsATS.201411-507FR
16. Ledford JG, Addison KJ, Foster MW, Que LG. Eosinophil-Associated Lung Diseases A Cry for Surfactant Proteins A and D Help? *Am J Respir Cell Mol Biol* (2014) 51(5):604–14. doi: 10.1165/rcmb.2014-0095TR
17. Gardai SJ, Xiao YQ, Dickinson M, Nick JA, Voelker DR, Greene KE, et al. By Binding SIRPalpha or Calreticulin/CD91, Lung Collectins Act as Dual Function Surveillance Molecules to Suppress or Enhance Inflammation. *Cell* (2003) 115(1):13–23. doi: 10.1016/s0092-8674(03)00758-x
18. Kudo K, Sano H, Takahashi H, Kuronuma K, Yokota SI, Fujii N, et al. Pulmonary Collectins Enhance Phagocytosis of Mycobacterium Avium Through Increased Activity of Mannose Receptor. *J Immunol* (2004) 172 (12):7592–602. doi: 10.4049/jimmunol.172.12.7592
19. LeVine AM, Elliott J, Whitsett JA, Srikiatkhachorn A, Crouch E, DeSilva N, et al. Surfactant Protein-D Enhances Phagocytosis and Pulmonary Clearance of Respiratory Syncytial Virus. *Am J Respir Cell Mol Biol* (2004) 31(2):193–99. doi: 10.1165/rcmb.2003-0107OC
20. Gasser M, Wick P, Clift MJ, Blank F, Diener L, Yan B, et al. Pulmonary Surfactant Coating of Multi-Walled Carbon Nanotubes (MWCNTs) Influences Their Oxidative and Pro-Inflammatory Potential *In Vitro*. *Part Fibre Toxicol* (2012) 9:17. doi: 10.1186/1743-8977-9-17
21. Shaw CA, Mortimer GM, Deng ZJ, Carter ES, Connell SP, Miller MR, et al. Protein Corona Formation in Bronchoalveolar Fluid Enhances Diesel Exhaust Nanoparticle Uptake and Pro-Inflammatory Responses in Macrophages. *Nanotoxicology* (2016) 10(7):981–91. doi: 10.3109/17435390.2016.1155672
22. Pondman KM, Paudyal B, Sim RB, Kaur A, Kouser L, Tsolaki AG, et al. Pulmonary Surfactant Protein SP-D Opsonises Carbon Nanotubes and Augments Their Phagocytosis and Subsequent Pro-Inflammatory Immune Response. *Nanoscale* (2017) 9(3):1097–109. doi: 10.1039/c6nr08807d
23. Xu JG, Futakuchi M, Shimizu H, Alexander DB, Yanagihara K, Fukamachi K, et al. Multi-Walled Carbon Nanotubes Translocate Into the Pleural Cavity and Induce Visceral Mesothelial Proliferation in Rats. *Cancer Sci* (2012) 103 (12):2045–50. doi: 10.1111/cas.12005
24. Mirshafiee V, Kim R, Park S, Mahmoudi M, Kraft ML. Impact of Protein Pre-Coating on the Protein Corona Composition and Nanoparticle Cellular Uptake. *Biomaterials* (2016) 75:295–304. doi: 10.1016/j.biomaterials.2015.10.019
25. Chroneos ZC, Sever-Chroneos Z, Shepherd VL. Pulmonary Surfactant: An Immunological Perspective. *Cell Physiol Biochem* (2010) 25(1):13–26. doi: 10.1159/000272047
26. Sano H, Chiba H, Iwaki D, Sohma H, Voelker DR, Kuroki Y. Surfactant Proteins A and D Bind CD14 by Different Mechanisms. *J Biol Chem* (2000) 275(29):22442–51. doi: 10.1074/jbc.M001107200
27. Stuart LM, Henson PM, Vandivier RW. Collectins: Opsonins for Apoptotic Cells and Regulators of Inflammation. *Curr Dir Autoimmun* (2006) 9:143–61. doi: 10.1159/000090778
28. Raesch SS, Tenzer S, Storck W, Rurainski A, Selzer D, Ruge CA, et al. Proteomic and Lipidomic Analysis of Nanoparticle Corona Upon Contact With Lung Surfactant Reveals Differences in Protein, But Not Lipid Composition. *ACS Nano* (2015) 9(12):11872–85. doi: 10.1021/acsnano.5b04215
29. Ruge CA, Kirch J, Canadas O, Schneider M, Perez-Gil J, Schaefer UF, et al. Uptake of Nanoparticles by Alveolar Macrophages is Triggered by Surfactant Protein A. *Nanomed-Nanotechnol Biol Med* (2011) 7(6):690–93. doi: 10.1016/j.nano.2011.07.009
30. Mortimer GM, Butcher NJ, Musumeci AW, Deng ZJ, Martin DJ, Minchin RF. Cryptic Epitopes of Albumin Determine Mononuclear Phagocyte System Clearance of Nanomaterials. *ACS Nano* (2014) 8(4):3357–66. doi: 10.1021/nn405830g
31. Zhang T, Tang M, Yao Y, Ma Y, Pu YP. MWCNT Interactions With Protein: Surface-Induced Changes in Protein Adsorption and the Impact of Protein Corona on Cellular Uptake and Cytotoxicity. *Int J Nanomed* (2019) 14:993–1009. doi: 10.2147/Ijn.S191689
32. Kondej D, Sosnowski TR. Alteration of Biophysical Activity of Pulmonary Surfactant by Aluminosilicate Nanoparticles. *Inhal Toxicol* (2013) 25(2):77–83. doi: 10.3109/08958378.2012.756087
33. Stern ST, Adiseshaiah PP, Crist RM. Autophagy and Lysosomal Dysfunction as Emerging Mechanisms of Nanomaterial Toxicity. *Particle Fibre Toxicol* (2012) 9:20–34. doi: 10.1186/1743-8977-9-20
34. Geunes-Boyer S, Oliver TN, Janbon G, Lodge JK, Heitman J, Perfect JR, et al. Surfactant Protein D Increases Phagocytosis of Hypocapsular Cryptococcus Neoformans by Murine Macrophages and Enhances Fungal Survival. *Infect Immun* (2009) 77(7):2783–94. doi: 10.1128/IAI.00088-09
35. Madan T, Reid KBM, Clark H, Singh M, Nayak A, Sarma PU, et al. Susceptibility of Mice Genetically Deficient in SP-A or SP-D Gene to Invasive Pulmonary Aspergillosis. *Mol Immunol* (2010) 47(10):1923–30. doi: 10.1016/j.molimm.2010.02.027
36. Sugimoto MA, Sousa LP, Pinho V, Perretti M, Teixeira MM. Resolution of Inflammation: What Controls Its Onset? *Front Immunol* (2016) 7:160. doi: 10.3389/fimmu.2016.00160
37. Bent R, Moll L, Grabbe S, Bros M. Interleukin-1 Beta-A Friend or Foe in Malignancies? *Int J Mol Sci* (2018) 19(8):2155–88. doi: 10.3390/ijms19082155

Conflict of Interest: The authors declare that the research was conducted in the absence of any commercial or financial relationships that could be construed as a potential conflict of interest.

frontiers | Frontiers in Immunology

ORIGINAL RESEARCH
published: 04 April 2022
doi: 10.3389/fimmu.2022.860262

Signaling Pathways That Mediate Alveolar Macrophage Activation by Surfactant Protein A and IL-4

Belén García-Fojeda[1†], Carlos M. Minutti[1†], Carlos Montero-Fernández[1], Cordula Stamme[2,3] and Cristina Casals[1*]*

[1] Department of Biochemistry and Molecular Biology, Complutense University of Madrid, Madrid, Spain, [2] Division of Cellular Pneumology, Research Center Borstel, Leibniz Lung Center, Borstel, Germany, [3] Department of Anesthesiology and Intensive Care, University of Lübeck, Lübeck, Germany

OPEN ACCESS

Edited by:
Taruna Madan,
National Institute for Research in Reproductive Health (ICMR), India

Reviewed by:
Joseph Alcorn,
University of Texas Health Science Center at Houston, United States
Julie Gunnells Ledford,
University of Arizona, United States
Faizah Bhatti,
University of Oklahoma Health Sciences Center, United States

***Correspondence:**
Cristina Casals
ccasalsc@ucm.es
Carlos M. Minutti
carlos.minutti@gmail.com

[†]These authors have contributed equally to this work

Specialty section:
This article was submitted to Molecular Innate Immunity, a section of the journal Frontiers in Immunology

Received: 22 January 2022
Accepted: 14 March 2022
Published: 04 April 2022

Citation:
García-Fojeda B, Minutti CM, Montero-Fernández C, Stamme C and Casals C (2022) Signaling Pathways That Mediate Alveolar Macrophage Activation by Surfactant Protein A and IL-4. Front. Immunol. 13:860262. doi: 10.3389/fimmu.2022.860262

Activation of tissue repair program in macrophages requires the integration of IL-4/IL-13 cytokines and tissue-specific signals. In the lung, surfactant protein A (SP-A) is a tissue factor that amplifies IL-4Rα-dependent alternative activation and proliferation of alveolar macrophages (AMs) through the myosin18A receptor. However, the mechanism by which SP-A and IL-4 synergistically increase activation and proliferation of AMs is unknown. Here we show that SP-A amplifies IL-4-mediated phosphorylation of STAT6 and Akt by binding to myosin18A. Blocking PI3K activity or the myosin18A receptor abrogates SP-A´s amplifying effects on IL-4 signaling. SP-A alone activates Akt, mTORC1, and PKCζ and inactivates GSK3α/β by phosphorylation, but it cannot activate arginase-1 activity or AM proliferation on its own. The combined effects of IL-4 and SP-A on the mTORC1 and GSK3 branches of PI3K-Akt signaling contribute to increased AM proliferation and alternative activation, as revealed by pharmacological inhibition of Akt (inhibitor VIII) and mTORC1 (rapamycin and torin). On the other hand, the IL-4+SP-A-driven PKCζ signaling axis appears to intersect PI3K activation with STAT6 phosphorylation to achieve more efficient alternative activation of AMs. Consistent with IL-4+SP-A-driven activation of mTORC1 and mTORC2, both agonists synergistically increased mitochondrial respiration and glycolysis in AMs, which are necessary for production of energy and metabolic intermediates for proliferation and alternative activation. We conclude that SP-A signaling in AMs activates PI3K-dependent branched pathways that amplify IL-4 actions on cell proliferation and the acquisition of AM effector functions.

Keywords: IL-4, surfactant protein A, macrophage alternative activation, proliferation, Pi3k-akt, mTORC1, PKCζ, metabolism

INTRODUCTION

Macrophages are crucial regulators of the initiation, maintenance, and resolution of repair following injury (1, 2). Tissue repair activities of macrophages are associated with type II cytokine activation (IL-4 and IL-13) through IL-4Rα. Global and myeloid cell-specific disruption of the IL-4Rα gene has been shown to cause tissue repair deficiencies in the lung and liver in different models of injury (3, 4).

Mechanistically, it has been proposed that IL-4Rα-activation of macrophages induces, either directly or through other cell types, the secretion of growth factors like IGF-1 and the production of repair factors like i) collagen type I, alpha 1, which forms the extracellular matrix; ii) resistin-like molecule alpha (Relmα), which serves to cross-link collagen with fibrils; and iii) arginine-derived polyamines, which are necessary for collagen synthesis and cell proliferation (1, 2, 5). Furthermore, IL-4Rα signaling instructs macrophage proliferation, resulting in local expansion of this effector population (6).

We recently reported that IL-4 may not be sufficient for the full induction of alternative activation and proliferation of tissue macrophages and that involvement of local tissue signals is also required (4). Surfactant protein (SP-) A, in the lung, and the first component of the complement system (C1q), in the liver, enhance IL-4Rα-dependent alternative activation, proliferation, and tissue-repair functions of resident macrophages through binding their collagen domains to the myosin 18A receptor (4). SP-A and C1q are versatile recognition proteins, which belong to the group of secreted soluble defense collagens that includes C1q, collectins (e.g., SP-A, SP-D, mannan-binding lectin), ficolins, and adiponectin (7). SP-A is secreted to the alveolar fluid by epithelial type II cells. This protein has important functions in the lung, integrating intrinsic host-defense properties in a lipid-rich medium (pulmonary surfactant) required to protect the lung against alveolar collapse during the breathing cycle (7–9). Thus, SP-A performs its host defense functions and at the same time facilitates the surface-active biophysical functions of the surfactant system (10).

SP-A significantly boosted IL-4-mediated proliferation and alternative activation induced by IL-4 in human, mouse, and rat alveolar macrophages (AMs) (4). Mice lacking SP-A exhibited reduced IL-4-dependent activation and proliferation of AMs. Interestingly, IL-4 increases the production of SP-A by epithelial type II cells and the expression of myosin 18A receptor (Myo18A) on the surface of AMs for full IL-4-dependent alternative activation and proliferation (4). Studies with SP-A-deficient mice infected with the lung-migrating nematode *Nippostrongylus brasiliensis* demonstrated that SP-A is required for i) accelerating parasite clearance; ii) reducing pulmonary injury after infection; and iii) promoting tissue repair (4).

In this study we asked what are the intracellular signaling pathways by which SP-A amplifies IL-4-effects in AMs. IL-4 signals through both the type I receptor (expressed on myeloid cells and lymphocytes and composed of the IL-4Rα chain and IL-2Rγ chain, also called γc) and the type II receptor (expressed on myeloid cells and all non-hematopoietic cells and composed of the IL-4Rα and IL-13Rα1 chains). Both IL-4 receptors signal *via* the Janus kinase (JAK)/signal transducer and activator of transcription 6 (STAT6) pathway that induces robust expression of genes associated with alternative activation in bone marrow-derived macrophages (BMDM) and peritoneal macrophages (pMs) (11, 12). IL-4 activation of the type I receptor also induces highly efficient tyrosine phosphorylation of insulin receptor substrate 2 (IRS2). Although IRS2 does not possess intrinsic enzymatic activities, it functions as an activator for a few other signaling proteins such as phosphatidylinositol-3 kinase (PI3K). Thus, IRS2 triggers the PI3K/Akt/mTORC1 pathway that activates cell growth, proliferation, and synthesis of extracellular matrix macromolecules in BMDM and pMs (12–15). PI3K/Akt activation also enhances the expression of a subset of alternative activation markers, such as *Arg1* and *Retnla* in BMDM (13, 14) and pMs (15). Given that SP-A activates the PI3K signal transduction pathway to upregulate the mannose receptor expression in human monocyte derived macrophages (16) and promote atypical protein kinase C ζ (PKCζ) phosphorylation (17) and regulation of endolysosomal trafficking dependent on the PI3K/PKCζ axis (18), we hypothesized that the induction of PI3K signaling by SP-A could increase IL-4 actions on AMs.

The objective of this study was to dissect SP-A-dependent signaling pathways that strengthen IL-4 signaling in AMs and to determine the metabolic profile of these cells. Our results indicate that SP-A enhances IL-4 effects in AMs through activation of PI3K, Akt, mTORC1, and PKCζ, and inactivation of GSK3α/β. In addition, we found that SP-A and IL-4 act synergistically to increase mitochondrial respiration and glycolysis. These processes provide energy and metabolic intermediates that sustain alternative activation and proliferation of alveolar macrophages.

MATERIALS AND METHODS

Reagents

Cell culture media and reagents were from Lonza (Basel, Switzerland). Western blotting materials were obtained from Bio-Rad (Hercules, California). Akt inhibitor VIII and PKCζ pseudosubstrate inhibitor myristoylated were from Calbiochem, (Darmstadt, Germany). PI3K inhibitor (LY294002), rapamycin and torin-1, as well as antibodies against phospho-STAT6 (Tyr641), phospho-Akt (Ser 473), phospho-PKCζ/λ (Thr410/403), phospho-4E-BP1 (Ser65), phospho-GSK3β (Ser 9), phospho-FoxO3a (Thr32), their respective total protein antibodies, and α-tubulin were purchased at Cell Signaling Technologies (Danvers, Massachusetts). Antibodies against anti-β actin, anti-PKCζ H1 and anti-EEA1 were from Santa Cruz Biotechnology (Dallas, Texas), and anti-STAT6, Alexa Fluor 488 anti-mouse IgG, and Alexa Fluor 633 anti-rabbit IgG were from Thermo Fisher Scientific (Waltham, Massachusetts). All other reagents were of analytical grade, purchased from Sigma-Aldrich (St. Louis, Missouri) unless otherwise specified.

Isolation, Purification and Characterization of Native SP-A

Surfactant protein A was isolated from bronchoalveolar lavages (BAL) of patients with alveolar proteinosis using a sequential butanol and octylglucoside extraction (4, 19–23). The purity of SP-A was checked by one-dimensional SDS-PAGE in 12% acrylamide under reducing conditions and mass spectrometry. The oligomerization state of SP-A was assessed by electrophoresis under non-denaturing conditions (22, 23), electron microscopy (23), and analytical ultracentrifugation as reported elsewhere (22). SP-A consisted of supratrimeric oligomers of at least 18 subunits.

Each subunit had a relative molecular mass (Mr) 36 kDa. The endotoxin content of native or recombinant human SP-A was < 0.1 endotoxin units/mg of SP-A as determined by Limulus amebocyte lysate assay (Lonza).

Isolation and Culture of Primary AMs

AMs were obtained from BAL of male Sprague–Dawley rats (Envigo). Rats (∼350 g) were anesthetized with ketamine (80 mg/kg; Merial, Duluth, GA) and xylazine (10 mg/kg; Bayer, Leverkusen, Germany) and the cardiopulmonary block was extracted to perform BALs with 40ml of PBS (0.2mM EDTA). Animal handling procedures to obtain BAL were reviewed and approved by the local ethics committee (both Complutense University of Madrid and Autonomous Community of Madrid), according to Directive 2010/63/EU of the European Parliament and the Spanish law RD53/2013 on protection of animals used for experimentation. In some experiments, AMs were obtained from BAL of SP-A-deficient mice as previously reported (4, 24). Importantly, AMs from SP-A-deficient mice were normal in number, phenotype and ability to respond to IL-4 (4). Animal care was conducted according to the Schleswig-Holstein Ministry of Energy, Agriculture, the Environment, Nature and Digitalization. Mice were housed under pathogen-free conditions with an inverted 12-hour light/dark cycle and had free access to food and water.

Bronchoalveolar cells were separated from lavage fluid by centrifugation (250 g, 7 min). The sedimented cells were washed twice with PBS, and the cell pellet was resuspended in RPMI 1640 medium (10% heat inactivated FBS, 100 U/ml penicillin, and 100 mg/ml streptomycin, supplemented with 2 mM glutamine). AMs were purified by adherence for 90 min at 37°C under a 95% air-5% CO_2 atmosphere in 150-mm culture dishes as reported previously (4, 19, 24). Adherent cells were 94.0 ± 1.1% viable (trypan blue exclusion test). To evaluate the purity of the isolated macrophages, rat AMs were immuno-stained with anti-CD11c (AbD Serotec, Kidlington, U.K.) and were analyzed by flow cytometry. Adherent cells were found to be composed of 90 ± 1% AMs.

Incubation Conditions

Adherent cells were gently scraped, plated in 96-well plastic dishes (7.5 x 10^4 cells/well) in 0.2 ml RPMI 1640 medium supplemented with 5% FBS, 2 mM glutamine, 100 U/ml penicillin, and 100 mg/ml streptomycin, and pre-cultured overnight. Cells were cultured in the presence or absence of rat recombinant IL-4 (1 μg/ml) (ImmunoTools, Berlin, Germany) and/or SP-A (25, 50 and 100 μg/ml) as reported previously (4). SP-A was added simultaneously with IL-4 to cells. Lower doses of IL-4 (0.1-1 μg/ml) were also assayed. Different concentrations of inhibitors were titrated to minimize undesired effects and toxicity. After titration the following concentrations were used: 50 nM LY294002 (PI3K inhibitor), 25 or 100 nM Akt inhibitor VIII (Isozyme-selective, Akti-1/2) as indicated, 30 μM PKCζ Pseudosubstrate inhibitor, myristoylated, 25 or 100 nM torin-1, and 5 or 20 nM rapamycin, as indicated. Cell viability was 95 or 97% under assay conditions and after treatment with inhibitors. Macrophage cultures were plated in triplicate wells, and each series of experiments was repeated at least three times.

siRNA-Targeted Silencing of Myo18A

After isolation, primary AMs were resuspended in Amaxa® mouse macrophage nucleofector solution (Lonza) and nucleofected with 100 nM siRNA using a nucleofector 2b device (Lonza) as previously reported (4). Experiments were conducted using two Stealth siRNAs directed against rat Myo18A (RSS322720 and RSS322721) (Applied Biosystems, Carlsbad, California). Medium GC Stealth siRNA was used as control (12935300) (Applied Biosystems). Myo18A expression was detected by Western blot analysis with an anti-Myo18A antibody as reported previously (4). After 48 hours post nucleofection, Myo18A expression was reduced 72 ± 4% for RSS322720 and 71 ± 5% for RSS322721 compared to control. At this time-point, cells were stimulated.

Immunoprecipitation of PKCζ

AMs were stimulated with SP-A, IL-4 or combinations thereof for 8 minutes. PKCζ immunoprecipitation was performed as in (17), with modifications. After culture, cells were lysed at 4°C for 30 min in 500 μl of lysis buffer: 50 mM Tris-HCl (pH 8.0), 150 mM NaCl, 0.5 mM EDTA, 0.5% IGEPAL, 1 mM benzamidine, 200 μg/ml aprotinin, 200 μg/ml leupeptin, 1 mM phenylmethylsulfonyl fluoride (PMSF), 20 mM β-glycerophosphate, 10 mM NaF, 10 mM sodium pyrophosphate and 2 mM orthovanadate. The lysates were centrifuged at 10 000 × g for 10 min, and the supernatants were precleared by adding protein A-agarose (50 μl) and incubated at 4°C for 45 min, followed by centrifugation at 10 000 × g for 10 min. The precleared supernatant was incubated with anti-PKCζ antibody or control IgG at 4°C overnight, after which 50 μl of protein A-agarose was added for 3 h at 4°C with gentle rotation. The immune complexes were collected by centrifugation at 10,000 × g for 5 min at 4°C, washed three times with cold lysis buffer, and released by boiling with Laemmli loading buffer. Phosphorylation of PKCζ was subsequently analyzed by Western blot using an anti-Phospho-PKCζ/λ (Thr410/403) and anti-PKCζ, as described below.

Western Blot Analysis

AMs were stimulated with SP-A, IL-4 or combinations thereof for 90 min to determine p-STAT6(Tyr641), 30 min to analyze p-Akt (Ser473) and p-4E-BP1 (Ser65), 10 min for p-GSK3 α/β (Ser21/9), and 45 min for p-FoxO3a (Thr32). Cells were lysed by shaking 30 min at 4°C with a buffer containing: 10 mM HEPES (pH 7.9), 15 mM $MgCl_2$, 10 mM KCl, 0.5 mM EDTA, 0.2% Triton X-100, 1 mM benzamidine, 200 μg/ml aprotinin, 200 μg/mL leupeptin, 1 mM phenylmethylsulfonyl fluoride (PMSF), 20 mM β-glycerophosphate, 10 mM NaF, 10 mM sodium pyrophosphate and 2 mM orthovanadate (Sigma-Aldrich). Samples were resolved by SDS-PAGE under reducing conditions and transferred to polyvinylidene fluoride membranes (Bio-Rad). After blocking with 2.5% (m/v) skim milk, membranes were washed in PBS 0.1% Tween20 and incubated with anti-phospho or anti-total protein antibodies, as indicated, overnight at 4°C. The membranes were washed, incubated with HRP-labeled anti-

rabbit/mouse IgG, and exposed to ECL reagents (Merck Millipore, Darmstadt, Germany). Immunoreactive bands intensity were quantified (Quantity One Software; Bio-Rad), and then normalized to the respective total protein for quantification of phosphorylated proteins, except p-4E-BP1 which was normalized relative to β-Actin.

Arginase Activity Assay

Arginase activity was measured as previously reported (4). Activated AMs with or without IL-4 and/or SP-A at 37°C for 48h were lysed with 50 µl of 50 mM Tris–HCl (pH 7.5), 0.1% Triton X-100, 1 mM benzamidine, 200 µg/ml aprotinin, and 200 µg/ml leupeptin. After 30 min shaking at 4°C, arginase was activated with 50 µl of 10 mM $MnCl_2$ and 50 mM Tris-HCl, pH 7.5, for 10 min at 55°C. L-arginine hydrolysis was measured by incubating the cell lysate with 25 µl of 0.5 M L-arginine (Sigma-Aldrich) (pH 9.7) at 37°C for 1 h. The reaction was stopped by addition of 200 µl $H_2SO_4/H_3PO_4/H_2O$ (1:3:7 v/v). The produced urea was quantified at 570 nm after addition of 25 µl of α-isonitrosopropiophenone (dissolved in 100% ethanol) followed by heating at 99°C for 45 min. Urea production was normalized to cell number for each treatment by quantifying cells with the WST-1 reagent (Roche), following manufacturer' instructions. One unit of arginase activity is defined as the amount of enzyme that catalyses the formation of 1 µmol urea per min.

Cell Proliferation Assays

For 5-Bromo-2'-deoxyuridine (BrdU) incorporation analysis (4), cells were treated with IL-4 and/or SP-A for 24h. Then, cells were exposed to 10 µM BrdU for another 24h. Detection of BrdU incorporation was performed by ELISA using BrdU cell proliferation assay (Cell Signaling Technologies) as previously reported (4). Briefly, cells are fixed, and DNA is denatured. Then, a BrdU mouse monoclonal antibody is added to detect the incorporated BrdU, followed by anti-mouse IgG linked to HRP secondary antibody. Finally, the HRP substrate tetra methylbenzidine is added to develop color. The retention of the cells at the bottom of the well after the removal of the supernatant was checked by the WST-1 assay. Cell number in all treatments was similar before and after supernatant removal.

Bioenergetic Characterization of AMs

AMs were plated at 2 x 10^5 cells/well in 1-, 5- or 11-mM glucose RPMI, during 24 h in a poly-L-lysine-coated Seahorse XFe24 microplate. RPMI was supplemented with 2 mM glutamine, 5% heat-inactivated FBS and 100 U or µg/ml of penicillin/streptomycin. Then, macrophages were stimulated with SP-A, IL-4 or combinations thereof for 24 h. Afterwards, cells were incubated in bicarbonate-free RPMI supplemented with glucose (1-, 5- or 11-mM), 2mM glutamine, and 2% FBS, at 37°C in a CO2-free incubator. Oxygen consumption rate (OCR) and extracellular acidification rate (ECAR) were simultaneously measured in a Seahorse XFe24 Extracellular Flux Analyzer (Agilent Technologies, CA). After four measurements under basal conditions, cells were treated sequentially with 1 µM oligomycin, 0.6 µM carbonyl cyanide p-(trifluoromethoxy) phenylhydrazone (FCCP), 0.4 µM FCCP, and 1 µM rotenone plus 1 µM antimycin A, with three consecutive determinations under each condition. Nonmitochondrial respiration (OCR value after addition of rotenone plus antimycin A) was subtracted from all OCR measurements. Spare respiratory capacity was calculated by subtracting basal OCR from the maximal respiratory capacity, which is the maximal OCR in the presence of FCCP. Glycolytic reserve was calculated by subtracting basal ECAR from the ECAR rate obtained after oligomycin treatment.

Glucose Uptake Assays

Glucose uptake was measured as previously reported (25). Briefly, AMs were plated at 2 x 10^5 cells/well in 5mM glucose RPMI (supplemented with 2 mM glutamine, 5% heat-inactivated FBS and 100 U or µg/ml of penicillin/streptomycin) in a 24-well plate. The next day, cells were stimulated with SP-A, IL-4 or combinations thereof for 24 h. Then, the fluorescent glucose analogue, 2-deoxy-2-[(7-nitro-2,1,3-benzoxadiazol-4-yl) amino]-D-glucose (2-NBDG) was added to the wells at a concentration of 50 µg/ml and cells were incubated for 20 minutes at 37°C under a 95% air-5% CO2 atmosphere. The 2-NBDG uptake reaction was stopped by removing the incubation medium and washing the cells twice with PBS. Fluorescence was measured by flow cytometry using a FACScalibur (Becton Dickinson, New Jersey) flow cytometer and Cell Quest software. Background fluorescence was measured in control cells without 2-NBDG.

Confocal Microscopy/PKCζ Membrane Translocation

AMs from SP-A-deficient mice were used to avoid confounding effects of the endogenous protein. Macrophages were seeded at 1x10^5 cells/well on 8-well Lab-TekII chamber slides (Nunc, Wiesbaden, Germany) and allowed to adhere for 90 min at 37°C in a 5% CO_2 atmosphere. After treatment, the cells were fixed with ice-cold (-20°C) methanol, washed with PBS, followed by permeabilization with 0.25% Triton X-100. Subsequently, the cells were blocked with 10% BSA/PBS, washed and incubated with anti-PKCζ H1 and rabbit anti-EEA1 antibodies (1:250 and 1:60, respectively, Santa Cruz). Alexa Fluor 488 anti-mouse IgG and Alexa Fluor 633 anti-rabbit IgG (1:500, Thermo Fisher Scientific) was used as secondary antibody. Cell nuclei were counterstained with DAPI (Thermo Fisher Scientific). Samples were analyzed using a Leica TCS SP5 confocal laser scanning microscope (Leica Microsystems, Wetzlar, Germany). Confocal images were acquired with the Leica Application Suite AF software and analysis was performed with the Sync Windows Plugin for Image J.

Statistics

Statistical evaluation of different groups was performed by analysis of variance (ANOVA) followed by the Bonferroni multiple comparison test. An α level $\leq$ 5% ($p \leq 0.05$) was considered significant. All statistical calculations were performed using PRISM (Graphpad La Jolla, CA).

RESULTS

SP-A Enhances IL-4 Signaling Through the Myo18A Receptor

First, we determined whether SP-A could drive IL-4-mediated activation of STAT6 and Akt. These are the two signaling branches that are triggered in response to IL-4 type I receptor activation and are essential for alternative activation and proliferation of macrophages (6, 11, 12). **Figure 1A** shows the phosphorylation of STAT6 (Tyr 641) and Akt (Ser 473) induced by IL-4 stimulation of AMs. Phosphorylation of STAT6 and Akt was potentiated by SP-A in a dose-dependent manner. In the absence of IL-4, SP-A could induce significant phosphorylation of Akt, but not STAT6, confirming the observation that SP-A induces activation of the PI3K-Akt axis in AMs (16–18).

To analyze whether the Myo18A receptor is mediating SP-A signaling in alveolar macrophages, we silenced the Myo18A gene and studied the phosphorylation of STAT6 and Akt in IL-4-stimulated macrophages in the presence or absence of SP-A. Silencing Myo18A resulted in a reduction of its expression by 72 ± 4% for RSS322720 siRNA and 71 ± 5% for RSS322721 siRNA compared to control (**Supplementary Figure 1**). **Figure 1B** shows that silencing the Myo18A receptor abrogated the effects of SP-A on STAT6 and Akt phosphorylation in macrophages stimulated with

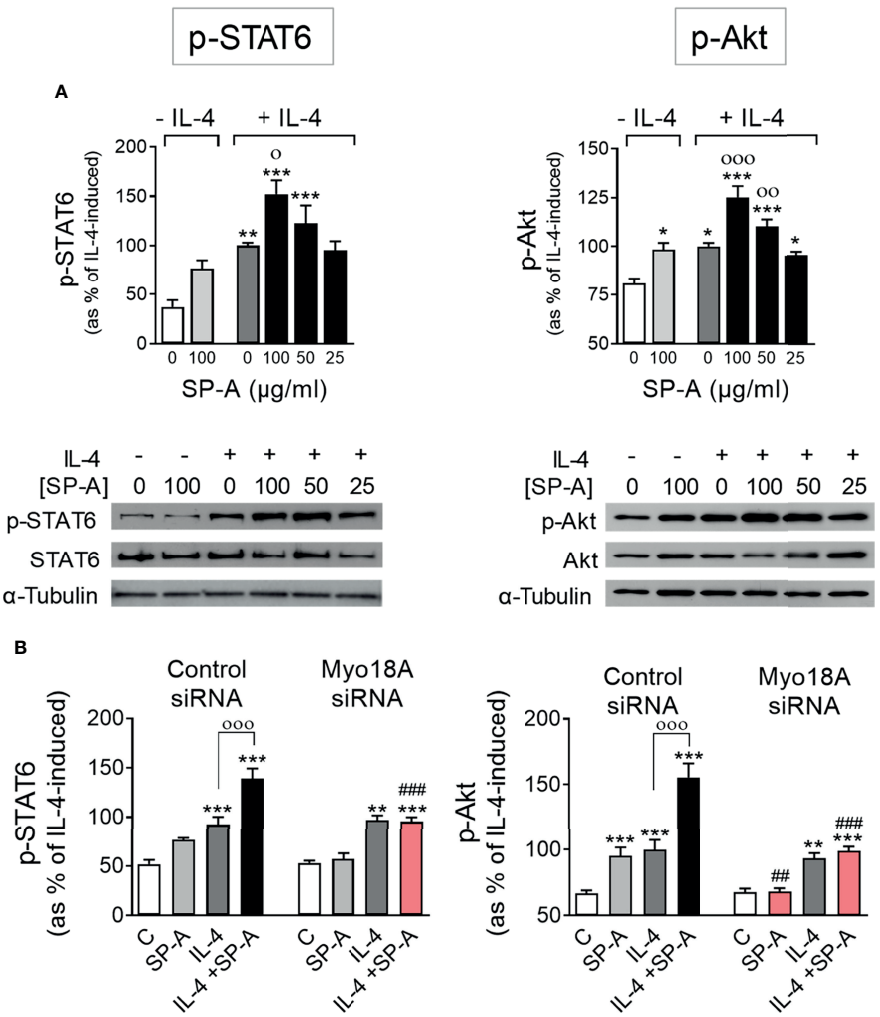

FIGURE 1 | SP-A acts through Myo18A to enhance STAT6 and Akt activation elicited by IL-4 in AMs. **(A)** Purified rat AMs were treated with or without IL-4 (1 µg/ml) in the presence or absence of SP-A at the indicated concentrations. STAT6 and Akt phosphorylation relative to total STAT6 or Akt, respectively, were analyzed by Western blot. A representative Western blot for p-STAT6 (Tyr641) or p-Akt (Ser473) is shown below each graph. **(B)** AMs were nucleofected with Myo18A (RSS322720) or control siRNA. Cells were then stimulated with or without IL-4 (1 µg/ml) and/or SP-A (100 µg/ml), and p-STAT6 and p-Akt were analyzed by Western blot. The data shown are means ± SEM of three different AM cultures with at least three biological replicates. ANOVA followed by the Bonferroni multiple-comparison test was used. $^{*}p < 0.05$, $^{**}p < 0.01$, and $^{***} < 0.001$ when compared with untreated cells. $^{o}p < 0.05$, $^{oo}p < 0.01$, and $^{ooo}p < 0.001$ when SP-A+IL-4-treated macrophages were compared with IL-4-treated macrophages. $^{\#\#}p < 0.01$ and $^{\#\#\#}p < 0.001$ when the effect of Myo18A siRNA is compared with siRNA control.

IL-4. In the absence of IL-4, we observed that silencing the Myo18A receptor also abolished Akt phosphorylation induced by SP-A (**Figure 1B**), indicating that SP-A induces PI3K/Akt activation by binding to the Myo18A receptor. However, Myo18A silencing had no impact on p-STAT6 and p-Akt induced by IL-4 alone, in the absence of SP-A. Together, these data suggest that the binding of SP-A to the Myo18A receptor amplifies IL-4-mediated phosphorylation of STAT6 and Akt. In addition, our data demonstrate that IL-4R signaling does not require Myo18A and therefore the synergy between IL-4 and SP-A must occur at the level of intracellular signaling.

SP-A Amplification of IL-4 Actions Depends on PI3K Activation

To assess if SP-A amplification of IL-4 actions depends on PI3K activation, we inhibited PI3K with 50 nM LY294002 in IL-4-stimulated macrophages with or without SP-A and analyzed the phosphorylation of STAT6 (**Figure 2A**) and Akt (**Figure 2B**), as well as alternative activation of AM by measuring arginase activity (**Figure 2C**), and proliferation by analyzing BrdU incorporation in DNA (**Figure 2D**). As expected, IL-4 did depend on PI3K to induce p-Akt, but not STAT6 phosphorylation. However, PI3K inhibitor abrogated SP-A-

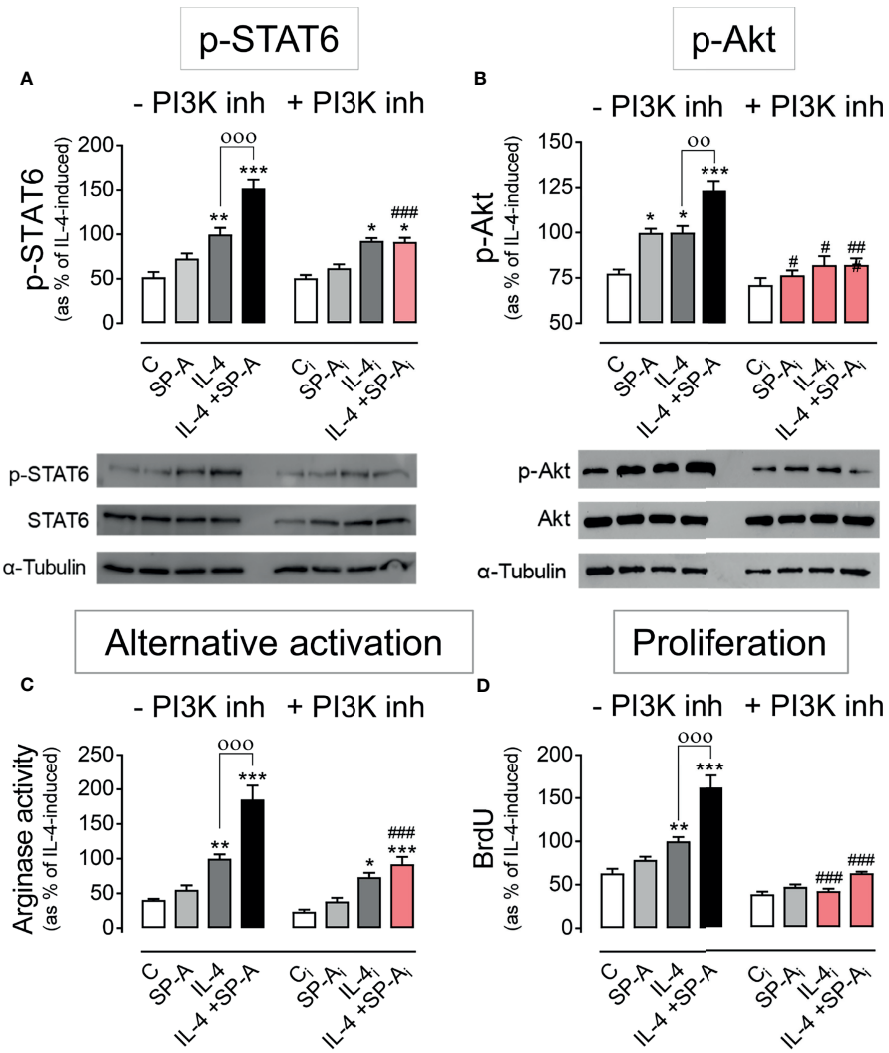

FIGURE 2 | PI3K inhibition abrogates SP-A effects on IL-4 signaling. Purified rat AMs were pretreated with 50 nM LY294002 (PI3K inhibitor) or vehicle (DMSO) for two hours. Subsequently, cells were stimulated with or without IL-4 (1 μg/ml) in the presence or absence of SP-A (100 μg/ml) and exposed to 10 μM BrdU for proliferation analysis. Quantification of **(A)** p-STAT6 (Tyr641) relative to total STAT6, **(B)** p-Akt (Ser473) relative to total Akt, **(C)** arginase activity, and **(D)** BrdU incorporation in the newly synthesized DNA of AMs. A representative Western blot for p-STAT6 and p-Akt is shown below each graph. The results are presented as means (± SEM) from three different cell cultures with at least three biological replicates. ANOVA followed by the Bonferroni multiple-comparison test was used. $^{*}p < 0.05$, $^{**}p < 0.01$, and $^{***}p < 0.001$ when compared with untreated macrophages. $^{oo}p < 0.01$ and $^{ooo}p < 0.001$ when SP-A+IL-4-treated macrophages were compared with IL-4-treated macrophages. $^{\#}p < 0.05$, $^{\#\#}p < 0.01$ and $^{\#\#\#}p < 0.001$ when the effect of PI3K inhibitor is compared with the same sample without inhibitor.

driven enhancement of both STAT6 and Akt phosphorylation in IL4-stimulated cells. The inhibition of PI3K nullified SP-A-driven enhancement of alternative activation and proliferation of IL4-stimulated alveolar macrophages (**Figures 2C, D**). However, only proliferation, but not alternative activation, was PI3K-dependent in macrophages treated with IL-4 alone. This is consistent with the fact that IL-4R signals *via* the JAK/STAT6 pathway induces robust alternative activation. Taken together, these results indicate that SP-A activates Myo18A/PI3K-dependent coordinated signaling pathways that amplify IL-4 actions.

Akt Activation Is Essential for SP-A and IL-4-Mediated Macrophage Proliferation

One of the best-characterized targets of PI3K is the Akt/mTORC signaling pathway (26). Upon PI3K activation, Akt is phosphorylated by PDK1 at Thr 308 and by mTORC2 at Ser 473. Maximal activation of Akt requires phosphorylation of Ser473 at the hydrophobic motif. We next evaluated whether the phosphorylation of Akt at Ser 473 induced by SP-A, IL-4, or both was dependent on mTORC2. **Figure 3A** shows that the increase in p-Akt (Ser473) elicited by SP-A, IL-4, and SP-A+IL-4 was completely suppressed by torin (inhibitor of mTORC1 and

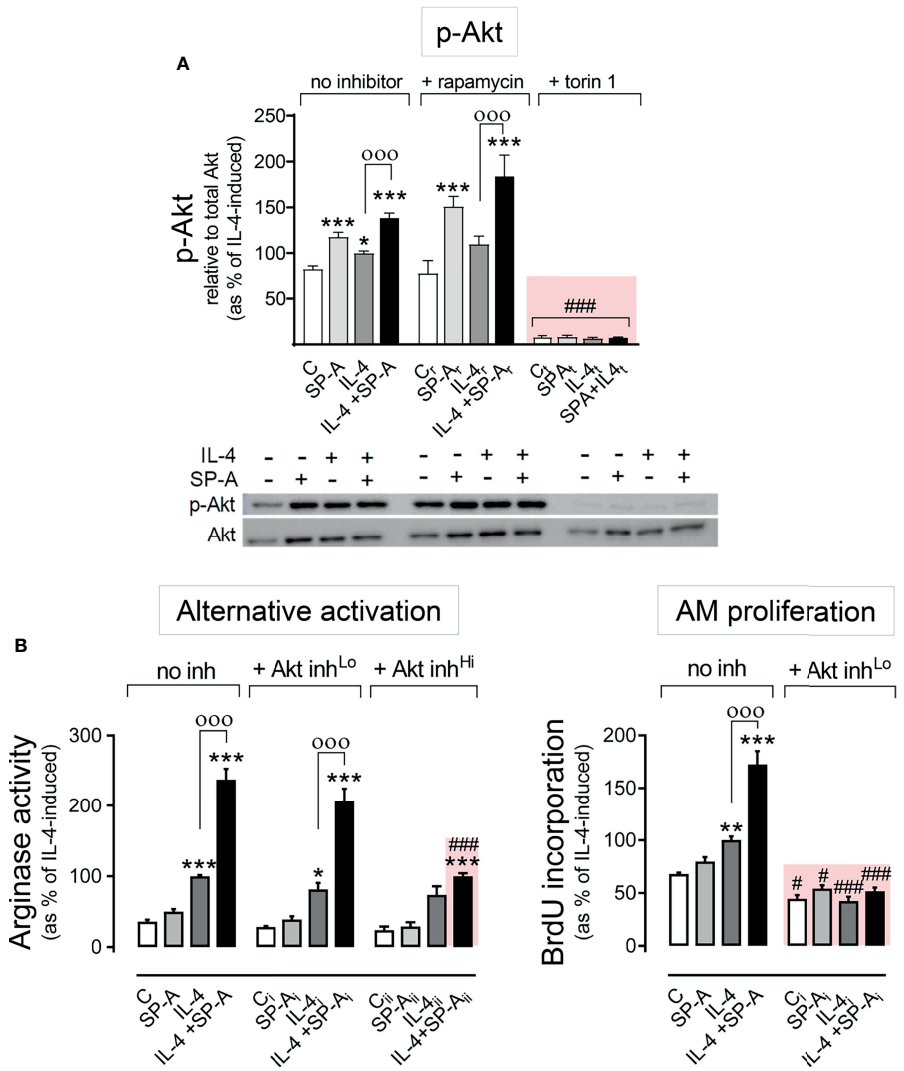

FIGURE 3 | SP-A and IL-4 induce Akt activation to enhance alternative activation and proliferation of AMs. **(A)** Purified rat AMs were pre-treated with 20 nM rapamycin, 100 nM torin 1, or vehicle for one hour. Cells were then stimulated with or without IL-4 (1 μg/ml) in the presence or absence of SP-A (100 μg/ml) 30 minutes, then Western blot for quantification of p-Akt (Ser473) relative to total Akt was performed. A representative Western blot image is shown below the graph. In **(B)** arginase activity and BrdU incorporation were measured in purified rat AMs pretreated with 25 nM (Lo), 100 nM (Hi) Akt inhibitor VIII, or vehicle for two hours, and then stimulated with or without IL-4 (1 μg/ml) and/or SP-A (100 μg/ml). The results are presented as means (± SEM) from three different cell cultures with at least three biological replicates. ANOVA followed by the Bonferroni multiple-comparison test was used. $^{*}p < 0.05$, $^{**}p < 0.01$, and $^{***}p < 0.001$ when compared with untreated macrophages. $^{ooo}p < 0.001$ when SP-A+IL-4-treated macrophages were compared with IL-4-treated macrophages. $^{\#}p < 0.05$ and $^{\#\#\#}p < 0.001$ when the effect of any inhibitor (Akt inhibitor VIII or torin1) is compared with the same sample without inhibitor.

mTORC2) but not by rapamycin (specific inhibitor of mTORC1), confirming that the complex responsible for phosphorylation of Akt at Ser473 was mTORC2.

To evaluate whether Akt affects the proliferation and alternative activation of alveolar macrophages stimulated with IL-4 and/or SP-A, we inhibited Akt activation with the Akt inhibitor VIII at concentrations of 25 or 100 nM (**Figure 3B**). We observed that 25 nM Akt inhibitor VIII drastically suppressed AM proliferation by IL-4 alone, which confirmed previous observations (15), and by IL-4 in combination with SP-A. In contrast, low concentrations of Akt inhibitor VIII did not affect arginase activity measured in alveolar macrophages stimulated with IL-4 or IL-4+SP-A (**Figure 3B**). Higher concentrations of Akt inhibitor VIII are needed to block arginase activity stimulated by IL-4+SP-A. These results demonstrate that while Akt activation is essential for macrophage proliferation, other signaling pathways, in addition to the PI3K/Akt pathway, are directly involved in signaling that promotes alternative activation of alveolar macrophages.

SP-A and IL-4 Inactivate GSK3α/β by Akt-Dependent Phosphorylation and Enhance mTORC1 Kinase Activity

The three best-established downstream targets of Akt are glycogen synthase kinase 3 (GSK3), forkhead box O family of transcription factors (FoxO), and mTORC 1 (26). We first analyzed whether IL-4 and/or SP-A affected the phosphorylation of GSK3αβ and FoxO3a in alveolar macrophages. Akt-dependent phosphorylation of the α and β subunits of GSK3 blocks the inhibitory actions of GSK3 on metabolism, proliferation, or cell survival (26). **Figure 4A** shows that SP-A, IL-4, and IL-4+SP-A (no additive effect) significantly increased phosphorylation of GSK3α and β subunits (in the residues Ser 21 and 9, respectively), which is consistent with the role of IL-4 and IL-4+SP-A in increasing macrophage proliferation. Inhibition of Akt suppressed GSK3 phosphorylation (data not shown). Regarding FoxO3a, a gene transcriptional activator also known as a tumor suppressor, we found that FoxO3a phosphorylation was not affected by IL-4 and/or SP-A stimulation of alveolar macrophages (**Supplementary Figure 2**).

We next analyzed whether IL-4 and/or SP-A affected mTORC1 activation, which promotes anabolic processes, cell growth, and proliferation (26) and enhances the expression of a subset of alternative activation markers in BMDM (13, 14). One of the main targets of mTORC1 activation is eukaryotic translation initiation factor 4E-binding protein 1 (4E-BP1), which is used as a canonical mTORC1 substrate. We evaluated phosphorylation of 4E-BP1 (**Figure 4B**) and found that the kinase activity of mTORC1 increased in the presence of SP-A, IL-4, and IL-4+SP-A. The activity of mTORC1 kinase was completely inhibited by rapamycin and torin 1 (**Figure 4B**).

Pharmacological Inhibition of mTORC1 suppresses IL-4- and IL-4+SP-A-Mediated Alternative Activation and Proliferation of Alveolar Macrophages

Figure 5A shows that mTORC1 was involved in IL-4- and IL-4 +SP-A-dependent alternative activation (synergistic effect),

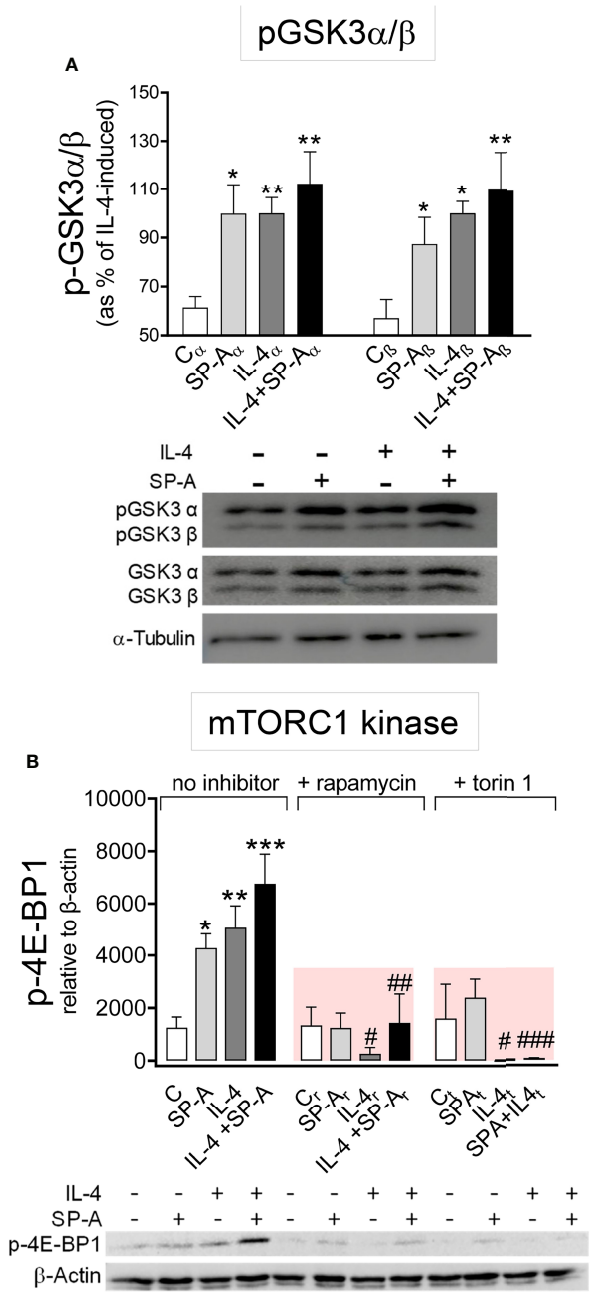

FIGURE 4 | SP-A and IL-4 enhance GSK3α/β phosphorylation and mTORC1 activation. **(A)** AMs were stimulated with or without IL-4 (1μg/ml) and/or SP-A (100 μg/ml) and phosphorylation of GSK3-α/β(Ser21/9) was measured. **(B)** Purified rat AMs were pretreated with 20 nM rapamycin, 100 nM torin 1, or vehicle (no inhibitor) for one hour. Cells were then stimulated with or without IL-4 (0.5 μg/ml) in the presence or absence of SP-A (40 μg/ml). p-4E-BP1(Ser65) relative to β-actin was quantified by Western blot. Representative Western blot analyses are shown below each graph. The results are presented as means (± SEM) from three different AM cultures with at least three biological replicates. ANOVA followed by the Bonferroni multiple-comparison test was used. $^{*}p < 0.05$, $^{**}p < 0.01$, and $^{***}p < 0.001$ when compared with untreated macrophages. $^{\#}p < 0.05$, $^{\#\#}p < 0.01$, and $^{\#\#\#}p < 0.001$ when the effect of either rapamycin or torin1 is compared with the same sample without inhibitor.

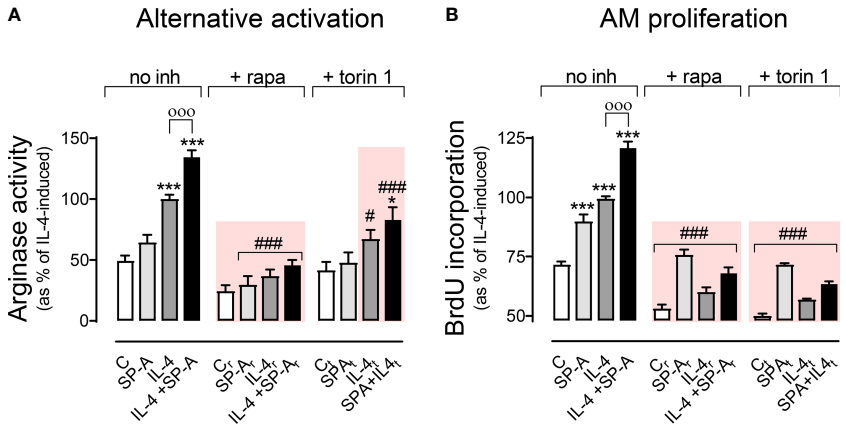

FIGURE 5 | Effect of pharmacological inhibition of mTORC1 on arginase activity and AM proliferation. Purified rat AMs were pretreated with 20 nM **(A)** or 5 nM **(B)** rapamycin, 100 nM **(A)** or 25nM **(B)** torin 1, or vehicle (DMSO) for one hour. Cells were then stimulated with or without IL-4 and/or SP-A and arginase activity **(A)** and AM proliferation **(B)** were measured. The results are presented as means (± SEM) from three different AM cultures with at least three biological replicates. ANOVA followed by the Bonferroni multiple-comparison test was used. *p < 0.05 and ***$p < 0.001$ when compared with untreated macrophages. $^{ooo}p < 0.001$ when SP-A+IL-4-treated macrophages were compared with IL-4-treated macrophages. $^{\#}p < 0.05$ and $^{\#\#\#}p < 0.001$ when the effect of either rapamycin or torin1 is compared with the same sample without inhibitor.

which was sensitive to torin and rapamycin. SP-A alone did not induce a significant increase in arginase activity. Regarding proliferation (**Figure 5B**), IL-4 and IL-4+SP-A (additive effect) induced proliferation dependent on mTORC1 (torin and rapamycin-sensitive). Taken together, these results suggest that the combined effects of IL-4 and SP-A on the mTORC1 and GSK3 branches of Akt signaling likely contribute to increased proliferation, and alternative activation of AMs.

SP-A Enhancement of IL-4-Dependent Macrophage Alternative Activation Also Requires PKCζ Activation

Atypical protein kinase Cζ (PKCζ) is another protein kinase activated through binding to phosphatidylinositol (3–5) trisphosphate in the plasma membrane and subsequent phosphorylation by PDK1. PKCζ-deficient T cells show reduced STAT6 phosphorylation in response to IL-4 stimulation (27). Accordingly, we analyzed the phosphorylation of PKCζ in alveolar macrophages stimulated with IL-4 and/or SP-A. **Figure 6A** shows that both SP-A and IL-4 induced PKCζ phosphorylation at Thr410, which was significantly increased when alveolar macrophages were stimulated by both factors. The PI3K inhibitor abrogated PKCζ phosphorylation induced by SP-A, IL-4, or SP-A+IL-4, confirming that this process depends on PI3K activation. We hypothesized that SP-A should activate the PI3K/PKCζ axis to enhance IL-4-dependent STAT6 phosphorylation and alternative activation of macrophages, since the SP-A-induced increase in STAT6 phosphorylation was blocked by the PI3K inhibitor (**Figure 2A**).

Figure 6B shows that PKCζ inhibition with the PKCζ pseudosubstrate prevented the increase of STAT6 phosphorylation induced by IL-4+SP-A, but not the increase induced by IL-4 alone. As a control experiment, we verified whether Akt was involved in the activation of STAT6 caused by IL-4 or IL-4+SP-A. **Supplementary Figure 3** shows that the production of p-STAT6 by AMs stimulated with IL-4 or IL-4+SP-A did not change in the presence of Akt inhibitor VIII.

Next, we studied the role of PKCζ in SP-A-mediated increase of alternative activation and proliferation of AMs stimulated with IL-4. We found that the PKCζ pseudosubstrate suppressed SP-A enhancement of IL-4-stimulated alternative activation (**Figure 6C**) but not IL-4- and IL-4+SP-A-induced macrophage proliferation (**Figure 6D**). Inhibition of PKCζ kinase activity did not modify IL-4-induced STAT6 phosphorylation (**Figure 6B**) or arginase activity (**Figure 6C**). Together, these results demonstrate that SP-A enhances IL-4-induced alternative activation of alveolar macrophages by sustaining a PI3K/PKCζ/STAT6 signaling axis.

To gain more insight into the functional consequences of cooperative PKCζ phosphorylation by IL-4 and SP-A (**Figure 6A**) for SP-A-mediated enhancement of IL-4-dependent STAT6 activation (**Figure 6B**), we analyzed translocation of PKCζ to the plasma membrane by confocal microscopy of AMs isolated from SP-A-deficient mice, stimulated with IL-4, SP-A, or both (**Figures 6E, F**). We found that IL-4 and SP-A significantly increased PKCζ translocation to the membrane. However, PKCζ appeared to redistribute to endosomes or the cytosol when AMs were stimulated with both agonists (**Figures 6E, F**). It is possible that IL-4+SP-A induces a faster translocation of PKCζ to the plasma membrane than that induced by IL-4 or SP-A alone, so we were unable to detect significant changes at selected times in our experiments. However, our results indicate changes in the cellular location of PKCζ when both agonists are present. On the other hand, it is known that following IL-4 stimulation, activated IL-4 receptors are preferentially associated with cortical endosomes, and there is a link between endocytosis and IL-4R signal transduction (28–30). To know whether SP-A, IL-4, or both agonists increase

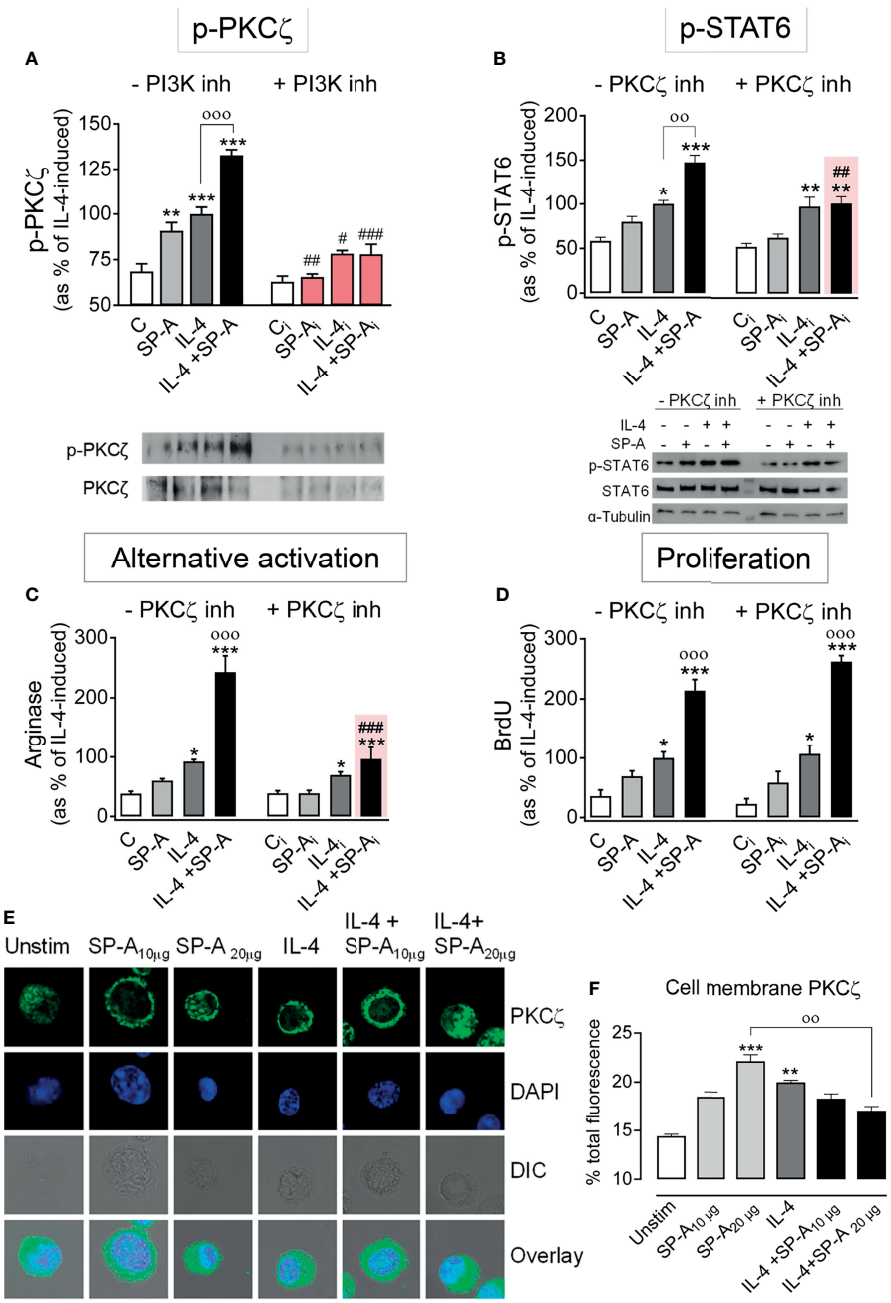

FIGURE 6 | SP-A enhancement of IL-4-induced p-STAT6 and arginase activity is mediated by PKCζ. **(A)** Purified rat AMs were pretreated with 50 nM LY294002 (PI3K inhibitor) or vehicle for two hours. Subsequently, cells were stimulated with or without IL-4 (1 μg/ml) in the presence or absence of SP-A (100 μg/ml). Then p-PKCζ (Thr410/403) relative to total PKCζ was quantified by Western blot. In **(B–D)** cells were pretreated with 30 μM of PKCζ pseudosubstrate inhibitor or vehicle for two hours. Subsequently, cells were stimulated with or without IL-4 (1 μg/ml) and/or SP-A (100 μg/ml). STAT6 phosphorylation relative to total STAT6 **(B)**, arginase activity **(C)**, and proliferation **(D)** of AMs were analyzed. Representative Western blot for p-PKCζ or p-STAT6 are shown below each graph. The results are presented as means (± SEM) from three different AM cultures with at least three biological replicates. **(E)** PKCζ plasma membrane localization after IL-4 and/or SP-A stimulation. Representative IF for PKCζ localization in AMs from SP-A$^{-/-}$ mice left untreated or treated with IL-4 (0.5 μg/ml) in the absence or presence of SP-A (10-20 μg/ml). Confocal images shown are representative of three independent experiments with similar results. Upper panels show PKCζ staining, middle panels show DAPI counterstaining of cell nuclei and differential interference contrast (DIC), lower panels show overlay. **(F)** Quantification of pixel density of cell-membrane PKCζ from total PKCζ values. Data are expressed as percentage ± SEM of three independent experiments with at least 20 cells per condition. Results were statistically analyzed by one-way ANOVA followed by the Bonferroni multiple-comparison test. $^{*}p < 0.05$, $^{**}p < 0.01$, and $^{***}p < 0.001$ when compared with untreated macrophages. $^{oo}p < 0.01$ and $^{ooo}p < 0.001$ when SP-A+IL-4-treated macrophages were compared with IL-4 or SP-A-treated macrophages. $^{\#}p < 0.05$, $^{\#\#}p < 0.01$ and $^{\#\#\#}p < 0.001$ when the effect of PI3K or PKCζ inhibitor is compared with the same sample without inhibitor.

redistribution of PKCζ to cortical/early endosomes, we determined co-localization of PKCζ and early endosome antigen 1 (EEA1) marker in AMs stimulated with or without these agonists. We found that SP-A, IL-4, and IL-4+SP-A significantly increased PKCζ/EEA1 co-localization, confirming redistribution of PKCζ to early endosomal membranes (**Supplementary Figure 4**).

SP-A and IL-4 Synergistically Increase Mitochondrial Respiration and Glycolysis in AMs

Metabolic changes in macrophages support and are closely related to the activated macrophage phenotype (31, 32). An increase in both glycolysis and mitochondrial respiration occurs in alternative activation of macrophages. mTORC1 and mTORC2 stimulate glycolysis, mitochondrial function, and induce an anabolic response to promote proliferation and survival (13, 31). Since we have shown that IL-4 and SP-A activate mTORC1 and mTORC2, our aim was to analyze whether the metabolic profile of macrophages stimulated with these agonists is affected. Therefore, we investigate the glycolysis rate and mitochondrial respiration of alveolar stimulated macrophages cultured in RPMI containing 5 mM glucose and 2 mM glutamine, using the mitochondrial stress test (Seahorse XFe24). Measurements of oxygen consumption rate (OCR) were achieved by the combined use of oligomycin (inhibitor of mitochondrial ATP synthase), FCCP (protonophore that uncouples mitochondrial respiration from ATP synthesis), and rotenone plus antimycin A (which blocks mitochondrial respiration by inhibiting complexes I and III, respectively), as previously described (33).

Alveolar macrophages stimulated with IL-4 and SP-A exhibited significantly higher basal OCR than macrophages not stimulated or stimulated with each agonist separately. Furthermore, macrophages stimulated with IL-4+SP-A showed a higher level of oligomycin-sensitive respiration, which would be associated with a higher production of ATP in the mitochondria. Respiratory capacity after administration of FCCP was also significantly higher in macrophages stimulated with IL-4+SP-A compared to macrophages not stimulated or stimulated separately with each agonist (**Figures 7A, B**).

The rate of glycolysis, estimated from ECAR values (a proxy for the rate of lactate formation), was also significantly higher in macrophages stimulated with IL-4+SP-A than in those unstimulated or stimulated with IL-4 or SP-A alone. Furthermore, glycolytic capacity, determined after inhibition of mitochondrial ATP synthesis by oligomycin, was also significantly higher in macrophages stimulated with IL-4+SP-A than in those unstimulated or stimulated separately with IL-4 or SP-A. The ability of AMs (stimulated and unstimulated) to induce glycolysis after inhibition of mitochondrial ATP production by oligomycin indicated that alveolar macrophages are not entirely dependent on mitochondria for cellular energy, despite the fact that their natural energy source *in vivo* must be oxidative degradation of surfactant phospholipids (32) (**Figures 7A, B**).

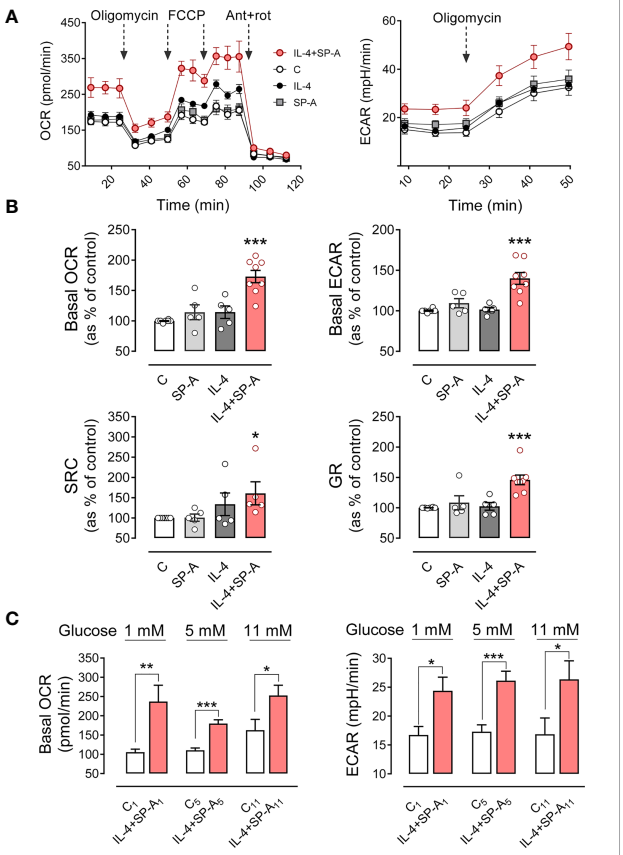

FIGURE 7 | SP-A and IL-4 synergistically increase mitochondrial respiration and glycolysis in AMs. The effect of IL-4 (1μg/ml) and/or SP-A (100 μg/ml) on the oxygen consumption rate (OCR) and the extracellular acidification rate (ECAR) in AM cultures was measured using Seahorse XFe24. **(A)** (left) Alveolar macrophages were treated sequentially with 1 μM oligomycin (ATP synthase inhibitor), 1 μM FCCP (uncoupler of oxidative phosphorylation in mitochondria), and 1 μM rotenone/1 μM antimycin A (inhibitors of mitochondrial complex I and III, respectively) to measure OCR under basal conditions and under mitochondrial stress. (Right) Glycolysis, measured as ECAR, in basal conditions and with oligomycin treatment to evaluate glycolysis intensification in response to mitochondrial inhibition. **(B)** Bar graphs to quantify the effect of IL-4 and/or SP-A on (left) basal OCR and spare respiratory capacity and (right) basal ECAR and glycolytic reserve (increase of ECAR after oligomycin addition). **(C)** Effect of glucose concentration in the culture medium on basal mitochondrial respiration and glycolysis induced by IL-4+SP-A. Data are mean ± SEM from five to eight independent experiments with three to five biological replicates. ANOVA followed by the Bonferroni multiple-comparison test **(A, B)** or Student's t-test **(C)** was used. *$p < 0.05$, **$p < 0.01$, and ***$p < 0.001$ when compared with untreated macrophages.

All these parameters indicate that IL-4 and SP-A synergically increased the metabolic activity of alveolar macrophages. As a control, the glucose transport was measured by determining the uptake of the fluorescently labeled deoxyglucose analog 2-NBDG (25) by AMs in the presence or absence of SP-A, IL-4, and both. No differences in glucose transport were observed between stimulated and unstimulated macrophages (**Supplementary Figure 5**), suggesting that there is no upregulation of primary glucose transporter in macrophages (GLUT1) (34) by IL-4.

The level of glucose in alveolar fluid is strongly regulated and is about 12 times lower than the blood glucose concentration (32, 35). Since AMs are exposed *in vivo* to a unique environment with minimal glucose availability, the bioenergetics profile of these cells was also performed in RPMI containing either very low (1mM) or high (11 mM) glucose concentrations. We found similar results regarding the synergistic action of IL-4 and SP-A on mitochondrial respiration and glycolysis (**Figure 7C**), although the increment in mitochondrial respiration of AMs stimulated with IL-4+SP-A decreased with increasing glucose concentration (**Figure 7C**).

Importantly, IL-4 alone did not induce any increase in mitochondrial respiration or glycolysis at glucose concentrations of 1 or 5 mM. However, at a higher glucose concentration of 11 mM, IL-4 alone significantly increased basal OCR and showed a tendency to increase basal ECAR. Both values were further increased in the presence of IL-4+SP-A, confirming that SP-A significantly boosted IL-4-mediated actions in macrophages (**Supplementary Figure 6A**). The bioenergetics profile of cells, defined as the ratio between basal OCR and basal ECAR, was measured in unstimulated and IL-4+SP-A-stimulated macrophages at various glucose concentrations. **Supplementary Figure 6B** shows that the OCR/ECAR ratio in IL-4+SP-A-stimulated compared to unstimulated macrophages was significantly higher at glucose concentrations of 1 mM, but not at glucose concentrations of 5 or 11 mM, indicating that, at low glucose concentrations, IL-4+SP-A notably increased mitochondrial respiration (OCR) for energy production, although macrophages also showed increased anaerobic glycolysis (ECAR) (**Figure 6C**).

DISCUSSION

Alveolar macrophages are tissue-resident immune cells that colonize the lung around the time of birth and can self-maintain for extended periods in an adult organism. Due to their localization in the airspace of the alveoli, these cells continuously patrol the alveoli and maintain alveolar homeostasis by efficiently removing pathogens, apoptotic cells, and pulmonary surfactant. Under inflammatory conditions such as active bacterial or viral infections, TLR signals and IFN-γ initiate a functional switch in AMs to a pro-inflammatory phenotype. Then, following stimulation with type 2 cytokines (IL-4/IL-3), the macrophage activation state changes to a tissue repair phenotype M(IL-4) (2, 11, 36). This process is driven and amplified by pulmonary surfactant protein A and the uptake of apoptotic cells (4, 37), and it is important to restore tissue homeostasis after injury. However, it can lead to allergy and fibrosis if not properly regulated (1, 2, 11).

In this study we focus on the alternative activation and cell cycling of alveolar macrophages stimulated by IL-4 alone and in combination with SP-A, at SP-A concentrations within the ranges found in the alveolar fluid of rat and human lungs (38, 39). We analyze the signaling pathways by which IL-4 and SP-A synergistically increase arginase-1 activity and cell proliferation (4) and determine the influence of these two factors on the metabolic profile of AMs. **Figure 8** summarizes the intracellular signaling pathways of IL-4, SP-A, and IL-4+SP-A analyzed in this study. By examining the phosphorylation of key transcription factors and regulatory enzymes and using pharmacological inhibitors, we found that SP-A activates coordinated PI3K-dependent signaling pathways that amplify the actions of IL-4 in alveolar macrophages. SP-A alone activates Akt, mTORC1, and PKCζ, and inactivates GSK3α/β by phosphorylation, but cannot activate arginase-1 activity or AM proliferation. Our results indicate that the combined effects of IL-4 and SP-A on the mTORC1 and GSK3 branches of the PI3K-Akt signaling axis contribute to increased proliferation and alternative activation of AMs. On the other hand, IL-4+SP-A-mediated PKCζ signaling appears to intersect PI3K activation with STAT6 phosphorylation, which increases alternative activation of IL-4-stimulated macrophages (**Figure 8**).

PKCζ is highly expressed in the lung (40), where it plays a critical role in several biological processes, including cell polarity and signaling. Regarding PKCζ signaling, in this study we found that IL-4 and SP-A synergistically increase (i) phosphorylation of PKCζ at $Thr^{410/403}$ in a PI3K-dependent manner; ii) phosphorylation of STAT6 in a PI3K- and PKCζ-dependent manner; and iii) alternative activation, but not proliferation, of AMs in a PI3K- and PKCζ-dependent manner. Macrophages stimulated with SP-A alone show increased PKCζ phosphorylation, as previously reported (17), but not STAT6 phosphorylation. On the other hand, macrophages stimulated with IL-4 alone show increased PKCζ phosphorylation, but STAT6 phosphorylation and macrophage alternative activation were not affected by pharmacological inhibition of PKCζ. These results contrast with those obtained for lymphocytes (27, 41, 42), where the loss of PKCζ impaired Jak1 activation, STAT6 phosphorylation, and secretion of Th2 cytokines *in vitro* and *in vivo*, indicating that PKCζ is necessary for Th2 differentiation (27, 41, 42). $PKC\zeta^{-/-}$ mice show dramatic inhibition of ovalbumin-induced allergic airway disease (40), strongly suggesting that PKCζ is critical for IL-4 signaling in the lung. In this study we show that SP-A, *via* PKCζ, increased IL-4-dependent phosphorylation of STAT6, essential for downstream targets of IL-4 signaling.

The catalytic potential of PKCζ, and other PKCs, is dictated by 'priming' phosphorylation in their catalytic domains, which are largely conserved (40, 43). But, as in other members of the PKC family, phosphorylated enzymes are maintained in a self-inhibited conformation through the interaction of their inhibitory pseudosubstrate domain with their catalytic domain (40, 43). Activation of PKCζ and other PKCs involves their binding to the membrane surface (43). For PKCζ, membrane binding occurs through two mechanisms that work in tandem: i) binding of the scaffold protein Par6 (bound to the N-terminal PB1 domain of PKCζ) to CDC42/Crumbs (bound to membrane) (43, 44), and ii) electrostatic interaction between the polybasic region of the PKCζ inhibitory pseudosubstrate with anionic phospholipids (PI4P and PI4,5P2) present in the plasma membrane and endosomal membranes (44). Binding of PKCζ to the membrane surface facilitates conformational changes in the protein that lead to dissociation of the pseudosubstrate from the catalytic domain and trigger PKCζ kinase activity (43, 44). In this

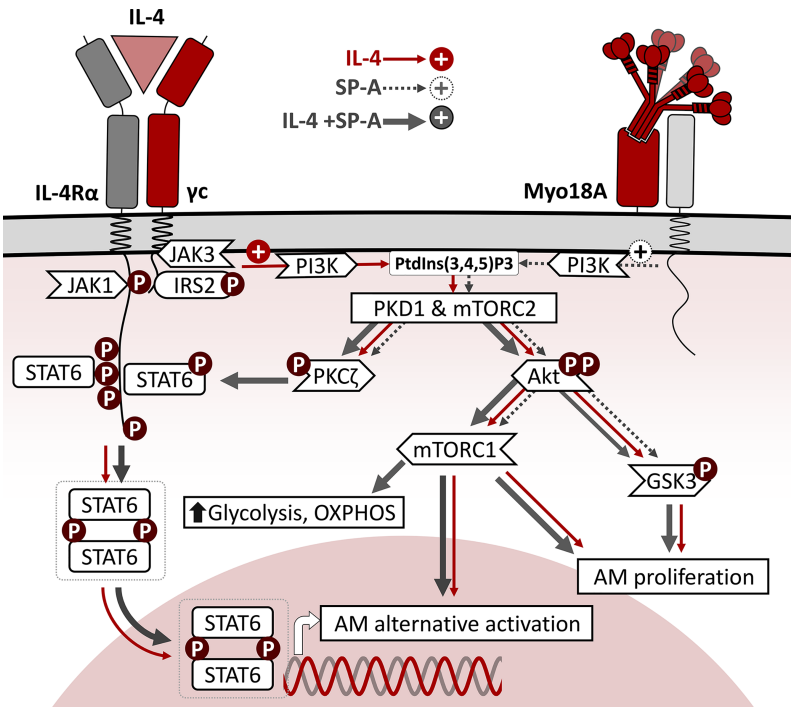

FIGURE 8 | Schematic representation of intracellular signaling pathways of IL-4, SP-A, and IL-4+SP-A in alveolar macrophages. The binding of IL-4 to the ectodomains of IL-4Rα and γc chains results in phosphorylation of critical tyrosine residues in IL-4Rα cytosolic domain, which serves as docking sites for SH domains of intracellular signaling molecules such as STAT6 and IRS2. Once STAT6 is activated by phosphorylation, they homodimerize *via* their Src homology 2 domains and translocate to the nucleus, where they bind to specific DNA sequences that induce expression of genes associated with alternative activation. In parallel, efficient tyrosine phosphorylation of IRS2 triggers the PI3K/Akt pathway, associated to the plasma and/or endosomal membranes. This signaling pathway activates cell proliferation and AM alternative activation. SP-A, *via* the Myo18A receptor, activates PI3K, Akt, mTORC1, and PKCζ, and inactivates GSK3α/β by phosphorylation, but cannot activate arginase-1 activity or AM proliferation. The combined effects of IL-4 and SP-A on the mTORC1 and GSK3 branches of PI3K-Akt signaling contribute to increased AM proliferation and alternative activation. Consistent with mTORC1 activation, SP-A+IL-4 synergistically increased mitochondrial respiration and glycolysis in AMs. In addition, SP-A+IL-4-mediated PKCζ signaling seems to intersect PI3K activation with STAT6 phosphorylation, increasing alternative activation of IL-4-stimulated macrophages.

study, we analyzed the effect of SP-A and/or IL-4 on the recruitment of PKCζ to the plasma membrane and endosomal membranes using confocal microscopy. Macrophages stimulated with IL-4 or SP-A alone show a significant increase in translocation of PKCζ to the plasma membrane and cortical/early endosomes. Interestingly, when macrophages were stimulated with IL-4+SP-A, PKCζ appeared to redistribute to early endosomes or the cytosol, suggesting a rapid alteration of the cell location of PKCζ in the presence of both agonists. It is possible that the presence of both agonists induces a faster internalization of the IL-4Rα receptor (28–30) and the movement of PKCζ from the plasma membrane to early endosomes. The presence of SP-A would improve the phagocytic and endocytic capacity of AMs (18, 45). SP-A uptake by AMs precede the initiation of SP-A signaling (18). It remains to be determined whether SP-A could affect other factors that regulate the activity and location of PKCζ. A potential candidate is the soluble lipid mediator sphingosine-1-phosphate (S1P), which is an allosteric activator of PKCζ catalytic activity (46).

Following IL-4 stimulation, IL-4Rα/γc is thought to be internalized, leading to increased receptor density in endosomal membranes (28, 29). Whether IL-4Rα/γc endocytosis is essential for downstream signaling transduction is still debated, but Bai et al. (30) recently demonstrated that endocytosis of IL-4Rα/γc is essential for Akt activation, but not STAT6 activation. Macrophage stimulation by both agonists, IL-4 and SP-A, converges on activation of the PI3K-Akt signaling pathway. In this study, we found that an increase in Akt phosphorylation was elicited by SP-A, IL-4 or SP-A+IL-4 macrophage stimulation and was completely suppressed by PI3K inhibitor and torin (inhibitor of mTORC1 and 2) but not by rapamycin (specific inhibitor of mTORC1).

The phosphorylation of GSK3, FOXO3, and the activation of mTORC1, which are downstream targets of Akt (26), were also evaluated. Consistent with the activation of Akt, we show that SP-A, IL-4, and IL-4+SP-A significantly increased phosphorylation of GSK3α and β subunits, which results in the inhibition of their kinase activity. GSK3 is a soluble monomeric enzyme that shows constitutively high basal kinase activity in resting cells, which phosphorylates and inactivates several proteins involved in proliferation (e.g., the transcription factors c-Myc and c-JUN), survival (e.g., MCL-1 that belongs to the Bcl-2 family), or

metabolism (e.g., glycogen synthase) (26, 47, 48). Akt inhibits GSK3 by phosphorylation of serine Ser21 at GSK3α and Ser9 at GSK3β, activating cell metabolism, proliferation, and survival (26, 47, 48). This suggests that GSK3 phosphorylation induced by IL-4 or IL-4 +SP-A macrophage stimulation might be involved in macrophage proliferation since Akt inhibitor VIII drastically suppressed macrophage proliferation induced by IL-4 alone and IL-4+SP-A as well as the phosphorylation of GSK3. Evidence supports that GSK3 phosphorylation is involved in the resolution of inflammation, tissue repair, and macrophage proliferation (47, 48). On the contrary, active GSK3 suppresses STAT3/6 phosphorylation to promote classical macrophage activation (49). Regarding FoxO3a, we did not find a significant effect of SP-A and/or IL-4 on FoxO3a phosphorylation, a transcription factor also involved in cell proliferation (26).

Another consequence of Akt activation in macrophages stimulated with SP-A, IL-4, and IL-4+SP-A was a significant increase in mTORC1 activity. The activity of mTORC1, measured by phosphorylation of 4E-BP1, was completely inhibited by rapamycin and torin1. The ability of IL-4 and IL-4 +SP-A to increase arginase activity and macrophage proliferation was sensitive to torin and rapamycin, and therefore, dependent on mTORC1 and mTORC2. According to these results, the PI3K/Akt/mTORC1 axis was reported to be involved in IL-4-induced alternative activation and proliferation of BMDM (13, 14). Increased alternative macrophage activation is reported to be mediated by increased acetylation of histones that controls upregulation of alternative activation genes (*Arg*1 and *Retnla*) and genes involved in proliferation, DNA replication (13, 50), and glycolysis (50, 51). Histone acetylation depends on the levels of acetyl-CoA in the cytosol derived from glucose and produced by the cytosolic enzyme ATP citrate lyase (Acly) (51). The Akt-mTORC1 pathway is involved in the regulation of Acly: Akt phosphorylates and activates Acly (52), and mTORC1 increases the expression of Acly in macrophages (13). Cultured Acly-deficient macrophages show decreased IL-4 response, which may be explained by lower acetylation of histone 3 lysine 27 (53).

The metabolic profile of *in vitro* cultured alveolar macrophages, stimulated with IL-4+SP-A but not with SP-A or IL-4 alone, is consistent with IL-4+SP-A-induced cooperative activation of mTORC1 and mTORC2, which play a prominent role in increasing glycolysis and anabolic processes for cell growth and proliferation (31, 54, 55). We found that alveolar macrophages exhibited significantly higher mitochondrial respiration (basal OCR values) when cells were stimulated with both IL-4 and SP-A but not when stimulated with each agonist separately at 5 mM glucose. Likewise, the rate of anaerobic glycolysis (ECAR values, as a proxy for the rate of lactate formation) was significantly higher in macrophages stimulated with IL-4+SP-A than in those not stimulated or stimulated with IL-4 or SP-A separately. Therefore, IL-4 and SP-A act synergistically to increase mitochondrial respiration (required to produce energy for biosynthetic reactions and proliferation) and the glycolysis pathway, which provides intermediate metabolites for the pentose phosphate pathway, glycosylation reactions and synthesis of key biomass constituents, including serine, glycine, glycerol-3-P, and acetyl-CoA for lipid synthesis (56).

An important limitation of these studies is that *in vitro* studies cannot reproduce the unique environment in which AMs reside, which is rich in lipids but very poor in glucose and amino acids (32, 35). Since glucose levels can influence the expression of Acly (57), the metabolic profile of AMs was also carried out with RPMI supplemented with glutamine and very low (1mM) or high (11 mM) glucose concentrations. Regardless of glucose concentration, IL-4 and SP-A acted synergistically to increase mitochondrial respiration and glycolysis, indicating the importance of SP-A in driving IL-4-mediated metabolic reprogramming in macrophages. Interestingly, at the highest glucose concentration (11 mM), but not at glucose concentrations of 5 or 1 mM, IL-4 alone significantly increased basal OCR and showed a tendency to increase basal ECAR, indicating the influence of the medium's glucose concentration on the response of AMs to IL-4.

In summary, this study provides a novel mechanism for the action of SP-A on IL-4-dependent signal transduction underlying macrophage repair responses (**Figure 8**). Although IL-4-activated macrophages have recently emerged as important players in homeostatic processes, chronic respiratory diseases such as fibrosis, asthma, and allergy are associated with a dysregulated type 2 response (1, 2, 11). The pro-M(IL-4) effects of SP-A reported here and in (4) contrast with reports that associate SP-A with protection in asthma and fibrosis (58–60). However, in addition to promoting IL-4-dependent activation and proliferation of alveolar macrophages, the anti-inflammatory and protective properties of SP-A (7–9, 60) may suppress the strong inflammatory responses that are responsible for more severe asthma and fibrosis. Type 2 cytokines are also important regulators of type 1- and TH17-driven inflammatory responses. Thus, several studies have revealed that blocking type 2 cytokines can dysregulate this cross-regulatory mechanism and promote type 1- and TH17-driven inflammation (1, 61). However, dual blockade of IL-13 and IFNγ leads to a marked reduction in fibrosis and eliminates the type 1 rebound inflammation and associated damage (62). Moreover, inhibition of PI3K/Akt/mTOR and TLR4/MyD88/NF-κB signaling with targeted molecules can attenuate pathological mechanisms of asthma and play an important role in protecting airways against allergic response and inflammation pathology (63). The signaling events that drive the SP-A-dependent amplification of IL-4 effects on alveolar macrophages may aid in the development of new approaches to control lung diseases caused by exaggerated repair responses.

DATA AVAILABILITY STATEMENT

The raw data supporting the conclusions of this article will be made available by the authors, without undue reservation.

ETHICS STATEMENT

The animal study was reviewed and approved by Local ethics committee of Complutense University of Madrid and Autonomous Community of Madrid (Spain).

AUTHOR CONTRIBUTIONS

Conceptualization, BG-F, CM, CS, and CC. Methodology and Investigation, BG-F, CM, CM-F, and CS. Formal analysis, all authors. Writing—original draft preparation, BG-F and CM. Writing—review and editing, CC. Supervision, CC. Project administration, CC. Funding acquisition for this study, CC. All authors read and agreed to the published version of the manuscript.

FUNDING

This study was supported by the Spanish Ministry of Science, Innovation and and Universities through Grants SAF2015-65307-R and RTI2018-094355-B-I00 to CC.

ACKNOWLEDGMENTS

We thank the animal facility of the Faculty of Biology and the Cytometry and Confocal Microscopy Unit of the Complutense University of Madrid for their excellent technical support. We also thank the Cell Culture Center of the Margarita Salas-Biological Research Center, CSIC, for facilitating the use of the Seahorse XFe24 device and for providing technical support.

SUPPLEMENTARY MATERIAL

The Supplementary Material for this article can be found online at: https://www.frontiersin.org/articles/10.3389/fimmu.2022.860262/full#supplementary-material

REFERENCES

1. Gieseck RL, Wilson MS, Wynn TA. Type 2 Immunity in Tissue Repair and Fibrosis. *Nat Rev Immunol* (2018) 18:62–76. doi: 10.1038/nri.2017.90
2. Puttur F, Gregory LG, Lloyd CM. Airway Macrophages as the Guardians of Tissue Repair in the Lung. *Immunol Cell Biol* (2019) 97:246–57. doi: 10.1111/imcb.12235
3. Chen F, Liu Z, Wu W, Rozo C, Bowdridge S, Millman A, et al. An Essential Role for T H 2-Type Responses in Limiting Acute Tissue Damage During Experimental Helminth Infection. *Nat Med* (2012) 18:260–6. doi: 10.1038/nm.2628
4. Minutti CM, Jackson-Jones LH, García-Fojeda B, Knipper JA, Sutherland TE, Logan N, et al. Local Amplifiers of IL-4Ra-Mediated Macrophage Activation Promote Repair in Lung and Liver. *Science* (2017) 356:1076–80. doi: 10.1126/science.aaj2067
5. Minutti CM, Knipper JA, Allen JE, Zaiss DMW. Tissue-Specific Contribution of Macrophages to Wound Healing. *Semin Cell Dev Biol* (2017) 61:3–11. doi: 10.1016/j.semcdb.2016.08.006
6. Jenkins SJ, Ruckerl D, Cook PC, Jones LH, Finkelman FD, van Rooijen N, et al. Local Macrophage Proliferation, Rather Than Recruitment From the Blood, is a Signature of T H2 Inflammation. *Science* (2011) 332:1284–8. doi: 10.1126/science.1204351
7. Casals C, García-Fojeda B, Minutti CM. Soluble Defense Collagens: Sweeping Up Immune Threats. *Mol Immunol* (2019) 112:291–304. doi: 10.1016/j.molimm.2019.06.007
8. Casals C, Campanero-Rhodes MA, García-Fojeda B, Solís D. The Role of Collectins and Galectins in Lung Innate Immune Defense. *Front Immunol* (2018) 9:1998. doi: 10.3389/fimmu.2018.01998
9. Nathan N, Taytard J, Duquesnoy P, Thouvenin G, Corvol H, Amselem S, et al. Surfactant Protein A: A Key Player in Lung Homeostasis. *Int J Biochem Cell Biol* (2016) 81:151–5. doi: 10.1016/j.biocel.2016.11.003
10. Casals C, Cañadas O. Role of Lipid Ordered/Disordered Phase Coexistence in Pulmonary Surfactant Function. *Biochim Biophys Acta - Biomembr* (2012) 1818:2550–62. doi: 10.1016/j.bbamem.2012.05.024
11. van Dyken SJ, Locksley RM. Interleukin-4-and Interleukin-13-Mediated Alternatively Activated Macrophages: Roles in Homeostasis and Disease. *Annu Rev Immunol* (2013) 31:317–43. doi: 10.1146/annurev-immunol-032712-095906
12. Junttila IS. Tuning the Cytokine Responses: An Update on Interleukin (IL)-4 and IL-13 Receptor Complexes. *Front Immunol* (2018) 9:888. doi: 10.3389/fimmu.2018.00888
13. Covarrubias AJ, Aksoylar HI, Yu J, Snyder NW, Worth AJ, Iyer SS, et al. Akt-Mtorc1 Signaling Regulates Acly to Integrate Metabolic Input to Control of Macrophage Activation. *eLife* (2016) 5:e11612. doi: 10.7554/eLife.11612
14. Byles V, Covarrubias AJ, Ben-Sahra I, Lamming DW, Sabatini DM, Manning BD, et al. The TSC-mTOR Pathway Regulates Macrophage Polarization. *Nat Commun* (2013) 4:2834. doi: 10.1038/ncomms3834
15. Rückerl D, Jenkins SJ, Laqtom NN, Gallagher IJ, Sutherland TE, Duncan S, et al. Induction of IL-4rα-Dependent microRNAs Identifies PI3K/Akt Signaling as Essential for IL-4-Driven Murine Macrophage Proliferation *In Vivo*. *Blood* (2012) 120:2307–16. doi: 10.1182/blood-2012-02-408252
16. Beharka AA, Crowther JE, McCormack FX, Denning GM, Lees J, Tibesar E, et al. Pulmonary Surfactant Protein A Activates a Phosphatidylinositol 3-Kinase/Calcium Signal Transduction Pathway in Human Macrophages: Participation in the Up-Regulation of Mannose Receptor Activity. *J Immunol* (2005) 175:2227–36. doi: 10.4049/jimmunol.175.4.2227
17. Moulakakis C, Adam S, Seitzer U, Schromm AB, Leitges M, Stamme C. Surfactant Protein A Activation of Atypical Protein Kinase C ζ in Iκb-α-Dependent Anti-Inflammatory Immune Regulation. *J Immunol* (2007) 179:4480–91. doi: 10.4049/jimmunol.179.7.4480
18. Moulakakis C, Stamme C. Role of Clathrin-Mediated Endocytosis of Surfactant Protein a by Alveolar Macrophages in Intracellular Signaling. *Am J Physiol Lung Cell Mol Physiol* (2009) 296:L430–41. doi: 10.1152/ajplung.90458.2008
19. Minutti CM, García-Fojeda B, Sáenz A, de las Casas-Engel M, Guillamat-Prats R, de Lorenzo A, et al. Surfactant Protein A Prevents IFN-γ/IFN-γ Receptor Interaction and Attenuates Classical Activation of Human Alveolar Macrophages. *J Immunol* (2016) 197:590–8. doi: 10.4049/jimmunol.1501032
20. Coya JM, Akinbi HT, Sáenz A, Yang L, Weaver TE, Casals C. Natural Anti-Infective Pulmonary Proteins: *In Vivo* Cooperative Action of Surfactant Protein SP-A and the Lung Antimicrobial Peptide SP-B N. *J Immunol* (2015) 195:1628–36. doi: 10.4049/jimmunol.1500778
21. García-Verdugo I, Sánchez-Barbero F, Bosch FU, Steinhilber W, Casals C. Effect of Hydroxylation and N187-Linked Glycosylation on Molecular and Functional Properties of Recombinant Human Surfactant Protein A. *Biochemistry* (2003) 42:9532–42. doi: 10.1021/bi0347196
22. Sánchez-Barbero F, Rivas G, Steinhilber W, Casals C. Structural and Functional Differences Among Human Surfactant Proteins SP-A1, SP-A2 and Co-Expressed SP-A1/SP-A2: Role of Supratrimeric Oligomerization. *Biochem J* (2007) 406:479–89. doi: 10.1042/BJ20070275
23. Sánchez-Barbero F, Strassner J, García-Cañero R, Steinhilber W, Casals C. Role of the Degree of Oligomerization in the Structure and Function of Human Surfactant Protein A. *J Biol Chem* (2005) 280:7659–70. doi: 10.1074/jbc.M410266200
24. Freundt K, Herzmann C, Biedziak D, Scheffzük C, Gaede KI, Stamme C. Surfactant Protein A Enhances the Degradation of LPS-Induced TLR4 in Primary Alveolar Macrophages Involving Rab7, β-Arrestin2, and Mtorc1. *Infect Immun* (2022) 90:e0025021. doi: 10.1128/IAI.00250-21
25. Zou C, Wang Y, Shen Z. 2-NBDG as a Fluorescent Indicator for Direct Glucose Uptake Measurement. *J Biochem Biophys Methods* (2005) 64:207–15. doi: 10.1016/j.jbbm.2005.08.001
26. Manning BD, Toker A. AKT/PKB Signaling: Navigating the Network. *Cell* (2017) 169:381–405. doi: 10.1016/j.cell.2017.04.001
27. Diaz-Meco MT, Moscat J. The Atypical PKCs in Inflammation: NF-κB and Beyond. *Immunol Rev* (2012) 246:154–67. doi: 10.1111/j.1600-065X.2012.01093.x

28. Gandhi H, Worch R, Kurgonaite K, Hintersteiner M, Schwille P, Bökel C, et al. Dynamics and Interaction of Interleukin-4 Receptor Subunits in Living Cells. *Biophys J* (2014) 107:2515–27. doi: 10.1016/j.bpj.2014.07.077
29. Kurgonaite K, Gandhi H, Kurth T, Pautot S, Schwille P, Weidemann T, et al. Essential Role of Endocytosis for Interleukin-4-Receptor-Mediated JAK/STAT Signalling. *J Cell Sci* (2015) 128:3781–95. doi: 10.1242/jcs.170969
30. Bai JY, Li Y, Xue GH, Li KR, Zheng YF, Zhang ZQ, et al. Requirement of Gαi1 and Gαi3 in Interleukin-4-Induced Signaling, Macrophage M2 Polarization and Allergic Asthma Response. *Theranostics* (2021) 11:4894–909. doi: 10.7150/thno.56383
31. Jones RG, Pearce EJ. MenTORing Immunity: mTOR Signaling in the Development and Function of Tissue-Resident Immune Cells. *Immunity* (2017) 46:730–42. doi: 10.1016/j.immuni.2017.04.028
32. Ogger PP, Byrne AJ. Macrophage Metabolic Reprogramming During Chronic Lung Disease. *Mucosal Immunol* (2021) 14:282–95. doi: 10.1038/s41385-020-00356-5
33. Brand MD, Nicholls DG. Assessing Mitochondrial Dysfunction in Cells. *Biochem J* (2011) 435:297–312. doi: 10.1042/BJ20110162
34. Freemerman AJ, Johnson AR, Sacks GN, Milner JJ, Kirk EL, Troester MA, et al. Metabolic Reprogramming of Macrophages: Glucose Transporter 1 (GLUT1)-Mediated Glucose Metabolism Drives a Proinflammatory Phenotype. *J Biol Chem* (2014) 289:7884–96. doi: 10.1074/jbc.M113.522037
35. Pezzulo AA, Gutiérrez J, Duschner KS, McConnell KS, Taft PJ, Ernst SE, et al. Glucose Depletion in the Airway Surface Liquid is Essential for Sterility of the Airways. *PloS One* (2011) 6:e16166. doi: 10.1371/journal.pone.0016166
36. Guilliams M, Svedberg FR. Does Tissue Imprinting Restrict Macrophage Plasticity? *Nat Immunol* (2021) 22:118–27. doi: 10.1038/s41590-020-00849-2
37. Bosurgi L, Cao YG, Cabeza-Cabrerizo M, Tucci A, Hughes LD, Kong Y, et al. Macrophage Function in Tissue Repair and Remodeling Requires IL-4 or IL-13 With Apoptotic Cells. *Science* (2017) 356:1072–6. doi: 10.1126/science.aai8132
38. Wright JR. Immunomodulatory Functions of Surfactant. *Physiol Rev* (1997) 77:931–62. doi: 10.1152/physrev.1997.77.4.931
39. Baughman RP, Sternberg RI, Hull W, Buchsbaum JA, Whitsett J. Decreased Surfactant Protein A in Patients With Bacterial Pneumonia. *Am Rev Respir Dis* (1993) 147:653–7. doi: 10.1164/ajrccm/147.3.653
40. Reina-Campos M, Diaz-Meco MT, Moscat J. The Dual Roles of the Atypical Protein Kinase Cs in Cancer. *Cancer Cell* (2019) 36:218–35. doi: 10.1016/j.ccell.2019.07.010
41. Durán A, Rodriguez A, Martin P, Serrano M, Flores JM, Leitges M, et al. Crosstalk Between PKCζ and the IL4/Stat6 Pathway During T-Cell-Mediated Hepatitis. *EMBO J* (2004) 23:4595–605. doi: 10.1038/sj.emboj.7600468
42. Martin P, Villares R, Rodriguez-Mascarenhas S, Zaballos A, Leitges M, Kovac J, et al. Control of T Helper 2 Cell Function and Allergic Airway Inflammation by Pkcζ. *Proc Natl Acad Sci U.S.A.* (2005) 102:9866–71. doi: 10.1073/pnas.0501202102
43. Parker PJ, Brown SJ, Calleja V, Chakravarty P, Cobbaut M, Linch M, et al. Equivocal, Explicit and Emergent Actions of PKC Isoforms in Cancer. *Nat Rev Cancer* (2021) 21:51–63. doi: 10.1038/s41568-020-00310-4
44. Dong W, Lu J, Zhang X, Wu Y, Lettieri K, Hammond GR, et al. A Polybasic Domain in aPKC Mediates Par6-Dependent Control of Membrane Targeting and Kinase Activity. *J Cell Biol* (2020) 219:e201903031. doi: 10.1083/JCB.201903031
45. Sender V, Moulakakis C, Stamme C. Pulmonary Surfactant Protein A Enhances Endolysosomal Trafficking in Alveolar Macrophages Through Regulation of Rab7. *J Immunol* (2011) 186:2397–411. doi: 10.4049/jimmunol.1002446
46. Kajimoto T, Caliman AD, Tobias IS, Okada T, Pilo CA, Van AAN, et al. Activation of Atypical Protein Kinase C by Sphingosine 1-Phosphate Revealed by an aPKC-Specific Activity Reporter. *Sci Signal* (2019) 12:eaat6662. doi: 10.1126/scisignal.aat6662
47. Patel S, Werstuck GH. Macrophage Function and the Role of GSK3. *Int J Mol Sci* (2021) 22:2206. doi: 10.3390/ijms22042206
48. Hoffmeister L, Diekmann M, Brand K, Huber R. GSK3: A Kinase Balancing Promotion and Resolution of Inflammation. *Cells* (2020) 9:820. doi: 10.3390/cells9040820
49. Mcalpine CS, Huang A, Emdin A, Banko NS, Beriault DR, Shi Y, et al. Deletion of Myeloid GSK3α Attenuates Atherosclerosis and Promotes an M2 Macrophage Phenotype. *Arterioscler Thromb Vasc Biol* (2015) 35:1113–22. doi: 10.1161/ATVBAHA.115.305438
50. Dominguez M, Brüne B, Namgaladze D. Exploring the Role of ATP-Citrate Lyase in the Immune System. *Front Immunol* (2021) 12:632526. doi: 10.3389/fimmu.2021.632526
51. Wellen KE, Hatzivassiliou G, Sachdeva UM, Bui TV, Cross JR, Thompson CB. ATP-Citrate Lyase Links Cellular Metabolism to Histone Acetylation. *Science* (2009) 324:1076–80. doi: 10.1126/science.1164097
52. Lee JV, Carrer A, Shah S, Snyder NW, Wei S, Venneti S, et al. Akt-Dependent Metabolic Reprogramming Regulates Tumor Cell Histone Acetylation. *Cell Metab* (2014) 20:306–19. doi: 10.1016/j.cmet.2014.06.004
53. Baardman J, Verberk SGS, van der Velden S, Gijbels MJJ, van Roomen CPPA, Sluimer JC, et al. Macrophage ATP Citrate Lyase Deficiency Stabilizes Atherosclerotic Plaques. *Nat Commun* (2020) 11:1–15. doi: 10.1038/s41467-020-20141-z
54. Linke M, Fritsch SD, Sukhbaatar N, Hengstschläger M, Weichhart T. mTORC1 and mTORC2 as Regulators of Cell Metabolism in Immunity. *FEBS Lett* (2017) 591:3089–103. doi: 10.1002/1873-3468.12711
55. González A, Hall MN, Lin SC, Hardie DG. AMPK and TOR: The Yin and Yang of Cellular Nutrient Sensing and Growth Control. *Cell Metab* (2020) 31:472–92. doi: 10.1016/j.cmet.2020.01.015
56. O'Neill LAJ, Kishton RJ, Rathmell J. A Guide to Immunometabolism for Immunologists. *Nat Rev Immunol* (2016) 16:553–65. doi: 10.1038/nri.2016.70
57. Fukuda H, Katsurada A, Iritani N. Effects of Nutrients and Hormones on Gene Expression of ATP Citrate-Lyase in Rat Liver. *Eur J Biochem* (1992) 209:217–22. doi: 10.1111/j.1432-1033.1992.tb17279.x
58. Goto H, Ledford JG, Mukherjee S, Noble PW, Williams KL, Wright JR. The Role of Surfactant Protein A in Bleomycin-Induced Acute Lung Injury. *Am J Respir Crit Care Med* (2010) 181:1336–44. doi: 10.1164/rccm.200907-1002OC
59. Francisco D, Wang Y, Conway M, Hurbon AN, Dy ABC, Addison KJ, et al. Surfactant Protein-A Protects Against IL-13–Induced Inflammation in Asthma. *J Immunol* (2020) 204:2829–39. doi: 10.4049/jimmunol.1901227
60. Ledford JG, Addison KJ, Foster MW, Que LG. Eosinophil-Associated Lung Diseases: A Cry for Surfactant Proteins A and D Help? *Am J Respir Cell Mol Biol* (2014) 51:604–14. doi: 10.1165/rcmb.2014-0095TR
61. Henderson NC, Rieder F, Wynn TA. Fibrosis: From Mechanisms to Medicines. *Nature* (2020) 587:555–66. doi: 10.1038/s41586-020-2938-9
62. Ramalingam TR, Gieseck RL, Acciani TH, M Hart K, Cheever AW, Mentink-Kane MM, et al. Enhanced Protection From Fibrosis and Inflammation in the Combined Absence of IL-13 and IFN-γ. *J Pathol* (2016) 239:344–54. doi: 10.1002/path.4733
63. Ma B, Athari SS, Mehrabi Nasab E, Zhao L. PI3K/AKT/mTOR and TLR4/MyD88/NF-κB Signaling Inhibitors Attenuate Pathological Mechanisms of Allergic Asthma. *Inflammation* (2021) 44:1895–907. doi: 10.1007/s10753-021-01466-3

Conflict of Interest: The authors declare that the research was conducted in the absence of any commercial or financial relationships that could be construed as a potential conflict of interest.

frontiers | Frontiers in Immunology

ORIGINAL RESEARCH
published: 27 April 2022
doi: 10.3389/fimmu.2022.853611

Comparison of the Toponomes of Alveolar Macrophages From Wild Type and Surfactant Protein A Knockout Mice and Their Response to Infection

David S. Phelps[1], Vernon M. Chinchilli[2], Xuesheng Zhang[1], Debra Shearer[3], Judith Weisz[3†] and Joanna Floros[1,3]**

[1]Penn State Center for Host Defense, Inflammation, and Lung Disease (CHILD) Research and Departments of Pediatrics, The Pennsylvania State University College of Medicine, Hershey, PA, United States, [2] Public Health Sciences, The Pennsylvania State University College of Medicine, Hershey, PA, United States, [3] Obstetrics and Gynecology, The Pennsylvania State University College of Medicine, Hershey, PA, United States

Background: Surfactant protein-A (SP-A) plays a critical role in lung innate immunity by regulating alveolar macrophages (AM), expression of inflammatory mediators, and other host defense proteins. The toponome imaging system (TIS), a serial immunostainer, was used to study the AM toponome because it characterizes the localization of multiple markers and identifies marker combinations in each pixel as combinatorial molecular phenotypes (CMPs). We used TIS to study the AM toponome from wild type (WT) and SP-A knockout (KO) mice and changes following *Klebsiella pneumoniae* exposure.

Methods: WT or KO mice received intratracheal *K. pneumoniae* or vehicle and AM were obtained by bronchoalveolar lavage after one hour. AM were attached to slides and underwent TIS analysis. Images were analyzed to characterize all pixels. AM CMPs from WT vehicle (n=3) and infected (n=3) mice were compared to each other and to AM from KO (n=3 vehicle; n=3 infected). Histograms provided us with a tool to summarize the representation of each marker in a set of CMPs.

Results: Using the histograms and other tools we identified markers of interest and observed that: 1) Both comparisons had conserved (present in all group members) CMPs, only in vehicle AM and only in infected AM, or common to both vehicle and infected AM, (i.e., unaffected by the condition). 2) the CMP number decreased with infection in WT and KO versus vehicle controls. 3) More infection-specific CMPs in WT vs KO AM. 4) When AM from WT and KO vehicle or infected were compared, there were more unique CMPs exclusive to the KO AM. 5) All comparisons showed CMPs shared by both groups.

OPEN ACCESS

Edited by:
Nicole Thielens,
UMR5075 Institut de Biologie Structurale (IBS), France

Reviewed by:
Jiegou Xu,
Anhui Medical University, China
Elena Lopez-Rodriguez,
Charité Universitätsmedizin Berlin, Germany

***Correspondence:**
Joanna Floros
jfloros@psu.edu
David S. Phelps
dsp4@psu.edu

[†]Deceased

Specialty section:
This article was submitted to Molecular Innate Immunity, a section of the journal Frontiers in Immunology

Received: 12 January 2022
Accepted: 23 March 2022
Published: 27 April 2022

Citation:
Phelps DS, Chinchilli VM, Zhang X, Shearer D, Weisz J and Floros J (2022) Comparison of the Toponomes of Alveolar Macrophages From Wild Type and Surfactant Protein A Knockout Mice and Their Response to Infection. Front. Immunol. 13:853611. doi: 10.3389/fimmu.2022.853611

Conclusions: The decrease of CMPs exclusive to infected AM in KO mice may underlie the observed susceptibility of KO mice to infection. However, both KO groups had more exclusive CMPs than the corresponding WT groups, perhaps indicating a vigorous effort by KO to overcome deficits in certain proteins and CMPs that are dysregulated by the absence of SP-A. Moreover, the presence of shared CMPs in the compared groups indicates that regulation of these CMPs is not dependent on either infection or the presence or absence of SP-A.

Keywords: phagocytosis, phenotype, SP-A, surfactant, innate immunity, immunohistochemistry, immunophenotype

INTRODUCTION

In a number of previous reports we have studied the effect of SP-A on the function of the alveolar macrophage (AM) (1). These studies have examined the expression of inflammatory mediators (2–5), the AM proteome (6–9), miRNome (10–12), and AM gene expression (1, 13), and more recently the AM toponome (14–16), i.e. the organization of proteins within the cells. These studies of inflammatory mediators were done, for the most part, by either comparing wild type (WT) mice or transgenic mice expressing human SP-A with SP-A knockout mice (KO), or by "rescuing" SP-A KO mice by administering exogenous SP-A. The results consistently showed differences between AM exposed to SP-A, either chronically or acutely, and AM not exposed to SP-A. The implications of these differences have been demonstrated in survival studies in a pneumonia model where mice were infected intratracheally with bacteria. SP-A KO mice showed markedly increased mortality compared to WT or "SP-A rescued" mice (17, 18). We showed that this was likely due, at least in part, to a reduction in the phagocytic index of the KO mice lacking SP-A (17).

Although we have demonstrated multiple changes in the AM in the absence of SP-A, the increased susceptibility to infection (17, 18) and reduced phagocytic efficiency (19) is likely due to many factors. The results of the proteomic studies strengthen this supposition since many proteins are affected, where some are increased and others decreased (6–9). We have previously shown that within a very short time after the introduction of bacteria to the lungs, binding of bacteria by the AM and phagocytosis of the pathogen are highly dependent on the presence of SP-A (17). The enhancement of bacterial clearance by SP-A is likely due to several mechanisms. The most proximal is the ability of SP-A to enhance phagocytosis by serving as an opsonin – binding the pathogen and enhancing its binding to cell surface receptors (20–22) . The second level is SP-A dependent regulation in the AM of various cell surface receptors involved in phagocytosis (18, 23, 24). Several of these cell surface proteins are targeted in this study, including sialoadhesin, CD206, CD44, and TLR4 (25–29). The third level is an apparent activation or boost of overall function of the AM due to SP-A (1, 22). Activation may be affected by a number of the studied proteins, including CD45, TLR4, Ly-6C, and CD200R, among others (21, 30–36). These and other proteins involved in cell-cell and cell-matrix interactions that can also influence activation were investigated in the present study.

The technology used in the present study, the Toponome Imaging System (TIS), is an ideal tool with which one may study these events because it looks at combinations of proteins, rather than individual proteins. TIS, also known as Imaging Cycler Microscopy, or Multi-epitope ligand cartography (MELC), allows one to study the toponome or the expression and/or the presence of multiple markers in their spatial networks in intact AM after different experimental manipulations (14–16, 37–39).

TIS is a robotically-driven system using immunofluorescent microscopy developed by Schubert (37–40) that involves repeated cycles of immunostaining, imaging, and photobleaching of antibodies conjugated with fluorescein isothiocyanate (FITC). A key feature of TIS is its utilization of dedicated software programs to process the captured images and construct a pixel-by-pixel map of the cells that provides information about co-localization and co-expression of proteins. This approach is significant because proteins rarely operate in isolation and their behavior may be a function of other proteins in close proximity forming multiprotein complexes. TIS generates these data by mapping each cell for the localization of multiple markers, allowing the investigator to identify and enumerate supramolecular structures formed by protein clusters, rather than simply co-localizing the proteins. These protein clusters are referred to as Combinatorial Molecular Phenotypes or CMPs, and they may identify candidate proteins that are potentially involved in important protein-protein interactions. Evidence is increasing that many proteins function as part of supramolecular complexes composed of multiple proteins working together. The scientific literature contains many examples of these interactions in pathway diagrams that illustrate various pathways such as that involving the LPS/CD14/TLR4/MyD88-mediated LPS receptor pathway (41).

In the composite images generated by TIS there are 2^n possible CMPs or marker combinations where n = the number of markers used (37, 40, 42, 43). CMPs are used to characterize and compare cell populations. This is important because there is evidence that various conditions result in differences in both the

Abbreviations: AM, alveolar macrophage; CMP, combinatorial molecular phenotype; FITC, fluorescein isothiocyanate; KO, SP-A knockout; KOI, knockout infected; KOV, knockout vehicle-treated; SP-A, surfactant protein-A; TIS, toponome imaging system; WI, wild type infected; WT, wild type; WV, wild type vehicle.

number and composition of CMPs; and there are conditions that may be identified by CMPs with a unique composition (37, 40, 42, 43). Thus, TIS serves as an ideal tool for addressing potential causes of alterations in AM function.

Several studies from our laboratory have employed both *in vitro* and *in vivo* assays to assess the phagocytic index of alveolar macrophages and the role of SP-A in this process (1, 44–46). The current study employed the same conditions described previously (19) for *in vivo* phagocytosis to investigate the impact of infection and/or SP-A on the AM toponome. We studied patterns of protein expression in AM harvested from lungs of WT or SP-A KO mice one hour after the intratracheal instillation of *Klebsiella pneumoniae*. The one-hour time frame used in these studies is notable in that it is unlikely that the effects we see result from new protein synthesis. Therefore, differences between vehicle-instilled and bacteria-instilled AM within a group (WT or KO) are probably a function of previously synthesized proteins moving within the cell, being secreted by the cell, or being broken down by metabolic events related to neutralizing phagocytosed bacteria. All of these events have the potential to alter the organization of proteins within the cell and change CMPs. A panel of antibodies to proteins known to have roles in AM cell-cell interactions and innate immune function was used. Our goal was to determine whether the introduction of bacteria during the time interval needed to alter the phagocytic index of the AM changed their toponome with respect to the studied group of proteins, and whether SP-A played a role, as assessed by comparison studies of the toponome of AM from WT or KO mice.

METHODS AND MATERIALS

This study used male mice on the C57BL6/J genetic background. Two strains were used – Wild Type (WT) (n=6; vehicle n=3 and infected n=3) and SP-A knockout (KO) (n=6; vehicle n=3 and infected n=3) at 8-12 weeks of age. The mice were bred in our breeding colony at the Penn State College of Medicine and raised under pathogen-free conditions or in barrier facilities with free access to food and water. Sentinel animals in the same animal rooms showed no evidence of respiratory pathogens. The Institutional Animal Care and Use Committee of the Penn State College of Medicine approved this study.

Preparation of Bacteria

Klebsiella pneumoniae bacteria were obtained from the American Type Culture Collection (ATCC 43816) and cryopreserved until needed for an experiment. The bacteria were grown overnight at 37°C in TS Broth with shaking at 120 RPM for 18 hours. An aliquot was then diluted and grown for 3 hours to achieve mid-log phase growth.

Experimental Procedure

Mice from each strain were anesthetized and received an intratracheal instillation of an aliquot of 1.2 x 10^7 mid-log phase bacteria in 50 microliters of PBS instilled into the trachea. Control mice from each strain received vehicle (50 microliters of PBS) only. After 1 hour, AM were harvested by BAL with 5 x 500 ul of PBS, 1 mM EDTA. The infection time was determined from earlier AM phagocytosis studies (19). The cells were washed and plated, then incubated for 1 hour to allow them to attach to slides. The slides were then dried, fixed, and stored at -80°C until TIS was done.

TIS

TIS was performed as described previously (14–16). As discussed in previous studies, the choice of antibodies was limited by the presence of artifacts in fluorescent images from some samples that may prevent the use of some of these images/markers for study. Good quality images for all 3 samples in all 4 experimental groups are needed to do a comparative CMP analysis. For our comparison study we analyzed data sets with 9 markers, although we originally performed the TIS with more markers.

Antibody Panel

Table 1 lists the nine antibodies or reagents we used in the image analysis, their gene names (where appropriate), their Uniprot accession numbers, the commercial source, and the catalog number of each antibody. Calibration and optimization of antibodies for the TIS procedure was done as previously described (14–16). Briefly, commercially available antibodies were tested at several dilutions. The time for incubation was held constant for all antibodies (30 minutes). The antibody concentration selected was one at which we obtained a good fluorescence signal with minimal background. We experimented with different exposure times for imaging so that we obtained good signals that were below saturation. After confirming concentration and exposure times, TIS runs were set up with the whole series of antibodies. This process was conducted for each new antibody that was added to an experiment or when there was a change in lot number for a given antibody.

Potential interactions between the markers used are shown in an interaction diagram (**Figure 1**) generated by the information present in the String database (https://string-db.org). It should be noted that we used FITC-labeled phalloidin to detect F-actin and for the interaction diagrams we used the gene symbol for beta-actin (*actb*), the main constituent of F-actin as a surrogate for phalloidin.

The selected antibodies shown here were chosen because they reliably produced good staining with a minimal number of artifacts.

TIS Image Analysis

The process employed to generate TIS data from a collection of immunofluorescent images has been described in detail in our previous publications (14–16) and is summarized in **Figure 2**. Briefly, a sample slide is subjected to repeated cycles of immunostaining with fluorescein-labeled antibodies, an image captured, the fluorescence bleached out, and the cycle repeated with the next antibody. After the immunostaining is completed, all of the resulting images are subjected to a binarization process in which a threshold level is set and areas with levels below the threshold designate the marker as absent and areas above the threshold as present. Following binarization the series of images

TABLE 1 | Markers for phagocytosis study (Wild Type) and comparison with knockout (KO).

Marker #	Marker or protein name	Accession #	Gene name	Supplier	Catalog #
1	Sialoadhesin (Siglec 1; CD169)	Q62230	Siglec1	Bioss	bs-10751R-FITC
2	CD44, Pgp-1, H_CAM, Ly-24	P15379	Cd44	BD Pharmingen	553133
3	CD200R (Mox-2; Ox-2)	O54901	Cd200r1	ThermoFisher	MA5-17984
4	CD206 (mannose receptor; C type 1)	Q61830	Mrc1	ThermoFisher	MA5-16870
5	CD45 (Receptor-type tyrosine-protein phosphatase C	P06800	Ptprc	BD Pharmingen	553080
6	CD18 (LFA-1, Mac-1) Integrin B2	P11835	Itgb2	BD Pharmingen	553292
7	Toll-like receptor 4 (TLR4), CD284	Q9QUK6	Tlr4	ThermoFisher	MA5-16212
8	Lymphocyte antigen-6c2 (Ly-6C2; Ly-6C)	P0CW03	Ly6c2 (Ly6c)	BD Pharmingen	553104
9	Phalloidon	-	-	ThermoFisher	F432

List of Markers: The markers used in this study are listed together with the accession number, gene name, supplier, and catalog number.

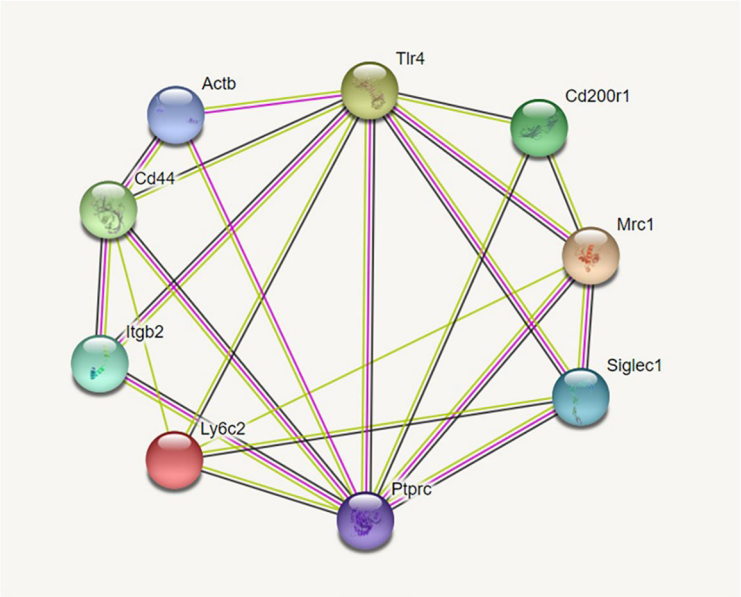

FIGURE 1 | Interaction diagram from String database. **Figure 1** shows the 9-marker set of proteins we studied. Proteins more closely identified with innate immune function, and specifically phagocytosis, are grouped on the right. Proteins known for their roles in cell-cell or cell-matrix interaction/adhesion are grouped on the left. As is evident from the large number of interactions each has, TLR4 and Ptprc (CD45) are placed at the top and bottom center and play pivotal roles in both groups. The interaction diagram was generated by https://string.db.org.

for a given sample are combined digitally. The presence or absence of each marker is tabulated in every pixel in the image. This is denoted in data tables, such as that shown in **Figure 3**, Panel A, as (0) for absent and (1) for present. The CMPs in order of abundance are listed in the column on the far left. The columns labeled 0 to 8 list the presence or absence of each marker. The column on the far right lists the frequency (i.e. abundance; # of pixels) occupied by that CMP. Each of the tabulated CMPs is assigned a color which is used to pseudocolor the image shown in **Figure 3**, Panel B.

In this study image analysis was restricted to whole images. In some samples, cell aggregation prevented us from delineating and analyzing separate cells. We used several tools within the TIS software to analyze the data in the images from the various experimental groups. One tool is a histogram that provides a snapshot of the group of CMPs being analyzed. An example is shown in **Figure 4**. Each marker is represented as a bar rising from the x-axis. The y-axis shows the frequency of each marker in all the CMPs being graphed. Note that in most cases this value would differ from the absolute amount of each marker because the CMPs themselves may vary considerably in terms of their abundance or the number of pixels in which they are found. In this example marker #2 (CD44) is found in about 83% of the CMPs and marker #5 (CD45) is found in about 12%.

The TIS software also allowed us to analyze the data in a number of ways that are subsequently shown in the histograms. These operations are summarized in **Figure 5** and include the ability to merge datasets, to find the intersection of multiple datasets, and determine the CMPs unique to one dataset compared to another (i.e. complement). These operations

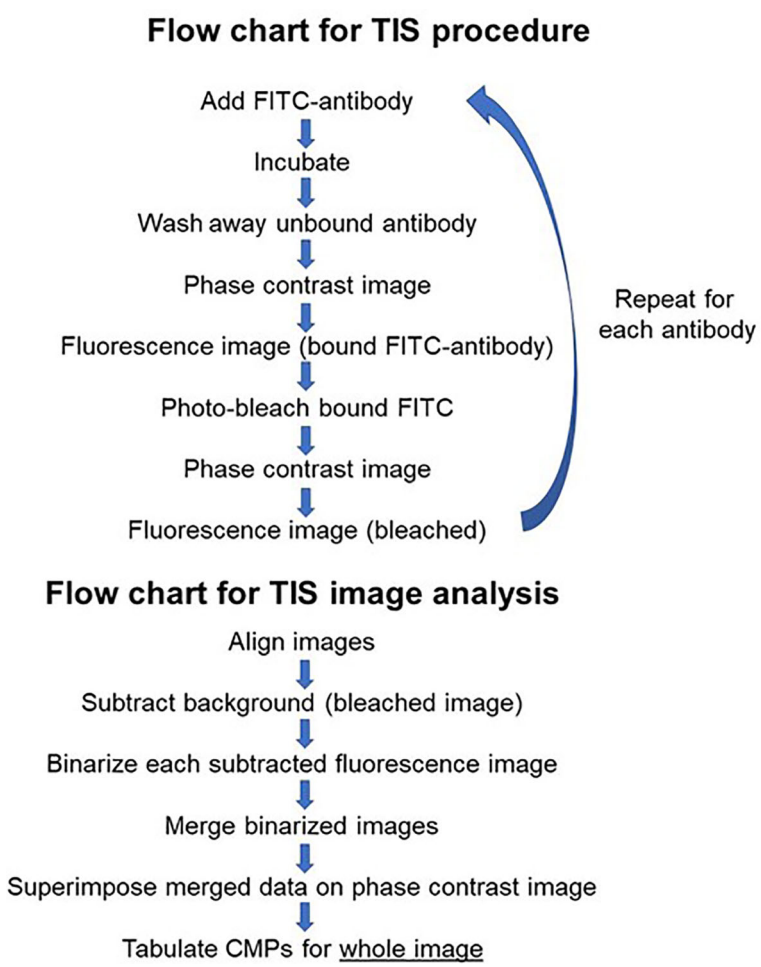

FIGURE 2 | Flow chart. **Figure 2** is flow chart that describes the TIS procedure and the steps involved in the analysis of images generated by TIS.

allowed us to identify conserved CMPs (i.e. CMPs present in multiple datasets).

RESULTS

Marker Interactions

Using the STRING database (https://string-db.org) we constructed diagrams of potential interactions between the proteins listed in **Table 1** from the information in the STRING database. The selected markers were proteins known to be important in AM function with a number of "potential" interactions among themselves. Two proteins, TLR4 and CD45 (Ptprc), exhibit interactions with the other eight proteins included in **Figure 1**. The interaction diagram has been constructed so that proteins involved in cell-cell interactions and cell adhesion are grouped on the left side of the diagram and proteins implicated in host defense function are on the right side. However, as the diagram illustrates these are not clear divisions and there are numerous interactions among the proteins. Five of the nine molecules potentially interact with more than half of the other molecules. The large number of documented interactions in various systems depicted by the diagram shows the relevance of these proteins and their likely importance in macrophage function.

Effect of Infection on the Toponomes of WT and SP-A KO AM

In order to assess how infection with *Klebsiella pneumoniae* affects the AM toponome and the influence of SP-A, we compared the response of AM to treatment with vehicle or bacteria in WT AM and SP-A KO AM. To do this it was necessary to have immunofluorescent images in all three samples that were free of artifacts for all four groups. The resultant set of 108 images included nine markers. **Figure 3**, Panel B is an example of a representative AM sample after pseudocoloring by the TIS software.

Comparison of WT Vehicle vs. WT Infected Toponomes

The six WT samples in this analysis (n=3 vehicle; n=3 infected) had an average of 263 CMPs (range = 163 to 343). The details for each

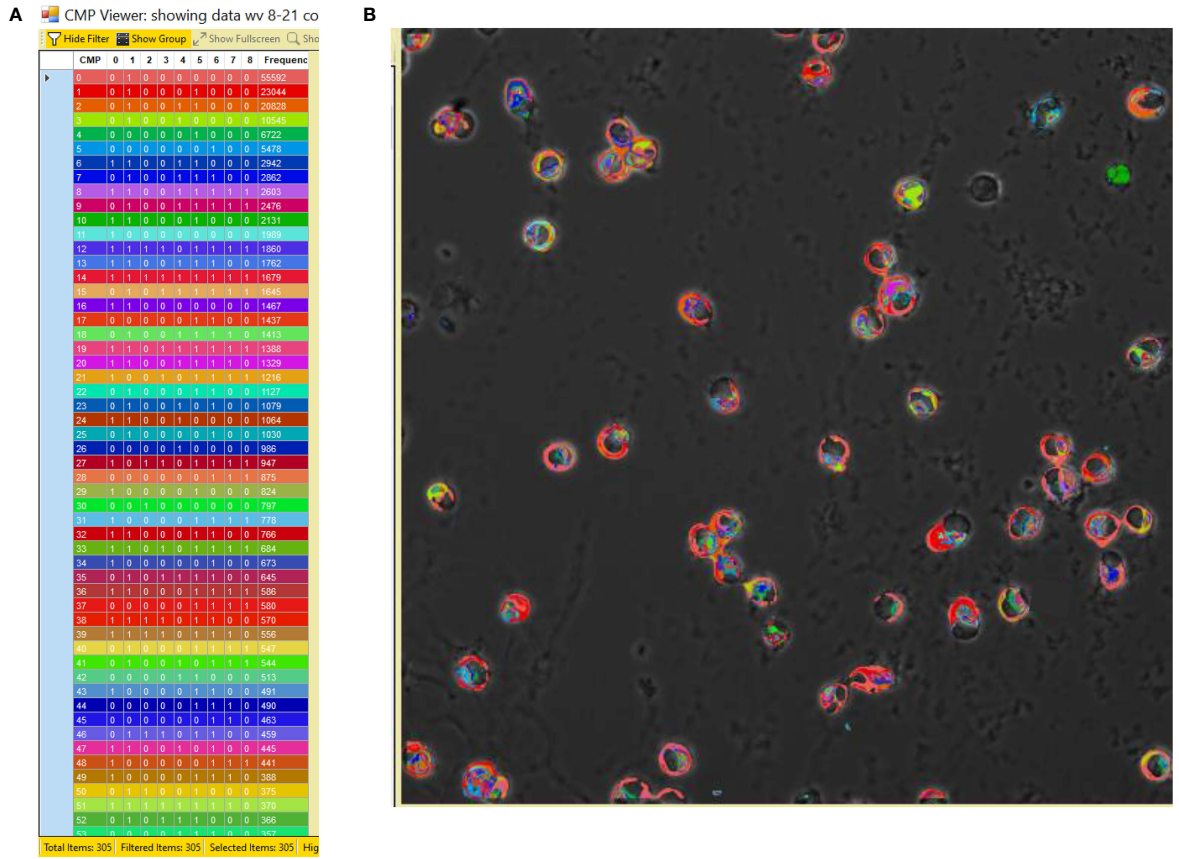

FIGURE 3 | CMP data and pseudocolored image. Panel **(A)** depicts an example of a portion of a CMP data table generated by the TIS software from a combined image after binarization of each of the 9 immunostained images. The CMPs are numbered in the left-hand column and are listed in order of frequency (i.e. abundance; # of pixels) (in the right-hand column) in which that CMP is present. The intervening columns (numbered 0 to 8) indicate the absence (0) or presence (1) of each marker in a given CMP. The colors in the table **(A)** are assigned by the program and also used to pseudocolor the image from which the data were derived **(B)**.

group are listed in **Table 2**, which shows the number of CMPs in each sample and their average. When the three WT vehicle (WV) samples are merged there are a total of 392 unique CMPs among the samples in the group. Determining the intersection of the three samples in each group provides a tabulation of CMPs that are present in all three samples in the group. We refer to these as "conserved" CMPs because they are found in all samples in a group. In the case of the WT vehicle group the intersection is comprised of 176 CMPs.

The second column of **Table 2** lists the CMP numbers for the WT infected (WI) group. The number of CMPs from the WT vehicle and WT infected samples did not differ significantly from one another. Merging the three WT infected samples also resulted in a set of 392 unique CMPs. The intersection of the WT infected group consisted of 102 CMPs. The data set formed by merging all of the vehicle samples with all of the infected samples contained a total of 449 unique CMPs. The theoretical maximum number of CMPs in a 9-marker study is 2^9 or 512 CMPs. The last two columns in **Table 2** show comparable data for the KO-vehicle and KO-infected samples and are discussed below in the next section.

We next looked at the histograms depicting intersection of all samples in the two groups which shows the marker composition of all "conserved" CMPs that were present in every sample (3-out-of 3) of each group. These and subsequent data sets are characterized in histograms, such as the one described above (**Figure 4**); these show the relative frequency of each marker in the sampled CMPs. As stated above, we identified 176 CMPs that were present in every WT vehicle sample (**Figure 6A**) and 102 CMPs that were present in the three WT infected samples (**Figure 6B**). The observed reduction (**Figure 6B**) in the number of CMPs after infection (102 in WI vs 176 in WV, **Figure 6A**) may indicate that exposure to bacteria results in a loss of phenotypic diversity as the AM mobilize to deal with the infectious threat. Merging these two sets (vehicle and infected) of conserved CMPs revealed that in the WT AM there were 209 unique CMPs that were conserved in at least one sample (**Figure 6C**).

When this set of 209 conserved CMPs was subjected to the complement procedure we were able to determine how many of the CMPs present in all three samples were: a) exclusive to the WT vehicle group (**Figure 6D**); b) exclusive to the WT infected group (**Figure 6E**) or; c) common to both groups (i.e. present in all three samples of both groups) (**Figure 6F**). The broken arrow originating at **Figure 6C** and terminating at **Figures 6D–F**

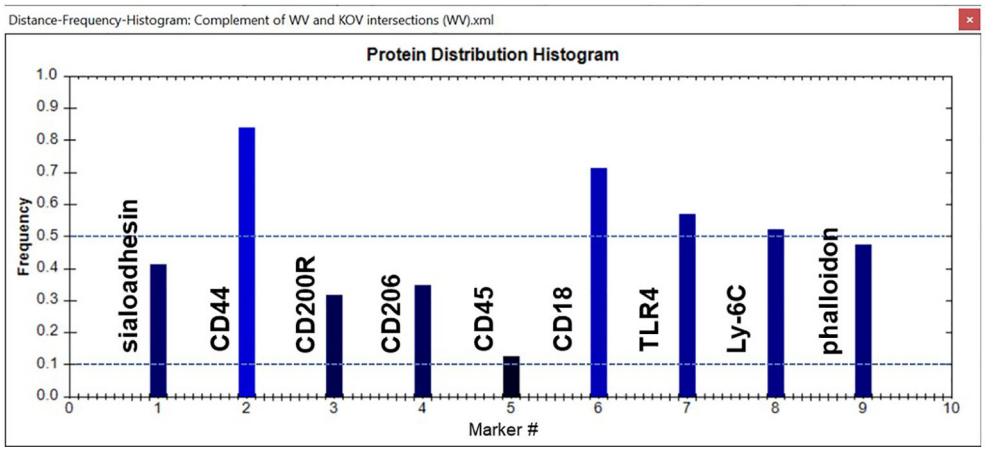

FIGURE 4 | Sample histogram. An example of a CMP histogram for one of the samples is shown. Reference lines (dotted blue) have been added for frequencies of 0.1 (10%) and 0.5 (50%). The frequency shows the relative abundance of a given marker in the set of CMPs used to generate the histogram. In this case Marker #2 (CD44) is found in 83% of the CMPs, whereas Marker #4 (CD206) is only found in 12% of the graphed CMPs. The names of the markers represented by each bar are shown.

Glossary of TIS image processing terms

1. **Merge – combines multiple data sets into a single data set listing all unique CMPs.**

(i.e. combines 3 samples into a single set listing all CMPs present; CMPs may be present in one or more samples)

2. **Intersection – lists only CMPs that are present in all samples in selected datasets.**

(i.e. analyzes multiple samples and generates a list of CMPs present in all samples)

3. **Conserved CMP – a CMP that is found in all samples in a group by performing the intersection operation.**

4. **Complement – compares two data sets and identifies the conserved CMPs exclusive to one set or the other, and those CMPs present in both data sets.**

5. **Histogram – a graphic representation of the relative abundance of each marker in the selected set of CMPs. (i.e. a value of 0.45 indicates that a given marker is in 45% of the CMPs in the analyzed data set).**

FIGURE 5 | Glossary of TIS terms. The TIS software enables probing the CMP data in a variety of ways. Several terms and the operations are listed and described in this figure.

illustrates this process. These conserved CMPs were mostly found in the vehicle group (n=107) (**Figure 6D**) and may be viewed as being characteristic of the normal AM. There are 33 CMPs that are exclusive to the infected group (**Figure 6E**) and these are probably triggered by the bacterial exposure and are likely to be involved in host defense processes against the bacteria. Finally, there are 69 conserved CMPs that are common to both groups (**Figure 6F**) and these may represent

TABLE 2 | Summary of CMPs in original samples and created data sets.

	WT-vehicle	WT-infected	KO-vehicle	KO-infected
Sample A	305	163	347	270
Sample B	211	254	294	214
Sample C	343	300	239	271
Average	286	239	293	252
Intersection	176	102	207	123
Merged (A,B,C)	392	392	449	390
Merged (veh+inf)	449		476	

*The four columns list data for each experimental group. The three samples (A, B, C) for each group are listed along with their average. The samples were then analyzed for their intersection (CMPs common to all three samples) (see **Table 2**) and the three samples were merged to obtain the total number of unique CMPs in each group of three samples. In the bottom row of the table is the number of unique CMPs found in the merged wild type group and the KO group.*

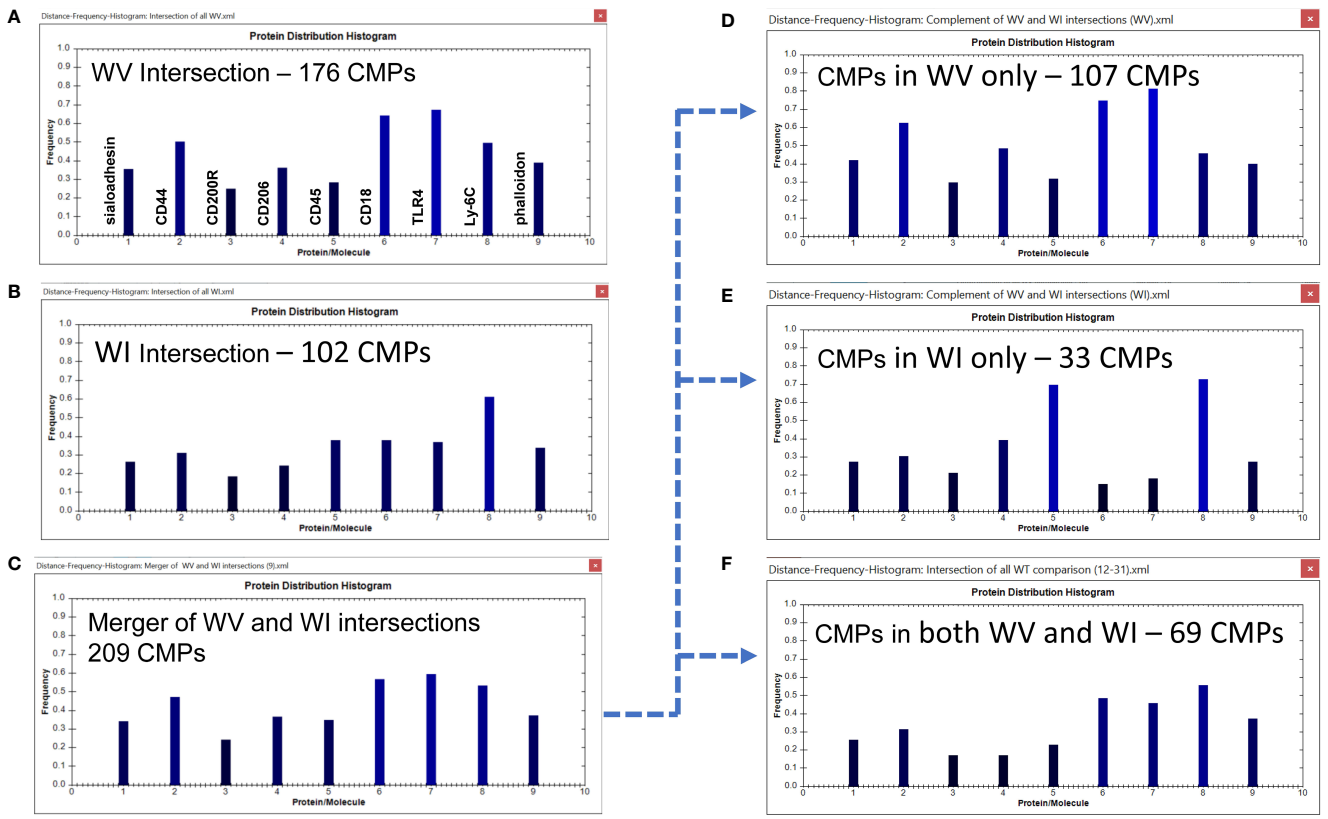

FIGURE 6 | CMP comparison of wild type AM with nine markers. The names of the proteins represented by each histogram bar are shown in Panel **(A)**. The same order applies to all other histogram panels in this and subsequent figures. Panels **(A, B)** show the intersection of the three wild type vehicle and three wild type infected samples. The intersection feature identifies the "conserved" CMPs present in all three samples of each group. Panel **(C)** depicts the merged results of Panels **(A, B)** and shows the characteristics of the 209 CMPs that are conserved in the vehicle and/or infected groups. Panels **(D–F)** use the complement feature of the TIS software to identify from the merged 209 CMPs, CMPs present in vehicle AM only **(D)**, infected AM only **(E)**, or common to both groups **(F)**. The arrow originating at Panel **(C)** and terminating at Panels **(D–F)** illustrates this process.

housekeeping functions since they are present in both groups and not affected by infection.

Using all of the CMP data the mean levels of each marker were calculated in each of the three samples/group. When these were compared using the Wilcoxon Rank Sum test the WT vehicle and WT infected data sets were found to be significantly different (p=0.0424).

Some of the features of these groups offer some insight into differences resulting from the exposure to bacteria. For example, the conserved CMPs found in the vehicle-treated AM (**Figure 6A**) generated a histogram that was quite different from that in the WT infected AM (**Figure 6B**). WT vehicle AM were characterized by high levels of CD44, CD18, and TLR4 (**Figure 6A**), whereas most of those markers were at lower levels

in the group of conserved CMPs found in the infected AM (**Figure 6B**). The overall differences between vehicle-treated and infected were more pronounced in the histograms of the group-exclusive CMPs (**Figures 6D, E**). As with the whole group of conserved CMPs the vehicle treated AM had higher levels of CD44, CD18, and TLR4, but it is also notable that levels of CD45 and Ly-6C were markedly lower in the WT vehicle AM than in their infected counterparts. These differences are likely to be part of the AM response to bacterial challenge.

It is also of interest to note that the overall profile of the histogram bars in the common CMPs (**Figure 6F**) for many of the markers was more similar to the profile of CMPs exclusive to the vehicle-treated group (**Figure 6D**), albeit at lower frequencies. The profile of CMPs exclusive to the infected AM (**Figure 6E**) differs from the subset of CMPs common to both groups (**Figure 6F**) in terms of many of the proteins.

Comparison of SP-A KO Vehicle vs. SP-A KO Infected

An analysis similar to the one described above for the WT was performed on the AM from KO mice. The six samples in this analysis (three vehicle; three infected) had an average of 273 CMPs (range = 214 to 347). The CMP data for the KO vehicle (KOV) and KO infected (KOI) groups are listed in **Table 2**. When the data for the three KO samples in each group were merged, a total of 449 unique CMPs were identified in the vehicle AM and 390 in the infected. A merging of these two sets (vehicle and infected) resulted in 476 unique CMPs.

Using the TIS software we obtained histograms for the intersection of all samples in the two groups; this tabulates all "conserved" CMPs that were present in every sample (3-out-of-3) of each group. We identified 207 (out of the total of 449) CMPs to be present in all three KO vehicle samples (**Figure 7A**) and 123 CMPs (out of 390) in the three KO infected samples (**Figure 7B**). This reduction in conserved CMPs after infection mirrors what we observed in the WT AM and provides another example in support of our conjecture that exposure to bacteria results in a loss of phenotypic diversity as the AM mobilize to deal with the potential infection.

Merging these two sets of intersecting CMPs (**Figures 7A, B**) revealed that they comprised of 223 unique CMPs that were conserved in at least one of the KO groups (**Figure 7C**). As with

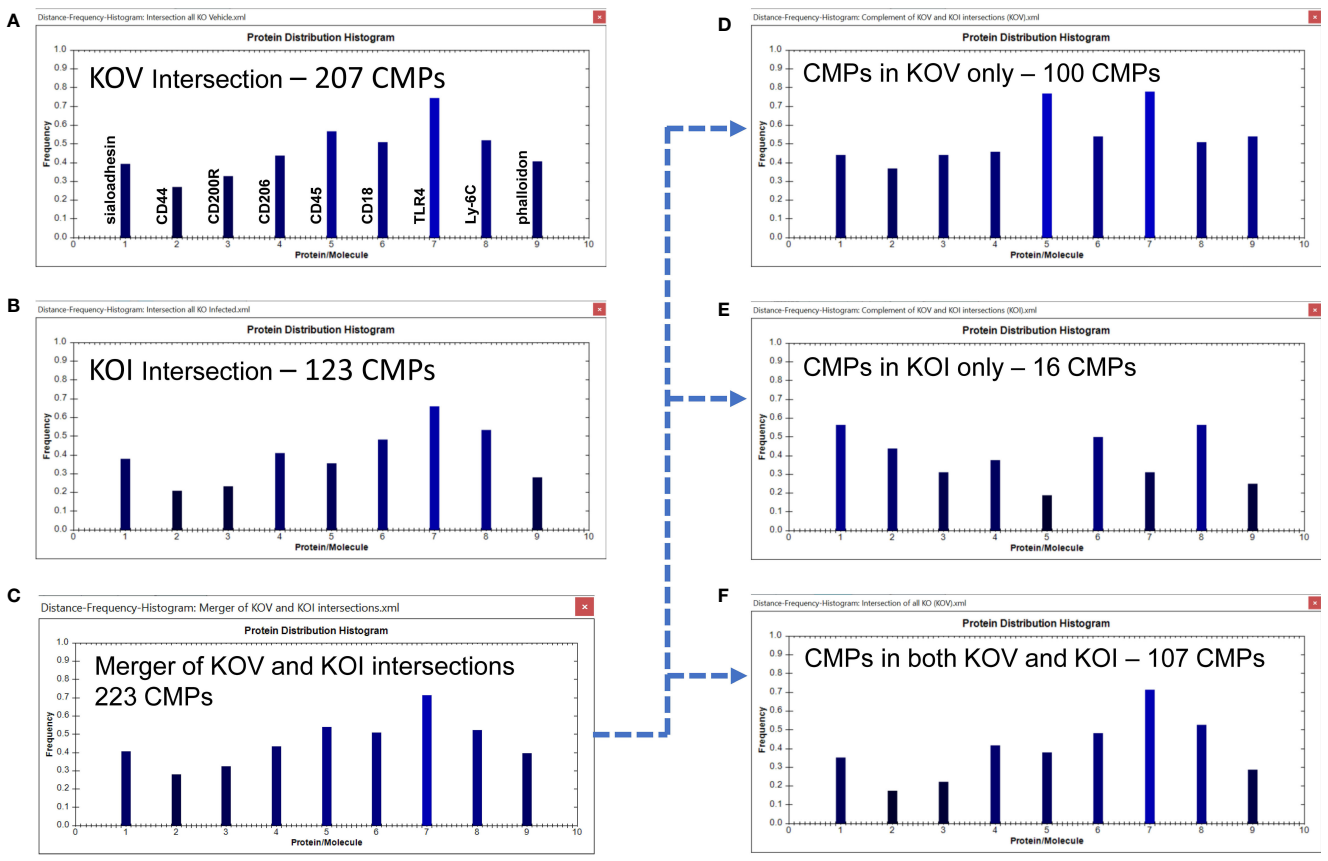

FIGURE 7 | CMP comparison of KO AM. As described in **Figure 6**, Panels **(A, B)** show the intersection of the three KO vehicle and three KO infected samples. Panel **(C)** depicts the merger of Panels **(A, B)** and shows the characteristics of the 223 CMPs that are conserved in the vehicle and/or infected groups. Panels **(D–F)** use the complement feature of the TIS software to identify from the merged 223 CMPs, CMPs present in KO vehicle AM only **(D)**, KO infected AM only **(E)**, or common to both KO groups **(F)**. The arrow originating at Panel **(C)** and terminating at Panels **(D–F)** illustrates this process.

the WT data, when we subjected this set of 223 CMPs to the complement procedure with the TIS software, we found that there were 100 conserved CMPs (i.e. present in all three samples) that were: a) exclusive to the vehicle-treated group (**Figure 7D**); b) 16 conserved CMPs that were exclusive to the infected group (**Figure 7E**); and c) 107 CMPs that were common to both groups (**Figure 7F**). As in **Figure 6** the arrow originating at **Figure 7C** and terminating at **Figures 7D–F** illustrates this process. As described above, we broadly characterize these three categories as baseline, infection-related, and housekeeping functions, respectively. When the KO vehicle and KO infected data sets were compared using the Wilcoxon Rank Sum test they approached (p=0.076), but did not reach significance. The lack of significance in this comparison is probably a function of the blunted response to bacteria by the KO AM.

We observed one major difference from the WT comparison when we compare the histograms of the conserved CMPs in KOV and KOI AM (**Figures 7A, B**). The two histograms in KO are similar to one another, although CD45 is substantially greater in the KOV AM, and TLR4 and phalloidin had slightly higher frequencies in the KOV than in KOI. This overall impression differs from that of the corresponding histograms in the WT AM (**Figures 6A, B**) where more differences in both magnitude and pattern of the histogram bars were observed.

The differences between groups are much more pronounced in the histograms of the CMPs exclusive to the KO vehicle-treated and KO infected groups (**Figures 7D, E**). In these histograms the frequencies of CD45 and TLR4, and to a lesser extent phalloidin, are higher in the KOV AM. An opposite trend was observed for CD45 in the WT AM (**Figures 6D, E**) where CD45 was much higher in the infected AM. TLR4 followed the same pattern in both WT and KO AM with much higher levels in the vehicle-treated versus infected. Whether this difference, and the lack of differences in CD44, CD18, and Ly-6C that we observed in WT (**Figures 6D, E**) are responsible for the increased susceptibility to infection in KO mice remains to be determined.

Effect of SP-A on the AM Toponome of Vehicle and Infected Groups

We next compared the WT and KO vehicle groups to each other (**Figure 8**) and the WT and KO infected groups to each other (**Figure 9**) to better assess the role of SP-A on the regulation of the AM toponome in the presence or absence of SP-A.

Vehicle Groups

As shown previously the WV samples had 176 conserved (i.e. present in all three samples) CMPs (**Figures 6A**, **8A**) and the KOV samples had 207 conserved CMPS (**Figures 7A**, **8B**). For this analysis we compared the two (WT and KO) vehicle data sets. In the conserved CMPs from the two vehicle groups some slight differences in marker content were apparent (compare 8A and 8B). These included a somewhat higher frequency of CMPs containing CD44 and CD18, and a lower frequency of those containing CD45 (marker 5) in WV versus KOV (compare **Figures 8A, B**). Following merger of the data for the three samples in each vehicle group, we obtained 270 unique CMPs (**Figure 8C**). When the complement procedure was applied to these 270 conserved CMPs, it showed: a) 63 that were exclusive to the WV group only (**Figure 8D**); b) 94 CMPs that were present in KOV only (**Figure 8E**); and c) 113 CMPs were common to both groups (**Figure 8F**). As in **Figure 6** the arrow originating at **Figure 8C** and terminating at **Figures 8D–F** illustrates this process. These three sets of CMPs are likely to correspond to CMPs that are SP-A dependent, those that result from the absence of SP-A, and those whose expression in independent of the presence of SP-A, respectively. The histograms show that the relative abundance of the markers in the exclusive groups (**Figures 8D, E**) was similar to that described above for the corresponding conserved CMP sets defined by the intersection of the three samples in each group (**Figures 8A, B**), respectively, but more accentuated. Namely, CD44 and CD18 were much increased in WV vs KOV, and CD45 was much lower in WV than in KOV.

A comparison of these two groups (WV and KOV) with the Wilcoxon Rank Sum test, as done above with the other comparisons, found no difference between the WV and KOV groups (p=0.711).

Infected Groups

The WI samples had 102 conserved CMPs (**Figures 6B**, **9A**) and the KOI had 123 conserved CMPs in KOI samples (**Figures 7B**, **9B**). Note that, as discussed above, there are substantially fewer conserved CMPs in the infected AM than in the vehicle-treated AM (**Figure 8**). When we identified conserved CMPs exclusive to either WI or KOI we found: a) 41 CMPs that were only in WI samples (**Figure 9D**); b) 62 only in KOI samples (**Figure 9E**); and c) 61 CMPs that were common to both groups (**Figure 9F**). As in **Figure 6** the arrow originating at **Figure 9C** and terminating at **Figures 9D–F** illustrates this process. This categorization of these groups, as described above, includes CMPs dependent on the presence of SP-A, the absence of SP-A, and independent of SP-A, respectively. Although the marker differences might have been rather subtle in the histograms for all conserved CMPs in each group (**Figures 9A, B**), the differences in marker frequencies were more prominent when the histograms depicting the profiles of conserved CMPs found only in one group or the other were compared (**Figures 9D, E**). In WI versus KOI the histograms showed that the frequency of CD44 and Ly-6C (markers 2 and 8) in conserved CMPs was higher, and that of sialoadhesin, CD206, CD18, and TLR4 was lower (see markers 1, 4, 6, and 7) in **Figures 9D, E**). The differences in so many markers involved in phagocytosis and AM activation may be part of the reason for the compromised host defense function in KO mice. However, despite these differences when a statistical comparison involving all marker means was subjected to the Wilcoxon Rank Sum test, no significant difference was found (p=0.518).

DISCUSSION

Numerous studies have investigated the effects of SP-A on various aspects of innate immune function (17, 18, 47). These effects are demonstrated in studies from our laboratory and

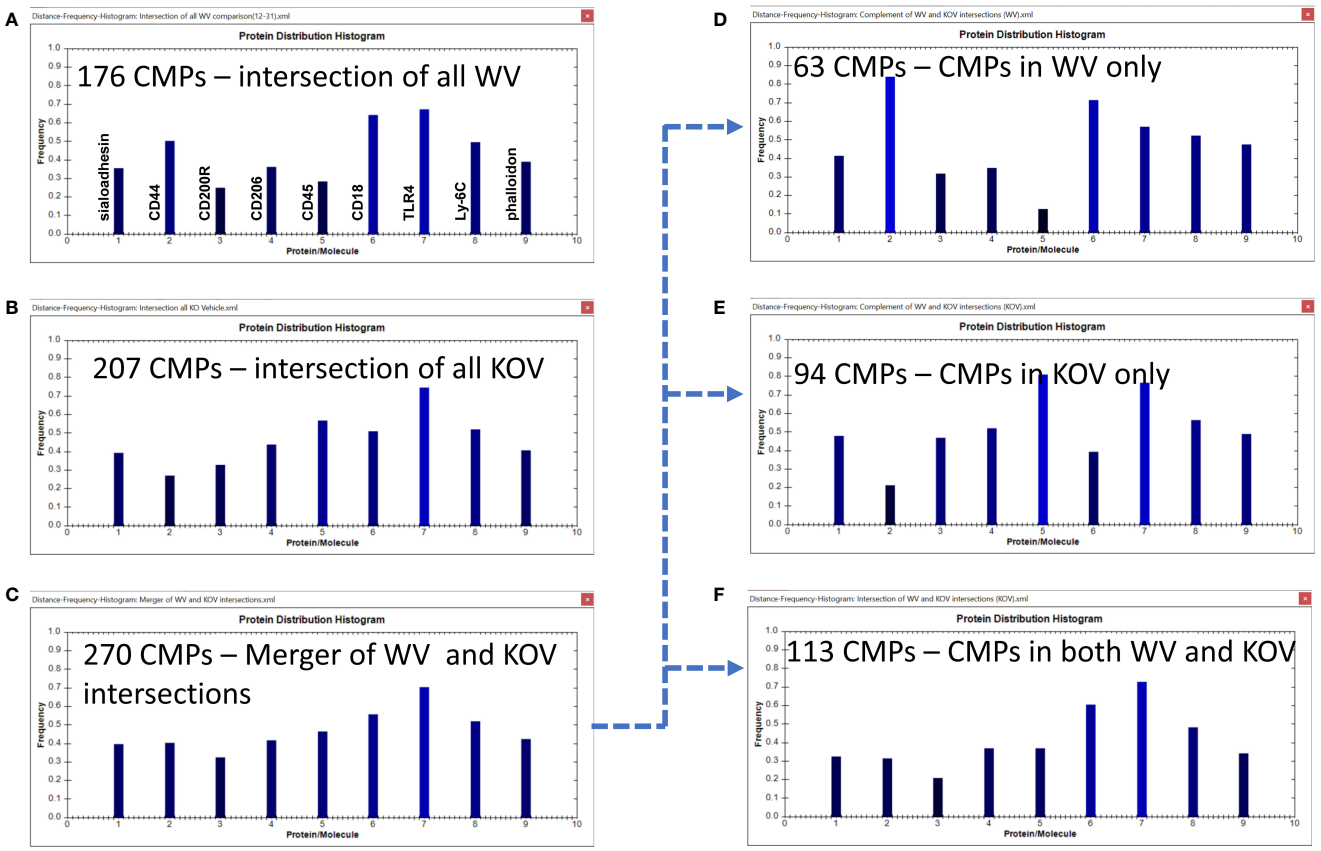

FIGURE 8 | CMP comparison of wild type vehicle (WV) and KO vehicle (KOV) samples. Panels **(A, B)** show the intersection of the three wild type vehicle and three KO vehicle samples. Panel **(C)** shows the results when the data in Panels **(A, B)** are merged and shows the characteristics of the 270 CMPs that are conserved in vehicle-treated WT and/or KO groups. Panels **(D–F)** use the complement feature of the TIS software to identify, from the 270 merged CMPs, CMPs present in wild type vehicle AM only **(D)**, KO vehicle AM only **(E)**, or common to both vehicle groups **(F)**. The arrow originating at Panel **(C)** and terminating at Panels, **(D–F)** illustrates this process.

others that show the vulnerability to infection of mice lacking SP-A (17, 18). Although there are many different ways that host defense in the lung can be influenced, arguably one of the most important is at the point where an infectious organism comes into contact with the alveolar macrophage, the sentinel cell of lung innate immune function. This event triggers a cascade of downstream events that profoundly influence the ability of a cell and eventually of the organism to deal with a threat from a pathogen and survive. As mentioned earlier, the fact that this study employs a relatively short time frame (i.e. harvest of AM 1 hr after instillation of vehicle or bacteria) lessens the likelihood that we are looking at new protein synthetic events. Thus, the changes we observed are probably the result of the re-organization of existing proteins into new CMPs, making TIS an ideal tool to study this.

In previous TIS studies of the AM we have described a way to assess the phenotypic consistency or diversity of the AM in an experimental group by determining whether specific CMPs are consistently expressed or "conserved" among members of that experimental group (14–16). Given the large number of potential protein combinations or CMPs that could be identified with TIS (i.e. 2^n where n = number of markers tested) (14–16) it is likely that the presence of specific CMPs in multiple samples is not random, but rather due to regulatory influences characteristic of that experimental group. Although in this study we were unable to characterize individual cells, the histograms provided us with a tool to summarize the marker content of a group of CMPs and identify markers whose variability could be important. Our assumption is that these conserved CMPs mediate critical functions and/or are characteristic of the presence or absence of a key regulator, such as SP-A. In the present study, we addressed this problem by analyzing our data sets in two ways. In the first part of the study we did direct comparisons of AM treated with vehicle to infected AM to assess the effects of infection on the AM toponome in the presence or absence of SP-A. In the second part of the study we compared: a) vehicle-treated WT and KO to assess the role of SP-A on the baseline AM proteome (i.e. unprovoked AM toponome); and b) infected WT and KO AM to assess, *via* this comparison, the role of SP-A on the AM toponome in response to infection.

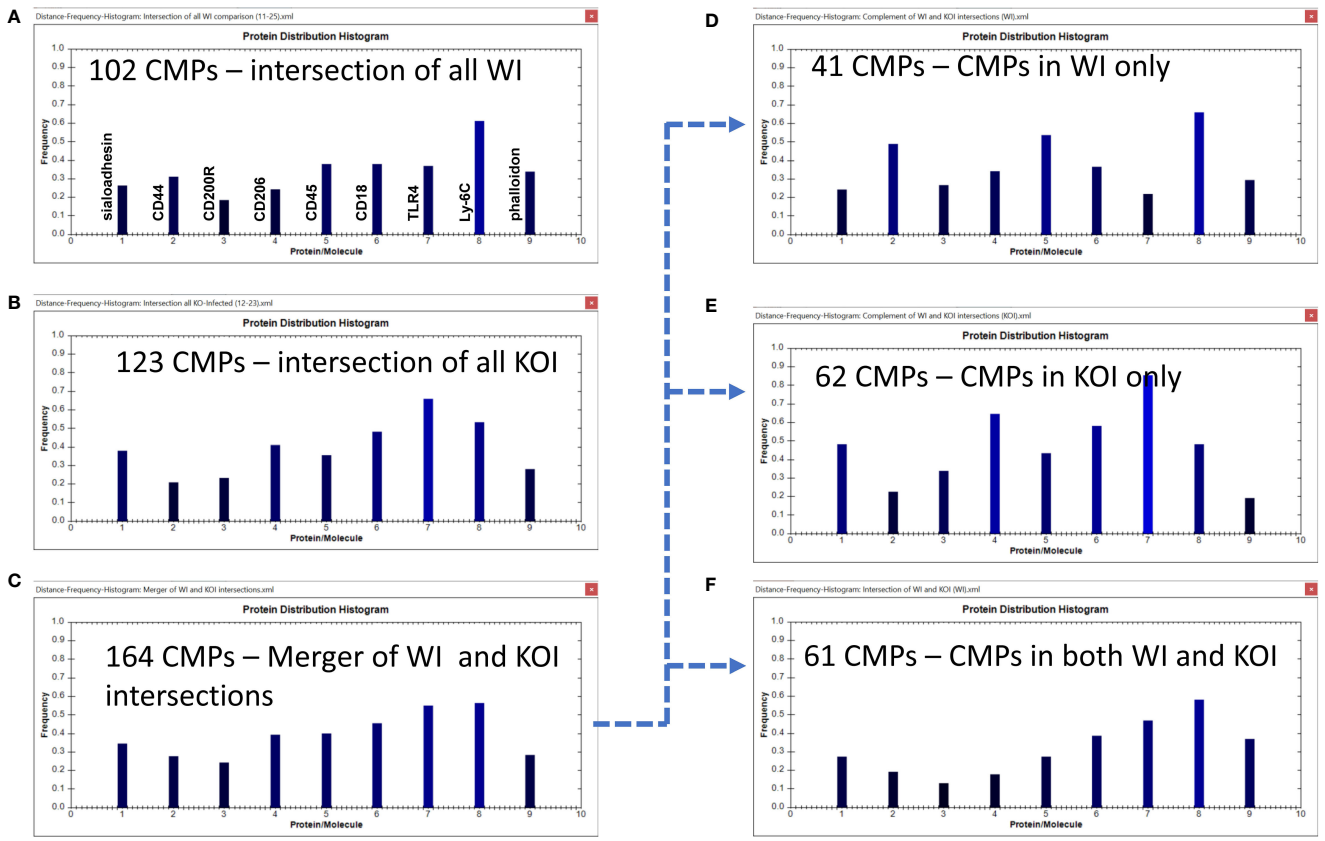

FIGURE 9 | CMP comparison of wild type infected (WI) and KO infected (KOI) AM. Panels **(A, B)** show the intersection of the three wild type infected and three KO infected samples. Panel **(C)** shows the results when the data in Panels **(A, B)** are merged and shows the characteristics of the 164 CMPs that are conserved in the WT and/or KO infected groups. Panels **(D–F)** use the complement feature of the TIS software to identify, from the 164 merged CMPs, CMPs present in wild type infected AM only **(D)**, KO infected AM only **(E)**, or common to both vehicle groups **(F)**. The arrow originating at Panel **(C)** and terminating at Panels **(D–F)** illustrates this process.

Impact of Infection on the AM Toponome in the Presence or Absence of SP-A

In the first set of comparisons, which consisted of CMPs exclusive to either vehicle or infected AM, we observed that there were far more conserved CMPs in the vehicle group than in the infected group. We speculate that this reflected the fact that normally populations of AM have the potential to differentiate along multiple pathways, as predicted by the heterogeneity that typically characterizes AM populations (14–16, 48) and that the larger number of conserved CMPs in the vehicle-treated cells reflect AM pluripotentiality. However, when a challenge occurs, such as infection, many of these conserved CMPs reorganize into a smaller group of CMPs that are focused on dealing with the pathogen. Thus, a decrease in the number of conserved CMPs is observed as the AM redirects its proteins to focus on innate immune defenses against the bacteria rather than maintaining readiness to proceed down many potential pathways. Moreover, the general reorganization of CMPs to a smaller group of CMPs in response to infection may be independent of SP-A, as both WT and KO were identified with a reduced number of CMPs when each was compared to its corresponding vehicle group. However, the specific nature of CMPs varies as differences between the CMP histograms of the WT vehicle and WT infected AM as well as KO vehicle and KO infected were observed. These may reflect qualitative differences between WT and KO in the attempt to combat infection. Furthermore, although the number of CMPs in WT vehicle and KO vehicle didn't differ significantly (107 vs 100), the number of CMPs in their corresponding infected group was quite different. The KO infected had about half as many exclusive CMPs (i.e. CMPs found only in that group) compared to WT infected (16 vs 33). This may indicate that the KO AM is only capable of invoking a limited number of pathways to combat infection, because: a) its baseline or readiness of AM is compromised in the absence of SP-A; b) the AM is unable to recognize and ingest a pathogen and initiate a successful response in the absence of SP-A; or c) both of these possibilities are contributing to the poorer outcome of KO animals in response to infection.

Of interest, in the absence of SP-A, the KO AM is not dormant and it still generates unique CMPs either in response

to vehicle or infection. However, the relatively small number of infection-specific CMPs in the KOI AM versus the KOV, and the presence of twice as many infection-specific CMPs in the WT infected AM versus the KOI, indicate a greater capacity for WT to respond to an infectious challenge and a potential inadequacy of the KO to respond and successfully overcome the challenge as we have shown by survival studies (12, 17, 18), Moreover, these CMPs constitute only a fraction of the AM's repertoire and there are likely to be other subsets, when more or other markers are used, enabling other macrophage functions to occur, such as responses to tissue damage, toxins, particulates, etc. In summary, infection appears to cause a shift of proteins into CMPs needed to respond to the insult. The importance of SP-A in this function is demonstrated by the more vigorous response in the WT AM.

Impact of SP-A on the AM Toponome

In our second set of comparisons we shifted the focus to the effects of SP-A on the AM toponome under baseline conditions and in response to infection by studying vehicle-treated AM from WT and KO mice and then WT and KO AM from infected mice. Knockout mice lacking a functional SP-A gene have been studied for many years (47). Although there is no major apparent phenotypic difference between the two types of mice (WT and KO) under normal, unchallenged conditions (49), our study utilizing TIS and examining expression and localization of nine markers with important roles in host defense function shows that the potential of AM from these two groups is not equivalent. Even though in the present study the number of CMPs didn't seem to differ significantly in AM from WT and KO vehicle (i.e. at baseline) the quality of these differs, as shown by the histograms. The histograms provided us with a tool to identify markers that differed between groups of CMPs. Proteomic studies also have shown that the AM proteome from KO also differs from that of the WT and that upon SP-A rescue the KO proteome becomes similar to that of the WT (6). Although the present findings are consistent with previous published studies, these further indicate that AM protein clusters or combinatorial molecular phenotypes (i.e, CMPs), rather than single protein levels, may underlie the previously observed differences at either baseline (15) or in response to infection (17). For the latter, both quantitative (i.e. the number of CMPs) and qualitative CMPs differences between WT and KO were observed. These CMPs may, in part, be SP-A-dependent and responsible for the poorer outcome in KO of either AM function in terms of their phagocytic index (17) or other AM functions (47, 49).

In the absence of an infectious challenge, the marked differences observed in the histograms in the CMP frequency of CD44, CD45, and CD18 between WT and KO may be predictive of potential host defense deficits in the AM given the importance of these proteins to host defense function (1, 30–32, 35, 36, 50). These differences were confirmed when we compared the two groups after an infectious challenge with *K. pneumoniae*, as differences in the infected groups in the same markers were observed as those seen in the vehicle-treated groups. However, in response to infection, marked differences were also observed in the CMP frequency of CD206, TLR4 and Ly-6C, all of which have important host defense functions (27, 28, 33, 34, 51).

The comparisons of the histograms from the two vehicle AM sets (**Figure 8**) and the two infected AM sets (**Figure 9**) offer some additional insight into the importance of SP-A. In previously published BAL proteomic studies (7, 52) we have observed that KO AM may overcompensate for deficits resulting from the lack of SP-A. The higher numbers of conserved CMPs in the present study in the KO groups versus the WT may be a manifestation of this. Not only are there overall more conserved CMPs in the two KO groups (vehicle and infected) but the sets of CMPs exclusive to KOV and KOI AM (**Figures 8E** and **9E**) are ~50% greater than the corresponding WT groups. However, despite the increased number of CMPs, the host defense function of the KO AM is inadequate, probably due to dysregulation of some important proteins, as shown by differences in the histograms of the two infected groups. CD45 (marker 5), a marker that varies considerably in the histograms from different groups, is a good example of the potential loss of mechanisms that may enable the formation of CMPs. The cellular localization of CD45 is dynamic and its distribution can be altered by conditions (30). Its baseline (vehicle) levels are low in WT AM and high in KO AM and just the reverse with infection, implying that its incorporation into CMPs varies with SP-A status. CD45 has many different forms and many different ligands and is involved in numerous aspects of immune cell function (30–32, 50). Given the multiple roles of SP-A in immune cell regulation it is likely that SP-A is involved in CD45's regulation or the regulation of its ligands and thus further investigation in this area is needed.

Common CMPs

There are also a number of conserved CMPs that are common to both vehicle and infected groups. The CMPs common to both vehicle and infected AM may be important for baseline or "housekeeping" functions in the AM. This notion is further supported by the observation that common CMPs exist in both WT vehicle and KO vehicle AM, as well as in WT infected and KO infected. These may, in part, provide a basis for the fact that KO mice, in the absence of infectious or inflammatory challenge, exhibit no major phenotypic differences from WT (49), although differences in the AM proteome between KO and WT have been observed previously (7). However, their histograms in the present study share more similarities than differences indicating that the AM baseline phenotype or its "prepared" state for future host defense is similar, but not identical between WT and KO. The common CMPs between WT and KO may be thought of as SP-A-independent. CMPs unique to WT and absent in KO at either baseline or in response to infection may be thought of as SP-A-dependent and it is likely that at least some of these play a role in mounting an effective response to infection.

In summary, using TIS and a set of nine macrophage markers we showed: a) sets of CMPs present in both WT and KO AM whose expression is independent of SP-A; b) CMP differences between vehicle-treated WT and KO AM probably due to the presence or absence of SP-A; c) a decrease in the total number of conserved CMPs in the infected AM of both groups vs vehicle,

possibly due to the mobilization of proteins into specific CMPs needed to deal with infection; and d) after an infectious challenge a number of differences in the relative CMP frequencies of different proteins existed between CMPs exclusive to the challenged AM from WT and KO AM. For the latter we postulate: 1) that these differences are responsible for the effective and ineffective response to infection of WT and KO AM, respectively, as shown by survival studies (17, 18); and 2) that these would largely be reversed by administration of exogenous SP-A, as shown previously with proteomic studies of the SP-A rescued KO AM (7) and lead to an improved survival rate after infection (17, 18). Thus, SP-A is important for the organization of AM CMPs in response to infection and to a lesser degree at AM baseline conditions.

CONCLUSION

In the absence of SP-A, a dysregulation may occur with regard to mechanisms that may lead to optimal outcomes, and this may be reflected in the number and composition of CMPs, as shown in the present study. Moreover, SP-A may contribute directly to CMP formation *via* interactions with various cell surface molecules, and in its absence these CMPs cannot be formed. The KO AM is not dormant and it still generates unique CMPs in both the baseline state and in response to infection, but these are not sufficient to enable a successful response in numerous readouts, as shown by published studies (19, 47). Although the mechanisms for CMP generation are not known, SP-A may play a direct or indirect role, as noted above. CMPs, in the presence and absence of SP-A at baseline conditions or in response to infection, consist of proteins whose levels may differ as well as proteins whose levels may not change. Although, the latter may be equally important in enabling the formation of protein patterns necessary to combat an insult, the present study was not designed to address this. However, the present study provides part of the foundation for further investigation. Future studies are needed to explore CMP differences by employing additional markers or antibodies, exogenous SP-A treatment (in WT mice) or rescue (in KO mice), or other, in order to experimentally manipulate specific markers that differ in WT vs KO AM CMPs. It is also possible that the binding of SP-A, either by itself or bound to pathogens, to cell surface molecules such as those studied here may play a role in the organization of CMPs that are important in host defense against infection. Such studies using technologies like TIS may identify key proteins responsible for the integrity of given CMPs necessary for host defense and other functions and help determine whether these potentially could serve as therapeutic agents or targets (52).

DATA AVAILABILITY STATEMENT

The raw data supporting the conclusions of this article will be made available by the authors, without undue reservation.

ETHICS STATEMENT

The animal study was reviewed and approved by The Institutional Animal Care and Use Committee of the Penn State College of Medicine.

AUTHOR CONTRIBUTIONS

DSP conducted TIS experiments, processed data, interpreted results, and wrote the manuscript. VMC converted .xml data files to SAS, allowing more extensive analysis and performed the statistical analyses on the dataset. XZ prepared bacteria, treated mice with vehicle or bacteria, recovered AM from mice, and prepared slides for TIS. DS provided helpful suggestions for antibody calibration, operation of the TIS system, and use of TIS software for processing of data. JW provided guidance and suggestions for conducting TIS experiments and processing data and participated in planning of the manuscript. JF was responsible for overall direction of the project including: developing experimental design, interpreting results, and manuscript preparation. All authors contributed to the article and approved the submitted version except JW (who passed away prior to its completion).

FUNDING

This work was supported by a grant from the National Institutes of Health (NIH 1R21AI113050-01A1) and by the G. Pedlow Research Fund.

ACKNOWLEDGMENTS

Purchase and partial support of the Toponome Imaging System was made possible by a generous gift from the Joir and Kato Weisz Charitable Foundation, UK.

REFERENCES

1. Floros J, Thorenoor N, Tsotakos N, Phelps DS. Human Surfactant Protein SP-A1 and SP-A2 Variants Differentially Affect the Alveolar Microenvironment, Surfactant Structure, Regulation and Function of the Alveolar Macrophage, and Animal and Human Survival Under Various Conditions. *Front Immunol* (2021) 12:2889. doi: 10.3389/fimmu.2021.681639
2. Koptides M, Umstead TM, Floros J, Phelps DS. Surfactant Protein A Activates NF-Kappa B in the THP-1 Monocytic Cell Line. *Am J Physiol* (1997) 273(2 Pt 1):L382–8. doi: 10.1152/ajplung.1997.273.2.L382
3. Kremlev SG, Phelps DS. Surfactant Protein A Stimulation of Inflammatory Cytokine and Immunoglobulin Production. *Am J Physiol* (1994) 267(6 Pt 1): L712–9. doi: 10.1152/ajplung.1994.267.6.L712
4. Kremlev SG, Umstead TM, Phelps DS. Surfactant Protein A Regulates Cytokine Production in the Monocytic Cell Line THP-1. *Am J Physiol* (1997) 272(5 Pt 1):L996–1004. doi: 10.1152/ajplung.1997.272.5.L996
5. Wang G, Phelps DS, Umstead TM, Floros J. Human SP-A Protein Variants Derived From One or Both Genes Stimulate TNF-Alpha Production in the THP-1 Cell Line. *Am J Physiol Lung Cell Mol Physiol* (2000) 278(5):L946–54. doi: 10.1152/ajplung.2000.278.5.L946

6. Phelps DS, Umstead TM, Quintero OA, Yengo CM, Floros J. *In Vivo* Rescue of Alveolar Macrophages From SP-A Knockout Mice With Exogenous SP-A Nearly Restores a Wild Type Intracellular Proteome; Actin Involvement. *Proteome Sci* (2011) 9:67. doi: 10.1186/1477-5956-9-67
7. Phelps DS, Umstead TM, Floros J. Sex Differences in the Response of the Alveolar Macrophage Proteome to Treatment With Exogenous Surfactant Protein-A. *Proteome Sci* (2012) 10(1):44. doi: 10.1164/ajrccm-conference.2012.185.1_MeetingAbstracts.A1374
8. Phelps DS, Umstead TM, Silveyra P, Hu S, Wang G, Floros J. Differences in the Alveolar Macrophage Proteome in Transgenic Mice Expressing Human SP-A1 and SP-A2. *J Proteom Genom Res* (2013) 1(2):2–26. doi: 10.14302/issn.2326-0793.jpgr-12-207
9. Phelps DS, Umstead TM, Floros J. Sex Differences in the Acute *In Vivo* Effects of Different Human SP-A Variants on the Mouse Alveolar Macrophage Proteome. *J Proteomics* (2014) 108:427–44. doi: 10.1016/j.jprot.2014.06.007
10. Noutsios GT, Thorenoor N, Zhang X, Phelps DS, Umstead TM, Durrani F, et al. SP-A2 Contributes to miRNA-Mediated Sex Differences in Response to Oxidative Stress: Pro-Inflammatory, Anti-Apoptotic, and Anti-Oxidant Pathways are Involved. *Biol Sex Differ* (2017) 8(1):37. doi: 10.1186/s13293-017-0158-2
11. Thorenoor N, Kawasawa YI, Gandhi CK, Zhang X, Floros J. Differential Impact of Co-Expressed SP-A1/SP-A2 Protein on AM Mirnome; Sex Differences. *Front Immunol* (2019) 10:1960. doi: 10.3389/fimmu.2019.01960
12. Thorenoor N, Phelps DS, Floros J. Differential Sex-Dependent Regulation of the Alveolar Macrophage Mirnome of SP-A2 and Co-Ex (SP-A1/SP-A2) and Sex Differences Attenuation After 18 H of Ozone Exposure. *Antioxid (Basel)* (2020) 9(12). doi: 10.3390/antiox9121190
13. Thorenoor N, Kawasawa YI, Gandhi CK, Floros J. Sex-Specific Regulation of Gene Expression Networks by Surfactant Protein A (SP-A) Variants in Alveolar Macrophages in Response to Klebsiella Pneumoniae. *Front Immunol* (2020) 11:1290. doi: 10.3389/fimmu.2020.01290
14. Phelps DS, Chinchilli VM, Weisz J, Yang L, Shearer D, Zhang X, et al. Differences in the Alveolar Macrophage Toponome in Humanized SP-A1 and SP-A2 Transgenic Mice. *JCI Insight* (2020) 5(24). doi: 10.1172/jci.insight.141410
15. Phelps DS, Chinchilli VM, Weisz J, Shearer D, Zhang X, Floros J. Using Toponomics to Characterize Phenotypic Diversity in Alveolar Macrophages From Male Mice Treated With Exogenous SP-A1. *Biomark Res* (2020) 8:5. doi: 10.1186/s40364-019-0181-z
16. Phelps DS, Chinchilli VM, Yang L, Shearer D, Weisz J, Zhang X, et al. The Alveolar Macrophage Toponome of Female SP-A Knockout Mice Differs From That of Males Before and After SP-A1 Rescue. *Sci Rep* (2022) 12:5039. doi: 110.1038/s41598-022-08114-2
17. Mikerov AN, Haque R, Gan X, Guo X, Phelps DS, Floros J. Ablation of SP-A has a Negative Impact on the Susceptibility of Mice to Klebsiella Pneumoniae Infection After Ozone Exposure: Sex Differences. *Respir Res* (2008) 9:77. doi: 10.1186/1465-9921-9-77
18. Thorenoor N, Umstead TM, Zhang X, Phelps DS, Floros J. Survival of Surfactant Protein-A1 and SP-A2 Transgenic Mice After Klebsiella Pneumoniae Infection, Exhibits Sex-, Gene-, and Variant Specific Differences; Treatment With Surfactant Protein Improves Survival. *Front Immunol* (2018) 9:2404. doi: 10.3389/fimmu.2018.02404
19. Mikerov AN, Gan X, Umstead TM, Miller L, Chinchilli VM, Phelps DS, et al. Sex Differences in the Impact of Ozone on Survival and Alveolar Macrophage Function of Mice After Klebsiella Pneumoniae Infection. *Respir Res* (2008) 9:24. doi: 10.1186/1465-9921-9-24
20. Phelps DS. Surfactant Regulation of Host Defense Function in the Lung: A Question of Balance. *Pediatr Pathol Mol Med* (2001) 20:269–92. doi: 10.1080/15513810109168822
21. Jakel A, Qaseem AS, Kishore U, Sim RB. Ligands and Receptors of Lung Surfactant Proteins SP-A and SP-D. *Front Biosci (Landmark Ed)* (2013) 18 (3):1129–40. doi: 10.2741/4168
22. Kuroki Y, Takahashi M, Nishitani C. Pulmonary Collectins in Innate Immunity of the Lung. *Cell Microbiol* (2007) 9(8):1871–9. doi: 10.1111/j.1462-5822.2007.00953.x
23. Henning LN, Azad AK, Parsa KV, Crowther JE, Tridandapani S, Schlesinger LS. Pulmonary Surfactant Protein A Regulates TLR Expression and Activity in Human Macrophages. *J Immunol* (2008) 180(12):7847–58. doi: 10.4049/jimmunol.180.12.7847
24. Beharka AA, Gaynor CD, Kang BK, Voelker DR, McCormack FX, Schlesinger LS. Pulmonary Surfactant Protein A Up-Regulates Activity of the Mannose Receptor, a Pattern Recognition Receptor Expressed on Human Macrophages. *J Immunol* (2002) 169(7):3565–73. doi: 10.4049/jimmunol.169.7.3565
25. Crocker PR, Paulson JC, Varki A. Siglecs and Their Roles in the Immune System. *Nat Rev Immunol* (2007) 7(4):255–66. doi: 10.1038/nri2056
26. Amash A, Wang L, Wang Y, Bhakta V, Fairn GD, Hou M, et al. CD44 Antibody Inhibition of Macrophage Phagocytosis Targets Fcgamma Receptor- and Complement Receptor 3-Dependent Mechanisms. *J Immunol* (2016) 196(8):3331–40. doi: 10.4049/jimmunol.1502198
27. Tsuchiya K, Suzuki Y, Yoshimura K, Yasui H, Karayama M, Hozumi H, et al. Macrophage Mannose Receptor CD206 Predicts Prognosis in Community-Acquired Pneumonia. *Sci Rep* (2019) 9(1):18750. doi: 10.1038/s41598-019-55289-2
28. Ciesielska A, Matyjek M, Kwiatkowska K. TLR4 and CD14 Trafficking and its Influence on LPS-Induced Pro-Inflammatory Signaling. *Cell Mol Life Sci* (2021) 78(4):1233–61. doi: 10.1007/s00018-020-03656-y
29. Gordon S. Phagocytosis: An Immunobiologic Process. *Immunity* (2016) 44 (3):463–75. doi: 10.1016/j.immuni.2016.02.026
30. Saunders AE, Johnson P. Modulation of Immune Cell Signalling by the Leukocyte Common Tyrosine Phosphatase, CD45. *Cell Signal* (2010) 22 (3):339–48. doi: 10.1016/j.cellsig.2009.10.003
31. Al Barashdi MA, Ali A, McMullin MF, Mills K. Protein Tyrosine Phosphatase Receptor Type C (PTPRC or CD45). *J Clin Pathol* (2021) 74(9):548–52. doi: 10.1136/jclinpath-2020-206927
32. St-Pierre J, Ostergaard HL. A Role for the Protein Tyrosine Phosphatase CD45 in Macrophage Adhesion Through the Regulation of Paxillin Degradation. *PloS One* (2013) 8(7):e71531. doi: 10.1371/journal.pone.0071531
33. Fitzgerald KA, Kagan JC. Toll-Like Receptors and the Control of Immunity. *Cell* (2020) 180(6):1044–66. doi: 10.1016/j.cell.2020.02.041
34. Lu MY, Lin YL, Kuo Y, Chuang CF, Wang JR, Liao F. Muscle Tissue Damage and Recovery After EV71 Infection Correspond to Dynamic Macrophage Phenotypes. *Front Immunol* (2021) 12:2792. doi: 10.3389/fimmu.2021.648184
35. Fagerholm SC, Guenther C, Llort AM, Savinko T, Uotila LM. Beta2-Integrins and Interacting Proteins in Leukocyte Trafficking, Immune Suppression, and Immunodeficiency Disease. *Front Immunol* (2019) 10:254. doi: 10.3389/fimmu.2019.00254
36. Hollingsworth JW, Li Z, Brass DM, Garantziotis S, Timberlake SH, Kim A, et al. CD44 Regulates Macrophage Recruitment to the Lung in Lipopolysaccharide-Induced Airway Disease. *Am J Respir Cell Mol Biol* (2007) 37(2):248–53. doi: 10.1165/rcmb.2006-0363OC
37. Bhattacharya S, Mathew G, Ruban E, Epstein DB, Krusche A, Hillert R, et al. Toponome Imaging System: *In Situ* Protein Network Mapping in Normal and Cancerous Colon From the Same Patient Reveals More Than Five-Thousand Cancer Specific Protein Clusters and Their Subcellular Annotation by Using a Three Symbol Code. *J Proteome Res* (2010) 9(12):6112–25. doi: 10.1021/pr100157p
38. Schubert W. Systematic, Spatial Imaging of Large Multimolecular Assemblies and the Emerging Principles of Supramolecular Order in Biological Systems. *J Mol Recognit* (2014) 27(1):3–18. doi: 10.1002/jmr.2326
39. Schubert W, Dress A, Ruonala M, Krusche A, Hillert R, Gieseler A, et al. Imaging Cycler Microscopy. *Proc Natl Acad Sci USA* (2014) 111(2):E215. doi: 10.1073/pnas.1319017111
40. Schubert W. Exploring Molecular Networks Directly in the Cell. *Cytom A* (2006) 69(3):109–12. doi: 10.1002/cyto.a.20234
41. Palsson-McDermott EM, O'Neill LA. Signal Transduction by the Lipopolysaccharide Receptor, Toll-Like Receptor-4. *Immunology* (2004) 113 (2):153–62. doi: 10.1111/j.1365-2567.2004.01976.x
42. Bode M, Irmler M, Friedenberger M, May C, Jung K, Stephan C, et al. Interlocking Transcriptomics, Proteomics and Toponomics Technologies for Brain Tissue Analysis in Murine Hippocampus. *Proteomics* (2008) 8(6):1170–8. doi: 10.1002/pmic.200700742
43. Schubert W, Bonnekoh B, Pommer AJ, Philipsen L, Bockelmann R, Malykh Y, et al. Analyzing Proteome Topology and Function by Automated Multidimensional Fluorescence Microscopy. *Nat Biotechnol* (2006) 24 (10):1270–8. doi: 10.1038/nbt1250
44. Mikerov AN, Umstead TM, Huang W, Liu W, Phelps DS, Floros J. SP-A1 and SP-A2 Variants Differentially Enhance Association of Pseudomonas

Aeruginosa With Rat Alveolar Macrophages. *Am J Physiol Lung Cell Mol Physiol* (2005) 288(1):L150–8. doi: 10.1152/ajplung.00135.2004
45. Mikerov AN, Wang G, Umstead TM, Zacharatos M, Thomas NJ, Phelps DS, et al. Surfactant Protein A2 (SP-A2) Variants Expressed in CHO Cells Stimulate Phagocytosis of Pseudomonas Aeruginosa More Than do SP-A1 Variants. *Infect Immun* (2007) 75(3):1403–12. doi: 10.1128/IAI.01341-06
46. Mikerov AN, Umstead TM, Gan X, Huang W, Guo X, Wang G, et al. Impact of Ozone Exposure on the Phagocytic Activity of Human Surfactant Protein A (SP-A) and SP-A Variants. *Am J Physiol Lung Cell Mol Physiol* (2008) 294(1): L121–30. doi: 10.1152/ajplung.00288.2007
47. Depicolzuane L, Phelps DS, Floros J. Surfactant Protein-A Function: Knowledge Gained From SP-A Knockout Mice. *Front Pediatr* (2021) 9:799693. doi: 10.3389/fped.2021.799693
48. Tsotakos N, Phelps DS, Yengo CM, Chinchilli VM, Floros J. Single-Cell Analysis Reveals Differential Regulation of the Alveolar Macrophage Actin Cytoskeleton by Surfactant Proteins A1 and A2: Implications of Sex and Aging. *Biol Sex Differ* (2016) 7:18. doi: 10.1186/s13293-016-0071-0
49. Korfhagen TR, Bruno MD, Ross GF, Huelsman KM, Ikegami M, Jobe AH, et al. Altered Surfactant Function and Structure in SP-A Gene Targeted Mice. *Proc Natl Acad Sci USA* (1996) 93(18):9594–9. doi: 10.1073/pnas.93.18.9594
50. Rheinlander A, Schraven B, Bommhardt U. CD45 in Human Physiology and Clinical Medicine. *Immunol Lett* (2018) 196:22–32. doi: 10.1016/j.imlet.2018.01.009
51. Zamze S, Martinez-Pomares L, Jones H, Taylor PR, Stillion RJ, Gordon S, et al. Recognition of Bacterial Capsular Polysaccharides and Lipopolysaccharides by the Macrophage Mannose Receptor. *J Biol Chem* (2002) 277(44):41613–23. doi: 10.1074/jbc.M207057200
52. Ali M, Umstead TM, Haque R, Mikerov AN, Freeman WM, Floros J, et al. Differences in the BAL Proteome After Klebsiella Pneumoniae Infection in Wild Type and SP-A-/- Mice. *Proteome Sci* (2010) 8:34. doi: 10.1186/1477-5956-8-34

Conflict of Interest: The authors declare that the research was conducted in the absence of any commercial or financial relationships that could be construed as a potential conflict of interest.

frontiers | Frontiers in Immunology

ORIGINAL RESEARCH
published: 02 June 2022
doi: 10.3389/fimmu.2022.842745

Single Nucleotide Polymorphisms (SNP) and SNP-SNP Interactions of the Surfactant Protein Genes Are Associated With Idiopathic Pulmonary Fibrosis in a Mexican Study Group; Comparison With Hypersensitivity Pneumonitis

*Ata Abbasi[1,2], Chixiang Chen[3†], Chintan K. Gandhi[4], Rongling Wu[3], Annie Pardo[5], Moises Selman[6] and Joanna Floros[4,7]**

[1] Cellular and Molecular Research Center, Cellular and Molecular Medicine Institute, Urmia University of Medical Sciences, Urmia, Iran, [2] Department of Pathology, Faculty of Medicine, Urmia University of Medical Sciences, Urmia, Iran, [3] Department of Public Health Science, Pennsylvania State University College of Medicine, Hershey, PA, United States, [4] Department of Pediatrics, Pennsylvania State University College of Medicine, Hershey, PA, United States, [5] Facultad de Ciencias, Universidad Nacional Autónoma de México, Mexico City, Mexico, [6] Unidad de Investigación, Instituto Nacional de Enfermedades Respiratorias "Ismael Cosio Villegas", Mexico City, Mexico, [7] Department of Obstetrics & Gynecology, Pennsylvania State University College of Medicine, Hershey, PA, United States

Surfactant proteins (SPs) are important for normal lung function and innate immunity of the lungs and their genes have been identified with significant genetic variability. Changes in quantity or quality of SPs due to genetic mutations or natural genetic variability may alter their functions and contribute to the host susceptibility for particular diseases. Alternatively, SP single nucleotide polymorphisms (SNPs) can serve as markers to identify disease risk or response to therapies, as shown for other genes in a number of other studies. In the current study, we evaluated associations of *SFTP* SNPs with idiopathic pulmonary fibrosis (IPF) by studying novel computational models where the epistatic effects (dominant, additive, recessive) of SNP-SNP interactions could be evaluated, and then compared the results with a previously published hypersensitivity pneumonitis (HP) study where the same novel models were used. Mexican Hispanic patients (IPF=84 & HP=75) and 194 healthy control individuals were evaluated. The goal was to identify SP SNPs and SNP-SNP interactions that associate with IPF as well as SNPs and interactions that may be unique to each of these interstitial diseases or common between them. We observed: 1) in terms of IPF, i) three single *SFTPA1* SNPs to associate with decreased IPF risk, ii) three *SFTPA1* haplotypes to associate with increased IPF risk, and iii) a number of three-SNP interactions to associate with IPF susceptibility. 2) Comparison of IPF and HP, i) three *SFTPA1* and one *SFTPB* SNP associated with decreased risk in IPF but increased risk in HP, and one *SFTPA1* SNP associated with

OPEN ACCESS

Edited by:
Taruna Madan, National Institute for Research in Reproductive Health (ICMR), India

Reviewed by:
Bartosz Pilecki, University of Southern Denmark, Denmark
Haruhiko Furusawa, Tokyo Medical and Dental University, Japan

***Correspondence:**
Joanna Floros
jfloros@pennstatehealth.psu.edu

[†]Present address:
Chixiang Chen, Department of Epidemiology and Public Health, University of Maryland School of Medicine, Baltimore, MD

Specialty section:
This article was submitted to Molecular Innate Immunity, a section of the journal Frontiers in Immunology

Received: *24 December 2021*
Accepted: *09 May 2022*
Published: *02 June 2022*

Citation:
Abbasi A, Chen C, Gandhi CK, Wu R, Pardo A, Selman M and Floros J (2022) Single Nucleotide Polymorphisms (SNP) and SNP-SNP Interactions of the Surfactant Protein Genes Are Associated With Idiopathic Pulmonary Fibrosis in a Mexican Study Group; Comparison With Hypersensitivity Pneumonitis. Front. Immunol. 13:842745. doi: 10.3389/fimmu.2022.842745

decreased risk in both IPF and HP, ii) a number of three-SNP interactions with the same or different effect pattern associated with IPF and/or HP susceptibility, iii) one of the three-SNP interactions that involved SNPs of *SFTPA1*, *SFTPA2*, and *SFTPD*, with the same effect pattern, was associated with a disease-specific outcome, a decreased and increased risk in HP and IPF, respectively. This is the first study that compares the SP gene variants in these two phenotypically similar diseases. Our findings indicate that SNPs of all *SFTPs* may play an important role in the genetic susceptibility to IPF and HP. Importantly, IPF and HP share some SP genetic variants, suggesting common pathophysiological mechanisms and pathways regarding surfactant biogenesis, but also some differences, highlighting the diverse underlying pathogenic mechanisms between an inflammatory-driven fibrosis (HP) and an epithelial-driven fibrosis (IPF). Alternatively, the significant SNPs identified here, along with SNPs of other genes, could serve as markers to distinguish these two devastating diseases.

Keywords: surfactant protein, single nucleotide polymorphism, idiopathic pulmonary fibrosis, hypersensitivity pneumonitis, SNP-SNP interactions

INTRODUCTION

Idiopathic pulmonary fibrosis (IPF) is one of the most common interstitial diseases of unknown etiology and poor prognosis (1, 2). It is characterized by aberrant activation of the lung epithelium which provokes the increase and activation of the fibroblasts population that finally leads to the replacement of lung parenchyma with destructive fibrotic bundles leading to respiratory failure and death (3, 4). IPF is a chronic, progressive, irreversible, and usually lethal disease of middle-aged and elderly patients (5, 6). Multiple efforts on different aspects to find out the etiology of this disease have been made but with little progress (3, 7–10). The clinical course of IPF is heterogeneous and considerable overlap exists in presentation of IPF and chronic hypersensitivity pneumonitis (HP) (11).

Hypersensitivity pneumonitis (HP) is another type of interstitial lung disease caused by an exaggerated immune response to environmental antigens, such as fugal, bacterial or bird proteins (12). Although antigens that cause HP have been identified and are distributed worldwide, only a very small percent of the world population gets affected and the distribution among different nations is not similar (12). In Mexico, the pigeon breeder's disease is the most common type of HP, caused by proteins from avian serum, feces, and feathers (12).

IPF and HP are different diseases with different etiologies. Validated risk factors for IPF include mainly aging and smoking; exposure to metal dust, wood dust, pesticide, and occupational history of farming or agriculture also increased the risk of IPF. Likewise, the risk of HP is associated mainly to the exposure to organic particles and varies with regional disparities in climate, occupational exposures, and environmental exposures, but not ethnicity. Respiratory viral infections, and high pesticide exposure, have been revealed as risk factors. Paradoxically, cigarette smoke reduces the risk of HP, but when smokers develop HP, they often follow a chronic fibro-proliferative course. However, there is a considerable overlap in pathophysiology and clinical presentation (6, 12–14). In fact, a previous study has shown that almost half of IPF patients, were, subsequently, diagnosed with chronic fibrotic HP, and often the clinical, functional and radiological behavior of both diseases are indistinguishable (13, 14). In both diseases, several members of the same family may be affected, indicating the role of genetic factors in the pathogenesis and progression of these diseases (15, 16). However, the interplay of genetics, environmental factors, and perhaps other factors is poorly understood.

Pulmonary surfactant and surfactant proteins (SPs), have been shown to play roles in host-defense functions, i.e. regulation of pro-inflammatory cytokine production, chemotaxis, and tissue repair (17–20), and in surfactant-related functions, i.e. lowering surface tension and stabilizing the alveoli. Hence, derangement in functional ability, structure, and/or levels of SPs (SP-A, SP-B, SP-C, SP-D) may contribute to the development of interstitial lung diseases, such as IPF and HP (21, 22). Alternatively, genetic polymorphisms of these important molecules may serve, along with other gene variants, as markers to distinguish these two diseases that share overlapping pathology and clinical presentation. Being able to distinguish these two diseases early on is of great importance. In this context, it has been recently reported a diagnostic algorithm which allow a better differential diagnosis between fibrotic HP and IPF (23). Accurate diagnosis is essential for appropriate treatment and management of these diseases. Currently, Nintedanib and pirfenidone, inhibitors of fibrosis pathways, are the treatments of choice for IPF (24). In contrast, HP treatment is based on corticosteroids and immunosuppressive therapy and importantly, administration of corticosteroids and immunosuppressants in some of the IPF

Abbreviations: IPF, Interstitial pulmonary fibrosis; HP, Hypersensitivity Pneumonitis; SP, surfactant protein; *SFTPA1*, gene encoding *SP-A1*; *SFTPA2*, gene encodi ng *SP-A2*; *SFTPB*, gene encoding SP-B; *SFTPC*, gene encoding SP-C; *SFTPD*, gene encoding SP-C; SNPs, single nucleotide polymorphisms.

patients can worsen their clinical condition, primarily those with severe telomere shortening, causing adverse effects and increased mortality (25). A better understanding of the pathobiology of fibrotic HP and of IPF as well as the genetic and molecular differences between them might help to identify biomarkers that allow distinguishing those patients who would benefit from antigen-exposure avoidance and immunosuppression (i.e., HP), from those with IPF in which the use of these drugs is not only unhelpful but increases the risk of hospitalization and death (12, 23, 25–27). There have been numerous examples in the literature where specific SNPs have been associated with disease susceptibility (28) or drug-response in certain disease populations (27, 29–31). For example, as reviewed and analyzed elsewhere (32) genotypes of molecules carrying certain SNPs were associated with response rates after imatinib treatment in patients with chronic myeloid leukemia. Furthermore, surfactant protein A2 genetic variants and genotypes of the donor lung have been associated with post-transplant clinical outcome i.e., survival in lung transplant patients (33).

The human SP-A is encoded by two similar genes, *SFTPA1* and *SFTPA2*, located on chromosome 10 (19, 34–36). Several genetic polymorphisms of each *SFTPA* gene, have been identified and characterized, and these are found with different frequencies in the general population (18, 19, 37–39). SP-A plays an important role in both innate lung host defense and surfactant-related processes (40) and the human variants may differentially affect these processes (19). SP-B, SP-C, and SP-D are each encoded by a single gene, *SFTPB, SFTPC*, and *SFTPD*, respectively (41), and several polymorphisms have been described for each of these genes (42–44). SP-D also plays a role in lung host defense and the primary role of SP-B and SP-C is in surfactant-related functions/processes. Furthermore, multiple studies showed associations of SPs genetic variants with various acute and chronic lung diseases including acute respiratory distress syndrome (ARDS) (43, 44), chronic obstructive pulmonary disease (COPD) (45, 46), cystic fibrosis (47), and other (44).

In a previous study, we showed associations of SP single nucleotide polymorphisms (SNPs) with IPF in a Mexican population (22). In addition, a number of studies identified significant associations between SP genetic variants or mutations and IPF, pointing to a potential role of SPs in the pathogenesis or specific processes of IPF (1, 7, 10, 48–52). Furthermore, to date many gene polymorphisms are known to be present in both IPF and HP interstitial lung disorders. Common genetic variants in TERC, DSP, MUC5B, ATP11A, FAM13A, and IVD described initially as risk gene factors for IPF also represent risk variants for HP, especially for the fibrotic HP (53, 54). Likewise, rare variants in telomere-related genes, such as TERT, TERC, DKC1, RTEL1, and PARN, have been identified in familial and sporadic IPF, and recently the same mutations were identified in patients with HP (55, 56).

In the present study, we used a statistical approach (57) where novel statistical models were studied to enable investigation of the epistatic effects of SNP-SNP interactions as has been done for other pulmonary diseases (21, 47, 58, 59). Using this novel approach, we reanalyzed IPF data that were previously published. The published study used regression analysis nearly 20 years ago (22). Next we compared these newly analyzed IPF data with our recently published HP data where the same novel statistical models were investigated (21). This comparison study is the first such study where SP variants were compared between IPF and HP. The objectives of the current study are: a) to re-analyze the existing IPF database (22), using the Wang's newer analytical approach (57), to gain further insight into complex SNP-SNP interactions, and b) to compare the IPF and HP data of SNP-SNP interactions, from the current IPF study and our recently HP published work (21), to identify unique interactions to each disease. The rationale for the latter is that both IPF and HP are members of the ILD family and some unique interactions may help to differentiate these two diseases, while shared interactions may reveal some common pathways.

METHODS

Study Population

The IPF and HP study population are the same as the ones described before (21, 22). Briefly, eighty-four and seventy-five unrelated patients were enrolled in the IPF and HP study groups, respectively. The diagnoses of both diseases were supported by clinical observation, pulmonary function, high-resolution computed tomography, and bronchoalveolar lavage findings (4, 12). In some cases, surgical biopsy was done to confirm the diagnosis. Patients with the diagnosis of other interstitial lung disease were excluded. All enrolled HP patients were classified to have a fibrotic HP (4). For both studies, one hundred and ninety-four healthy individuals served as controls. All study members were Hispanic Mexican individuals and enrolled at the National Institute of Respiratory Diseases in Mexico City. The protocol was approved by the Ethics Committee. The demographics and clinical characteristics of the study groups are shown in **Table 1**. Blood samples from enrolled subjects were collected and the genotyping was done using the PCR-RFLP method as described in the previous studies (21, 22).

Surfactant Protein Genes and Single Nucleotide Polymorphisms

We evaluated, as shown in **Table 2**, 17 SNPs of the SP genes using the single SNP model and the two and three-SNP-SNP

TABLE 1 | Demographics and clinical characteristics of the study groups.

Characteristic	Idiopathic pulmonary fibrosis (n = 84)	Hypersensitivity Pneumonitis (n = 75)	Healthy controls (n = 194)
Sex, male/female (%)	59/25 (70/30)	5/70 (8/92)	124/70(64/36)
Age (years)	62.3 ± 10.9	44 ± 13.2	41 ± 14.5
Nonsmokers/smokers (%)	54/30 (64/36)	61/14 (81/19)	103/91(53/47)
FVC % predicted	62.6 ± 14.6	56.6 ± 21.6	106.5 ± 11.3*
FEV1% predicted	65.6 ± 15.8	59.6 ± 21.7	99.7 ± 12.8*
FEV1/FVC%	88.0 ± 10.1	90.7 ± 8.5	79.3 ± 5.5*

*Performed in 122 healthy controls.

interaction models described by Wang et al. (57). These included five from *SFTPA1*, four from *SFTPA2*, four from *SFTPB*, two from *SFTPC*, and two from *SFTPD*.

Statistical Analysis

As mentioned previously (57), we used a SNP–SNP interaction method in a case-control setting to study associations of SP genes SNPs with IPF. Wang et al. developed a computational model for detecting additive, dominant and epistatic effects by integrating quantitative genetic theory into a case-control design context (57). This approach integrates the principle of quantitative genetics, and decomposes the overall genetic effect of each SNP into different components: additive (a), dominant (d), and recessive (r) and can characterize high-order epistatic interactions. For example, consider two genes A and B, which may have four types of epistasis, additive x additive, additive x dominant, dominant x additive, dominant x dominant. These four types function differently to affect disease risk. For example, if a x a is important, this means that the two-marker genotype AABB (homozygote AA at gene A and homozygote BB at gene B) performs differently from the two-marker genotype AAbb (homozygote AA at gene A and homozygote bb at gene B). However, if d x d is significant, this means that double heterozygote AaBb performs differently from the other genotypes. Therefore, it is important to distinguish these four types of epistasis.

This SNP-SNP interaction approach (57) has been used and validated in studying associations of high order epistatic interactions with various acute and chronic pulmonary diseases (21, 47, 58, 59). The cases and controls were converted into a 2×2 contingency table and various types of epistatic interactions at different orders were tested. The p-value was adjusted for sex and smoking due to their modifying effects on both diseases. To account for multiple testing, false discovery rate (FDR) was set at 5%. The Cochran-Mantel-Haenszel test was used to calculate the Odds ratios (OR) with 95% of confidence interval (95%CI). All possible interactions for two- and three-SNP interaction models were tested and those with p value less than 0.05 are reported.

RESULTS

IPF

Main Effect Analysis of the IPF Group (n = 84) vs the Control Group (n = 194)

In the present study, we observed significant differences in the studied groups with the single- and the three-SNP interaction model. We did not observe any significant SNP-SNP interactions in the two-SNP interaction model.

Single SNP Model

Three SNPs, rs1059047, rs1136450, and rs1059057 of *SFTPA1*, were each associated with decreased risk of IPF (OR: 0.42 to 0.46, p value: 0.008-0.010) (**Table 3**).

Association of SNP-SNP Interaction with IPF in the Three-SNP Interaction Model

As previously described, each SNP can have additive, dominant or recessive effect on the disease phenotype and these are noted as a, d, and r, respectively. In our analysis, each SNP had dominant or additive effects, and no recessive effect was observed (**Supplementary Tables 1–6**).

Comparison of the IPF Group (n = 84) vs the Control Group (n = 194)

We found a total of 277 significant SNP-SNP interactions associated with IPF in the three-SNP model. The interactions are shown in detail in **Supplementary Tables 1–6**. Out of these 277 interactions, we observed the following. First, a) 30 interactions with two additive effects and one dominant effect. Four of these exhibited the axdxa effect pattern and 26 the dxaxa; b) 121 interactions with two dominant and one additive effect, (dxdxa (n=65), axdxd (n=27), dxaxd (n=29)) and c) 126 interactions with three dominant effects (dxdxd). Second, 44 were among SNPs of hydrophilic SPs (*SFTPA1, SFTPA2, SFTPD*) alone, 14 were among hydrophobic SPs (*SFTPB, SFTPC*) alone, and the others were among SNPs of both the hydrophilic and hydrophobic SPs. Third, most interactions (n=196) were associated with increased risk of IPF (p=0.001-0.046, OR= 1.48-11.4) and the remaining (n=81) were associated with decreased risk of IPF (p=0.001- 0.049, OR= 0.12-0.69). Among the interactions with increased risk of IPF, 7 were in the same SP gene (intragenic). Of these, 6 were in *SFTPA1* (4 with dxdxd, 1 with axdxd and 1 with dxdxa interactions effect) and 1 in *SFTPB* (with dxaxd interaction effect). Among the interactions with decreased risk of IPF, 2 were intragenic in the *SFTPB* with dxdxa interactions. No significant interactions were observed with recessive (r x r x r) or additive effects (a x a x a) only.

Overall, out of the 17 SNPs studied, 14 were found in SNP-SNP interactions shown to significantly associate with IPF in the three-SNP model. Of the 14 SNPs, six were SNPs of *SFTPA* (4 *SFTPA1* and 2 *SFTPA2*), 4 of *SFTPB*, 2 of *SFTPC* and 2 of *SFTPD*. Although all of these SNPs were frequently present in the significant SNP-SNP interactions, the rs1059046 of *SFTPA2* encoding amino acid 9 ((AA9), Asn>Thr) was the most frequently present followed by *SFTPC* SNPs. The frequency of

TABLE 2 | SNPs of each surfactant protein gene analyzed in this study.

SFTPA1	SFTPA2	SFTPB	SFTPC	SFTPD
rs1059047	rs1059046	rs2077079	rs4715	rs721917
rs1136450	rs17886395	rs3024798	rs1124	rs2243639
rs1136451	rs1965707	rs1130866		
rs1059057	1965708	rs7316		
rs4253527				

TABLE 3 | IPF association with *SFTPA1* single SNPs.

	SNP	Odds ratio (OR)	OR range	adjusted-P value
1	rs1059047	0.461	0.28-0.75	0.010
2	rs1136450	0.422	0.25-0.7	0.008
3	rs1059057	0.442	0.27-0.7	0.008

each of the 14 SNPs found in significant SNP-SNP interactions associated IPF are shown in **Table 4**.

Thirteen interactions had OR greater than 5 indicating a strong association with increased risk of IPF (**Table 5**). Among them one was an intragenic interaction of *SFTPB* SNPs (rs2077079, rs3024798, rs7316) and twelve interactions had two-SNPs with additive and one with dominant effect. In all but one, the *SFTPA1* SNP (rs1136450, (AA50), leu>val) was the one with the dominant effect.

Haplotype Analysis

Haplotype analysis showed that three haplotypes TG (rs1059047 x rs1136450), GA (rs1136450 x rs1136451) and GG (rs1136451 x rs1059057) of the *SFTPA1* were associated with increased risk of IPF (OR=2.372, p=0.004, OR=2.368, p=0.004 and OR=2.265, p=0.004, respectively) and all exhibited a dominant effect (**Table 6** and **Figure 1**). The dominant effect of, for example, the TG haplotype displays a higher risk of IPF compared to the combination of non-risk haplotypes (CC, TT, GG). This is also true for haplotypes GA and GG of *SFTPA1*.

TABLE 4 | Frequency of SNPs in significant SNP-SNP interactions.

SNP	Amino Acid (AA) No.	Surfactant Protein (SP)	frequency in interactions	Amino acid change
rs1136451	AA62	SP-A1	56	–
rs1136450	AA50	SP-A1	60	leu>val
rs1059047	AA19	SP-A1	56	val>Ala
rs1059057	AA133	SP-A1	55	–
rs1059046	AA9	SP-A2	76	Asn>Thr
rs1130866	AA131	SP-B	63	Thr131Ile
rs2077079	AA2	SP-B	60	His2Leu
rs3024798		SP-B	55	–
rs17886395	AA91	SP-A2	57	Pro>Aln
rs2243639	AA180	SP-D	52	Thr180Ala
rs4715	AA138	SP-C	71	Thr138Asn
rs1124	AA186	SP-C	74	Ser186Asn
rs7316		SP-B	43	–
rs721917	AA31	SP-D	53	Met31Thr

Amino acid (AA) designation for SP-A (36, 60) is based on the precursor molecule that includes the signal peptide. Amino designation for SP-B, SP-C, and SP-D does not include the signal peptide (https://www.ncbi.nlm.nih.gov/snp). After signal peptide cleavage both proSP-B and proSP-C undergo several peptide cleavages to give rise to the mature SP-B and SP-C, respectively.

TABLE 5 | SNP interactions associated with IPF with odds ratio higher than 5.

Single nucleotide polymorphism (SNP)			interaction	Odds ratio (OR)	OR interval
rs2077079	rs3024798	rs7316	dxaxd	5.483	2.3-14.5
rs1136450	rs1136451	rs4715	dxaxa	11.430	2.5-107.1
rs1136450	rs1136451	rs1124		10.978	2.4-104.5
rs1136450	rs1059057	rs4715		5.964	2.1-19.1
rs1136450	rs1059057	rs1124		6.238	2.2-20
rs1136450	rs2077079	rs1130866		8.835	2.8-33.8
rs1136450	rs3024798	rs1130866		6.926	2.3-24.1
rs1136450	rs7316	rs4715		6.796	2.7-18.5
rs1136450	rs7316	rs1124		8.904	3.3-26.9
rs1136450	rs4715	rs1124		6.360	2.9-14.9
rs1059047	rs1136450	rs4715	axdxa	5.964	2.1-19.1
rs1059047	rs1136450	rs1124		6.027	2.1-19.3
rs4715	rs1124	rs2243639		9.266	2.3-55.1

TABLE 6 | Haplotype association with IPF susceptibility.

	SNPi	SNPj	Risk haplotype	Odds ratio (OR)	OR range	Adjusted P value
1	rs1059047	rs1136450	TG	2.372	1.437-3.916	0.004
2	rs1136450	rs1136451	GA	2.368	1.434-3.910	0.004
3	rs1136451	rs1059057	GG	2.265	1.398-3.669	0.004

All SNPs shown are from SFTPA1.

Comparison Between IPF (n = 84) and HP (n = 75) Using the Same Control Group (n = 194)

Comparison of SNP Associations in the Single-SNP Model

As shown in **Figure 2**, the rs1136450 of the *SFTPA1* was associated with a decreased risk for both diseases. The rs1059047 and the rs1059057 of the *SFTPA1* were associated with decreased risk of IPF, whereas the rs1136451 of the *SFTPA1* was associated with increased risk of HP. The rs1130866 of the *SFTPB* was associated with decreased risk of HP.

Common SNP-SNP Interactions Between IPF and HP After Comparison to the Same Control Group (n = 194) in the Three SNP Model

We studied the common SNP-SNP interactions in the three SNP model between the 277 interactions resulting from the comparison of the IPF group vs the control group (present study) and the 97 interactions resulting from the comparison of the HP group vs the control group in the three SNP model from our previous study (21). Of the 227 interactions in IPF comparison, as noted above, 81 interactions were associated with decreased risk of IPF, and the remaining 196 with increased risk of the disease. Of the 97 HP interactions, 68 and 29 were associated with decreased and increased risk of HP, respectively. However, in a large number of SNP-SNP interactions, the same SNPs were involved in IPF and HP. These SNP interactions exhibited either the same effect pattern between the two groups, IPF and HP, for example dxdxa (**Table 7**) or a different effect pattern between the two group comparisons i.e., dxdxa vs dxaxd (**Table 8**).

Same SNPs and Same Pattern Effect in IPF and HP

We observed 28 interactions that involved the same SNPs (n=28) that exhibited the same effect pattern (n=29); Interaction #4 (**Table 7**) exhibited two different effect patterns. Of the 28 interactions, 13 of them were associated with decreased risk in both diseases and 12 of them with increased risk in both diseases. However, 4 interactions shown in bold in **Table 7**, involving the same SNPs and exhibiting the same pattern effect were associated with a decreased risk in HP and an increased risk in IPF indicating disease specificity. Moreover, one of these four interactions (rs1059046, rs1136450, rs721917 of *SFTPA2, SFTPA1, SFTPD*, respectively), noted as #4 in **Table 7**,

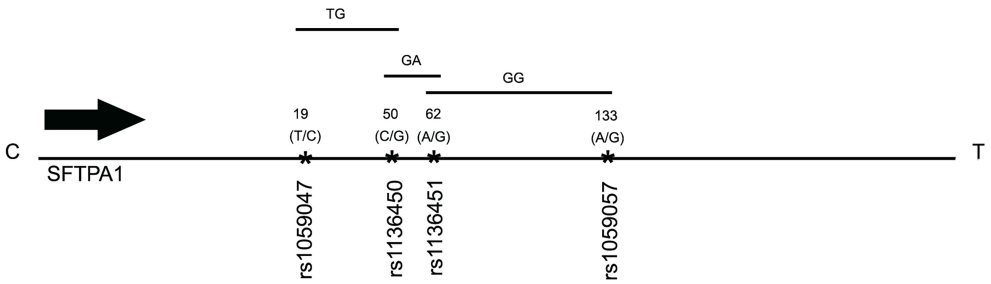

FIGURE 1 | A schematic presentation of the *SFTPA1* gene SNPs is shown. The relative location of the gene is shown from centromere (C) to telomere (T). The numbers above the solid black line indicate the amino acid number with the corresponding nucleotide change shown in parenthesis. The SNP id is noted below the black line. The arrow indicates transcriptional orientation. The transmitted haplotypes (TG, GA, and GG) are shown in a two-SNP model and are associated with increased risk of IPF (OR: OR = 2.372, p = 0.004, OR = 2.368, p = 0.004 and OR = 2.265, p = 0.004, respectively). The TG haplotype is constituted by the rs1059047 Val (T) at codon 19 and the rs1136450 Val(G) at codon 50, the GA haplotype by the rs1136450 Val(G) at codon 50 and the rs1136451 Prol(A) at codon 62 and the GG by the rs1136451 Prol(G) at codon 62 and the rs1059057 Thr(G) at codon 133. Of note, the T/C and C/G alleles change the encoded amino acids at codons 19 Val/Ala and 50 Val/Leu, respectively, but the SNPs at codons 62 and 133 do not change the encoding amino acids (19).

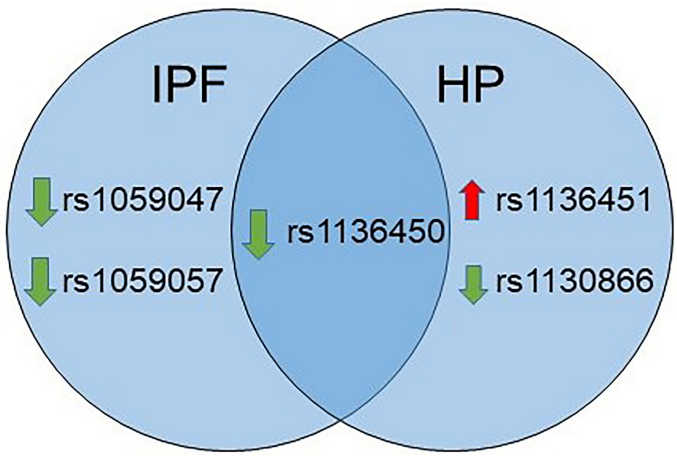

FIGURE 2 | Venn diagram showing similarities and differences in association of SNPs with IPF and HP in a single SNP model. The green and red arrows besides SNPs show association of a given SNP with decreased and increased risk, respectively.

exhibited two different patterns (dxdxd, dxdxa) in both IPF and HP, with the dxdxd (shown in bold) pattern being associated with an outcome that seemed to be disease-specific i.e., with a decreased risk in HP and an increased risk in IPF.

Same SNPs and Different Pattern Effect in IPF and HP

The interactions with the same SNPs (n=37) but with different pattern effects exhibited altered susceptibility in the two diseases and are shown in **Table 8**. For example, interactions #26 and #27, rs1136450 x rs1136451 x rs4715 and rs1136450 x rs1136451 x rs1124 (**Table 8**) with the dxaxa pattern were strongly associated with IPF (OR=11.43, 10.98, respectively), but the same SNP interactions in the dxdxd pattern were both associated with low risk of HP (OR=0.36 and 0.5, respectively). The rs1136450 x rs4715 x rs1124 (interaction #29, **Table 8**) is another interaction which was associated with increased risk of IPF in the dxaxa, dxdxa and dxdxd patterns (OR=6.36, 3.44 and 1.61, respectively) but associated with decreased risk of IPF and HP in the axdxd pattern (interaction #23, **Table 7**).

Of note, rs1059057 and rs7316 were not present in any of the common SNP-SNP interactions.

DISCUSSION

Surfactant proteins (SPs) are important in normal lung function and also in innate immunity of the lungs. Changes in quantity or quality of SPs due to genetic alterations may alter their functions, whether in host defense and/or surfactant-related processes, and contribute to the host susceptibility for particular diseases. SP-A, for example, plays an important role in innate host defense against various pathogens, irritants, and other (40) and its natural genetic variability may differentially affect these

TABLE 7 | Interactions with the same SNPs and the same pattern effect in IPF and HP patients.

Number	SNPs involved in interactions			pattern	OR for HP	OR for IPF
1	rs1059046 *SFTPA2*	rs1136450 *SFTPA1*	rs1136451 *SFTPA1*	axdxd	0.08	0.33
2	rs1059047 *SFTPA1*	rs1136450 *SFTPA1*	rs1136451 *SFTPA1*	dxdxd	1.87	2.09
3	rs1059047 *SFTPA1*	rs2077079 *SFTPB*	rs3024798 *SFTPB*	dxdxd	2.070	2.36
4	**rs1059046**	**rs1136450**	**rs721917**	**dxdxd**	**0.44**	**2.05**
	rs1059046 *SFTPA2*	rs1136450 *SFTPA1*	rs721917 *SFTPD*	dxdxa	3.66	2.37
5	rs1136450 *SFTPA1*	rs1136451 *SFTPA1*	rs721917 *SFTPD*	dxdxa	3.16	2.77
6	rs17886395 *SFTPA2*	rs2077079 *SFTPB*	rs3024798 *SFTPB*	dxdxd	2.18	2
7	rs1136450 *SFTPA1*	rs1136451 *SFTPA1*	rs721917 *SFTPD*	dxdxa	3.16	2.77
8	**rs1059046** *SFTPA2*	**rs2077079** *SFTPB*	**rs4715** *SFTPC*	**dxdxa**	**0.38**	**2.38**
9	**rs3024798** *SFTPB*	**rs4715** *SFTPC*	**rs1124** *SFTPC*	**dxdxd**	**0.45**	**2.54**
10	**rs1130866** *SFTPB*	**rs4715** *SFTPC*	**rs1124** *SFTPC*	**dxdxa**	**0.33**	**2.7**
11	rs1136450 *SFTPA1*	rs2077079 *SFTPB*	rs1130866 *SFTPB*	dxdxd	2.14	2.11
12	rs1136450 *SFTPA1*	rs3024798 *SFTPB*	rs1130866 *SFTPB*	dxdxd	1.89	2.09
13	rs1136451 *SFTPA1*	rs2077079 *SFTPB*	rs1124 *SFTPC*	dxdxd	1.87	2.1
14	rs17886395 *SFTPA2*	rs1136451 *SFTPA1*	rs2077079 *SFTPB*	dxdxa	3.75	2.86
15	rs2077079 *SFTPB*	rs3024798 *SFTPB*	rs721917 *SFTPD*	dxdxa	7.86	3.7
16	rs3024798 *SFTPB*	rs721917 *SFTPD*	rs2243639 *SFTPD*	axdxd	3.43	2.57
17	rs1059046 *SFTPA2*	rs17886395 *SFTPA2*	rs1124 *SFTPC*	dxdxa	0.38	0.46
18	rs1059046 *SFTPA2*	rs1136451 *SFTPA1*	rs4715 *SFTPC*	dxdxd	0.36	0.53
19	rs17886395 *SFTPA2*	rs3024798 *SFTPB*	rs1130866 *SFTPB*	dxdxa	0.33	0.306
20	rs17886395 *SFTPA2*	rs4715 *SFTPC*	rs721917 *SFTPD*	dxdxa	0.29	0.35
21	rs1059047 *SFTPA1*	rs3024798 *SFTPB*	rs1130866 *SFTPB*	dxdxa	0.24	0.43
22	rs1136450 *SFTPA1*	rs2077079 *SFTPB*	rs3024798 *SFTPB*	axdxd	0.2	0.29
23	rs1136450 *SFTPA1*	rs4715 *SFTPC*	rs1124 *SFTPC*	axdxd	0.12	0.32
24	rs1136450 *SFTPA1*	rs3024798 *SFTPB*	rs721917 *SFTPD*	dxdxd	0.44	0.69
25	rs1136450 *SFTPA1*	rs1136451 *SFTPA1*	rs4715 *SFTPC*	dxdxd	0.36	0.63
26	rs1130866 *SFTPB*	rs4715 *SFTPC*	rs1124 *SFTPC*	axdxd	0.33	0.32
27	rs1136451 *SFTPA1*	rs3024798 *SFTPB*	rs1130866 *SFTPB*	dxdxa	0.29	0.48
28	rs2077079 *SFTPB*	rs3024798 *SFTPB*	rs1130866 *SFTPB*	dxdxa	0.24	0.19

Interactions with different disease associations are in bold; OR, odds ratio.

processes (19). In the current study, we evaluated associations of *SFTP* SNPs with IPF using a novel statistical method and compared the results of the current study with a previously published HP study (21). The goal here was to find SNPs and SNP-SNP interactions that are unique to each of these interstitial lung diseases or common between them. Importantly, IPF is an epithelial-driven fibrosis and is typically progressive, while HP is an immune inflammatory-driven disease, often evolving to

TABLE 8 | Interactions with the same SNPs and different effect pattern in IPF and HP patients.

No	Interactions			HP		IPF	
				pattern	OR	pattern	OR
1	rs1059046	rs1130866	rs721917	dxdxd	0.473	axdxa	0.117
	SFTPA2	*SFTPB*	*SFTPD*				
2	rs1059046	rs1130866	rs2243639	dxdxd	0.348	dxaxa	0.202
	SFTPA2	*SFTPB*	*SFTPD*				
3	rs1059046	rs17886395	rs1136450	dxaxd	0.27	axdxd	0.285
	rs1059046	rs17886395	rs1136450	dxdxa	0.274		
	SFTPA2	*SFTPA2*	*SFTPA1*				
4	rs1059046	rs17886395	rs1130866	dxdxa	0.27	axdxd	0.332
	SFTPA2	*SFTPA2*	*SFTPB*				
5	rs1059046	rs1136451	rs1130866	dxdxa	0.18	axdxd	0.368
	SFTPA2	*SFTPA1*	*SFTPB*				
6	rs1059046	rs3024798	rs4715	dxdxa	0.4	axdxd	0.389
	SFTPA2	*SFTPB*	*SFTPC*				
7	rs1059046	rs1124	rs721917	dxdxd	0.409	dxaxd	0.208
	SFTPA2	*SFTPC*	*SFTPD*				
8	rs1059046	rs3024798	rs721917	dxdxd	0.56	axdxd	0.327
	SFTPA2	*SFTPB*	*SFTPD*				
9	rs1136450	rs3024798	rs4715	dxdxa	0.34	axdxd	0.389
	SFTPA1	*SFTPB*	*SFTPC*				
10	rs1059047	rs1130866	rs2243639	axdxd	3.2	dxdxd	1.51
	SFTPA1	*SFTPB*	*SFTPD*				
11	rs1059046	rs1059047	rs2077079	axaxd	6.5	dxaxa	4.221
						dxdxa	2.515
						dxdxd	1.503
	SFTPA2	*SFTPA2*	*SFTPB*				
12	rs1059046	rs1059047	rs2243639	dxaxd	3.51	dxdxd	1.787
	SFTPA2	*SFTPA1*	*SFTPD*				
13	rs1136451	rs1130866	rs2243639	dxdxa	3.11	dxdxd	1.556
	SFTPA1	*SFTPB*	*SFTPD*				
14	rs17886395	rs1059047	rs1136451	dxdxa	5.96	dxdxd	1.995
	SFTPA2	*SFTPA1*	*SFTPA1*				
15	rs17886395	rs2077079	rs1130866	dxdxd	2.048	dxdxa	0.298
	SFTPA2	*SFTPB*	*SFTPB*				
16	rs1136450	rs2077079	rs1130866	dxdxd	2.14	axdxd	0.373
	SFTPA1	*SFTPB*	*SFTPB*				
17	rs1136450	rs3024798	rs2243639	dxdxd	1.96	axdxd	0.38
	SFTPA1	*SFTPB*	*SFTPD*				
18	rs1059047	rs1136450	rs721917	axaxa	0.053	dxdxd	1.506
	SFTPA1	*SFTPA1*	*SFTPD*				
19	rs1059046	rs2077079	rs3024798	axdxd	0.2	dxdxa	3.018
						dxaxd	3.589
						dxdxd	1.458
	SFTPA2	*SFTPB*	*SFTPB*				
20	rs1059046	rs17886395	rs2077079	axaxd	0.15	dxdxa	2.983
						dxdxd	1.807
	SFTPA2	*SFTPA2*	*SFTPB*				
21	rs1059046	rs17886395	rs1136450	dxdxa	0.274	dxdxd	1.756
	rs1059046	rs17886395	rs1136450	dxaxd	0.277		
	SFTPA2	*SFTPA2*	*SFTPA1*				
22	rs1059046	rs17886395	rs3024798	axaxd	0.073	dxdxd	1.565
	SFTPA2	*SFTPA2*	*SFTPB*				
23	rs1059046	rs17886395	rs1124	dxaxd	0.228	dxdxd	1.731
	rs1059046	rs17886395	rs1124	dxdxa	0.387		
	SFTPA2	*SFTPA2*	*SFTPC*				
24	rs1059046	rs17886395	rs1130866	dxdxa	0.270	dxdxd	1.502
	SFTPA2	*SFTPA2*	*SFTPB*				
25	rs1059046	rs3024798	rs4715	dxdxa	0.407	dxdxd	2.293
	SFTPA2	*SFTPB*	*SFTPC*				
26	rs1136450	rs1136451	rs4715	dxdxd	0.369	dxaxa	11.43
	SFTPA1	*SFTPA1*	*SFTPC*				
27	rs1136450	rs1136451	rs1124	dxdxd	0.502	dxaxa	10.98

(Continued)

TABLE 8 | Continued

No	Interactions			HP		IPF	
				pattern	OR	pattern	OR
	SFTPA1	*SFTPA1*	*SFTPC*				
28	rs1136450	rs2077079	rs3024798	axdxd	0.2	dxdxd	2.592
	SFTPA1	*SFTPB*	*SFTPB*				
29	rs1136450	rs4715	rs1124	axdxd	0.124	dxaxa	6.36
						dxdxa	3.448
						dxdxd	1.615
	SFTPA1	*SFTPC*	*SFTPC*				
30	rs1136451	rs3024798	rs1130866	dxdxa	0.292	dxdxd	1.858
	SFTPA1	*SFTPB*	*SFTPB*				
31	rs17886395	rs1136451	rs1130866	dxdxa	0.303	dxdxd	2.941
	SFTPA2	*SFTPA1*	*SFTPB*				
32	rs17886395	rs3024798	rs1130866	dxdxa	0.332	dxdxd	1.778
	SFTPA2	*SFTPB*	*SFTPB*				
33	rs17886395	rs1059047	rs1130866	dxdxa	0.294	dxdxd	1.673
	SFTPA2	*SFTPA1*	*SFTPB*				
34	rs2077079	rs3024798	rs2243639	axaxd	0.216	dxdxa	3.457
	SFTPB	*SFTPB*	*SFTPD*				
35	rs3024798	rs1130866	rs2243639	dxdxd	0.50	dxdxa	2.171
	SFTPB	*SFTPB*	*SFTPD*				
36	rs1059046	rs1136450	rs1136451	dxaxd	0.07	dxdxd	1.915
	rs1059046	rs1136450	rs1136451	dxdxa	3.551		
	SFTPA2	*SFTPA1*	*SFTPA1*				
37	rs1136451	rs2077079	rs3024798	dxaxd	0.162	dxdxd	1.661
	rs1136451	rs2077079	rs3024798	axdxd	9.198		
	SFTPA1	*SFTPB*	*SFTPB*				

OR, odds ratio.

fibrosis, and may also develop a progressive fibrotic phenotype. We observed, 1) in terms of IPF: i) three single *SFTPA1* SNPs to associate with decreased IPF risk, ii) three *SFTPA1* haplotypes to associate with increased IPF risk, and iii) a number of three-SNP interactions to associate with IPF susceptibility. 2) After comparison of IPF and HP, i) three *SFTPA1* and one *SFTPB* SNP were found to associate with decreased or increased risk in IPF and HP and one *SFTPA1* SNP to associate with decreased risk in both IPF and HP, ii) a number of three-SNP interactions with the same or different effect pattern associated with IPF and/or HP susceptibility; iii) one of the three-SNP interactions that involved SNPs of *SFTPA2*, *SFTPA1*, and *SFTPD*, with the same effect pattern, was associated with a disease-specific outcome, a decreased and increased risk in HP and IPF, respectively. The findings of the current study may provide an example to start differentiating these two diseases based on their genetic background.

For the current study, we took advantage of the same ethnic background of cases for both diseases (IPF and HP) and controls, i.e. All study subjects were Mexican Hispanic patients and all of them were enrolled from the same center. We hoped that this will help identify genetic patterns that in turn may enable distinguishing these two diseases or at the very least provide a paradigm for further work where genetic models could be used to find disease-specific markers.

IPF

The *SFTPA1* gene is shown in the present study, *via* different analyses, including the use of a single SNP model, haplotype analysis and SNP-SNP interactions, to associate with IPF susceptibility. One of its SNPs, rs1136450, was the most frequently observed *SFTPA1* SNP in the 3-SNP interactions. This SNP was found to be significant either by itself, as part of significant haplotypes, or part of significant 3-SNP interactions and has been found previously to associate with susceptibility with other pulmonary diseases including community acquired pneumonia (61), cystic fibrosis (47), acute respiratory distress of the newborn (59) and pediatric acute and chronic respiratory failure (58, 62). The rs1136450 SNP encodes (leu/val) amino acid 50 (AA50), and it is located within the collagen-like region of SP-A1. In the absence of the collagen-like region, functional defects of surfactant are observed as well as the absence of an extracellular structural form of surfactant, the tubular myelin (63). This region is also important for the oligomerization and stability of SP-A (64). This SNP change is SP-A1 variant-specific and not gene-specific. All of the most frequently found and studied SP-A1 variants (6A, $6A^3$, and $6A^4$) have a leucine at AA50 except the $6A^2$ variant that has a valine. On the other hand, all frequently found and studied SP-A2 variants have a valine (19, 38, 39). These two amino acids (Leu/Val), although they share a lot of similarities, as they are both essential non-polar amino acids with aliphatic side chains and neutral charge at pH 7.4, they may however provide differential sites for proteases. Proteases are often highly specific in their proteolytic activity, and even a conservative substitution as this one, provided by the rs1136450 SNP, may have a significant differential effect on the proteolylic process, as demonstrated in detailed studies for the matrix metalloproteinases family (65). Whether and how the AA50

change imparted by this SNP differentially affects any of the studied properties affected by the collagen-like region or provides preferential sites for various enzymes remains to be determined.

Of interest, a previous analysis of the same cohort using the traditional logistic regression analysis showed association of three SNPs of the *SFTPA1*, rs4253527 (AA219_T), rs1136450 (AA50_C), and rs1136451 (AA62_G) with increased risk of IPF (22). In the present study, the "G" allele of the rs1136450 SNP was associated with decreased risk of IPF. Although these findings appear to contradict one another, both studies do identify the same significant SNPs. Also, this comparison provides an opportunity for a cautionary note where one needs to take into consideration the method of assigning, reference and alternate alleles of a given SNP. Wang et al.'s approach employed in the present study uses the dbSNP database of the NCBI (66) to assign the reference and the alternate alleles, whereas, in the logistic regression analysis, alleles were assigned based on the frequencies in the studied group, i.e., the more frequent allele in that study group was the reference allele. Furthermore, in the current study, we did not observe association of the rs4253527 (AA219_T) with IPF either in the single-SNP or in the three-SNP model. This may be due to the difference in statistical approaches used for the two studies. Although we did not observe association of rs1136451 in the single-SNP model either, this SNP was observed in several SNP-SNP interactions (**Table 1**).

However, what is of considerable interest are the observations made regarding associations with relative risk or protection of IPF. In the single SNP model, the *SFTPA1* SNP (rs1136450) and two other *SFTPA1* SNPs (rs1059047, rs1059057) were shown to associate with decreased risk but haplotypes that included the rs1136450 and/or the other two SNPs were associated with increased risk. Moreover, a number of 3-SNP interactions, where the rs1136450 had a dominant effect and any other two SNPs had an additive effect, exhibited a high odds ratio indicating risk. However, when the rs1136450 in 3-SNP interactions was found with different effect patterns, the interactions were associated with either increased or decreased risk. An example to demonstrate this is depicted in the 3-SNP interactions, #9 and #28 in **Table 8**, where in the former the pattern effect is axdxd and in the latter is dxdxd, where the rs1136450 has additive (a) and dominant (d) effect, respectively. These different effect patterns of the rs113650, were associated with decreased (axdxd) and increased (dxdxd) risk of IPF, respectively. A similar effect pattern observation in 3-SNP interactions was made for the *SFTPA2* rs1059046 (interactions, 3 & 21, 4 & 24, 6 & 25, **Table 8**). We postulate that the effect pattern, whether dominant (d) or additive (a) (no recessive effect was observed in this study), plays an important role in disease susceptibility. Although what contributes to a SNP to exhibit a different effect pattern is not entirely clear, we speculate that the overall cellular microenvironment, its interaction with other SNPs, and other unknown factors contribute to the specific effect pattern and its consequences, as it may be assessed by the strength of the given association with disease susceptibility. For example, different effect patterns among the same SNPs were observed, where each was associated with varying degree of IPF susceptibility as assessed by the odds ratio. Interaction #11 (**Table 8**) exemplifies this point. Three different effect patterns observed and each was associated with increased IPF risk albeit each exhibited a different odds ratio (range 1.5-4.2). These observations collectively indicate that fully understanding SNP-SNP interactions that may alter the risk of an individual to a disease, is a challenging problem (67, 68) due to the phenomenon of epistasis where the combined effect of one or more genes/SNPs on the phenotype could not have been predicted by their separate effects (69). Thus, this type of observations requires further consideration.

The central pathogenesis path of IPF is a progressive deposition of fibrotic tissue in the lungs secondary to dysregulated activity of the alveolar epithelium to repeated injury (7). Actually, mutations in genes encoding surfactant proteins, have been identified in adults with the phenotype of pulmonary fibrosis through a gain-of-toxic function mechanism (70). In the present study, we show that the *SFTP* genes play a role in IPF as shown by the numerous 3-SNP significant interactions that included SNPs of all the *SFTP* genes. Although, single SNPs or haplotypes of *SFTPA1* exhibited significant association with IPF susceptibility, no SNPs of other *SFTP* genes showed any significant associations. Considering the vital role of SP-A in innate immunity and host responses of the lung to foreign particles, these findings are not surprising. Of interest, *SFTPA1*, compared to *SFTPA2*, has been shown to be more efficient in surfactant lipid reorganization and in preventing surfactant inhibition by serum proteins, indicating that the importance of this gene in IPF may in part be due to its dual role in host defense and surfactant-related activities. Because the 3-SNP interactions involved SNPs from all *SFTPs*, we postulate that collectively *SFTP* variants contribute to IPF in ways that we are not able, to yet fully understand. Further research is needed in studying the impact of the actual SNP-SNP interactions on levels and biophysical/biochemical properties of SPs in appropriate biological models. This may shed light into the complexities of their interactions and advance our understanding of these interactions on complex diseases, such as IPF.

Comparison of IPF and HP

When we compared findings of the current IPF study with a previously published HP study (21), using the same statistical approach, and cohort as control, a number of similarities and differences were identified between these interstitial lung diseases. Although one single *SFTPA1* SNP (rs1136450), was found to associate with decreased risk in both diseases, other *SFTPA1* SNPs were associated with IPF or HP disease-specific susceptibility. Thus, these point to a potential use of these SNPs as markers to distinguish between these two diseases. The *SFTPA1* significant SNPs that change the encoded amino acid may affect functional aspects of the protein variant. The significance of the rs1136450 has been discussed above under IPF. The rs1059047 of *SFTPA1* that associates with decreased risk in IPF, changes amino acid 19 (Val/Ala). This amino acid may or may not be part of all the mature SP-A1 molecules (60)

and therefore it is unclear whether and how this may affect the processing of the precursor protein and/or the functional capability of the mature molecules that contain this amino acid.

Moreover, one *SFTPB* SNP (rs1130866) was associated specifically with decreased risk in HP. The SP-B protein plays a crucial role in surfactant function and some mutations are not compatible with life (71). The *SFTPB* SNP noted above is responsible for a missense codon (ACT/ATT) that changes amino acid 131 from a Threonine (ACT) to Isoleucine (ATT) and eliminates an N-linked glycosylation site (Asp^{129}-Gln-Thr^{131}) (72). Although amino acid 131 is part of the N-terminal peptide of the SP-B preprotein and not the mature SP-B, animal models have shown that the alleles of this SNP differentially affect the number of lamellar bodies, an extracellular structural form of surfactant, surface tension and levels of SP-B (73). Whether this SNP modifies any surfactant properties in humans and whether the consequences of these contribute to HP susceptibility is unknown. Its location is near a mutation hotspot and whether this, under certain circumstances, impacts other events is currently unknown (74).

Furthermore, we observed four 3-SNP interactions to exhibit a disease specific outcome. These interactions involved the same SNPs with similar effect patterns and associated with increased and decreased risk of IPF and HP, respectively (**Table 7**). These interactions involved SNPs from all *SFTPs*, with two of these (interactions #9 and 10) containing SNPs only from the hydrophobic surfactant proteins (*SFTPB and SFTPC*), one (interaction #4) contained SNPs only from the hydrophilic proteins (*SFTPA2, SFTPA1, SFTPD*) and one (interaction #8) contained SNPs from both groups (*SFTPA2, SFTPB, SFTPC*). Collectively, these indicate a role of all the surfactant proteins in the susceptibility of these diseases. Furthermore, the disease-specific lung microenvironment may alter the susceptibility of the host (75) and thus SNP interactions of the same SNPs with the same effect pattern may lead to different outcomes, as shown with the 3-SNP interactions in the present study. These interactions indicate that is plausible to distinguish the two similar interstitial lung diseases (IPF and HP), based on genetic interactions. Furthermore, we observed a number of 3-SNP interactions, with the same SNPs but with different effect patterns, to associate with IPF and HP disease susceptibility (**Table 8**). These observations are difficult to understand at the current time, as there may be a nonlinear relationship (dominant) between the gene products and disease outcomes, due perhaps to the gene dosage/imbalance and other sources of "more than-additive genetic interactions" that may lead to variable phenotypes of either over-, under- or non-function of the gene products in a given disease state (76).

The strengths of the current study are: a) the use of a newer statistical analysis to study SNP-SNP interactions with adjustment of important variables such as age, sex, and smoking status, b) enrollment of a patient population and control study groups with a similar ethnic background from the same center; therefore, the population structure of the studied groups may not be a major issue. Although, the second strength maybe a limitation (i.e., whether it can be generalized to include other groups of a different race or ethnicity), to our current knowledge ethnicity is not a significant risk factor as both diseases occur similarly in different ethnic groups as reported worldwide. However, there is limited information to determine whether differences in the frequency of the surfactant protein genetic variants, epigenetics, or differences in the SNP-SNP effect patterns studied here exist among different groups that could potentially point to different underlying processes in the pathogenesis of these disease. Thus, it is prudent to replicate the present findings in a larger sample size by case control studies with clinically confirmed cases of IPF and HP of other groups of heterogeneous non-Hispanic patients from various ethnicities in order to validate and strengthen the differential diagnostic potential of the identified SNPs and SNP interactions.

In conclusion, SNPs of all *SFTPs* appear to play an important role in identifying disease susceptibility in IPF and HP interstitial lung diseases. Similarities between these two diseases with regards to the surfactant protein genes variants were observed in haplotypes or in 3-SNP interactions, as well as differences highlighting the different underlying pathogenic mechanisms between an inflammatory-driven fibrosis (HP) and an epithelial-driven fibrosis (IPF). In addition, the disease-specific associations of the SP polymorphisms hold the potential for these SNPs to be used as markers to distinguish between these two diseases. The information obtained in the current study was enabled *via* the use of newer/novel statistical methods to study models of single SNPs as well as SNP-SNP interactions where epistasis could be addressed. *SFTPA1* and *SFTPB* SNPs might be of particular interest for future studies, where these could be used as markers either individually or together with other biomarkers in an attempt to distinguish between these two similar diseases. This is of great importance as it could help downstream decision-making of diagnosis and disease-specific therapies of these two devastating diseases.

DATA AVAILABILITY STATEMENT

The datasets presented in this study can be found in online repositories. The names of the repository/repositories and accession number(s) can be found below:

dbSNP, accession number: 1063345.

ETHICS STATEMENT

The studies involving human participants were reviewed and approved by National Institute of Respiratory Diseases in Mexico City. The patients/participants provided their written informed consent to participate in this study.

AUTHOR CONTRIBUTIONS

AA analyzed the data and wrote the original draft of the manuscript. CC performed the statistical analysis. CG contributed to the manuscript writing. MS and AP were responsible for sample collection and patient screening as

noted in previous publications and contributed in manuscript writing. RW worked closely with CC and guided the statistical analysis. JF supervised the entire project and worked closely with all co-authors and especially with AA to ensure quality of data analysis and finalize the manuscript. All authors contributed to the article and approved the submitted version.

FUNDING

This work was supported by NIH HL34788 to JF.

ACKNOWLEDGMENTS

The authors thank the study participants. We thank Susan DiAngelo for her technical assistance in genotyping samples.

SUPPLEMENTARY MATERIAL

The Supplementary Material for this article can be found online at: https://www.frontiersin.org/articles/10.3389/fimmu.2022.842745/full#supplementary-material

REFERENCES

1. van Moorsel CH, Hoffman TW, van Batenburg AA, Klay D, van der Vis JJ, Grutters JC. Understanding Idiopathic Interstitial Pneumonia: A Gene-Based Review of Stressed Lungs. *BioMed Res Int* (2015) 2015:304186. doi: 10.1155/2015/304186
2. Selman M, Pardo A. The Leading Role of Epithelial Cells in the Pathogenesis of Idiopathic Pulmonary Fibrosis. *Cell Signalling* (2020) 66:109482. doi: 10.1016/j.cellsig.2019.109482
3. Ntolios P, Tzilas V, Bouros E, Avdoula E, Karakasiliotis I, Bouros D, et al. The Role of Microbiome and Virome in Idiopathic Pulmonary Fibrosis. *Biomedicines* (2021) 9(4):442. doi: 10.3390/biomedicines9040442
4. Raghu G, Remy-Jardin M, Myers JL, Richeldi L, Ryerson CJ, Lederer DJ, et al. Diagnosis of Idiopathic Pulmonary Fibrosis. An Official ATS/ERS/JRS/ALAT Clinical Practice Guideline. *Am J Respir Crit Care Med* (2018) 198(5):e44–68. doi: 10.1164/rccm.201807-1255ST
5. Pardo A, Selman M. The Interplay of the Genetic Architecture, Aging, and Environmental Factors in the Pathogenesis of Idiopathic Pulmonary Fibrosis. *Am J Respir Cell Mol Biol* (2021) 64(2):163–72. doi: 10.1165/rcmb.2020-0373PS
6. King TE Jr, Pardo A, Selman M. Idiopathic Pulmonary Fibrosis. *Lancet* (2011) 378(9807):1949–61. doi: 10.1016/S0140-6736(11)60052-4
7. Taskar VS, Coultas DB. Is Idiopathic Pulmonary Fibrosis an Environmental Disease? *Proc Am Thorac Soc* (2006) 3(4):293–8. doi: 10.1513/pats.200512-131TK
8. Seibold MA, Wise AL, Speer MC, Steele MP, Brown KK, Loyd JE, et al. A Common MUC5B Promoter Polymorphism and Pulmonary Fibrosis. *New Engl J Med* (2011) 364(16):1503–12. doi: 10.1056/NEJMoa1013660
9. Molyneaux PL, Maher TM. The Role of Infection in the Pathogenesis of Idiopathic Pulmonary Fibrosis. *Eur Respir Rev* (2013) 22(129):376–81. doi: 10.1183/09059180.00000713
10. Doubková M, Kozubík KS, Radová L, Pešová M, Trizuljak J, Pál K, et al. A Novel Germline Mutation of the SFTPA1 Gene in Familial Interstitial Pneumonia. *Hum Genome Variation* (2019) 6(1):1–6. doi: 10.1038/s41439-019-0044-z
11. Chiba S, Tsuchiya K, Akashi T, Ishizuka M, Okamoto T, Furusawa H, et al. Chronic Hypersensitivity Pneumonitis With a Usual Interstitial Pneumonia-Like Pattern: Correlation Between Histopathologic and Clinical Findings. *Chest* (2016) 149(6):1473–81. doi: 10.1016/j.chest.2015.12.030
12. Costabel U, Miyazaki Y, Pardo A, Koschel D, Bonella F, Spagnolo P, et al. Hypersensitivity Pneumonitis. *Nat Rev Dis Primers* (2020) 6(1):1–19. doi: 10.1038/s41572-020-0191-z
13. Morell F, Villar A, Montero M-Á, Muñoz X, Colby TV, Pipvath S, et al. Chronic Hypersensitivity Pneumonitis in Patients Diagnosed With Idiopathic Pulmonary Fibrosis: A Prospective Case-Cohort Study. *Lancet Respir Med* (2013) 1(9):685–94. doi: 10.1016/S2213-2600(13)70191-7
14. Yang MM, Wolters PJ. Cut From the Same Cloth: Similarities Between Hypersensitivity Pneumonitis and IPF. *Am J Respir Crit Care Med* (2021) 205(1):4-6. doi: 10.1164/rccm.202109-2211ED
15. Kaur A, Mathai SK, Schwartz DA. Genetics in Idiopathic Pulmonary Fibrosis Pathogenesis, Prognosis, and Treatment. *Front Med* (2017) 4:154. doi: 10.3389/fmed.2017.00154
16. Falfán-Valencia R, Camarena A, Pineda CL, Montaño M, Juárez A, Buendía-Roldán I, et al. Genetic Susceptibility to Multicase Hypersensitivity Pneumonitis Is Associated With the TNF-238 GG Genotype of the Promoter Region and HLA-DRB1*04 Bearing HLA Haplotypes. *Respir Med* (2014) 108(1):211–7. doi: 10.1016/j.rmed.2013.11.004
17. Haque R, Umstead TM, Ponnuru P, Guo X, Hawgood S, Phelps DS, et al. Role of Surfactant Protein-A (SP-A) in Lung Injury in Response to Acute Ozone Exposure of SP-A Deficient Mice. *Toxicol Appl Pharmacol* (2007) 220(1):72–82. doi: 10.1016/j.taap.2006.12.017
18. Floros J, Wang G, Mikerov AN. Genetic Complexity of the Human Innate Host Defense Molecules, Surfactant Protein A1 (SP-A1) and SP-A2—impact on Function. *Crit Reviews™ Eukaryotic Gene Expression* (2009) 19(2):125–37. doi: 10.1615/CritRevEukarGeneExpr.v19.i2.30
19. Floros J, Thorenoor N, Tsotakos N, Phelps DS. Human Surfactant Protein SP-A1 and SP-A2 Variants Differentially Affect the Alveolar Microenvironment, Surfactant Structure, Regulation and Function of the Alveolar Macrophage, and Animal and Human Survival Under Various Conditions. *Front Immunol* (2021) 12:2889. doi: 10.3389/fimmu.2021.681639
20. Perez-Gil J, Weaver TE. Pulmonary Surfactant Pathophysiology: Current Models and Open Questions. *Physiology* (2010) 25(3):132–41. doi: 10.1152/physiol.00006.2010
21. Gandhi CK, Chen C, Amatya S, Yang L, Fu C, Zhou S, et al. SNP and Haplotype Interaction Models Reveal Association of Surfactant Protein Gene Polymorphisms With Hypersensitivity Pneumonitis of Mexican Population. *Front Med* (2020) 7:1043. doi: 10.3389/fmed.2020.588404
22. Selman M, Lin H-M, Montaño M, Jenkins AL, Estrada A, Lin Z, et al. Surfactant Protein A and B Genetic Variants Predispose to Idiopathic Pulmonary Fibrosis. *Hum Genet* (2003) 113(6):542–50. doi: 10.1007/s00439-003-1015-4
23. Guler SA, Wohlfarth E, Berezowska S, Geiser TK, Ebner L, Funke-Chambour M. Performance of a Diagnostic Algorithm for Fibrotic Hypersensitivity Pneumonitis. A Case–Control Study. *Respir Res* (2021) 22(1):1–7. doi: 10.1186/s12931-021-01727-7
24. Pleasants R, Tighe RM. Management of Idiopathic Pulmonary Fibrosis. *Ann Pharmacother* (2019) 53(12):1238–48. doi: 10.1177/1060028019862497
25. Network IPFCR. Prednisone, Azathioprine, and N-Acetylcysteine for Pulmonary Fibrosis. *N Engl J Med* (2012) 366(21):1968–77. doi: 10.1056/NEJMoa1113354
26. Newton CA, Zhang D, Oldham JM, Kozlitina J, Ma S-F, Martinez FJ, et al. Telomere Length and Use of Immunosuppressive Medications in Idiopathic Pulmonary Fibrosis. *Am J Respir Crit Care Med* (2019) 200(3):336–47. doi: 10.1164/rccm.201809-1646OC
27. Oldham JM, Ma S-F, Martinez FJ, Anstrom KJ, Raghu G, Schwartz DA, et al. TOLLIP, MUC5B, and the Response to N-Acetylcysteine Among Individuals With Idiopathic Pulmonary Fibrosis. *Am J Respir Crit Care Med* (2015) 192(12):1475–82. doi: 10.1164/rccm.201505-1010OC
28. Chen H, Xu X, Hua C, Zhang H, Jian J, Ge T, et al. Polymorphisms of Matrix Metalloproteinases Affect the Susceptibility of Esophageal Cancer: Evidence From 20412 Subjects, Systematic Review and Updated Meta-Analysis. *Medicine* (2021) 100(38):e27229. doi: 10.1097/MD.0000000000027229

29. Megías-Vericat J, Herrero M, Rojas L, Montesinos P, Bosó V, Moscardó F, et al. A Systematic Review and Meta-Analysis of the Impact of WT1 Polymorphism Rs16754 in the Effectiveness of Standard Chemotherapy in Patients With Acute Myeloid Leukemia. *Pharmacogenomics J* (2016) 16 (1):30–40. doi: 10.1038/tpj.2015.80
30. Ojha RP, Gurney JG. Methylenetetrahydrofolate Reductase C677T and Overall Survival in Pediatric Acute Lymphoblastic Leukemia: A Systematic Review. *Leukemia Lymphoma* (2014) 55(1):67–73. doi: 10.3109/10428194.2013.792336
31. Daver N, Schlenk RF, Russell NH, Levis MJ. Targeting FLT3 Mutations in AML: Review of Current Knowledge and Evidence. *Leukemia* (2019) 33 (2):299–312. doi: 10.1038/s41375-018-0357-9
32. Cargnin S, Ravegnini G, Soverini S, Angelini S, Terrazzino S. Impact of SLC22A1 and CYP3A5 Genotypes on Imatinib Response in Chronic Myeloid Leukemia: A Systematic Review and Meta-Analysis. *Pharmacol Res* (2018) 131:244–54. doi: 10.1016/j.phrs.2018.02.005
33. D'Ovidio F, Floros J, Aramini B, Lederer D, DiAngelo SL, Arcasoy S, et al. Donor Surfactant Protein A2 Polymorphism and Lung Transplant Survival. *Eur Respir J* (2020) 1900618. doi: 10.1183/13993003.00618-2019
34. Hoover RR, Floros J. Organization of the Human SP-A and SP-D Loci at 10q22-Q23. Physical and Radiation Hybrid Mapping Reveal Gene Order and Orientation. *Am J Respir Cell Mol Biol* (1998) 18(3):353–62. doi: 10.1165/ajrcmb.18.3.3035
35. Bruns G, Stroh H, Veldman GM, Latt SA, Floros J. The 35 Kd Pulmonary Surfactant-Associated Protein Is Encoded on Chromosome 10. *Hum Genet* (1987) 76(1):58–62. doi: 10.1007/BF00283051
36. Floros J, Steinbrink R, Jacobs K, Phelps D, Kriz R, Recny M, et al. Isolation and Characterization of cDNA Clones for the 35-kDa Pulmonary Surfactant-Associated Protein. *J Biol Chem* (1986) 261(19):9029–33. doi: 10.1016/S0021-9258(19)84483-6
37. DiAngelo S, Lin Z, Wang G, Phillips S, Ramet M, Luo J, et al. Novel, non-Radioactive, Simple and Multiplex PCR-cRFLP Methods for Genotyping Human SP-A and SP-D Marker Alleles. *Dis Markers* (1999) 15(4):269–81. doi: 10.1155/1999/961430
38. Floros J, Hoover RR. Genetics of the Hydrophilic Surfactant Proteins A and D. *Biochim Biophys Acta* (1998) 1408(2-3):312–22. doi: 10.1016/S0925-4439(98)00077-5
39. Floros J, Wang G, Lin Z. Genetic Diversity of Human SP-A, A Molecule With Innate Host Defense and Surfactant-Related Functions; Characteristics, Primary Function, and Significance. *Curr Pharmacogenomics* (2005) 3 (2):87–95. doi: 10.2174/1570160054022935
40. Lynnlee Depicolzuane DSP, Floros J. Surfactant Protein-A Function: Knowledge Gained From SP-A Knockout Mice. *Front Pediatrics* (2021) 9:799693. doi: 10.3389/fped.2021.799693
41. Floros J, Phelps D. Pulmonary Surfactant. In: Yaksh TL, Lynch C III, Zapol WM, Maze M, Biebuyck JF, Saidman LJ, editors. *Anesthesia: Biologic Foundations*. Philadelphia, PA, USA: Lippincott-Raven, Philadelphia (1997). p. 1259–79.
42. Wert SE, Whitsett JA, Nogee LM. Genetic Disorders of Surfactant Dysfunction. *Pediatr Dev Pathol* (2009) 12(4):253–74. doi: 10.2350/09-01-0586.1
43. Lin Z, Pearson C, Chinchilli V, Pietschmann S, Luo J, Pison U, et al. Polymorphisms of Human SP-A, SP-B, and SP-D Genes: Association of SP-B Thr131Ile With ARDS. *Clin Genet* (2000) 58(3):181–91. doi: 10.1034/j.1399-0004.2000.580305.x
44. Silveyra P, Floros J. Genetic Variant Associations of Human SP-A and SP-D With Acute and Chronic Lung Injury. *Front Biosci: J Virtual library* (2012) 17:407. doi: 10.2741/3935
45. Guo X, Lin H, Lin Z, Montano M, Sansores R, Wang G, et al. Surfactant Protein Gene A, B, and D Marker Alleles in Chronic Obstructive Pulmonary Disease of a Mexican Population. *Eur Respir J* (2001) 18(3):482–90. doi: 10.1183/09031936.01.00043401
46. Seifart C, Plagens A, Brödje D, Müller B, Von Wichert P, Floros J. Surfactant Protein B Intron 4 Variation in German Patients With COPD and Acute Respiratory Failure. *Dis Markers* (2002) 18(3):129–36. doi: 10.1155/2002/194075
47. Lin Z, Thorenoor N, Wu R, DiAngelo SL, Ye M, Thomas NJ, et al. Genetic Association of Pulmonary Surfactant Protein Genes, SFTPA1, SFTPA2, SFTPB, SFTPC, and SFTPD With Cystic Fibrosis. *Front Immunol* (2018) 9:2256. doi: 10.3389/fimmu.2018.02256
48. Nathan N, Giraud V, Picard C, Nunes H, Dastot-Le Moal F, Copin B, et al. Germline SFTPA1 Mutation in Familial Idiopathic Interstitial Pneumonia and Lung Cancer. *Hum Mol Genet* (2016) 25(8):1457–67. doi: 10.1093/hmg/ddw014
49. van Moorsel CH, Ten Klooster L, van Oosterhout MF, de Jong PA, Adams H, Wouter van Es H, et al. SFTPA2 Mutations in Familial and Sporadic Idiopathic Interstitial Pneumonia. *Am J Respir Crit Care Med* (2015) 192 (10):1249–52. doi: 10.1164/rccm.201504-0675LE
50. Liu L, Qin J, Guo T, Chen P, Ouyang R, Peng H, et al. Identification and Functional Characterization of a Novel Surfactant Protein A2 Mutation (P. N207Y) in a Chinese Family With Idiopathic Pulmonary Fibrosis. *Mol Genet Genomic Med* (2020) 8(9):e1393. doi: 10.1002/mgg3.1393
51. Takezaki A, Tsukumo S-i, Setoguchi Y, Ledford JG, Goto H, Hosomichi K, et al. A Homozygous SFTPA1 Mutation Drives Necroptosis of Type II Alveolar Epithelial Cells in Patients With Idiopathic Pulmonary Fibrosis. *J Exp Med* (2019) 216(12):2724–35. doi: 10.1084/jem.20182351
52. Nureki S-I, Tomer Y, Venosa A, Katzen J, Russo SJ, Jamil S, et al. Expression of Mutant Sftpc in Murine Alveolar Epithelia Drives Spontaneous Lung Fibrosis. *J Clin Invest* (2018) 128(9):4008–24. doi: 10.1172/JCI99287
53. Fingerlin TE, Murphy E, Zhang W, Peljto AL, Brown KK, Steele MP, et al. Genome-Wide Association Study Identifies Multiple Susceptibility Loci for Pulmonary Fibrosis. *Nat Genet* (2013) 45(6):613–20. doi: 10.1038/ng.2609
54. Furusawa H, Peljto AL, Walts AD, Cardwell J, Molyneaux PL, Lee JS, et al. Common Idiopathic Pulmonary Fibrosis Risk Variants are Associated With Hypersensitivity Pneumonitis. *Thorax* (2022) 77(5):508–10. doi: 10.1164/ajrccm-conference.2021.203.1_MeetingAbstracts.A3143
55. Kam ML, Nguyen TT, Ngeow JY. Telomere Biology Disorders. *NPJ Genomic Med* (2021) 6(1):1–13. doi: 10.1038/s41525-021-00198-5
56. Ley B, Torgerson DG, Oldham JM, Adegunsoye A, Liu S, Li J, et al. Rare Protein-Altering Telomere-Related Gene Variants in Patients With Chronic Hypersensitivity Pneumonitis. *Am J Respir Crit Care Med* (2019) 200 (9):1154–63. doi: 10.1164/rccm.201902-0360OC
57. Wang Z, Liu T, Lin Z, Hegarty J, Koltun WA, Wu R. A General Model for Multilocus Epistatic Interactions in Case-Control Studies. *PloS One* (2010) 5 (8):e11384. doi: 10.1371/journal.pone.0011384
58. Gandhi CK, Chen C, Wu R, Yang L, Thorenoor N, Thomas NJ, et al. Association of SNP–SNP Interactions of Surfactant Protein Genes With Pediatric Acute Respiratory Failure. *J Clin Med* (2020) 9(4):1183. doi: 10.3390/jcm9041183
59. Amatya S, Ye M, Yang L, Gandhi CK, Wu R, Nagourney B, et al. Single Nucleotide Polymorphisms Interactions of the Surfactant Protein Genes Associated With Respiratory Distress Syndrome Susceptibility in Preterm Infants. *Front Pediatr* (2021) 9(1065). doi: 10.3389/fped.2021.682160
60. Wang G, Bates-Kenney SR, Tao J-Q, Phelps DS, Floros J. Differences in Biochemical Properties and in Biological Function Between Human SP-A1 and SP-A2 Variants, and the Impact of Ozone-Induced Oxidation. *Biochemistry* (2004) 43(14):4227–39. doi: 10.1021/bi036023i
61. García-Laorden M, de Castro FR, Solé-Violán J, Rajas O, Blanquer J, Borderías L, et al. Influence of Genetic Variability at the Surfactant Proteins A and D in Community-Acquired Pneumonia: A Prospective, Observational, Genetic Study. *Crit Care* (2011) 15(1):1–12. doi: 10.1186/cc10030
62. Gandhi CK, Thomas NJ, Meixia Y, Spear D, Fu C, Zhou S, et al. SNP-SNP Interactions of Surfactant Protein Genes in Persistent Respiratory Morbidity Susceptibility in Previously Healthy Children. *Front Genet* (2022) 13:815727. doi: 10.3389/fgene.2022.815727
63. Ikegami M, Elhalwagi BM, Palaniyar N, Dienger K, Korfhagen T, Whitsett JA, et al. The Collagen-Like Region of Surfactant Protein A (SP-A) Is Required for Correction of Surfactant Structural and Functional Defects in the SP-A Null Mouse. *J Biol Chem* (2001) 276(42):38542–8. doi: 10.1074/jbc.M102054200
64. Palaniyar N, Ikegami M, Korfhagen T, Whitsett J, McCormack FX. Domains of Surfactant Protein A That Affect Protein Oligomerization, Lipid Structure and Surface Tension. *Comp Biochem Physiol Part A: Mol Integr Physiol* (2001) 129(1):109–27. doi: 10.1016/S1095-6433(01)00309-9
65. Eckhard U, Huesgen PF, Schilling O, Bellac CL, Butler GS, Cox JH, et al. Active Site Specificity Profiling of the Matrix Metalloproteinase Family: Proteomic Identification of 4300 Cleavage Sites by Nine MMPs Explored With Structural and Synthetic Peptide Cleavage Analyses. *Matrix Biol* (2016) 49:37–60. doi: 10.1016/j.matbio.2015.09.003

66. Sherry ST, Ward MH, Kholodov M, Baker J, Phan L, Smigielski EM, et al. dbSNP: The NCBI Database of Genetic Variation. *Nucleic Acids Res* (2001) 29 (1):308–11. doi: 10.1093/nar/29.1.308
67. Cao X, Liu J, Guo M, Wang J. HiSSI: High-Order SNP-SNP Interactions Detection Based on Efficient Significant Pattern and Differential Evolution. *BMC Med Genomics* (2019) 12(7):139. doi: 10.1186/s12920-019-0584-6
68. Cordell HJ. Detecting Gene–Gene Interactions That Underlie Human Diseases. *Nat Rev Genet* (2009) 10(6):392–404. doi: 10.1038/nrg2579
69. Frankel WN, Schork NJ. Who's Afraid of Epistasis? *Nat Genet* (1996) 14 (4):371–3. doi: 10.1038/ng1296-371
70. Nogee LM. Genetic Causes of Surfactant Protein Abnormalities. *Curr Opin Pediatrics* (2019) 31(3):330. doi: 10.1097/MOP.0000000000000751
71. Nogee LM, Garnier G, Dietz HC, Singer L, Murphy AM, DeMello DE, et al. A Mutation in the Surfactant Protein B Gene Responsible for Fatal Neonatal Respiratory Disease in Multiple Kindreds. *J Clin Invest* (1994) 93(4):1860–3. doi: 10.1172/JCI117173
72. Wang G, Christensen ND, Wigdahl B, Guttentag SH, Floros J. Differences in N-Linked Glycosylation Between Human Surfactant Protein-B Variants of the C or T Allele at the Single-Nucleotide Polymorphism at Position 1580: Implications for Disease. *Biochem J* (2003) 369(Pt 1):179–84. doi: 10.1042/bj20021376
73. Yang F, Zhang J, Yang Y, Ruan F, Chen X, Guo J, et al. Regulatory Roles of Human Surfactant Protein B Variants on Genetic Susceptibility to Pseudomonas Aeruginosa Pneumonia-Induced Sepsis. *Shock* (2020) 54 (4):507–19. doi: 10.1097/SHK.0000000000001494
74. Lin Z, deMello DE, Wallot M, Floros J. An SP-B Gene Mutation Responsible for SP-B Deficiency in Fatal Congenital Alveolar Proteinosis: Evidence for a Mutation Hotspot in Exon 4. *Mol Genet Metab* (1998) 64(1):25–35. doi: 10.1006/mgme.1998.2702
75. Gosens R, Hiemstra PS, Adcock IM, Bracke KR, Dickson RP, Hansbro PM, et al. Host–microbe Cross-Talk in the Lung Microenvironment: Implications for Understanding and Treating Chronic Lung Disease. *Eur Respir J* (2020) 56 (2):1902320. doi: 10.1183/13993003.02320-2019
76. Veitia RA, Bottani S, Birchler JA. Gene Dosage Effects: Nonlinearities, Genetic Interactions, and Dosage Compensation. *Trends Genet* (2013) 29(7):385–93. doi: 10.1016/j.tig.2013.04.004

Conflict of Interest: The authors declare that the research was conducted in the absence of any commercial or financial relationships that could be construed as a potential conflict of interest.

Publisher's Note: All claims expressed in this article are solely those of the authors and do not necessarily represent those of their affiliated organizations, or those of the publisher, the editors and the reviewers. Any product that may be evaluated in this article, or claim that may be made by its manufacturer, is not guaranteed or endorsed by the publisher.

frontiers | Frontiers in Immunology

ORIGINAL RESEARCH
published: 01 July 2022
doi: 10.3389/fimmu.2022.854434

The Lung Alveolar Cell (LAC) miRNome and Gene Expression Profile of the SP-A-KO Mice After Infection With and Without Rescue With Human Surfactant Protein-A2 ($1A^0$)

Nithyananda Thorenoor[1,2] *and Joanna Floros*[1,3]*

[1] Department of Pediatrics, College of Medicine, The Pennsylvania State University, Hershey, PA, United States, [2] Department of Biochemistry and Molecular Biology, College of Medicine, The Pennsylvania State University, Hershey, PA, United States, [3] Department of Obstetrics and Gynecology, College of Medicine, The Pennsylvania State University, Hershey, PA, United States

OPEN ACCESS

Edited by:
Taruna Madan, National Institute for Research in Reproductive Health (ICMR), India

Reviewed by:
Lakshna Mahajan, University of Delhi, India
Julie Gunnells Ledford, University of Arizona, United States

***Correspondence:**
Joanna Floros
jfloros@pennstatehealth.psu.edu

Specialty section:
This article was submitted to Molecular Innate Immunity, a section of the journal Frontiers in Immunology

Received: *14 January 2022*
Accepted: *24 May 2022*
Published: *01 July 2022*

Citation:
Thorenoor N and Floros J (2022) The Lung Alveolar Cell (LAC) miRNome and Gene Expression Profile of the SP-A-KO Mice After Infection With and Without Rescue With Human Surfactant Protein-A2 ($1A^0$). Front. Immunol. 13:854434. doi: 10.3389/fimmu.2022.854434

Human surfactant protein (SP)-A1 and SP-A2 exhibit differential qualitative and quantitative effects on the alveolar macrophage (AM), including a differential impact on the AM miRNome. Moreover, SP-A rescue (treatment) of SP-A-knockout (KO) infected mice impoves survival. Here, we studied for the first time the role of exogenous SP-A protein treatment on the regulation of lung alveolar cell (LAC) miRNome, the miRNA-RNA targets, and gene expression of SP-A-KO infected mice of both sexes. Toward this, SP-A-KO mice of both sexes were infected with *Klebsiella pneumoniae*, and half of them were also treated with SP-A2 ($1A^0$). After 6 h of infection/SP-A treatment, the expression levels and pathways of LAC miRNAs, genes, and target miRNA-mRNAs were studied in both groups. We found 1) significant differences in the LAC miRNome, genes, and miRNA-mRNA targets in terms of sex, infection, and infection plus SP-A2 ($1A^0$) protein rescue; 2) an increase in the majority of miRNA-mRNA targets in both study groups in KO male vs. female mice and involvement of the miRNA-mRNA targets in pathways of inflammation, antiapoptosis, and cell cycle; 3) genes with significant changes to be involved in TP-53, tumor necrosis factor (TNF), and cell cycle signaling nodes; 4) when significant changes in the expression of molecules from all analyses (miRNAs, miRNA-mRNA targets, and genes) were considered, two signaling pathways, the TNF and cell cycle, referred to as "integrated pathways" were shown to be significant; 5) the cell cycle pathway to be present in all comparisons made. Because SP-A could be used therapeutically in pulmonary diseases, it is important to understand the molecules and pathways involved in response to an SP-A acute treatment. The information obtained contributes to this end and may help to gain insight especially in the case of infection.

Keywords: surfactant protein A2, lung alveolar cells, alveolar macrophages, *Klebsiella pneumoniae*, miRNome, gene expression, cell cycle, TP-53

INTRODUCTION

Lung diseases due to bacterial infection result in a significant increase in mortality and morbidity. The Gram-negative bacterium *Klebsiella pneumoniae* (*K. pneumoniae*) was isolated from a pneumonia patient, and it is a major source of community- and hospital-acquired respiratory infection (1–3). It is found in nature (1, 2, 4, 5) and colonizes human mucosal surfaces, such as the gastrointestinal tract and oropharynx (4–6), causing infections in a number of organs including the lung, liver, urinary tract, and others, associated with increased mortality and morbidity (7). In neonates and elderly individuals, *K. pneumoniae* infection is a major health problem (8).

In pulmonary infections due to rapid *K. pneumoniae* progress, the time interval for effective treatment is minimized (9). In humans and mouse model studies, within hours of *K. pneumoniae* infection, there are significant changes in the neutrophils at lung air spaces and pulmonary edema (10–12). The lung resident key effector cells of innate immunity, the alveolar macrophages (AMs), *via* bacterial phagocytosis can effectively eliminate the bacterial infection in the lung (13). A reduction in the number of AM cells in the lungs has been associated with a decrease in the killing of *K. pneumoniae in vivo* (14). During the early and later stages of lung infection, AM cells produce inflammatory cytokines to aid in the control of the infection (15, 16).

The hydrophilic lung surfactant proteins (SPs), SP-A and SP-D, members of the family of collectins (17), provide the first line of contact for inhaled bacteria. SP-A serves important roles in both the lung innate immunity and host defense as well as in surfactant-related functions (13, 18–21). SP-A consists of a number of functional regions/domains (21), and its C-terminal carbohydrate recognition domain is important for binding to pathogens, allergens, and others (20–24). SP-A interacts with AM and *via* this interaction modulates the function and regulation of AM (13, 25–29). SP-A may also play a role in linking innate immunity and adaptive immunity (30). In the absence of SP-A, there is a significant increase in the susceptibility to pneumonia and other types of lung injury (31–35).

In humans, SP-A is encoded by two functional genes, *SFTPA1* and *SFTPA2* (21, 36, 37), that are differentially regulated (38). These genes encode SP-A1 and SP-A2, respectively. SP-A1 and SP-A2 differ virtually in all studied aspects that include qualitative (21) and quantitative (38) differences. The qualitative differences include their differential ability to regulate the AM proteome, toponome, and many others (21, 39–43). However, in the absence of SP-A, as in SP-A knockout (KO) mice, the AM proteome profile was significantly and differentially changed in response to SP-A1 or SP-A2 protein treatment (39). Furthermore, humanized transgenic mice that each expresses SP-A1 or SP-A2 exhibited, after infection, sex differences in survival and in lung function mechanics (44, 45), and the SP-A2-expressing mouse exhibited sex-dependent AM NAD(H) redox levels (46).

miRNAs are ~22-nucleotide-long non-coding RNAs with important roles in posttranscriptional regulation usually of gene silencing of target mRNAs under various conditions (47–52). SP-A1 and SP-A2 have been shown to differentially regulate the AM (53) and the Type II cell (54) miRNome in a sex-specific manner (21). The presence of SP-A2 or the presence of both SP-A1 and SP-A2 in humanized transgenic mice resulted in significant differences in AM miRNome and miRNA-mRNA target gene regulation (53, 55). However, at a later time point, an attenuation of sex differences was observed (56), implicating an interplay of post-exposure time, sex, and SP-A genotype.

Previously, we observed 1) improved survival after treatment of SP-A-KO infected mice with SP-A, and this was independent of the time of protein treatment, i.e., prior, after, or at the same time as the infection (44); and 2) a significant change in the AM miRNome and AM gene expression profile after exposure to various insults (i.e., ozone or infection) in mice that were constitutively/chronically exposed to SP-A2 (42, 53, 56). Because innate immunity and SP-A, in particular, play an important role in mitigating infection severity, we wished to investigate mechanisms in response to acute SP-A2 treatment, as this may be relevant to cases of lung infection if one were to use SP-A-regulated miRNAs or target certain genes/pathways for therapeutic purposes.

Here, we studied the impact of infection and infection plus SP-A2 ($1A^0$) protein rescue on the regulation of lung alveolar cell (LAC) miRNome and gene expression in SP-A-KO mice. The majority of LACs after 6 h following infection are AMs (~70%–75%), as assessed by differential cell count after Papanicolaou staining (see *Materials and Methods*). The KO mice of both sexes were infected with *K. pneumoniae* with or without SP-A2 ($1A^0$) protein rescue. Six hours later, the expression levels of LAC miRNAs, genes, and miRNA-mRNA targets of significantly changed miRNAs as well as various pathways were studied. A number of molecules (miRNAs, miRNA-mRNA targets, and genes) were identified with significantly changed levels as a function of exposure and sex, and specific pathways were identified as being significant in these processes. The cell cycle was ubiquitous, as this was significant in all comparisons made, although the specific molecules involved differed under the different studied conditions. The pro-inflammatory pathway was another important pathway. In the gene expression study, an unexpected pathway known to play a role in cancer, the TP-53, was identified. To our knowledge, this is the first study to investigate SP-A treatment in response to infection, and the information obtained may provide useful insight, as SP-A is moving toward therapeutic considerations (57, 58).

MATERIALS AND METHODS

Animals

Male and female SP-A-KO mice (~12 weeks old) were used in the current study. All of the animals were kept in a pathogen-free environment, as described previously (44, 45). The estrous cycle in female mice was synchronized, as previously noted (44, 45). Twenty-eight mice were used (16 for miRNA and gene

expression profiling and 12 for miRNA target gene validation). The Pennsylvania State University Medical Center Institute Animal Care and Use Committee (IACUC) approved the procedures and the animal protocol (#44968) used.

Klebsiella pneumoniae Preparation and Infection of Mice

K. pneumoniae bacteria (ATCC 43816) were obtained (Rockville, MD, USA) and prepared as described previously (32, 44, 45, 59). Approximately, 450 colony forming units (CFUs) in a 50 µl suspension were used to infect each mouse. The CFU/ml values were calculated based on the standard curve obtained by measuring the growth of bacteria at OD_{660}. The mice were infected oropharyngeally (42, 60) after being anesthetized with a mixture of ketamine and xylazine as described previously (32, 44, 45, 59, 60). Male and female SP-A-KO mice (n = 4/group for miRNA and gene expression profile and n = 3/group for qRT-PCR validation) were used. Based on previous study findings (39, 42, 61, 62), the 6-h time point was selected to study LAC miRNAs and gene expression profile from KO mice in response to bacterial infection with and without rescue with SP-A. We hypothesized that the 6-h time interval would allow for the study of relatively early events.

Treatment of Mice With SP-A2 ($1A^0$) Protein

SP-A-KO mice were anesthetized, and one group of mice was infected with *K. pneumoniae* (~450 CFU/mouse) as described above. Another group was infected as described above and, at the same time, these mice received 10 µg (50 µl) of purified SP-A2 ($1A^0$) protein (42, 44, 60). In this study, 10 µg of purified protein was chosen, as this was shown in a previous rescue study (44) to significantly improve the survival of infected mice. The protein used for the rescue was obtained from stably transfected CHO cell lines as described (63). The mice were monitored for 6 h after infection.

Isolation of Lung Alveolar Cells From Infected Mice

LAC were obtained from SP-A-KO mice by bronchoalveolar lavage (BAL) at 6 h, after infection alone, and after infection plus SP-A2 ($1A^0$) protein treatment as described previously (42, 61). The cells in the BAL were separated by centrifugation (150 × *g* for 5 min) (31, 53), and a total cell count was performed, and cells were frozen (-80°C) until further use for either miRNA or gene expression studies. Briefly, the cell pellet was washed with 1× PBS (Gibco, Waltham, MA, USA), and the LACs, as a whole, were used in the present study without any cell sorting. Randomly, a fraction of the cells from 2 samples from each group was used to prepare cytospins, cells were subjected to Papanikolaou staining, and a differential cell count was performed. The majority of LACs at 6 h after infection are AMs (~70%–75%). Other cells early in the response to infection may include neutrophils (10–12). SP-A treatment is not expected to change the AM cell population (39, 61).

RNA Extraction, Library Construction, and Sequencing

Total RNA extracted from LACs was used for library construction and sequencing, as described previously (42, 55).

miRNA Analysis

Small RNA sequencing (RNA-seq) libraries were generated by NEXTflex Small RNA Library Prep Kit v3 for Illumina (BioO Scientific, Austin, TX, USA), followed by deep sequencing on an Illumina HiSeq 2500 as per the manufacturer's instructions. Briefly, 1–2 ng of total RNA was ligated with chemically modified 3′ and 5′ adapters that can specifically bind to mature microRNAs, followed by reverse transcription and PCR amplification. Unique index sequence tags were introduced during PCR to enable multiplexed sequencing. Each library was assessed for the presence of desired microRNA population and approximate library quantity by Bioanalyzer High Sensitivity DNA Kit (Agilent Technologies). Pooled libraries were denatured and loaded onto a TruSeq Rapid flow cell on an Illumina HiSeq 2500 and run for 50 cycles using a single-read recipe according to the manufacturer's instructions. De-multiplexed sequencing reads passed the default purify filtering of Illumina CASAVA pipeline (released version 1.8) and were quality trimmed/filtered using The FASTX-Toolkit (http://hannonlab.cshl.edu/fastx_toolkit). The filtered reads were further trimmed with both 5′ and 3′ adapter sequences and subjected to Chimira suite to align and count miRNA expression (64).

The differentially expressed miRNAs between male and female mice under the studied condition were identified by using edgeR test method (65) and TCC v1.14.0 R package (66) with a false discovery rate (FDR)-adjusted p-value of 0.1 as a significance cutoff for miRNA identification. Outliers and other inconsistencies were removed based on 1) the lack of good correlation of data count among the groups in at least 3 replicates and on average tag count data and 2) whether the value was higher than twice the standard deviation. The differentially expressed miRNAs (n = 178) used for further analysis were selected based on their fold change and their p-value ($p < 0.05$).

Gene Expression Analysis

QuantSeq 3′ mRNA-Seq Library Prep Kit FWD from Illumina (Lexogen, Vienna, Austria) was used to generate mRNA-Seq libraries as per manufacturer's recommendation, followed by deep sequencing on an Illumina HiSeq-2500 as per the manufacturer's instructions. Briefly, 0.5–1 ng of total RNA was subjected to the first cDNA strand that is initiated by oligo dT priming. The synthesis of the second cDNA strand is performed by random priming in a manner that DNA polymerase is efficiently stopped when reaching the next hybridized random primer, so only the fragment closest to the 3′ end gets captured for later indexed adapter ligation and PCR amplification. The processed libraries were assessed for fragment size distribution and quantity using a BioAnalyzer High Sensitivity DNA kit (Agilent Technologies). Pooled libraries were denatured and loaded onto a TruSeq Rapid flow cell on an Illumina HiSeq 2500 (Illumina) and run for 50

cycles using a single-read recipe (TrueSeq SBS kit v3, Illumina) according to the manufacturer's instructions. Illumina CASAVA pipeline (released version 1.8, Illumina) was used to obtain de-multiplexed sequencing reads (fastq files) that passed the default purifying filter. These were further subjected to QuantSeq data analysis pipeline on a Bluebee genomics analysis platform (Bluebee, Cambridge, MA, USA). The differentially expressed genes between male and female mice under the studied condition were identified by using the edgeR test method (65) and TCC v1.14.0 R package (66). We chose genes for further analysis based on their p-value ($p < 0.05$) and their expression levels (≥2-fold change) in LACs from infected and infection plus protein rescue mice.

Lung Alveolar Cell miRNA and Gene Data Analysis

Changes in the levels of miRNAs and gene expression after infection and infection plus SP-A2 ($1A^0$) were compared. Differentially expressed miRNAs and genes in SP-A-KO male and female mice were identified (data count from 3 out of 4 mice, **Supplementary Materials 1**, **2**). The fold differences for the identified miRNAs and genes between male and female mice were determined by dividing a specific individual male miRNA or gene value by the corresponding specific female miRNA or gene value and *vice versa* for the same miRNA or gene (**Supplementary Materials 1**,**2**).

Ingenuity Pathway Analysis

Ingenuity Pathway Analysis (IPA; www.qiagen.com/ingenuity Qiagen, Redwood City) was performed as described (42, 53, 55, 67) and used values that met the cutoff of 2-fold up and downregulation in the male and female groups in the studied conditions. IPA helped to identify miRNA-mRNA targets of the significantly changed miRNAs and signaling pathways of the miRNA targets and regulatory networks of the differentially expressed genes as well as identify "integrated" signaling networks of the significantly changed miRNAs, their targets, and the differentially expressed genes under the studied conditions.

Validation of miRNA-mRNA Target Gene Expression

The expression levels of individual miRNA targets were validated in LACs isolated from KO male and female mice after infection alone and after infection in combination with exogenous SP-A2 ($1A^0$) protein by qRT-PCR as described previously (42, 55). The expression levels of BCL2, CASP9, CCND1, CCND2, CDK7, CDKN2A, E2F1, E2F2, E2F3, EGR2, FOXO1, FOXO3, IL-6, MYC, PPARA, PPARG, SMAD2, STAT-3, TLR2, TNF, and TNFSF12 were assessed by real-time PCR using RT2 SYBR Breen ROX qPCR master mix (#330520, Qiagen) on a QuantStudio 12K Flex Real-Time PCR system (Applied Biosystems, Waltham, MA, USA) at the Pennsylvania State University College of Medicine Genomic Core Facility. The RT2 qPCR Primer assays were purchased from Qiagen. The LAC samples [3 animals/sex/treatment—infection alone or in combination with SP-A2 ($1A^0$) protein] were analyzed in triplicate/animal. The glyceraldehyde 3-phosphate dehydrogenase (GAPDH) level was used, as a standard, to quantify the relative expression levels of the studied genes. The relative expression levels of genes were determined by the $2^{-\Delta CT}$ in which ΔCT was calculated as follows: $\Delta CT = CT_{\text{gene-of-interest}} - CT_{\text{housekeeping gene}}$.

Statistical Analysis

Significant differences of the miRNAs and gene expression levels in male and female mice after infection and after infection plus SP-A2 ($1A^0$) protein were assessed by a two-tailed t-test and nonparametric Mann–Whitney test. Multiple comparison analysis was performed by one-way analysis of variance (ANOVA) followed by Bonferroni correction for multiple comparisons. A $p < 0.05$ was considered statistically significant. All of the data points are means ± standard deviation, and analyses were performed using GraphPad Prism software version 5.0 (GraphPad Software, San Diego, CA, USA).

RESULTS

Lung Alveolar Cell miRNome

Effect of Infection and Infection Plus Exogenous SP-A2 ($1A^0$) Protein Rescue on Lung Alveolar Cell miRNome

A total of 178 LAC miRNAs were found in male and female mice of both study groups (**Supplementary Material 1**). A two-tailed t-test and nonparametric Mann–Whitney test were used to assess differences ($p < 0.05$) (**Figures 1A–D**). No significant differences were observed in any of the comparisons by one-way ANOVA or Bonferroni multiple comparison analysis (data not shown).

miRNAs That Changed ≥2-Fold After Infection and Infection Plus SP-A2 ($1A^0$) Protein Rescue

We next studied LAC miRNAs that exhibited ≥2-fold changes in response to infection vs infection plus SP-A2 ($1A^0$) protein rescue in KO male and female mice.. A comparison of LAC miRNAs from infected KO male and female mice revealed 1) 47 miRNAs in male mice and 7 miRNAs in female mice in response to infection and 2) 53 miRNAs in male mice and 12 miRNAs in female mice after infection plus SP-A2 ($1A^0$) (**Supplementary File 1)**. Another comparison of LAC miRNAs that changed in response to infection vs. infection plus SP-A2 ($1A^0$) protein rescue in the same sex revealed that, in male mice, 25 miRNAs were differentially expressed (≥2-fold) in response to infection compared to 12 miRNAs in response to infection plus SP-A2 ($1A^0$) protein, and in female mice, 26 miRNAs were differentially expressed (≥2-fold) in response to infection compared to 15 miRNAs in response to infection plus SP-A2 ($1A^0$) protein rescue (**Supplementary File 1**). In both comparisons, miRNAs with ≥2-fold expression level were specific to infection or infection plus SP-A2 ($1A^0$) protein rescue. No miRNA was found to be in common in either sex between the two conditions (**Supplementary File 1**).

Ingenuity Pathway Analysis

IPA was used to assess biological functions and miRNA targets of significantly changed miRNAs. The miRNA-mRNA targets of the significantly changed miRNAs and the signaling pathways that these are involved in are shown in **Figure 2**. The miRNA-mRNA targets include BCL2, CASP9, CCND1, CCND2, CDK7, CDKN2A, E2F1, E2F2, E2F3, EGR2, FOXO1, FOXO3, IL-6, MYC, PPARA, PPARG, SMAD2, STAT-3, TLR2, TNF, and TNFSF12. The miRNAs that were changed significantly in KO male and female mice under the studied conditions and their targets are listed in **Table 1**.

miRNA-mRNA Target Validation by qRT-PCR Analysis

LACs derived from mice of either sex from the two studied conditions were used for this analysis (**Figure 3**). The expression levels of CASP9, CCND1, CCND2, E2F1, E2F2, E2F3, EGR2, FOXO1, FOXO3, MYC, PPARG, SMAD2, STAT-3, TLR2, TNF, and TNFSF12 were significantly upregulated in KO male vs. female mice under both studied conditions (**Figure 3A**). On the other hand, the expression levels of BCL2, CDKN2A, IL-6, and PPARA remained similar in both male and female mice after infection but were significantly upregulated in male mice after infection in combination with exogenous SP-A2 ($1A^0$) protein (**Figure 3B**). The expression level of CDK7 was significantly increased in male mice after infection but decreased significantly compared to female mice in response to infection in combination with exogenous SP-A2 ($1A^0$) protein (**Figure 3B**).

Gene expression of Lung Alveolar Cells From Infected Mice and Infected Plus SP-A2 ($1A^0$) Protein Rescue Mice

Ingenuity Pathway Analysis

The genes that exhibited significant changes (≥2-fold) in response to infection and infection plus SP-A2 ($1A^0$) protein between KO male and female mice were used for IPA. Three signaling nodes, tumor necrosis factor (TNF), TP-53, and cell cycle, were identified where each node had direct interactions with 4 or more molecules in the studied conditions. The TNF node even though lacked direct interactions with 4 or more molecules is shown in **Figure 4** because a large number of genes (n = 8) with ≥2-fold change had indirect interactions. The functional relationship plots of the signaling nodes in both sexes in KO under the studied conditions are presented in **Figure 4** and **Supplementary Figure 1**. These together show that many of the observed genes with ≥2-fold changes were previously shown to contribute, *via* either direct (solid lines) or indirect (dashed lines) interactions, to TNF, cell cycle, and TP-53 signaling nodes under the studied conditions (**Figure 4**, **Supplementary Figure 1**).

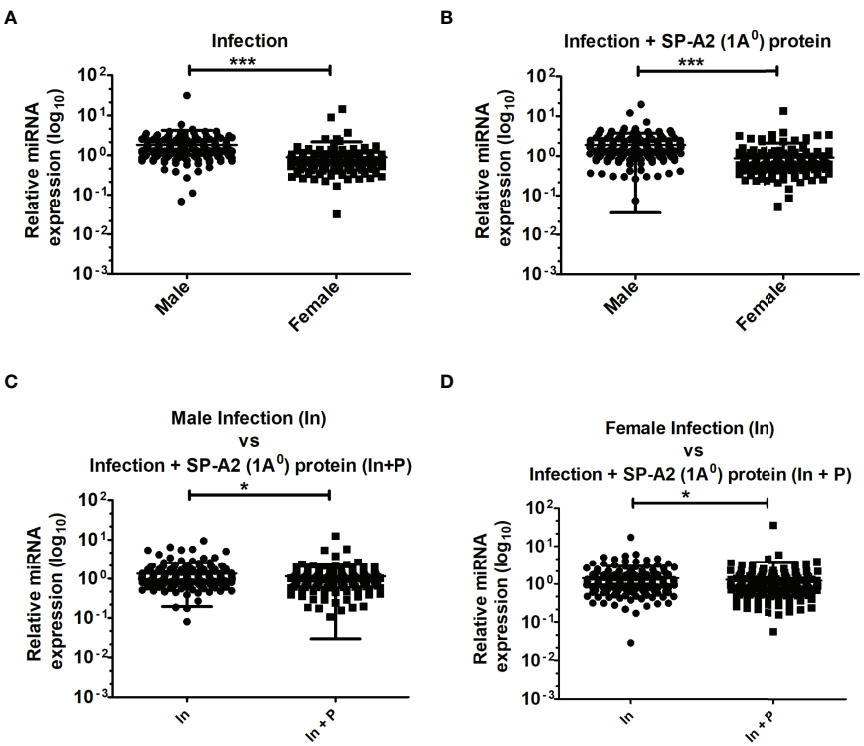

FIGURE 1 | LAC miRNome in KO males and females mice after *K. pneumoniae* infection and infection plus SP-A2 ($1A^0$) protein rescue. Comparisons between miRNAs identified in KO, M vs. F, after infection **(A)**, M vs. F, after infection plus SP-A2 ($1A^0$) protein rescue **(B)**. Male mice: infection vs. infection plus SP-A2 ($1A^0$) protein **(C)**. Female mice: infection vs. infection plus SP-A2 ($1A^0$) protein **(D)**. Significant differences were observed between sexes and between bacterial infection and infection plus rescue (**A–D**; $p < 0.05$). *$p < 0.05$, ***$p < 0.001$. In; Infection, In + P; infection plus SP-A2 (1A0) protein.

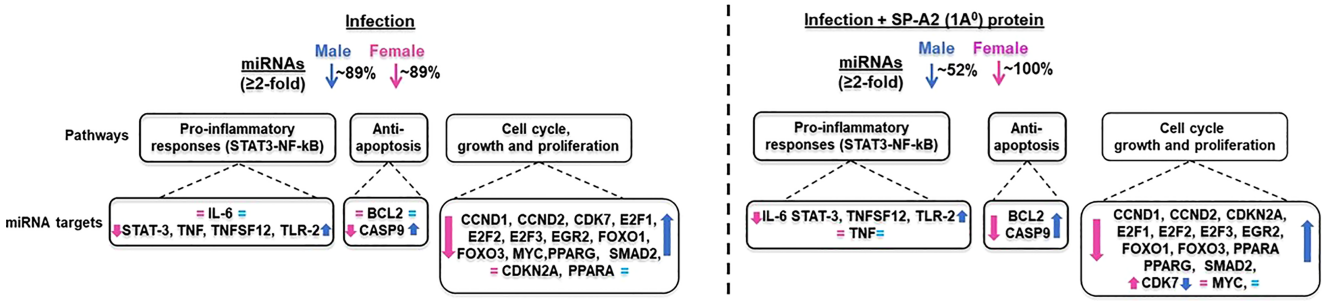

FIGURE 2 | Effect of infection and infection plus SP-A2 ($1A^0$) protein rescue on the miRNome, miRNA-mRNA targets, and pathways of the LAC KO male and female mice. A comparison is shown of the miRNAs, target genes, and pathways of the LAC KO after infection and infection plus SP-A2 ($1A^0$) rescue in the left and right panels, respectively. The significantly regulated miRNAs (n = 19) each present in KO male and female groups in response to infection were largely decreased by ~89% in male (blue arrow) and female (pink arrow) mice. In the infection plus SP-A2 ($1A^0$) protein rescue, ~52% of the significantly regulated miRNAs (n = 19) were decreased in male (blue arrow) and 100% in female (pink arrow) mice; a few miRNAs showed an increase **(Table 1)**). Three pathways are depicted as assessed by IPA of the significantly changed miRNAs. The upregulated miRNA-mRNA targets in KO male mice (blue arrow) and the downregulated targets in female mice (pink arrows) are depicted after infection and infection plus rescue in the left and right panels, respectively. The mRNA targets that did not change after infection and infection plus SP-A2 ($1A^0$) protein are shown in pink and blue equal sign.

TABLE 1 | LAC KO miRNA levels in male and female mice and their mRNA targets after infection and infection plus SP-A2 ($1A^0$) rescue.

miRNA ID	Infection		Infection + SP-A2 ($1A^0$) Protein		#Target molecule
	Fold change				
	Male mice	Female mice	Male mice	Female mice	
let-7a-5p	1.16*	0.86*	1.64*	0.61*	CCND1, CCND2, CDKN2A, E2F1, E2F2, E2F3, MYC, PPARA, TNF, TNFSF12
miR-16-5p	0.83*	1.21*	1.39*	0.72*	BCL2, CCND1, CCND2,CDK7, E2F1, E2F2, E2F3, TNFSF12
miR-17-5p	2.09	0.48*	1.67*	0.60*	CCND1, CDK7, E2F1, E2F2, E2F3, EGR2, MYC, STAT-3, PPARA, TNFSF12,
miR-22-3p	0.44*	2.28	1.32*	0.76*	E2F1, E2F3
miR-23a-3p	1.23*	0.81*	1.98	0.51*	E2F1, E2F3,TNFSF12
miR-30c-5p	1.74*	0.57*	1.64*	0.61*	PPARA
miR-34a-5p	1.30*	0.77*	3.49	0.29*	PPARA, PPARG
miR-103-3p	0.80*	1.24*	1.38*	0.72*	E2F1, E2F3, PPARA
miR-125b-5p	1.10*	0.91*	1.48*	0.68*	TLR2
miR-143-3p	0.51*	1.94	0.73*	1.38*	E2F1, E2F3, PPARA
miR-155-5p	2.45	0.41*	3.01	0.33*	IL-6, TLR2, TNF
miR-181a-5p	1.09*	0.91*	2.44	0.41*	SMAD2
miR-182-5p	1.08*	0.93*	1.53*	0.66*	FOXO1, PPARA
miR-185-5p	0.70*	1.42*	2.18	0.46*	SMAD2
miR-191-5p	1.20*	0.83*	2.10	0.48*	IL-6
miR-200b-3p	1.15*	0.87*	1.28*	0.78*	PPARA
miR-221-3p	0.96*	1.04*	2.17	0.46*	E2F1, E2F2, E2F3
miR-378a-3p	1.27*	0.79*	2.37	0.42*	CASP9, FOXO3, PPARA
miR-423-5p	1.94	0.52*	3.11	0.32*	SMAD2

Indicates downregulation. #Identified by IPA.

Differentially Expressed Genes in Knockout Lung Alveolar Cells From Mice Under the Studied Conditions, Infection and Infection Plus Rescue

We identified differentially expressed genes ($p < 0.05$) for several of the comparisons made. These include a) M vs. F, infection, n = 169 genes; b) M vs. F, infection plus SP-A2 ($1A^0$) protein, n = 105 genes; c) male mice, infection vs. infection plus SP-A2 ($1A^0$), n = 245 genes; and d) female mice, infection vs. infection plus SP-A2 ($1A^0$), n = 188 genes (**Supplementary File 2**).

Next, we assessed changes in specific genes that either increased (≥2-fold) or decreased (≤2-fold) significantly in either sex under each studied condition. After infection, out of the 169 significantly changed genes (≥2-fold), 38 were increased and 131 were decreased in male vs. female mice and *vice versa*

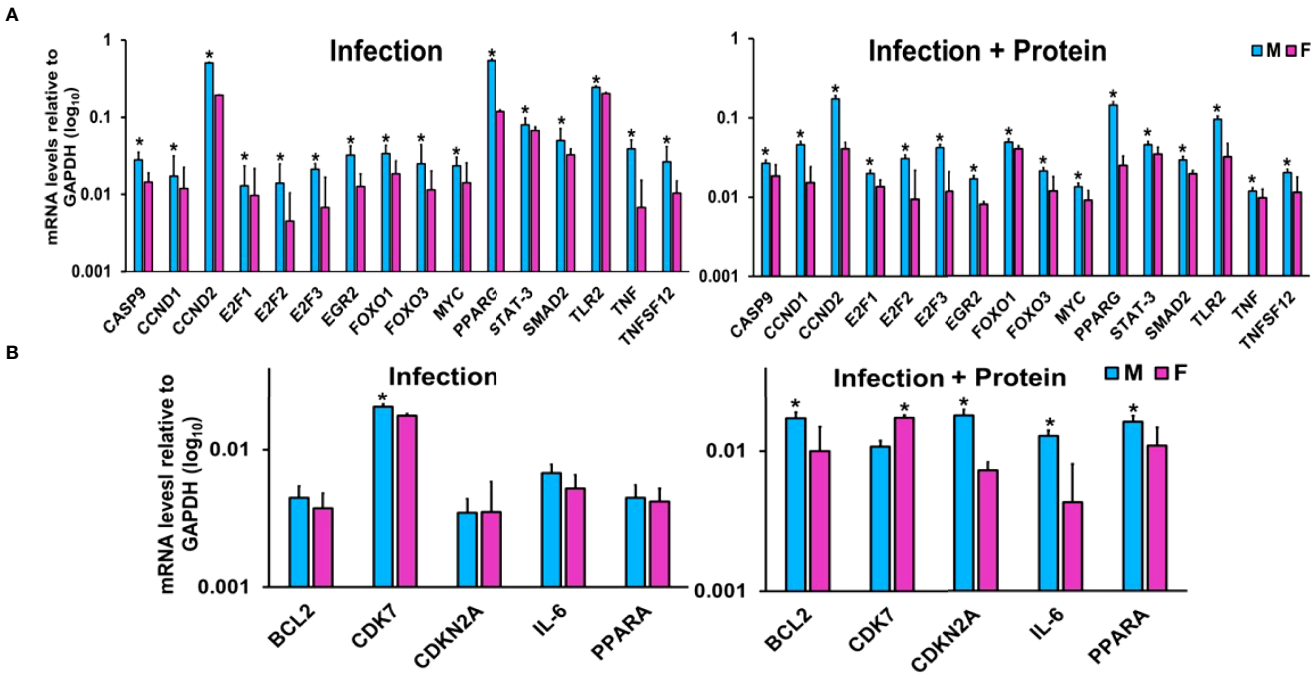

FIGURE 3 | Effect of infection and infection plus SP-A2 ($1A^0$) protein rescue on miRNA-mRNA targets. Panels **A, B** show the gene expression levels in KO male and female mice. Significant sex differences after infection in the expression levels of CASP9, CCND1, CCND2, E2F1, E2F2, E2F3, EGR2, FOXO1, FOXO3, MYC, PPARG, SMAD2, STAT-3, TLR2, TNF, and TNFSF12 (upregulated in male mice compared to female mice) are shown in panel **(A)** on the left. The expression levels of BCL2, CDK7, CDKN2A, IL-6, and PPARA after infection that exhibited no changes between sexes in response to infection except CDK7 (showed a significant increase in male mice) are shown in panel **(B)** on the left. However, in response to infection plus protein rescue, all of the genes exhibited an increase in male vs. female mice (**A, B** on the right) except the CDK7 that exhibited an increase ($p < 0.05$) in female mice (**B** on the right). The expression levels of specific mRNA targets were normalized to GAPDH and are depicted by blue and pink bars, respectively, for male and female mice. An asterisk (*) marks the differences ($p < 0.05$) between male and female mice.

(**Supplementary File 2**). In response to infection plus SP-A2 ($1A^0$), out of the 105 significantly changed genes (≥2-fold), 22 and 84 had increased and decreased levels, respectively, in male vs. female mice and *vice versa* (**Supplementary File 2**). In male mice, out of 245 significantly changed genes (≥2-fold), 178 and 65 had increased and decreased levels, respectively, in response to infection vs. infection plus SP-A2 ($1A^0$) and *vice versa* (**Supplementary File 2**). Whereas in female mice, out of the 188 significantly changed genes, 127 and 61 exhibited increased and decreased levels, respectively, in response to infection vs. infection plus SP-A2 ($1A^0$) and *vice versa* (**Supplementary File 2**). Next, we compared genes identified under the studied condition in male and female mice and found 45 genes to be in common under all studied conditions (**Table 2**).

Sex and Treatment Differences in Lung Alveolar Cell Gene Expression After Infection and After Infection Plus SP-A2 ($1A^0$) Protein

The two-tailed t-test and nonparametric Mann–Whitney U-test were used to study the relative expression levels ($p < 0.05$) of genes in the LAC under the studied conditions. The results showed significant differences both as a function of sex and treatment after infection or infection plus SP-A2 ($1A^0$) protein (**Figures 5A–D**).

Significant Pathways After Integration of miRNAs, miRNA-mRNA Target Genes, and Genes Expressed Under the Studied Conditions

In response to infection and infection plus SP-A2 ($1A^0$) protein rescue, a subset of the miRNAs, miRNA-mRNA targets, and genes identified with significant changes in their levels in male and female mice were involved in TNF and cell cycle signaling pathways (**Figure 6**). These are referred to as "integrated" pathways in the *Discussion*.

In Response to Infection

Two signaling pathways were identified, the TNF and the cell cycle. 1) In TNF signaling, the expression level of miRNAs let-7a-5p, miR-34a-5p, and miR-155-5p was downregulated ($p < 0.05$) in both sexes, except miR-155-5p that showed a significant increase in male mice. The identified miRNAs were predicted to bind and regulate TNF and PPARG, and their altered expression was associated with an increase in the expression ($p < 0.05$) of these target molecules in male vs. female mice (**Figure 6A**). IPA revealed that several of the identified genes in the gene expression study (ATP6V0D2, COTL1, SRGN, SNAP23, LITAF, CDC42, PPT1, SCARB2, and PANK3) have an indirect interaction with the

miRNA targets especially TNF, whereas the MBNL1 has a direct interaction with PPARG (**Figure 6A**). The expression of the ATP6V0D2, SNAP23, LITAF, CDC42, PPT1, and SCARB2 genes was downregulated ($p < 0.05$), and the expression of SRGN, PANK3, and MBNL1 was upregulated ($p < 0.05$) in male vs. female mice. However, the expression of the COTL1 gene was upregulated ($p < 0.05$) in both sexes (**Figure 6A**).

2) In cell cycle signaling, the expression level of miRNAs let-7a-5p, miR-16-5p, miR-17-5p, miR-182-5p, and miR-378a-3p was downregulated ($p < 0.05$) in male and female mice, except miR-17-5p that showed a significant increase in male mice. These miRNAs were predicted to bind and regulate CCND1 and FOXO1. These target molecules showed a significant increase in their expression in male vs. female mice (**Figure 6B**). IPA revealed that several of the identified genes (ARPC1B, PRKAR1A, CDC42, RNF187, and TBCA) have indirect interaction with the miRNA target CCND1, and the NDUFA7 gene has a direct interaction with FOXO1 (**Figure 6B**).

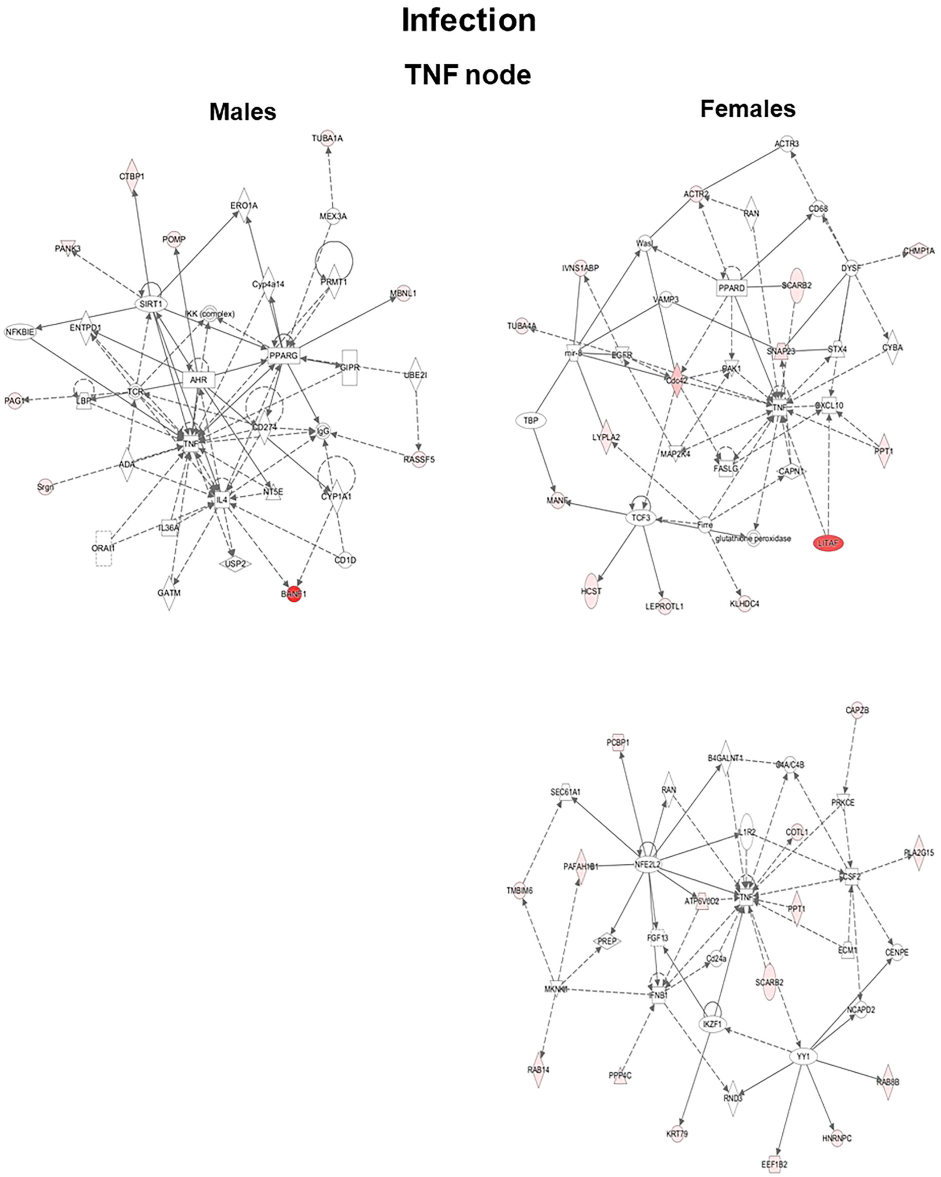

FIGURE 4 | Ingenuity pathway analysis. Biological networks for the TNF signaling of genes with ≥2-fold changes in their expression level are shown for the KO LAC of both sexes at 6 h after infection. Direct and indirect gene interactions are marked with solid and dashed lines, respectively. Networks on the left and right show one pathway for male mice and two pathways for female mice, respectively. The different shapes depict different functional classes as follows: Square and concentric (double) circles denote cytokines and complex/groups, respectively. Diamonds denote peptidases and enzymes. Ovals denote transmembrane receptors and transcription regulators; triangle, kinases and phosphatases; rectangles, ion channels, G-protein-coupled receptors, and ligand-dependent nuclear receptors; and trapezoids, microRNAs and transporters.

TABLE 2 | Relative content (≥2-fold or ≤2-fold) of genes found to be in common in KO male vs. female (M/F) mice and *vice versa* after infection and infection plus SP-A2($1A^0$) rescue are shown.

Gene Symbol	Fold change (≥2 or ≤2)					
	Male mice			Female mice		
	Infection	Infection plus Protein	p-value	Infection	Infection plus Protein	p-value
Anxa2	10.500	0.095	0.012	14.943	0.067	0.005
App	9.888	0.101	0.019	23.387	0.043	0.002
Arl6ip1	48.327	0.021	0.001	7.220	0.138	0.040
Atp6v1b2	11.270	0.089	0.040	7.451	0.134	0.033
B2m	7.368	0.136	0.046	14.988	0.067	0.007
Cd47	15.293	0.065	0.027	0.003	391.712	0.000
Cd63	36.338	0.028	0.004	11.236	0.089	0.009
Cd74	42.953	0.023	0.001	9.876	0.101	0.012
Cebpb	8.023	0.125	0.025	15.958	0.063	0.007
Chmp1a	0.112	8.899	0.012	11.532	0.087	0.024
Chmp4b	0.143	6.990	0.009	44.313	0.023	0.000
Cotl1	8.627	0.116	0.031	7.323	0.137	0.028
Cox6a1	13.444	0.074	0.023	43.058	0.023	0.004
Ctsz	101.999	0.010	0.000	10.138	0.099	0.020
Dazap2	15.871	0.063	0.013	64.249	0.016	0.000
Ear2	14.074	0.071	0.007	6.663	0.150	0.026
Furin	18.289	0.055	0.012	41.871	0.024	0.001
Gm10076	15.460	0.065	0.015	11.796	0.085	0.019
Gm23935	146.087	0.007	0.000	52.072	0.019	0.001
Gpx1	24.106	0.041	0.004	29.036	0.034	0.000
Grn	17.153	0.058	0.006	24.312	0.041	0.001
Iqgap1	7.248	0.138	0.048	7.978	0.125	0.029
Itgb1	18.834	0.053	0.024	28.461	0.035	0.010
Itm2c	19.639	0.051	0.016	156.657	0.006	0.000
Lcp1	12.632	0.079	0.013	33.804	0.030	0.001
Lsp1	0.113	8.849	0.042	8.749	0.114	0.045
Pafah1b1	0.084	11.933	0.011	40.320	0.025	0.007
Pla2g15	36.258	0.028	0.007	6.479	0.154	0.045
Psap	45.531	0.022	0.000	38.107	0.026	0.001
Ptprc	13.997	0.071	0.040	17.303	0.058	0.006
Rab14	11.907	0.084	0.040	12.096	0.083	0.004
Rpl36a	42.542	0.024	0.002	16.947	0.059	0.005
Rpl37	8.835	0.113	0.041	11.783	0.085	0.017
Rps25	38.956	0.026	0.000	12.910	0.077	0.009
Rps3	18.131	0.055	0.014	54.118	0.018	0.001
Rps5	7.865	0.127	0.042	9.942	0.101	0.017
Rps9	7.408	0.135	0.045	30.685	0.033	0.001
Shisa5	33.361	0.030	0.002	49.892	0.020	0.000
Tmbim6	7.950	0.126	0.031	24.143	0.041	0.001
Tmed10	84.217	0.012	0.001	13.154	0.076	0.035
Tubb5	14.562	0.069	0.013	49.324	0.020	0.001
Txnip	10.103	0.099	0.033	51.432	0.019	0.000
Ube2d3	17.291	0.058	0.024	29.690	0.034	0.006
Vdac2	0.116	8.650	0.016	0.121	8.268	0.040
Wfdc21	148.952	0.007	0.000	10.742	0.093	0.026

The significantly changed genes were downregulated ($p < 0.05$) in male vs. female mice (**Figure 6B**).

In Response to Infection Plus SP-A2 ($1A^0$) Protein Rescue

One signaling pathway was identified under this condition, namely, the cell cycle. In this pathway, the expression level of miRNAs let-7a-5p, miR-17-5p, miR-30c-3p, miR-34a-5p, miR-103-3p, miR-143-3p, miR-182-5p, miR-200b-3p, and miR-378a-3p was significantly downregulated in male and female mice, except miR-34a-5p and miR-378-3p. These two showed a significant increase in male mice. These miRNAs were predicted to bind and regulate MYC, E2F1, and PPARA; these target molecules showed an increase ($p < 0.05$) in their expression in male vs. female mice (**Figure 6C**). IPA revealed that several of the identified genes (RPL6, RPS21, RPL4, RPL35A, RPS3, RPS9, RPL37, RPL36a, RPS25, RPL31, TSPO, DBI, ACAA1b, and UQCR11) have direct interaction with the miRNA-mRNA targets, i.e., MYC, E2F1, and PPARA, whereas PIM1, SRGN, and IVNS1ABP have indirect interaction with MYC (**Figure 6C**). The expression level of RPS21, RPL4, UQCR11, SRGN, and IVNS1ABP genes was upregulated ($p <$

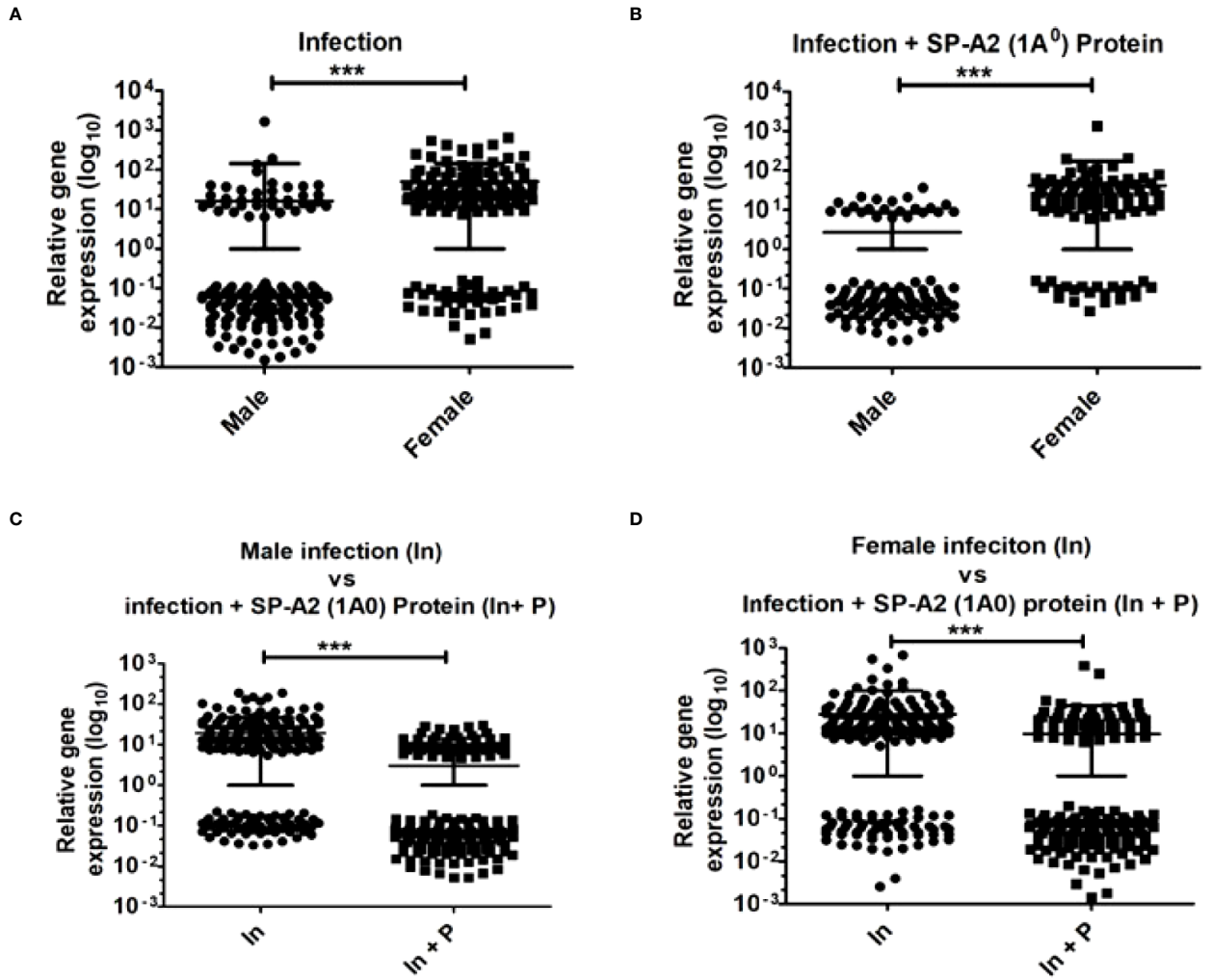

FIGURE 5 | Gene expression in KO mice of both sexes at 6 h after *K. pneumoniae* infection and infection plus SP-A2 ($1A^0$) protein rescue. A total of 169 genes in M vs. F after infection **(A)**, 105 genes in M vs. F after infection plus SP-A2 ($1A^0$) protein rescue **(B)**, 245 genes in male mice of infection vs. infection plus SP-A2 ($1A^0$) protein rescue groups **(C)**, and 188 genes in female mice of infection vs. infection plus SP-A2 ($1A^0$) protein rescue groups **(D)** were changed significantly and used in these analyses. These comparisons (n = 4/group) were significant ($p < 0.05$). Sex and treatment differences (***$p < 0.001$) were observed under studied conditions.

0.05) in male vs. female mice, but the expression of RPL35A was upregulated ($p < 0.05$) in female vs. male mice (**Figure 6C**). The expression of the other genes that interacted with MYC, E2F1, and PPARA was downregulated in both sexes under the studied condition. Together, these may provide some insight into the sex-specific response in the presence or absence of SP-A, observed here and in other studies, following bacterial infection.

DISCUSSION

AMs are key effector cells in the innate immunity of the lung, and their regulation and function can be affected by SP-A (13, 20, 21, 32, 59, 68–70). Several studies have shown in response to *K. pneumoniae* infection differences in survival as a function of sex in various types of mice including wild-type, SP-A-KO, and humanized transgenic mice, where each mouse line expresses a different human SP-A1 and SP-A2 variant (21, 32, 44, 59). In fact, the rescue of SP-A-KO mice with exogenous SP-A has been shown to significantly improve survival after bacterial infection regardless of whether the SP-A treatment occurred before or after infection or simultaneously with infection (44). Human SP-A1 and SP-A2 variants exhibit sex differences in their ability to regulate *in vivo* the miRNome (21) of AM (53) and Type II cells (54). Here, we studied the effect of *K. pneumoniae* infection and infection plus SP-A2 ($1A^0$) protein rescue on the differential regulation of the LAC miRNome and gene expression of SP-A-KO mice. Mice were infected with *K. pneumoniae* or infected plus rescue with SP-A2 ($1A^0$) protein. LAC miRNAs and gene expression levels were studied at 6 h after infection and infection plus rescue. The miRNA-mRNA target genes and signaling networks of the significant miRNAs were studied by IPA and

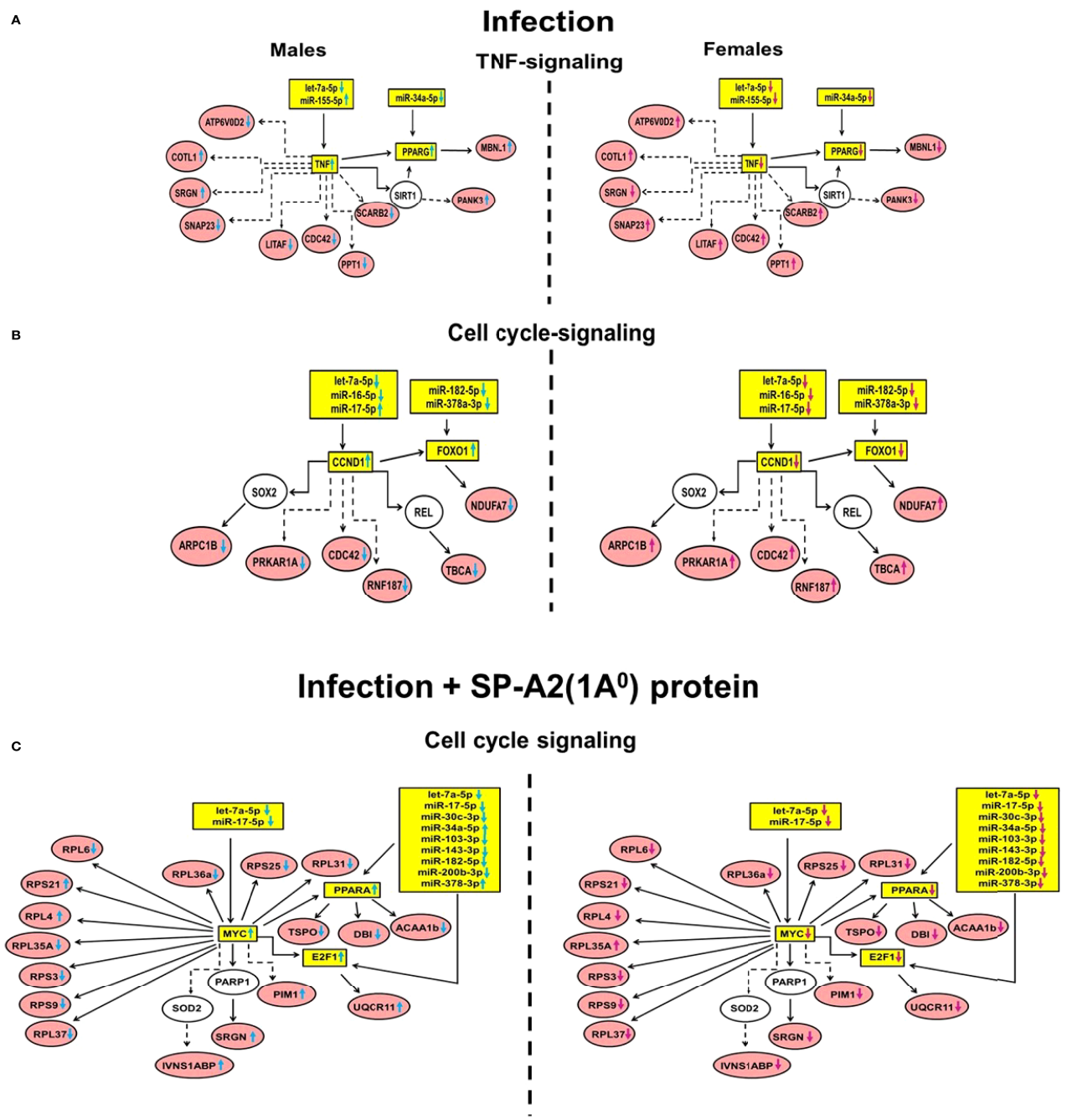

FIGURE 6 | Significant pathways that involve miRNAs, miRNA-mRNA targets and genes expressed following infection (Panel **A, B**) and infection plus SP-A2 (1A0) protein rescue (Panel **C**) are shown for males (left side diagrams) and for females (right side diagrams). Interactions of miRNA targets with genes identified from the gene expression analysis are shown. The molecules in these interactions are involved in the TNF and cell signaling pathways ($p < 0.05$). The miRNAs and their targets validated by qRT-PCR are highlighted in yellow. The genes that interact with miRNA targets are highlighted in red, and genes not identified in our study but exhibited interactions with the identified genes are shown in white. Direct and indirect interactions are shown with solid and dashed lines, respectively. The up and downregulation of miRNAs and genes are shown in blue and pink colored arrows indicating males and females, respectively.

validated by qRT-PCR and the gene expression profile by IPA. We observed the following: 1) differences ($p < 0.05$) in the LAC miRNome and gene expression of KO as a function of sex and condition; 2) significant increases in the overwhelming majority of miRNA target genes in KO male mice in response to infection and infection plus rescue; 3) involvement of the miRNA-mRNA targets in various pathways that included pathways involved in inflammation, antiapoptosis, and cell cycle; 4) based on LAC

gene expression, signaling pathways of TP-53, TNF, and cell cycle signaling nodes were identified; and 5) miRNA-mRNA target and gene expression was significantly increased in KO male mice compared to female mice. A subset of the significantly changed targets, genes, and miRNAs was connected *via* the TNF and cell cycle signaling pathways in response to infection and the cell cycle signaling pathway alone in response to infection plus SP-A2 ($1A^0$) protein rescue.

The role of sex and sex hormones on lung immunity in both humans and animals has been previously documented (71–81). A number of animal models have shown differences in survival after infection as a function of sex (13, 21, 32, 44, 59, 82) as well as in disease susceptibility and severity (32, 44, 59, 83–87). In humans, both prematurely born males vs. females exhibit higher susceptibility to neonatal respiratory distress syndrome (RDS) (73, 74), and adult males exhibit a higher susceptibility in Idiopathic pulmonary fibrosis (IPF), and Chronic obstructive pulmonary disease (COPD) (77, 88) and others, as well as in different types of pneumonia (79, 80, 88, 89).

In the current study, we found significant differences in the LAC miRNome, gene expression, and miRNA-mRNA target gene expression in KO, in terms of sex, under the studied conditions. An interesting and consistent observation was made, as also observed in previous related studies (42, 55, 56). The upregulation and downregulation of the majority of miRNAs, miRNA-mRNA targets, and genes were largely opposite in male and female mice, and the relevant discussion below pertains primarily to male mice. The sex differences observed are not surprising, as these have been observed before with other mouse models (13, 21). However, the present study, apart from contributing to a strong foundation that sex is an important variable that cannot be ignored, is the first study where the miRNome of infected mice was studied using mice that were never exposed to SP-A until the time of experimentation. In the published miRNome studies, the mice were exposed to ozone (and not to infection as in the current study) and were chronically exposed to SP-A. The available data indicate that the sex variable is important regardless of the exposure insult (i.e., ozone exposure, infection, others) and the studied conditions (13, 21). Although the detailed mechanisms for this sex-dependent regulation are not entirely clear, the collective literature points to a need of taking sex into consideration in study design and decisions that may impact biological processes. Moreover, the significantly changed molecules, whether miRNAs, miRNA-mRNA targets, or genes alone, were found to be involved in various signaling pathways. A subset of all three types of molecules whose expression was studied (miRNAs, miRNA-mRNA targets, and genes) converged in namely the TNF and cell cycle signaling pathways. We refer to these two pathways as "integrated' pathways.

Integrated Pathways

Cell Cycle Signaling in Response to Infection

The expression levels of both CCND1 and FOXO1 were increased in KO male mice, and the significant miRNAs shown to target these genes were for the most part downregulated compared to female mice. In the current study, the miRNAs that target CCND1, i.e., let-7a-5p, miR-16-5p, and miR-17-5p, may play a role in its regulation (90–93). CCND1 contributes to the regulation of G1-S phase transition, and the expression of CCND1 is induced by various stimuli (94, 95). The increase of CCND1 in KO male mice in response to infection may benefit LAC growth and G1-S phase progression (95), and decreased expression of CCND1 in female mice may contribute to the inhibition of cellular proliferation by a mechanism yet to be defined.

The expression level of FOXO1 as noted above was increased in KO male mice compared to female mice, and the miRNAs that target FOXO1, miR-182-5p, and miR-378-3p (**Table 1**) were significantly downregulated. FOXOs are transcription factors and may serve as a negative feedback loop in the control of cellular ROS homeostasis (96). FOXOs regulate different genes in different cell types (97) and activate the stress resistance genes and proapoptotic genes in response to different stimuli (97). Thus, the upregulation of FOXO1 may be a mechanism to alleviate stress-induced damage on LACs in KO male mice compared to female mice in response to infection. Of interest, previous studies (reviewed in Floros et al. (21)) have indicated that AMs from KO mice (i.e., AMs not exposed to SP-A) may be in a state of oxidative stress. Furthermore, a redox imaging study of a comparison of the KO AM redox status with AMs from humanized transgenic mice expressing a human SP-A transgene showed the KO AMs to be more oxidized after *in vivo* exposure of mice to ozone (46). It is possible that a similar mechanism is involved in response to infection, and FOXO1 plays a protective role in this. FOXO1, as did CCND1 (discussed above), was detected only in the infection group and not in the infection plus rescue. However, in the rescue group, one of the miRNAs (miR378a-3p) (**Table 1**) that targets FOXOs was increased, indicating that in KO LACs, additional/varied pathways may contribute to the regulation of this gene family.

Cell Cycle Signaling in Response to Infection Plus SP-A Protein Rescue

Even though this pathway was significant in both response to infection and response to infection plus rescue, different cell cycle molecules were significant in each. In the rescue group, three miRNA-mRNA targets (MYC, E2F1, and PPARA) were identified as targets for several miRNAs and potential regulators of several genes involved in this pathway. MYC gets activated in the G1 phase of cell growth and may serve, along with CCND1, as a G1-S phase transition regulator. The expression of E2F1 is induced by MYC (98, 99). The levels of both E2F1 and MYC were increased in KO male mice in the presence of SP-A2 ($1A^0$) protein rescue at the time of infection, even though most (except miR-378-3p, in KO male mice) of the miRNAs that target these genes were decreased in both sexes.

TNF Signaling in Response to Infection

The "integrated" TNF pathway was identified only for the infection group and not for the infection plus rescue. This pathway in both male and female mice contained two target genes, the TNF and PPARG. SP-A is shown to modulate TNF

expression in AMs (28) and in a macrophage-like cell line (100) *via* NF-κB activation/signaling (101, 102). In the latter, NF-κB inhibitors were shown to inhibit the SP-A-dependent TNF increase (101). In the absence of SP-A, TNF production was reduced (103) and an altered NF-κB pathway may play a role in SP-A-mediated TNF regulation after ozone exposure (103), a condition shown to reduce significantly the activity of SP-A (104). Whether infection in the absence of SP-A modulates TNF expression *via* different or modified NF-κB-mediated pathways, as shown previously under other conditions, is currently unknown. Although two miRNAs were identified to target TNF, the fact that their level was increased (miR-155-5p) and decreased (let-7a-5p) provides at present little insight into potential miRNA-mediated mechanisms without further experimentation.

However, upregulation of TNF may have an impact on NF-κB signaling by enhancing its nuclear translocation, which is key for NF-κB-mediated transcription of genes necessary to combat infection. In KO male mice, the IKK complex that may be activated indirectly by the TNF is increased at 6 h post-infection with or without rescue (**Figure 3**). In unstimulated cells, IKK molecules are associated with NF-κB to retain it in the cytoplasm. A variety of stimuli that include bacterial products could posttranslationally modify, *via* phosphorylation, the IKK molecules (105). This in turn initiates their destruction, which is key to freeing the NF-κB to enable its move to the nucleus in order to modulate transcription of various genes that are necessary to combat infection (105, 106). In addition, phosphorylation of IKK triggers MAPK signaling pathways, ERK1/2, JNK, and p38 (107). It would be of interest to investigate whether TNF induces prosurvival NF-κB and MAPK-dependent signaling in the studied infection models.

Furthermore, the peroxisome proliferator-activated receptors (PPARs) are transcriptional factors and members of the nuclear hormone receptor superfamily (108). One of its members, PPARG, is upregulated in the integrated pathway, and the miRNA (miR-34a-5p) that targets it is downregulated, pointing to a potential miRNA-mediated regulation of this gene in KO male mice. PPARs play a crucial role in anti-inflammatory activities in AMs (109, 110), and PPARG ligands significantly reduce cytokine production including TNF-α in human and mouse AMs (111, 112). However, the exact mechanism involved in the present model is yet to be determined.

In summary, the information from the integrated pathways that connects the three molecules (miRNAs, miRNA-mRNA targets, and genes) whose expression changed significantly shows that the general cell cycle signaling is important in both groups of study, although the actual molecules involved in each study group differ. This indicates that the presence or absence of SP-A is a key factor in the specificity of the overall process. The TNF signaling, on the other hand, was present only in the infection group. As noted above and reviewed elsewhere (21), the KO AM, which is the predominant cell in LACs, may exhibit certain deficits. Proteomics studies have shown that the proteomics profile of AM KO differs from that of wild type at baseline (113) and in response to infection (114). It is possible that the TNF signaling is necessary, as it may enable the AM KO or other cells in LACs to overcome potential inherent deficits.

Knockout Lung Alveolar Cell miRNome After Infection or After Infection Plus Rescue With SP-A

The cell cycle signaling and a pro-inflammatory pathway were identified as being important in response to infection and infection plus rescue when the miRNA-mRNA targets were analyzed by IPA. Both of these pathways involved several of the molecules whose expression changed significantly. The cell cycle was a ubiquitous pathway, as it was significant in all comparisons made. The overwhelming majority of changed miRNAs were downregulated after infection and infection plus SP-A2 ($1A^0$) protein rescue, and these were predicted to target genes that play a role in cell cycle and growth and proliferation pathways, such as CCND1, CCND2, CDK7, CDKN2A, E2F1, E2F2, E2F3, and MYC (**Table 1**). For example, miR-16-5p and miR-17-5p are predicted to bind CCND1, CCND2, CDK7, E2F1, E2F3, E2F3, and MYC mRNAs. Several studies have shown that these miRNAs play a role in the regulation of these genes (90–93). In the present study, the mRNA levels of CCND1, CCND2, CDK7, E2F1, E2F3, E2F3, and MYC were increased in male mice. As a downregulated miRNA usually associates with a target gene exhibiting increased expression, in male mice, it seems to be a concordance between the downregulation and upregulation of miRNAs and target genes, respectively, in response to infection and infection plus SP-A2 ($1A^0$) protein rescue. In female mice, however, despite the miRNA downregulation, there was a decreased expression of these genes. These indicate that different mechanisms may be operative in the LAC miRNome in male and female mice, as also observed in previous studies (53, 55, 56).

The pro-inflammatory responses were mediated *via* STAT-3 and NF-κB. These pathways have been shown to be involved in inflammatory processes and lung disease (115–120). The expression of miR-17-5p, predicted to bind and regulate STAT-3, was significantly decreased, and this was associated with an increased expression of STAT-3 in male mice. Previously, we have shown that STAT-3 levels were significantly increased after 4 h of post-oxidative stress due to ozone exposure in male AMs from mice expressing the human SP-A2 ($1A^0$) transgene (53) or after 4 h following infection in mice expressing the human SP-A ($1A^0$) or both human SP-A transgenes (55). Whereas after 18 h following infection, the STAT-3 levels were also increased in female mice (55, 56), indicating a time-dependent and sex-specific regulation of STAT-3. Furthermore, in male mice, the level of EGR2 that contributes, *via* STAT-3, to the upregulation of pro-inflammatory cytokines was also upregulated compared to female mice. These data indicate that the NF-κB and STAT-3-mediated pathways are important in the pro-inflammatory gene expression in KO male mice. However, in female mice, these pathways may be compromised. Moreover, the role of the sex-dependent miRNA-target genes in the regulation of the inflammatory response to infection in the presence or absence of SP-A warrants further investigation.

Lung Alveolar Cell Knockout Gene Expression in Response to Infection or Infection Plus SP-A Rescue

The cell cycle signaling node and the TP-53 node were found to be important in the gene expression study of both groups,

infection and infection plus rescue. The former has been discussed above. The TP-53 node was unexpected, as this one is shown to associate with lung cancer (121). SP-A1 ($6A^4$) and SP-A2 variants have been shown previously to associate with lung carcinoma (122–124). Although SP-A may regulate the tumor microenvironment *via* its ability to modulate cytokine expression and the polarization of macrophages in lung cancer (125), given the short time interval (6 h) in the present study from infection to data analysis, the changes in the expression of these various genes are likely due to bacterial infection. It is unlikely that this could be due to any true carcinogenic modulation, as this would require a considerably longer time than the 6-h time point used here. Several of the identified genes from the gene expression study had direct interaction with TP-53 in response to infection and infection plus SP-A2 ($1A^0$) protein rescue. In response to infection, in male mice, the TACC2, BUB1B, ATP5MC3, and MYO1E, and in female mice, the CAP1, MRPL2, COX5A, KLHL21, PDIA6, TSPO, and USP14 had direct interaction with TP-53 (**Supplementary Figure 1**). In response to SP-A2 ($1A^0$) protein rescue in male mice, the PGD, NAB1, RPL10, CDC42, and PDCD6IP had direct interaction with TP-53, whereas the NFAM1, PSMC1, and TP2B had indirect interaction with TP-53 (**Supplementary Figure 1**). In female mice, MDH2, NDUFS6, CSTB, LRRC17, TALDO1, CTSD, PFN1, S100A4, FAM120A, HUWE1, MCAM, GLUL, and UQCRQ had direct interaction with TP-53 (**Supplementary Figure 1**). These indicate that regardless of the role of TP-53 in infection, significant differences exist in the specific genes involved and the number of genes that interact with TP-53 as a function of sex, infection, and SP-A genotype that warrant further investigation.

COMMENTS AND SUMMARY

A number of studies with similar mouse models exposed to different insults have, previously, been carried out. In the grand scheme of things, similar observations were made in terms of pathways involved, albeit with some differences among the molecules involved. In the previously published mouse models where the miRNome and signaling pathways were studied, the mice were exposed to ozone and these were chronically/constitutively exposed to SP-A (53–56), whereas in the current study, the SP-A-KO mice were never exposed to SP-A until experimentation where they were acutely treated with SP-A at the time of infection. Interestingly, regardless of the insult/exposure (i.e., infection or ozone exposure), a number of similarities in the general response were observed. For example, after infection or ozone exposure, miRNAs were largely decreased in male and female mice, although differences in the levels of their target genes in terms of increases or decreases were observed between males and females. Even though LACs after infection in the present SP-A rescue study consist of ~70%–75% AMs and LACs after ozone exposure of humanized transgenic mice exposed chronically to human SP-A1 and SP-A2 constist of ~95% AMs (53, 55), following IPA, some of the signaling pathways were similar for the miRNA-mRNA targets regardless of exposure conditions.

Knowing the pathways and molecules involved in response to infection after an acute treatment of SP-A-KO mice with SP-A may have clinical importance if SP-A is used as a therapy. One potential example is the prematurely born infant who has low levels of SP-A, and infection has been identified as a major complication in these infants (126–128). Other conditions that may benefit from SP-A therapy include RSV and asthma, where SP-A or specific fragments/peptides of SP-A have already been used in preclinical studies as a potential therapy (57, 58). The present study provides insights that may be useful, as considerations for the therapeutic value of SP-A may expand in the future.

In related mouse models (regardless of the type of insult) where the miRNome and/or the gene expression profile of the AM or of the LAC was studied, two of the signaling pathways that were found to be significant in more than one study were rather unexpected. One of these was TP-53, which is shown to associate with lung cancer and is discussed in the previous section. Another one was the cell cycle signaling pathway. This pathway was ubiquitous, as this was not only significant in all comparisons made in the current study but in previously published studies of related mouse models (42, 55, 56). This observation, although it is surprising and difficult to explain because the AM (the predominant cell in LACs 6 h after infection or after 4 h of ozone exposure), and macrophages, in general, are not known to multiply. However, a rather recent literature challenges this notion. In a recent review, Röszer (129) discusses the self-renewal of macrophages at various tissue locations. For AMs, in particular, local proliferation was noted in mice and humans under certain conditions, and this capacity of self-renewing was also demonstrated *in vitro* (129). A number of mitogenic signals have been shown to play a role in macrophage proliferation. These include macrophage colony-stimulating factor (M-CSF) and granulocyte-macrophage (GM)-CSF (130) and IL-1α (131). The latter in certain conditions modulates the proliferation of a subset of AMs (131). Of interest, IL-1α levels in BAL were shown to be increased after infection (132), and during asthmatic inflammation, the AM pool at the early stages of the process depends on local proliferation (133). Furthermore, because the cell cycle pathway has been observed not only after infection (present study) where AMs are ~70%–75% of the LAC but also after 4 h of ozone exposure where AMs are ~95% of the LAC (53, 55), it is likely that this pathway occurs in AMs rather than other LACs that may constitute a fairly small portion of the LACs. Although it is currently unknown whether infection under the studied conditions can cause local AM proliferation, this possibility, however, cannot be excluded at this point, as the present data provide a general support that this may occur. This is an interesting possibility and warrants further investigation.

The novelty of the present study is to the best of our knowledge that this is the first such study where the SP-A-KO mice were rescued with/exposed to SP-A at the time of infection and the LAC miRNome was studied. The similarity of molecules/pathways observed in response to SP-A among various studies, whether acute or chronic exposure (as discussed above), points to an important role of SP-A in LACs under various conditions. However, studying, as done here, LACs as a whole instead of a

given cell type is a limitation, and in future studies, investigation of individual types of cells and the use of other methods is needed. For example, studying alveolar cells after cell sorting will better determine which miRNAs/pathways are attributed to AMs and which ones are attributed to other cells in BAL under the studied conditions.

In summary, the present study showed that 1) sex differences exist in all analyses performed; 2) the cell cycle pathway is significant in all study groups, although miRNAs and molecules involved in the cell cycle may differ under the different studied conditions; 3) pro-inflammatory pathways play an important role, and these may be more pronounced in the absence of SP-A; and 4) the gene expression profile identified the TP-53 and the cell cycle nodes as significant pathways. These unexpected findings are of particular interest and warrant further study. These together provide the foundation for future mechanistic studies where the details of SP-A-mediated pathways after bacterial infection could be investigated in a pure LAC population after employing cell sorting purification techniques (134).

DATA AVAILABILITY STATEMENT

The datasets presented in this study can be found in online repositories. The names of the repository/repositories and accession number(s) can be found in the article/**Supplementary Material**.

ETHICS STATEMENT

The protocols used were approved by the Pennsylvania State University College of Medicine Institutional Animal Care and Use Committee. The content on the care and use of laboratory animals were according to the guidelines of the National Institutes of Health.

AUTHOR CONTRIBUTIONS

NT and JF designed the study. NT performed the experiments, data analysis, and synthesis and contributed to the article writing. JF provided oversight in data analysis and integration and in the writing of the article. All of the authors read and approved the final article.

FUNDING

This work was supported by the John Ardell Pursley Memorial Research Fund and the Center for Host Defense, Inflammation and Lung Disease (CHILD) Fund, Department of Pediatrics, Penn State University College of Medicine.

ACKNOWLEDGMENTS

We thank Dr. Yuka Imamura Kawasawa, Institute for Personalized Medicine, Department of Biochemistry and Molecular Biology, Pennsylvania State University College of Medicine, for the identification of miRNAs by RNA sequencing.

SUPPLEMENTARY MATERIAL

The Supplementary Material for this article can be found online at: https://www.frontiersin.org/articles/10.3389/fimmu.2022.854434/full#supplementary-material

Supplementary File 1 | LAC KO miRNAs of both sexes at 6h after infection and after infection plus SP-A2 ($1A^0$) protein rescue.

Supplementary File 2 | LAC KO gene expression of both sexes at 6h after infection and after infection plus SP-A2 ($1A^0$) protein rescue.

Supplementary Figure 1 | Biological networks for the cell cycle and TP-53 signaling pathways of genes with ≥ 2-fold expression levels in both sexes are shown for the KO at 6 h after infection with or without SP-A2 (1A0) protein rescue. Direct and indirect gene interactions are marked with solid and dashed lines, respectively. Networks on the left and right sides of the figure show pathways for male and female mice, respectively. Each gene or group of genes is represented as a node. The different shapes depict different functional classes as follows: Square and concentric (double) circles denote cytokines and complex/groups, respectively. Diamonds denote peptidases and enzymes; Ovals denote transmembrane receptors and transcription regulators; Triangle kinases and phosphatases; Rectangles ion channels, Gprotein coupled receptors, and ligand-dependent nuclear receptors; and Trapezoids microRNAs and transporters.

REFERENCES

1. Kofteridis DP, Papadakis JA, Bouros D, Nikolaides P, Kioumis G, Levidiotou S, et al. Nosocomial Lower Respiratory Tract Infections: Prevalence and Risk Factors in 14 Greek Hospitals. *Eur J Clin Microbiol Infect Dis* (2004) 23 (12):888–91. doi: 10.1007/s10096-004-1245-y
2. Podschun R, Ullmann U. Klebsiella Spp. As Nosocomial Pathogens: Epidemiology, Taxonomy, Typing Methods, and Pathogenicity Factors. *Clin Microbiol Rev* (1998) 11(4):589–603. doi: 10.1128/CMR.11.4.589
3. Ko WC, Paterson DL, Sagnimeni AJ, Hansen DS, Von Gottberg A, Mohapatra S, et al. Community-Acquired Klebsiella Pneumoniae Bacteremia: Global Differences in Clinical Patterns. *Emerg Infect Dis* (2002) 8(2):160–6. doi: 10.3201/eid0802.010025
4. Bagley ST. Habitat Association of Klebsiella Species. *Infect Control* (1985) 6 (2):52–8. doi: 10.1017/S0195941700062603
5. Rock C, Thom KA, Masnick M, Johnson JK, Harris AD, and Morgan DJ, et al. Frequency of Klebsiella Pneumoniae Carbapenemase (KPC)-Producing and non-KPC-Producing Klebsiella Species Contamination of Healthcare Workers and the Environment. *Infect Control Hosp Epidemiol* (2014) 35(4):426–9. doi: 10.1086/675598
6. Dao TT, Liebenthal D, Tran TK, Ngoc ThiVu B, Ngoc ThiNguyen D, Thi Tran HK, et al. Klebsiella Pneumoniae Oropharyngeal Carriage in Rural and Urban Vietnam and the Effect of Alcohol Consumption. *PLoS One* (2014) 9 (3):e91999. doi: 10.1371/journal.pone.0091999
7. Paczosa MK, Mecsas J. Klebsiella Pneumoniae: Going on the Offense With a Strong Defense. *Microbiol Mol Biol Rev* (2016) 80(3):629–61. doi: 10.1128/MMBR.00078-15
8. Magill SS, Edwards JR, Bamberg W, Beldavs ZG, Dumyati G, Kainer MA, et al. Multistate Point-Prevalence Survey of Health Care-Associated Infections. *N Engl J Med* (2014) 370(13):1198–208. doi: 10.1056/NEJMoa1306801

9. Munoz-Price LS, Poirel L, Bonomo RA, Schwaber MJ, Daikos GL, Cormican M, et al. Clinical Epidemiology of the Global Expansion of Klebsiella Pneumoniae Carbapenemases. *Lancet Infect Dis* (2013) 13(9):785–96. doi: 10.1016/S1473-3099(13)70190-7
10. Burns AR, Smith CW, Walker DC. Unique Structural Features That Influence Neutrophil Emigration Into the Lung. *Physiol Rev* (2003) 83 (2):309–36. doi: 10.1152/physrev.00023.2002
11. Mizgerd JP. Molecular Mechanisms of Neutrophil Recruitment Elicited by Bacteria in the Lungs. *Semin Immunol* (2002) 14(2):123–32. doi: 10.1006/smim.2001.0349
12. Mizgerd JP. Acute Lower Respiratory Tract Infection. *N Engl J Med* (2008) 358(7):716–27. doi: 10.1056/NEJMra074111
13. Depicolzuane L, Phelps DS, Floros J. Surfactant Protein-A Function: Knowledge Gained From SP-A Knockout Mice. *Front Pediatr* (2022) 9 (1542). doi: 10.3389/fped.2021.799693
14. Broug-Holub E, et al. Alveolar Macrophages are Required for Protective Pulmonary Defenses in Murine Klebsiella Pneumonia: Elimination of Alveolar Macrophages Increases Neutrophil Recruitment But Decreases Bacterial Clearance and Survival. *Infect Immun* (1997) 65(4):1139–46. doi: 10.1128/iai.65.4.1139-1146.1997
15. Nau GJ, Richmond JF, Schlesinger A, Jennings EG, Lander ES, and Young RA. Human Macrophage Activation Programs Induced by Bacterial Pathogens. *Proc Natl Acad Sci USA* (2002) 99(3):1503–8. doi: 10.1073/pnas.022649799
16. Pittet LA, Quinton LJ, Yamamoto K, Robson BE, Ferrari JD, Algul H, et al. Earliest Innate Immune Responses Require Macrophage RelA During Pneumococcal Pneumonia. *Am J Respir Cell Mol Biol* (2011) 45(3):573–81. doi: 10.1165/rcmb.2010-0210OC
17. Holmskov U, Thiel S, Jensenius JC. Collections and Ficolins: Humoral Lectins of the Innate Immune Defense. *Annu Rev Immunol* (2003) 21:547–78. doi: 10.1146/annurev.immunol.21.120601.140954
18. Kishore U, Greenhough TJ, Waters P, Shrive AK, Ghai R, Kamran MF, et al. Surfactant Proteins SP-A and SP-D: Structure, Function and Receptors. *Mol Immunol* (2006) 43(9):1293–315. doi: 10.1016/j.molimm.2005.08.004
19. Wright JR. Pulmonary Surfactant: A Front Line of Lung Host Defense. *J Clin Invest* (2003) 111(10):1453–5. doi: 10.1172/JCI200318650
20. Phelps DS. Surfactant Regulation of Host Defense Function in the Lung: A Question of Balance. *Pediatr Pathol Mol Med* (2001) 20(4):269–92.
21. Floros J, Thorenoor N, Tsotakos N, Phelps DS. Human Surfactant Protein SP-A1 and SP-A2 Variants Differentially Affect the Alveolar Microenvironment, Surfactant Structure, Regulation and Function of the Alveolar Macrophage, and Animal and Human Survival Under Various Conditions. *Front Immunol* (2021) 12:681639. doi: 10.3389/fimmu.2021.681639
22. Crouch E, Hartshorn K, Ofek I. Collectins and Pulmonary Innate Immunity. *Immunol Rev* (2000) 173:52–65. doi: 10.1034/j.1600-065X.2000.917311.x
23. Crouch E, Wright JR. Surfactant Proteins a and D and Pulmonary Host Defense. *Annu Rev Physiol* (2001) 63:521–54. doi: 10.1146/annurev.physiol.63.1.521
24. Crouch EC. Collectins and Pulmonary Host Defense. *Am J Respir Cell Mol Biol* (1998) 19(2):177–201. doi: 10.1165/ajrcmb.19.2.140
25. Wright JR, Youmans DC. Pulmonary Surfactant Protein A Stimulates Chemotaxis of Alveolar Macrophage. *Am J Physiol* (1993) 264(4 Pt 1): L338–44. doi: 10.1152/ajplung.1993.264.4.L338
26. Mariencheck WI, Savov J, Dong Q, Tino MJ, Wright JR. Surfactant Protein A Enhances Alveolar Macrophage Phagocytosis of a Live, Mucoid Strain of P. Aeruginosa. *Am J Physiol* (1999) 277(4):L777–86. doi: 10.1152/ajplung.1999.277.4.L777
27. Khubchandani KR, Snyder JM. Surfactant Protein A (SP-A): The Alveolus and Beyond. *FASEB J* (2001) 15(1):59–69. doi: 10.1096/fj.00-0318rev
28. Kremlev SG, Umstead TM, Phelps DS. Effects of Surfactant Protein A and Surfactant Lipids on Lymphocyte Proliferation In Vitro. *Am J Physiol* (1994) 267(4 Pt 1):L357–64. doi: 10.1152/ajplung.1994.267.4.L357
29. Borron P, McCormack FX, Elhalwagi BM, Chroneos ZC, Lewis JF, Zhu S, et al. Surfactant Protein A Inhibits T Cell Proliferation via its Collagen-Like Tail and a 210-kDa Receptor. *Am J Physiol* (1998) 275(4):L679–86. doi: 10.1152/ajplung.1998.275.4.L679
30. Brinker KG, Garner H, Wright JR. Surfactant Protein A Modulates the Differentiation of Murine Bone Marrow-Derived Dendritic Cells. *Am J Physiol Lung Cell Mol Physiol* (2003) 284(1):L232–41. doi: 10.1152/ajplung.00187.2002
31. Haque R, Umstead TM, Ponnuru P, Guo X, Hawgood S, Phelps DS, et al. Role of Surfactant Protein-A (SP-A) in Lung Injury in Response to Acute Ozone Exposure of SP-A Deficient Mice. *Toxicol Appl Pharmacol* (2007) 220 (1):72–82. doi: 10.1016/j.taap.2006.12.017
32. Mikerov AN, Haque R, Gan X, Guo X, Phelps DS, Floros J, et al. Ablation of SP-A has a Negative Impact on the Susceptibility of Mice to Klebsiella Pneumoniae Infection After Ozone Exposure: Sex Differences. *Respir Res* (2008) 9:77. doi: 10.1186/1465-9921-9-77
33. LeVine AM, Bruno MD, Huelsman KM, Ross GF, Whitsett JA, Korfhagen TR. Surfactant Protein A-Deficient Mice are Susceptible to Group B Streptococcal Infection. *J Immunol* (1997) 158(9):4336–40.
34. LeVine AM, Kurak KE, Bruno MD, Stark JM, Whitsett JA, Korfhagen TR. Surfactant Protein-A-Deficient Mice are Susceptible to Pseudomonas Aeruginosa Infection. *Am J Respir Cell Mol Biol* (1998) 19(4):700–8. doi: 10.1165/ajrcmb.19.4.3254
35. Madan T, Reid KB, Clark H, Singh M, Nayak A, Sarma PU, et al. Susceptibility of Mice Genetically Deficient in SP-A or SP-D Gene to Invasive Pulmonary Aspergillosis. *Mol Immunol* (2010) 47(10):1923–30. doi: 10.1016/j.molimm.2010.02.027
36. Di Angelo S, Lin Z, Wang G, Phillips S, Ramet M, Luo J, et al. Novel, non-Radioactive, Simple and Multiplex PCR-cRFLP Methods for Genotyping Human SP-A and SP-D Marker Alleles. *Dis Markers* (1999) 15(4):269–81. doi: 10.1155/1999/961430
37. Karinch AM, Floros J. 5' Splicing and Allelic Variants of the Human Pulmonary Surfactant Protein A Genes. *Am J Respir Cell Mol Biol* (1995) 12(1):77–88. doi: 10.1165/ajrcmb.12.1.7811473
38. Floros J, Tsotakos N. Differential Regulation of Human Surfactant Protein A Genes, SFTPA1 and SFTPA2, and Their Corresponding Variants. *Front Immunol* (2021) 12:766719. doi: 10.3389/fimmu.2021.766719
39. Phelps DS, Umstead TM, Floros J. Sex Differences in the Acute In Vivo Effects of Different Human SP-A Variants on the Mouse Alveolar Macrophage Proteome. *J Proteomics* (2014) 108:427–44. doi: 10.1016/j.jprot.2014.06.007
40. Phelps DS, Umstead TM, Silveyra P, Hu S, Wang G, Floros J, et al. Differences in the Alveolar Macrophage Proteome in Transgenic Mice Expressing Human SP-A1 and SP-A2. *J Proteom Genom Res* (2013) 1 (2):2–26. doi: 10.14302/issn.2326-0793.jpgr-12-207
41. Tsotakos N, Phelps DS, Yengo CM, Chinchilli VM, Floros J. Single-Cell Analysis Reveals Differential Regulation of the Alveolar Macrophage Actin Cytoskeleton by Surfactant Proteins A1 and A2: Implications of Sex and Aging. *Biol Sex Differ* (2016) 7:18. doi: 10.1186/s13293-016-0071-0
42. Thorenoor N, Kawasawa YI, Gandhi CK, Floros J. Sex-Specific Regulation of Gene Expression Networks by Surfactant Protein A (SP-A) Variants in Alveolar Macrophages in Response to Klebsiella Pneumoniae. *Front Immunol* (2020) 11:1290. doi: 10.3389/fimmu.2020.01290
43. Phelps DS, Chinchilli VM, Weisz J, Yang L, Shearer D, Zhang X, et al. Differences in the Alveolar Macrophage Toponome in Humanized SP-A1 and SP-A2 Transgenic Mice. *JCI Insight* (2020) 5(24):e141410. doi: 10.1172/jci.insight.141410
44. Thorenoor N, Umstead TM, Zhang X, Phelps DS, Floros J. Survival of Surfactant Protein-A1 and SP-A2 Transgenic Mice After Klebsiella Pneumoniae Infection, Exhibits Sex-, Gene-, and Variant Specific Differences; Treatment With Surfactant Protein Improves Survival. *Front Immunol* (2018) 9:2404. doi: 10.3389/fimmu.2018.02404
45. Thorenoor N, Zhang X, Umstead TM, Scott Halstead E, Phelps DS, Floros J, et al. Differential Effects of Innate Immune Variants of Surfactant Protein-A1 (SFTPA1) and SP-A2 (SFTPA2) in Airway Function After Klebsiella Pneumoniae Infection and Sex Differences. *Respir Res* (2018) 19(1):23. doi: 10.1186/s12931-018-0723-1
46. Xu HN, Floros J, Li LZ, Amatya S.). Imaging NAD(H) Redox Alterations in Cryopreserved Alveolar Macrophages from Ozone-Exposed Mice the Impact of Nutrient Starvation during Long Lag Times. *Antioxid (Basel)* (2020) 10(5). doi: 10.3390/antiox10050767
47. Ezzie ME, Crawford M, Cho JH, Orellana R, Zhang S, Gelinas R, et al. Gene Expression Networks in COPD: microRNA and mRNA Regulation. *Thorax* (2012) 67(2):122–31. doi: 10.1136/thoraxjnl-2011-200089

48. Sayed D, Abdellatif M. MicroRNAs in Development and Disease. *Physiol Rev* (2011) 91(3):827–87. doi: 10.1152/physrev.00006.2010
49. Sessa R, Hata A. Role of microRNAs in Lung Development and Pulmonary Diseases. *Pulm Circ* (2013) 3(2):315–28. doi: 10.4103/2045-8932.114758
50. Feketea G, Bocsan CI, Popescu C, Gaman M, Stanciu LA, Zdrenghea MT, et al. A Review of Macrophage MicroRNAs' Role in Human Asthma. *Cells* (2019) 8(5):420. doi: 10.3390/cells8050420
51. Hoefel G, Tay H, Foster P. MicroRNAs in Lung Diseases. *Chest* (2019) 156 (5):991–1000. doi: 10.1016/j.chest.2019.06.008
52. Miao C, Xiong Y, Zhang G, Chang J. MicroRNAs in Idiopathic Pulmonary Fibrosis, New Research Progress and Their Pathophysiological Implication. *Exp Lung Res* (2018) 44(3):178–90. doi: 10.1080/01902148.2018.1455927
53. Noutsios GT, Thorenoor N, Zhang X, Phelps DS, Umstead TM, Durrani F, et al. SP-A2 Contributes to miRNA-Mediated Sex Differences in Response to Oxidative Stress: Pro-Inflammatory, Anti-Apoptotic, and Anti-Oxidant Pathways are Involved. *Biol Sex Differ* (2017) 8(1):37. doi: 10.1186/s13293-017-0158-2
54. Noutsios GT, Thorenoor N, Zhang X, Phelps DS, Umstead TM, Durrani F, et al. Major Effect of Oxidative Stress on the Male, But Not Female, SP-A1 Type II Cell Mirnome. *Front Immunol* (2019) 10:1514. doi: 10.3389/fimmu.2019.01514
55. Thorenoor N, Kawasawa YI, Gandhi CK, Zhang X, Floros J. Differential Impact of Co-Expressed SP-A1/SP-A2 Protein on AM Mirnome; Sex Differences. *Front Immunol* (2019) 10:1960. doi: 10.3389/fimmu.2019.01960
56. Thorenoor N, Phelps DS, Floros J. Differential Sex-Dependent Regulation of the Alveolar Macrophage Mirnome of SP-A2 and Co-Ex (SP-A1/SP-A2) and Sex Differences Attenuation After 18 H of Ozone Exposure. *Antioxidants (Basel)* (2020) 9(12):1190. doi: 10.3390/antiox9121190
57. Watson A, Kronqvist N, Spalluto CM, Griffiths M, Staples KJ, Wilkinson T, et al. Novel Expression of a Functional Trimeric Fragment of Human SP-A With Efficacy in Neutralisation of RSV. *Immunobiology* (2017) 222(2):111–8. doi: 10.1016/j.imbio.2016.10.015
58. Francisco D, Wang Y, Conway M, Hurbon AN, Dy AB.C, Addison KJ, et al. Surfactant Protein-A Protects Against IL-13-Induced Inflammation in Asthma. *J Immunol* (2020) 204(10):2829–39. doi: 10.4049/jimmunol.1901227
59. Mikerov AN, Gan X, Umstead TM, Miller L, Chinchilli VM, Phelps DS, et al. Sex Differences in the Impact of Ozone on Survival and Alveolar Macrophage Function of Mice After Klebsiella Pneumoniae Infection. *Respir Res* (2008) 9:24. doi: 10.1186/1465-9921-9-24
60. Allen IC. Bacteria-Mediated Acute Lung Inflammation. *Methods Mol Biol* (2013) 1031:163–75. doi: 10.1007/978-1-62703-481-4_19
61. Phelps DS, Umstead TM, Floros J. Sex Differences in the Response of the Alveolar Macrophage Proteome to Treatment With Exogenous Surfactant Protein-a. *Proteome Sci* (2012) 10(1):44. doi: 10.1164/ajrccm-conference.2012.185.1_MeetingAbstracts.A1374
62. Wang G, Guo X, Diangelo S, Thomas NJ, Floros J. Humanized SFTPA1 and SFTPA2 Transgenic Mice Reveal Functional Divergence of SP-A1 and SP-A2: Formation of Tubular Myelin In Vivo Requires Both Gene Products. *J Biol Chem* (2010) 285(16):11998–2010. doi: 10.1074/jbc.M109.046243
63. Wang G, Umstead TM, Phelps DS, Al-Mondhiry H, Floros J. The Effect of Ozone Exposure on the Ability of Human Surfactant Protein a Variants to Stimulate Cytokine Production. *Environ Health Perspect* (2002) 110(1):79–84. doi: 10.1289/ehp.0211079
64. Vitsios DM, Enright AJ. Chimira: Analysis of Small RNA Sequencing Data and microRNA Modifications. *Bioinformatics* (2015) 31(20):3365–7. doi: 10.1093/bioinformatics/btv380
65. Robinson MD, McCarthy DJ, Smyth GK. Edger: A Bioconductor Package for Differential Expression Analysis of Digital Gene Expression Data. *Bioinformatics* (2010) 26(1):139–40. doi: 10.1093/bioinformatics/btp616
66. Sun J, Nishiyama T, Shimizu K, Kadota K. TCC: An R Package for Comparing Tag Count Data With Robust Normalization Strategies. *BMC Bioinf* (2013) 14:219. doi: 10.1186/1471-2105-14-219
67. Thorenoor N, Phelps DS, Kala P, Ravi R, Floros Phelps A, Umstead T M, et al. Impact of Surfactant Protein-A Variants on Survival in Aged Mice in Response to Klebsiella Pneumoniae Infection and Ozone: Serendipity in Action. *Microorganisms* (2020) 8(9):1276. doi: 10.3390/microorganisms8091276
68. Beharka AA, Gaynor CD, Kang BK, Voelker DR, McCormack FX, Schlesinger LS, et al. Pulmonary Surfactant Protein A Up-Regulates Activity of the Mannose Receptor, a Pattern Recognition Receptor Expressed on Human Macrophages. *J Immunol* (2002) 169(7):3565–73. doi: 10.4049/jimmunol.169.7.3565
69. Kuronuma K, Sano H, Kato K, Kudo K, Hyakushima N, Yokota S, et al. Pulmonary Surfactant Protein A Augments the Phagocytosis of Streptococcus Pneumoniae by Alveolar Macrophages Through a Casein Kinase 2-Dependent Increase of Cell Surface Localization of Scavenger Receptor a. *J Biol Chem* (2004) 279(20):21421–30. doi: 10.1074/jbc.M312490200
70. Gil M, McCormack FX, Levine AM. Surfactant Protein A Modulates Cell Surface Expression of CR3 on Alveolar Macrophages and Enhances CR3-Mediated Phagocytosis. *J Biol Chem* (2009) 284(12):7495–504. doi: 10.1074/jbc.M808643200
71. Schuurs AH, Verheul HA. Effects of Gender and Sex Steroids on the Immune Response. *J Steroid Biochem* (1990) 35(2):157–72. doi: 10.1016/0022-4731(90)90270-3
72. Verthelyi D. Sex Hormones as Immunomodulators in Health and Disease. *Int Immunopharmacol* (2001) 1(6):983–93. doi: 10.1016/S1567-5769(01)00044-3
73. Nielsen HC. Testosterone Regulation of Sex Differences in Fetal Lung Development. *Proc Soc Exp Biol Med* (1992) 199(4):446–52. doi: 10.3181/00379727-199-43379
74. Perelman RH, Palta M, Kirby R, Farrell PM. Discordance Between Male and Female Deaths Due to the Respiratory Distress Syndrome. *Pediatrics* (1986) 78(2):238–44. doi: 10.1542/peds.78.2.238
75. Spitzer JA. Gender Differences in Some Host Defense Mechanisms. *Lupus* (1999) 8(5):380–3. doi: 10.1177/096120339900800510
76. Weinstein Y, Ran S, Segal S. Sex-Associated Differences in the Regulation of Immune Responses Controlled by the MHC of the Mouse. *J Immunol* (1984) 132(2):656–61.
77. Caracta CF. Gender Differences in Pulmonary Disease. *Mt Sinai J Med* (2003) 70(4):215–24.
78. FitzSimmons SC. The Changing Epidemiology of Cystic Fibrosis. *J Pediatr* (1993) 122(1):1–9. doi: 10.1016/S0022-3476(05)83478-X
79. Gannon CJ, Pasquale M, Tracy JK, McCarter RJ, Napolitano LM. Male Gender is Associated With Increased Risk for Postinjury Pneumonia. *Shock* (2004) 21(5):410–4. doi: 10.1097/00024382-200405000-00003
80. Gutierrez F, Masia M, Mirete C, Soldan B, Rodriguez JC, Padilla S, et al. The Influence of Age and Gender on the Population-Based Incidence of Community-Acquired Pneumonia Caused by Different Microbial Pathogens. *J Infect* (2006) 53(3):166–74. doi: 10.1016/j.jinf.2005.11.006
81. Kaplan V, Angus DC, Griffin MF, Clermont G, Scott Watson R, Linde-Zwirble WT, et al. Hospitalized Community-Acquired Pneumonia in the Elderly: Age- and Sex-Related Patterns of Care and Outcome in the United States. *Am J Respir Crit Care Med* (2002) 165(6):766–72. doi: 10.1164/ajrccm.165.6.2103038
82. Durrani F, Phelps DS, Weisz J, Silveyra P, Hu S, Mikerov AN, et al. Gonadal Hormones and Oxidative Stress Interaction Differentially Affects Survival of Male and Female Mice After Lung Klebsiella Pneumoniae Infection. *Exp Lung Res* (2012) 38(4):165–72. doi: 10.3109/01902148.2011.654045
83. Mikerov AN, Hu S, Durrani F, Gan X, Wang G, Umstead TM, et al. Impact of Sex and Ozone Exposure on the Course of Pneumonia in Wild Type and SP-A (-/-) Mice. *Microb Pathog* (2012) 52(4):239–49. doi: 10.1016/j.micpath.2012.01.005
84. Yamamoto Y, Tomioka H, Sato K, Saito H, Yamada Y, Setogawa T, et al. Sex Differences in the Susceptibility of Mice to Infection Induced by Mycobacterium Intracellulare. *Am Rev Respir Dis* (1990) 142(2):430–3. doi: 10.1164/ajrccm/142.2.430
85. Guilbault C, Stotland P, Lachance C, Tam M, Keller A, Thompson-Snipes L, et al. Influence of Gender and Interleukin-10 Deficiency on the Inflammatory Response During Lung Infection With Pseudomonas Aeruginosa in Mice. *Immunology* (2002) 107(3):297–305. doi: 10.1046/j.1365-2567.2002.01508.x
86. Yamamoto Y, Saito H, Setogawa T, Tomioka H. Sex Differences in Host Resistance to Mycobacterium Marinum Infection in Mice. *Infect Immun* (1991) 59(11):4089–96. doi: 10.1128/iai.59.11.4089-4096.1991

87. Yancey AL, Watson HL, Cartner SC, Simecka JW. Gender is a Major Factor in Determining the Severity of Mycoplasma Respiratory Disease in Mice. *Infect Immun* (2001) 69(5):2865–71. doi: 10.1128/IAI.69.5.2865-2871.2001
88. Gordon HS, Rosenthal GE. The Relationship of Gender and in-Hospital Death: Increased Risk of Death in Men. *Med Care* (1999) 37(3):318–24. doi: 10.1097/00005650-199903000-00011
89. Loeb M, McGeer A, McArthur M, Walter S, Simor AE. Risk Factors for Pneumonia and Other Lower Respiratory Tract Infections in Elderly Residents of Long-Term Care Facilities. *Arch Intern Med* (1999) 159 (17):2058–64. doi: 10.1001/archinte.159.17.2058
90. Yu Z, Wang C, Wang M, Li Z, Casimiro MC, Liu M, et al. A Cyclin D1/microRNA 17/20 Regulatory Feedback Loop in Control of Breast Cancer Cell Proliferation. *J Cell Biol* (2008) 182(3):509–17. doi: 10.1083/jcb.200801079
91. Attar M, Arefian E, Nabiuni M, Adegani FJ, Bakhtiari SH, Karimi Z, et al. MicroRNA 17-92 Expressed by a Transposone-Based Vector Changes Expression Level of Cell-Cycle-Related Genes. *Cell Biol Int* (2012) 36 (11):1005–12. doi: 10.1042/CBI20110089
92. Shu J, Xia Z, Li L, Liang ET, Slipek N, Shen D, et al. Dose-Dependent Differential mRNA Target Selection and Regulation by Let-7a-7f and miR-17-92 Cluster microRNAs. *RNA Biol* (2012) 9(10):1275–87. doi: 10.4161/rna.21998
93. Wang F, Mao A, Tang J, Zhang Q, Yan J, Wang Y, et al. microRNA-16-5p Enhances Radiosensitivity Through Modulating Cyclin D1/E1-pRb-E2F1 Pathway in Prostate Cancer Cells. *J Cell Physiol* (2018) 234(8):13182–13190. doi: 10.1002/jcp.27989
94. Albanese C, Johnson J, Watanabe G, Eklund N, Vu D, Arnold A, et al. Transforming P21ras Mutants and C-Ets-2 Activate the Cyclin D1 Promoter Through Distinguishable Regions. *J Biol Chem* (1995) 270(40):23589–97. doi: 10.1074/jbc.270.40.23589
95. Fu M, Wang C, Li Z, Sakamaki T, Pestell RG. Minireview: Cyclin D1: Normal and Abnormal Functions. *Endocrinology* (2004) 145(12):5439–47. doi: 10.1210/en.2004-0959
96. Essers MA, Weijzen S, de Vries-Smits AM, Saarloos I, de Ruiter ND, Bos JL, et al. FOXO Transcription Factor Activation by Oxidative Stress Mediated by the Small GTPase Ral and JNK. *EMBO J* (2004) 23(24):4802–12. doi: 10.1038/sj.emboj.7600476
97. Carter ME, Brunet A. FOXO Transcription Factors. *Curr Biol* (2007) 17(4): R113–4. doi: 10.1016/j.cub.2007.01.008
98. Matsumura I, Tanaka H, Kanakura Y. E2F1 and C-Myc in Cell Growth and Death. *Cell Cycle* (2003) 2(4):333–8. doi: 10.4161/cc.2.4.428
99. O'Donnell KA, Wentzel EA, Zeller KI, Dang CV, Mendell JT. C-Myc-Regulated microRNAs Modulate E2F1 Expression. *Nature* (2005) 435 (7043):839–43. doi: 10.1038/nature03677
100. Kremlev SG, Umstead TM, Phelps DS. Surfactant Protein A Regulates Cytokine Production in the Monocytic Cell Line THP-1. *Am J Physiol* (1997) 272(5 Pt 1):L996–1004. doi: 10.1152/ajplung.1997.272.5.L996
101. Koptides M, Umstead TM, Floros J, Phelps DS. Surfactant Protein A Activates NF-Kappa B in the THP-1 Monocytic Cell Line. *Am J Physiol* (1997) 273(2 Pt 1):L382–8. doi: 10.1152/ajplung.1997.273.2.L382
102. Song M, Phelps DS. Interaction of Surfactant Protein A With Lipopolysaccharide and Regulation of Inflammatory Cytokines in the THP-1 Monocytic Cell Line. *Infect Immun* (2000) 68(12):6611–7. doi: 10.1128/IAI.68.12.6611-6617.2000
103. Janic B, Umstead TM, Phelps DS, Floros J. Modulatory Effects of Ozone on THP-1 Cells in Response to SP-A Stimulation. *Am J Physiol Lung Cell Mol Physiol* (2005) 288(2):L317–25. doi: 10.1152/ajplung.00125.2004
104. Wang G, Umstead TM, Hu S, Mikerov AN, Phelps DS, Floros J. Differential Effects of Human SP-A1 and SP-A2 on the BAL Proteome and Signaling Pathways in Response to Klebsiella Pneumoniae and Ozone Exposure. *Front Immunol* (2019) 10:561. doi: 10.3389/fimmu.2019.00561
105. Israel A. The IKK Complex, a Central Regulator of NF-kappaB Activation. *Cold Spring Harb Perspect Biol* (2010) 2(3):a000158. doi: 10.1101/cshperspect.a000158
106. Scheidereit C. IkappaB Kinase Complexes: Gateways to NF-kappaB Activation and Transcription. *Oncogene* (2006) 25(51):6685–705. doi: 10.1038/sj.onc.1209934
107. Sabio G, Davis RJ. TNF and MAP Kinase Signalling Pathways. *Semin Immunol* (2014) 26(3):237–45. doi: 10.1016/j.smim.2014.02.009
108. Desvergne B, Wahli W. Peroxisome Proliferator-Activated Receptors: Nuclear Control of Metabolism. *Endocr Rev* (1999) 20(5):649–88. doi: 10.1210/edrv.20.5.0380
109. Becker J, Delayre-Orthez C, Frossard N, Pons F. Regulation of Inflammation by PPARs: A Future Approach to Treat Lung Inflammatory Diseases? *Fundam Clin Pharmacol* (2006) 20(5):429–47. doi: 10.1111/j.1472-8206.2006.00425.x
110. Moraes LA, Piqueras L, Bishop-Bailey D. Peroxisome Proliferator-Activated Receptors and Inflammation. *Pharmacol Ther* (2006) 110(3):371–85. doi: 10.1016/j.pharmthera.2005.08.007
111. Asada K, Sasaki S, Suda T, Chida K, Nakamura H. Antiinflammatory Roles of Peroxisome Proliferator-Activated Receptor Gamma in Human Alveolar Macrophages. *Am J Respir Crit Care Med* (2004) 169(2):195–200. doi: 10.1164/rccm.200207-740OC
112. Reddy RC, Keshamouni VG, Jaigirdar SH, Zeng X, Leff T, Thannickal VJ, et al. Deactivation of Murine Alveolar Macrophages by Peroxisome Proliferator-Activated Receptor-Gamma Ligands. *Am J Physiol Lung Cell Mol Physiol* (2004) 286(3):L613–9. doi: 10.1152/ajplung.00206.2003
113. Phelps DS, Umstead TM, Quintero OA, Yengo CM, Floros J. In Vivo Rescue of Alveolar Macrophages From SP-A Knockout Mice With Exogenous SP-A Nearly Restores a Wild Type Intracellular Proteome; Actin Involvement. *Proteome Sci* (2011) 9:67. doi: 10.1186/1477-5956-9-67
114. Ali M, Umstead TM, Haque R, Mikerov AN, Freeman WM, Floros J, et al. Differences in the BAL Proteome After Klebsiella Pneumoniae Infection in Wild Type and SP-A-/- Mice. *Proteome Sci* (2010) 8:34. doi: 10.1186/1477-5956-8-34
115. Geraghty P, Wyman AE, Garcia-Arcos I, Dabo AJ, Gadhvi S, Foronjy R, et al. STAT3 Modulates Cigarette Smoke-Induced Inflammation and Protease Expression. *Front Physiol* (2013) 4:267. doi: 10.3389/fphys.2013.00267
116. El Kasmi KC, Holst J, Coffre M, Mielke L, de Pauw A, Lhocine N, et al. General Nature of the STAT3-Activated Anti-Inflammatory Response. *J Immunol* (2006) 177(11):7880–8. doi: 10.4049/jimmunol.177.11.7880
117. Gao H, Ward PA. STAT3 and Suppressor of Cytokine Signaling 3: Potential Targets in Lung Inflammatory Responses. *Expert Opin Ther Targets* (2007) 11(7):869–80. doi: 10.1517/14728222.11.7.869
118. Ruwanpura SM, McLeod L, Miller A, Jones J, Vlahos R, Ramm G, et al. Deregulated Stat3 Signaling Dissociates Pulmonary Inflammation From Emphysema in Gp130 Mutant Mice. *Am J Physiol Lung Cell Mol Physiol* (2012) 302(7):L627–39. doi: 10.1152/ajplung.00285.2011
119. Saleh A, Shan L, Halayko AJ, Kung S, Gounni AS. Critical Role for STAT3 in IL-17A-Mediated CCL11 Expression in Human Airway Smooth Muscle Cells. *J Immunol* (2009) 182(6):3357–65. doi: 10.4049/jimmunol.0801882
120. Caetano MS, Hassane M, Van HT, Bugarin E, Cumpian AM, McDowell CL, et al. Sex Specific Function of Epithelial STAT3 Signaling in Pathogenesis of K-Ras Mutant Lung Cancer. *Nat Commun* (2018) 9(1):4589. doi: 10.1038/s41467-018-07042-y
121. Gu J, Zhou Y, Huang L, Ou W, Wu J, Li S, et al. TP53 Mutation is Associated With a Poor Clinical Outcome for non-Small Cell Lung Cancer: Evidence From a Meta-Analysis. *Mol Clin Oncol* (2016) 5(6):705–13. doi: 10.3892/mco.2016.1057
122. Grageda M, Silveyra P, Thomas NJ, DiAngelo SL, Floros J. DNA Methylation Profile and Expression of Surfactant Protein A2 Gene in Lung Cancer. *Exp Lung Res* (2015) 41(2):93–102. doi: 10.3109/01902148.2014.976298
123. Seifart C, Lin HM, Seifart U, Plagens A, DiAngelo S, von Wichert P, et al. Rare SP-A Alleles and the SP-A1-6A(4) Allele Associate With Risk for Lung Carcinoma. *Clin Genet* (2005) 68(2):128–36. doi: 10.1111/j.1399-0004.2005.00470.x
124. Lin Z, Thomas NJ, Bibikova M, Seifart C, Wang Y, Guo X, et al. DNA Methylation Markers of Surfactant Proteins in Lung Cancer. *Int J Oncol* (2007) 31(1):181–91. doi: 10.3892/ijo.31.1.181
125. Mitsuhashi A, Goto H, Kuramoto T, Tabata S, Yukishige S, Abe S, et al. Surfactant Protein A Suppresses Lung Cancer Progression by Regulating the Polarization of Tumor-Associated Macrophages. *Am J Pathol* (2013) 182 (5):1843–53. doi: 10.1016/j.ajpath.2013.01.030
126. deMello DE, Heyman S, Phelps DS, Floros J. Immunogold Localization of SP-A in Lungs of Infants Dying From Respiratory Distress Syndrome. *Am J Pathol* (1993) 142(5):1631–40.
127. Stevens PA, Schadow B, Bartholain S, Segerer H, Obladen M. Surfactant Protein A in the Course of Respiratory Distress Syndrome. *Eur J Pediatr* (1992) 151(8):596–600. doi: 10.1007/BF01957730
128. deMello DE, Phelps DS, Patel G, Floros J, Lagunoff D. Expression of the 35kda and Low Molecular Weight Surfactant-Associated Proteins in the Lungs of

Infants Dying With Respiratory Distress Syndrome. *Am J Pathol* (1989) 134 (6):1285–93.
129. Röszer T. Understanding the Biology of Self-Renewing Macrophages. *Cells* (2018) 7(8):1285–93. doi: 10.3390/cells7080103
130. Hashimoto D, Chow A, Noizat C, Teo P, Beasley MB, Leboeuf M, et al. Tissue-Resident Macrophages Self-Maintain Locally Throughout Adult Life With Minimal Contribution From Circulating Monocytes. *Immunity* (2013) 38(4):792–804. doi: 10.1016/j.immuni.2013.04.004
131. Huaux F, et al. IL-1α Induces CD11b(low) Alveolar Macrophage Proliferation and Maturation During Granuloma Formation. *J Pathol* (2015) 235(5):698–709. doi: 10.1002/path.4487
132. Mikerov AN, Phelps DS, Gan X, Umstead TM, Haque R, Wang G, et al. Effect of Ozone Exposure and Infection on Bronchoalveolar Lavage: Sex Differences in Response Patterns. *Toxicol Lett* (2014) 230(2):333–44. doi: 10.1016/j.toxlet.2014.04.008
133. Zasłona Z, Przybranowski S, Wilke C, van Rooijen N, Teitz-Tennenbaum S, Osterholzer JJ, et al. Resident Alveolar Macrophages Suppress, Whereas Recruited Monocytes Promote, Allergic Lung Inflammation in Murine Models of Asthma. *J Immunol* (2014) 193(8):4245–53. doi: 10.4049/jimmunol.1400580
134. Nayak DK, Mendez O, Bowen S, Mohanakumar T. Isolation and In Vitro Culture of Murine and Human Alveolar Macrophages. *J Vis Exp* (2018) 134: e57287. doi: 10.3791/57287

Conflict of Interest: The authors declare that the research was conducted in the absence of any commercial or financial relationships that could be construed as a potential conflict of interest.

Publisher's Note: All claims expressed in this article are solely those of the authors and do not necessarily represent those of their affiliated organizations, or those of the publisher, the editors and the reviewers. Any product that may be evaluated in this article, or claim that may be made by its manufacturer, is not guaranteed or endorsed by the publisher.

GLOSSARY

ACAA1b	acetyl-CoA acyltransferase 1
AM	alveolar macrophage
ANOVA	analysis of variance
ARPC1B	actin-related protein 2/3 complex subunit 1B
ATP6V0D2	ATPase H+ transporting V0 subunit D2
ATP5MC3	ATP synthase membrane subunit C locus 3
BAL	bronchoalveolar lavage
BCL2	B-cell lymphoma 2
BUB1B	mitotic checkpoint serine/threonine kinase B
CAP1	cyclase-associated actin cytoskeleton regulatory protein 1
CASP9	caspase 9
CCND1	cyclin D1
CCND2	cyclin D2
CDC42	cell division cycle 42
CDK7	cyclin-dependent kinase 7
CDKN2A	cyclin-dependent kinase inhibitor 2
COTL1	coactosin-like F-actin binding protein 1
COX5A	cytochrome C oxidase subunit 5A
CSTB	cystatin B
CTSD	cathepsin D
DBI	diazepam-binding inhibitor acyl-CoA binding protein
E2F1	E2F transcription factor 1
E2F2	E2F transcription factor 2
E2F3	E2F transcription factor 3
EGR2	early growth response 2
FAM120A	family with sequence similarity 120A
FOXO1	Forkhead box O1
FOXO3	Forkhead box O3
GAPDH	glyceraldehyde 3-phosphate dehydrogenase
hTG	humanized transgenic
HUWE1	HECT UBA and WWE domain-containing E3 ubiquitin protein ligase 1
GLUL	glutamate-ammonia ligase
IL-6	interleukin 6
IPA	Ingenuity Pathway Analysis
IVNS1ABP	influenza virus NS1A-binding protein
KLHL21	Kelch-like family member 21
KO	knockout
LAC	lung alveolar cell
LITAF	lipopolysaccharide-induced TNF
LRRC17	leucine-rich repeat containing 17
MBNL1	muscleblind-like splicing regulator 1
MCAM	melanoma cell adhesion molecule
MDH2	malate dehydrogenase 2
miRNAs	microRNAs
MRPL2	mitochondrial ribosomal protein L2
MYC	MYC proto-oncogene
MYO1E	myosin IE
NAB1	NGFI-A-binding protein 1
NDUFA7	NADH:ubiquinone oxidoreductase subunit A7
NDUFS6	NADH:ubiquinone oxidoreductase subunit S6
NFAM1	NFAT-activating protein with ITAM motif 1
PANK3	pantothenate kinase 3
PDIA6	protein disulfide isomerase family A member 6
PDCD6IP	programmed cell death 6-interacting protein
PFN1	profilin 1
PGD	phosphogluconate dehydrogenase
PIM1	proto-oncogene serine/threonine kinase
PPT1	palmitoyl-protein thioesterase 1
PPARA	peroxisome proliferator-activated receptor alpha
PPARG	peroxisome proliferator-activated receptor gamma
PRKAR1A	protein kinase CAMP-dependent Type I regulatory subunit alpha
PSMC1	proteasome 26S subunit ATPase 1
RNF187	ring finger protein 187
RPL4	ribosomal protein L4
RPL6	ribosomal protein L6
RPL10	ribosomal protein L10
RPL31	ribosomal protein L31
RPL35A	ribosomal protein L35a
RPL36a	ribosomal protein L36a
RPL37	ribosomal protein L37
RPS3	ribosomal protein S3
RPS9	ribosomal protein S9
RPS21	ribosomal protein S21
RPS25	ribosomal protein S25
SCARB2	scavenger receptor Class B Member 2
S*FTPA*1	gene-encoding SP-A1
S*FTPA2*	gene-encoding SP-A2
SMAD2	SMAD family member 2
SNAP23	synaptosome-associated protein 23
SP-A	surfactant protein A
SRGN	serglycin
STAT-3	signal transducer and activator of transcription 3
S100A4	S100 calcium-binding protein A4
TACC2	transforming acidic coiled-coil containing protein 2
TALDO1	transaldolase 1
TBCA	tubulin-folding cofactor A
TLR2	Toll-like receptor 2
TNF	tumor necrosis factor
TNFSF12	TNF super family member 12
TP-53	tumor protein 53
TSPO	translocator protein
UQCRQ	ubiquinol-cytochrome C reductase complex III subunit VII
UQCR11	ubiquinol-cytochrome C reductase complex III subunit XI
USP14	ubiquitin-specific peptidase 14

frontiers | Frontiers in Immunology

ORIGINAL RESEARCH
published: 07 July 2022
doi: 10.3389/fimmu.2022.930449

Immunomodulatory Role of Surfactant Protein-D in a Transgenic Adenocarcinoma of Mouse Prostate (TRAMP) Model

Kasturi Ganguly[1], *Uday Kishore*[2,3], *Siddhanath M. Metkari*[4] *and Taruna Madan*[1]*

[1] *Department of Innate Immunity, Indian Council of Medical Research (ICMR)- National Institute for Research in Reproductive and Child Health, Mumbai, India,* [2] *Biosciences, College of Health and Life Sciences, Brunel University London, Uxbridge, United Kingdom,* [3] *Department of Veterinary Medicine, United Arab Emirates (U.A.E) University, Al Ain, United Arab Emirates,* [4] *Indian Council of Medical Research (ICMR)- National Institute for Research in Reproductive and Child Health, Mumbai, India*

Surfactant protein D (SP-D), a pattern recognition molecule, is emerging as a potent anti-tumoural innate immune defense molecule in a range of cancers. Previously, SP-D expression was found to be significantly downregulated at the malignant sites of human prostate adenocarcinoma and associated with an increasing Gleason score and severity. We recently reported selective induction of intrinsic apoptosis by a recombinant fragment of human SP-D (rfhSP-D) in the human Prostate cancer (PCa) biopsy explants and cells with glucose regulated protein of 78 (GRP78) as one of the key interacting partners. The present study evaluated the expression of SP-D in early and advanced stages of PCa using transgenic adenocarcinoma of mouse prostate (TRAMP) model. Both early and late stages of PCa showed significantly decreased SP-D mRNA expression and increased proteolytic degradation of SP-D protein. Systemic and tumoural immunophenotyping of TRAMP model revealed increased serine proteases producing granulocytes and polymorphonuclear myeloid-derived suppressor cells (PMN MDSCs) in the late stage; the serine proteases secreted by these cells could be involved in the degradation of SP-D. Susceptibility of rfhSP-D to elastase-mediated proteolysis provided the rationale to use an elastase-inhibitor to sustain intact rfhSP-D in the tumour microenvironment. The study revealed an immunomodulatory potential of rfhSP-D and elastase inhibitor, sivelestat, to induce macrophage polarization towards M1 with downregulation of PMN MDSCs in *ex-vivo* cultured TRAMP tumours. Furthermore, rfhSP-D induced immunogenic cell death in murine PCa cells and in TRAMP explants. The findings highlight that SP-D plays an anti-tumourigenic role in PCa by inducing immunogenic cell death and immunomodulation while the prostate tumour milieu adversely impacts SP-D by inhibiting its transcription, and enhancing its proteolytic degradation. Transformation of an immunologically “cold tumour” into a “hot tumour” implicates therapeutic potential of rfhSP-D in PCa.

Keywords: prostate cancer, SP-D, TRAMP model, immunomodulaion, innate immunity, immunogenic cell death (ICD), collectin

OPEN ACCESS

Edited by:
Jagadeesh Bayry,
Indian Institute of Technology Palakkad, India

Reviewed by:
Kenneth Reid,
University of Oxford, United Kingdom
Chiara Agostinis,
Institute for Maternal and Child Health Burlo Garofolo (IRCCS), Italy

***Correspondence:**
Taruna Madan
taruna_m@hotmail.com

Specialty section:
This article was submitted to Molecular Innate Immunity, a section of the journal Frontiers in Immunology

Received: *28 April 2022*
Accepted: *23 May 2022*
Published: *07 July 2022*

Citation:
Ganguly K, Kishore U, Metkari SM and Madan T (2022) Immunomodulatory Role of Surfactant Protein-D in a Transgenic Adenocarcinoma of Mouse Prostate (TRAMP) Model. Front. Immunol. 13:930449. doi: 10.3389/fimmu.2022.930449

INTRODUCTION

Prostate cancer (PCa) is one of the deadliest cancer in men with second highest incidence rate globally (1). Although its incidence in Asia is much lower as compared to the U.S.A. and the Europe, the cancer statistics of China demonstrates a stably increasing trend of the incidence and mortality due to PCa (2). The conventional anti-cancer treatments, mainly androgen-deprivation therapy (ADT), are efficacious by providing a high rate of progression-free survival. However, 30–50% of patients experience recurrence and eventually progress to metastatic castration-resistant prostate cancer (mCRPC) (3). Tumour antigen-specific adaptive immunotherapies have improved clinical outcomes and revolutionized the treatment paradigm in many hematological and solid malignancies (4–6). These approaches, however, have been largely unsuccessful for mCRPC, owing to the "cold tumour" microenvironment which is characterized by immunosuppression, low tumour mutation burden (TMB), low immunogenicity, minimal T-cell infiltration, and downregulated MHC-I molecules (3–5, 7). Lack of pre-requisites for successful prostate cancer-specific adaptive immune therapy has given rise to a sub-category of poor responders (6). This necessitates consideration of tumour antigen-independent, innate immune responses mediated by pattern recognition receptors (PRRs) as an alternative or complementary means to target cancer cells.

Surfactant protein D (SP-D), a soluble pattern recognition receptor (PRR) belonging to carbohydrate-binding lectins or C-type lectin receptors (CLRs) family, plays a key role in host defence. They serve as an innate immune molecule in the control of inflammation, infection, allergy, and cancer (8, 9). Structurally it is composed of an N-terminal cysteine-rich domain, a triple-helical collagen domain consisting of Gly-X-Y repeating triplets, an α-helical coiled coil neck region, and C-terminal carbohydrate recognition domain (CRD) or C-type lectin domain (10). Depending on its structural oligomerization and interaction with cell surface receptors, SP-D performs a dual immune surveillance role by triggering either pro-inflammatory or anti-inflammatory signaling (11, 12). Though it was initially considered as a lung collectin due to its association with pulmonary surfactant, the immunological roles of SP-D at extrapulmonary and mucosal sites are now well established (10, 13). In rat prostate, upregulation of SP-D in response to *Escherichia coli* infection as well as the presence of SP-D in human prostate and prostatic secretions suggested that SP-D could be involved in prostate immunity (14). Kankavi et al. first reported decreased expression of SP-D and SP-A proteins at the malignant site of human prostate adenocarcinoma compared to non-malignant areas in the same tissue sections (15). The potential of SP-D acting as an immunosurveillance molecule in PCa was subsequently demonstrated by our group with the use of a recombinant fragment of human SP-D (rfhSP-D) comprising 8 Gly-X-Y repeats trimeric neck and CRD that selectively induced intrinsic apoptosis in human prostate biopsy explants as well as in human prostate cancer cells including androgen-responsive LNCaP and androgen-resistant PC3 (16). In-silico and *in-vitro* analyses of the membrane interactome of rfhSP-D in PC3 cell line revealed that rfhSP-D bound glucose regulated protein of 78 kDa (GRP78) through its CRD region and interfered with the pro-survival signaling (17). rfhSP-D has also been shown to differentially induce TNF-α and Fas-mediated pro-apoptotic signaling pathway and activate caspase cascade, and thus, induce apoptosis in pancreatic ductal adenocarcinoma (PDAC) cell lines such as Panc-1 Capan-2, and MiaPaCa-2 as well as in an ovarian cancer cell line SKOV3 (18, 19). rfhSP-D also inhibited epithelial-to-mesenchymal transition (EMT) by inhibiting transforming growth factor-β (TGF-β) pathway and downregulating mesenchymal specific markers, such as zinc finger E-box binding homeobox 1 (Zeb1), Snail, and Vimentin in PDAC cell lines such as Panc-1, and MiaPaCa-2 (20). SP-D has also been shown to interrupt epidermal growth factor (EGF) signaling by blocking the EGF–EGFR interaction in human lung adenocarcinoma A549 cell line (21). Proteomics analysis of rfhSP-D-treated eosinophilic cell line, AML14.3D10 line resulted in oxidative stress-mediated apoptotic signaling with downregulation of HMGA1, a pro-survival factor (22).

With established potent anti-cancer activity of rfhSP-D at the cellular level mediated through several molecular mechanisms, it is important to explore therapeutic implication of rfhSP-D in the murine models of PCa. In context to this, it has been observed that several serine proteases, mainly neutrophil elastase (NE), are known to cleave SP-D at the CRD and give rise to stable non-functional degraded fragment of ~35kDa (23, 24). Thus, it is of great interest to analyze the susceptibility of SP-D to proteolysis in NE-rich PCa microenvironment.

In this study, using a transgenic adenocarcinoma mouse prostate (TRAMP) model that is a spontaneous PCa model closely resembling the development and stages of human PCa, we evaluated the expression of SP-D in early and advanced stage of tumour progression. A stage-dependent downregulated expression of SP-D in tumour was observed possibly due to increased proteolysis of the protein. In addition, susceptibility of rfhSP-D to elastase, a serine protease, highlighted the importance of a new therapeutic strategy that maintained the stability of rfhSP-D in elastase-rich PCa tumoural microenvironment (TME). Furthermore, immunosuppressive TME can be altered with the exogenous treatment of rfhSP-D combined with elastase inhibitor in the *ex vivo* cultured TRAMP tumours. For the first time, we show that, rfhSP-D can induce immunogenic cell death (ICD) in murine PCa cells and in TRAMP explants. Together, our results provide a rationale for exploiting the therapeutic potential of rfhSP-D to treat immunologically unresponsive tumours.

MATERIALS AND METHODS

Transgenic Adenocarcinoma of Mouse Prostate (TRAMP) Model

All animal experiments were approved by the Institutional Animal Ethics Committee (IAEC No. 09/18). Mice representing Transgenic Adenocarcinoma of Mouse Prostate (TRAMP) were purchased from the Jackson Laboratory (C57BL/6-Tg (TRAMP)8247Ng/J); the model closely resembles the pattern of disease progression and stages of human PCa.

Mice hemizygous to the transgene, where prostate-specific rat probasin promoter is used to drive expression of the Simian Virus 40 large tumour T antigen, spontaneously develop progressive forms of PCa from pre-cancerous prostatic intraepithelial neoplasia (PIN), well-differentiated carcinoma (WD), poorly differentiated adenocarcinoma (PD) of the prostate gland, and finally metastasis (25). Hemizygous TRAMP mice were maintained in C57BL/6 background as the stock colony, whereas TRAMP mice were bred to non-transgenic normal FVB/NJ mice to obtain non-transgenic and hemizygous transgenic [C57BL/6 TRAMP x FVB/NJ] F1 male progenies that were used for the experiments. Prior to the start of the experiments, mice were allowed to acclimatize for one week. During the course of the experiment, mice were monitored weekly for general health, food consumption, and body weight. Mice were kept under controlled temperature, and humidity condition with 12-hour light: 12-hour dark cycle and were fed *ad libitum*.

Genotyping of TRAMP Mice

TRAMP mice were genotyped for confirmation as reported (26). Briefly, tail DNA was isolated using RED Extract-N-Amp Tissue PCR Kit (Sigma, USA). The primers recommended by the Jackson Laboratory protocol for Tg (TRAMP) 8247Ng stock mice, specific for rat probasin gene (Transgene; Tg), and as internal positive control (IPC) primers specific for beta-actin gene, were used for PCR. The PCR end products were run on a 2% agarose (GeNei, India) gel to confirm the presence or absence of the transgene.

RNA Isolation and Quantitative Reverse Transcription PCR (RT-qPCR) Analysis

Total RNA was isolated from prostate tumour or control dorsal lobe prostate using the TRIzol reagent (Ambion by Life technologies, USA) and quantified in multimode plate reader (BioTek Synergy H1, USA). 1 µg RNA was reverse transcribed using Superscript III first-strand synthesis kit (Invitrogen, USA). RT-qPCR was performed using Bio-Rad CFX 96^{TM} Thermal Cycler machine (Bio-Rad, USA) with 1.25 µl of the first-strand cDNA for each 25 µl real time PCR reaction using SYBR green (BioRad, USA) and forward and reverse primers. The semi-quantitation of the relative target mRNA was carried out using the ΔΔCT comparative method after normalizing with GAPDH abundance in the same sample. The specificity of each amplified product was validated by analysing their melt curve and by visualizing the band size of the amplified products on a 2% (w/v) agarose gel. The assay was performed in triplicates and the mean value was taken for further calculations. The primers were designed from NCBI Primer BLAST Software. Primer pair sequences, amplicon sizes, and their annealing temperatures are listed in **Table 1**.

Immunohistochemistry (IHC) Analysis

Formalin-fixed prostate tumours of TRAMP mice or dorsal lobe of control prostate tissues were paraffin-embedded, sectioned, and mounted on poly-L-lysine coated slides. 5 µm sections were deparaffinized in xylene and gradually rehydrated in a methanol gradient of 100%, 90%, 70%, 50%, 30%, and distilled water, each for 5 min. Blocking of endogenous peroxidase activity was done by immersing the rehydrated sections in a 3% hydrogen peroxide solution for 30 minutes. To improve antigen retrieval, the slides were boiled in sodium citrate buffer (pH 6.0) in a microwave. After the slides cooled down, they were washed with PBS, and any non-specific binding was blocked with 5% BSA in Tris buffer saline with Tween 20 (TBS-T) for an hour at room temperature (RT). The slides were incubated with a rabbit polyclonal primary antibody against mouse SP-D (Ab203309, Abcam, UK, 1:50 dilution in PBS) overnight at 4°C in a humidified chamber. For negative control, tissue sections were treated with the antibody diluent, PBS alone, without primary antibody. Next day, slides were washed in PBS, incubated with horseradish peroxidase (HRP)-conjugated polyclonal goat anti-rabbit IgG (ab205718, Abcam, 1:15000 dilution in PBS) at RT for an hour. Visualization was done using diaminobenzidine (DAB) (Sigma, USA) incubation for 10 min. Next, the nuclei were counterstained with Mayer's haematoxylin (SRL, India), followed by dehydration and mounting using DPX (SRL, India). Images were taken with Leica AS LMD microsystem at 40× magnification. The immunostaining was quantified using the open-source plugin, IHC profiler compatible with the open resource digital image analysis software, ImageJ, followed by calculation of the H score as previously described (27). For each tissue section, a minimum of three to four areas were scanned and the average H score was calculated and plotted as the mean ± SEM.

Total Protein Isolation and Immunoblot Analysis

TRAMP prostate tumour tissue or dorsal lobe of the prostate from control mice (~100 mg) were minced and homogenized in RIPA lysis buffer (Millipore Sigma, USA) with protease inhibitor cocktail (Thermo Fisher Scientific, USA). The homogenate was

TABLE 1 | Details of murine primers.

Target	Forward primer (5' → 3')	Reverse primer (3' → 5')	Amplicon size (bp)
Transgene	TACAACTGCCAACTGGGATG	CAGGCACTCCTTTCAAGACC	264
Internal Positive Control (β-actin)	CTGTCCCTGTATGCCTCTGG	AGATGGAGAAAGGACTAGGCTACA	415
SP-D	GCAGGACATGCTGCCCTTTCT	ACCCTTCTCACCCCGTGGACC	196
SP-A	ACCTGGATGAGGAGCTTCAGACTC	TGCTTGCGATGGCCTCGTTCT	225
MBL-A1	ACCAGGTCAAGGGCTCAGGGG	TGCCAGCTTCTCCTCAATGGCTC	141
GAPDH	CTGAGCAAGAGAGGCCCTATCC	CTCCCTAGGCCCCTCCTGTT	101

incubated for 30 min on ice followed by centrifugation at 14,000× g for 30 min at 4°C. The supernatant was collected and the total protein content was determined by BCA Protein Assay (Thermo Fisher Scientific, USA). 30 μg of protein was loaded in each lane and resolved on 12% v/v SDS-PAGE under reducing conditions. The resolved proteins were transferred onto an activated polyvinylidene fluoride (PVDF) membrane (Pall Corporation, USA), then blocked with 5% BSA in TBS containing 0.1% (v/v) Tween-20 (GeNei, India) (TBS-T) for 1h at RT. The membrane was probed overnight at 4°C with a rabbit polyclonal primary antibody raised against mouse SP-D (ab203309, Abcam, USA, 1:500 dilution in PBS) and a rabbit monoclonal antibody against mouse GAPDH (2118S, Cell signalling Technology, 1:1000 dilution in PBS) as the reference control. Next day, the blots were washed in TBS-T and probed with HRP-conjugated polyclonal goat anti-rabbit IgG (ab205718; Abcam, 1:15000 dilution in PBS) for 1 h at RT. Finally, the protein bands were detected with ECL Western Blotting Substrate (Thermo Fisher Scientific, USA). Quantitative densitometric analysis of the protein bands corresponding to intact SP-D and cleaved SP-D was conducted using ImageJ software and the band intensity was normalized using corresponding GAPDH as the loading control. The quantitative data were presented as mean ± SEM.

Immunophenotyping by Flow Cytometry

For phenotypic characterization of circulatory and prostate-resident immune cells, mice were euthanized, prostate tissue and whole blood (collected by trans-cardiac bleeding into K_2EDTA tubes to prevent clot formation) were collected, and stained with nine-colour combinations of fluorescently labelled monoclonal antibodies. Single cell suspensions were prepared as reported previously (28). Briefly, prostate tumour tissues from TRAMP or control prostate were harvested, washed with ice-cold PBS, enzymatically digested with collagenase IV (Gibco, USA) at 37°C for 2 h, and centrifuged at 400 x g for 5 min. The samples were treated with warm 0.05% trypsin-EDTA and 500U DNase I (Sigma, USA). The enzyme digested suspensions were passed through a 70-μm cell strainer (Corning, USA), centrifuged for 5 min, and re-suspended in FACS staining buffer [phosphate-buffered saline (PBS) with 0.2% foetal bovine serum (FBS)]. Dissociated cells were then collected, washed, counted, and distributed in tubes (10^6 cells/ml) for multicolour flow cytometry. The fresh EDTA-collected blood cells and single-cell suspensions (200 μl) were incubated with fluorescently labelled monoclonal antibodies for 20 min at RT. In the blood samples, RBCs were lysed using BD Pharm lyse (BD Biosciences) and washed twice with staining buffer (PBS with 0.2% FBS). Antibodies utilized for flow cytometry are listed in **Table 2**; antibodies were individually titrated to determine optimal staining dilutions. Data acquisition was performed on BD ACCURI C6 flow cytometer (BD Biosciences) where at least 50,000 events gated on the $CD45^+$leukocyte population were acquired. Anti-rat Ig, κ/ Negative Control compensation beads (BD Biosciences) were used to set compensation parameters. Fluorescence minus one (FMO) and unstained controls were used to identify and gate cells. Data analysis was carried out using FlowJo v10.8.1(Tree Star Inc., Oregon, USA). A representative flow cytometry gating strategy is displayed in **Figure S1** with initial gating on overall morphology, singlets, live cells, and CD45 positivity before proceeding with further analyses.

Production of rfhSP-D

The homotrimeric recombinant fragment of human SP-D (rfhSP-D), comprising 8 N-terminal Gly-X-Y triplets of the collagen region, α-helical coiled-coil neck region, and a C-terminal CRD, was expressed in *Escherichia coli*, purified and, characterized, as described previously (29). Endotoxin level in the rfhSP-D preparation was determined using the QCL-1000 Limulus amoebocyte lysate system (BioWhittaker Inc., USA). The amount of endotoxin in rfhSP-D preparations was found to be <4 pg/μg of rfhSP-D.

Cell Culture

TRAMP-C2 cells were purchased from the American Type Culture Collection (ATCC) and grown in high glucose Dulbecco's Modified Eagle Medium (DMEM) media (Gibco, USA) supplemented with 10 nm trans-dehydroandrosterone (D4000, Sigma, China), 0.005 mg/ml bovine insulin (Sigma, USA), 5% FBS (Gibo, USA), and 5% Serose (Himedia, India) at 37°C in a humidified chamber containing 5% CO_2.

MTT Assay

5×10^3 TRAMP-C2 (passage no. 7-9) cells were plated and grown overnight in 96-well culture plates. Post-starving the cells in serum-free media for 18 h, they were treated with rfhSP-D (20μg/ml) for 24, 48, and 72 h. Cells with only culture medium served as the media control and cells treated with PBS served as

TABLE 2 | List of antibodies used for immunophenotyping.

Antigen (mouse)	Label	Clone	Vendor	Catalog #
CD45	Brilliant Violet 605	30-F11	BioLegend	103140
CD11c	APC-eFluor 780	N418	Invitrogen	47-0114-82
CD206	Brilliant Violet 785	C068C2	BioLegend	141729
F4/80	PE/Cy7	BM8	BioLegend	123114
MHC Class II	eFluor 450	M5/114.15.2	Invitrogen	48-5321-82
Ly-6C	PE	HK1.4	Invitrogen	12-5932-82
CD11b	Alexa Fluor 488	M1/70	BioLegend	101217
Ly-6G	Alexa Fluor 647	1A8	BioLegend	127610
7-AAD	–	–	BioLegend	420403

the vehicle control. After incubation, 10µl MTT [3-(4, 5-dimethylthiazol-2-yl)-2, 5-diphenyltetrazolium bromide], from 5 mg/ml stock solution, was added to each well and incubated at 37°C overnight. Next day, after removing the MTT solution, acidified isopropanol was added to dissolve the formazan crystals and absorbance was read at 570 nm in BioTek Synergy H1 (Winooski, VT, USA).

Immunogenic Cell Death (ICD) Assay

5×10^3 TRAMP-C2 cells were grown on coverslips overnight. Cells were incubated with rfhSP-D (20 µg/ml) or PBS (vehicle control) in a serum-free DMEM medium. After 24h treatment, the medium was removed, and cells were washed, fixed in paraformaldehyde (4% in PBS) at RT for 15 min. For intracellular high mobility group protein B1 (HMGB1) immunofluorescence, cells were permeabilized using 0.25% Triton X-100 (Sigma, USA), blocked with 5% BSA in PBST for 1h at 37° followed by overnight incubation with rabbit antibody against HMGB1 (3935S, Cell signalling Technology, 1:100 dilution) at 4°C in a humified chamber. Next day, the cells were washed and probed with Alexa Fluor 488- tagged goat anti-rabbit IgG (A11034, Invitrogen, USA, 1:400 dilution) for 1h at RT followed by staining with DAPI, and were mounted on the slides. For negative controls, only secondary antibodies were used. The fluorescence signals were observed and captured under the confocal microscope (Carl Zeiss, Germany).

Cell-surface expression of calreticulin (CRT) was evaluated with the surface-staining protocol of flow cytometry using rabbit monoclonal antibody against mouse CRT (12238S, Cell signalling Technology, 1:400 dilution in PBS) for 40 min followed by Alexa Fluor 488-tagged goat anti-rabbit IgG (A11034, Invitrogen, USA, 1:400 dilution in PBS) for 1h at RT. Similarly, intracellular CRT was evaluated by flow cytometry with staining of permeabilized cells.

To evaluate the extracellular release of HMGB1 and CRT from *ex-vivo* cultured TRAMP tumours, the culture supernatant was collected, and approx 40µl of culture supernatant was resolved on the SDS-PAGE under reducing conditions. Western blotting was performed using the above-mentioned HMGB1 and CRT antibodies (1:1000 dilution in PBS). Coomassie blue staining was used for assessing the protein load. Quantitative densitometric analysis was carried out as described above using total protein for normalization.

Elastase-Mediated Degradation Assay

This experiment was carried out as per the previously reported protocol with some modifications (24). Briefly, 2µg rfhSP-D was incubated with 2.5µg porcine pancreas elastase (E7885, Sigma, USA) or 2.5 µg heat-inactivated elastase (HI elastase) for 30 minutes at 37 ° water bath. For heat inactivation, elastase was heated at 95° for 30 minutes before it was added to rfhSP-D. For inhibition of elastase activity, 5mM phenylmethylsulfonylfluoride (PMSF, Roche, Germany) was used. In addition, 2µg rfhSP-D was incubated with 2.5µg elastase in the presence or absence of 10mM $CaCl_2$ and LPS (10µg/ml). Reactions were stopped by heating the protein sample with Laemmli buffer at 95° for 10 min. The samples were resolved on 15% SDS-PAGE under reducing conditions and the gels were Coomassie blue stained or silver stained.

Short-Term *Ex Vivo* Culture of TRAMP Biopsies

Late TRAMP biopsies were cultured as previously described (30). Briefly, fresh tumour tissues were washed in Hanks' Balanced Salt Solution (HBSS) (Gibco, USA), and then cut into ~1mm pieces. Tumour sections were transferred to a 24-well plate and soaked in DMEM high glucose medium (Gibco, USA) 2% with PenStrep (Sigma, USA). TRAMP tumour biopsies were divided into 4 groups: vehicle control (PBS), rfhSP-D treated (40 µg/ml), sivelestat treated (S7198, Sigma, China) (4µmol), and rfhSP-D and sivelestat treated. Biopsies were cultured for 72 hour in a culture medium at 37°C with 5% CO_2. After treatment, biopsies were dissociated in a single cell suspension for flow cytometry. The culture supernatants were collected to evaluate the expression of HMGB1 and calreticulin *via* western blot.

Statistical Analysis

GraphPad Prism Software version 9.00 was used for Statistical analyses. The number of technical replicates, biological replicates, and independent experiments performed are listed in the figure legends. Unpaired two-tailed Student's t-test, one-way Analysis of Variance (ANOVA) with *post-hoc* Tukey, and two-way ANOVA with *post-hoc* Dunnett's test were utilized as appropriate. Data are presented as mean ± standard error of the mean (S.E.M.). For all analyses, results were considered statistically significant with *P < 0.05, **P < 0.01, ***P < 0.001, and ****P < 0.0001.

RESULTS

Differential Expression of Surfactant Protein-D (SP-D) in PIN and PD

Using the TRAMP mice, which is an autochthonous, spontaneous, heterogeneous, and progressive, clinically relevant animal model for prostate cancer, we determined the expression of different collectin molecules throughout the tumour progression. TRAMP mice closely recapitulate the key features of human prostate cancer with respect to progression, androgen independence, and biochemical characteristics. Based on the previous reports, about 80% of C57BL/6 TRAMP mice develop prostatic intraepithelial neoplasia (PIN) by 8 weeks and more than 70% of the dorsal and lateral lobe of the prostate showed the predominant pathology of PIN at this age. The tumour progresses into poorly-differentiated adenocarcinoma (PD) by 24-28 weeks (31). Based on these characteristics of disease progression in TRAMP x FVB F1, the preclinical study was designed (**Figure 1**). TRAMP x FVB F1 mice were genotyped and grouped into non-transgenic control (lacking rat probasin gene) and transgenic TRAMP (containing rat probasin gene) (**Figure 1A**). Transgenic mice were further grouped based on their ages which reflected different stages of prostate cancer. In the first group, TRAMP males were euthanized at about 8-12 weeks (or, 2-3 months) of age to represent PIN stage, referred as 'early TRAMP' and tissues were collected for further

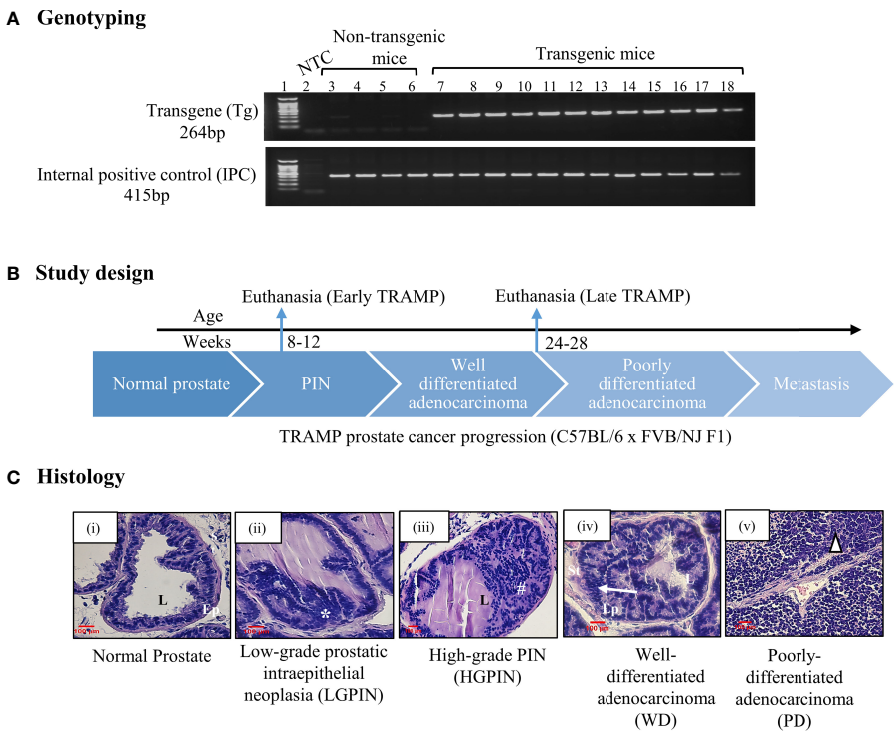

FIGURE 1 | **(A)** Genotyping of TRAMP mice. PCR amplified products of murine tail DNA using rat probasin gene (Transgene; Tg)-specific primers and internal positive control (IPC) primers were run on the agarose gel to confirm the presence Tg in transgenic mice (Lane No. 7-18) whereas non-transgenic mice show no Tg-specific amplification at 264 base pairs (bp) (Lane No. 3-6), Lane 2 represents non template control (NTC). **(B)** A brief study design for sample collection. **(C)** Histology. Histological photomicrographs of normal dorsal prostate and TRAMP dorsal prostate depicting different lesions at different stages of the tumour development. (i) Normal (Control) prostate lobe with columnar epithelial lining surrounding the lumen and presence of dense stroma, (ii) Low-grade intraepithelial neoplasia (LGPIN): represents stratification of epithelial cells (*), (iii) High-grade intraepithelial neoplasia (HGPIN): represents epithelial stratification in papillary and cribriform pattern in lumen (#), (iv) Well-differentiated adenocarcinoma (WD) represents migration of epithelial cells towards smooth muscle lining of stroma (arrow), (v) Poorly differentiated adenocarcinoma (PD) represents lack of glandular architecture (triangle). L, lumen; Ep, epithelium; St, stroma. Sections stained with hematoxylin–eosin. scale =100 µm.

analysis. The second group of transgenic males were allowed to mature and develop advanced tumours *i.e.* to the poorly differentiated adenocarcinoma (PD) stage, and euthanized at about 24–28 weeks (or, 6-7 months) of age, referred as 'late TRAMP' (**Figure 1B**). Age-matched non-transgenic littermates were used as controls, referred as '2M control' and '6M control'. Haematoxylin and Eosin (H&E) staining of the dorsal prostate lobe were carried out for confirming the histological features (**Figure 1C**).

In order to evaluate the expression of collectins in prostate tumour pathogenesis, we determined the mRNA levels of Surfactant protein-D (SP-D), Surfactant protein-A (SP-A) and Mannan-binding lectin-A (MBL-A) in the prostate of TRAMP mice during early and late stage of tumour, compared to the age-matched non-transgenic littermates (2M control and 6M control). The mRNA expression revealed significantly reduced expression of SP-D transcript ~14.87-fold in the early TRAMP and ~2.7-fold in late TRAMP when compared with control mice (**Figure 2A**). Since extrahepatic MBL-A expression has been reported in the murine testis (32) and human prostate (33), prostatic production of MBL-A transcript in TRAMP was compared with controls. MBL mRNA was not detectable in the prostate of control and TRAMP mice (**Figure S2**). Since the presence of SP-A mRNA in the human prostate has also been reported, the expression of SP-A transcript was evaluated in the murine prostate. Similar to MBL-A, SP-A expression was undetectable probably due to its lower expression in control and TRAMP prostate (**Figure S2**). None of the tested control or TRAMP mice prostate tissues had cycle threshold values <40 for SP-A mRNA.

Next, the localization of SP-D protein in prostate of early and late TRAMP was evaluated *via* immunohistochemistry. SP-D immunostaining was uniformly intracytoplasmic in TRAMP and control tissue sections. Positive immunoreactivity for SP-D was observed in the basal cell layer surrounding the acini and in the stroma of dorsal prostate of the control mice (**Figure 2B**). The expression pattern was completely altered in the poorly differentiated late TRAMP. Compared to the controls, a relatively strong homogenous staining for SP-D was detected in both early and late TRAMP mice. Densitometric analysis revealed ~1.66-fold higher SP-D immunostaining in the late TRAMP mice (**Figure 2C**).

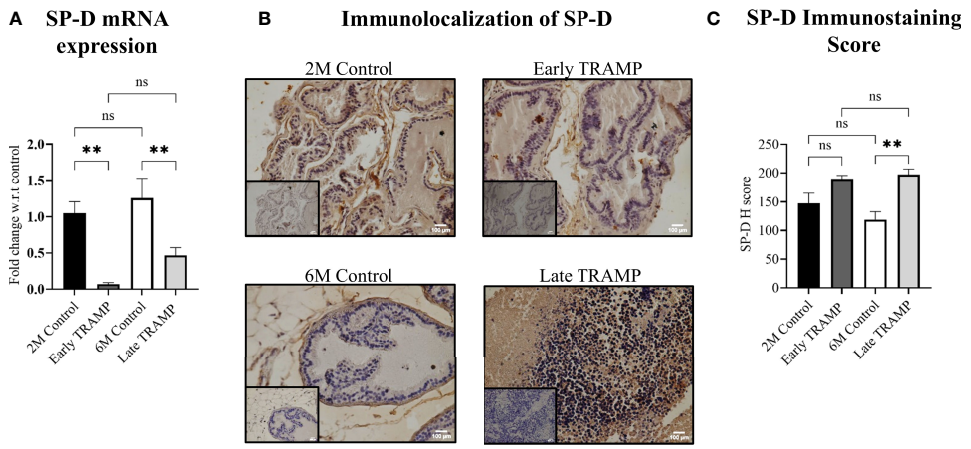

FIGURE 2 | Altered expression of SP-D mRNA and protein in the early and late stages. **(A)** qRTPCR of SP-D transcript in 2M Control (n= 4), Early TRAMP (n=5), 6M Control (n=5) and Late TRAMP (n=8) normalized with GAPDH. **(B)** Representative images of SP-D immunolocalization. **(C)** Semi-quantitative immunohistochemical (IHC) analysis of SP-D protein in TRAMP (early and late) and age-matched control mice. The intensity of SP-D staining was quantitated by an open source plugin, IHC profiler compatible with open resource digital image analysis software, Image J followed by calculation of H score. For each tissue section, a minimum of three to four areas were scanned and average H score was calculated. The bar graphs represent the average H score of 2M Control (n= 3), Early TRAMP (n=3), 6M Control (n=4), Late TRAMP (n= 5) tissue samples. Inner boxes represent negative staining. Statistical significance was tested using one-way ANOVA followed Tukey's multiple comparisons test (**p < 0.01). The data presented are mean ± SEM. ns, Non-significant.

Increased Proteolytic Degradation of SP-D in TRAMP Prostate Tumour

Pericellular proteases are reported as the key initiators of major proteolytic cascades involved in prostate tumour progression (34). Activated serine proteases are up-regulated during prostate tumour progression that can cleave SP-D to a non-functional form (23, 24, 35). Hence, it was important to evaluate if the levels of intact SP-D were altered in prostate tumour tissues due to increased proteolysis. Western blot analysis revealed less amount of the intact monomeric 43 kDa (~6.5-fold, p<0.0001) and differentially glycosylated 50 kDa forms of the SP-D protein in the late TRAMP when compared to control mice (**Figures 3B, D**). The 43 kDa form of intact SP-D protein was not significantly altered in the early TRAMP (**Figures 3A, C**). In addition, we observed a higher amount (~2.3-fold) of cleaved SP-D fragments of molecular weights ranging from ~35kDa to 33kDa in late TRAMP when compared to control mice (**Figure 3E**). Furthermore, early TRAMP prostate showed non-significant alteration in the cleaved SP-D fragments when compared to controls (**Figure 3E**). Also, there was a significant increase in the cleaved SP-D from early to advanced stage of tumour, suggesting a stage-dependent degradation of SP-D (**Figure 3E**). Similar to the IHC data, the total SP-D proteins (cleaved+intact) were significantly higher in the late TRAMP (~1.95 fold) whereas early TRAMP did not show any significant association (**Figure 3F**). Ratio of intact and cleaved SP-D was found to be significantly downregulated in late TRAMP (**Figure 3G**), suggesting increased proteolysis of SP-D protein.

Susceptibility of rfhSP-D to Elastase-Mediated Degradation

In view of the promising therapeutic potential of rfhSP-D in prostate cancer, it was important to know its stability in the TME. As previously reported, neutrophil elastase is one of the key serine proteases actively involved in PCa progression and is also known to cleave SP-D. Incubation of 2µg rfhSP-D with 2.5µg elastase for 30 mins at 37°C resulted in complete degradation of rfhSP-D (**Figure 4A**, Lane 4). With complete heat inactivation of the elastase at 95° for 30min, most of the rfhSP-D protein was intact with minimal degradation (**Figure 4A**, Lane 5). The proteolytic degradation products of rfhSP-D are visible below 10kDa marker (**Figure 4A**, Lane 4-6). In addition, the serine protease inhibitor PMSF (5mM), when incubated simultaneously with elastase and rfhSP-D, partially inhibited rfhSP-D degradation (**Figure 4A**, Lane 6). Further, addition of calcium chloride ($CaCl_2$, 10mM) also partially inhibited elastase activity (**Figure 4B**, Lane 4). LPS did not show any effect on this degradation (**Figure 4B**, Lane 5). Thus, a specific inhibitor for elastase-mediated proteolytic activity could potentiate the impact of rfhSP-D in TME.

Circulatory and Tumour-Derived Innate Immune Landscape Revealed Increased Elastase-Producing Immune Suppressive Cells

Since myeloid innate immune cells are known to play an important role in solid tumours, it was important to assess their systemic and tumoural distribution in the early and advanced stages of PCa in the TRAMP model. First, we assessed tumour-infiltrating innate immune cells in the early and late TRAMP and compared it with the immune profile of control mice (**Figures 5A–H**). The gating strategies were adopted from previous studies (36, 37). Flow cytometry gating on CD45 and CD11b showed a significantly increased accumulation of granulocytes (30.98 ± 7.98%) in the late TRAMP when compared to the 6-month-old control group (4.59 ± 0.922%) (**Figure 5A**). Also, late TRAMP revealed significantly

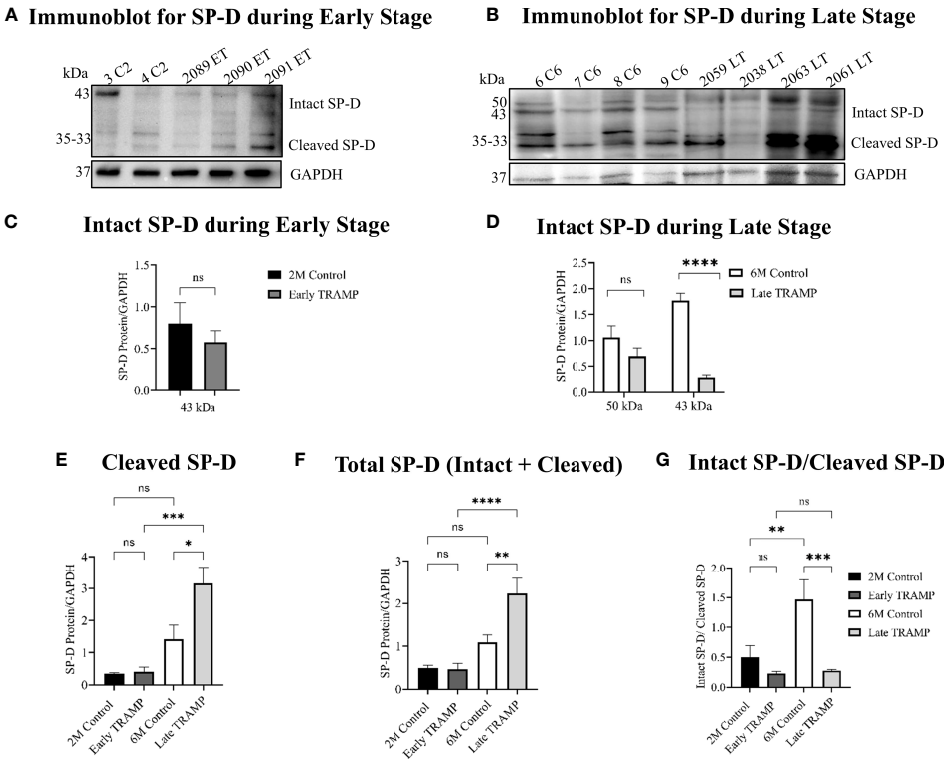

FIGURE 3 | Impaired expression of the intact form of SP-D throughout the tumour progression. Total protein lysates were analysed by Western blot for SP-D and GAPDH. **(A)** Immunoblot analyses of intact monomeric form of SP-D (~45kDa) and cleaved SP-D fragments (~35kDa-~33kDa) in the Early TRAMP compared with the corresponding 2M controls. C2: 2M Control mice; ET: Early TRAMP; 3 C2: 2M Control mice no. 3; 4 C2: 2M Control mice no. 4; 2089 ET: Early TRAMP mice no. 2089; 2090 ET: Early TRAMP mice no. 2090; 2091 ET: Early TRAMP mice no. 2091. **(B)** Immunoblot analyses of intact monomeric form of SP-D (~43kDa), differentially glycosylated form of SP-D (~50kDa) and cleaved SP-D fragments (~35kDa-~33kDa) in the Late TRAMP, compared with the corresponding 6M controls. C6: 6M Control mice; LT: Late TRAMP; 6 C6: 6M Control mice no. 6; 7 C6: 6M Control mice no. 7; 8 C6: 6M Control mice no. 8; 9 C6: 6M Control mice no. 9; 2059 LT: Late TRAMP mice no. 2059; 2038 LT: Late TRAMP mice no. 2038; 2063 LT: Late TRAMP mice no. 2063; 2061 LT: Late TRAMP mice no. 2061. GAPDH was used as a loading control. **(C–G)** Densitometric analysis of proteins normalized with GAPDH. n=3-6 for each group. Data are represented as mean ± SEM. Statistical significance was determined using two-tailed Student's t-test **(C)**; one-way ANOVA followed Tukey's multiple comparisons test **(D–G)**, NS, Non-significant. (*p < 0.05, **p < 0.01, ***p < 0.001, ****p < 0.0001).

increased infiltration of the PMN-MDSCs (32.18 ± 8.945%) over control (4.354 ± 0.344%) (**Figure 5B**). While comparing early and late-stage tumours, it was observed that the late TRAMP showed a ~5.13 fold increase in granulocytes and a~4.62 fold increase in PMN-MDSCs over the early TRAMP (**Figures 5A, B**). The percentage of monocytic MDSCs (M-MDSCs) showed an increasing trend in TRAMP but could not attain a significance level (**Figure 5C**). Furthermore, the late TRAMP showed a significantly decreased abundance of both immature (2.9 ± 1.19% vs. 12.81 ± 3.76%) and mature dendritic cells (DCs) (0.98 ± 0.28% vs. 4.98 ± 0.68%) within the TME as compared to controls (**Figures 5D, E**). Tumour-associated macrophages (TAM) showed decreased accumulation of classical macrophages (M1) (12.066 ± 1.12 vs. 38 ± 8.98) and increased infiltration of alternative macrophages (M2) (17.36 ± 2.97 vs. 7.71 ± 2.06) in the late tumour as compared to control (**Figures 5F–H**). A stage-dependent alteration in the M1 and M2 population between early and late TRAMP was noticed (**Figures 5G, H**). Thus, the increased percentage of granulocytes and PMN-MDSCs may serve as the main contributor to increased elastase activity which may eventually inhibit SP-D-mediated immune surveillance by degrading SP-D into a non-functional form. Increased percentage of M2 and PMN-MDSCs may also contribute to the immune-unresponsive or immunologically "cold" TME to allow immune evasion.

Next, the number of circulating myeloid cells in peripheral blood was evaluated by flow cytometry (**Figures 5I, J**). Immunosuppressive PMN-MDSCs and granulocyte populations were found to be significantly expanded in the circulation of late TRAMP as compared to the control group. The percentage of circulatory M-MDSCs did not alter significantly in TRAMP mice (**Figure S3B**). No alteration in the ratio of inflammatory and anti-inflammatory monocytes was observed in TRAMP as compared to controls (**Figure S3A**).

Combined Treatment With rfhSP-D and Elastase Inhibitor, Sivelestat, Modulates Immune Phenotype in *Ex Vivo* TRAMP Prostate Tumour Biopsies

We first assessed whether *ex vivo* treatment of TRAMP biopsies with rfhSP-D and sivelestat could influence the phenotype of

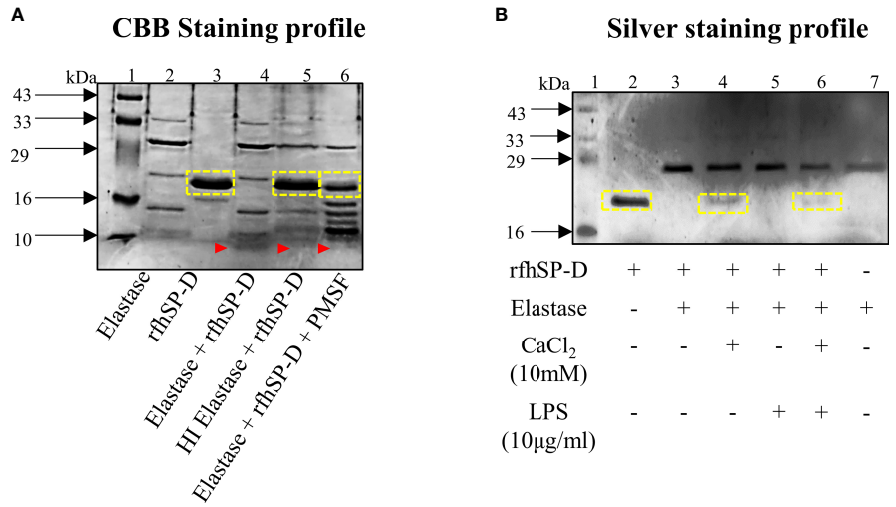

FIGURE 4 | Elastase mediated degradation of rfhSP-D. **(A)** CBB-stained profile of 2µg rfhSP-D treated with 2.5µg elastase for 30 mins at 37°C. Heat-inactivated elastase was used as the negative control. Assessment of partial inhibition of elastase activity by the serine protease inhibitor PMSF (5mM). **(B)** Effect of $CaCl_2$ (10mM) and LPS (10µg/ml) on elastase-mediated degradation of rfhSP-D. Yellow boxes represent band of rfhSP-D; red arrow-heads represent cleaved fragment of rfhSP-D (below 10kDa) due to elastase activity.

macrophages found in PCa. Freshly harvested TRAMP tumour biopsies were divided into 4 groups: vehicle control (PBS); rfhSP-D treated (40 µg/ml); sivelestat treated (4µmol); and rfhSP-D+ sivelestat treated. Biopsies were cultured for 72 h in a standard culture medium (**Figure 6A**). Moreover, to avoid the possibility of complement activation-induced alteration of immune cell phenotype, we used serum-free medium. At the end of the treatment, biopsies were fixed and stained for immune cells markers.

As previously observed, a comparison of immune cell marker expression (CD45, MHC-II, CD206) within viable cells by flow cytometry between immediately processed tumour tissues and those cultured for 72h did not show any significant difference (**Figure 6B**) (30). We next analysed the expression of the M1 and M2 markers within the macrophage population defined as $CD45^+/CD11b^+/F4/80^+$ $Ly6G^-$ cells. The TAM population represented about 60% of the $CD45^+$ leukocytes found in the biopsies (data not shown). While comparing between different treatment groups and PBS control biopsies, we observed a non-significant change in the percentage of TAM (**Figure 6C**) and a significant difference in the proportion of cells expressing the M1 and M2 markers within the TAM population. Flow cytometric analyses of tumour-derived immune cells showed that, when treated with rfhSP-D and sivelestat, the TAM skewed towards the M1 phenotype (**Figure 6D**). The treatment induced a reduction in the proportion of cells concomitantly expressing high levels of the M2-associated marker ($CD206^+$ $MHC\text{-}II^-$) when compared to the control PBS group (**Figure 6E**). Treatment with rfhSP-D alone or sivelestat alone did not induce such phenotypic changes in macrophages with respect to the PBS-treated control. In addition, we also observed a significant reduction in the immunosuppressive PMN-MDSCs count ($CD11b^+Ly6G^+Ly6C^{Low}$) in the rfhSP-D+sivelestat treated group over the PBS control group (**Figure 6F**). Since macrophages and MDSCs are one of the major immune cells within the prostate TME, we sought to evaluate how they are modulated by rfhSP-D using short-term *ex vivo* cultured TRAMP prostate biopsies. Immunologically unresponsive "cold" TME appeared to be altered by rfhSP-D in the presence of sivelestat by polarizing TAM towards M1 phenotype; reduction in PMN-MDSCs percentage is suggestive of the immunomodulatory potential of rfhSP-D in PCa.

Induction of Immunogenic Cell Death (ICD) by rfhSP-D

Previously, we have reported the anti-tumourigenic potential of rfhSP-D on human prostate cancer cells *in vitro* (16, 17). Interestingly, *in vitro* culture of the murine TRAMP-C2 cells with rfhSP-D (20µg/ml) resulted in cell death in a time-dependent manner and confirmed that rfhSP-D had a similar anti-tumour effect on the murine PCa cell line (**Figure 7A**). To investigate if the immunogenic cell death (ICD) contributed to this effect, HMGB1 and CRT, two major ICD damage-associated molecular patterns (DAMPs), were evaluated in TRAMP-C2 cells treated with 20µg/ml rfhSP-D for 24 hour. The rfhSP-D treated TRAMP-C2 cells showed a decreased nuclear HMGB1 staining by ~1.5 fold over PBS treated cells, signifying increased release of HMGB1 from the nucleus (**Figures 7B, C**). Percentage of cells expressing surface and intracellular CRT was evaluated by flow cytometry. rfhSP-D treatment induced a significantly increased CRT translocation to the cell surface (~8.77 fold) in non-permeabilized TRAMP-C2 and caused a ~2.8 fold reduction in the intracellular CRT expression in permeabilized cells when compared to the PBS control group (**Figures 7D, E**).

Similar to the *in-vitro* observations, induction of ICD by rfhSP-D was evaluated using *ex-vivo* cultured TRAMP tumour biopsies. Flow cytometric analysis of PI+ dead cells showed a significant increase in the cell death in rfhSP-D+sivelestat group (**Figure 8A**).

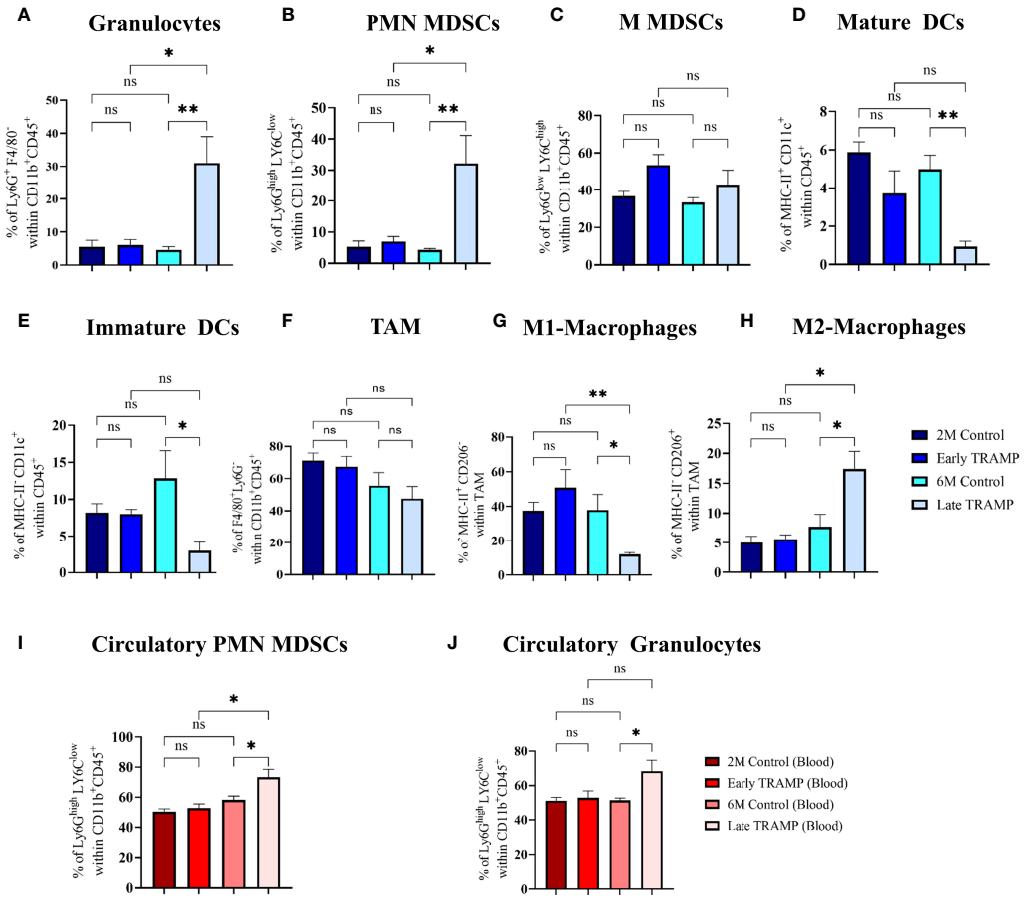

FIGURE 5 | Tumour-stage-specific altered tumoural, and circulatory innate immune landscape. Control and tumour tissues were harvested at the indicated time points, single-cell suspensions were prepared and immune-phenotyped to characterize different innate immune cells like **(A)** Granulocytes ($Ly6G^+$ $F4/80^-$); **(B)** Polymorpho-nuclear myeloid-derived suppressor cells (PMN-MDSCs) ($Ly6G^{high}$ $LY6C^{low}$); **(C)** Monocytic MDSCs (MMDSCs) ($Ly6G^{low}$ $LY6C^{high}$); **(D)** Mature dendritic cells (DCs) (MHC-II^+ $CD11c^+$); **(E)** Immature DCs (MHC-II^- $CD11c^+$) **(F)** Tumour associated macrophages (TAM) ($F4/80^+$ Ly6G) **(G)** M1 macrophages (MHC-II^+ $CD206^-$ $F4/80^+$ $Ly6G^-$); **(H)** M2 macrophages (MHC-II^- $CD206^+$ $F4/80^+$ $Ly6G^-$). Circulatory PMN-MDSCs and granulocytes were analysed using peripheral blood **(I, J).** n=4-5/group (tissue), n=5-7/group (blood)E; Data are represented as mean ± SEM. Statistical significance was determined using one-way ANOVA followed by Tukey's multiple comparisons test, ns, Non-significant; (*$p < 0.05$, **$p < 0.01$).

Extracellular expression of HMGB1 and CRT was evaluated in the culture medium of tumour explant. Both rfhSP-D treated and rfhSP-D+sivelestat treated groups showed a ~17.88 fold (p=0.003) and ~18.64 fold (p=0.002) upregulation in HMGB1 release, respectively, when compared to the PBS control (**Figure 8B**). There was no change in the extracellular CRT expression (**Figure 8C**) following treatment.

DISCUSSION

The role of SP-D has been extended to anti-tumoural innate immune surveillance beyond its well-established protective functions against pathogens and allergens (38). A correlation between presence/levels of SP-D transcript/protein and the cancer development was proposed recently to highlight the prognostic value of SP-D in several cancers (38). Downregulated SP-D expression has been reported in the lung, breast, and gastric cancers as compared to the healthy controls, whereas high transcriptional and protein expression of SP-D is found in the ovarian adenocarcinoma (19, 38). However, the bioinformatics studies revealed that only in the lung adenocarcinoma, SP-D mRNA had a favourable prognostic effect, whereas the presence of SP-D mRNA was negatively associated with the overall survival rate in the patients with breast, ovarian, and gastric carcinoma (38). Further, down-regulated expression of SP-D (and SP-A) at the malignant sites of human prostate adenocarcinomas as compared to the non-malignant sites and an association of weak SP-D (and SP-A) protein expression with an increasing Gleason score have been reported earlier (15). Thus, a complex regulatory mechanism involving SP-D seems to be operational in various cancers.

In order to delineate the molecular mechanisms for the initiation and progression of metastatic PCa, the TRAMP

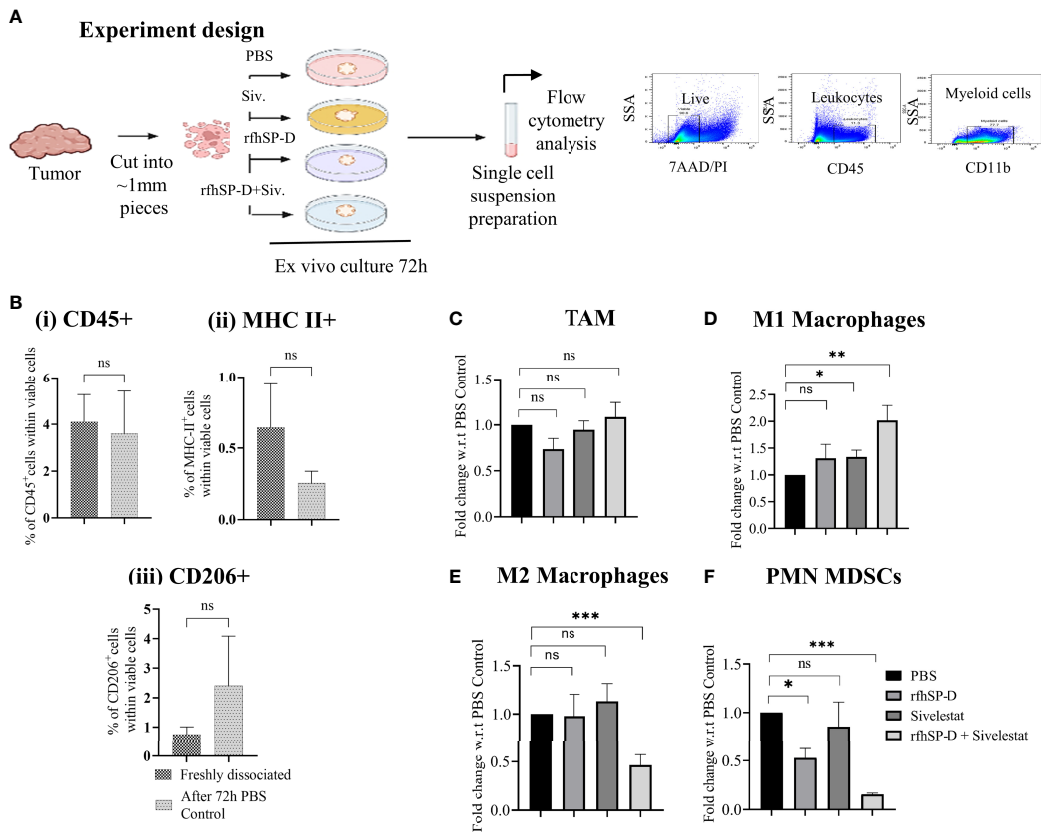

FIGURE 6 | Treatment with rfhSP-D+sivelestat induced polarisation of macrophages in *ex vivo* cultured TRAMP tumours. **(A)** Study design. **(B)** Comparison of (i) CD45+, (ii) MHC-II+ and (iii) CD206+ cells percentage between freshly dissociated TRAMP tumours and tumours after 72h culture in DMEM media.**(C–F)** Tumour tissues were collected from the late TRAMP and cultured in the serum-free DMEM with PBS/rfhSP-D/sivelestat/rfhSP-D+sivelestat treatment for 72h. After treatment, single cell suspensions were prepared and percentages of different immune cell types were analysed by flow cytometry. Fold change of **(C)** tumour-associated macrophages (TAM), **(D)** M1; **(E)** M2 and, **(F)** PMN-MDSCs in *ex vivo* cultured TRAMP tumours were calculated with respect to PBS control. n=3/treatment group. Data represented as mean ± SEM. Statistical significance was determined by the two-tailed Student's t-test. (*p < 0.05, **p < 0.01, ***p < 0.001); ns, Non-significant.

model was used as a pre-clinical autochthonous model of PCa. This genetically engineered model develops progressive, multifocal, and heterogeneous tumour which resembles various human PCa stages, thus facilitating pre-clinical studies (25, 31).

In this study, the expression of SP-D was evaluated at different stages of prostate cancer using TRAMP. Significantly downregulated transcript of SP-D was observed in both early stage (PIN: precancerous) and advanced stage (poorly differentiated adenocarcinoma; PD) of tumour development compared to age-matched non-transgenic littermates (control), a finding similar to our earlier report of a significant downregulation of SP-D mRNA in the androgen-sensitive human LNCaP cells (16). In this context, it is important to note that the glucocorticoids stimulate SP-D mRNA expression in the lung, and glucocorticoid receptor expression is low in the human prostatic carcinoma patients (39). Therefore, SP-D mRNA in the TRAMP mice could be indirectly regulated through the glucocorticoid receptor pathway in the prostate. Similarly, estrogen receptor-α was reported to stimulate SP-A expression in the fetal lung cells. In addition, a significant decrease in estrogen and androgen receptors from PIN to PD in TRAMP has been reported previously (40). Thus, it is likely that the alteration in the levels of these receptors may regulate the synthesis of SP-D in TRAMP mice. Interestingly, there was a relatively higher SP-D transcript expression in the late stage than in the early stage, most plausibly a rescue mechanism by the host. As advanced prostate tumours are histopathologically very heterogeneous (41), the expression profile of SP-D gene from late TRAMP tissues could be substantially influenced by contamination with surrounding noncancerous cells which could explain the increased expression of SP-D transcript in late TRAMP as compared to the small localized lesion of PIN or early TRAMP.

Immunolocalization in the control prostate revealed expression of SP-D in basal epithelial lining of acini and in the stromal compartment. This expression pattern was altered in the poorly differentiated late TRAMP. Thus, the considerable immunostaining of SP-D in TRAMP tumour, compared to control, may be due to its extra-prostatic origin. Since SP-D is a hydrophilic soluble PRR and is present in serum, it may circulate to the tumoural compartment as a consequence of host response (42, 43).

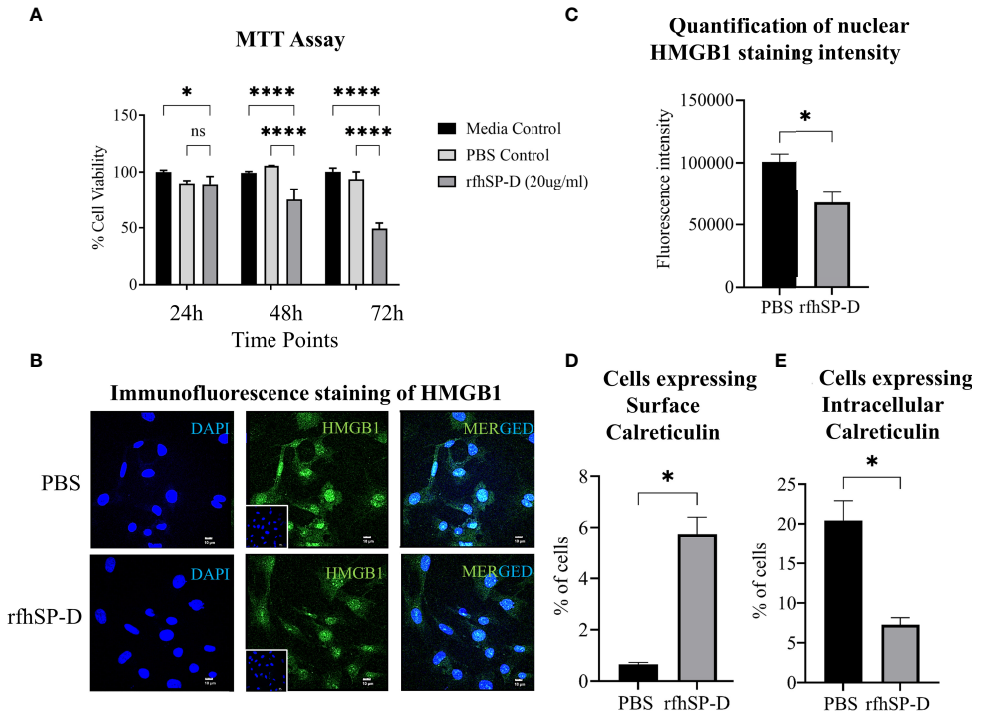

FIGURE 7 | rfhSP-D induces immunogenic cell death (ICD) in TRAMP-C2 cells. **(A)** TRAMP-C2 cells were incubated in the serum-free media for 12h and then treated with or without rfhSP-D (20μg/ml in PBS). PBS was used as the vehicle control. Treatment was given for the indicated time intervals (24, 48, and 72 h). After treatment, MTT assay was done. Each bar represents % viability ± SEM of three independent experiments relative to the untreated controls or PBS control. After 24h treatment TRAMP C2 cells were analysed by immunofluorescence or flow cytometry. **(B)** Representative images showing immunofluorescence staining of nuclear high mobility group box protein 1 (HMGB1) (Green) and DAPI (Blue) **(C)** Quantification of nuclear HMGB1 staining intensity using ImageJ. **(D)** Flow cytometric analysis of cell-surface exposed calreticulin (CRT) in the non-permealized cells; and **(E)** intra-cellular calrticulin in permealized cells. Samples were analyzed in triplicate and represented as mean ± SEM. Statistical significance was determined by two-way ANOVA **(A)**, two-tailed Student's t-test **(B–E)**. ns, Non-significant. *p < 0.05, ****p < 0.0001.

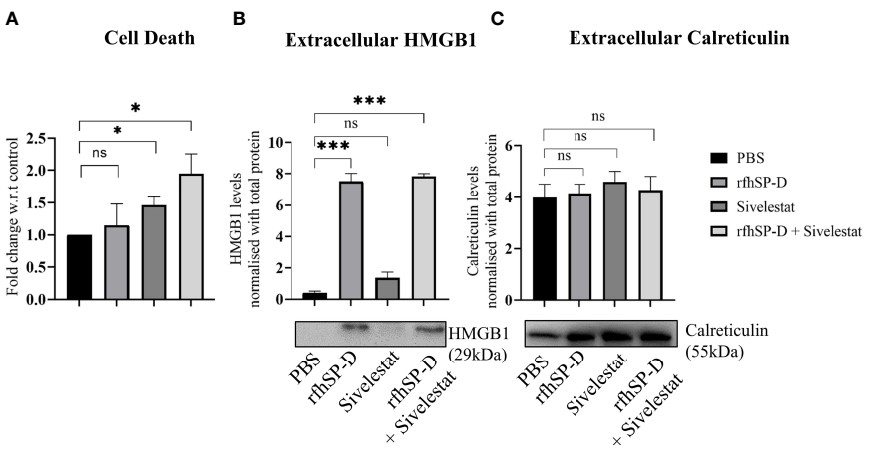

FIGURE 8 | Assessment of cell death and released ICD markers in *ex vivo* cultured TRAMP tumours. Tumour tissues were collected from the late TRAMP and cultured in serum-free DMEM with PBS, rfhSP-D, sivelestat and rfhSP-D+sivelestat treatment for 72h. **(A)** After treatment, single cell suspensions were prepared and percentage of Propidium Iodide-positive (PI^+) (dead) cells were analysed by flow cytometry. **(B, C)** After treatment, the culture-media were subjected to western blot. **(B)** Representative immunoblot and densitometric analysis of extracellular HMGB1. **(C)** Representative immunoblot and densitometric analysis of extracellular calreticulin. n=3/treatment group. Data represented as mean ± SEM. Statistical significance was determined by one-way ANOVA **(A)**, two-tailed Student's t-test **(B, C)**. ns, Non-significant. *p < 0.05, ***p < 0.001.

Tumour-infiltrating neutrophils and PMN-MDSCs are associated with a poor prognosis in many solid tumours including PCa (44). It has been observed that the stromal area of both primary and invasive PCa tissue is enriched with PMN-MDSCs more than the epithelial counterpart (45). The pro-tumourigenic effect exerted by these granulocytic myeloid cells is mainly by releasing a serine protease, neutrophil elastase (NE); importantly, these cells show a progressive increase from normal to early to advanced prostate tumours of TRAMP (34). The role of NE in promoting tumour growth, angiogenesis, and metastasis has been addressed in many cancers (46). Endocytosis of NE by the lung adenocarcinoma cells caused upregulation of PI3K-AKT survival signalling, whereas in PCa, extracellular NE triggered ERK signaling *via* the combined activation of receptor tyrosine kinases AXL and EGF (46). These pro-tumoural activities were further confirmed when inhibition of NE by the genetic deletion approach or pharmacological inhibitors showed a reduction in tumour growth in mice (46).

There are several serine proteases known to cleave SP-D. Elastase is known to cleave SP-D within the CRD region to produce a stable but non-functional 35-kDa fragment (23, 24). In the cystic fibrosis lung (35), SP-D-mediated host defense is compromised due to the increased proteolysis of SP-D. In this study, a significant increment in the cleaved SP-D and total SP-D (cleaved+intact) was found in the late TRAMP as compared to both the early TRAMP and control mice, suggesting that though the amount of total SP-D protein increased, most of it was functionally inactive. It has been shown previously that elastase-mediated degradation impairs CRD-dependent activities of SP-D can could hamper several defense mechanisms such as SP-D mediated chemotaxis of immune cells, opsonization, internalization, and killing of microbes by leukocytes (23, 24). As previously reported, immunophenotyping of the early and late TRAMP also revealed a significantly increased presence of PMN-MDSCs and granulocytes in the tumour as well as in the peripheral blood. Therefore, it is interesting to postulate that the intra-tumoural factors may be associated with an increased accumulation of MDSCs that results in the increased intra-tumoural NE level (46). Interestingly, endogenous NE inhibitors, like SERPINB1, are down-regulated in early and advanced prostate cancer, which is indicative of another strategy to establish high NE activity in tumours (41, 47). Thus, degradation of SP-D may have resulted from the plausibly increased PMN-MDSCs-derived NE activity. Several *in vitro* studies exemplified the anti-tumourigenic potential of rfhSP-D, comprising of CRD and eight Gly-X-Y repeats, but this study for the first time demonstrated that rfhSP-D is highly susceptible to the elastase-mediated degradation in tumor tissues. Hence, to maintain the stability of exogenous rfhSP-D in TME, it is important to inhibit the elastase activity.

A complex and dynamic communication between the cancer cells and immune cells within the prostate TME greatly influences tumour survival and growth. Macrophages, one of the key immune cells present within the tumour and its periphery, contribute to tumour resistance and metastases (30). The advanced TRAMP TME is marked by an abundance of immunosuppressive M2 macrophages, PMN-MDSCs with decreased M1, and mature DCs.

Hence, it is important to evaluate the anti-prostate tumour potential of SP-D in the TME. After several unsuccessful attempts to generate TRAMP-C2 syngeneic model [following reported protocols using $1x10^6$ or $5x10^6$ TRAMP-C2 cells by intraprostatic or subcutaneous routes in young (6-8 wk), and old mice (24 wk) (48, 49)] for evaluating the anti-prostate tumour effect of rfhSP-D+sivelestat *in-vivo*, we pursued the *ex-vivo* approach to evaluate the anti-tumourigenic potential of rfhSP-D. To overcome the limitations encountered with spontaneous tumour development, the usage of highly tumourigenic androgen-insensitive cell lines derived from androgen-deprived parental TRAMP-C1 or TRAMP-C2 can be used as an alternative means (50, 51).

Here we report, for the first time, the ability of rfhSP-D combined with sivelestat to modulate the immunosuppressive TME. rfhSP-D+sivelestat treated *ex vivo* cultured tumour explants showed dynamic polarization of macrophages from M2 to M1 with significant alteration in the PMN-MDSCs. Consistent with this observation, the potential of de-oligomerized SP-D in macrophages polarization was also reported in the animal model of acute kidney injury (AKI), in which induction of M1 macrophages through CRT/p38 MAPK signaling cascade was observed by the recombinant SP-D (11). The efficacy of sivelestat, in suppressing prostate as well as colon cancer xenografts in athymic mice was recently reported (44, 52). Sivelestat functions by directly inhibiting NETosis, NE-induced cancer cell proliferation, and invasion (44, 52). Here, sivelestat alone treatment resulted in significant cell death but was neither able to modulate immune profile nor HMGB1 release from the TRAMP explant. However, the impact of rfhSP-D was found to be greatly stabilized when combined with sivelestat, which suggests a new therapeutic approach for PCa (**Figure 8**). The molecular mechanisms underlying macrophage polarisation remain to be deciphered.

According to the current concept, ICD relies on the ability of specific apoptotic cancer cells treated with chemotherapeutics or radiotherapy to convey spatiotemporally coordinated release of immunogenic signals in the form of damage-associated molecular patterns (DAMPs), which provoke an active immune response (53). DAMPs exert robust immunostimulatory effects upon binding to the pattern recognition receptors (PRRs) expressed on the immune cells. The hallmarks of ICD are CRT cell surface exposure, and secretion of ATP and HMGB1 (53, 54). Here we provide evidence that rfhSP-D treatment increased the release of HMGB1 from the nucleus and a significant translocation of CRT to the cell surface, suggesting a novel mechanism through which rfhSP-D enhances immunogenicity of the tumour via ICD induction. In *ex-vivo* cultured TRAMP tumour, treatment with rfhSP-D, with or without sivelestat, induced a robust HMGB1 release in the culture medium, suggesting an enhanced ICD. Since, secreted HMGB1 is known to serve as a ligand for the receptor for advanced glycocylation end products (RAGE) and TLRs and helps in the recruitment, maturation of DCs, induction of HMGB1 by

rfhSP-D may modulate immune unresponsiveness in the TME (55).

Accumulation of hyaluronic acid (HA) has been extensively reported in epithelial cancers, such as prostate, where the presence of tumour cell HA matrices is both histopathologically correlated with aggressive cancer and functionally implicated in metastatic spread (56, 57). It has been reported that HA binds to rfhSP-D and hampers its anti-apoptotic potential against the breast cancer cells (58). HA has also been reported to be involved in PCa progression, and thus, the impact of interplay between HA with SP-D in PCa is definitely worth examining. It will be interesting to analyse the impact of HA on various anti-tumour mechanisms of SP-D like EGF-EGFR interaction, ICD, and immunomodulation of rfhSP-D besides the previously reported inhibition of SP-D mediated apoptosis of cancer cells.

In summary, the present study demonstrates that the tumour milieu adversely impacts functional SP-D levels *via* reduced transcription and enhanced proteolytic degradation. We report, for the first time, an immunomodulatory role of the recombinant fragment of human SP-D (rfhSP-D) in the TRAMP tumour explants. Dynamic phenotype changes of macrophages with the downregulation of immunosuppressive PMN-MDSCs within tumour indicates a novel anti-tumour effector mechanism of rfhSP-D leading to the transformation of an immunologically unresponsive "cold tumour" into a responsive "hot tumour" microenvironment. In addition, ICD mediated by rfhSP-D is being reported in the TRAMP tumour explants for the first time. The current study provides a snapshot of the involvement of SP-D in the immunomodulation in TME of prostate cancer. Future studies would be directed to elucidate the synergistic potential of rfhSP-D and sivelestat in prostate cancer *in vivo*.

DATA AVAILABILITY STATEMENT

The original contributions presented in the study are included in the article/**Supplementary Material**. Further inquiries can be directed to the corresponding author.

ETHICS STATEMENT

The animal study was reviewed and approved by Institutional Animal Ethics Committee (IAEC), ICMR-National Institute for Research in Reproductive and Child Health, (IAEC Project No. 09/18).

AUTHOR CONTRIBUTIONS

KG coordinated the study, designed, performed the experiments, analyzed the experimental data, and wrote the paper. UK provided purified and characterized rfhSP-D for the study and edited the paper. SM helped in animal handling and dissection. TM supervised the entire study, analyzed the data, and edited the paper. All authors reviewed the results and approved the final version of the manuscript.

FUNDING

This work was financially supported by the Institutional Grant provided by ICMR-NIRRCH (Accession no. 1239). KG was supported by Junior and Senior Research Fellowships of the Council of Scientific and Industrial Research (CSIR, India).

ACKNOWLEDGMENTS

We thank Dr. Geetanjali Sachdeva, Director, ICMR- National Institute for Research in Reproductive and Child Health, Mumbai (ICMR-NIRRCH), for providing financial support, experimental facilities and TRAMP mice to carry out the study. We sincerely acknowledge Ms. Junita Desouza for helping in TRAMP breeding. We thank Dr. Vainav Patel, Ms. Sameen Khan for their help in flow cytometry experiments. We are grateful to Dr. Vikas Dighe and Mr. Praveen Salunkhe for their help in histological sectioning. We also thank Dr. Nafisa Balasinor and Ms. Shobha Banage for their help in confocal microscopy.

SUPPLEMENTARY MATERIAL

The Supplementary Material for this article can be found online at: https://www.frontiersin.org/articles/10.3389/fimmu.2022.930449/full#supplementary-material

REFERENCES

1. Sung H, Ferlay J, Siegel RL, Laversanne M, Soerjomataram I, Jemal A, et al. Global Cancer Statistics 2020: GLOBOCAN Estimates of Incidence and Mortality Worldwide for 36 Cancers in 185 Countries. *CA Cancer J Clin* (2021) 71:209–49. doi: 10.3322/caac.21660
2. Chen W, Zheng R, Baade PD, Zhang S, Zeng H, Bray F, et al. Cancer Statistics in China, 2015. *CA Cancer J Clin* (2016) 66:115–32. doi: 10.3322/caac.21338
3. Rizzo A, Mollica V, Cimadamore A, Santoni M, Scarpelli M, Giunchi F, et al. Is There a Role for Immunotherapy in Prostate Cancer? *Cells* (2020) 9:2051. doi: 10.3390/cells9092051
4. Patel D, McKay R, Parsons JK. Immunotherapy for Localized Prostate Cancer: The Next Frontier? *Urol Clin* (2020) 47:443–56. doi: 10.1016/j.ucl.2020.07.008
5. Adamaki M, Zoumpourlis V. Immunotherapy as a Precision Medicine Tool for the Treatment of Prostate Cancer. *Cancers (Basel)* (2021) 13:173. doi: 10.3390/cancers13020173
6. Fay EK, Graff JN. Immunotherapy in Prostate Cancer. *Cancers (Basel)* (2020) 12:1752. doi: 10.3390/cancers12071752
7. Ryan MJ, Bose R. Genomic Alteration Burden in Advanced Prostate Cancer and Therapeutic Implications. *Front Oncol* (2019) 9:1287. doi: 10.3389/fonc.2019.01287
8. Yan H, Kamiya T, Suabjakyong P, Tsuji NM. Targeting C-Type Lectin Receptors for Cancer Immunity. *Front Immunol* (2015) 6:408. doi: 10.3389/fimmu.2015.00408
9. Ganguly K, Kishore U, Madan T. Interplay Between C-Type Lectin Receptors and microRNAs in Cellular Homeostasis and Immune Response. *FEBS J* (2021) 288:4210–29. doi: 10.1111/febs.15603

10. Kishore U, Greenhough TJ, Waters P, Shrive AK, Ghai R, Kamran MF, et al. Surfactant Proteins SP-A and SP-D: Structure, Function and Receptors. *Mol Immunol* (2006) 43:1293–315. doi: 10.1016/j.molimm.2005.08.004
11. Li D, Pan L, Zhang X, Jiang Z. Lower Oligomeric Form of Surfactant Protein D in Murine Acute Lung Injury Induces M1 Subtype Macrophages Through Calreticulin/p38 MAPK Signaling Pathway. *Front Immunol* (2021) 12:687506. doi: 10.3389/fimmu.2021.687506
12. Gardai SJ, Xiao Y-Q, Dickinson M, Nick JA, Voelker DR, Greene KE, et al. By Binding Sirpα or Calreticulin/CD91, Lung Collectins Act as Dual Function Surveillance Molecules to Suppress or Enhance Inflammation. *Cell* (2003) 115:13–23. doi: 10.1016/S0092-8674(03)00758-X
13. Sorensen GL. Surfactant Protein D in Respiratory and Non-Respiratory Diseases. *Front Med* (2018) 5:18. doi: 10.3389/fmed.2018.00018
14. Oberley RE, Goss KL, Quintar AA, Maldonado CA, Snyder JM. Regulation of Surfactant Protein D in the Rodent Prostate. *Reprod Biol Endocrinol* (2007) 5:1–9. doi: 10.1186/1477-7827-5-42
15. Kankavi O, Baykara M, Eren Karanis MI, Bassorgun CI, Ergin H, Ciftcioglu MA. Evidence of Surfactant Protein A and D Expression Decrement and Their Localizations in Human Prostate Adenocarcinomas. *Ren Fail* (2014) 36:258–65. doi: 10.3109/0886022X.2013.846831
16. Thakur G, Prakash G, Murthy V, Sable N, Menon S, Alrokayan SH, et al. Human SP-D Acts as an Innate Immune Surveillance Molecule Against Androgen-Responsive and Androgen-Resistant Prostate Cancer Cells. *Front Oncol* (2019) 9:565. doi: 10.3389/fonc.2019.00565
17. Thakur G, Sathe G, Kundu I, Biswas B, Gautam P, Alkahtani S, et al. Membrane Interactome of a Recombinant Fragment of Human Surfactant Protein D Reveals GRP78 as a Novel Binding Partner in PC3, a Metastatic Prostate Cancer Cell Line. *Front Immunol* (2021) 11:600660. doi: 10.3389/fimmu.2020.600660
18. Kaur A, Riaz MS, Murugaiah V, Varghese PM, Singh SK, Kishore U. A Recombinant Fragment of Human Surfactant Protein D Induces Apoptosis in Pancreatic Cancer Cell Lines *via* Fas-Mediated Pathway. *Front Immunol* (2018) 9:1126. doi: 10.3389/fimmu.2018.01126
19. Kumar J, Murugaiah V, Sotiriadis G, Kaur A, Jeyaneethi J, Sturniolo I, et al. Surfactant Protein D as a Potential Biomarker and Therapeutic Target in Ovarian Cancer. *Front Oncol* (2019) 9:542. doi: 10.3389/fonc.2019.00542
20. Kaur A, Riaz MS, Singh SK, Kishore U. Human Surfactant Protein D Suppresses Epithelial-to-Mesenchymal Transition in Pancreatic Cancer Cells by Downregulating TGF-β. *Front Immunol* (2018) 9:1844. doi: 10.3389/fimmu.2018.01844
21. Hasegawa Y, Takahashi M, Ariki S, Asakawa D, Tajiri M, Wada Y, et al. Surfactant Protein D Suppresses Lung Cancer Progression by Downregulation of Epidermal Growth Factor Signaling. *Oncogene* (2015) 34:838–45. doi: 10.1038/onc.2014.20
22. Mahajan L, Pandit H, Madan T, Gautam P, Yadav AK, Warke H, et al. Human Surfactant Protein D Alters Oxidative Stress and HMGA1 Expression to Induce P53 Apoptotic Pathway in Eosinophil Leukemic Cell Line. *PLos One* (2013) 8:e85046. doi: 10.1371/journal.pone.0085046
23. Alcorn JF, Wright JR. Degradation of Pulmonary Surfactant Protein D by Pseudomonas Aeruginosa Elastase Abrogates Innate Immune Function. *J Biol Chem* (2004) 279:30871–9. doi: 10.1074/jbc.M400796200
24. Griese M, Wiesener A, Lottspeich F, von Bredow C. Limited Proteolysis of Surfactant Protein D Causes a Loss of Its Calcium-Dependent Lectin Functions. *Biochim Biophys Acta (BBA)-Mol Basis Dis* (2003) 1638:157–63. doi: 10.1016/S0925-4439(03)00063-2
25. Greenberg NM, DeMayo F, Finegold MJ, Medina D, Tilley WD, Aspinall JO, et al. Prostate Cancer in a Transgenic Mouse. *Proc Natl Acad Sci* (1995) 92:3439–43. doi: 10.1073/pnas.92.8.3439
26. Rokade S, Kishore U, Madan T. Surfactant Protein D Regulates Murine Testicular Immune Milieu and Sperm Functions. *Am J Reprod Immunol* (2017) 77:e12629. doi: 10.1111/aji.12629
27. Pirker R, Pereira JR, Von Pawel J, Krzakowski M, Ramlau R, Park K, et al. EGFR Expression as a Predictor of Survival for First-Line Chemotherapy Plus Cetuximab in Patients With Advanced Non-Small-Cell Lung Cancer: Analysis of Data From the Phase 3 FLEX Study. *Lancet Oncol* (2012) 13:33–42. doi: 10.1016/S1470-2045(11)70318-7
28. Nath D, White JR, Bratslavsky G, Kotula L. Identification, Histological Characterization, and Dissection of Mouse Prostate Lobes for *In Vitro* 3D Spheroid Culture Models. *J Vis Exp* (2018) 139:58397. doi: 10.3791/58397
29. Mahajan L, Madan T, Kamal N, Singh VK, Sim RB, Telang SD, et al. Recombinant Surfactant Protein-D Selectively Increases Apoptosis in Eosinophils of Allergic Asthmatics and Enhances Uptake of Apoptotic Eosinophils by Macrophages. *Int Immunol* (2008) 20:993–1007. doi: 10.1093/intimm/dxn058
30. Boibessot C, Joncas F-H, Park A, Berrehail Z, Pelletier J-F, Gris T, et al. Using Ex Vivo Culture to Assess Dynamic Phenotype Changes in Human Prostate Macrophages Following Exposure to Therapeutic Drugs. *Sci Rep* (2021) 11:1–10. doi: 10.1038/s41598-021-98903-y
31. Kaplan-Lefko PJ, Chen T, Ittmann MM, Barrios RJ, Ayala GE, Huss WJ, et al. Pathobiology of Autochthonous Prostate Cancer in a Pre-Clinical Transgenic Mouse Model. *Prostate* (2003) 55:219–37. doi: 10.1002/pros.10215
32. Wagner S, Lynch NJ, Walter W, Schwaeble WJ, Loos M. Differential Expression of the Murine Mannose-Binding Lectins A and C in Lymphoid and Nonlymphoid Organs and Tissues. *J Immunol* (2003) 170:1462–5. doi: 10.4049/jimmunol.170.3.1462
33. Seyfarth J, Garred P, Madsen HO. Extra-Hepatic Transcription of the Human Mannose-Binding Lectin Gene (Mbl2) and the MBL-Associated Serine Protease 1–3 Genes. *Mol Immunol* (2006) 43:962–71. doi: 10.1016/j.molimm.2005.06.033
34. Bok RA, Hansell EJ, Nguyen TP, Greenberg NM, McKerrow JH, Shuman MA. Patterns of Protease Production During Prostate Cancer Progression: Proteomic Evidence for Cascades in a Transgenic Model. *Prostate Cancer Prostatic Dis* (2003) 6:272–80. doi: 10.1038/sj.pcan.4500676
35. Von Bredow C, Wiesener A, Griese M. Proteolysis of Surfactant Protein D by Cystic Fibrosis Relevant Proteases. *Lung* (2003) 181:79–88. doi: 10.1007/s00408-003-1008-z
36. Ager CR, Reilley MJ, Nicholas C, Bartkowiak T, Jaiswal AR, Curran MA. Intratumoural STING Activation With T-Cell Checkpoint Modulation Generates Systemic Antitumour Immunity. *Cancer Immunol Res* (2017) 5:676–84. doi: 10.1158/2326-6066.CIR-17-0049
37. Annels NE, Simpson GR, Denyer M, Arif M, Coffey M, Melcher A, et al. Oncolytic Reovirus-Mediated Recruitment of Early Innate Immune Responses Reverses Immunotherapy Resistance in Prostate Tumours. *Mol Ther* (2021) 20:434–46. doi: 10.1016/j.omto.2020.09.010
38. Mangogna A, Belmonte B, Agostinis C, Ricci G, Gulino A, Ferrara I, et al. Pathological Significance and Prognostic Value of Surfactant Protein D in Cancer. *Front Immunol* (2018) 9:1748. doi: 10.3389/fimmu.2018.01748
39. Mohler JL, Chen Y, Hamil K, Hall SH, Cidlowski JA, Wilson EM, et al. Androgen and Glucocorticoid Receptors in the Stroma and Epithelium of Prostatic Hyperplasia and Carcinoma. *Clin Cancer Res* (1996) 2:889–95.
40. Ślusarz A, Jackson GA, Day JK, Shenouda NS, Bogener JL, Browning JD, et al. Aggressive Prostate Cancer Is Prevented in Erαko Mice and Stimulated in Erβko TRAMP Mice. *Endocrinology* (2012) 153:4160–70. doi: 10.1210/en.2012-1030
41. Ashida S, Nakagawa H, Katagiri T, Furihata M, Iiizumi M, Anazawa Y, et al. Molecular Features of the Transition From Prostatic Intraepithelial Neoplasia (PIN) to Prostate Cancer: Genome-Wide Gene-Expression Profiles of Prostate Cancers and PINs. *Cancer Res* (2004) 64:5963–72. doi: 10.1158/0008-5472.CAN-04-0020
42. Greene KE, Wright JR, Steinberg KP, Ruzinski JT, Caldwell E, Wong WB, et al. Serial Changes in Surfactant-Associated Proteins in Lung and Serum Before and After Onset of ARDS. *Am J Respir Crit Care Med* (1999) 160:1843–50. doi: 10.1164/ajrccm.160.6.9901117
43. Liu H, Jensen L, Hansen S, Petersen SV, Takahashi K, Ezekowitz AB, et al. Characterization and Quantification of Mouse Mannan-Binding Lectins (MBL-A and MBL-C) and Study of Acute Phase Responses. *Scand J Immunol* (2001) 53:489–97. doi: 10.1046/j.1365-3083.2001.00908.x
44. Lerman I, de la Luz Garcia-Hernandez M, Rangel-Moreno J, Chiriboga L, Pan C, Nastiuk KL, et al. Infiltrating Myeloid Cells Exert Protumourigenic Actions *via* Neutrophil Elastase. *Mol Cancer Res* (2017) 15:1138–52. doi: 10.1158/1541-7786.MCR-17-0003
45. Wen J, Huang G, Liu S, Wan J, Wang X, Zhu Y, et al. Polymorphonuclear MDSCs Are Enriched in the Stroma and Expanded in Metastases of Prostate Cancer. *J Pathol Clin Res* (2020) 6:171–7. doi: 10.1002/cjp2.160
46. Lerman I, Hammes SR. Neutrophil Elastase in the Tumour Microenvironment. *Steroids* (2018) 133:96–101. doi: 10.1016/j.steroids.2017.11.006

47. Altintas DM, Allioli N, Decaussin M, de Bernard S, Ruffion A, Samarut J, et al. Differentially Expressed Androgen-Regulated Genes in Androgen-Sensitive Tissues Reveal Potential Biomarkers of Early Prostate Cancer. *PLos One* (2013) 8:e66278. doi: 10.1371/journal.pone.0066278
48. Anker JF, Mok H, Naseem AF, Thumbikat P, Abdulkadir SA. A Bioluminescent and Fluorescent Orthotopic Syngeneic Murine Model of Androgen-Dependent and Castration-Resistant Prostate Cancer. *J Vis Exp* (2018) 133:57301. doi: 10.3791/57301
49. Lardizabal J, Ding J, Delwar Z, Rennie PS, Jia W. A TRAMP-Derived Orthotopic Prostate Syngeneic (TOPS) Cancer Model for Investigating Anti-Tumour Treatments. *Prostate* (2018) 78:457–68. doi: 10.1002/pros.23490
50. Jeet V, Ow K, Doherty E, Curley B, Russell PJ, Khatri A. Broadening of Transgenic Adenocarcinoma of the Mouse Prostate (TRAMP) Model to Represent Late Stage Androgen Depletion Independent Cancer. *Prostate* (2008) 68:548–62. doi: 10.1002/pros.20714
51. Wu C-T, Chen W-C, Chen M-F. The Response of Prostate Cancer to Androgen Deprivation and Irradiation Due to Immune Modulation. *Cancers (Basel)* (2018) 11:20. doi: 10.3390/cancers11010020
52. Ho A-S, Chen C-H, Cheng C-C, Wang C-C, Lin H-C, Luo T-Y, et al. Neutrophil Elastase as a Diagnostic Marker and Therapeutic Target in Colorectal Cancers. *Oncotarget* (2014) 5:473. doi: 10.18632/oncotarget.1631
53. Kepp O, Senovilla L, Vitale I, Vacchelli E, Adjemian S, Agostinis P, et al. Consensus Guidelines for the Detection of Immunogenic Cell Death. *Oncoimmunology* (2014) 3:e955691. doi: 10.4161/21624011.2014.955691
54. Colangelo T, Polcaro G, Ziccardi P, Muccillo L, Galgani M, Pucci B, et al. The miR-27a-Calreticulin Axis Affects Drug-Induced Immunogenic Cell Death in Human Colorectal Cancer Cells. *Cell Death Dis* (2016) 7:e2108–8. doi: 10.1038/cddis.2016.29
55. Yu Y, Tang D, Kang R. Oxidative Stress-Mediated HMGB1 Biology. *Front Physiol* (2015) 6:93. doi: 10.3389/fphys.2015.00093
56. Bharadwaj AG, Kovar JL, Loughman E, Elowsky C, Oakley GG, Simpson MA. Spontaneous Metastasis of Prostate Cancer Is Promoted by Excess Hyaluronan Synthesis and Processing. *Am J Pathol* (2009) 174:1027–36. doi: 10.2353/ajpath.2009.080501
57. Gomez CS, Gomez P, Knapp J, Jorda M, Soloway MS, Lokeshwar VB. Hyaluronic Acid and HYAL-1 in Prostate Biopsy Specimens: Predictors of Biochemical Recurrence. *J Urol* (2009) 182:1350–6. doi: 10.1016/j.juro.2009.06.070
58. Murugaiah V, Agostinis C, Varghese PM, Belmonte B, Vieni S, Alaql FA, et al. Hyaluronic Acid Present in the Tumour Microenvironment can Negate the Pro-Apototic Effect of a Recombinant Fragment of Human Surfactant Protein D on Breast Cancer Cells. *Front Immunol* (2020) 11:1171. doi: 10.3389/fimmu.2020.01171

Conflict of Interest: The authors declare that the research was conducted in the absence of any commercial or financial relationships that could be construed as a potential conflict of interest.

Publisher's Note: All claims expressed in this article are solely those of the authors and do not necessarily represent those of their affiliated organizations, or those of the publisher, the editors and the reviewers. Any product that may be evaluated in this article, or claim that may be made by its manufacturer, is not guaranteed or endorsed by the publisher.

frontiers | Frontiers in Immunology

ORIGINAL RESEARCH
published: 08 July 2022
doi: 10.3389/fimmu.2022.900022

Small Peptide Derivatives Within the Carbohydrate Recognition Domain of SP-A2 Modulate Asthma Outcomes in Mouse Models and Human Cells

Dave Francisco[1,2], Ying Wang[1,2], Craig Marshall[1], Michelle Conway[1], Kenneth J. Addison[2], Dean Billheimer[2], Hiroki Kimura[1,2], Mari Numata[3], Hong W. Chu[3], Dennis R. Voelker[3], Monica Kraft[1,2†] and Julie G. Ledford[2,4*†]*

[1] Department of Medicine, University of Arizona, Tucson, AZ, United States, [2] Asthma and Airway Disease Research Center, University of Arizona Health Sciences, Tucson, AZ, United States, [3] Department of Medicine, National Jewish Health, Denver, CO, United States, [4] Department of Cellular and Molecular Medicine, University of Arizona, Tucson, AZ, United States

Surfactant Protein-A (SP-A) is an innate immune modulator that regulates a variety of pulmonary host defense functions. We have shown that SP-A is dysfunctional in asthma, which could be partly due to genetic heterogeneity. In mouse models and primary bronchial epithelial cells from asthmatic participants, we evaluated the functional significance of a particular single nucleotide polymorphism of SP-A2, which results in an amino acid substitution at position 223 from glutamine (Q) to lysine (K) within the carbohydrate recognition domain (CRD). We found that SP-A 223Q humanized mice had greater protection from inflammation and mucin production after IL-13 exposure as compared to SP-A-2 223K mice. Likewise, asthmatic participants with two copies the major 223Q allele demonstrated better lung function and asthma control as compared to asthmatic participants with two copies of the minor SP-A 223K allele. In primary bronchial epithelial cells from asthmatic participants, full-length recombinant SP-A 223Q was more effective at reducing IL-13-induced MUC5AC gene expression compared to SP-A 223K. Given this activity, we developed 10 and 20 amino acid peptides of SP-A2 spanning position 223Q. We show that the SP-A 223Q peptides reduce eosinophilic inflammation, mucin production and airways hyperresponsiveness in a house dust mite model of asthma, protect from lung function decline during an IL-13 challenge model in mice, and decrease IL-13-induced MUC5AC gene expression in primary airway epithelial cells from asthmatic participants. These results suggest that position 223 within the CRD of SP-A2 may modulate several outcomes relevant to asthma, and that short peptides of SP-A2 retain anti-inflammatory properties similar to that of the endogenous protein.

Keywords: asthma, surfactant protein, SP-A, SP-A peptides, genetics

OPEN ACCESS

Edited by:
Taruna Madan, National Institute for Research in Reproductive Health (ICMR), India

Reviewed by:
Yusuke Murakami, Musashino University, Japan
Lakshna Mahajan, University of Delhi, India

***Correspondence:**
Julie G. Ledford
jledford@email.arizona.edu
Monica Kraft
kraftm@email.arizona.edu

†These authors have contributed equally to this work

Specialty section:
This article was submitted to Molecular Innate Immunity, a section of the journal Frontiers in Immunology

Received: *19 March 2022*
Accepted: *16 June 2022*
Published: *08 July 2022*

Citation:
Francisco D, Wang Y, Marshall C, Conway M, Addison KJ, Billheimer D, Kimura H, Numata M, Chu HW, Voelker DR, Kraft M and Ledford JG (2022) Small Peptide Derivatives Within the Carbohydrate Recognition Domain of SP-A2 Modulate Asthma Outcomes in Mouse Models and Human Cells. Front. Immunol. 13:900022. doi: 10.3389/fimmu.2022.900022

INTRODUCTION

Surfactant Protein A (SP-A) belongs to a class of macromolecules produced in the lung known as collectins and possesses host defense and innate immune properties (1). We have shown that SP-A also has specific anti-inflammatory properties relevant to asthma and can be dysfunctional or deficient (2, 3). Specifically, we have shown that SP-A derived from asthmatic participants is defective in reducing *Mycoplasma pneumoniae*-induced inflammation and mucin gene expression (2). From our group, Lugogo et al. showed that SP-A was significantly decreased in asthmatic participants who were obese and that this correlated with worse lung function and asthma status (3). Recently, we have shown that SP-A can mediate Interleukin (IL)-13 induced allergic inflammation in both *in vitro* primary human lung epithelial cells and *in vivo* mouse models (4).

SP-A is a hydrophilic calcium-dependent (C-type) lectin produced in the lung epithelium of the distal airways, club cells and mucosal cells (5). A complete SP-A protein consists of a trimeric assembly of two molecules, SP-A1 and SP-A2, which oligomerize into an octadecamer possessing six trimers (6). Although SP-A1 and SP-A2 share approximately 96% amino acid sequence homology, the latter is believed to be more biologically active (7, 8). Wang et al. demonstrated that asthmatic participants have higher levels of SP-A1/total SP-A compared to healthy individuals, suggesting a reduction in SP-A2 or dysfunction with this protein may correlate with increased disease pathogenesis (2).

A single monomer of SP-A2, encoded by the SFTPA2 gene, is 248 amino acids in length and structurally composed of 4 domains: an N terminal sequence, collagen-like domain, neck-region, and a carbohydrate recognition domain (CRD) (9). In particular, the CRD recognizes oligosaccharide motifs and encourages the binding and opsonization of pathogens. Allelic variations corresponding to the CRD of SP-A2 have been associated with several respiratory diseases including tuberculosis, allergic rhinitis, respiratory syncytial virus, and influenza (10).

We identified a single nucleotide polymorphism (SNP) of SP-A2 (rs1965708) present in some of our asthma patients, which results in an amino acid substitution at position 223 and replaces a glutamine (Q) for a lysine (K) in the CRD. Our studies show that asthmatic individuals who possess two copies of the minor SP-A 223K allele are more likely to have lower lung function and worse asthma control as compared to asthmatic participants with two copies of the major SP-A 223Q allele.

Furthermore, *ex vivo* studies using primary bronchial epithelial cells show that exogenous SP-A2 223Q reduces IL-13-induced mucin gene expression more effectively than the SP-A 223K protein. To gain further insight into the importance of the major allele, SP-A223 Q, 10 and 20 amino acid peptides containing this region of interest were developed and studied using *in vitro* primary human lung epithelial cells and *in vivo* mouse models of asthma. We demonstrate that these truncated peptides retain anti-inflammatory properties similar to that of the full-length endogenous SP-A protein and may have potential therapeutic benefits in asthma.

MATERIALS AND METHODS

Study Approvals

The Duke University and University of Arizona Institutional Review Boards (IRB) approved all protocols for recruitment of participants for these human studies. All animal experiments were carried out according to IACUC approved protocols at both Duke University and the University of Arizona.

Human Studies

Description of Research Participants

Participants were recruited from the population in Durham, North Carolina, Tucson, Arizona and their surrounding areas. Informed consent was obtained from each participant (18-65 years of age). Asthmatic participants met criteria for mild and moderate asthma per GINA guidelines (11), including the presence of reversibility of airflow obstruction or airways responsiveness with a provocative concentration of methacholine resulting in a 20% fall in FEV_1 (PC_{20} FEV_1) of ≤ 8mg/ml or < 16 mg/ml if they were taking inhaled corticosteroids. The presence of atopy was determined using skin testing and peripheral eosinophils and were measured in a subset of participants. Healthy participants had no evidence of airflow obstruction, and no history of pulmonary disease. Exclusion criteria included an exacerbation of asthma within four weeks of study requiring antibiotics and/or corticosteroids, greater than 10-pack year history of tobacco use or any cigarette use in the last year, and any other significant medical conditions.

Research Bronchoscopy and Cell Culture

Participants underwent bronchoscopy with endobronchial-protected brushing and bronchoalveolar lavage, as previously described (12). The brushing of the proximal airways to obtain bronchial epithelial cells was performed under direct visualization using a separate protected cytologic brush for each pass, for a total of eight passes. Bronchoalveolar lavage (BAL) was performed *via* instillation of warm sterile saline in 60-ml aliquots, with return *via* gentle hand suction, for a total of 300 ml. Participants were discharged when their FEV_1 achieved 90% of their pre-bronchoscopy, post-albuterol value. Freshly isolated airway bronchial epithelial cells from endobronchial brushing were cultured with BEGM (Lonza, Walkersville, MD) as previously described (12). Culture media contained the following supplements: Bovine pituitary extract, Insulin, Gentamycin-amphotericin, Retinoic Acid, Transferrin, Triiodothyronine, Epinephrine, and human Epidermal Growth Factor. After reaching confluence, cells were trypsinized and seeded onto collagen-coated polyester Transwell insert membranes of 12-mm diameter, at a concentration of 4×10^4/well. Then the cells were cultured at air–liquid interface for 2 weeks to allow for differentiation.

SP-A Preparation

SP-A was purified from the BAL fluid of patients with alveolar proteinosis that were seen at Duke University Medical Center and were under IRB approval using previously described methods (13). Extracted SP-A was passed over a polymyxin B-agarose column to

reduce endotoxin contamination and had final endotoxin concentrations of <0.01pg/mg SP-A as determined by the Limulus amoebocyte lysate assay [QCL-1000, BioWhittaker (Lonza)]. Recombinant SP-A was expressed in Freestyle HEK-293 cells and purified as previously described (14). This affinity purification procedure, which requires the C-type lectin activity of the protein be functional, ensures that the purified SP-A is properly folded. Small peptides were purchased from Genscript (Piscataway, NJ) and were received as lyophilized powder. All peptides were resuspended under sterile conditions in PCR-grade H_2O. Peptide purity was greater than 95% and preparations were tested to confirm they were endotoxin-free. The SP-A 20-mer peptide sequence: PAGRGKEQCVEMYTDGQWND; the SP-A 10-mer peptide sequence: KEQCVEMYTD.

Sequencing of hSP-A2 Gene

Genomic DNA was extracted from peripheral blood using a PAXgene Blood DNA kit (Qiagen) according to manufacturer's instructions. The region of interest containing SP-A2 coding sequence was assessed through allelic discrimination using TaqMan™ probes labeled with either HEX (encoding 223Q) or FAM (encoding 223K).

SP-A Binding Assay

Plates were coated with 100 ng/well of rIL-13 in PBS and placed at 4°C overnight. Wells were blocked with 5% non-fat milk in PBS/1% Triton X-100 for 2 hrs at 37°C after which purified samples of SP-A (1 mg/ml) were added in blocking buffer and incubated for an additional 2 hrs at 37°C. The plate was washed 5 times with PBS/1% Triton X-100 and HRP conjugated anti-human SP-A was added (1:2000) in blocking buffer for 1 hr at 37°C, after which the plate was washed an additional 5 times as described above. Finally, orthophenylene diamine substrate was added for 5 min, after which stop solution was added and samples were assessed using an ELISA plate reader at absorbance of 490 nm.

Western Analysis of STAT Activation

Human bronchial epithelial cells were grown on transwell inserts at an air-liquid interface for two weeks prior to experimentation. Some wells received chronic IL-13 challenge (10 ng/ml each day for 5 days on the apical surface) in the presence of absence of SP-A (20 μg/ml, 30 min prior to IL-13 on the apical surface). For collection of human epithelial cells or mouse lungs, radioimmunoprecipitation assay (RIPA) buffer (Millipore) with protease inhibitors (Roche) were added to each sample for cell lysis or tissue homogenization. Each sample was homogenized, sonicated, and insoluble material was removed by centrifugation. The protein concentration of each lysate was determined by BCA and an equal amount of lysate was loaded onto electrophoretic gels for each sample to be analyzed by Western. Antibodies for phospho-Stat3, Stat3 and β-actin were all used according to manufacturer's (Cell Signaling) recommendations and analyzed in the order listed respectively for each blot.

Statistical Analysis

For human data analysis, associations between SPA2 SNP rs1965708 and asthma status were evaluated using Fisher's exact test, and separately, logistic regression with the number of "A" alleles as an explanatory variable. Lung function measurements (FEV_1, FVC, and FEV_1/FVC ratio), blood cell types (eosinophils, neutrophils) and BAL cell types (macrophages, eosinophils, neutrophils, epithelial cells) were evaluated using linear models with asthma status and SPA2 SNP genotype as categorical explanatory variables. Because no non-asthmatic participants with AA genotype have blood or BAL cell type data, these comparisons combined the heterozygote AC and homozygote AA SPA2 genotypes into a single category. Analysis of variance was used to assess asthma and SPA2 SNP factors, as well as their interaction. Tukey's HSD is used for pairwise comparisons. Note that Tukey's procedure accounts for all pairwise comparisons within a single analysis in computing p-values. P-values less than 0.05 were considered statistically significant, but no adjustment was made for testing the multiple related outcomes in these exploratory clinical data. Airways hyperresponsiveness, as measured by the provocative concentration of methacholine resulting in a 20% fall in FEV1 (PC20 FEV1) was compared between the AC and CC asthmatic groups using Student's t test of the logPC20 FEV1.

MUC5AC expression fold-change, relative to control, was computed for IL-13 alone, IL-13 + AA10, and IL-13 + AA20. We used log10 transformed data to reduce skewness, and a linear mixed model for statistical analysis. The mixed model extends the usual analysis of variance model to reflect the ALI intra-subject treatments with IL-13 + SP-A peptides, and the inter-subject asthma vs. control groups. Inference proceeded hierarchically, first requiring main effects or interactions be significant ($p < 0.05$) before proceeding to *post hoc* comparisons. Tukey's honestly significant difference was used for pairwise comparison of groups with a significance level of 0.05.

Mouse Studies

Description of Mice

SP-A humanized transgenic mice were generated as previously described (15). SP-$A^{-/-}$ mice on C57BL/6 background (16) were bred in-house and wild-type (WT) mice were purchased from Jackson Laboratories (Bar Harbor, ME) and bred in house for experiments. Age-matched (approximately 6-8 weeks) male mice were used for experiments since they have more robust methacholine sensitivity for lung function measurements compared to female mice. Mice were anesthetized under inhaled isoflurane and given 3.9 μg of recombinant IL-13 (Peprotech) in 50 μl of sterile saline *via* oropharyngeal delivery (17). At the desired time point, mice were euthanized and the lungs lavaged with PBS (0.1 mM EDTA) and lung tissue was obtained for further analysis. Differential cell counts were analyzed from the lavage fluid after H&E staining. Viability was assessed by Trypan blue exclusion.

House Dust-Mite Model

The common allergic airway model was used in which 6-8 weeks old C57BL/6 male mice were sensitized and challenged with 100 μg house-dust mite extract (HDM; prepared from dry

weight, Greer) over the course of three intranasal instillations while under isoflurane anesthesia. Mice received either vehicle, SP-A 10-mer or 20-mer peptides 24 hrs after HDM challenge *via* oropharyngeal delivery while under isofluorane anesthesia.

On the day of pulmonary function testing (PFT), mice were anesthetized with urethane (Sigma, U2500) prepared at a concentration of 125 mg/ml in sterile dH2O and dosed at 16 µl/gram of body weight intraperitoneally (ip). Once a surgical plane of anesthesia is reached, the trachea was cannulated with a 19-gauge metal cannula using previously described methods (18, 19). Mice were connected to a commercial computer-controlled piston-ventilator (flexiVent, SCIREQ Inc., Montreal, Qc, Canada) for mechanical ventilation and PFTs (19). Pancuronium bromide (0.8 mg/ml in saline, Sigma P1918) was administered to the anesthetized mouse *via* ip injection at a volume of 10 µl/gram of body weight to prevent any interference from the subject during the PFTs. Following an equilibration period under default mechanical ventilation settings (150 breaths/min, tidal volume of 10 ml/kg, and a PEEP of 3 cmH_2O), two recruitment maneuvers (inflation to a standard pressure of 30 cmH_2O over a 3 second and holding for an additional 3 seconds) were performed to open and close lung areas and to standardize lung volume history. Methacholine challenges were carried out as previously described (20). Mice that were not subject to PFTs were euthanized and the lung lavaged with PBS (0.1 mM EDTA) and lung tissue was obtained for further analysis. Differential cells counts were analyzed from the lavage fluid after H&E staining. Viability was assessed by Trypan blue exclusion.

RT-PCR

Mouse tissues and human bronchial epithelial cells were collected into 1 ml of TRI Reagent® (Sigma). RNA was isolated using the standard TRI reagent/chloroform extraction method. DNA was synthesized from 1 µg of total RNA using Bio-Rad™ cDNA Synthesis kit. Real-time polymerase chain reaction (RT-PCR) was performed using Bioline 2x SensiFAST SYBR no-ROX mix. The samples were analyzed for expression levels of mouse MUC5AC using forward and reverse primers specific to the gene (forward 5' GAG GGC CCA GTG AGC ATC TCC 3', reverse 5' TGG GAC AGC AGC AGT ATT CAG T 3'). The relative levels of expression obtained were normalized to the mammalian housekeeper gene Cyclophilin using primers specific to the gene (forward 5' AGC ACT GGA GAG AAA GGA TTT GG 3', reverse 5' TCT TCT TGC TGG TCT TGC CAT T 3'). For human bronchial epithelial cells, each condition is compared to its unexposed negative control after standardization to the housekeeper gene, GAPDH.

Histological Analysis

Mice were euthanized by CO_2 asphyxiation. Left lung lobes were dissected and immersed in 10% buffered formalin for fixation. After 3 days, the lung lobes were transferred from formalin to 70% ethanol, then routinely processed and paraffin embedded for PAS staining to assess for mucin production. Stained sections were scored blinded according to standard methods (21).

Statistical Analysis

For murine experiments, analyses were performed using Graph Pad Prism and Student's t-Test or one-way ANOVA, as necessary. F-test was used to compare variances between data analyzed and Welch's correction applied if variances were significantly different ($p<0.05$) between groups statistical significance was defined as a p-value < 0.05.

RESULTS

Humans: Genetic Variation in SP-A2 is Associated With Changes in Lung Function

Seventy-five participants with mild-moderate asthma (FEV_1: 87 ± 2% predicted), and sixty-eight non-asthmatic participants (FEV_1: 100 ± 2% predicted) underwent blood sampling for gene sequencing of the SP-A2 gene (**Table 1**). By Fisher's exact test, the SP-A2 SNP associated with asthma status ($p=0.023$), with the "A" allele (Lysine/K at position 223) associated with greater odds of disease. Logistic regression with number of "A" as a factor indicates increasing odds of disease (ChiSq=7.5, df=2, $p=0.023$) with the minor allele. While there is an association of the minor allele and asthma status, there does not appear to be an association with increased reported disease severity ($p=0.65$).

In addition, there is an association between SP-A2 SNP, asthma status and lung function (FEV_1%, FVC% and FEV_1/FVC ratio). This effect may be modified with combined modeling of subjects' SP-A2 SNP and asthma status. FEV_1 (% predicted) is associated with both asthma status ($p<0.001$) and SP-A2 SNP ($p=0.003$), with a possible interaction ($p=0.16$). Pairwise group comparisons indicated that among asthmatics, the AA genotype (encodes for 223K/K) exhibits reduced FEV_1 (% predicted) with an approximately 16% reduction compared with CC (223Q/Q, $p=0.057$) and AC ($p=0.002$), respectively. Among non-asthmatics, significant differences in lung function are not demonstrated between genotypes. FVC (% predicted) is associated with both asthma status ($p<0.003$) and SP-A2 SNP ($p=0.003$), with a possible interaction ($p=0.08$). Pairwise group comparisons indicated that among asthmatics, the AA genotype exhibits reduced FVC (about 17%) compared with CC ($p=0.021$) and AC ($p=0.003$), respectively. Among non-asthmatics, strong differences are not indicated. The FEV_1/FVC ratio is associated with asthma status ($p<0.001$), but not with the SP-A2 SNP. The ratios average 0.07 lower for participants with asthma as compared to non-asthma. Within the group who underwent bronchoscopy (**Table 2**), the methacholine PC20 FEV1 was significantly lower in the AC asthma group compared to CC asthma group, suggesting greater hyperresponsiveness in the AC asthmatic group ($p=0.03$)

A subset of the SP-A2 genotyped asthmatic participants was further analyzed for inflammatory cells in the peripheral blood. Due to the relatively small number of homozygous 223K individuals carrying the minor allele AA which translates to the amino acids KK, participants carrying one (223Q/K) or two

TABLE 1 | Demographics for patients undergoing asthma phenotyping and blood genotyping for SP-A2.

rs1965708 SFTPA2	AA		AC		CC	
	Asthma	Normal	Asthma	Normal	Asthma	Normal
Asthma/Normal	8	1	35	30	32	37
Males**	3	0	11	8	11	12
Females**	5	1	24	21	21	25
White	1	0	17	14	21	24
Black	5	1	16	14	8	10
Hispanic	0	0	0	0	2	1
Asian	2	0	2	2	1	2
Age*	36 ± 5.2	28	30 ± 1.6	31 ± 1.9	29 ± 2	29 ± 1.5
FEV1 (%)*	72.62 ± 3.4†	109	91.17 ± 2.2†	101.89 ± 2.6	87.77 ± 2.2	99.75 ± 1.9
FVC (%)*	81.62 ± 3.7¥	117	99.5 ± 2.2¥	105.92 ± 3.1	98.83 ± 1.6¥	101.55 ± 2.0
FEV1/FVC (%)*	73.37 ± 1.9	80	75.62 ± 1.5	81.82 ± 1.3	75.09 ± 1.5	83.61 ± 1.1
PC20 (mg/ml)*	0.63 ± 0.35	16	1.23 ± 0.3	16.34 ± 0.3	0.91 ± 0.2	16
ACQ*	2.82 ± 0.2	N/A	1.19 ± 0.2	N/A	1.59 ± 0.1	N/A
Exacerbations per year*	1	N/A	1.14 ± 0.1	N/A	0.75 ± 5	N/A
Atopy (% positive)	75	0	93	37	84	47
Total Peripheral Eosinophils	N/A	N/A	1.78 x 10^10 ± 1	8.37 x 10^9 ± 0.8	3.25 X 10^9 ± 1.3	1.9^10^9 ± 0.4
Total Peripheral Neutrophils	N/A	N/A	2.58 x 10^11 ± 0.5	3.27 x 10^11 ± 0.5	6.29 X 10^10 ± 0.3	5.02 x 10^10 ± 0.5
Medications						
Short acting beta agonist	7	N/A	33	N/A	29	N/A
Leukotriene modifier	2	N/A	2	N/A	3	N/A
Inhaled corticosteroid (ICS)	1	N/A	3	N/A	2	N/A
Antihistamine	3	N/A	10	N/A	11	N/A
Combination therapy (ICS/LABA)	3	N/A	5	N/A	5	N/A
Short acting anticholinergic	1	N/A	N/A	N/A	N/A	N/A

**Mean ± SE; **One participant did not specify gender.*
†p = 0.002 AA < AC; ¥ p< 0.05; AA < AC and CC.
N/A, not applicable.

TABLE 2 | Demographics for patients that underwent bronchoscopy for analysis of bronchial epithelial cells.

rs1965708 SFTPA2	AC		CC	
	Asthma	Normal	Asthma	Normal
Asthma/Normal	4	4	7	5
Males	3	1	1	2
Females	1	3	6	3
White	0	2	4	3
Black	4	2	2	2
Hispanic	0	0	0	0
Asian	0	0	1	0
Age*	24 ± 2.3	35 ± 6.1	26 ± 2.2	30 ± 1.4
FEV1 (%)	90.5 ± 6.0	100.8 ± 9.0	88.3 ± 4.2	101.5 ± 2.4
FVC (%)	99.5 ± 6.0	99.75 ± 8.3	101.3 ± 3.0	100 ± 2.5
FEV1/FVC (%)	77.0 ± 3.4	83.0 ± 1.6	74.4 ± 2.7	84.3 ± 2.6
PC20 (mg/ml)	0.5 ± 0.2†	N/A	1.8 ± 0.4†	N/A
ACQ	1.5 ± 0.2	N/A	1.3 ± 0.1	N/A
Exacerbations per year	1.5 ± 0.5	N/A	1	N/A
Atopy (% positive)	100	25	83	60
Total Eosinophils	2.7 x 10^10 ± 1.5	9 x 10^9 ± 3.9	2.5 x 10^10 ± 1	N/A
Total Neutrophils	3.5 x 10^11 ± .48	4.5 x 10^11 ± 1.5	2.9 x 10^11 ± .3	N/A
Medications				
Short acting beta agonist	4	N/A	7	N/A
Leukotriene modifier	N/A	N/A	N/A	N/A
Inhaled corticosteroid (ICS)	N/A	N/A	N/A	N/A
Antihistamine	N/A	N/A	3	N/A
Combination therapy (ICS/LABA)	N/A	N/A	1	N/A
Short acting anticholinergic	N/A	N/A	N/A	N/A

**Mean ± SE; †Significant p<0.05.*
N/A, not applicable.

copies (223K/K) of the minor allele were grouped for analysis. Blood eosinophils were increased in participants with asthma (p=0.002), but no significant association was observed in our cohort for blood neutrophils. There was no significant association between the SP-A2 SNP and blood eosinophils or neutrophils.

Mice: SP-A2 Genetic Variation Influences Protection Against IL-13

In order to determine the consequence of SP-A2 223Q and 223K variations *in vivo*, we examined the response to IL-13 challenge in humanized SP-A2 transgenic mice. These mice are devoid of mouse SP-A and express either the human version of SP-A2 223Q or SP-A 223K at similar RNA gene expression and protein levels, as described previously (15). There were no gross differences in the humanized SP-A transgenic mice prior to challenge and saline treated controls had similar levels of BAL cells across all genotypes of mice examined which consisted of >95% macrophages (**Figure S1**).

When challenged with IL-13, there were significantly more total cells in BAL of SP-A$^{-/-}$ mice as compared to WT mice (**Figure 1A**), which was contributed by increases in macrophages, neutrophils and eosinophils (**Figures 1B–D**). However, mice that were homozygous for human 223Q had significantly decreased total BAL cells (**Figure 1A**) as compared to SP-A$^{-/-}$ mice; the differential counts were not significantly different from WT mice (**Figures 1B–D**). In contrast, mice homozygous for 223K, had less protection as defined by total cells in BAL when compared to SP-A$^{-/-}$ mice and 223Q/Q mice.

After IL-13 challenge, the 223Q-expressing mice had significantly less mucin production as compared to SP-A$^{-/-}$ mice and were similar to WT mice (**Figures 1E, F**). There were no differences in mucin production in the saline control mice across the different genotypes (data not shown). Since we had previously determined that SP-A regulated Stat3 phosphorylation in response to IL-13 (4), we next wanted to assess whether there were differences in Stat3 phosphorylation in the lung tissue of the humanized mice challenged with IL-13. As shown in **Figures 1F, G**, there was significantly more Stat3 phosphorylation in lungs from IL-13 challenged 223K mice as compared to WT mice. There was no discernable difference in Stat3 phosphorylation when comparing 223Q mice to WT mice.

Humans: SP-A2 Genetic Variation Modulates Protection Against IL-13 in Epithelial Cells

Previously, we have shown that SP-A extracted from participants with mild asthma is dysfunctional in the immune regulation of pathogens (2). One possibility for defective function of SP-A in asthma is genetic variation in the setting of type 2 inflammation. Since our clinical data showed an association between the SP-A2 SNP, asthma status and lung function, we further tested the ability of two SP-A recombinant genetic variants (full-length containing either 223Q or 223K) to suppress inflammation to IL-13 *ex vivo*. We used an affinity purification procedure, which requires the C-type lectin activity of the protein be functional, thus ensuring that we are purifying properly folded and active forms of SP-A. We observed minimal responses from IL-13 challenged cells derived from normal participants (**Figure 2A**). However, IL-13 challenged bronchial epithelial cells from a separate cohort of asthmatic participants (see **Table 2** for demographics) resulted in an approximately 30-fold increase in MUC5AC when the cells were exposed over the course of 5 days. When co-cultured with recombinant SP-A2 223Q at a physiologic concentration (20 μg/ml), MUC5AC expression was significantly attenuated in the IL-13 challenged/exposed cells derived from asthmatic participants (p=0.029), whereas the SP-A2 223K variant was not as effective (p=0.157) (**Figure 2A**). Further examination of common variants in SP-A2 at position 223 revealed that variants 223Q and 223K, which had different effects against MUC5AC, bound to IL-13 similarly (**Figure 2B**) suggesting the function of SP-A2 is independent of binding to IL-13.

Mice: Development and *In Vivo* Testing of SP-A Peptides on Inflammation in an Asthma Model

The use of house dust-mite is a well-established model of allergic airways disease in mice that is known to induce recruitment of eosinophils, mucin production and enhance airways hyperresponsiveness. To test the SP-A 20-mer and 10-mer peptides on inflammation associated with allergic airways disease, SP-A deficient mice were challenged with HDM on days 0, 7 and 14 as described in **Figure 3A**. At day 15, when inflammation is at a maximum, 1 dose of SP-A peptides (20-mer or 10-mer, both containing Q from site 223) or vehicle were delivered. The timing of this model and dosing were based on our previous study in which full-length SP-A was given at the peak of eosinophils (24 hrs after the last challenge) and eosinophils assessed in BAL 4 days later (22). Eosinophils and mucin production were examined four days after peptide therapy as an indicator of inflammation. As demonstrated in **Figure 3B**, both the 20-mer and the 10-mer resulted in significantly decreased eosinophils in the BAL as compared to the vehicle treated control. There were no eosinophils detected in the BAL of control non-HDM challenged mice that received vehicle (**Figure S1**). In addition, treatment with either the 20-mer or the 10-mer led to significanlty reduced mucin production as detected in PAS stained lung histology (**Figures 3C, D**). There were no differences in mucin production in the non-HDM challenged mice that received vehicle or SP-A peptides (not shown).

Mice: *In Vivo* Testing of SP-A Peptides on Airway Hyperresponsiveness in an Asthma Model

In another set of experiments, pulmonary function tests (PFTs) during methacholine challenge were carried out in WT male mice and we chose to use the 10-mer peptide since we anticipate the smaller peptides will be easier to deliver with the use of inhalers in future drug development models. For these studies, mice were challenged with HDM on days 0, 7 and 14 as described in **Figure 4A**. Twenty four hours after each HDM challenge, mice received either vehicle or SP-A peptides (10-mer). We

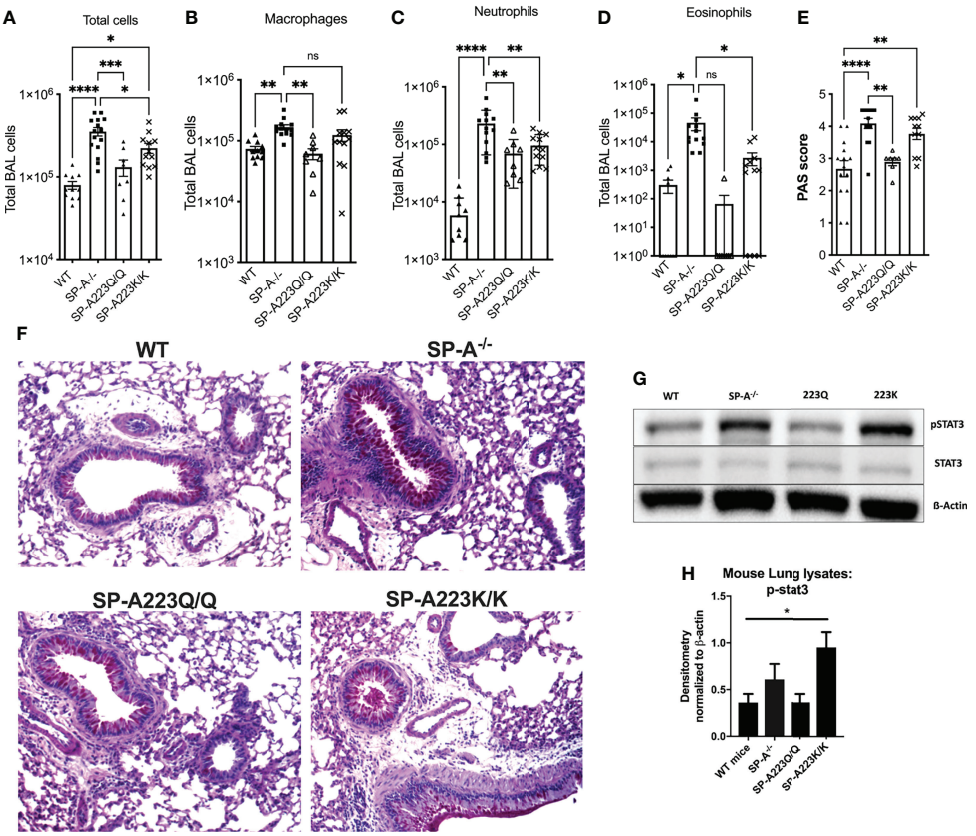

FIGURE 1 | Genetic variation in SP-A2 determines extent of protection against IL-13 induced inflammation in humanized SP-A transgenic mice. BAL cells from **(A)** IL-13 challenged mice, which consisted of and **(B)** macrophages, **(C)** neutrophils and **(D)** eosinophils. **(E)** PAS scored lung histology from IL-13 challenged mice. N=12 WT; 15 SP-A$^{-/-}$; 8 SP-A223Q/Q; 12 SP-A223K/K per group from 3 separate experimental repeats. *p < 0.05, **p < 0.01, ***p < 0.001. ****p < 0.0001 by One-way Anova with Dunnett's test for multiple comparisons. **(F)** Representative PAS images of each genotype treated with IL-13. **(G, H)** Stat3 phosphorylation by Western blot and densitometry from representative lung samples; *p<0.05 by One-Way Anova with Tukey's multiple comparisons.

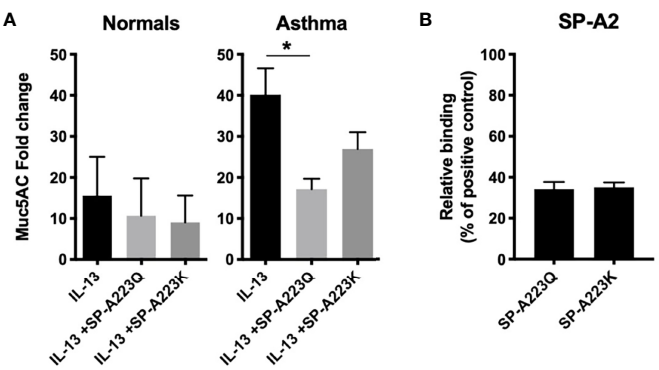

FIGURE 2 | Genetic variation in SP-A2 determines extent of protection against IL-13-induced inflammation from bronchial epithelial cells from asthmatic participants. **(A)** MUC5AC RNA expression from bronchial epithelial cells (n=3 normal, n=3 asthma) grown at ALI and treated with IL-13 for 5 days in the presence of absence of full-length recombinant SP-A2(223K) (20 μg/ml) or SP-A2(223Q) (20 μg/ml) that were added 30 min prior to challenge. After standardization to the housekeeper gene, data are displayed as fold relative to the non-IL-13 challenged control for each respective patient set, with the standard deviation shown. Average fold change and standard deviation are displayed. *p < 0.05. **(B)** Genetic variants of SP-A2 that differ only at position 223 (Q and K) were examined for relative binding to IL-13 relative to extracted human oligomeric control SP-A.

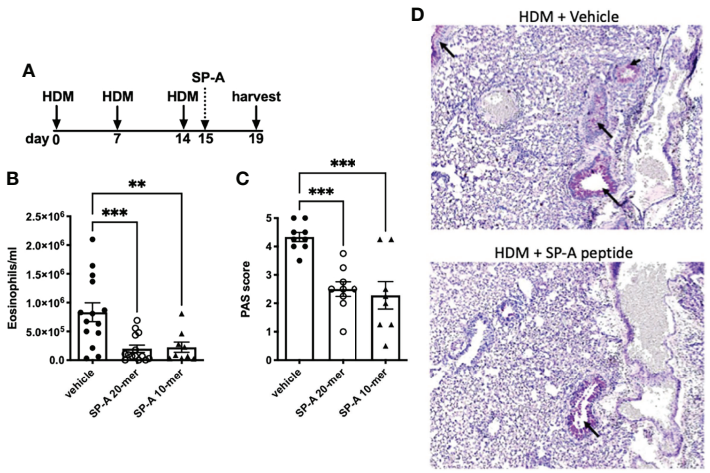

FIGURE 3 | HDM-challenged SP-A deficient mice treated with SP-A peptides have reduced hallmarks of inflammation. **(A)** SP-A deficient mice challenged intra-nasally with HDM on days 0, 7, and 14. On day 15 mice were divided into groups and given either vehicle or SP-A peptides (10-mer or 20-mer) *via* oropharyngeal instillation at 25 μg/ml concentration (~1 mg/kg body weight). On day 19, mice were sacrificed and **(B)** eosinophils in the BAL and **(C)** mucin production in **(D)** lung histological sections were assessed. n = 10,10, **p < 0.01, ***p < 0.001 by One-way Anova for multiple comparisons.

chose to deliver a dose of our test peptides after each HDM challenge in order to assess their impact on overall lung function and not merely clearance of eosinophils, which are but one of several contributors to the asthma phenotype. PFTs were assessed four days after the last SP-A treatment. HDM provoked an elevated response to methacholine compared to the negative control saline treated mice (**Figure S1**). The resistance of the respiratory system (R_{rs}), which reflects the overall airflow resistance at the breathing frequency, was significantly decreased in the SP-A peptide treatment group as compared to vehicle control group (**Figure 4B**). This measurement includes a contribution from the conducting and peripheral airways, the tissue, and the chest wall. In addition, the Newtonian resistance (R_n), which is dominated by the resistance of the large conducting airways not involved in gas exchange, was also significantly reduced in the peptide treated group as compared to the vehicle treated group (**Figure 4C**).

The respiratory system elastance (E_{rs}), which quantifies the overall stiffness of the entire respiratory system during tidal breathing was also significantly reduced at the highest doses of methacholine challenge in the peptide treated group as compared to the vehicle treated group (**Figure 4D**). Finally, tissue damping (G), which reflects a measure of the amount of energy that is lost within the tissues as a result of friction and includes resistance to air flow in the peripheral airways, was significantly reduced at the highest doses of methacholine challenge in the peptide treated group as compared to the vehicle treated group (**Figure 4E**).

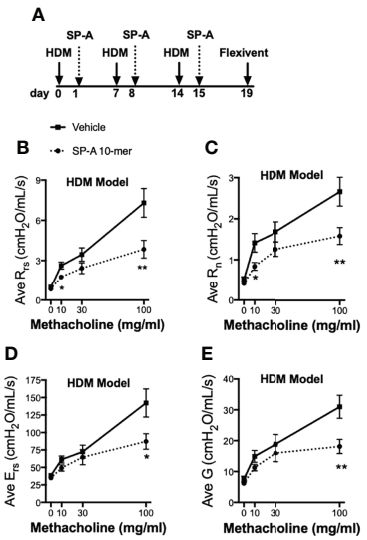

FIGURE 4 | HDM-challenged WT mice treated with SP-A peptides have reduced sensitivity to methacholine challenge. **(A)** WT male mice challenged intra-nasally with HDM on days 0, 7, and 14. On days 1, 8 and 15 mice were divided into groups and given either vehicle or SP-A peptides (10-mer, 25 μg/ml, ~1 mg/kg body weight) *via* oropharyngeal instillation. On day 19, pulmonary function tests during a methacholine challenge were performed while mice were under anesthesia. **(B)** Total airways resistance (Rrs), **(C)** Newtonian resistance (Rn), **(D)** total airways Elastance (Ers) and **(E)** tissue damping **(G)** were assessed by flexivent. Data graphed are mean +/- SEM. n = 12,12, *p < 0.05, **p < 0.01 by t-test at each indicated dose.

Mice: *In Vivo* Testing of SP-A Peptides on Pulmonary Function During Non-allergic IL-13 Challenge

In order to test whether the SP-A 10-mer was effective in a non-allergic model of asthma, we tested the SP-A peptides (10-mer) in the IL-13 challenge model. For this, WT male mice were challenged with vehicle or IL-13 by oropharyngeal delivery for 3

consecutive days. Two hours after each IL-13 challenge, mice received either vehicle (saline) or SP-A 10-mer peptide (25 μg) also *via* oropharyngeal delivery. Pulmonary function tests were conducted on day 4 on a Flexivent machine (SCIREQ) with the negative pressure-driven forced expiration (NPFE) extension. Since IL-13 is such a strong inducer of lung function decline by non-allergic mechanisms, a methacholine challenge was not necessary to determine the effectiveness of SP-A peptides in this model. As shown in **Figure 5**, IL-13 challenge resulted in significantly increased Newtonian resistance (Rn) and decreased forced expiratory volumes (FEV) at 0.05, 0.1 and 0.2 seconds. Treatment with SP-A 10-mer peptide led to significant protection against IL-13-induced increase in Rn and decreases in FEV across all time points assessed.

Humans: Small SP-A 20-mer Peptide Attenuates IL-13 Induced MUC5AC in Epithelial Cells From Asthma

Since our findings in asthmatic participants as well as mouse models indicated that SP-A2 expressing glutamine at position 223 was active in reducing type 2 inflammation, we sought to determine if our small peptides encompassing the 223 area of interest have activity in human cells from asthmatic participants. Based on our previous findings with 20 amino acid peptides spanning this region, we tested the 20-mer containing a glutamine at position 223 with surrounding amino acids identical to those in endogenous SP-A (23) and also a shortened 10-mer version. Bronchial epithelial cells obtained from normal and asthmatic participants were exposed to IL-13 in the presence of SP-A 20-mer, 10-mer or vehicle and assessed for MUC5AC by RT-PCR. Assessment of treatment (vehicle vs SP-A-mer) was done for the same set of patient cells and graphically displayed as a fold change over their respective control, which is the level of MUC5AC in a non-challenged control set of wells. As shown in **Figure 6**, MUC5AC gene expression was significantly reduced in asthmatic and normal participants with SP-A 20-mer treatment as compared to IL-13 with vehicle (p=0.004).

DISCUSSION

We recently published that SP-A decreases mucin secretion and inflammation in response to IL-13 challenge using a combination of SP-A deficient mice and primary human airway epithelial cells from participant with and without asthma (4). In mice lacking SP-A, we demonstrated that IL-13 significantly increased airway neutrophil and eosinophil recruitment and mucin production compared to WT mice. Likewise, phenotypes observed in human primary cells grown at an ALI and exposed to IL-13 were significantly reduced when SP-A was administered alongside IL-13 (4). Mechanistically, we showed that SP-A modulated IL-13-induced inflammation *via* mediating downstream IL-6/Stat3 signaling. While we have previously shown that SP-A demonstrates anti-inflammatory effects relevant to asthma, our new findings suggest there is genetic heterogeneity in these functions.

In this report, we first identified a polymorphism at position 223 of the CRD of SP-A2 peptide as relevant to asthma based upon human SP-A2 gene sequencing. Participants with two copies of the SNP rs1965708, which results in a substitution of a glutamine for a lysine at position 223 of SP-A2 peptide, were more likely to have lower lung function and worse asthma control, as discussed in the results section. To further investigate the functional significance of this SNP, we bred

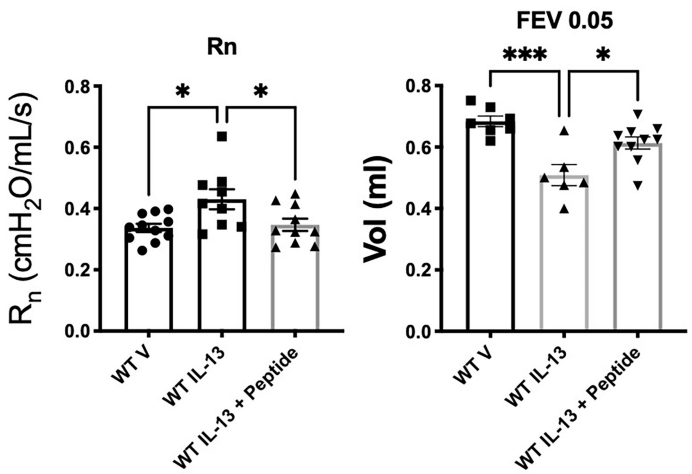

FIGURE 5 | IL-13-challenged mice treated with SP-A 10-mer peptide have improved lung function. WT male mice were challenged with vehicle (saline) or IL-13 (3.9 μg) by oropharyngeal delivery for 3 consecutive days. Two hours after each IL-13 challenge, mice received either vehicle (saline) or SP-A 10-mer peptide (25 μg/ml; ~1mg/kg body weight) *via* oropharyngeal delivery. Pulmonary function tests were conducted on day 4 on a flexiVent machine (SCIREQ) with the negative pressure-driven forced expiration (NPFE) extension. IL-13 challenge resulted in significantly increased Newtonian resistance (Rn) and decreased forced expiratory volumes (FEV) at 0.05 seconds. Treatment with SP-A 10-mer peptide protected against IL-13 induced increase in Rn and decreases in FEV. Average mean +/- SEM is graphed, n= as shown from 2 independent experiments. *p < 0.05, ***p < 0.001 by ANOVA for multiple comparisons.

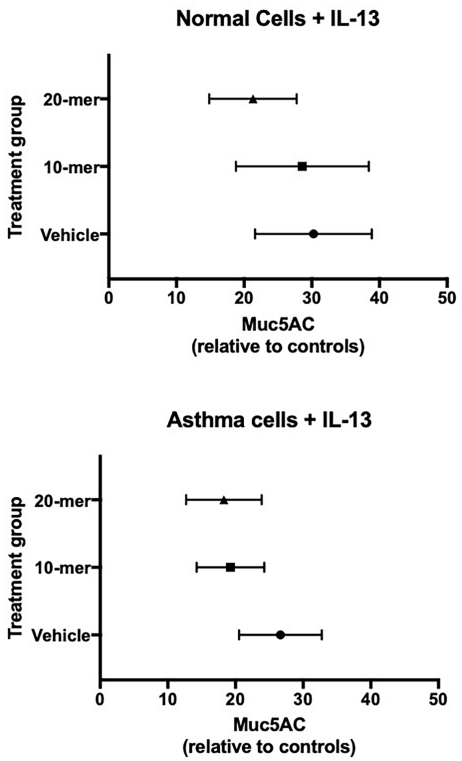

FIGURE 6 | Primary human lung epithelial cells treated with SP-A peptides have reduced IL-13 induced MUC5AC gene expression. Primary human bronchial epithelial cells derived from normal and asthmatic participants were incubated for 30 minutes with either 20-mer or 10-mer SP-A peptide (20 µg/ml) before stimulation with IL-13 (10 ng/ml) for 5 days. When taken together (asthma and normal cells), MUC5AC gene expression was significantly reduced in the SP-A 20-mer treatment group compared with IL-13 alone (p=0.004).

mice to express two copies of the major or minor allele of this SNP (15). Similar to what we observed in humans, the mice expressing two copies of the minor allele where a glutamine (Q/Q) was substituted for a lysine (K/K), these mice were not as protected from IL-13 challenge with increased inflammation compared to the mice expressing two copies of the major allele (Q/Q).

Recognizing the importance surrounding this amino acid change, we created 10- and 20-mer SP-A2 peptides that included position 223 from the CRD in order to determine if replacement of SP-A with a functional variant would modulate endpoints relevant to asthma. We chose this particular region of the CRD based on our findings in asthma patients as described above and based on our studies in which full-length SP-A that contains the Q at position 223 was able to induce eosinophil apoptosis, which was CRD-dependent, while SP-A containing K at position 223 was not active in this function, as we reported previously (22). Here we report that the CRD-containing peptides that included Q at position 223 were effective at reducing inflammation in SP-A deficient during HDM challenge, reducing AHR in WT mice following HDM challenge, and protecting from lung function decline in WT mice following a high dose IL-13 challenge. Lastly, we also show that the Q variant is more effective than the K variant at inhibiting Stat3 phosphorylation in SP-A deficient mice challenged with IL-13, suggesting a possible mechanism of action of the SP-A peptides.

Reports over the last decade have linked SP-A and asthma. Pastva and colleagues showed in 2011 that SP-A deficient mice sensitized and challenged with OVA manifested a robust type 2 inflammatory response with increased airway eosinophils, interleukin-4, 5 and IgE (24). Our group showed that SP-A extracted from bronchoalveolar lavage (BAL) from participants with asthma ineffectively reduced inflammation due to *M. pneumoniae* infection of airway epithelial cells compared to SP-A extracted from participants without asthma (2). Additionally, we reported that SP-A levels in BAL are reduced in asthmatic participants who are obese, and this reduction correlated with BMI and asthma status (3). These data, coupled with our recent report demonstrating inhibition of Stat3 phosphorylation by SP-A as a potential mechanism suggest that SP-A exhibits immune modulatory effects in asthma. We report here that the effects are not uniform across all genotypes of SP-A as K at position 223 of SP-A2 results in reduced phosphorylation of Stat3 as compared to the Q variant. These observations have allowed creation of a construct that replacement of SP-A with the more effective variant may be a possible treatment for asthma.

Our report has several limitations. It is certainly possible that other variants of SP-A1 and 2 may also exhibit immune modulatory effects in diseases such asthma. We chose to study the SP-A2 variant with an amino acid substitution at position 223 based upon genotyping of a relatively small cohort of asthmatic participants with type 2 asthma. We did not compare peptide 223Q to 223K as we focused our 10 and 20-mer peptide experiments on the use of 223Q based upon our full-length SP-A and humanized mouse model data showing efficacy. Additionally, we acknowledge that our SP-A replacement/rescue experimental data may be slightly more compelling than the data from transgenic mice, which may be due to concentrations delivered to the source of inflammation given that we can give higher doses of peptides as opposed to the endogenous levels of SP-A that are expressed in the mice. Third, at this early time in development, we do not know the stability and half-life of our peptides in these model systems, which will be the focus of future studies. Finally, we also realize that inhibition of Stat3, as reported here and in our recent publication (4), may be one of many mechanisms, as SP-A is also known to exhibit immune modulatory functions in macrophages, eosinophils, mast cells and dendritic cells (21, 25, 26).

In summary, we report that SP-A exhibits genetic heterogeneity of function in models of HDM and IL-13 exposure. Using mouse models and primary human lung epithelial cells, a particular region of SP-A2 that includes position 223 has efficacy regarding inhibition of airway inflammation, MUC5AC gene expression and mucin production. Additionally, we provide evidence that our SP-A-derived peptides reduce one of the key features of asthma, a

reduction in bronchoconstriction to methacholine challenge, in two mouse models. We have evidence that SP-A does this through interactions on two key cell types: eosinophils and epithelial cells. SP-A induces eosinophil apoptosis which is in line with the reduced eosinophilia detected in the peptide treated mice in the HDM model (22). Furthermore, SP-A works through a newly discovered receptor on eosinophils for this activity, MYADM, which may also be the therapeutic target for the peptides in the HDM model (27). SP-A works directly on epithelial cells to reduce STAT-3 signaling, which may also be true of the SP-A peptides, however additional testing is needed (4). A reduction in STAT-3 signaling leads to less inflammatory cytokine production and less mucus- key features we observe with our peptide treatment. While the effect of these SP-A2 peptides in the setting of oropharyngeal delivery of IL-13 and HDM and cellular exposure of IL-13 are interesting, more work is needed to determine if SP-A peptides delivered by aerosol are a viable therapeutic strategy for human disease.

DATA AVAILABILITY STATEMENT

The raw data supporting the conclusions of this article will be made available by the authors, without undue reservation.

ETHICS STATEMENT

The studies involving human participants were reviewed and approved by Institutional Review Board at the University of Arizona. The patients/participants provided their written informed consent to participate in this study. The animal study was reviewed and approved by Institutional Animal Care and Use Committee at the University of Arizona.

AUTHOR CONTRIBUTIONS

DF, YW, CM, MC, KA performed experiments. DB and HK performed statistical analysis. MN, HC, DV provided reagents and helped with data interpretation. DF, YW, MK and JL conceived of experiments. DF, MK and JL wrote the manuscript. All authors reviewed the manuscript.

FUNDING

This work was funded by NIH grants from NHLBI and NIAID and from the Arizona Biomedical Research Commission. HL125602 (Ledford), AI135935 (Ledford), AI125357 (Kraft, Voelker, Chu) and ADHS16-162519 (Kraft).

SUPPLEMENTARY MATERIAL

The Supplementary Material for this article can be found online at: https://www.frontiersin.org/articles/10.3389/fimmu.2022.900022/full#supplementary-material

Supplementary Figure 1 | C57BL/6 negative controls. **(A)** BAL analysis for IL-13 model of all genotypes, **(B)** BAL analysis for HDM model, **(C)** lung function of WT males to methacholine challenge.

Supplementary Figure 2 | Full Western blots for Stat3. Representative Western blot analysis of p-Stat3, Stat3 and b-actin.

REFERENCES

1. Casals C, Campanero-Rhodes MA, Garcia-Fojeda B, Solis D. The Role of Collectins and Galectins in Lung Innate Immune Defense. *Front Immunol* (2018) 9:1998. doi: 10.3389/fimmu.2018.01998
2. Wang Y, Voelker DR, Lugogo NL, Wang G, Floros J, Ingram JL, et al. Surfactant Protein A is Defective in Abrogating Inflammation in Asthma. *Am J Physiol Lung Cell Mol Physiol* (2011) 301(4):L598–606. doi: 10.1152/ajplung.00381.2010
3. Lugogo N, Francisco D, Addison KJ, Manne A, Pederson W, Ingram JL, et al. Obese Asthmatic Patients Have Decreased Surfactant Protein A Levels: Mechanisms and Implications. *J Allergy Clin Immunol* (2018) 141(3):918–26.e3. doi: 10.1016/j.jaci.2017.05.028
4. Francisco D, Wang Y, Conway M, Hurbon AN, Dy ABC, Addison KJ, et al. Surfactant Protein-A Protects Against IL-13-Induced Inflammation in Asthma. *J Immunol* (2020) 204(10):2829–39. doi: 10.4049/jimmunol.1901227
5. Auten RL, Watkins RH, Shapiro DL, Horowitz S, Surfactant apoprotein A. (SP-A) Is Synthesized in Airway Cells. *Am J Respir Cell Mol Biol* (1990) 3 (5):491–6. doi: 10.1165/ajrcmb/3.5.491
6. Sano H, Kuroki Y. The Lung Collectins, SP-A and SP-D, Modulate Pulmonary Innate Immunity. *Mol Immunol* (2005) 42(3):279–87. doi: 10.1016/j.molimm.2004.07.014
7. Mikerov AN, Umstead TM, Huang W, Liu W, Phelps DS, Floros J. SP-A1 and SP-A2 Variants Differentially Enhance Association of Pseudomonas Aeruginosa With Rat Alveolar Macrophages. *Am J Physiol Lung Cell Mol Physiol* (2005) 288(1):L150–8. doi: 10.1152/ajplung.00135.2004
8. Wang G, Umstead TM, Hu S, Mikerov AN, Phelps DS, Floros J. Differential Effects of Human SP-A1 and SP-A2 on the BAL Proteome and Signaling Pathways in Response to Klebsiella Pneumoniae and Ozone Exposure. *Front Immunol* (2019) 10:561. doi: 10.3389/fimmu.2019.00561
9. Kishore U, Greenhough TJ, Waters P, Shrive AK, Ghai R, Kamran MF, et al. Surfactant Proteins SP-A and SP-D: Structure, Function and Receptors. *Mol Immunol* (2006) 43(9):1293–315. doi: 10.1016/j.molimm.2005.08.004
10. Silveyra P, Floros J. Genetic Variant Associations of Human SP-A and SP-D With Acute and Chronic Lung Injury. *Front Biosci (Landmark Ed)* (2012) 17:407–29. doi: 10.2741/3935
11. GINA. *Global Initiative for Asthma*. (2020). Available at: https://ginasthma.org/gina-reports/.
12. Kraft M, Adler KB, Ingram JL, Crews AL, Atkinson TP, Cairns CB, et al. Mycoplasma Pneumoniae Induces Airway Epithelial Cell Expression of MUC5AC in Asthma. *Eur Respir J* (2008) 31(1):43–6. doi: 10.1183/09031936.00103307
13. McIntosh JC, Mervin-Blake S, Conner E, Wright JR. Surfactant Protein A Protects Growing Cells and Reduces TNF-Alpha Activity From LPS-Stimulated Macrophages. *Am J Physiol* (1996) 271(2 Pt 1):L310–9. doi: 10.1152/ajplung.1996.271.2.L310
14. Foster MW, Thompson JW, Ledford JG, Dubois LG, Hollingsworth JW, Francisco D, et al. Identification and Quantitation of Coding Variants and Isoforms of Pulmonary Surfactant Protein a. *J Proteome Res* (2014) 13(8):3722–32. doi: 10.1021/pr500307f
15. Ledford JG, Voelker DR, Addison KJ, Wang Y, Nikam VS, Degan S, et al. Genetic Variation in SP-A2 Leads to Differential Binding to Mycoplasma

Pneumoniae Membranes and Regulation of Host Responses. *J Immunol* (2015) 194(12):6123–32. doi: 10.4049/jimmunol.1500104
16. Korfhagen TR, Bruno MD, Ross GF, Huelsman KM, Ikegami M, Jobe AH, et al. Altered Surfactant Function and Structure in SP-A Gene Targeted Mice. *Proc Natl Acad Sci U S A* (1996) 93(18):9594–9. doi: 10.1073/pnas.93.18.9594
17. Hollingsworth JW, Theriot BS, Li Z, Lawson BL, Sunday M, Schwartz DA, et al. Both Hematopoietic-Derived and Non-Hematopoietic-Derived {Beta}-Arrestin-2 Regulates Murine Allergic Airway Disease. *Am J Respir Cell Mol Biol* (2010) 43(3):269–75. doi: 10.1165/rcmb.2009-0198OC
18. Hartney JM, Robichaud A. Assessment of Airway Hyperresponsiveness in Mouse Models of Allergic Lung Disease Using Detailed Measurements of Respiratory Mechanics. *Methods Mol Biol* (2013) 1032:205–17. doi: 10.1007/978-1-62703-496-8_16
19. McGovern TK, Robichaud A, Fereydoonzad L, Schuessler TF, Martin JG. Evaluation of Respiratory System Mechanics in Mice Using the Forced Oscillation Technique. *J Vis Exp* (2013) 75):e50172. doi: 10.3791/50172
20. Addison KJ, Morse J, Robichaud A, Daines MO, Ledford JG. A Novel *In Vivo* System to Test Bronchodilators. *J Infect Pulm Dis* (2017) 3(1):1–5. doi: 10.16966/2470-3176.120
21. Ledford JG, Mukherjee S, Kislan MM, Nugent JL, Hollingsworth JW, Wright JR. Surfactant Protein-A Suppresses Eosinophil-Mediated Killing of Mycoplasma Pneumoniae in Allergic Lungs. *PloS One* (2012) 7(2):e32436. doi: 10.1371/journal.pone.0032436
22. Dy ABC, Arif MZ, Addison KJ, Que LG, Boitano S, Kraft M, et al. Genetic Variation in Surfactant Protein-A2 Delays Resolution of Eosinophilia in Asthma. *J Immunol* (2019) 203(5):1122–30. doi: 10.4049/jimmunol.1900546
23. Younis US, Chu HW, Kraft M, Ledford JG. A 20-Mer Peptide Derived From the Lectin Domain of SP-A2 Decreases Tumor Necrosis Factor Alpha Production During Mycoplasma Pneumoniae Infection. *Infect Immun* (2020) 88(9):99–106. doi: 10.1128/IAI.00099-20
24. Pastva AM, Mukherjee S, Giamberardino C, Hsia B, Lo B, Sempowski GD, et al. Lung Effector Memory and Activated CD4+ T Cells Display Enhanced Proliferation in Surfactant Protein A-Deficient Mice During Allergen-Mediated Inflammation. *J Immunol* (2011) 186(5):2842–9. doi: 10.4049/jimmunol.0904190
25. Ledford JG, Lo B, Kislan MM, Thomas JM, Evans K, Cain DW, et al. Surfactant Protein-A Inhibits Mycoplasma-Induced Dendritic Cell Maturation Through Regulation of HMGB-1 Cytokine Activity. *J Immunol* (2010) 185(7):3884–94. doi: 10.4049/jimmunol.1000387
26. Ledford JG, Pastva AM, Wright JR. Review: Collectins Link Innate and Adaptive Immunity in Allergic Airway Disease. *Innate Immunity* (2010) 16(3):183–90. doi: 10.1177/1753425910368446
27. Dy ABC, Langlais PR, Barker NK, Addison KJ, Tanyaratsrisakul S, Boitano S, et al. Myeloid-Associated Differentiation Marker Is a Novel SP-A-Associated Transmembrane Protein Whose Expression on Airway Epithelial Cells Correlates With Asthma Severity. *Sci Rep* (2021) 11(1):23392. doi: 10.1038/s41598-021-02869-w

Conflict of Interest: Authors JL and MK are co-founders of RaeSedo Inc, a start-up company with the goal of developing novel peptidomimetic based therapeutics derived from an active area of SP-A.

The remaining authors declare that the research was conducted in the absence of any commercial or financial relationships that could be construed as a potential conflict of interest.

Publisher's Note: All claims expressed in this article are solely those of the authors and do not necessarily represent those of their affiliated organizations, or those of the publisher, the editors and the reviewers. Any product that may be evaluated in this article, or claim that may be made by its manufacturer, is not guaranteed or endorsed by the publisher.

frontiers | Frontiers in Immunology

ORIGINAL RESEARCH
published: 12 July 2022
doi: 10.3389/fimmu.2022.922956

Hydrophilic But Not Hydrophobic Surfactant Protein Genetic Variants Are Associated With Severe Acute Respiratory Syncytial Virus Infection in Children

Lynnlee C. Depicolzuane[1], Catherine M. Roberts[1], Neal J. Thomas[1], Keenan Anderson-Fears[2], Dajiang Liu[2], João Paulo Pereira Barbosa[3], Felipe Rodrigues Souza[3], André Silva Pimentel[3], Joanna Floros[1,4] and Chintan K. Gandhi[1]**

[1] Center for Host defense, Inflammation, and Lung Disease (CHILD) Research, Department of Pediatrics, The Pennsylvania State College of Medicine, Hershey, PA, United States, [2] Department of Public Health Science, The Pennsylvania State College of Medicine, Hershey, PA, United States, [3] Departamento de Química, Pontifícia Universidade Católica do Rio de Janeiro, Rio de Janeiro, Brazil, [4] Department of Obstetrics & Gynecology, The Pennsylvania State College of Medicine, Hershey, PA, United States

OPEN ACCESS

Edited by:
Taruna Madan,
National Institute for Research in Reproductive Health (ICMR), India

Reviewed by:
Masoumeh Tavakoli-Yaraki,
Iran University of Medical Sciences, Iran
Karen Bohmwald,
Pontificia Universidad Católica de Chile, Chile

***Correspondence:**
Joanna Floros
jfloros@pennstatehealth.psu.edu
Chintan K. Gandhi
cgandhi@penntatehealth.psu.edu

Specialty section:
This article was submitted to Molecular Innate Immunity, a section of the journal Frontiers in Immunology

Received: 18 April 2022
Accepted: 07 June 2022
Published: 12 July 2022

Citation:
Depicolzuane LC, Roberts CM, Thomas NJ, Anderson-Fears K, Liu D, Barbosa JPP, Souza FR, Pimentel AS, Floros J and Gandhi CK (2022) Hydrophilic But Not Hydrophobic Surfactant Protein Genetic Variants Are Associated With Severe Acute Respiratory Syncytial Virus Infection in Children. Front. Immunol. 13:922956. doi: 10.3389/fimmu.2022.922956

Respiratory syncytial virus (RSV) is the leading cause of lower respiratory tract infection-related hospitalization in the first year of life. Surfactant dysfunction is central to pathophysiologic mechanisms of various pulmonary diseases including RSV. We hypothesized that RSV severity is associated with single nucleotide polymorphisms (SNPs) of surfactant proteins (SPs). We prospectively enrolled 405 RSV-positive children and divided them into moderate and severe RSV disease. DNA was extracted and genotyped for sixteen specific SP gene SNPs. SP-A1 and A2 haplotypes were assigned. The association of RSV severity with SP gene SNPs was investigated by multivariate logistic regression. A likelihood ratio test was used to test the goodness of fit between two models (one with clinical and demographic data alone and another that included genetic variants). $p \leq 0.05$ denotes statistical significance. A molecular dynamics simulation was done to determine the impact of the *SFTPA2* rs1965708 on the SP-A behavior under various conditions. Infants with severe disease were more likely to be younger, of lower weight, and exposed to household pets and smoking, as well as having co-infection on admission. A decreased risk of severe RSV was associated with the rs17886395_C of the *SFTPA2* and rs2243639_A of the *SFTPD*, whereas an increased risk was associated with the rs1059047_C of the *SFTPA1*. RSV severity was not associated with SNPs of *SFTPB* and *SFTPC*. An increased risk of severe RSV was associated with the $1A^0$ genotype of *SFTPA2* in its homozygous or heterozygous form with $1A^3$. A molecular dynamic simulation study of SP-A variants that differ in amino acid 223, an important amino acid change (Q223K) between $1A^0$ and $1A^3$, showed no major impact on the behavior of these two variants except for higher thermodynamic stability of

the K223 variant. The likelihood ratio test showed that the model with multi-allelic variants along with clinical and demographic data was a better fit to predict RSV severity. In summary, RSV severity was associated with hydrophilic (but not with hydrophobic) SPs gene variants. Collectively, our findings show that SP gene variants may play a key role in RSV infection and have a potential role in prognostication.

Keywords: respiratory sycytial virus, surfacant protein genetic variant, single nucelotide polymorphisms, SFTPA1, SFTPA2, SFTPB, SFTPC, SFTPD

INTRODUCTION

Respiratory syncytial virus (RSV) is a major burden to the health of children worldwide. It is the leading cause of lower respiratory tract infection and hospitalization in the first year of life in developed countries (1–5). In the United States, it is the most common viral cause of death in children under 5 years of age. While nearly all children are infected with RSV by 2 years of age, only 2-3% of these need hospitalization and of the hospitalized children, 5-10% require mechanical ventilation (2). In a small subset of infants, the risk of death from RSV is as high as 1% even in developed countries (5). Currently, there is no vaccine available for the prevention of RSV infection. Passive immunization is given using anti-RSV monoclonal antibody prophylactically only to high-risk children; for example, to those, who are born extremely premature (<29 weeks), with certain types of congenital heart diseases, chronic lung disease, and certain immunologic disorders (6).

RSV has a heterogeneous presentation and interactions, among virus, host, and environmental factors, all of which have been implicated in affecting RSV disease severity (7). Though environmental factors, sex, and socioeconomic status play a role in the severity of RSV, the underlying mechanisms of this wide spectrum of contributing factors, have not yet been understood. A study of > 12,000 twins showed that genetic factors contributed approximately 20% in determining RSV severity (8) and multiple genetic studies have shown RSV bronchiolitis–associated loci in genes encoding proteins such as surfactant proteins, toll-like receptors, Vitamin D receptor, and various cytokines (9, 10). Thus, genetic variability may partially explain the individual disease susceptibility to RSV infection.

Pulmonary surfactant, a lipoprotein complex, is essential for normal lung function. It prevents alveolar collapse at low lung volumes by lowering the surface tension at the alveolar air-liquid surface. Its components, and especially the surfactant proteins, play important roles both in surfactant-related functions and in innate immune host defense of the lung. In general, the hydrophobic surfactant proteins (SP-B and SP-C) play important roles in surfactant function and structure, and the hydrophilic surfactant proteins (SP-A and SP-D) in innate immunity, as well as in surfactant function (SP-A) (11–16). Because of the diverse functions of the surfactant proteins, any derangement in their structure, function, and/or composition could lead to the development of a wide variety of pulmonary disorders.

Human SP-A is encoded by two functional genes, *SFTPA1* and *SFTPA2* (16, 17), and several genetic polymorphisms are found frequently in the general population (16, 18–21). SP-B, SP-C, and SP-D are each encoded by a single gene, *SFTPB, SFTPC*, and *SFTPD*, respectively (22), and several polymorphisms have been described for each (23–26). Moreover, SP genetic polymorphisms have been shown to associate with RSV (27–30), as well as other pulmonary diseases, such as neonatal respiratory distress syndrome (RDS) (31–35), cystic fibrosis (CF) (36), chronic obstructive pulmonary disease (COPD) (37, 38), acute respiratory distress syndrome (ARDS) (23), hypersensitivity pneumonitis (39, 40), pediatric acute respiratory failure (ARF) (41), and persistent respiratory morbidity in pediatric ARF survivors (42). However, the majority of previous RSV association studies with SP genetic variants were case-control in design, comparing RSV-infected children with healthy children without RSV infection (27, 28, 30, 43). Predicting which infants are at risk of developing RSV infection is less important because virtually all infants are at risk. Hence, in the current study, we took the unique approach of enrolling only RSV-infected children, regardless of their risk factors, and categorizing them by their disease severity to study associations of severe RSV infection with SP genetic variants.

We hypothesized that severe RSV infection is associated with natural SP genetic variants and such associations, in addition to clinical demographic information, may help to identify at-risk children for severe RSV. We further hypothesized that the genetic variation of two significant SP-A haplotypes has an impact on the molecular dynamics of SP-A protein.

MATERIALS AND METHODS

Subjects: We prospectively enrolled and collected blood samples from 416 children (ages between 7 days and 3 years old) admitted with a diagnosis of RSV infection at two academic children's hospitals, Penn State Health Children's Hospital and the University of Virginia Children's Hospital, during three consecutive winters. The diagnosis of RSV was made by either direct fluorescent assay or viral culture of nasopharyngeal swabs. Clinical data were extracted from their medical records, including demographics, risk factors for RSV infection, history of parental smoking, pet exposure, length of stay, and co-infections.

For this study, severe RSV was defined *a priori* as the need for admission to the intensive care unit with or without mechanical

ventilation. Children admitted to the general pediatric ward were considered as having moderate RSV infection. In the current study, 171 (42%) and 234 (58%) children were diagnosed with moderate and severe RSV disease, respectively. We observed 32 (out of 171) and 123 (out of 234) cases of co-infection in moderate and severe RSV groups, respectively. Out of the 32 cases of co-infection in the moderate RSV group, 8 cases were of otitis media, 9 were with clinical and radiographic pneumonia of unknown bacterial etiology, 2 cases of each Streptococcus pneumoniae and staphylococcus aureus pneumonia, 3 cases of influenza, 2 cases of sinus infection, 1 case of each adenovirus, Moraxella catarrhalis, group b streptococcus urinary tract infection, Hemophilus influenzae bacteremia, coagulase-negative staphylococcus bacteremia, and clostridium difficile. Out of the 123 cases of co-infection in the severe RSV group, the majority of them were due to bacterial infection, n=112 (Hemophilus influenzae = 31, Moraxella catarrhalis = 27, Streptococcus pneumoniae = 22, Staphylococcus aureus = 16, Klebsiella pneumoniae = 4, Escherichia coli = 3, Bordetella pertussis = 2, Enterobacter cloacae = 2, coagulase-negative staphylococcus =2, Pseudomonas aeruginosa = 1, Neisseria meningitidis = 1, Serratia marcescens = 1); 5 cases were each of viral (influenza = 2, 1 case each of adenovirus, rhinovirus, and parainfluenza) and fungal infections (candida albicans = 5) and 1 case of otitis media. The majority of the co-infections were due to a wide variety of bacteria; hence, we have clumped them together and adjusted them as a co-infection covariate.

For statistical analysis purposes, children with severe and moderate RSV infection were considered as cases and controls, respectively. The protocol to collect human samples in this study was approved by the Human Subjects Protection Office of The Pennsylvania State University College of Medicine and the Institutional Review Board for Health Sciences Research at The University of Virginia, and informed consent was obtained from each parent or guardian.

DNA Isolation

The samples received from the participating sites, were numbered sequentially upon arrival with no other identifiers. DNA extraction and genotyping, each was performed in a blinded fashion to reduce any potential bias. A total of 416 children were enrolled for the current study, however, eleven subjects were excluded from analysis due to lack of genotyping information secondary to degradation of the original sample quality, leaving the final sample size of 405 subjects.

Genomic DNA was extracted from blood samples using QIAamp Blood kit (Qiagen, Valencia, CA USA) following the manufacturer's instructions as described earlier (19).

Selection of Genetic Variants

A total of 16 target SNPs of SP genes, *SFTPA1*, *SFTPA2*, *SFTPB*, *SFTPC*, and *SFTPD* were selected that included, 5 SNPs from *SFTPA1*, rs1059047, rs1136450, rs1136451, rs1059057, and rs4253527; 4 SNPs from *SFTPA2*, rs1059046, rs17886395, rs1965707, and 1965708; 3 SNPs from *SFTPB*, rs2077079, rs3024798, and rs1130866; 2 SNPs from *SFTPC*, rs4715 and rs1124; and 2 SNPs from *SFTPD*, rs721917 and rs2243639. Several acute and chronic pulmonary diseases of all age groups, such as, neonatal RDS (31–35), CF (36), COPD (37, 38), ARDS (23), hypersensitivity pneumonitis (39, 40), pediatric ARF (41), and persistent respiratory morbidity in pediatric ARF survivors (42) have been shown to be associated with the studied SNPs. The SP-A1 (6A, $6A^m$, m=0-13) and SP-A2 (1A, $1A^n$, n=0-15) genotypes were assigned as described (19).

Genotype Analysis

We used polymerase chain reaction-restriction fragment length polymorphism (PCR-RFLP), as described earlier (19), to analyze *SFTPA1*, *SFTPA2*, *SFTPD* (19, 23), *SFTPB* (23, 36), and *SFTPC* (44) gene polymorphisms. The PCR primer sequences and restriction enzymes used are given in **Supplementary Table 1** and the detailed method is described elsewhere (36). This method was used for genotyping of approximately half of the samples. The other half of the samples were processed using a multiplexed polymerase chain reaction workflow of Ampliseq utilizing custom designed panels from Illumina, (Illumina, San Diego, CA) (**Supplementary Table 2**). The library was prepared according to manufacturer's instructions. All reagents for the library preparation were from Illumina, San Diego, CA, unless specified otherwise. Briefly, 20 nanograms of DNA (in low EDTA TE buffer solution, 10 mM Tris-HCl +1 mM EDTA, pH 7.0) were used and mixed with 4.5 µl of ampliseq Hi-fi mix (Illumina, San Diego, CA) and 2 µl of custom primer design panels to a final volume of 20 µl (**Supplementary Table 2**). PCR was performed at 99°C for 2 min, 21 cycles of 99°C for 15 seconds, and 60°C for 8 minutes (instead of 4 minutes recommended in manufacturer's instructions) to optimize amplification of the studied genes. Next, we used 2 µl of the FuPa Reagent (Illumina, San Diego, CA) to digest primer dimers and amplicons. The library prep was vortexed and then centrifuged briefly at 280 x g for 10 seconds. The following volumes of reagents were added in the order listed to each sample (switch solution - 4 µl, unique index adapters for each sample - 2 µl, and DNA ligase – 2 µl) to the 22 µl of amplicons to make the final volume of 30 µl to ligate the index adapters. The ligation program was performed at 22°C for 30 minutes, 68°C for 5 minutes, and then at 72°C for 5 minutes. Libraries were cleaned up using AMPure XP beads per manufacturer's instructions (Beckman Coulter, CA, USA) and amplified a second time after adding 1X Lib Amp Mix (45 µl) and 10X Library Amp primers (5 µl) at 98°C for 2 min, 7 cycles of 98°C for 15 seconds, 64°C for 1 minute. The second cleanup of libraries was done using AMPure XP beads as noted above and sequenced at the Penn State College of Medicine Genome Sciences Facility (Hershey, PA). SNPs, rs1059047, rs1136450, rs2243639, were not included in the final analysis because it was challenging to make appropriate calls with the sequencing method.

Statistical Analysis

We used descriptive statistics to define the study population and a t-test to compare the two groups (moderate vs severe). For the genetic analysis, we used a total of 5 dummy variables to represent the six ancestral covariates, i.e. Hispanic, Black, Asian, others (Hawaiian and Pacific Islanders), and Mixed. The sixth ancestral category, White, was used as the baseline (0,0,0,0,0). Using these encodings as well as additional covariates of sex, age, smoking exposure, pet

exposure, and co-infection, logistic regression models were constructed for each of the 16 SNPs using PLINK 2.0. Additional models, both logistic regression (PLINK 2.0) and associations (PLINK 1.9), were constructed *via* variation of the covariates as well as including additional interaction and dominant/recessive features.

Given that certain SNPs were in linkage disequilibrium, permutation tests were used to correct for the multiple comparisons. In each permutation, we shuffled the phenotype so that the connections between the phenotype and the genetic variants are broken and a null distribution can be generated. A regression model is then run on each permuted dataset in the same way it is used to analyze the original dataset. The minimal p-value of all tested SNPs in each permuted dataset forms an empirical distribution, which is used to determine the corrected p-value after controlling for the family-wise error rate. The corrected p-value for each SNP is determined by:

$$corrected\ P-value = (\#\ of\ Permuted\ minimal\ P-values > Original\ P-value)/(\text{Total \# of Permutatations})$$

Odds ratios (OR) were calculated for the tested SNPs to determine whether variants were associated with risk (> 1) or protection (< 1). To test the 42 genotypes of multi-allelic variants of SP-A1 and SP-A2 i.e., $1A/1A^0$, $6A/6A^2$, etc, a multivariate logistic model was used including all covariates previously described, following our published approach for analyzing multi-allelic variants in genetic association studies (45). A likelihood ratio test (LRT) was used to compare models of clinical demographic data only and clinical demographic data with genotype information to determine if the multi-allelic variants are associated. Analysis was performed using the R framework, with regression models using both PLINK 2.0 for individual SNP tests and the stats package for multi-allelic models and PLINK 1.9 for individual SNP association tests. The lmtest package was used for likelihood ratio test.

Software Versions:
PLINK – 1.9 & 2.0
R (stats package included) – 4.0.2
Readxl – 1.3.1
Dplyr – 1.0.4
Tidyr – 1.1.2
biomaRt – 2.44.4
forcats – 0.5.1
Biobase – 2.48.0
lmtest – 0.9-48
data.table – 1.14.0
kableExtra – 1.3.4

Molecular Modeling of Human SP-A

Next, we studied the impact of rs1965708 on the molecular dynamics of SP-A. This SNP changes a glutamine (Q) to lysine (K) at amino acid position 223 of SP-A2. The rationale for studying this particular SNP is based on the following: a) a previous association of RSV with the *SFTPA2* rs1965708 has been observed (43); b) in the current study an association of RSV severity with SP-A2 protein variants was observed, as assessed by the logistic regression analysis (see results below); and c) the location of the rs1965708 SNP is in the SP-A C-terminal carbohydrate recognition domain (CRD), a region shown to bind carbohydrates on the surface of pathogens in a calcium-dependent manner to enable neutralization and clearance of pathogens including RSV (16, 46).

The three-dimensional structure of human SP-A is not available in any database, and one way to solve this problem is to apply comparative/homology modeling. This modeling is based on identifying the three-dimensional structure of known proteins that resemble the structure of the query sequence, producing an alignment between the amino acids of the known structure and the amino acid sequence of the desired structure (47, 48). To obtain the three-dimensional structure of human SP-A, we used as a template, the crystallographic structure of *Rattus norvegicus* SP-A, obtained from the protein data bank (49), code 5FFT (50) with a resolution of 2.20 Å. We obtained the SP-A three-dimensional structure through the Swiss-Model server (48, 51–54), and compared and verified the possible structural errors using the SPDB Viewer (55).

The SP-A variants investigated in the present study consisted of amino acids 104-244 and as such, these variants enabled the study of the amino acid change of interest at residue 223. The variation occurring at the amino acid Q223 was studied by using the PyMOL software by Schrödinger Inc. Applying the mutagenesis tool, we chose the conformation of amino acid K223. The molecular dynamics (MD) simulations of the SP-A K223 and the Q223 variants followed the same protocol and these simulations are described below. One of the smaller SP-A oligomers is a trimer, consisting of three monomer subunits, two SP-A1 and one SP-A2 monomers, i.e., a hetero-oligomer (56) or a homo-trimer consisting of three monomers of either SP-A1 or SP-A2 as shown by electrophoresis under non-denaturing conditions (57, 58). All the gene-specific differences are found in the collagen-like domain of SP-A, specifically at amino acid positions 66, 73, 81, 85 (16, 20, 21). Because the structural information of the first 100 amino acid residues of SP-A is not available in any database, we focused our attention on residues 104-244 to perform MD simulations, as this region contains the amino acid change at position 223 encoded by the rs1965708. An SP-A trimer was created using three identical monomers. The MD simulations mentioned below were performed once with each trimer but we analyzed the data of the three monomers separately in order to study the behavior of each SP-A trimer under various conditions.

MD simulations were performed applying the bonded and non-bonded parameters for the all-atom force field, OPLS-AA (59). The tri-dimensional coordinates and topology of the protein were generated by pdb2gmx, which is part of the GROMACS 2019 package (60–63), and used in this work to perform all MD simulations.

Protein and calcium were placed in an octahedron-shaped box, with a volume of 1393 nm^3 and filled with 43602 water molecules of the TIP4P model (64–66). Periodic boundary conditions were applied on all axes of the box (67). The system was submitted to the minimization step applying the steepest descent algorithm with the convergence criterion of 100.00 $kJ.mol^{-1}.nm^{-1}$ or 20000 steps. The equilibration of pressure and temperature was achieved with a time of 100 picoseconds (ps) following a two-step through the simulation. Towards this we used: (i) the canonical ensemble (NVT) (68), keeping the number of particles, volume, and temperature constant, and (ii) the isothermal-isobaric ensemble (NpT) (69), keeping the number of particles, pressure, and temperature constant. After the equilibration step, the systems were submitted to a production step of 50 nanosecond (ns). All MD simulations were performed at 310 K and 1 bar, using 2 fs of integration time with the lists of pairs being updated at every 5 steps. The cut-off for Lennard Jones and Coulomb interactions was between 0 and 1.2 nm. The leap-frog algorithm was used in the production step with the Nose-Hoover thermostat (70) (τ = 0.5 ps) at 310 K and the Parrinello-Rahman barostat (68) (τ = 2.0 ps) at 1 bar. All Arg and Lys residues were assigned with positive charges and all Glu and Asp residues were assigned with negative charges. The Visual Molecular Dynamics (71) software were used to visualize the simulation trajectories.

We analyzed the root-mean-square deviation (RMSD), the root-mean-square fluctuation (RMSF), the radius of gyration, hydrogen bond, Dictionary of Secondary Structure of Proteins (DSSP), and principal component analysis (PCA), to assess the conformational influence of the Q223/K223 on SP-A behavior. The RMSD is calculated from the comparison of the overlap of two structures, one of which is taken as a reference (72). For example, in our work, each structure from the molecular dynamic trajectory was compared to the initial structure. The RMSF calculates the fluctuation of each atom of each amino acid from its average position, indicating the flexibility of the amino acids throughout the simulation. The radius of gyration of a protein is the measure of the stability of protein folding. If a protein is stably folded, it will likely maintain a relatively steady value of radius of gyration (Rg). Hydrogen bonds were determined based on the cutoffs of the angle formed between the hydrogen, the donor atom and the acceptor atom and the distance between the donor atom and the acceptor atom. The DSSP computes the secondary structure for each time frame and describes the stability of the secondary structure of proteins throughout the simulation (72). PCA is a statistical technique applied in molecular modeling to reduce the complexity of the data that characterize dominant conformational movements in proteins during molecular dynamics simulations (73). PCA describes them through the significance of the collective movements of the structure that are converted into main movements during the molecular dynamics simulations, that is, the number of dimensions necessary to describe the conformation dynamics is reduced by decomposing its movements from a larger spatial scale to those of a smaller scale (74, 75). For this work, the default values of the gmx hbond module were used from the Gromacs 2019 modules.

The torsional entropy of the proteins was calculated using the gmentro.py program (76). We generated a tabulated data file from the dynamics angle trajectory. Using Gaussian mixtures of the torsional data, gmentro.py was used to calculate the configurational entropy from a conformational ensemble of the whole SP-A structure (76).

RESULTS

A. Associations of Severe RSV Risk With SP Polymorphisms and Demographic Variables

Out of the 405 enrolled RSV-positive children, 171 (42%) and 234 (58%) children were diagnosed with moderate and severe RSV disease, respectively. **Table 1** shows the demographic data describing the study population. There were no statistically significant differences in sex, race, ethnicity, and measures of risk factors previously known to be associated with severe RSV disease (e.g. history of prematurity, congenital heart disease) between the two groups (**Table 1**). The majority of the patients (~ 85%) were white. Infants with severe RSV were more likely to be younger, of lower weight, had exposure to household pets and smoking; as well as more likely to have a co-infection on admission. As one would expect, children with severe RSV required a longer hospital stay and supplemental oxygen at discharge ($p < 0.05$). The logistic regression analysis of the clinical data showed that history of pet exposure (OR 3.05, 95% CI 1.25-7.46, p=0.014), and co-infection on admission (OR 3.98, 95% CI 2.30-6.87, $p < 0.001$) were associated with increased risk of severe RSV, whereas higher age was associated with decreased risk of severe RSV (OR 0.89, 95% CI 0.84-0.94, $p < 0.001$) (**Figure 1**).

The observed frequency distribution of the majority of SNPs shown in **Supplementary Table 3** was in Hardy-Weinberg equilibrium. The logistic regression analysis of SNPs showed that decreased risk of severe RSV associated with two SNPs, the rs17886395_C allele of the *SFTPA2* (OR=0.63, 95% CI 0.46-0.85, p = 0.002) and the rs2243639_A allele of the *SFTPD* (OR 0.64, 95% CI 0.41-0.99, p = 0.045) after adjusting for significant covariates (age, ethnicity, co-infection, smoke and pet exposure), and increased risk of severe RSV with the rs1059047_C (OR= 3.8, 95% CI 1.1-12.6, p=0.032) allele of the *SFTPA1* after adjusting for the same covariates (**Table 2**). As shown in **Supplementary Table 4**, the logistic regression analysis of genotypes after adjusting for the same covariates showed similar association with RSV severity.

As shown in **Figure 1**, an increased risk of severe RSV was associated with the SP-A2 $1A^0$ variant in its homozygous ($1A^0$/$1A^0$, OR=5, 95% CI 1.5-16.4, p = 0.009) or heterozygous form with $1A^3$ ($1A^0$/$1A^3$, OR=7.2, 95% CI 1.1-47.2, p = 0.04).

To evaluate the overall addition of genotype information to demographic data, a likelihood ratio test was done. The model with the genotype information along with demographic data was a better fit to predict disease severity compared to demographic data alone (p = 0.029 and Chi sq of 57.445).

TABLE 1 | Demographics of the cohort stratified by moderate and severe RSV disease.

Variable	Whole cohort (n = 405)	Moderate RSV (n = 171)	Severe RSV (n = 234)	p value
Demographics				
Age on admission (months)	4 ± 5.3	5.35 ± 6.7	3 ± 3.7	<0.001
Weight on admission (kilogram)	5.5 ± 2.4	6.1 ± 2.8	5 ± 2.1	<0.001
Female/male (%/%)	218/187 (54/46)	88/83 (52/48)	130/104 (56/44)	0.45
Non-white race (%)	64 (16)	25 (15)	39 (17)	0.71
Hispanic ethnicity (%)	86 (21)	36 (21)	50 (22)	0.96
Past history (%)				
Prematurity	96 (24)	44 (26)	52 (22)	0.43
Cardiac disease	23 (6)	8 (5)	15 (6)	0.62
NICU admission	75 (19)	37 (22)	38 (16)	0.18
Congenital anomalies	29 (7)	16 (9)	13 (6)	0.1
Family history of asthma	166 (41)	77 (45)	89 (38)	0.14
Environmental exposures				
Exposure to household smoking	53 (13)	15 (9)	38 (16)	0.03
Pet exposure	53 (13)	8 (5)	45 (19)	<0.001
Co-infection	155 (38)	32 (19)	123 (53)	<0.001
Hospital days	8.9 ± 9.9	3.8 ± 2.3	12.7 ± 11.5	0.000
Duration of support (n=237)				
Ventilator days	5.7± 5.1		5.7± 5.1	
PICU days	7.8 ± 6		7.8 ± 6	
Outcomes: Discharged with				
Supplemental oxygen	24 (6)	5 (3)	19 (8)	0.03
Oral/inhaled corticosteroids	43 (11)	23 (14)	20 (9)	0.08
Bronchodilators	141 (35)	68 (40)	73 (31)	0.08

RSV, Respiratory Syncytial Virus; NICU, Neonatal Intensive Care Unit; Mean ± SD.

B. Impact of the *SFTPA2* SNP rs1965708 on SP-A Structure

This SNP encodes the only amino acid change that exists between the SP-A2, $1A^0$ and $1A^3$ protein variants (16, 20, 77). A glutamine (Q) in $1A^0$ is changed into a lysine (K) in $1A^3$ at residue 223, which is located in the CRD of SP-A. Because, in the present study, increased risk of severe RSV was associated with $1A^0/1A^0$ and $1A^0/1A^3$ genotypes, we sought to investigate the impact of rs1965708 SNP on SP-A structural parameters *via* the use of SP-A simulated structural data.

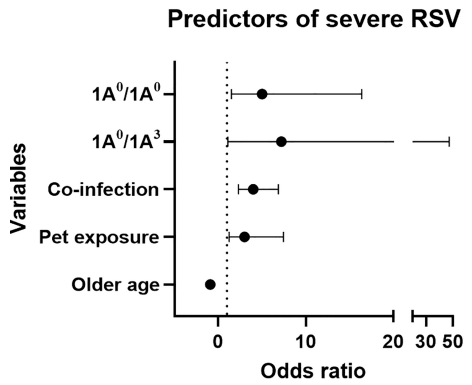

FIGURE 1 | Forest plot represents predictors of severe RSV using mutivariable logistic regression analysis. X-axis and Y-axis represents odds ratio (OR) and variables, respectively. Dotted line represents OR of 1. Based on OR, $1A^0/1A^0$, $1A^0/1A^3$, pet exposure and co-infection are associated with increase risk of severe RSV (OR > 1), whereas, older age is associated with decreased risk of severe RSV (OR < 1).

We studied the RMSF of the Q223 and K223 SP-A variants and **Figure 2** shows the RMSF of the backbone and sidechain of the Q223 and K223 variants. In the RMSF data, although the position of peaks did not differ significantly between Q223 and K223, we observed that the major peaks are in general, greater for Q223 compared to the K223 SP-A variant. The region around amino acid 223 (the site of variation), has more intense peaks indicating a region with great atomic movement. Furthermore, the RMSF values of each of the three identical monomers present in each trimer (Q223 or K223) analyzed did not differ significantly. The sidechain of both Q223 and K223 SP-A monomers showed higher RMSF values than the backbone (**Figure 2**) indicating a greater fluctuation of the sidechain atoms compared to the protein backbone.

The thermodynamic data on the torsional entropy show a larger entropy value for the K223 compared to Q223 SP-A variant (**Table 3**). Although entropy change in the variant process ($\Delta S_{mutation}$) seems small (< 70 J K-1 mol-1), it is not negligible and indicates larger stability of the K223 compared to the Q223 SP-A variant. These observations may also be associated with a greater fluctuation mostly in amino acids of the backbone and sidechain atoms of the K223 compared to the Q223 variant.

We did not observe a major difference in the RMSD of the center of mass in either Q223 or K223 SP-A (**Supplementary File 1**), indicating that the amino acid change at the specific site (223) at the protein chain does not significantly influence atomic movement in relation to the center of mass. Furthermore, there were no major differences, among the three monomers of each trimer (Q223 and K223), in the radius of gyration (a measure of protein folding stability), the DSSP (a description of secondary structure stability), hydrogen bonds (a measure of overall protein

TABLE 2 | Severe RSV vs moderate RSV using the multivariate logistic analysis after adjusting for covariates (age, ethnicity, co-infection, smoke and pet exposure).

Gene	Allele	OR (95% CI)	*p* value
SFTPA1	**rs1059047_C**	**3.80 (1.1-12.6)**	**0.032**
	rs1136450_C	0.68 (0.4-1.3)	0.227
	rs1136451_G	0.91 (0.3-2.7)	0.863
	rs1059057_G	0.60 (0.1-2.4)	0.472
	rs4253527_T	1.40 (0.5-3.9)	0.512
SFTPA2	rs1965708_A	0.58 (0.3-1.3)	0.187
	rs1965707_T	1.50 (0.7-3.0)	0.273
	rs17886395_C	**0.63 (0.5-0.8)**	**0.002**
	rs1059046_C	1.00 (0.5-2.1)	0.916
SFTPB	rs1130866_C	1.00 (0.7-1.5)	0.932
	rs3024798_A	0.36 (0.1-1.0)	0.056
	rs2077079_C	1.70 (0.6-4.4)	0.313
SFTPC	rs4715_A	1.00 (0.5-2.0)	0.959
	rs1124_A	0.96 (0.5-1.8)	0.894
SFTPD	**rs2243639_A**	**0.64 (0.4-0.9)**	**0.045**
	rs721917_C	1.20 (0.8-1.7)	0.427

SNP, single nucleotide polymorphism; OR, Odds ratio; CI, Confidence Interval; Bold text is statistically significant with p ≤ 0.05.

stability), and PCA (to reduce the complexity of the data that characterize dominant conformational movements of the protein during MD simulations). (**Supplementary File 1**).

DISCUSSION

Risk for RSV has been associated, in several studies, with genetic variants including SP genetic variants. However, most of the previous RSV association studies have used healthy children without RSV infection as controls. In the current study, we took the unique approach of enrolling only RSV-positive children to study association of disease severity with surfactant protein genetic variants. Our findings indicated that 1) a decreased risk of severe RSV is associated with the rs17886395_C of the *SFTPA2* and the rs2243639_A of the *SFTPD*, whereas, an increased risk is associated with the rs1059047_C of the *SFTPA1*. 2) RSV severity is not associated with the studied SNPs of *SFTPB* and *SFTPC*. 3) An increased risk of severe RSV is associated with the $1A^0$ haplotype of *SFTPA2* in its homozygous or heterozygous form with $1A^3$. 4) The model with the SP genetic information along with demographic data is a

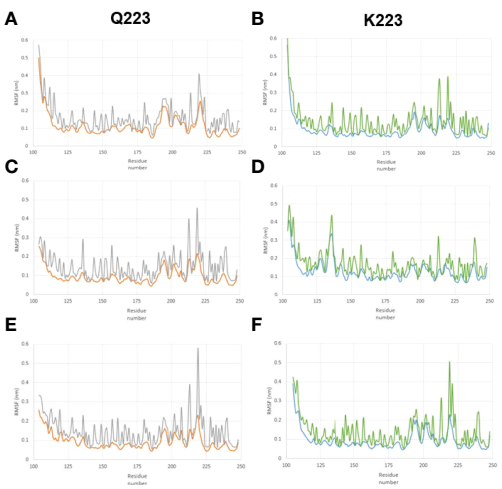

FIGURE 2 | Root-mean-square fluctuation (RMSF) in the backbone and sidechain of the Q223 and K223 SP-A variants. SP-A homo-trimers consisting of three identical monomers of SP-A1 or SP-A2 that included amino acids 104-224 were studied. The RMSF trimer data of each of the two variants (Q223 and K223) were analyzed for each of the 3 identical monomers present in each trimer to study the behavior of SP-A trimer. **(A–C)** represent monomers 1, 2, and 3, respectively, for Q223 trimer, and **(D–F)** represent monomers 1,2,3, respectively, for K223 trimer. The amino acid residue number is on the x-axis and RMSF is on the y-axis. The backbone and sidechain of the Q223 variant, are depicted in orange and gray colors, respectively. Whereas, blue and green colors depict the backbone and sidechain of the K223 SP-A, respectively. The position of peaks did not differ significantly between Q223 and K223 variants, however, the peak of each residue, in general, is greater for Q223 compared to the K223. The region around amino acid 223 (the site of variation), has more intense peaks, indicating a region with great atomic movement.

TABLE 3 | First order entropy change ($\Delta S_{mutation}$) in the mutation process for protein and for the backbone chain.

	First order entropy (J K^{-1} mol^{-1})	
	Protein	**Backbone**
Q223 SP-A	28331.24	28331.82
K223 SP-A	28400.87	28398.73
$\Delta S_{mutation}$	69.63	66.91

better fit to predict RSV disease severity compared to demographic data alone. 5) Based on the molecular dynamic studies, the K223 SP-A variant is more stable than the Q223 SP-A (the $1A^3$ haplotype has a lysine (K) and the $1A^0$ has a glutamine (Q) at residue 223).

A decreased risk of severe RSV is associated with the rs17886395_C allele of *SFTPA2* ($p < 0.002$). This SNP results in an amino acid substitution from alanine to proline at position 91 within the coding region (16, 20, 77). Similar to our findings, a decreased risk of RSV in Finnish children (43) and a decreased risk of RDS in white American neonates (35) was associated with the same SNP. Although direct comparison between studies is difficult, due to differences in study design, it is interesting that the rs17886395_C allele is associated with decreased risk of RSV and RDS in different populations and disease processes. It is shown that replacing alanine with proline stabilizes collagen triple helices due to conformational restrictions of the pyrrolidine ring (78). Whether this affects the concentration of a well-functioning SP-A and confers protection against severe RSV, is unknown as direct experimental evidence is lacking.

An increased risk of severe RSV was associated with the rs1059047_C of the *SFTPA1* (p=0.032) in our study. This SNP results in an amino acid substitution from valine to alanine at amino acid position 19, also within the coding region (16, 20, 26, 77), although it may or may not be part of all the molecules of the mature SP-A (57). Contrary to our observation, the aforementioned Finnish study found a protective effect of rs1059047_C on RSV disease (43). The difference in findings between the two studies could be due to differences a) in sample size (n=86 compared to n=405 in our study), b) definition of cases and controls, and c) patient population. The Finnish study used RSV-positive children as cases and healthy children without RSV as controls. In contrast, we enrolled only RSV-positive children and divided them between moderate (controls) and severe (cases) RSV disease. The fact that all children get infected with RSV by two years of age, it becomes less important to know who is at risk of getting RSV infection because virtually all children are at risk. For the current study, we enrolled only RSV-positive children to study RSV associations with SP SNPs, and determine who of the RSV-infected subjects is at risk for severe disease. If our findings are replicated and validated independently, the at-risk children for severe RSV could receive disease-modifying treatments without delay and be considered to receive prophylactic anti-RSV monoclonal antibodies in the future. The antibody treatment bears a considerable cost (79) and thus targeting it to those at the highest risk makes economic sense.

A decreased risk of severe RSV was associated with the rs2243639_A allele of *SFTPD* (p=0.045). This SNP results in an amino acid substitution from threonine to alanine at position 160 (26). Similar to our findings, previous studies have shown a decreased risk of severe RSV to associate with the rs2243639_A in the Chilean population (30) and in white American children (28). Although the exact mechanisms of how this SNP confers protection against severe RSV is not known, the rs2243639_A is shown to associate with a decreased level of serum SP-D and decreased risk of RDS in premature infants (80). Increased serum SP-D concentration is associated with worst respiratory outcomes in other viral infections, such as influenza and COVID-19 (81, 82), presumably, due to alveolar injury secondary to oxidative stress and infection. We did not measure SPs concentration in our patient population, and hence, we are unable to determine in the present study the impact of the rs2243639, if any, on SP-D concentration and its association with RSV.

An increased risk of severe RSV was associated with the $1A^0$ haplotype of *SFTPA2*, in its homozygous ($1A^0/1A^0$) or in its heterozygous ($1A^0/1A^3$) form. Previous studies have shown varying associations of *SFTPA2* haplotypes with RSV (28, 30, 43). In line with our observation, one study found an association of increased risk of RSV with $1A^0/1A^3$, but not with $1A^0/1A^0$ (43). However, another study found an association of decreased risk of severe RSV with the $1A^0/1A^0$ (29). Although the latter used the same definition for cases and controls as ours, the study population was very different. In that study, approximately 65% of the enrolled patients were African American compared to 85% of Caucasian children in our study. Liu et al. showed differences in frequencies of SP-A haplotypes based on race (83), therefore, the contrasting findings between the two studies could be due to baseline genetic differences in patient population. Furthermore, the sample size (29) was lower (n=277) than that in our study (n=405) and the authors compared the $1A^0/1A^0$ genotype vs other SP-A genotypes combined due to the low frequency of the other haplotypes in their patient population (29). Nevertheless, the majority of studies have found associations of *SFTPA2* haplotypes with RSV (28–30, 43). Similarly, a previous association study of *SFTPA* genetic variants with severity of Influenza A virus showed that the $1A^0$ of the *SFTPA2* was associated with a need for mechanical ventilation, acute respiratory failure, and acute respiratory distress syndrome in an adult population (84). These findings are not surprising because SP-A2 (encoded by *SFTPA2)* compared to SP-A1 (encoded by *SFTPA1)* exhibits higher activity in innate host defense/inflammatory processes (16).

In addition to RSV infection, the same SNPs and haplotypes have been studied with other infectious diseases such as tuberculosis (85, 86), pneumonia (87), otitis media (88, 89), and allergic bronchopulmonary aspergillosis (26, 90). Of interest, none of the individual studied SNPs were associated with the above-mentioned infectious diseases after correcting for significant covariates. However, similar to our findings, an increased risk of tuberculosis was associated with the $1A^3$ haplotype in Ethiopian (86) and Mexican (85) adult

populations. In the above-mentioned studies, there were other haplotypes of SP-A1 and SP-A2 (but not of the $1A^0$ and the $1A^3$ that are observed in the current study) associated with pneumonia, otitis media, and allergic bronchopulmonary aspergillosis. Nonetheless, associations of *SFTPA1* and *SFTPA2* SNPs and haplotypes with infectious diseases other than RSV underline the role of SP-A1 and SP-A2 in innate immunity and host defense functions.

The only amino acid difference, between SP-A2, $1A^0$ and $1A^3$ variants, is generated by the rs1965708 SNP at residue 223, where the amino acid is either a glutamine (Q) in $1A^0$ or a lysine (K) in $1A^3$ (16, 20). Glutamine is a neutral amino acid with a polar amide group, whereas lysine is a positively charged amino acid with a basic side chain. In simulation studies of molecular dynamics, we did not observe any major difference in structure or behavior of the SP-A variants, Q223 and K223, except a higher stability of the K223 as assessed by its higher conformational entropy compared to Q223 SP-A variant. In line with our findings, no significant differences were observed between the Q223K variants in a number of parameters studied *in vitro*, including their ability to form stable secreted complexes, oligomers, structural stability following limited proteolysis, and other (91). Yet, a transgenic mouse model of asthma carrying this SNP showed delayed resolution of eosinophils in bronchoalveolar lavage fluid of SP-A2 223K/K and SP-A knockout mice compared to SP-A2 223Q/Q > wild-type mice (92). It is well known that severe RSV infection early in life can predispose children to a later development of asthma (93, 94). Taken together, we speculate that the $1A^0/1A^3$ genotype predisposes children to severe RSV secondary to decrease binding and clearance of RSV and may predispose them to develop asthma later in life. In the future, we plan to study the impact of Q223K on the binding ability of SP-A2 to RSV and its subsequent clearance.

Most importantly, a likelihood ratio test revealed that the model that included information about the patients' genetic variants, along with clinical and demographic data is more accurate at predicting severe RSV infection compared to the model with only clinical and demographic data. The collective observations in this study contribute to an important foundation where, in the future, physicians could consider using this genetic information in clinical decision-making for high-risk children and identify those that may benefit from preventative measures such as an anti-RSV monoclonal antibody or aggressive early treatment such as surfactant replacement therapy.

Strengths of this study include the prospective study design and the well-characterized demographic, illness, and environmental exposure information for the cohort. There are a few limitations of our study. First, the relatively moderate sample size and homogeneous patient population may prevent the generalizability of our findings. Second, we did not serotype RSV in our patient population and RSV genetic variations may have accounted for altered disease severity rather than the host genetic variants (95, 96). Third, we used a direct fluorescent assay and viral culture to diagnose RSV infection instead of molecular testing. Although this holds the possibility of introducing a few false-positive results, a previous study has shown a good correlation between the direct fluorescent assay and molecular approaches, particularly for infants and young children (97). Subclinical infections with RSV are not common. Importantly, in the present study we have only enrolled children who were symptomatic and required hospitalization, hence, RSV was likely causally related to the illness. Therefore, we believe that the method of RSV detection may not change our conclusion. Fourth, we did not measure the level of inflammatory markers or SPs in our patient population, hence, the impact of these SNPs on these markers is unknown. Nonetheless, it is important that the associations observed in the present study be strengthened and validated by increasing the sample size and replicating the findings in other groups of heterogeneous patient populations with RSV, where measurements of other endpoints are performed.

In summary, multiple single SNPs and haplotypes of *SFTPA1, SFTPA2*, and *SFTPD* genes, encoding the hydrophilic SPs, but no SNPs or haplotypes of those (*SFTPB* and *SFTPC*) encoding the hydrophobic SPs were associated with RSV severity, indicating that SPs involved in innate immunity and host defense, play an important role in RSV severity. The model of genetic variants combined with demographic data was a better fit for predicting RSV severity than that of demographic data alone. This observation strengthens the argument that genetic variants do play a role along with environmental factors in the prediction of viral illness severity in children.

DATA AVAILABILITY STATEMENT

The data presented in the study have been deposited in the ClinVar repository, accession number SCV002506610.

ETHICS STATEMENT

The studies involving human participants were reviewed and approved by Human Subjects Protection Office of The Pennsylvania State University College of Medicine and the Institutional Review Board for Health Sciences Research at The University of Virginia. Written informed consent to participate in this study was provided by the participants' legal guardian/next of kin.

AUTHOR CONTRIBUTIONS

Data curation: CG, LD, CR, NT. Molecular modeling data: JB, FS, AP. Statistical Analysis: KA-F, DL. Methodology: CG, NT, JF. Resources: JF, CG, NT. Supervision: NT, JF. Writing original draft: CG, LD, KA-F, AP. Writing, reviewing & editing: CG, NT,

JF. All authors have read and agreed to the published version of the manuscript.

FUNDING

The study was supported in part by grants from Children's Miracle Network to CG and by NIH R37 HL 34788 to JF. The computational work was supported by the Fundação de Amparo à Pesquisa do Estado do Rio de Janeiro (FAPERJ) with the Rio Network of Innovation in nanosystems for the health (Nanohealth) - E-26/010.000983/2019. The National Council for Scientific and Technological Development (CNPq – 465259/2014-6), the Coordination for the Improvement of Higher Education Personnel (CAPES), the National Institute of Science and Technology Complex Fluids (INCT-FCx), and the São Paulo Research Foundation (FAPESP – 2014/50983-3) to ASP.

ACKNOWLEDGMENTS

The authors thank the parents and study participants. We thank Susan DiAngelo for organizing and cataloging the incoming samples and for genotyping about half of the samples studied.

SUPPLEMENTARY MATERIAL

The Supplementary Material for this article can be found online at: https://www.frontiersin.org/articles/10.3389/fimmu.2022.922956/full#supplementary-material

REFERENCES

1. Purcell K, Fergie J. Driscoll Children's Hospital Respiratory Syncytial Virus Database: Risk Factors, Treatment and Hospital Course in 3308 Infants and Young Children 1991 to 2002. *Pediatr Infect Dis J* (2004) 23(5):418–23. doi: 10.1097/01.inf.0000126273.27123.33
2. Hall CB, Weinberg GA, Iwane MK, Blumkin AK, Edwards KM, Staat MA, et al. The Burden of Respiratory Syncytial Virus Infection in Young Children. *N Engl J Med* (2009) 360(6):588–98. doi: 10.1056/NEJMoa0804877
3. Langley GF, Anderson LJ. Epidemiology and Prevention of Respiratory Syncytial Virus Infections Among Infants and Young Children. *Pediatr Infect Dis J* (2011) 30(6):510–7. doi: 10.1097/INF.0b013e3182184ae7
4. Shi T, McAllister DA, O'Brien KL, Simoes EAF, Madhi SA, Gessner BD, et al. Global, Regional, and National Disease Burden Estimates of Acute Lower Respiratory Infections Due to Respiratory Syncytial Virus in Young Children in 2015: A Systematic Review and Modelling Study. *Lancet* (2017) 390 (10098):946–58. doi: 10.1016/S0140-6736(17)30938-8
5. Stein RT, Bont LJ, Zar H, Polack FP, Park C, Claxton A, et al. Respiratory Syncytial Virus Hospitalization and Mortality: Systematic Review and Meta-Analysis. *Pediatr Pulmonol* (2017) 52(4):556–69. doi: 10.1002/ppul.23570
6. Diseases, A.A.o.P.C.o.I and Committee, A.A.o.P.B.G. Updated Guidance for Palivizumab Prophylaxis Among Infants and Young Children at Increased Risk of Hospitalization for Respiratory Syncytial Virus Infection. *Pediatrics* (2014) 134(2):415–20. doi: 10.1542/peds.2014-1665
7. Sonawane AR, Tian L, Chu CY, Qiu X, Wang L, Holden-Wiltse J, et al. Microbiome-Transcriptome Interactions Related to Severity of Respiratory Syncytial Virus Infection. *Sci Rep* (2019) 9(1):13824. doi: 10.1038/s41598-019-50217-w
8. Thomsen SF, Stensballe LG, Skytthe A, Kyvik KO, Backer V, Bisgaard H. Increased Concordance of Severe Respiratory Syncytial Virus Infection in Identical Twins. *Pediatrics* (2008) 121(3):493–6. doi: 10.1542/peds.2007-1889
9. Janssen R, Bont L, Siezen CL, Hodemaekers HM, Ermers MJ, Doornbos G, et al. Genetic Susceptibility to Respiratory Syncytial Virus Bronchiolitis is Predominantly Associated With Innate Immune Genes. *J Infect Dis* (2007) 196(6):826–34. doi: 10.1086/520886
10. Forton JT, Rowlands K, Rockett K, Hanchard N, Herbert M, Kwiatkowski DP, et al. Genetic Association Study for RSV Bronchiolitis in Infancy at the 5q31 Cytokine Cluster. *Thorax* (2009) 64(4):345–52. doi: 10.1136/thx.2008.102111
11. Wright JR. Immunoregulatory Functions of Surfactant Proteins. *Nat Rev Immunol* (2005) 5(1):58–68. doi: 10.1038/nri1528
12. Kishore U, Greenhough TJ, Waters P, Shrive AK, Ghai R, Kamran MF, et al. Surfactant Proteins SP-A and SP-D: Structure, Function and Receptors. *Mol Immunol* (2006) 43(9):1293–315. doi: 10.1016/j.molimm.2005.08.004
13. Serrano AG, Pérez-Gil J. Protein-Lipid Interactions and Surface Activity in the Pulmonary Surfactant System. *Chem Phys Lipids* (2006) 141(1-2):105–18. doi: 10.1016/j.chemphyslip.2006.02.017
14. Lopez-Rodriguez E, Pascual A, Arroyo R, Floros J, Perez-Gil J. Human Pulmonary Surfactant Protein SP-A1 Provides Maximal Efficiency of Lung Interfacial Films. *Biophys J* (2016) 111(3):524–36. doi: 10.1016/j.bpj.2016.06.025
15. Depicolzuane L, Phelps DS, Floros J. Surfactant Protein-A Function: Knowledge Gained From SP-A Knockout Mice. *Front Pediatr* (2021) 9:799693. doi: 10.3389/fped.2021.799693
16. Floros J, Thorenoor N, Tsotakos N, Phelps DS. Human Surfactant Protein SP-A1 and SP-A2 Variants Differentially Affect the Alveolar Microenvironment, Surfactant Structure, Regulation and Function of the Alveolar Macrophage, and Animal and Human Survival Under Various Conditions. *Front Immunol* (2021) 12:681639. doi: 10.3389/fimmu.2021.681639
17. Hoover RR, Floros J. Organization of the Human SP-A and SP-D Loci at 10q22-Q23. Physical and Radiation Hybrid Mapping Reveal Gene Order and Orientation. *Am J Respir Cell Mol Biol* (1998) 18(3):353–62. doi: 10.1165/ajrcmb.18.3.3035
18. Floros J, Hoover RR. Genetics of the Hydrophilic Surfactant Proteins A and D. *Biochim Biophys Acta* (1998) 1408(2-3):312–22. doi: 10.1016/s0925-4439(98)00077-5
19. DiAngelo S, Lin Z, Wang G, Phillips S, Ramet M, Luo J, et al. Novel, non-Radioactive, Simple and Multiplex PCR-cRFLP Methods for Genotyping Human SP-A and SP-D Marker Alleles. *Dis Markers* (1999) 15(4):269–81. doi: 10.1155/1999/961430
20. Floros J, Wang G, Lin Z. Genetic Diversity of Human SP-A, a Molecule With Innate Host Defense and Surfactant-Related Functions; Characteristics, Primary Function, and Significance. *Curr Pharmacogenom* (2005) 3(2):87–95. doi: 10.2174/1570160054022935
21. Floros J, Wang G, Mikerov AN. Genetic Complexity of the Human Innate Host Defense Molecules, Surfactant Protein A1 (SP-A1) and SP-A2–Impact on Function. *Crit Rev Eukaryot Gene Expr* (2009) 19(2):125–37. doi: 10.1615/critreveukargeneexpr.v19.i2.30
22. Floros J, Phelps D, Biebuyck J, Lynch C, Maze M, Saidamn L, et al. *Anesthesia: Biologic Foundations*. Lippincott-Raven, New York (1997).
23. Lin Z, Pearson C, Chinchilli V, Pietschmann SM, Luo J, Pison U, et al. Polymorphisms of Human SP-A, SP-B, and SP-D Genes: Association of SP-B Thr131Ile With ARDS. *Clin Genet* (2000) 58(3):181–91. doi: 10.1034/j.1399-0004.2000.580305.x
24. Lahti M, Marttila R, Hallman M. Surfactant Protein C Gene Variation in the Finnish Population - Association With Perinatal Respiratory Disease. *Eur J Hum Genet* (2004) 12(4):312–20. doi: 10.1038/sj.ejhg.5201137
25. Puthothu B, Krueger M, Heinze J, Forster J, Heinzmann A. Haplotypes of Surfactant Protein C are Associated With Common Paediatric Lung Diseases. *Pediatr Allergy Immunol* (2006) 17(8):572–7. doi: 10.1111/j.1399-3038.2006.00467.x

26. Silveyra P, Floros J. Genetic Variant Associations of Human SP-A and SP-D With Acute and Chronic Lung Injury. *Front Biosci (Landm Ed)* (2012) 17:407–29. doi: 10.2741/3935
27. Lahti M, Lofgren J, Marttila R, Renko M, Klaavuniemi T, Haataja R, et al. Surfactant Protein D Gene Polymorphism Associated With Severe Respiratory Syncytial Virus Infection. *Pediatr Res* (2002) 51(6):696–9. doi: 10.1203/00006450-200206000-00006
28. Thomas NJ, DiAngelo S, Hess JC, Fan R, Ball MW, Geskey JM, et al. Transmission of Surfactant Protein Variants and Haplotypes in Children Hospitalized With Respiratory Syncytial Virus. *Pediatr Res* (2009) 66(1):70–3. doi: 10.1203/PDR.0b013e3181a1d768
29. El Saleeby CM, Li R, Somes GW, Dahmer MK, Quasney MW, DeVincenzo JP. Surfactant Protein A2 Polymorphisms and Disease Severity in a Respiratory Syncytial Virus-Infected Population. *J Pediatr* (2010) 156(3):409–14. doi: 10.1016/j.jpeds.2009.09.043
30. Ampuero S, Luchsinger V, Tapia L, Palomino MA, Larrañaga CE. SP-A1, SP-A2 and SP-D Gene Polymorphisms in Severe Acute Respiratory Syncytial Infection in Chilean Infants. *Infect Genet Evol* (2011) 11(6):1368–77. doi: 10.1016/j.meegid.2011.04.033
31. Kala P, Ten Have T, Nielsen H, Dunn M, Floros J. Association of Pulmonary Surfactant Protein A (SP-A) Gene and Respiratory Distress Syndrome: Interaction With SP-B. *Pediatr Res* (1998) 43(2):169–77. doi: 10.1203/00006450-199802000-00003
32. Nogee LM, Wert SE, Proffit SA, Hull WM, Whitsett JA. Allelic Heterogeneity in Hereditary Surfactant Protein B (SP-B) Deficiency. *Am J Respir Crit Care Med* (2000) 161(3 Pt 1):973–81. doi: 10.1164/ajrccm.161.3.9903153
33. Rämet M, Haataja R, Marttila R, Floros J, Hallman M. Association Between the Surfactant Protein A (SP-A) Gene Locus and Respiratory-Distress Syndrome in the Finnish Population. *Am J Hum Genet* (2000) 66(5):1569–79. doi: 10.1086/302906
34. Floros J, Fan R, Diangelo S, Guo X, Wert J, Luo J. Surfactant Protein (SP) B Associations and Interactions With SP-A in White and Black Subjects With Respiratory Distress Syndrome. *Pediatr Int* (2001) 43(6):567–76. doi: 10.1046/j.1442-200x.2001.01474.x
35. Amatya S, Ye M, Yang L, Gandhi CK, Wu R, Nagourney B, et al. Single Nucleotide Polymorphisms Interactions of the Surfactant Protein Genes Associated With Respiratory Distress Syndrome Susceptibility in Preterm Infants. *Front Pediatr* (2021) 9:682160. doi: 10.3389/fped.2021.682160
36. Lin Z, Thorenoor N, Wu R, DiAngelo SL, Ye M, Thomas NJ, et al. Genetic Association of Pulmonary Surfactant Protein Genes, SFTPA1, SFTPA2, SFTPB, SFTPC, and SFTPD With Cystic Fibrosis. *Front Immunol* (2018) 9:2256. doi: 10.3389/fimmu.2018.02256
37. Guo X, Lin HM, Lin Z, Montaño M, Sansores R, Wang G, et al. Surfactant Protein Gene A, B, and D Marker Alleles in Chronic Obstructive Pulmonary Disease of a Mexican Population. *Eur Respir J* (2001) 18(3):482–90. doi: 10.1183/09031936.01.00043401
38. Seifart C, Plagens A, Brödje D, Müller B, von Wichert P, Floros J. Surfactant Protein B Intron 4 Variation in German Patients With COPD and Acute Respiratory Failure. *Dis Markers* (2002) 18(3):129–36. doi: 10.1155/2002/194075
39. Gandhi CK, Chen C, Amatya S, Yang L, Fu C, Zhou S, et al. SNP and Haplotype Interaction Models Reveal Association of Surfactant Protein Gene Polymorphisms With Hypersensitivity Pneumonitis of Mexican Population. *Front Med* (2021) 7:588404. doi: 10.3389/fmed.2020.588404
40. Abbasi A, Chen C, Gandhi CK, Wu R, Pardo A, Selman M, et al. Single Nucleotide Polymorphisms (SNP) and SNP-SNP Interactions of the Surfactant Protein Genes Are Associated With Idiopathic Pulmonary Fibrosis in a Mexican Study Group; Comparison With Hypersensitivity Pneumonitis. *Front Immunol* (2022) 13:842745. doi: 10.3389/fimmu.2022.842745
41. Gandhi CK, Chen C, Wu R, Yang L, Thorenoor N, Thomas NJ, et al. Association of SNP-SNP Interactions of Surfactant Protein Genes With Pediatric Acute Respiratory Failure. *J Clin Med* (2020) 9(4):1183. doi: 10.3390/jcm9041183
42. Gandhi CK, Thomas NJ, Meixia Y, Spear D, Fu C, Zhou S, et al. SNP–SNP Interactions of Surfactant Protein Genes in Persistent Respiratory Morbidity Susceptibility in Previously Healthy Children. *Front Genet* (2022) 13:815727. doi: 10.3389/fgene.2022.815727
43. Löfgren J, Rämet M, Renko M, Marttila R, Hallman M. Association Between Surfactant Protein A Gene Locus and Severe Respiratory Syncytial Virus Infection in Infants. *J Infect Dis* (2002) 185(3):283–9. doi: 10.1086/338473
44. Selman M, Lin HM, Montaño M, Jenkins AL, Estrada A, Lin Z, et al. Surfactant Protein A and B Genetic Variants Predispose to Idiopathic Pulmonary Fibrosis. *Hum Genet* (2003) 113(6):542–50. doi: 10.1007/s00439-003-1015-4
45. Jiang Y, Chen S, Wang X, Liu M, Iacono WG, Hewitt JK, et al. Association Analysis and Meta-Analysis of Multi-Allelic Variants for Large-Scale Sequence Data. *Genes* (2020) 11(5):586. doi: 10.3390/genes11050586
46. Watson A, Kronqvist N, Spalluto CM, Griffiths M, Staples KJ, Wilkinson T, et al. Novel Expression of a Functional Trimeric Fragment of Human SP-A With Efficacy in Neutralisation of RSV. *Immunobiology* (2017) 222(2):111–8. doi: 10.1016/j.imbio.2016.10.015
47. Ginalski K. Comparative Modeling for Protein Structure Prediction. *Curr Opin Struct Biol* (2006) 16(2):172–7. doi: 10.1016/j.sbi.2006.02.003
48. Guex N, Peitsch MC, Schwede T. Automated Comparative Protein Structure Modeling With SWISS-MODEL and Swiss-PdbViewer: A Historical Perspective. *Electrophoresis* (2009) 30(Suppl 1):S162–173. doi: 10.1002/elps.200900140
49. Berman HM, Westbrook J, Feng Z, Gilliland G, Bhat TN, Weissig H, et al. The Protein Data Bank. *Nucleic Acids Res* (2000) 28(1):235–42. doi: 10.1093/nar/28.1.235
50. Goh BC, Wu H, Rynkiewicz MJ, Schulten K, Seaton BA, McCormack FX. Elucidation of Lipid Binding Sites on Lung Surfactant Protein A Using X-Ray Crystallography, Mutagenesis, and Molecular Dynamics Simulations. *Biochemistry* (2016) 55(26):3692–701. doi: 10.1021/acs.biochem.6b00048
51. Bertoni M, Kiefer F, Biasini M, Bordoli L, Schwede T. Modeling Protein Quaternary Structure of Homo- and Hetero-Oligomers Beyond Binary Interactions by Homology. *Sci Rep* (2017) 7(1):10480. doi: 10.1038/s41598-017-09654-8
52. Bienert S, Waterhouse A, de Beer TA, Tauriello G, Studer G, Bordoli L, et al. The SWISS-MODEL Repository-New Features and Functionality. *Nucleic Acids Res* (2017) 45(D1):D313–9. doi: 10.1093/nar/gkw1132
53. Waterhouse A, Bertoni M, Bienert S, Studer G, Tauriello G, Gumienny R, et al. SWISS-MODEL: Homology Modelling of Protein Structures and Complexes. *Nucleic Acids Res* (2018) 46(W1):W296–303. doi: 10.1093/nar/gky427
54. Studer G, Rempfer C, Waterhouse AM, Gumienny R, Haas J, Schwede T. QMEANDisCo-Distance Constraints Applied on Model Quality Estimation. *Bioinformatics* (2020) 36(8):2647. doi: 10.1093/bioinformatics/btaa058
55. Guex N, Peitsch MC. SWISS-MODEL and the Swiss-PdbViewer: An Environment for Comparative Protein Modeling. *Electrophoresis* (1997) 18(15):2714–23. doi: 10.1002/elps.1150181505
56. Voss T, Melchers K, Scheirle G, Schäfer KP. Structural Comparison of Recombinant Pulmonary Surfactant Protein SP-A Derived From Two Human Coding Sequences: Implications for the Chain Composition of Natural Human SP-A. *Am J Respir Cell Mol Biol* (1991) 4(1):88–94. doi: 10.1165/ajrcmb/4.1.88
57. Wang G, Bates-Kenney SR, Tao JQ, Phelps DS, Floros J. Differences in Biochemical Properties and in Biological Function Between Human SP-A1 and SP-A2 Variants, and the Impact of Ozone-Induced Oxidation. *Biochemistry* (2004) 43(14):4227–39. doi: 10.1021/bi036023i
58. Wang G, Myers C, Mikerov A, Floros J. Effect of Cysteine 85 on Biochemical Properties and Biological Function of Human Surfactant Protein A Variants. *Biochemistry* (2007) 46(28):8425–35. doi: 10.1021/bi7004569
59. Kaminski GA, Friesner RA, Tirado-Rives J, Jorgensen WL. Evaluation and Reparametrization of the OPLS-AA Force Field for Proteins *via* Comparison With Accurate Quantum Chemical Calculations on Peptides. *J Phys Chem B* (2001) 105(28):6474–87. doi: 10.1021/jp003919d
60. Berendsen HJC, van der Spoel D, van Drunen R. GROMACS: A Message-Passing Parallel Molecular Dynamics Implementation. *Comput Phys Commun* (1995) 91(1):43–56. doi: 10.1016/0010-4655(95)00042-E
61. Van Der Spoel D, Lindahl E, Hess B, Groenhof G, Mark AE, Berendsen HJ. GROMACS: Fast, Flexible, and Free. *J Comput Chem* (2005) 26(16):1701–18. doi: 10.1002/jcc.20291

62. Hess B, Kutzner C, van der Spoel D, Lindahl E. GROMACS 4: Algorithms for Highly Efficient, Load-Balanced, and Scalable Molecular Simulation. *J Chem Theory Comput* (2008) 4(3):435–47. doi: 10.1021/ct700301q
63. Pronk S, Páll S, Schulz R, Larsson P, Bjelkmar P, Apostolov R, et al. GROMACS 4.5: A High-Throughput and Highly Parallel Open Source Molecular Simulation Toolkit. *Bioinformatics* (2013) 29(7):845–54. doi: 10.1093/bioinformatics/btt055
64. Jorgensen WL, Chandrasekhar J, Madura JD, Impey RW, Klein ML. Comparison of Simple Potential Functions for Simulating Liquid Water. *J Chem Phys* (1983) 79(2):926–35. doi: 10.1063/1.445869
65. Mark P, Nilsson L. Structure and Dynamics of the TIP3P, SPC, and SPC/E Water Models at 298 K. *J Phys Chem A* (2001) 105(43):9954–60. doi: 10.1021/jp003020w
66. Harrach MF, Drossel B. Structure and Dynamics of TIP3P, TIP4P, and TIP5P Water Near Smooth and Atomistic Walls of Different Hydroaffinity. *J Chem Phys* (2014) 140(17):174501. doi: 10.1063/1.4872239
67. Martínez L, Borin I, Skaf M. Metodos de Quí mica Teó rica e Modelageḿ Molecular; Morgon, N. H., Coutinho, K. Eds. *Editora Livraria da Física* (2007) (12):413–452.
68. Parrinello M, Rahman A. Polymorphic Transitions in Single Crystals: A New Molecular Dynamics Method. *J Appl Phys* (1981) 52(12):7182–90. doi: 10.1063/1.328693
69. Bosko JT, Todd BD, Sadus RJ. Molecular Simulation of Dendrimers and Their Mixtures Under Shear: Comparison of Isothermal-Isobaric (NpT) and Isothermal-Isochoric (NVT) Ensemble Systems. *J Chem Phys* (2005) 123 (3):34905. doi: 10.1063/1.1946749
70. Evans DJ, Holian BL. The Nose–Hoover Thermostat. *J Chem Phys* (1985) 83 (8):4069–74. doi: 10.1063/1.449071
71. Humphrey W, Dalke A, Schulten K. VMD: Visual Molecular Dynamics. *J Mol Graph* (1996) 14(1):33–38, 27-38. doi: 10.1016/0263-7855(96)00018-5
72. Singh S, Singh VK. "Molecular Dynamics Simulation: Methods and Application,". In: DB Singh and T Tripathi, editors. *Frontiers in Protein Structure, Function, and Dynamics*. Singapore: Springer Singapore (2020). p. 213–38.
73. David CC, Jacobs DJ. Principal Component Analysis: A Method for Determining the Essential Dynamics of Proteins. *Methods Mol Biol (Clifton N.J.)* (2014) 1084:193–226. doi: 10.1007/978-1-62703-658-0_11
74. Ndagi U, Mhlongo NN, Soliman ME. The Impact of Thr91 Mutation on C-Src Resistance to UM-164: Molecular Dynamics Study Revealed a New Opportunity for Drug Design. *Mol Biosyst* (2017) 13(6):1157–71. doi: 10.1039/c6mb00848h
75. Palaniappan C, Ramalingam R. Deciphering the Molecular Effects of Mutations on ATRX Cause ATRX Syndrome: A Molecular Dynamics Study. *J Cell Biochem* (2017) 118(10):3318–27. doi: 10.1002/jcb.25984
76. Gyimesi G, Závodszky P, Szilágyi A. Calculation of Configurational Entropy Differences From Conformational Ensembles Using Gaussian Mixtures. *J Chem Theory Comput* (2017) 13(1):29–41. doi: 10.1021/acs.jctc.6b00837
77. Floros J, Tsotakos N. Differential Regulation of Human Surfactant Protein A Genes, SFTPA1 and SFTPA2, and Their Corresponding Variants. *Front Immunol* (2021) 12:766719. doi: 10.3389/fimmu.2021.766719
78. Kersteen EA, Raines RT. Contribution of Tertiary Amides to the Conformational Stability of Collagen Triple Helices. *Biopolymers* (2001) 59(1):24–8. doi: 10.1002/1097-0282(200107)59:1<24::AID-BIP1002>3.0.CO;2-N
79. Prescott WAJr., Doloresco F, Brown J, Paladino JA. Cost Effectiveness of Respiratory Syncytial Virus Prophylaxis: A Critical and Systematic Review. *Pharmacoeconomics* (2010) 28(4):279–93. doi: 10.2165/11531860-000000000-00000
80. Sorensen GL, Dahl M, Tan Q, Bendixen C, Holmskov U, Husby S. Surfactant Protein-D-Encoding Gene Variant Polymorphisms Are Linked to Respiratory Outcome in Premature Infants. *J Pediatr* (2014) 165(4):683–9. doi: 10.1016/j.jpeds.2014.05.042
81. Delgado C, Krötzsch E, Jiménez-Alvarez LA, Ramírez-Martínez G, Márquez-García JE, Cruz-Lagunas A, et al. Serum Surfactant Protein D (SP-D) Is a Prognostic Marker of Poor Outcome in Patients With A/H1N1 Virus Infection. *Lung* (2015) 193(1):25–30. doi: 10.1007/s00408-014-9669-3
82. Tong M, Xiong Y, Zhu C, Xu H, Zheng Q, Jiang Y, et al. Serum Surfactant Protein D in COVID-19 Is Elevated and Correlated With Disease Severity. *BMC Infect Dis* (2021) 21(1):737. doi: 10.1186/s12879-021-06447-3
83. Liu W, Bentley CM, Floros J. Study of Human SP-A, SP-B and SP-D Loci: Allele Frequencies, Linkage Disequilibrium and Heterozygosity in Different Races and Ethnic Groups. *BMC Genet* (2003) 4:13. doi: 10.1186/1471-2156-4-13
84. Herrera-Ramos E, López-Rodríguez M, Ruíz-Hernández J, Horcajada J, Borderías L, Lerma E, et al. Surfactant Protein A Genetic Variants Associate With Severe Respiratory Insufficiency in Pandemic Influenza A Virus Infection. *Crit Care* (2014) 18(3):R127. doi: 10.1186/cc13934
85. Floros J, Lin H-M, García A, Salazar MA, Guo X, DiAngelo S, et al. Surfactant Protein Genetic Marker Alleles Identify a Subgroup of Tuberculosis in a Mexican Population. *J Infect Dis* (2000) 182(5):1473–8. doi: 10.1086/315866
86. Malik S, Greenwood CMT, Eguale T, Kifle A, Beyene J, Habte A, et al. Variants of the SFTPA1 and SFTPA2 Genes and Susceptibility to Tuberculosis in Ethiopia. *Hum Genet* (2006) 118(6):752–9. doi: 10.1007/s00439-005-0092-y
87. García-Laorden MI, Rodríguez de Castro F, Solé-Violán J, Rajas O, Blanquer J, Borderías L, et al. Influence of Genetic Variability at the Surfactant Proteins A and D in Community-Acquired Pneumonia: A Prospective, Observational, Genetic Study. *Crit Care* (2011) 15(1):R57. doi: 10.1186/cc10030
88. Rämet M, Löfgren J, Alho O-P, Hallman M. Surfactant Protein-A Gene Locus Associated With Recurrent Otitis Media. *J Pediatr* (2001) 138(2):266–8. doi: 10.1067/mpd.2001.110133
89. Pettigrew MM, Gent JF, Zhu Y, Triche EW, Belanger KD, Holford TR, et al. Association of Surfactant Protein A Polymorphisms With Otitis Media in Infants at Risk for Asthma. *BMC Med Genet* (2006) 7(1):68. doi: 10.1186/1471-2350-7-68
90. Saxena S, Madan T, Shah A, Muralidhar K, Sarma PU. Association of Polymorphisms in the Collagen Region of SP-A2 With Increased Levels of Total IgE Antibodies and Eosinophilia in Patients With Allergic Bronchopulmonary Aspergillosis. *J Allergy Clin Immunol* (2003) 111 (5):1001–7. doi: 10.1067/mai.2003.1395
91. Maitra M, Wang Y, Gerard RD, Mendelson CR, Garcia CK. Surfactant Protein A2 Mutations Associated With Pulmonary Fibrosis Lead to Protein Instability and Endoplasmic Reticulum Stress. *J Biol Chem* (2010) 285(29):22103–13. doi: 10.1074/jbc.M110.121467
92. Dy ABC, Arif MZ, Addison KJ, Que LG, Boitano S, Kraft M, et al. Genetic Variation in Surfactant Protein-A2 Delays Resolution of Eosinophilia in Asthma. *J Immunol* (2019) 203(5):1122–30. doi: 10.4049/jimmunol.1900546
93. Stein RT, Sherrill D, Morgan WJ, Holberg CJ, Halonen M, Taussig LM, et al. Respiratory Syncytial Virus in Early Life and Risk of Wheeze and Allergy by Age 13 Years. *Lancet* (1999) 354(9178):541–5. doi: 10.1016/S0140-6736(98)10321-5
94. Sigurs N, Bjarnason R, Sigurbergsson F, Kjellman B. Respiratory Syncytial Virus Bronchiolitis in Infancy Is an Important Risk Factor for Asthma and Allergy at Age 7. *Am J Respir Crit Care Med* (2000) 161(5):1501–7. doi: 10.1164/ajrccm.161.5.9906076
95. Midulla F, Nenna R, Scagnolari C, Petrarca L, Frassanito A, Viscido A, et al. How Respiratory Syncytial Virus Genotypes Influence the Clinical Course in Infants Hospitalized for Bronchiolitis. *J Infect Dis* (2018) 219(4):526–34. doi: 10.1093/infdis/jiy496
96. Human S, Hotard AL, Rostad CA, Lee S, McCormick L, Larkin EK, et al. A Respiratory Syncytial Virus Attachment Gene Variant Associated With More Severe Disease in Infants Decreases Fusion Protein Expression, Which May Facilitate Immune Evasion. *J Virol* (2020) 95(2):e01201–01220. doi: 10.1128/JVI.01201-20
97. Zhang Y, Sakthivel SK, Bramley A, Jain S, Haynes A, Chappell JD, et al. Serology Enhances Molecular Diagnosis of Respiratory Virus Infections Other Than Influenza in Children and Adults Hospitalized With Community-Acquired Pneumonia. *J Clin Microbiol* (2017) 55(1):79–89. doi: 10.1128/jcm.01701-16

Conflict of Interest: The authors declare that the research conducted was in the absence of any commercial or financial relationships construed as a potential conflict of interest.

this article, or claim that may be made by its manufacturer, is not guaranteed or endorsed by the publisher.

frontiers | Frontiers in Immunology

TYPE Original Research
PUBLISHED 07 September 2022
DOI 10.3389/fimmu.2022.927017

OPEN ACCESS

EDITED BY
Taruna Madan,
National Institute for Research in Reproductive Health (ICMR), India

REVIEWED BY
Ashwinkumar Subramenium Ganapathy,
College of Medicine, The Pennsylvania State University, United States
Julie Gunnells Ledford,
University of Arizona, United States

*CORRESPONDENCE
Cristina Casals
ccasalsc@ucm.es

†These authors have contributed equally to this work

SPECIALTY SECTION
This article was submitted to Molecular Innate Immunity, a section of the journal Frontiers in Immunology

RECEIVED 23 April 2022
ACCEPTED 10 August 2022
PUBLISHED 07 September 2022

CITATION
Coya JM, Fraile-Ágreda V, de Tapia L, García-Fojeda B, Sáenz A, Bengoechea JA, Kronqvist N, Johansson J and Casals C (2022) Cooperative action of SP-A and its trimeric recombinant fragment with polymyxins against Gram-negative respiratory bacteria.
Front. Immunol. 13:927017.
doi: 10.3389/fimmu.2022.927017

Cooperative action of SP-A and its trimeric recombinant fragment with polymyxins against Gram-negative respiratory bacteria

Juan Manuel Coya[1†], Víctor Fraile-Ágreda[1†], Lidia de Tapia[1], Belén García-Fojeda[1], Alejandra Sáenz[1], José A. Bengoechea[2], Nina Kronqvist[3], Jan Johansson[3] and Cristina Casals[1*]

[1]Department of Biochemistry and Molecular Biology, Complutense University of Madrid, Madrid, Spain, [2]Wellcome-Wolfson Institute for Experimental Medicine, Queen's University Belfast, Belfast, United Kingdom, [3]Department of Biosciences and Nutrition, Neo, Karolinska Institutet, Huddinge, Sweden

The exploration of therapies combining antimicrobial lung proteins and conventional antibiotics is important due to the growing problem of multidrug-resistant bacteria. The aim of this study was to investigate whether human SP-A and a recombinant trimeric fragment (rfhSP-A) have cooperative antimicrobial activity with antibiotics against pathogenic Gram-negative bacteria. We found that SP-A bound the cationic peptide polymyxin B (PMB) with an apparent dissociation constant (K_D) of 0.32 ± 0.04 μM. SP-A showed synergistic microbicidal activity with polymyxin B and E, but not with other antibiotics, against three SP-A-resistant pathogenic bacteria: *Klebsiella pneumoniae*, non-typable *Haemophilus influenzae* (NTHi), and *Pseudomonas aeruginosa*. SP-A was not able to bind to *K. pneumoniae, NTHi*, or to mutant strains thereof expressing long-chain lipopolysaccharides (or lipooligosaccharides) and/or polysaccharide capsules. In the presence of PMB, SP-A induced the formation of SP-A/PMB aggregates that enhance PMB-induced bacterial membrane permeabilization. Furthermore, SP-A bound to a molecular derivative of PMB lacking the acyl chain (PMBN) with a K_D of 0.26 ± 0.02 μM, forming SP-A/PMBN aggregates. PMBN has no bactericidal activity but can bind to the outer membrane of Gram-negative bacteria. Surprisingly, SP-A and PMBN showed synergistic bactericidal activity against Gram-negative bacteria. Unlike native supratrimeric SP-A, the trimeric rfhSP-A fragment had small but significant direct bactericidal activity against *K. pneumoniae*, NTHi, and *P. aeruginosa*. rfhSP-A did not bind to PMB under physiological conditions but acted additively with PMB and other antibiotics against these pathogenic bacteria. In summary, our results significantly improve our understanding of the antimicrobial actions of SP-A and its synergistic action with PMB. A peptide based on SP-A may aid the therapeutic use of PMB, a relatively cytotoxic antibiotic that is currently being reintroduced into clinics due to the global problem of antibiotic resistance.

KEYWORDS

collectin SP-A, recombinant trimeric fragment, multidrug-resistant bacteria, microbial infection, lung, polymyxin B, PMB nonapeptide, synergy

Introduction

Gram-negative respiratory infections are a persistent and pervasive public health problem (1, 2). This problem has been generated mainly by the uncontrolled expansion of respiratory pathogens resistant to multiple families of antibiotics (3, 4), such as *Klebsiella pneumoniae, Pseudomonas aeruginosa*, and *Haemophilus influenzae*, some of which are listed as ESKAPE pathogens (5, 6). The emergence of antimicrobial resistance in respiratory pathogens limits current antimicrobial treatments, leading to prolonged illness, higher health care expenditures, and an increase in mortality and morbidity rates.

Some of the most well studied virulence factors contributing to the pathogenicity and resistance of Gram-negative bacteria are the polysaccharide capsule (CPS) and lipopolysaccharide (LPS). CPS acts as an external barrier that protects bacteria and mediates the interaction with their environment. LPS is composed of a highly conserved and amphipathic part called lipid A, an oligosaccharide core, and a variable domain of repeated units of oligosaccharide called O-antigen (7). The O-antigen is much longer than the core oligosaccharide and contains the hydrophilic domain of LPS. Wild-type bacteria species with O-chains are termed "smooth," and hence their LPS are called smooth LPS (S-LPS). Mutants that produce LPS lacking O-specific chains are termed "rough" (R), and their LPS are designated Ra, Rb, Rc, Rd, and Re in order of decreasing core length (7). Both LPS and CPS cause the impermeabilization of bacteria to hydrophobic antibiotics and prevent bacterial recognition by the host's immune system (8, 9). These virulence factors are involved in bacterial resistance to antimicrobial factors, including antimicrobial proteins and peptides (AMPs) (10, 11).

Currently, clinical research has focused on development of new alternative therapies for replacing and/or supporting classic antimicrobial treatments to combat antibiotic resistance. In this context, proteins and peptides of the innate immune system have attracted huge clinical interest due to their ability to act against these multidrug-resistant pathogens and their reduced ability to induce new bacterial resistance compared to conventional antibiotics (12–14). In addition, they show other characteristics, including broad-spectrum activity, endotoxin neutralization, and potential synergy with antibiotics (15, 16).

Among human lung defense AMPs, surfactant protein A (SP-A) is an oligomeric extracellular protein secreted into the airway mucosa where it recognizes a great variety of immune and non-immune ligands (17–19). SP-A binds to surfactant membranes but also to membrane receptors present in epithelial and immune cells, modifying their response to pathogens or other stimuli. SP-A also recognizes pathogen-associated molecular patterns in some microorganisms, such as the fungi *Pneumocystis carinii* and *Aspergillus fumigatus* (20), the Gram-positive bacteria *Staphylococcus aureus* (21) and *Streptococcus pneumoniae* (22), respiratory syncytial virus (23), and influenza (24). By binding to these pathogens, SP-A facilitates their clearance by macrophages or recruited neutrophils (17, 19). SP-A-deficient mice show decreased microbe clearance and increased tissue markers of inflammation in the lung after infection with group B *Streptococcus*, *Klebsiella pneumoniae, Pseudomonas aeruginosa*, capsulated *Haemophilus influenzae*, respiratory syncytial virus, adenovirus, and influenza virus (25, 26). Although it has been suggested that SP-A has potent direct antibacterial activity *in vivo*, *in vitro* data supporting direct antimicrobial activity of SP-A are sparse. Respiratory pathogens like *K. pneumoniae*, *Bordetella pertussis*, and *P. aeruginosa* are resistant to SP-A (27–31). It is possible that multiple antimicrobial factors are released during immune responses *in vivo*, and lung antimicrobials could act in combination with SP-A. Consistent with this, we recently discovered synergistic antimicrobial action between SP-A and SP-B^{N}, an anionic antimicrobial peptide secreted to the alveolar fluid (32). Interaction between SP-A and SP-B^{N} confers new antimicrobial properties, including the ability to kill respiratory pathogens such as *K. pneumoniae* and *P. aeruginosa* that are resistant to either protein alone (30, 31).

Each SP-A subunit consists of an N-terminal segment containing cysteine residues involved in oligomerization followed by a collagen-like region, an alpha helical coiled neck region, and a globular region with a carbohydrate recognition domain (CRD) (17–19). SP-A is intracellularly assembled in multiples of three subunits *via* its collagen domain. Its supratrimeric assembly has an umbelliform-shaped structure of six trimers like mannose binding protein or C1q (17–19). Supratrimeric oligomerization of SP-A appears to be needed for many of its functions since it facilitates multivalent binding and increases the functional affinity of the globular domain for their

ligands (33, 34). However, there are clear advantages of using the smaller recombinant fragments of SP-A, in terms of ease of production and delivery, if they are as effective as native SP-A. In this study we use a recombinant trimeric fragment of human SP-A1 (rfhSP-A), which lacks the N-terminal domain and most of the collagen domain, to evaluate its bactericidal activity alone or in combination with antibiotics. We previously showed that rfhSP-A is highly effective in neutralizing respiratory syncytial virus (23).

We hypothesize that combinations of SP-A, or its recombinant fragments, with antibiotics against Gram-negative bacteria, such as polymyxins, could be an effective antibacterial strategy. Polymyxins are relatively cytotoxic antibiotics that have been reintroduced into clinics as the last-resort therapy for severe MDR infections (35). Polymyxins are pentacationic lipopeptide antibiotics expressed by *Bacilus polymyxia*, which act only against Gram-negative bacteria. They carry five free amino groups in a polycationic peptide ring and a tripeptide side chain with a fatty acid tail (36). The main mechanism of action consists of electrostatic interaction between the negative charge of LPS and the positive charge of the peptide, followed by insertion of the polymyxin molecule into the bacterial membrane. The cyclic lipopeptide cross-links the outer membrane and cytoplasmic bacterial membranes, leading to permeabilization of both membranes and resulting in lysis and cell death (36, 37). However, polymyxins' mechanism is more complex than their effects in membrane permeabilization because polymyxins bind ribosomes, prevent cell division, and inhibit bacterial respiration (37). Polymyxin derivatives have also acquired great interest with the aim of reducing lipopeptide toxicity and obtaining efficient antimicrobial therapies (38). For example, polymyxin B nonapeptide (PMBN), a PMB derivative that lacks the fatty acid tail and the N-terminal diaminobutyryl residue, retains polymyxin B's ability to bind to LPS and disturb the outer membrane of Gram-negative bacteria. However, PMBN has no bactericidal activity on its own and its use depends on efficient combination with other antimicrobial factors (38, 39).

The objectives of this article are to investigate i) the bactericidal activity of human SP-A and rfhSP-A, produced in a novel way using the spider silk derived solubility tag NT* (40, 41), against clinically relevant respiratory pathogens and isogenic mutants, and ii) the synergistic or additive antimicrobial activity of human SP-A and rfhSP-A with antibiotics such as polymyxins against these respiratory pathogens. Since SP-A is the most abundant protein in the alveolar space, comprehensive understanding of protein-polymyxin interactions would facilitate the development of new therapies against respiratory infections by Gram-negative bacteria, which induce airway attacks in patients who are elderly or who suffer from chronic obstructive pulmonary disease (COPD), cystic fibrosis, or asthma.

Material and methods

Materials

The antibiotics azithromycin (AZI), ciprofloxacin (CIPRO), tetracycline (TC), polymyxin B (PMB), colistin (PME) and PMB nonapeptide (PMBN) were obtained from Sigma-Aldrich (St. Louis, MO, USA). Antibiotics were prepared according to the manufacturer's instructions; the stocks of antibiotics were diluted in the corresponding dilution media and were used on the same day of dilution. The β-Nicotinamide adenine dinucleotide hydrate (β-NAD) and hemin were obtained from Sigma-Aldrich. Sytox Green, propidium iodide and 1,6-diphenyl-1,3,5-hexatriene (DPH) fluorescent dyes were from Molecular Probes (Eugene, OR, USA). The fluorescent dye 5 (6)-carboxyfluorescein diacetate *N*-succinimidyl ester (CFSE) was obtained from ThermoFisher Scientific (Waltham, MA, USA). Chocolate agar plates for the growth of nontypeable *Haemophilus influenzae* strains were from bioMérieux (Marcy l'Etoile, France). Rough lipopolysaccharide (Re 595, Re-LPS) from *Salmonella enterica* serotype Minnesota was obtained from Sigma-Aldrich. Dipalmitoylphosphatidylcholine (DPPC) was obtained from Avanti Polar Lipids (Birmingham, AL, USA). All other reagents were obtained from Sigma-Aldrich.

Bacterial strains and growth conditions

K. pneumoniae 52145 (serotype K2:O1), nontypeable *Haemophilus influenzae* strain 375 (NTHi), and *P. aeruginosa* (PAO1) are clinical isolates, as previously described (42–45). The chemical structure of *K. pneumoniae* and PAO1 capsules has been reported (46, 47). Table 1 summarized *K. pneumoniae* 52145 wildtype (WT) and isogenic mutants with or without capsule and expressing a range of different LPS phenotypes used in this study. Table 1 also shows NTHi 375 and mutant strains with defects in outer membranes (OM) used in this study. They were generated as previously described (47–49). *P. aeruginosa*, *K. pneumoniae* K2, and its mutant strains were grown in Luria–Bertani (LB) broth at 37°C with continuous shaking to the exponential phase. Frozen stocks of NTHi strains were thawed and then grown on chocolate agar plates during 18 h at 37°C in a humidified 5% CO_2 atmosphere. Then, NTHi were grown to the exponential phase on brain heart infusion broth (BHI) supplemented with 10 μg/ml hemin and 10 μg/ml β-NAD (sBHI) with continuous shaking at 37°C in a humidified 5% CO_2 atmosphere. Exponential-phase bacteria were then harvested, resuspended in PBS, and adjusted to the desired final concentration, as described in (30, 31).

TABLE 1 Bacterial strains used in this study.

Bacterial strains	Nomenclature in the text	LPS Serotype	CPS	Ref
Klebsiella				
K. pneumoniae 52145	wt Kp	S-LPS	CPS (K2)	(42, 48)
52145-Δwca_{K2}	wt Kp-CPS	S-LPS	–	(10)
52145-Δ*wabK*	Rc Kp+CPS	Rc-LPS	CPS (K2)	(47)
52145-Δwca_{K2}-Δ*wabK*	Rc Kp-CPS	Rc-LPS	–	(48)
52145-Δ*waaC*	Re Kp-CPS	Re-LPS	–	(48)
Haemophilus				
Nontypeable H. influenzae 375	wt-NTHi	S-LOS	–	(44, 49)
375 Δ*lgtF*-Δ*lpsA*	Rc-NTHi	Rc-LOS	–	(49)
375 Δ*opsX*	Re-NTHi	Re-LOS	–	(49)
Pseudomonas				
P. aeruginosa	PAO1	S-LPS	CPS (Alginate)	(43)

S-, smooth; R(c, e)-, rough; LOS, lipooligosaccharide; CPS, capsule.

Isolation of human SP-A

Surfactant protein A was isolated from bronchoalveolar lavage of patients with alveolar proteinosis using a sequential n-butanol and octylglucoside extraction (30, 31, 33, 34, 50, 51). The purity of SP-A was evaluated by one-dimensional SDS-PAGE in 12% acrylamide under reducing conditions and mass spectrometry. SP-A structure was analyzed by tryptophan fluorescence and circular dichroism as in (30, 31, 33, 34, 50, 51). SP-A hydrodynamic diameter was determined by dynamic light scattering as in (30, 51). The degree of SP-A oligomerization was assessed by electrophoresis under nondenaturing conditions, electron microscopy, and analytical ultracentrifugation as reported elsewhere (33, 34). SP-A consisted of supratrimeric oligomers of at least 18 subunits (molecular mass, 650 kDa). Each subunit had an apparent molecular mass of 36,000 Da. Endotoxin content of isolated human SP-A was about 300 pg endotoxin/mg SP-A, as determined by Limulus amebocyte lysate assay (Bio-Whittaker, Walkersville, MD, USA).

Expression and purification of rfhSP-A

The recombinant trimeric fragment of human SP-A (rfhSP-A) (molecular mass, 57 kDa), including the globular carbohydrate recognition domain (CRD), neck, and 8 x Gly-Xaa-Yaa repeats of the collagen stalk, was previously expressed in fusion with the wild-type NT solubility tag and purified by refolding (23). In the present study, rfhSP-A was sub-cloned into a pT7 expression vector containing the NT* tag N-terminally of the rfhSP-A (40, 41). A His_6-tag was included in the N-terminal of NT* to allow efficient purification. The cleavage site for coxsackievirus 3C protease was added between NT* and rfhSP-A to allow removal of the tag after purification. BL21 (DE3) *Escherichia coli* containing the plasmid encoding NT*-rfhSP-A were grown over night at 37°C in LB media containing 70 mg/L kanamycin. 10 mL culture was used to inoculate 1 L of LB medium with kanamycin and the cells were grown at 30°C to OD_{600} ~ 0.9. Isopropyl β-D-1-thiogalactopyranoside (IPTG) was added to a concentration of 0.5 mM and protein was expressed for 20 h at 20°C. Cells from 1 L culture were harvested by centrifugation at 4000 xg for 20 min and the pellet was resuspended to 60 mL in 20 mM Tris-HCl, 2 M urea, pH 8. The cell solution was sonicated (Sonics VC505 ultrasonic processor, converter model CV334, standard probe 13 mm) at 80% amplitude, 1 sec pulses, for a total of 2 min 40 sec. After lysis, a clear supernatant was obtained by centrifugation at 27,000 x g, 4°C for 30 min. The supernatant was loaded to a Ni-sepharose column (GE Healthcare) equilibrated with 20 mM Tris-HCl, 2 M urea, pH 8. The bound protein was washed with Tris buffer containing decreasing concentrations of urea (2 M, 1 M, 0.5 M and no urea) until the A_{280} baseline was reached. The protein was eluted with 20 mM Tris-HCl, 300 mM imidazole, pH 8 and imidazole was removed by over-night dialysis using a Spectra/Por® membrane with a 6-8 kDa molecular weight cut-off placed in 5 L of 20 mM Tris-HCl, pH 8 at 4°C. The fusion protein was cleaved at 4°C overnight using 1:10 (w/w) 3C protease in the presence of 1 mM DTT. An over-night dialysis was performed as described above to remove DTT, and rfhSP-A was purified by reapplication to an IMAC column to remove His-tagged NT* and 3C protease. The protein was concentrated to 1.4 mg/mL using a Vivaspin 20 centrifugal tube with a 5 kDa molecular weight cut-off (GE Healthcare). rfhSP-A identity was evaluated by one-dimensional SDS-PAGE. LPS contamination was removed by addition of polymyxin B-agarose to the rfhSP-A sample in 5 mM Tris, 150 mM NaCl, pH 7.4, at 1:5 (vol/vol). OGP (30

mM) was also added to the suspension. The sample was incubated for 30 min at room temperature in a rotator shaker and centrifuged at 500 g for 5 min at 4°C. The supernatant was then dialyzed, and the protein was quantified by the Lowry method. Endotoxin content was then determined by Limulus amebocyte lysate assay. Structural characteristics of rfhSP-A were assessed by tryptophan fluorescence and circular dichroism as in (33, 34, 50), and its hydrodynamic size by dynamic light scattering (30, 51).

Bacterial killing assays

The microbicidal activity of SP-A, rfhSP-A, and/or conventional antibiotics was evaluated by colony counts on plate assays (11, 30, 31). Five microliters of bacterial suspension (10^5 CFU/ml) were incubated with different concentrations of proteins (SP-A or rfhSP-A), antibiotics, and combinations thereof in 30 µL of 10 mM phosphate buffer, 100 mM NaCl, and 1% tryptic soy broth (*Liquid Testing Medium*, LTM) for 1 h at 37°C. At the end of incubation, bacterial suspensions were plated on LB agar for *K. pneumoniae* and PAO1 strains, or sBHI agar for NTHi strains, and incubated for 18 h at 37°C. Viable bacteria were enumerated by colony count. The results were expressed as a percentage of relative survival in comparison to untreated bacteria. The molar concentration of rfhSP-A used was 6 times higher than that of SP-A, since native SP-A is composed of 6 trimerics units.

Direct bactericidal activity of SP-A was assessed by fluorescence microscopy using *K. pneumoniae* 52145 and mutant strains transformed with pZsGreen-expressing GFP or NTHI strains stained with CFSE (52). Briefly, 100 µl of GFP expressing *K. pneumoniae* suspension, containing 10^8 CFU/ml, were incubated with or without 100 µg/ml SP-A in LTM for 1 h at 37°C. On the other hand, 100 µl of a CFSE-stained NTHi suspension, containing 10^8 CFU/ml, were incubated with or without 25 or 100 µg/ml SP-A in Hank's balanced salt solution (HBSS) (0.137 M NaCl, 5,4 mM KCl, 0.25 mM Na_2HPO_4, 0.44 mM KH_2PO_4, 1.3 mM $CaCl_2$, 1 mM $MgSO_4$, 4.2 mM $NaHCO_3$) supplemented with 1% tryptic soy broth for 1 h at 37°C in a humidified 5% CO_2 atmosphere. Polymyxin B was used as a positive killing control. Samples were then stained with 30 µM propidium iodide, a membrane-impermeable fluorescent probe, for 15 min under dark conditions. Bacteria were pelleted, re-suspended in the same buffer, and mounted on glass slides. Living (green) and dead/dying (red) bacteria were visualized by fluorescence microscopy (Leica TCS SP2 Confocal System).

Binding of SP-A to bacteria

To explore the ability of SP-A to bind to *K. pneumoniae* 52145 (or mutant strains) in the absence or presence of polymyxins (PMB and PMBN), binding assays were performed with biotinylated SP-A, which was prepared as previously described (51). Structure and functional activities of biotinylated SP-A were similar to those of unlabeled SP-A. The binding assay of biotinylated SP-A to bacteria was executed as previously described (30, 31). Briefly, 10^7 CFU/ml log-phase bacteria in 5 mM Tris-HCl buffer containing 150 mM NaCl and 2 mM Ca^{2+} were incubated with several concentrations of biotinylated SP-A in the absence or presence of PMB (5 µg/ml), PMBN (5 µg/ml), or human serum albumin (HSA) in 10% FBS-blocked microcentrifuge tubes by gentle orbital rotation for 30 min at room temperature. In all cases, bacteria were pelleted, washed twice, and resuspended in 200 ml carbonate buffer 0.1 M, pH 9.5. Controls were performed in the absence of bacteria to estimate nonspecific binding. Bacteria-associated SP-A was next measured by solid-phase binding as follows. Samples were applied to a 96-well plate MaxiSorp (Nunc, Rochester, NY, USA) and allowed to bind 1 h at 37°C. The plate was next blocked with 5 mM Tris-HCl containing 10% FBS for 1 h at 37°C. After extensive washing with PBS, streptavidin-HRP was added to the wells and incubations were performed for 1 h at room temperature. Biotinylated SP-A was detected by adding 3,3',5,5'-tetramethylbenzidine liquid substrate. The colorimetric reaction was halted with 4M sulfuric acid, and absorbance read at 450 nm on an ELISA reader (DigiScan, Asys HiTech GmbH, Eugendorf, Austria). Results were expressed as nanograms of SP-A per 10^7 bacteria.

Bacterial aggregation assays

Bacteria in exponential phase were re-suspended in HBSS buffer and adjusted to a final concentration of 10^9 CFU/ml (OD_{700} = 1). For PAO1, *K. pneumoniae* 52145 and mutant strains, either SP-A (25 µg/ml) or rfhSP-A (13 µg/ml) was added to 150 µl of the bacterial suspension and incubated for 30 min at 37°C with 30 seconds of gentle shaking every 5 min. Bacterial aggregation was determined by monitoring changes in absorbance at 700 nm during 2 h at 37°C without shaking, in a spectrophotometer DU-800 (Beckman Coulter, Fullerton, USA). Bacterial aggregation is observed as a decrease in absorbance as bacterial aggregates precipitate out of solution. SP-A-induced bacterial aggregation was also visualized by fluorescence microscopy (Leica TCS SP2 Confocal System) using *K. pneumoniae* 52145 and mutant strains expressing GFP. Bacterial suspensions (10^9 CFU/ml) in HBSS buffer were

incubated with SP-A (25 µg/ml) in FACS tubes in the conditions described above for direct visualization. For NTHi and mutant strains, which exhibit aggregation on their own (52), the process of SP-A-induced bacterial aggregation was measured immediately after addition of SP-A or buffer by measuring changes in light absorbance at 700 nm during 2 h without shaking.

Intrinsic fluorescence experiments

To assess the binding of human SP-A and its recombinant fragment to PMB or PMBN, the tryptophan fluorescence of rfhSP-A or SP-A was used as in (30, 50, 53, 54) to determine the apparent dissociation constant (K_D) at 25°C for protein-antibiotic complexes. Experiments were carried out in 5x5 quartz cuvettes using an SLM-Aminco AB-2 spectrofluorimeter equipped with a thermostated cuvette holder (± 0.1°C; Thermo Spectronic, Waltham, MA, USA). Fluorescence emission spectra of SP-A (15 nM) or rfhSP-A (0.3 µM) in the absence and presence of increasing concentrations of polymyxins were recorded from 305 to 400 nm on excitation at 295 nm at 25°C in 5 mM Tris-HCl buffer (pH 7.4) containing 150 mM NaCl or not. Each titration data point was performed in separated samples, and tryptophan fluorescence emission was monitored 10 min after PMB or PMBN addition. The change in the fluorescence of SP-A (or rfhSP-A) at the emission wavelength maximum was monitored as a function of PMB or PMBN concentration, and the titration data were analyzed by nonlinear least-squares fitting to the Hill equation, as previously reported (30, 53, 54):

$$\Delta F/\Delta F_{max} = [L]^{nH}/([L]^{nH} + K_D) \quad (1)$$

where ΔF is the change in fluorescence intensity at 337 nm relative to intensity of free SP-A (for free rfhSP-A, the emission wavelength maximum was 342 nm); ΔF_{max} is the change in fluorescence intensity at saturating polymyxin concentrations; K_D is the apparent equilibrium dissociation constant; [L] is the molar concentration of free PMB or PMBN; n_H is Hill coefficient.

Dynamic light scattering

These assays were carried out as in (30, 51, 54–56) to determine if there are changes in the size of the particles after the interaction of SP-A (or rfhSP-A) with the corresponding polymyxin (PMB or PMBN) in solution. Hydrodynamic diameters of PMB, PMBN, SP-A, rfhSP-A, and combinations thereof were measured at 25°C in a Zetasizer Nano S (Malvern Instruments, Malvern, UK) equipped with a 633-nm HeNe laser. Interaction of SP-A or rfhSP-A with polymyxins in solution was measured by addition of different concentrations of polymyxins to 15 nM SP-A (or rfhSP-A) in 5 mM Tris-HCl buffer (pH 7.4), in the absence or presence of 150 mM NaCl. Ten scans were performed for each sample, and experiments were performed in triplicate. The hydrodynamic diameters were calculated using the general purpose and multiple narrow modes algorithms available from the Malvern software for DLS analysis.

Bacterial membrane permeabilization

The ability of SP-A (or rfhSP-A), PMB, PMBN, and combinations thereof to permeabilize the outer and cytoplasmic bacterial membranes was studied in live bacteria by quantifying the internalization of the impermeant fluorescent Sytox Green, since its fluorescence increases when binding to bacterial DNA (31). For the measurement of Sytox Green influx, the probe (1 µM) was added to 1 ml of bacterial suspension ($2x10^7$ CFU/ml) in LTM and the sample was incubated for 15 min in darkness at room temperature. Then, the fluorescence of the Sytox Green/bacterial suspension mixture was monitored for 4 hours in a FLUOstar Omega microplate reader (BMG LabTechnologies, Ortenberg, Germany) at excitation and emission wavelengths of 485 and 520 nm, respectively. PBS was used as a negative control, whereas ethanol (70%) was used as a positive control. Background fluorescence was measured in non-labeled bacteria.

Bacterial membrane alteration

Exponential phase bacteria ($1×10^7$ CFU/mL) were treated with SP-A (100 µg/mL), PMB (1 µg/mL), PMBN (1 µg/mL) and combinations thereof at 37°C for 30 min in PBS buffer as previously described in (31). The suspension was incubated with 20 µM of DPH dissolved in N,N-dimethylformamide for 1h at 37°C in darkness. DPH fluorescence intensity was measured using an SLM-Aminco AB-2 spectrofluorimeter equipped with a thermostated cuvette holder (Thermo Spectronic, Waltham, MA, USA). Quartz cuvettes of 5x5-mm path length were used. Excitation and emission wavelengths: 350 and 450 nm, respectively. Non-labeled bacteria were used as background. All experiments were conducted in triplicate.

LPS aggregation assays

LPS aggregation induced by SP-A, PMB, PMBN, and combinations thereof was studied as described elsewhere (33, 34, 57) by measuring the change in absorbance at 400 nm in a Beckman DU-800 spectrophotometer. Briefly, the sample and reference cuvettes were first filled with Re-LPS in 5 mM Tris-HCl buffer (pH 7.4), 150 mM NaCl, and 0.2 mM EDTA. After a 10-min equilibration at 37°C, SP-A, PMB, PMBN, or combinations thereof were added to the sample cuvette, and the change in optical density at 400 nm was monitored. Next,

Ca^{2+} (2.5 mM) was added to both the sample and reference cuvettes, and the change in absorbance was monitored again. For LPS aggregation assay, final concentrations (58) were 40 μg/ml Re-LPS, 20 μg/ml (30 nM) SP-A, 1.5 μg/ml (1.08 μM) PMB, and 2.5 μg/ml (2.59 μM) PMBN. DPPC vesicle aggregation experiments were also performed as previously reported (33, 34).

Statistical analysis

Data are presented as means ± SDs. Differences in the means were analyzed by one-way ANOVA followed by the Bonferroni multiple-comparison test. For comparison of two groups, Student t test was used. An α level $\leq$ 5% ($p \leq 0.05$) was considered significant.

Results

Direct antimicrobial activity of SP-A against *K. pneumoniae* K2 and isogenic mutants

K. pneumoniae is a common nosocomial Gram-negative bacterium that expresses S-LPS and CPS, which can be classified into 77 serotypes; K1 and K2 serotypes are expressed by a significant number of clinical isolates (59). We investigated SP-A antimicrobial activity against *K. pneumoniae* 52145 (serotype K2) wild-type (WT) and isogenic mutants expressing a range of different LPS phenotypes (Table 1) by determining its ability to bind, aggregate, and kill bacteria (Figure 1). This *K. pneumoniae* strain encodes all the virulence determinants associated with invasive strains (60, 61). SP-A bound to both Rc and Re non-capsulated *K. pneumoniae* strains in a dose-dependent manner, but it did not bind to capsulated WT and Rc strains and the non-capsulated WT strain, as seen by solid-phase binding assay (Figure 1A). These results indicate that the K2 capsule and LPS glycoconjugate structures underneath the K2 capsule are not recognized by native SP-A. Consistent with bacterial binding assays, spectrophotometry experiments revealed that SP-A induces aggregation of non-capsulated Rc and Re strains in the presence of calcium, but not bacterial strains to which SP-A does not bind (Figure 1B). Bacterial aggregation is observed as a decrease in absorbance as bacterial aggregates precipitate out of solution. SP-A's ability to aggregate non-capsulated deep rough *K. pneumoniae* strains was confirmed by fluorescence microscopy using strains transformed with pZsGreen-expressing GFP (Figure 1C) and bacterial pellet formation (Figure 1D). SP-A exhibited direct microbicidal activity against non-capsulated Rc and Re strains, but not against capsulated WT and Rc and non-capsulated WT strains (Figure 1E). These results were confirmed using the membrane-impermeable DNA-specific dye propidium iodide. Following incubation with SP-A, the non-capsulated Rc strain, but not the *K. pneumoniae* K2 strain, formed aggregates, and most bacteria were propidium iodide-stained, indicating bacterial cell death (Figure 1F). Together, these results indicate that LPS and CPS glycoconjugates of *K. pneumoniae* confer protection from direct antimicrobial activity of native human SP-A.

Direct antimicrobial activity of SP-A against nontypeable *Haemophilus influenzae* and isogenic mutants.

Nontypeable *H. influenzae* (NTHi) is a human-restricted respiratory pathogen (62) expressing surface glycolipids that lack O-antigens and have been termed lipooligosaccharides (LOS) (49). Since LOS glycoconjugates of NTHi have been shown to be involved in NTHi pathogenicity and antimicrobial resistance (49), we next determined SP-A antibacterial activity against strain NTHi375, clinical isolate from a patient with otitis media, and isogenic mutants with truncated LOS variants (Table 1). SP-A exhibited direct microbicidal activity against the deep rough mutant Re-NTHi strain, which conserves only the KDO component of LOS, but did not significantly kill the wild-type strain (with complete LOS) and the Rc-NTHi strain (lacking the outer part of LOS) (Figure 2A). These results support the role of LOS glycoconjugates in NTHi resistance to SP-A. The results were confirmed by fluorescence microscopy using wt NTHi and mutant strains stained with CFSE. After SP-A treatment, the deep rough mutant Re-NTHi strain, but not the wild-type strain, were propidium iodide-stained, indicating bacterial death (Figure 2B). NTHi and mutant strains have the property to aggregate on their own in the presence of calcium (52). The rate of auto-aggregation of NTHi depends on the complexity of LOS. It decreases progressively with decreasing LOS extension in Rc-NTHi and Re-NTHi strains (Figure 2C). The presence of SP-A significantly increases aggregation of the deep rough mutant Re-NTHi strain, but not the wild-type and Rc-NTHi strains (Figures 2C, D).

Interaction of SP-A with antibiotics.

We next evaluated the potential synergy of SP-A with conventional antibiotics against Gram-negative bacteria. To achieve this, we used polymyxin B and E, azithromycin, tetracycline, and ciprofloxacin because they have different mechanisms of action and different targets on Gram-negative bacteria (58). Figure 3 shows that SP-A had synergistic antimicrobial activity with sub-inhibitory concentrations of polymyxin B (PMB) against *K. pneumoniae* (Figure 3A) and *P. aeruginosa* (Figure 3B), which are resistant to SP-A. However,

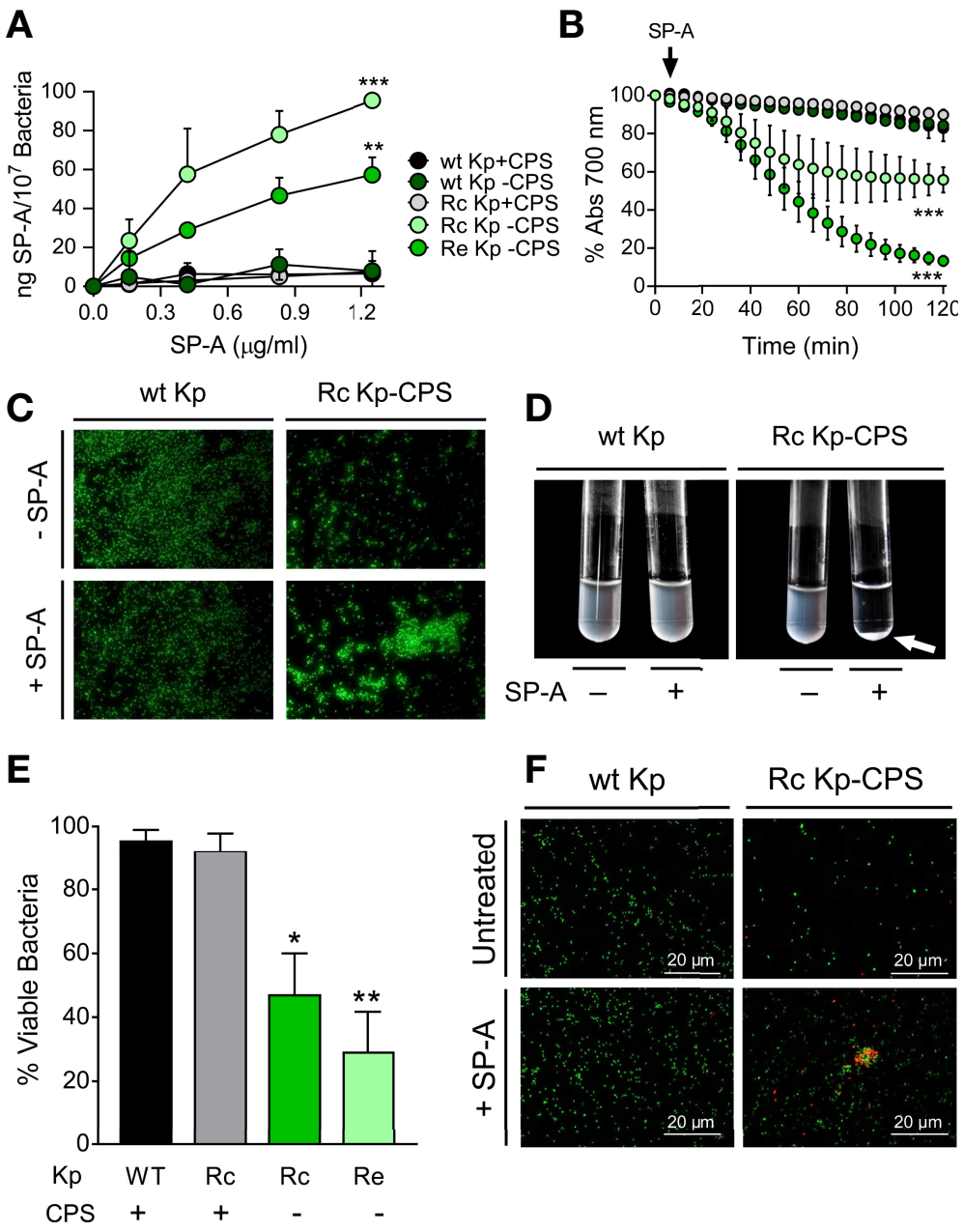

FIGURE 1
SP-A binds, aggregates, and kills deep rough non-capsulated *K pneumoniae*, but not strains expressing long-chain LPS and/or capsule. **(A)** *K pneumoniae* strains (10^7 CFU) were incubated with biotinylated SP-A (0 to 1.25 μg/ml), and total *Klebsiella*-associated SP-A was measured by solid-phase binding and expressed as total ng of SP-A/10^7 bacteria. Data are means ± SD of three independent experiments. A value of ***p < 0.001 was obtained for the one-way ANOVA, followed by the general multiple-comparison Bonferroni test. **(B)** Bacterial aggregation by SP-A (25 μg/ml) was determined by monitoring the changes in absorbance at 700 nm during 2 h at 37°C without shaking. Absorbance of strains incubated in the absence of SP-A corresponds to 100%. Data are means ± SD (n=3, each in triplicate). **(C)** SP-A-induced bacterial aggregation was visualized by fluorescence microscopy using wt and Rc-CPS *K pneumoniae* strains expressing GFP. Images shown are representative of three independent experiments with similar results. Scale bar, 20 μm. **(D)** SP-A-induced bacterial aggregation of the Rc-CPS strain but not of the wt strain was also visualized by the formation of bacterial pellets (white arrow) after 2 h of incubation with 25 μg/ml SP-A. **(E)** The antimicrobial activity of SP-A on *K pneumoniae* strains was determined by incubation of bacteria (10^5 CFUs/ml) in the absence or presence of SP-A (100 μg/ml) for 1 h at 37°C. Then, bacteria were plated on LB agar for CFU count after 18 h of incubation at 37°C. The results are shown as % viable bacteria (percentage of live colony counts compared with untreated control). Data are means ± SD of three independent experiments with three biological replicates. **(F)** Bacterial killing was also visualized by fluorescence microscopy. Strains expressing GTP (wt Kp and Rc Kp-CPS) were incubated with or without 100 μg/ml SP-A and stained with propidium iodide to assess viability. Images shown are representative of three independent experiments. Scale bar, 20 μm. In **(A)**, **(B)**, and **(E)**, results were statistically analyzed by one-way ANOVA followed by the Bonferroni multiple-comparison test. *p < 0.05, **p < 0.01, and ***p < 0.001 when comparing SP-A-treated with untreated *K pneumoniae* strains.

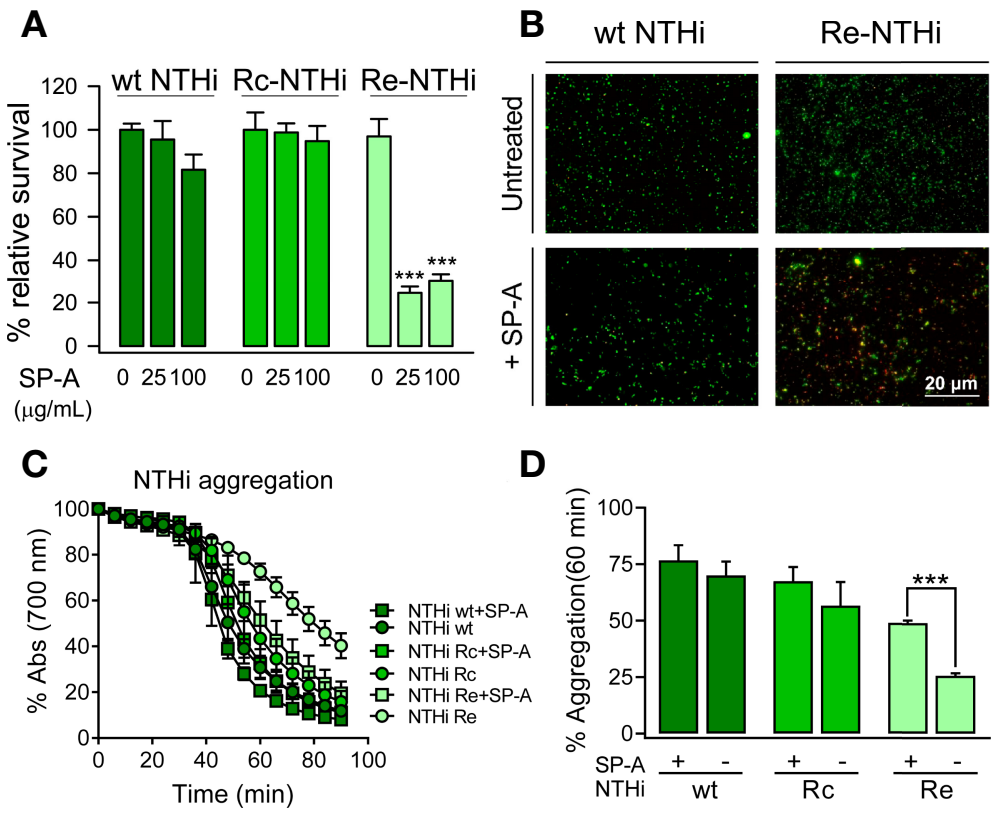

FIGURE 2
SP-A kills and induces aggregation of deep rough NTHi strains but not of NTHi strains expressing long-chain LOS. **(A)** Bacteria (10^5 CFUs/ml) were incubated with and without SP-A (25 and 100 μg/ml) and plated on sBHI agar for CFU count. The results are shown as % viable bacteria (percentage of live colony counts compared with untreated control). Data are means ± SD of three independent experiments with three biological replicates. **(B)** Bacterial killing was also visualized by fluorescence microscopy using wt NTHi and Re-NTHi stained with CFSE. Bacteria were incubated with 100 μg/ml SP-A for 1 h and then stained with 30 μM propidium iodide to assess viability. Images shown are representative of three independent experiments. Scale bar, 20 μm. **(C)** SP-A-induced aggregation of NTHi strains was monitored by changes in absorbance at 700 nm during 1.30 h at 37°C without shaking in HBSS buffer. **(D)** Percentage of aggregation at 60 min is shown. Data are means ± SD (n=3, each triplicate). In **(A, D)**, results were statistically analyzed by one-way ANOVA followed by the Bonferroni multiple-comparison test. ***$p < 0.001$ when the Re-NTHi strain treated with SP-A was compared with that not treated with SP-A.

SP-A did not show synergy with other antibiotics such as azithromycin, tetracycline and ciprofloxacin. In these experiments, both SP-A and the antibiotics were in solution. When bacteria were first incubated with SP-A in solution and then plated on Müller-Hinton agar supplemented with different antibiotics, the synergy between SP-A and PMB was lost (data not shown). Given the poor diffusion of SP-A in agar, these data suggest that the observed synergy is based on the SP-A/PMB interaction in solution.

We first determined the potential interaction of SP-A and PMB in solution by monitoring changes in the intrinsic fluorescence of SP-A after PMB binding (Figure 4A). The fluorescence of SP-A is dominated by the contribution of its two conserved tryptophan residues at the COOH-terminal end of the protein (50). Addition of increasing concentrations of PMB (0 to 150 μM) resulted in a significant PMB concentration-dependent decrease in the amplitude of the fluorescence emission spectrum of SP-A, without any shift in the wavelength of the emission maxima (Figure 4A, left). The estimated dissociation constant (K_D) for SP-A/PMB interaction was 0.32 ± 0.04 μM (Figure 4A, right), and the Hill coefficient value was greater than 1, indicating a positive cooperative binding.

We next evaluated whether SP-A interaction with PMB allows SP-A binding to *K. pneumoniae* by solid-phase binding assay (Figure 4B). SP-A alone did not bind to *K. pneumoniae*, not even in the presence of HSA. However, SP-A was able to bind this respiratory pathogen in the presence of PMB in a dose-dependent manner. Therefore, these results indicate that, through a protein-lipopeptide interaction mechanism, PMB facilitates the binding of SP-A to bacteria.

To determine if there are changes in the size of the particles after the interaction of SP-A with PMB in solution, we performed dynamic light scattering in the absence and

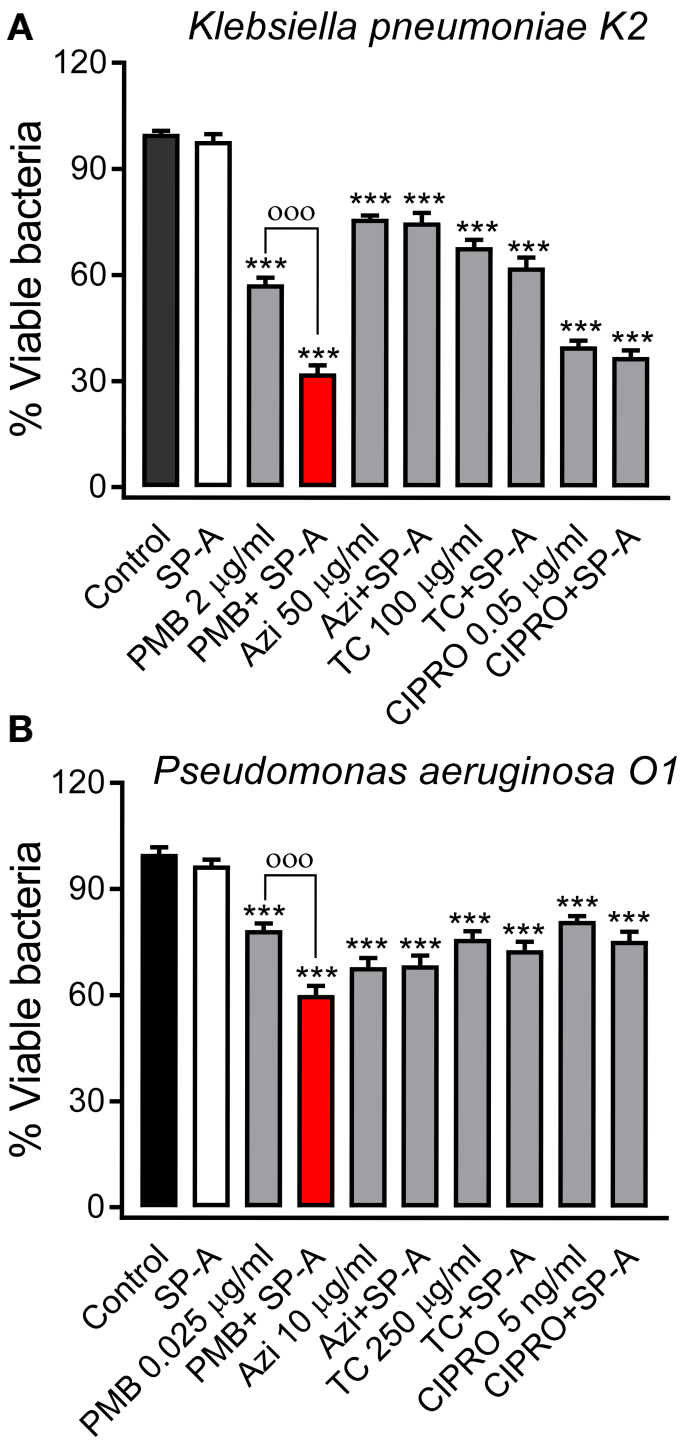

FIGURE 3
SP-A has synergic antimicrobial activity with polymyxin B (PMB), but not with azithromycin (AZI), tetracycline (TC), and ciprofloxacin (CIPRO), against Gram-negative bacteria. 10^5 CFU/ml of *K pneumoniae* **(A)** or PAO1 **(B)** were incubated with conventional antibiotics, at the indicated concentrations, in the absence or presence of SP-A (100 µg/ml) in 10 mM phosphate buffer (pH 7.4), 1% TSB, and 100 mM NaCl for 1h at 37°C. Then, the bacteria were plated on LB agar for CFU count after 18 h of incubation at 37°C. The results are shown as % viable bacteria (percentage of live colony counts compared with untreated control). SP-A alone was unable to kill capsulated *K pneumoniae* or PAO1, as previously reported (25). Data are the means ± SD of three independent experiments with at least three biological replicates. A value of $p < 0.001$ was obtained for the one-way ANOVA, followed by the general multiple-comparison Bonferroni test: ***$p < 0.001$ when comparing antibiotic treatment vs. the control untreated group; $^{ooo}p < 0.001$ when comparing SP-A+antibiotic treatment vs. the antibiotic-treated group.

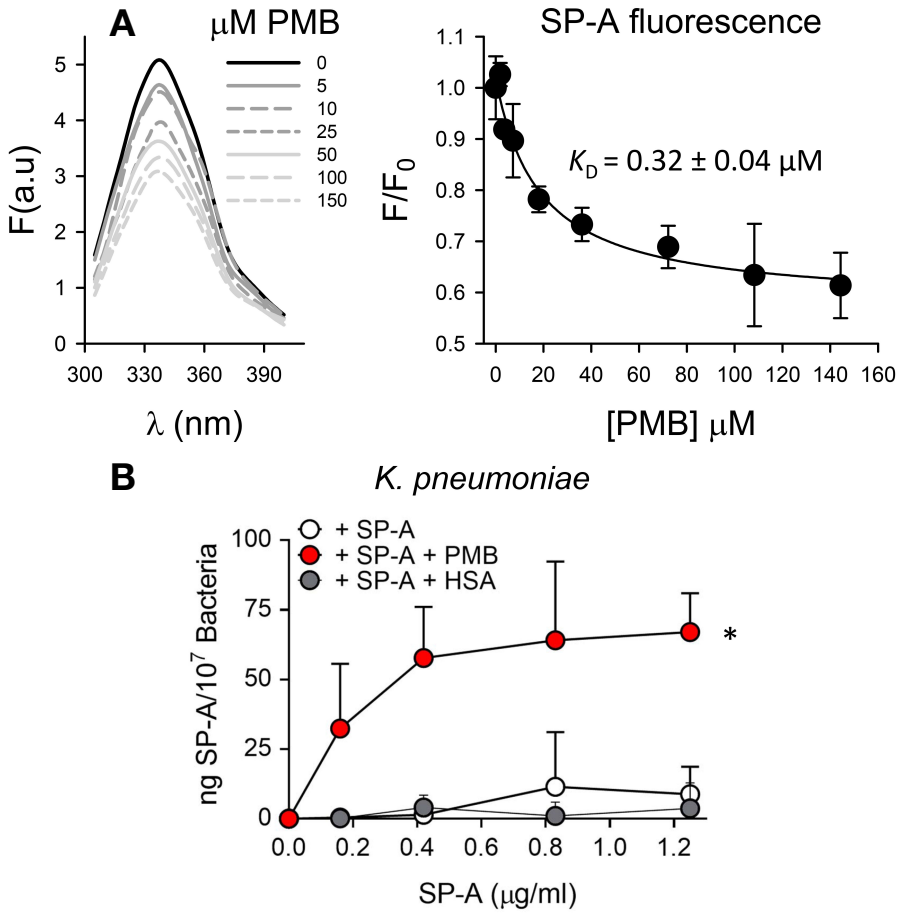

FIGURE 4
SP-A and polymyxin B interact in a dose-dependent manner, allowing binding of SP-A to *K pneumoniae*. **(A)** (Left) Tryptophan fluorescence emission spectra of SP-A (15 nM) (10 μg/ml) were measured with or without increasing concentrations of PMB (0-150 μM; 0-180 μg/ml) at 25°C in 5 mM Tris-HCl buffer (pH 7.4) containing 150 mM NaCl. SP-A samples (with and without PMB) and blank samples (PMB alone) were excited at 295 nm and the emission spectra recorded from 300 to 400 nm. One representative experiment of four is shown. (Right) Results are expressed as F/F_0, where F and F_0 are the corrected emission intensities at 337 nm in the presence and absence of PMB. Results are means ± SD of four experiments. **(B)** Binding capacity of biotinylated SP-A to *K pneumoniae* (10^7 CFU) in the presence and absence of PMB (5 μg/ml) or HSA (5 μg/ml). The concentration of biotinylated SP-A associated with *K pneumoniae* was measured by a solid phase binding assay. Data are means ± SD of three independent experiments with three biological replicates. A value of $*p < 0.05$ was obtained for the one-way ANOVA.

presence of salts to further determine the role of NaCl in the interaction between positively charged PMB particles and SP-A, a protein rich in negatively charged amino acids, whose isoelectric point varies between pH 4.5 and 5.2 (63). Figure 5A shows that addition of PMB to SP-A at neutral pH caused a PMB concentration-dependent increase of SP-A hydrodynamic size, both in the presence and absence of salts, resulting in the formation of SP-A-PMB aggregates of 800-900 nm (Figure 5B). Figure 5A also shows that PMB alone exhibited a unique peak (independent of concentration) corresponding to particles with a hydrodynamic diameter of 20 ± 3, in the absence of salts, and 150 ± 30 nm, in the presence of 150 mM NaCl (Figure 5, upper graphs). On the other hand, SP-A alone showed a hydrodynamic diameter of 34 ± 5 nm in the absence of salts, as previously described (51). In the presence of 150 mM NaCl, SP-A self-aggregates, as previously described (64) with a major peak at 320 ± 30 nm (30) (Figure 5A).

Synergistic antimicrobial activity of SP-A with polymyxin B and colistin

We next assessed whether SP-A/polymyxin complexes increase the antimicrobial activity of this lipopeptide antibiotic against *K. pneumoniae* K2, non-typable *H. influenzae* (NTHi), and *P. aeruginosa*, which are resistant to SP-A. For these experiments we use polymyxin B and E (colistin), both of which are available for clinical use. Colistin differs from

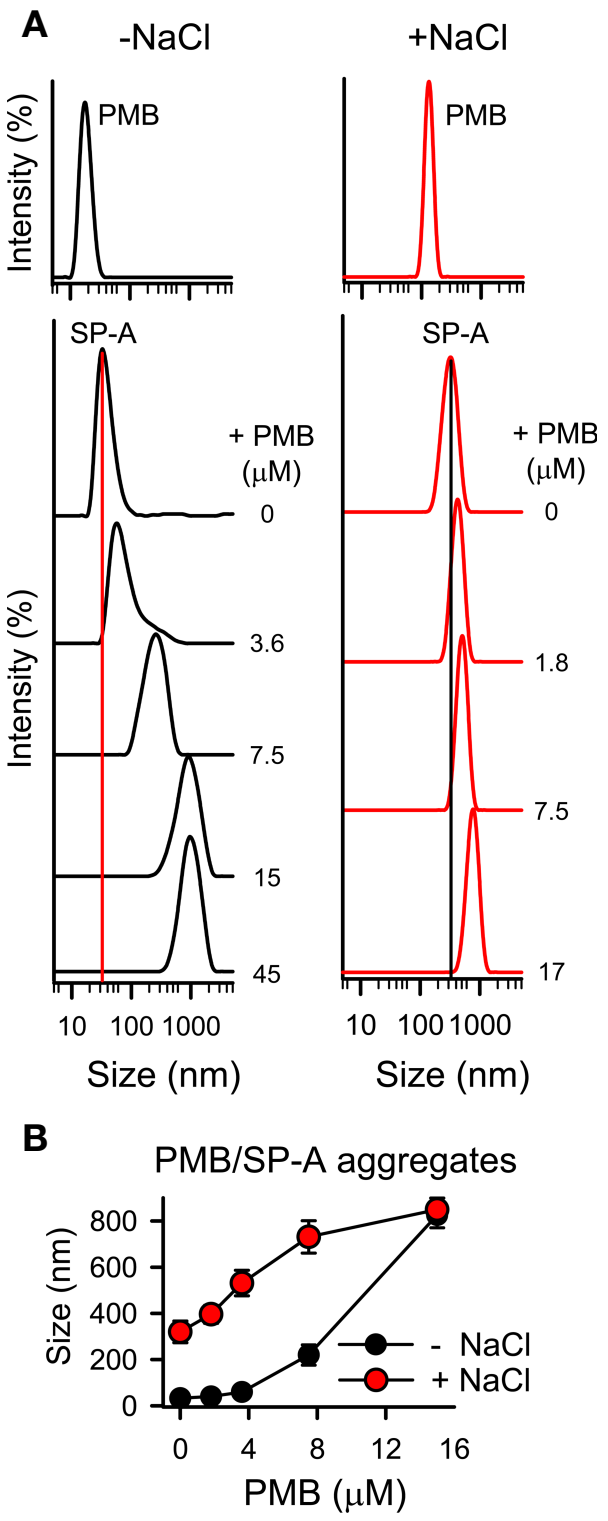

FIGURE 5
SP-A forms molecular aggregates with polymyxin B. The formation of SP-A and PMB complexes was examined by DLS. **(A)** DLS analysis of the hydrodynamic diameter of SP-A/PMB complexes in 5 mM Tris-HCl buffer (pH 7.4), in the presence or absence of 150 mM NaCl. The y-axis represents the relative intensity of the scattered light; the x-axis represents the hydrodynamic diameter of the particles present in the solution. DLS analyses of SP-A (15 nM) and PMB (15 μM) particles alone in both buffers are shown in the upper graphs. One representative experiment of four is shown. **(B)** Formation of SP-A/PMB aggregates is independent of salts. The results are the mean ± SD of four independent experiments, each in triplicate.

polymyxin B in the amino acid at R6 position of the cyclic heptapeptide part (i.e., residues R4–R10), which is D-phenylalanine in PMB and D-leucine in PME (35). Figure 6 shows that when bacteria were incubated with SP-A (at concentrations within the ranges found in the alveolar fluid of human lungs) (65) and increasing concentrations of PMB (Figure 6, upper panels) and colistin (PME) (Figure 6, lower panels), SP-A significantly increased polymyxin bactericidal activity against the three pathogens. Therefore, we demonstrated that human SP-A/polymyxin complexes exhibit significantly increased antimicrobial activity relative to PMB and PME alone.

Interaction and synergy of SP-A with nontoxic polymyxin nonapeptide

Given that SP-A is a lipid binding protein (63), we determined the role of the lipid moiety of this lipopeptide antibiotic in the interaction with SP-A using polymyxin B nonapeptide (PMBN), a PMB derivative that lacks the fatty acid tail. PMBN maintains polymyxin B's ability to bind to Gram-negative bacteria and disturb to some extent the outer membrane of these bacteria. However, PMBN alone does not have bactericidal activity (38, 39).

Figure 7A shows that SP-A interacted with PMBN with an estimated dissociation constant (K_D = 0.26 ± 0.04 μM) similar to that obtained for the lipopeptide antibiotic. The binding of SP-A to PMBN also resulted in the formation of molecular aggregates similar in hydrodynamic size to those formed with PMB, as determined by dynamic light scattering (Figure 7B). In addition, the formation of SP-A/PMBN aggregates, through a protein-protein interaction mechanism, facilitates the binding of SP-A to *K. pneumoniae* to which SP-A alone does not bind (Figure 7C).

Next, we sought to ascertain whether the formation of SP-A/PMBN aggregates confers new antimicrobial properties, including the ability to kill pathogenic Gram-negative bacteria that are otherwise resistant to either SP-A or PMBN alone. We found that SP-A/PMBN complexes were able to kill *K. pneumoniae*, non-typable *H. influenzae*, and *P. aeruginosa* (Figure 8), indicating that the combination of nontoxic PMBN and SP-A could be used as a new antimicrobial against respiratory Gram-negative infections.

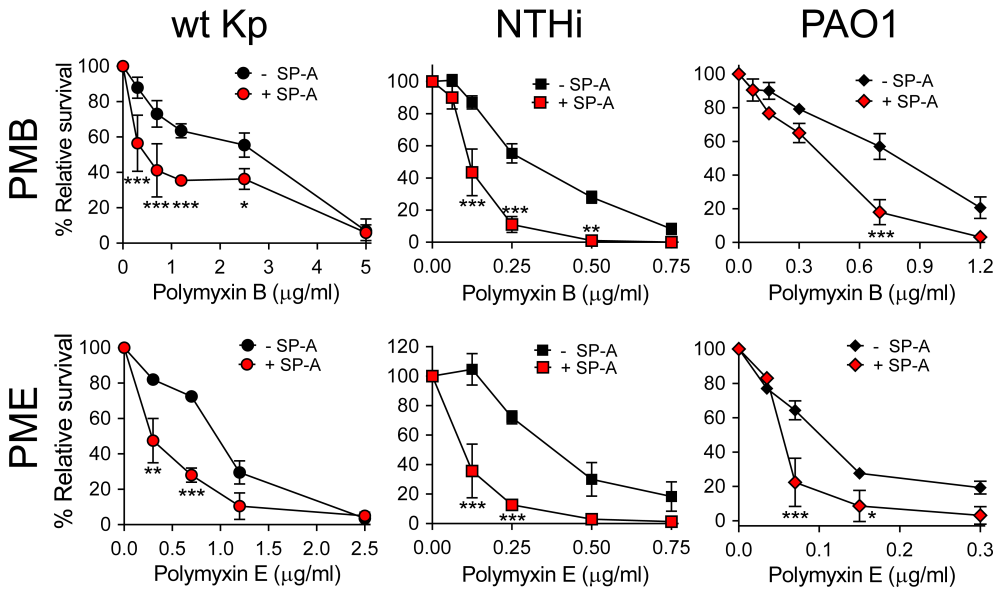

FIGURE 6
SP-A acts synergistically with polymyxin B and colistin (PME) against Gram-negative bacteria. 10^5 CFUs/ml of bacteria (*K. pneumoniae*, NTHi, and *P. aeruginosa* O1) were incubated with different concentrations of PMB (upper graphs) and PME (lower graphs) in the absence or presence of SP-A (100 μg/ml) in 10 mM phosphate, 1% TSB, and 100 mM NaCl buffer (pH 7.4) for 1 h at 37°C. Bacteria were then plated on LB agar (*Kp* and PAO1) or sBHI agar (NTHi) for CFU counting. Results are shown as a percentage of relative survival compared to untreated bacteria. Data are means ± SD of four independent experiments, with three biological replicates. Results were statistically analyzed by one-way ANOVA followed by the Bonferroni multiple-comparison test. *$p < 0.05$, **$p < 0.01$, and ***$p < 0.001$ when comparing SP-A-treated with SP-A-untreated *K. pneumoniae* strains.

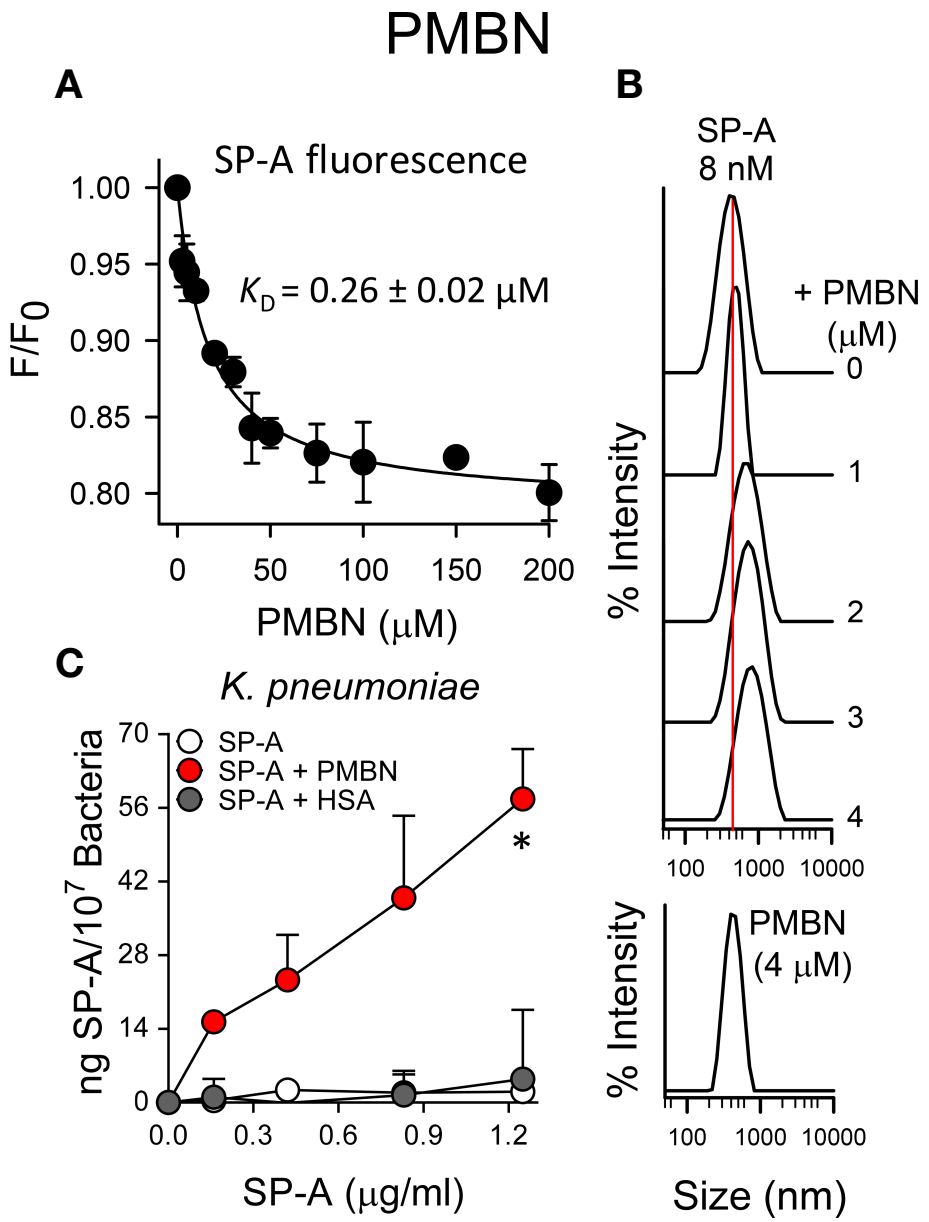

FIGURE 7
SP-A and PMBN interact in a dose-dependent manner, forming molecular aggregates that allow binding of SP-A to *K pneumoniae*. **(A)** Binding of SP-A and PMBN was examined by changes in intrinsic fluorescence emission spectra of SP-A (15 nM; 10 μg/ml)) by addition of increasing concentrations of PMBN (0 to 200 μM; 0-192 μg/ml)) at 25°C in 5 mM Tris-HCl buffer (pH 7.4) containing 150 mM NaCl. Results are expressed as F/F_0, where F and F_0 are the corrected emission intensities at 337 nm in the presence and absence of PMBN. Results are means ± SD of four experiments. **(B)** DLS analysis of the hydrodynamic diameter of SP-A/PMBN complexes in 5 mM Tris-HCl, 150 mM NaCl buffer (pH 7.4). The y-axis represents the relative intensity of the scattered light; the x-axis denotes the hydrodynamic diameter of the particles present in the solution. DLS analyses of SP-A and PMBN particles alone are also shown. One representative experiment of four is shown. **(C)** Binding capacity of biotinylated SP-A to *K pneumoniae* (10^7 CFU) in the presence and absence of PMBN (5 μg/ml) or HSA (5 μg/ml). The concentration of biotinylated SP-A associated with *K pneumoniae* was measured by a solid phase binding assay and expressed as total nanograms of SP-A/10^7 bacteria. The results are the mean ± SD of three independent experiments with three biological replicates. A value of $*p < 0.05$ was obtained for the one-way ANOVA.

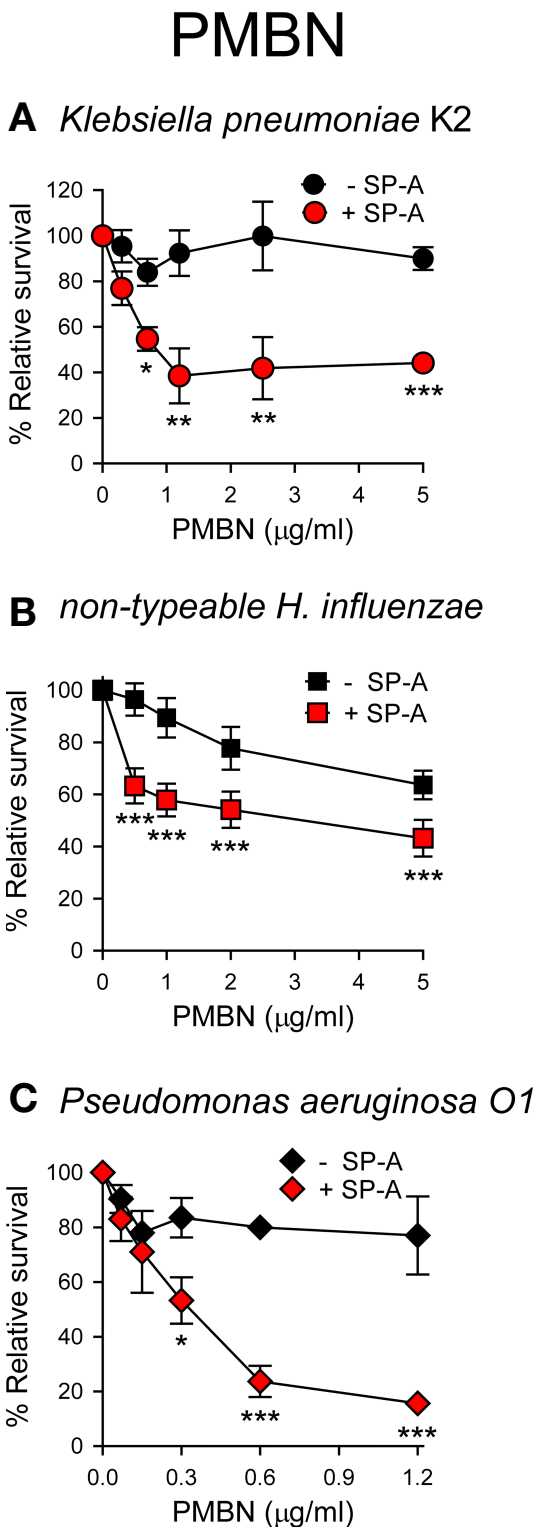

FIGURE 8
SP-A/PMBN complexes kill Gram-negative bacteria. 10^5 CFUs/ml of *K pneumoniae* **(A)**, NTHi **(B)**, and *P. aeruginosa* O1 **(C)** were incubated with increasing concentrations of PMBN in the absence or presence of SP-A (100 μg/ml for *Kp* and PAO1; 25 μg/ml for NTHi) for 1 h at 37°C. Bacteria were then plated on LB agar (*Kp* and PAO1) or sBHI agar (NTHi) for CFU counting. Results are shown as a percentage of relative survival compared to untreated bacteria. Data are means ± SD of four independent experiments, with three biological replicates. Results were statistically analyzed by one-way ANOVA followed by the Bonferroni multiple-comparison test. *$p < 0.05$, **$p < 0.01$, and ***$p < 0.001$ when bacteria treated with SP-A+PMBN were compared against bacteria treated with PMBN.

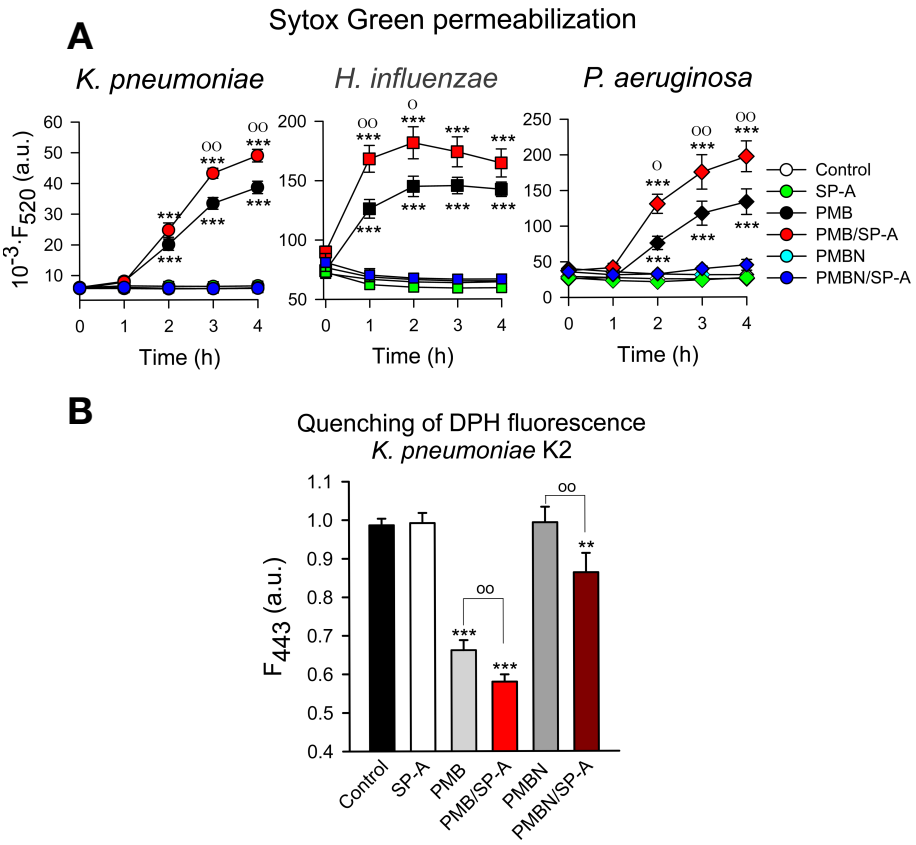

FIGURE 9
Membrane integrity of Gram-negative bacteria. **(A)** 10^7 CFU/ml of ***(K)*** *pneumoniae*, NTHi, and PAO1 were incubated with polymyxins (PMB or PMBN) and/or SP-A (100 μg/ml) in the presence of Sytox Green, and the change in the fluorescence of the dye was recorded as a function of time. The experiments were conducted at 37°C. PMB concentrations: 1 μg/ml for *K pneumoniae*; 0.5 μg/ml for NTHi and PAO1. PMBN concentrations: 1 μg/ml for *K pneumoniae*; 2 μg/ml for NTHi; 0.5 μg/ml for PAO1. **(B)** 10^7 CFU/ml of *K pneumoniae* were incubated with or without PMB (1μg/ml), PMBN (1μg/ml) and/or SP-A (100 μg/ml) in the presence of 1,6-diphenyl-1,3,5-hexatriene (DPH), and the change in the fluorescence of DPH was recorded as a function of time. Data shown correspond to the fluorescence of DPH after treatment with SP-A and/or polymyxins for 30 min. Experiments were performed at 37°C. The results are the mean ± SD of three independent experiments, each in triplicate. Results were statistically analyzed by one-way ANOVA followed by the Bonferroni multiple-comparison test: $^{**}p < 0.01$; $^{***}p < 0.001$ compared to untreated bacteria (control); $^{o}p < 0.05$; $^{oo}p < 0.01$ when bacteria treated with SP-A+polymyxin (PMB or PMBN) were compared with bacteria treated with PMB or PMBN alone.

Bacterial membrane permeabilization

The ability of SP-A, PMB, PMBN, and combinations thereof to permeabilize bacterial membranes of *K. pneumoniae*, NTHi and *P. aeruginosa* was assessed by using the fluorescent dye Sytox Green, whose fluorescence is enhanced upon binding to DNA once the bacterial cytoplasmic membrane is compromised (66). Addition of SP-A alone did not statistically affect the fluorescence of the dye (Figure 9A). These results align with the absence of SP-A binding to any of these pathogens and its incapacity to kill these bacteria on its own. However, PMB significantly increased the dye's fluorescence, consistent with the bacterial membrane permeabilization properties of PMB (36, 37). Moreover, bacteria treated with SP-A+PMB showed significantly greater Sytox Green permeabilization than those treated with PMB alone. Thus, the formation of SP-A/PMB aggregates significantly increases PMB-induced bacterial membrane permeabilization and consequent bacterial death.

In contrast to SP-A/PMB aggregates, SP-A/PMBN aggregates did not promote permeabilization of Sytox Green through Gram-negative bacterial membranes, nor did PMBN alone (Figure 9A). This suggests that the synergistic microbicidal activity of SP-A/PMBN aggregates could be related to mechanisms of action other than permeabilization of the cytoplasmic membrane. To determine if SP-A, PMB, PMBN, and combinations thereof alter the integrity of *K. pneumoniae* membranes, we measured the fluorescence of 1,6-diphenyl-1,3,5-hexatriene (DPH), a fluorescent dye that incorporates into the hydrophobic core of lipid bilayers. DPH has a low quantum yield and a very short lifetime when exposed to water. Thus, its fluorescence is sensitive

to the amount of water that penetrates the lipid bilayer (67). Figure 9B shows that SP-A or PMBN alone did not affect the fluorescence of the probe, while PMB alone and PMB/SP-A and PMBN/SPA mixtures significantly decreased the dye's fluorescence, indicating the presence of water molecules in the hydrophobic microenvironment of *K. pneumoniae* membranes. The effect of PMB/SP-A complexes on membrane alteration was significantly greater than that of PMB. Likewise, the effect of PMBN/SP-A on the integrity of *K. pneumoniae* membranes was significantly greater than that of PMBN, which did not exhibit any effect.

Bacterial lipopolysaccharide aggregation.

Polymyxins and SP-A are LPS binding peptides and induce LPS aggregation (16, 33, 34, 57, 68). Thus, we analyzed Re-LPS aggregation induced by SP-A, PMB, PMBN, and combinations thereof (Figure 10). We found that PMB/SP-A and PMBN/SP-A complexes exhibited higher LPS aggregation activity than PMB or PMBN alone at the concentrations analyzed.

Several lines of evidence have shown that the carbohydrate recognition domain (CRD) of SP-A is involved in its binding to the lipid A moiety of LPS and to dipalmitoylphosphatidylcholine (DPPC), a main pulmonary surfactant component (69–71). Thus, these experiments suggest that PMB (or PMBN) binds to SP-A at sites other than the lipid-binding site on the globular heads of SP-A. To confirm this assumption, we determined the ability of SP-A to bind and aggregate DPPC vesicles in the presence and absence of PMB, which does not bind zwitterionic phosphatidylcholine (72). Supplementary Figure 2 shows that PMB alone, in excessive concentration, did not aggregate DPPC vesicles, but SP-A/PMB complexes induced DPPC aggregation almost like SP-A alone. Together, these data indicate that the binding of PMB to SP-A does not interfere with the ability of SP-A to bind and aggregate lipids and that PMB/SP-A interaction might not occur *via* the globular domains of SP-A.

Direct antimicrobial activity of rfhSP-A against Gram-negative bacteria

We next evaluated the bactericidal activity of a recombinant trimeric fragment of human SP-A1 (rfhSP-A), which lacks the N-terminal domain and the collagen domain (Figure 11). In contrast to native supratrimeric SP-A, a small trimeric fragment of the protein (containing three globular heads) was able to kill also wt strains of respiratory pathogens (*K. pneumoniae*, NTHi, and *P. aeruginosa*). We found that rfhSP-A possesses identical antimicrobial activity against encapsulated and non-encapsulated wt strains of *K. pneumoniae*, indicating that CPS is not relevant if *K. pneumoniae* contains whole LPS glycoconjugates. However, the bactericidal activity of rfhSP-A was greater with the non-capsulated *K. pneumoniae* mutant expressing deep-rough lipopolysaccharide (Re-Kp-CPS) than with the non-capsulated wild-type strain (Figure 11). On the

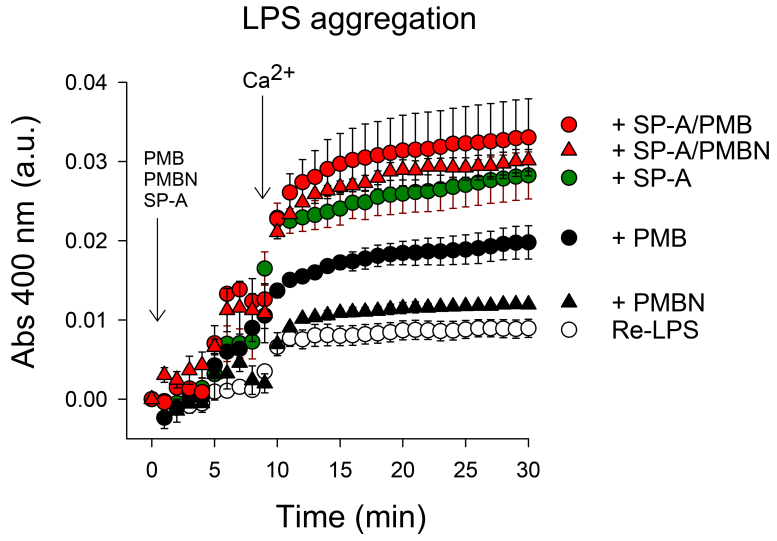

FIGURE 10
LPS aggregation induced by SP-A, PMB, PMBN, and combinations thereof. Ca^{2+}-dependent Re-LPS aggregation was studied by measuring the change in absorbance at 400 nm in a Beckman DU-800 spectrophotometer. Re-LPS was prepared at a final concentration of 40 µg/ml in 5 mM Tris-HCl buffer, pH 7.4, containing 150 mM NaCl and 0.1 mM EDTA. The final concentration of SP-A and polymyxins was 20 µg/ml (30 nM) SP-A, 1.5 µg/ml (1.08 µM) PMB, and 2.5 µg/ml (2.59 µM) PMBN. The concentration of Ca^{2+} was 2.5 mM. Results are the mean ± SD of three experiments.

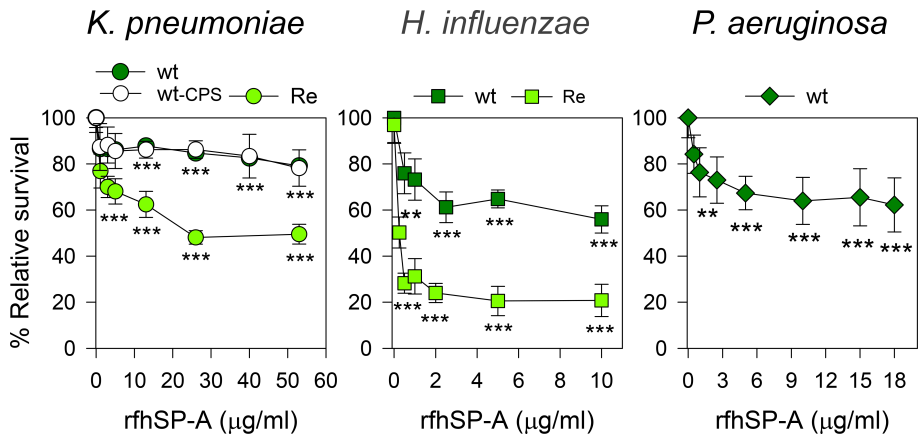

FIGURE 11
rfhSP-A kills Gram-negative bacteria. 10^5 CFUs/ml of different strains of Kp, NTHi, or PAO1 were incubated with increasing concentrations of rfhSP-A in 10 mM phosphate buffer (pH 7.4) containing 1% TSB and 100 mM NaCl for 1 h at 37°C. Bacteria were then plated on LB agar (Kp and PAO1) or sBHI agar (NTHi) for CFU counting. Results are shown as a percentage of relative survival compared to untreated bacteria. Importantly, SP-A had no effect on the survival of these pathogens at molar concentrations equivalent to or greater than the molar concentrations of rfhSP-A. Data are means ± SD of three independent experiments, with three biological replicates. Experiments were performed with both polymyxin-agarose treated and untreated rfhSP-A, to remove LPS contamination, with identical results. Results were statistically analyzed by one-way ANOVA followed by the Bonferroni multiple-comparison test. $^{**}p < 0.01$, and $^{***}p < 0.001$ when bacterial strains treated with rfhSP-A were compared with those not treated with rfhSP-A.

other hand, the rfhSP-A-induced killing of the Re-NTHi mutant strain expressing only KDO residues at its oligosaccharide moiety of LOS was much greater than that of the wild-type NTHi strain expressing long chains of LOS glycoconjugates. These results suggest that the umbelliform-shaped structure of native SP-A impedes SP-A binding to respiratory Gram-negative pathogens. Conversely, smaller fragments of SP-A, which retain the carbohydrate recognition domain and lipid binding site in their globular heads, bind to these pathogens and show bactericidal properties.

Although the small rfhSP-A protein binds and partially kills *P. aeruginosa*, NTHi, and *K. pneumoniae*, rfhSP-A is unable to aggregate not only wt PAO1 and *K. pneumoniae*, but also non-capsulated deep rough *K. pneumoniae* strains, which are aggregated by SP-A (Supplementary Figure S2). The inability of rfhSP-A to induce bacterial aggregation is consistent with the fact that SP-A requires an oligomeric assembly to induce aggregation of its different ligands (34).

Loss of interaction and synergy between rfhSP-A and polymyxin B

The trimeric recombinant fragment of human SP-A1 did not interact with PMB in solution at physiological concentrations of salts, as determined by intrinsic fluorescence of rfhSP-A after PMB binding (Figure 12A) and dynamic light scattering (Figure 12B). This suggests that the collagen-like domain and/or the supratrimeric structure of SP-A is essential for SP-A/PMB interaction and the formation of protein-lipopeptide aggregates. In the absence of salts, rfhSP-A weakly interacts with PMB with a K_D of 1.37 ± 0.5 μM.

Due to the loss of interaction under physiological conditions, rfhSP-A and PMB did not show synergistic action. However, rfhSP-A added in combination with PMB significantly increased antimicrobial efficacy against *K. pneumoniae*, non-typable *H. influenzae*, and *P. aeruginosa* (Figure 12C). The combination of rfhSP-A with other antibiotics against Gram-negative bacteria also significantly improved bactericidal efficacy against *K. pneumoniae*, indicating an additive effect of rfhSP-A with other antibiotics in addition to PMB (Supplementary Figure 3). Consistent with the lack of interaction and synergy between rfhSP-A and PMB, the recombinant fragment did not affect the ability of PMB to permeabilize bacterial membranes of Gram-negative bacteria (Figure 13). On the other hand, rfhSP-A did not affect bacterial membrane permeabilization on its own, suggesting a different mechanism for its bactericidal activity.

Discussion

SP-A is secreted into the airway mucosa by type II alveolar epithelial cells and non-ciliated bronchiolar cells, but it is also detected in the trachea, nasal mucosa, and other extrapulmonary mucosal surfaces, where it provides immune protection (17–19). It enhances phagocytosis of pathogens by opsonizing and/or up-regulating expression of the mannose receptor involved in microbial recognition (17, 19, 73, 74). In addition, SP-A can

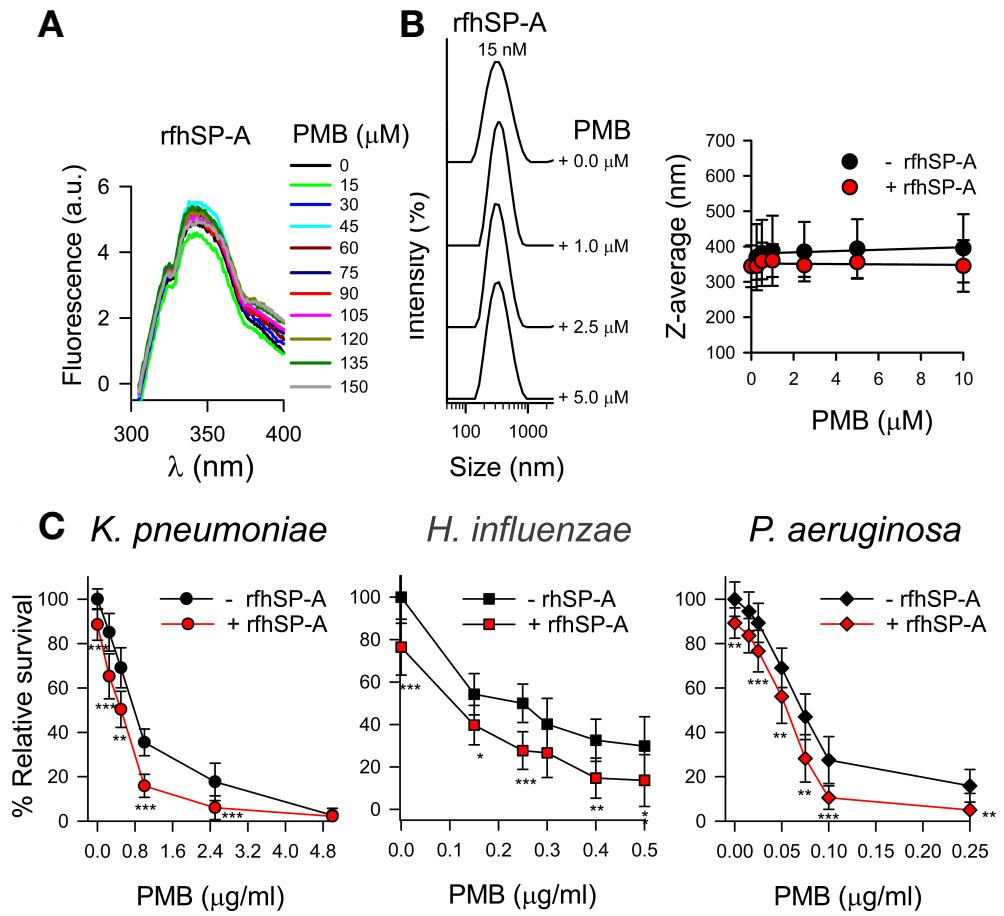

FIGURE 12
rfhSP-A does not interact with PMB and in combination with PMB increases the killing of Gram-negative bacteria. **(A)** Tryptophan fluorescence emission spectra of rfhSP-A (13 μg/ml) were measured with or without increasing concentrations of PMB (0-150 μM; 0-180 μg/ml) at 25°C in 5 mM Tris-HCl buffer (pH 7.4) containing 150 mM NaCl. Samples were excited at 295 nm and the emission spectra recorded from 300 to 400 nm. One representative experiment of four is shown. **(B)** (Left) Addition of increasing concentrations of PMB (ranging from 0 to 5 μM) to a solution containing a constant concentration of rfhSP-A (17.5 nM) in 5 mM Tris-HCl, 150 mM NaCl, buffer (pH 7.4) did not change the particle size of either SP-A or PMB. One representative experiment of four is shown. (Right) Dependence of Z-average on the PMB concentration in the presence or absence of rfhSP-A (17.5 nM). **(C)** 10^5 CFUs/ml of bacteria (*K. pneumoniae*, NTHi, and *P. aeruginosa* O1) were incubated with different concentrations of PMB in the absence or presence of rfhSP-A (1 μg/ml) (17.5 nM) in 10 mM phosphate, 1% TSB, and 100 mM NaCl buffer (pH 7.4) for 1 h at 37°C. Bacteria were then plated on LB agar (*Kp* and PAO1) or sBHI agar (NTHi) for CFU counting. Results are shown as a percentage of relative survival compared to untreated bacteria. The results in **(A)** and **(B)** correspond to rfhSP-A treated with polymyxin agarose in 5 mM Tris, 150 mM NaCl, pH 7.4 buffer to remove LPS contamination. In **(C)**, experiments were performed with both polymyxin-agarose treated and untreated rfhSP-A, with identical results. Data are means ± SD of three independent experiments, each in triplicate. Results were statistically analyzed by Student's t-test. *$p < 0.05$, **$p< 0.01$, and ***$p < 0.001$ when bacteria treated with rfhSP-A+PMB were compared with bacteria treated with PMB alone.

agglutinate some bacteria and has direct microbicidal activity on some microorganisms (20–24). However, reports of direct microbicidal activity of SP-A against clinically relevant Gram-negative bacteria are scarce, and several studies have shown that highly virulent respiratory pathogens are resistant to SP-A (27–31, 75).

In this study, we examined factors involved in the resistance of clinical isolates of *K. pneumoniae* and nontypeable *H. influenzae* to SP-A. Using *K. pneumoniae* 52145 and isogenic mutants with or without capsule and expressing a range of different LPS phenotypes, we show that both the K2 polysaccharide capsule and the underneath LPS glycoconjugates are not recognized by SP-A. SP-A exhibited direct antimicrobial activity (bacterial binding, aggregation, and killing) only against non-capsulated deep rough *K. pneumoniae* strains expressing Rc- and Re-LPS phenotypes. The small number of sugar residues in the rough strains makes it easier for SP-A to recognize the lipid A region of LPS (76, 77). Some lines of evidence suggest that *K. pneumoniae* may undergo phase variation between capsulated and non-capsulated phenotypes since non-capsulated phase variants of *K.*

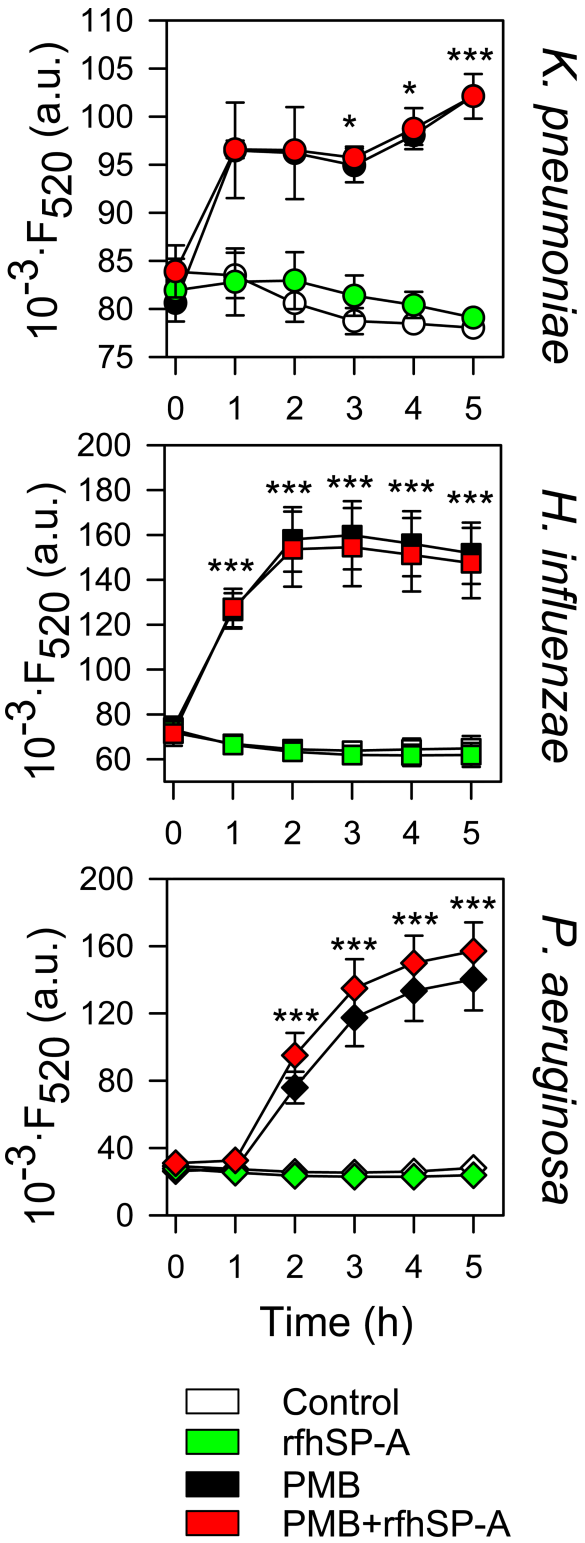

FIGURE 13
rfhSP-A does not affect the ability of PMB to permeabilize bacterial membranes. 10^7 CFU/ml of *K. pneumoniae*, NTHi, and PAO1 were incubated with PMB (1 μg/ml for *K. pneumoniae*; 0.5 μg/ml for NTHi and PAO1) and/or rfhSP-A (5 μg/ml) in the presence of Sytox Green, and the change in the fluorescence of the dye was recorded as a function of time. The results are the mean ± SD of three independent experiments, each in triplicate. A p-value < 0.001 was obtained for the one-way ANOVA followed by the Bonferroni multiple-comparison test: *p < 0.05 and ***p < 0.001 compared to untreated bacteria (control).

pneumoniae attach to and invade epithelial cells more efficiently (75, 78). SP-A would not have direct microbicidal activity against non-capsulated *Klebsiella* because of its long-chain lipopolysaccharides shield *K. pneumoniae* from SP-A. Interestingly, the macrophage mannose receptor together with SP-A provides protection against *K. pneumoniae* K21a serotype that expresses the Man-α2-Man sequence in its CPS, which is recognized by SP-A and the mannose receptor (27, 75). There is a significant correlation between the presence of this capsular glycoepitope, recognized by SP-A and other C-type lectins, and the low frequency of *K. pneumoniae* K21a in clinical isolates of patients (75).

Nontypeable *H. influenzae* is a non-capsulated Gram-negative bacterium that causes exacerbations in patients with chronic obstructive pulmonary disease (79, 80) and colonizes the lower respiratory tract of patients with neutrophilic asthma (81). NTHi express a lipooligosaccharide (LOS), which lacks the O-specific polysaccharide chains. LOS glycoconjugates are analogous to LPS found in other Gram-negative families, but tend to have short, nonrepeating oligosaccharides. They also share similar lipid A structures. Using clinical isolates of NTHi375 and isogenic mutants with truncated LOS variants, we showed that SP-A exhibited direct microbicidal activity against only the deep rough mutant Re-NTHi strain, which retains only the KDO component of LOS. These results indicate that LOS glycoconjugates of NTHi confer protection against the bactericidal and bacterial aggregation-inducing activities of SP-A.

Our results are consistent with other reports indicating that one of the factors conferring resistance to SP-A in *Bordetella pertussis* is the branched structure of the LPS core (29). For *P. aeruginosa*, several studies have indicated that there are multiple virulence factors that explain its resistance to SP-A: i) reduced expression of the outer membrane protein OprH (a ligand for SP-A) (82); ii) increased expression of glycoconjugates of long-chain LPS (82); and iii) expression of type IV pilus on the cell wall (83). In addition, *P. aeruginosa* secretes elastase and protease IV that degrade SP-A (84, 85). These adaptations of *P. aeruginosa* facilitate bacterial escape from SP-A-mediated phagocytic killing (82).

In contrast to SP-A, rfhSP-A, a trimeric recombinant fragment of the protein, surprisingly showed significant direct microbicidal activity against *K. pneumoniae*, NTHi, and *P. aeruginosa*. The trimeric recombinant fragment lacks the N-terminal domain and most of the collagen domain, which are domains involved in SP-A oligomerization. However, rfhSP-A retains ligand binding sites in the globular domains and the α-helical neck domain. The different functionality of SP-A and rfhSP-A could be related to the smaller size of rfhSP-A, which facilitates the transit of rfhSP-A through the glycoconjugate structures of CPS and LPS, or LOS in the case of NTHi. However, the bactericidal activity of rfhSP-A was higher with the non-encapsulated *K. pneumoniae* mutant expressing Re-LPS (Re-kp-CPS) and with the Re-NTHi mutant than with non-encapsulated *K. pneumoniae* and NTHi, which express long-chain glycoconjugate structures. These data indicate that these glycoconjugate assemblies also confer protection against the bactericidal action of rfhSP-A.

Direct *in vitro* killing of *K. pneumoniae*, NTHi, and *P. aeruginosa* by native human SP-A is negligible (27–31). It is possible that defense AMPs in the alveolar fluid act synergistically or cooperatively with SP-A in eliminating these pathogens, as we recently demonstrated for synergic SP-A/SP-B^N interaction (30, 31). It has recently been shown that the combined use of AMPs and antibiotics can kill drug-resistant pathogens, reduce antibiotic resistance, and significantly improve the therapeutic effects of antibiotics (86). In this study, we examined the potential cooperation of SP-A and its trimeric recombinant fragment with several antibiotics, including polymyxin B, azithromycin, tetracycline, and ciprofloxacin against Gram-negative bacteria. We chose these antibiotics because they have different mechanisms of action and different targets on Gram-negative bacteria (58). We found that SP-A only acted cooperatively with polymyxin B. SP-A bound PMB in solution with an estimated K_D of 0.32 ± 0.04 μM. Binding occurs through SP-A recognition of the polycationic peptide ring of polymyxin, since SP-A bound PMBN, a derivative of PMB lacking the fatty acid tail (33), with the same affinity. The binding of SP-A to PMB or PMBN resulted in the formation of macromolecular aggregates in the presence of physiological ionic strength. The formation of SP-A/PMB and SP-A/PMBN complexes facilitated the binding of SP-A to *K. pneumoniae*, to which SP-A alone does not bind.

We found that SP-A acted synergistically with PMB and colistin (PME) against *K. pneumoniae*, NTHi, and *P. aeruginosa*. Thus, SP-A potentiates the bactericidal action of two potent but relatively cytotoxic antibiotics. Since toxicity is dose-dependent, the potential use of these synergistic combinations offers a new strategy to improve the clinical utility and safety of polymyxins. Importantly, the interaction between SP-A and PMBN conferred significant bactericidal properties to the SP-A/PMBN complex against *K. pneumoniae*, NTHi, and *P. aeruginosa*, which are resistant to both PMBN and SP-A, individually. PMBN has no bactericidal activity but is still capable of binding to the outer membrane of Gram-negative bacteria, causing membrane disturbances that make Gram-negative bacteria susceptible to various hydrophobic antibiotics (38, 39). The markedly lower toxicity of the PMBN molecule compared to that of PMB suggests that the use of synergistic combinations of SP-A/PMBN could be a promising strategy to treat respiratory infections by multidrug-resistant bacteria.

In Gram-negative infections, killing of bacteria by antibiotics and antimicrobials from the innate immune system is accompanied by the release of LPS, an endotoxin that causes high inflammation. Here we show the ability of SP-A/PMB and SP-A/PMBN complexes to aggregate LPS. Aggregation of LPS

particles reduces LPS toxicity (87) and facilitates its phagocytosis by alveolar macrophages (88). Aggregation of LPS by SP-A or PMB blocks LPS interaction with its receptor complex, which reduces proinflammatory cytokine production (16, 57). Furthermore, in the lung, LPS promotes destabilization and alteration of the biophysical activity of pulmonary surfactant (89), and SP-A and PME act as a scavenger of LPS, protecting pulmonary surfactant from the inhibitory effects of LPS (90).

In contrast to SP-A, rfhSP-A did not bind to PMB in solution at physiological salt concentrations, suggesting that the N-terminal domain, the collagen domain, and/or the supratrimeric structure of SP-A are essential for polymyxin binding. Consistent with their lack of interaction, rfhSP-A and PMB did not show synergistic action. However, addition of rfhSP-A in combination with PMB significantly increased antimicrobial efficacy against *K. pneumoniae*, non-typable *H. influenzae*, and *P. aeruginosa*. Moreover, rfhSP-A added in combination with azithromycin, tetracycline, and ciprofloxacin significantly enhanced the killing of *K. pneumonia*e, indicating an additive effect of rfhSP-A with other antibiotics in addition to PMB. Another important difference between SP-A and rfhSP-A is the inability of rfhSP-A to induce bacterial aggregation or LPS aggregation (91), which is consistent with the fact that SP-A requires an oligomeric assembly to induce aggregation of its different ligands (34).

In relation to the possible site of interaction between SP-A and PMB, SP-A binds to the polycationic peptide ring of polymyxins, and the binding of PMB (or PMBN) to SP-A could occur at domains other than the globular domain or the α-helical domain, since rfhSP-A does not bind PMB. The fact that the binding of PMB to SP-A does not interfere with the ability of SP-A to bind and aggregate LPS or DPPC particles by its globular domains strongly suggests that PMB (or PMBN) binds to SP-A at sites other than the lipid-binding site on the globular heads of SP-A.

Regarding the mechanisms of bactericidal action of SP-A/polymyxin complexes, we show that the formation of SP-A/PMB aggregates significantly increased PMB-induced bacterial membrane permeabilization and consequent bacterial death of *K. pneumoniae*, NTHi, and *P. aeruginosa*. PMB-dependent alteration of the outer bacterial membrane could facilitate the binding of SP-A to the lipid A portion of LPS, allowing SP-A-mediated extraction of LPS molecules from the membrane (77). We propose a model in which SP-A/PMB aggregates bind onto the bacterial surface and cover it like a carpet. This high local protein concentration would facilitate the formation of lipoprotein aggregates, resulting in a loss of membrane lipids, leading to membrane leakage and permeabilization. Polymyxin appears to promote contacts between the periplasmic leaflets of the bacterial inner and outer membranes, which would promote lipid exchange between the inner and outer membrane and osmotic imbalance. In contrast to SP-A/PMB aggregates, SP-A/PMBN aggregates did not promote permeabilization of the Sytox Green fluorescent dye through Gram-negative bacterial membranes. However, SP-A/PMBN mixtures, like SP-A/PMB, significantly altered the hydrophobic microenvironment of *K. pneumoniae* membranes, as detected by DPH fluorescence. These data suggest that the interaction of SP-A/PMBN aggregates with the bacterial surface could decrease the dense packing of the bacterial outer membrane and produce transient defects that facilitate the passage of the cyclic peptide through the outer and cytoplasmic membrane. Polymyxins can inhibit crucial intracellular processes such as cell division and bacterial respiration (37). Furthermore, polymyxins bind to bacterial ribosomes to inhibit protein synthesis (37).

Our results suggest that the synergistic antimicrobial activity of SP-A and polymyxin combinations depends on the formation of protein aggregates, since rfhSP-A, which lacks domains necessary for oligomerization and self-aggregation, did not form aggregates with PMB in physiological solutions. Consequently, rfhSP-A did not show synergistic action with PMB. Many antimicrobial proteins and peptides form protein aggregates related to their bactericidal activity, such as human LL-37 (92), protegrine-1 (93), dermaseptin S9 (94), temporins B and L (95), SP-B^N at acidic pH (30), and the SP-A/SPB^N complex at neutral pH (30). However, the role of protein aggregates in direct killing of bacterial cells remains to be fully determined.

PMB and colistin are available for aerosol administration in humans. Colistin/SP-A complexes administered by nebulization could be beneficial in the treatment of Gram-negative bacterial infections and in LPS neutralization. Moreover, SP-A/colistin administration by nebulization could have the advantage of placing SP-A/polymyxin complexes in a strategic location at the air-liquid interface, which is the first line of defense against inhaled pathogens and endotoxins entering the alveoli. This location could prevent the transport of polymyxin to plasma through the alveolar-capillary barrier, since high concentrations of polymyxin in plasma are related to nephrotoxicity (35, 38, 96). Consistent with this hypothesis, clinical evidence indicates that nebulized colistimethate sodium is effective in treating lower respiratory tract infections caused by multidrug-resistant Gram-negative bacteria without increasing plasma colistin concentration (97). Importantly, it has recently been shown, in an animal model of pneumonia, that instillation of colistin mixed with exogenous pulmonary surfactant increases its bactericidal effect compared to instillation of colistin alone, suggesting that lung surfactant may serve as a vehicle to facilitate the efficient spread of colistin through the airways (98). We suggest that therapeutic SP-A/colistin complexes mixed with exogenous surfactant might be beneficial in treating resistant Gram-negative bacterial infections and protecting pulmonary surfactant from the inhibitory effects of LPS (90).

The combined use of SP-A and colistin to enhance the therapeutic effects of this antibiotic requires the development of recombinant SP-A as a clinical therapeutic agent. The

production of full-length oligomeric recombinant SP-A is expensive due to low expression yields in mammalian systems and difficulties in molecular characterization and handling of this protein (33, 34). Producing a small trimeric fragment of SP-A as an alternative to the full-length oligomeric protein has clear advantages in terms of ease of production, handling, and cost (40, 41). In this study, we show that rfhSP-A exhibited significant direct microbicidal activity against *K. pneumoniae*, NTHi, and *P. aeruginosa*.The mechanism of bactericidal action of rfhSP-A against these Gram-negative bacteria is unknown. rfhSP-A did not affect bacterial membrane permeability of these pathogens, as determined by Sytox Green, but might moderately alter the physical integrity of the outer membrane structure through its interaction with lipid A. The potential use of this fragment as antimicrobial is promising, as it additively enhanced the killing of bacteria when used with several conventional antibiotics. Its bactericidal activity could be improved by genetically modifying its structural amphipathicity. Furthermore, since rfhSP-A recognizes Gram-negative bacteria, the possibility of using this fragment as carrier for small antimicrobial molecules that bind to rfhSP-A could help develop new alternative treatments against Gram-negative bacteria.

Data availability statement

The raw data supporting the conclusions of this article will be made available by the authors, without undue reservation.

Author contributions

Conceptualization, JC, VF-Á, LT, AS, BG-F, JB, NK, JJ, and CC; Methodology and Investigation, JC, VF-Á, LT, AS, BG-F, and NK. Contribution with tools and expertise, JB, and JJ. Formal analysis, all authors. Writing—original draft preparation, JC and VF-Á; Writing—review and editing, CC; Supervision, CC; Project administration, CC Funding acquisition for this study, JB, JJ, and CC. All authors read and agreed to the published version of the manuscript.

Funding

This study was supported by the Spanish Ministry of Science, Innovation and Universities through Grants SAF2015-65307-R and RTI2018-094355-B-I00 to CC, and by the Swedish Research Council (2020-02434) to JJ, and by the Biotechnology and Biological Sciences Research Council (BB/T001976/1 and BB/L007223/1) and Medical Research Council (MR/R005893/1) to JB. VF-Á was the recipient of a postdoctoral contract from Complutense University of Madrid (POP-UCM, 2021-2022, CT17/17-CT18/17) and LT was the recipient of a contract (PEJ-2020-AI/BMD-17865) from the Consejería de Educación, Juventud y Deporte of Comunidad de Madrid (Spain) and the European Social Funding Program.

Acknowledgments

We thank the Confocal Microscopy Unit of the Complutense University of Madrid for their excellent technical support. We also thank Dr. Junkal Garmendia (Instituto de Agrobiotecnología, Mutilva, Spain) for providing nontypeable *H. influenzae* strains used in this study.

Conflict of interest

The authors declare that the research was conducted in the absence of any commercial or financial relationships that could be construed as a potential conflict of interest.

Publisher's note

Supplementary material

The Supplementary Material for this article can be found online at: https://www.frontiersin.org/articles/10.3389/fimmu.2022.927017/full#supplementary-material

References

1. Mizgerd JP. Acute lower respiratory tract infection. *N Engl J Med* (2008) 358:716–27. doi: 10.1097/inf.0b013e31816fc362

2. Peleg AY, Hooper DC. Hospital-acquired infections due to gram-negative bacteria. *N Engl J Med* (2010) 362:1804–13. doi: 10.1056/NEJMra0904124

3. Fair RJ, Tor Y. Antibiotics and bacterial resistance in the 21st century. *Perspect Medicin Chem* (2014) 6:25–64. doi: 10.4137/PMC.S14459

4. Fauci AS, Marston HD. The perpetual challenge of antimicrobial resistance. *JAMA - J Am Med Assoc* (2014) 311:1853–4. doi: 10.1001/jama.2014.2465

5. Pendleton JN, Gorman SP, Gilmore BF. Clinical relevance of the ESKAPE pathogens. *Expert Rev Anti Infect Ther* (2013) 11:297–308. doi: 10.1586/eri.13.12

6. De Oliveira DMP, Forde BM, Kidd TJ, Harris PNA, Schembri MA, Beatson SA, et al. Antimicrobial resistance in ESKAPE pathogens. *Clin Microbiol Rev* (2020) 33:e00181-19. doi: 10.1128/CMR.00181-19

7. Nikaido H. Molecular basis of bacterial outer membrane permeability revisited. *Microbiol Mol Biol Rev* (2003) 67:593–656. doi: 10.1128/mmbr.67.4.593-656.2003

8. Delcour AH. Outer membrane permeability and antibiotic resistance. *Biochim Biophys Acta - Proteins Proteomics.* (2009) 1794:808–16. doi: 10.1016/j.bbapap.2008.11.005

9. Hornef MW, Wick MJ, Rhen M, Normark S. Bacterial strategies for overcoming host innate and adaptive immune responses. *Nat Immunol* (2002) 3:1033–40. doi: 10.1038/ni1102-1033

10. Llobet E, Tomás JM, Bengoechea JA. Capsule polysaccharide is a bacterial decoy for antimicrobial peptides. *Microbiology* (2008) 154:3877–86. doi: 10.1099/mic.0.2008/022301-0

11. Ebbensgaard A, Mordhorst H, Aarestrup FM, Hansen EB. The role of outer membrane proteins and lipopolysaccharides for the sensitivity of escherichia coli to antimicrobial peptides. *Front Microbiol* (2018) 9:2153. doi: 10.3389/fmicb.2018.02153

12. Mookherjee N, Anderson MA, Haagsman HP, Davidson DJ. Antimicrobial host defence peptides: functions and clinical potential. *Nat Rev Drug Discovery* (2020) 19:311–32. doi: 10.1038/s41573-019-0058-8

13. Wiesner J, Vilcinskas A. Antimicrobial peptides: The ancient arm of the human immune system. *Virulence* (2010) 1:440–64. doi: 10.4161/viru.1.5.12983

14. Moravej H, Moravej Z, Yazdanparast M, Heiat M, Mirhosseini A, Moosazadeh Moghaddam M, et al. Antimicrobial peptides: Features, action, and their resistance mechanisms in bacteria. *Microb Drug Resist* (2018) 24:747–67. doi: 10.1089/mdr.2017.0392

15. Hancock REW, Sahl HG. Antimicrobial and host-defense peptides as new anti-infective therapeutic strategies. *Nat Biotechnol* (2006) 24:1551–7. doi: 10.1038/nbt1267

16. Schromm AB, Paulowski L, Kaconis Y, Kopp F, Koistinen M, Donoghue A, et al. Cathelicidin and PMB neutralize endotoxins by multifactorial mechanisms including LPS interaction and targeting of host cell membranes. *Proc Natl Acad Sci U S A* (2021) 118:1–12. doi: 10.1073/pnas.2101721118

17. Wright JR. Immunoregulatory functions of surfactant proteins. *Nat Rev Immunol* (2005) 5:58–68. doi: 10.1038/nri1528

18. Casals C, Campanero-Rhodes MA, García-Fojeda B, Solís D. The role of collectins and galectins in lung innate immune defense. *Front Immunol* (2018) 9:1998. doi: 10.3389/fimmu.2018.01998

19. Casals C, García-Fojeda B, Minutti CM. Soluble defense collagens: Sweeping up immune threats. *Mol Immunol* (2019) 112:291–304. doi: 10.1016/j.molimm.2019.06.007

20. Ordonez SR, Veldhuizen EJAA, van Eijk M, Haagsman HP. Role of soluble innate effector molecules in pulmonary defense against fungal pathogens. *Front Microbiol* (2017) 8:2098. doi: 10.3389/fmicb.2017.02098

21. Veith NT, Tschernig T, Gutbier B, Witzenrath M, Meier C, Menger M, et al. Surfactant protein a mediates pulmonary clearance of staphylococcus aureus. *Respir Res* (2014) 15:85. doi: 10.1186/s12931-014-0085-2

22. Kuronuma K, Sano H, Kato K, Kudo K, Hyakushima N, Yokota SI, et al. Pulmonary surfactant protein a augments the phagocytosis of streptococcus pneumoniae by alveolar macrophages through a casein kinase 2-dependent increase of cell surface localization of scavenger receptor a. *J Biol Chem* (2004) 279:21421–30. doi: 10.1074/jbc.M312490200

23. Watson A, Kronqvist N, Spalluto CM, Griffiths M, Staples KJ, Wilkinson T, et al. Novel expression of a functional trimeric fragment of human SP-a with efficacy in neutralisation of RSV. *Immunobiology* (2017) 222:111–8. doi: 10.1016/j.imbio.2016.10.015

24. Al-Qahtani AA, Murugaiah V, Bashir HA, Pathan AA, Abozaid SM, Makarov E, et al. Full-length human surfactant protein a inhibits influenza a virus infection of A549 lung epithelial cells: A recombinant form containing neck and lectin domains promotes infectivity. *Immunobiology* (2019) 224:408–18. doi: 10.1016/j.imbio.2019.02.006

25. LeVine AM, Whitsett JA. Pulmonary collectins and innate host defense of the lung. *Microbes Infect* (2001) 3:161–6. doi: 10.1016/S1286-4579(00)01363-0

26. LeVine AM, Hartshorn K, Elliott J, Whitsett J, Korfhagen T. Absence of SP-a modulates innate and adaptive defense responses to pulmonary influenza infection. *Am J Physiol - Lung Cell Mol Physiol* (2002) 282:563–72. doi: 10.1152/ajplung.00280.2001

27. Kabha K, Schmegner J, Keisari Y, Parolis H, Schlepper-Schaeffer J, Ofek I. SP-a enhances phagocytosis of klebsiella by interaction with capsular polysaccharides and alveolar macrophages. *Am J Physiol* (1997) 272:L344–52. doi: 10.1152/ajplung.1997.272.2.L344

28. Zhang S, Chen Y, Potvin E, Sanschagrin F, Levesque RC, McCormack FX, et al. Comparative signature-tagged mutagenesis identifies pseudomonas factors conferring resistance to the pulmonary collectin SP-a. *PloS Pathog* (2005) 1:0259–68. doi: 10.1371/journal.ppat.0010031

29. Schaeffer LM, McCormack FX, Wu H, Weiss AA. Bordetella pertussis lipopolysaccharide resists the bactericidal effects of pulmonary surfactant protein a. *J Immunol* (2004) 173:1959–65. doi: 10.4049/jimmunol.173.3.1959

30. Coya JM, Akinbi HT, Sáenz A, Yang L, Weaver TE, Casals C. Natural anti-infective pulmonary proteins: *In vivo* cooperative action of surfactant protein SP-a and the lung antimicrobial peptide SP-BN. *J Immunol* (2015) 195:1628–36. doi: 10.4049/jimmunol.1500778

31. Fraile-Ágreda V, Cañadas O, Weaver TE, Casals C. Synergistic action of antimicrobial lung proteins against klebsiella pneumoniae. *Int J Mol Sci* (2021) 22:11146. doi: 10.3390/ijms222011146

32. Yang L, Johansson J, Ridsdale R, Willander H, Fitzen M, Akinbi HT, et al. Surfactant protein b propeptide contains a saposin-like protein domain with antimicrobial activity at low pH. *J Immunol* (2010) 184:975–83. doi: 10.4049/jimmunol.0900650

33. Sánchez-Barbero F, Rivas G, Steinhilber W, Casals C. Structural and functional differences among human surfactant proteins SP-A1, SP-A2 and co-expressed SP-A1/SP-A2: Role of supratrimeric oligomerization. *Biochem J* (2007) 406:479–89. doi: 10.1042/BJ20070275

34. Sánchez-Barbero F, Strassner J, García-Cañero R, Steinhilber W, Casals C. Role of the degree of oligomerization in the structure and function of human surfactant protein a. *J Biol Chem* (2005) 280:7659–70. doi: 10.1074/jbc.M410266200

35. Vaara M. Polymyxins and their potential next generation as therapeutic antibiotics. *Front Microbiol* (2019) 10:1689. doi: 10.3389/fmicb.2019.01689

36. Hancock REW. Peptide antibiotics. *Lancet* (1997) 349:418–22. doi: 10.1016/S0140-6736(97)80051-7

37. Trimble MJ, Mlynárčik P, Kolář M, Hancock REW. Polymyxin: Alternative mechanisms of action and resistance. *Cold Spring Harb Perspect Med* (2016) 6:a025288. doi: 10.1101/cshperspect.a025288

38. Vaara M. Polymyxin derivatives that sensitize gram-negative bacteria to other antibiotics. *Molecules* (2019) 24:249. doi: 10.3390/molecules24020249

39. Tsubery H, Ofek I, Cohen S, Fridkin M. Structure–function studies of polymyxin b nonapeptide: Implications to sensitization of gram-negative bacteria. *J Med Chem* (2000) 43:3085–92. doi: 10.1021/jm0000057

40. Kronqvist N, Sarr M, Lindqvist A, Nordling K, Otikovs M, Venturi L, et al. Efficient protein production inspired by how spiders make silk. *Nat Commun* (2017) 8:15504. doi: 10.1038/ncomms15504

41. Kronqvist N, Rising A, Johansson J. A novel approach for the production of aggregation-prone proteins using the spidroin-derived NT* tag. *Methods Mol Biol* (2022) 2406:113–30. doi: 10.1007/978-1-0716-1859-2_6

42. Nassif X, Fournier JM, Arondel J, Sansonetti PJ. Mucoid phenotype of klebsiella pneumoniae is a plasmid-encoded virulence factor. *Infect Immun* (1989) 57:546–52. doi: 10.1128/iai.57.2.546-552.1989

43. Stover CK, Pham XQ, Erwin AL, Mizoguchi SD, Warrener P, Hickey MJ, et al. Complete genome sequence of pseudomonas aeruginosa PAO1, an opportunistic pathogen. *Nature* (2000) 406:959–64. doi: 10.1038/35023079

44. Bouchet V, Hood DW, Li J, Brisson JR, Randle GA, Martin A, et al. Host-derived sialic acid is incorporated into haemophilus influenzae lipopolysaccharide and is a major virulence factor in experimental otitis media. *Proc Natl Acad Sci U.S.A.* (2003) 100:8898–903. doi: 10.1073/pnas.1432026100

45. Morey P, Cano V, Martí-Lliteras P, López-Gómez A, Regueiro V, Saus C, et al. Evidence for a non-replicative intracellular stage of nontypable haemophilus influenzae in epithelial cells. *Microbiology* (2011) 157:234–50. doi: 10.1099/mic.0.040451-0

46. Sherbrock-Cox V, Russell NJ, Gacesa P. The purification and chemical characterisation of the alginate present in extracellular material produced by mucoid strains of pseudomonas aeruginosa. *Carbohydr. Res* (1984) 135:147–54. doi: 10.1016/0008-6215(84)85012-0

47. Regué M, Izquierdo L, Fresno S, Piqué N, Corsaro MM, Naldi T, et al. A second outer-core region in klebsiella pneumoniae lipopolysaccharide. *J Bacteriol.* (2005) 187:4198–206. doi: 10.1128/JB.187.12.4198-4206.2005

48. March C, Cano V, Moranta D, Llobet E, Pérez-Gutiérrez C, Tomás JM, et al. Role of bacterial surface structures on the interaction of klebsiella pneumoniae with phagocytes. *PLoS One* (2013) 8:1–16. doi: 10.1371/journal.pone.0056847

49. Morey P, Viadas C, Euba B, Hood DW, Barberán M, Gil C, et al. Relative contributions of lipooligosaccharide inner and outer core modifications to nontypeable haemophilus influenzae pathogenesis. *Infect Immun* (2013) 81:4100–11. doi: 10.1128/IAI.00492-13

50. Casals C, Miguel E, Perez-Gil J. Tryptophan fluorescence study on the interaction of pulmonary surfactant protein a with phospholipid vesicles. *Biochem J* (1993) 296:585–93. doi: 10.1042/bj2960585

51. Sáenz A, López-Sánchez A, Mojica-Lázaro J, Martínez-Caro L, Nin N, Bagatolli LA, et al. Fluidizing effects of c-reactive protein on lung surfactant membranes: Protective role of surfactant protein a. *FASEB J Off Publ. Fed Am Soc Exp Biol* (2010) 24:3662–73. doi: 10.1096/fj.09-142646

52. García-Fojeda B, González-Carnicero Z, De Lorenzo A, Minutti CM, De Tapia L, Euba B, et al. Lung surfactant lipids provide immune protection against haemophilus influenzae respiratory infection. *Front Immunol* (2019) 10:458. doi: 10.3389/fimmu.2019.00458

53. Cañadas O, Sáenz A, de Lorenzo A, Casals C. Pulmonary surfactant inactivation by β-d-glucan and protective role of surfactant protein a. *Colloids Surf. B Biointerfaces* (2022) 210:112237. doi: 10.1016/j.colsurfb.2021.112237

54. Carregal-Romero S, Groult H, Cañadas O, A-Gonzalez N, Lechuga-Vieco AV, García-Fojeda B, et al. Delayed alveolar clearance of nanoparticles through control of coating composition and interaction with lung surfactant protein A. *Biomater Adv* (2022) 134:112551. doi: 10.1016/j.msec.2021.112551

55. Minutti CM, García-Fojeda B, Sáenz A, de las Casas-Engel M, Guillamat-Prats R, de Lorenzo A, et al. Surfactant protein a prevents IFN-γ/IFN-γ receptor interaction and attenuates classical activation of human alveolar macrophages. *J Immunol* (2016) 197:590–8. doi: 10.4049/jimmunol.1501032

56. López-Sánchez A, Sáenz A, Casals C. Surfactant protein a (SP-a)-tacrolimus complexes have a greater anti-inflammatory effect than either SP-a or tacrolimus alone on human macrophage-like U937 cells. *Eur J Pharm Biopharm.* (2011) 77:384–91. doi: 10.1016/j.ejpb.2010.12.013

57. García-Verdugo I, Sánchez-Barbero F, Soldau K, Tobias PS, Casals C. Interaction of SP-a (surfactant protein a) with bacterial rough lipopolysaccharide (Re-LPS), and effects of SP-a on the binding of re-LPS to CD14 and LPS-binding protein. *Biochem J* (2005) 391:115–24. doi: 10.1042/BJ20050529

58. Walkenhorst WF. Using adjuvants and environmental factors to modulate the activity of antimicrobial peptides. *Biochim Biophys Acta - Biomembr.* (2016) 1858:926–35. doi: 10.1016/j.bbamem.2015.12.034

59. Podschun R, Ullmann U. Klebsiella spp. as nosocomial pathogens: Epidemiology, taxonomy, typing methods, and pathogenicity factors. *Clin Microbiol Rev* (1998) 11:589–603. doi: 10.1128/cmr.11.4.589

60. Lery LMS, Frangeul L, Tomas A, Passet V, Almeida AS, Bialek-Davenet S, et al. Comparative analysis of klebsiella pneumoniae genomes identifies a phospholipase d family protein as a novel virulence factor. *BMC Biol* (2014) 12:41. doi: 10.1186/1741-7007-12-41

61. Holt KE, Wertheim H, Zadoks RN, Baker S, Whitehouse CA, Dance D, et al. Genomic analysis of diversity, population structure, virulence, and antimicrobial resistance in klebsiella pneumoniae, an urgent threat to public health. *Proc Natl Acad Sci U S A* (2015) 112:E3574–81. doi: 10.1073/pnas.1501049112

62. Finney LJ, Ritchie A, Pollard E, Johnston SL, Mallia P. Lower airway colonization and inflammatory response in COPD: A focus on haemophilus influenza. *Int J COPD* (2014) 9:1119–32. doi: 10.2147/COPD.S54477

63. Casals C. Role of surfactant protein a (SP-a)/lipid interactions for SP-a functions in the lung. *Pediatr Pathol Mol Med* (2001) 20:249–68. doi: 10.1080/15513810109168821

64. Ruano MLF, García-Verdugo I, Miguel E, Pérez-Gil J, Casals C. Self-aggregation of surfactant protein a. *Biochemistry* (2000) 39:6529–37. doi: 10.1021/bi000188z

65. Baughman RP, Sternberg RI, Hull W, Buchsbaum JA, Whitsett J. Decreased surfactant protein a in patients with bacterial pneumonia. *Am Rev Respir Dis* (1993) 147:653–7. doi: 10.1164/ajrccm/147.3.653

66. Roth BL, Poot M, Yue ST, Millard PJ. Bacterial viability and antibiotic susceptibility testing with SYTOX green nucleic acid stain. *Appl Environ Microbiol* (1997) 63:2421–31. doi: 10.1128/aem.63.6.2421-2431.1997

67. Lakowicz JR. *Principles of fluorescence spectroscopy, 3rd ed.* (Boston, MA: Springer (2006). doi: 10.1117/1.2904580.

68. Domingues MM, Inácio RG, Raimundo JM, Martins M, Castanho MARB, Santos NC. Biophysical characterization of polymyxin b interaction with LPS aggregates and membrane model systems. *Biopolymers* (2012) 98:338–44. doi: 10.1002/bip.22095

69. Kuroki Y, McCormack FX, Ogasawara Y, Mason RJ, Voelker DR. Epitope mapping for monoclonal antibodies identifies functional domains of pulmonary surfactant protein a that interact with lipids. *J Biol Chem* (1994) 269:29793–800. doi: 10.1016/S0021-9258(18)43951-8

70. McCormack FX, Stewart J, Voelker DR, Damodarasamy M. Alanine mutagenesis of surfactant protein a reveals that lipid binding and pH-dependent liposome aggregation are mediated by the carbohydrate recognition domain. *Biochemistry* (1997) 36:13963–71. doi: 10.1021/bi970745q

71. Goh BC, Wu H, Rynkiewicz MJ, Schulten K, Seaton BA, McCormack FX. Elucidation of lipid binding sites on lung surfactant protein a using X-ray crystallography, mutagenesis, and molecular dynamics simulations. *Biochemistry* (2016) 55:3692–701. doi: 10.1021/acs.biochem.6b00048

72. Theretz A, Ranck JL, Tocanne JF. Polymyxin b-induced phase separation and acyl chain interdigitation in phosphatidylcholine/phosphatidylglycerol mixtures. *Biochim Biophys Acta* (1983) 732:499–508. doi: 10.1016/0005-2736(83)90226-2

73. Kuroki Y, Takahashi M, Nishitani C. Pulmonary collectins in innate immunity of the lung. *Cell Microbiol* (2007) 9:1871–9. doi: 10.1111/j.1462-5822.2007.00953.x

74. Nayak A, Dodagatta-Marri E, Tsolaki AG, Kishore U. An insight into the diverse roles of surfactant proteins, SP-a and SP-d in innate and adaptive immunity. *Front Immunol* (2012) 3:131. doi: 10.3389/fimmu.2012.00131

75. Sahly H, Keisari Y, Crouch E, Sharon N, Ofek I. Recognition of bacterial surface polysaccharides by lectins of the innate immune system and its contribution to defense against infection: The case of pulmonary pathogens. *Infect Immun* (2008) 76:1322–32. doi: 10.1128/IAI.00910-07

76. Van Iwaarden JF, Pikaar JC, Storm J, Brouwer E, Verhoef J, Oosting RS, et al. Binding of surfactant protein a to the lipid a moiety of bacterial lipopolysaccharides. *Biochem J* (1994) 303:407–11. doi: 10.1042/bj3030407

77. Cañadas O, García-Verdugo I, Keough KMW, Casals C. SP-a permeabilizes lipopolysaccharide membranes by forming protein aggregates that extract lipids from the membrane. *Biophys J* (2008) 95:3287–94. doi: 10.1529/biophysj.108.137323

78. Sahly H, Podschun R, Oelschlaeger TA, Greiwe M, Parolis H, Hasty D, et al. Capsule impedes adhesion to and invasion of epithelial cells by klebsiella pneumoniae. *Infect Immun* (2000) 68:6744–9. doi: 10.1128/IAI.68.12.6744-6749.2000

79. Van Eldere J, Slack MPE, Ladhani S, Cripps AW. Non-typeable haemophilus influenzae, an under-recognised pathogen. *Lancet Infect Dis* (2014) 14:1281–92. doi: 10.1016/S1473-3099(14)70734-0

80. Short B, Carson S, Devlin AC, Reihill JA, Crilly A, MacKay W, et al. Non-typeable haemophilus influenzae chronic colonization in chronic obstructive pulmonary disease (COPD). *Crit Rev Microbiol* (2021) 47:192–205. doi: 10.1080/1040841X.2020.1863330

81. Zhang J, Zhu Z, Zuo X, Pan H, Gu Y, Yuan Y, et al. The role of NTHi colonization and infection in the pathogenesis of neutrophilic asthma. *Respir Res* (2020) 21:1–12. doi: 10.1186/s12931-020-01438-5

82. Qadi M, Lopez-Causapé C, Izquierdo-Rabassa S, Mateu Borrás M, Goldberg JB, Oliver A, et al. Surfactant protein a recognizes outer membrane protein OprH on pseudomonas aeruginosa isolates from individuals with chronic infection. *J Infect Dis* (2016) 214:1449–55. doi: 10.1093/infdis/jiw387

83. Tan RM, Kuang Z, Hao Y, Lau GW. Type IV pilus of pseudomonas aeruginosa confers resistance to antimicrobial activities of the pulmonary surfactant protein-a. *J Innate Immun* (2014) 6:227–39. doi: 10.1159/000354304

84. Kuang Z, Hao Y, Walling BE, Jeffries JL, Ohman DE, Lau GW. Pseudomonas aeruginosa elastase provides an escape from phagocytosis by degrading the pulmonary surfactant protein-a. *PloS One* (2011) 6:e27091. doi: 10.1371/journal.pone.0027091

85. Malloy JL, Veldhuizen RAW, Thibodeaux BA, O'Callaghan RJ, Wright JR. Pseudomonas aeruginosa protease IV degrades surfactant proteins and inhibits surfactant host defense and biophysical functions. *Am J Physiol Lung Cell Mol Physiol* (2005) 288:L409–18. doi: 10.1152/ajplung.00322.2004

86. Zhu Y, Hao W, Wang X, Ouyang J, Deng X, Yu H, et al. Antimicrobial peptides, conventional antibiotics, and their synergistic utility for the treatment of drug-resistant infections. *Med Res Rev* (2022) 42:1377–1422. doi: 10.1002/med.21879

87. Takayama K, Mitchell DH, Din ZZ, Mukerjee P, Li C, Coleman DL. Monomeric re lipopolysaccharide from escherichia coli is more active than the aggregated form in the limulus amebocyte lysate assay and in inducing egr-1 mRNA in murine peritoneal macrophages. *J Biol Chem* (1994) 269:2241–4. doi: 10.1016/s0021-9258(17)42159-4

88. Kitchens RL, Munford RS. CD14-dependent internalization of bacterial lipopolysaccharide (LPS) is strongly influenced by LPS aggregation but not by cellular responses to LPS. *J Immunol* (1998) 160:1920–8. Available at: http://www.jimmunol.org/content/160/4/1920

89. Cañadas O, Keough KMW, Casals C. Bacterial lipopolysaccharide promotes destabilization of lung surfactant-like films. *Biophys J* (2011) 100:108–16. doi: 10.1016/j.bpj.2010.11.028

90. Calkovska A, Haegerstrand-Björkman M, Curstedt T. Restoration of surfactant activity by polymyxin b in lipopolysaccharide-potentiated injury of immature rabbit lungs. *Sci Rep* (2021) 11:1–9. doi: 10.1038/s41598-020-79679-z

91. De Tapia L, García-Fojeda B, Kronqvist N, Johansson J, Casals C. The collectin SP-A and its trimeric recombinant fragment protect alveolar epithelial cells from the cytotoxic and proinflammatory effects of human cathelicidin *in vitro*. *Front Immunol* (2022). doi: 10.3389/fimmu.2022.994328

92. Engelberg Y, Landau M. The human LL-37(17-29) antimicrobial peptide reveals a functional supramolecular structure. *Nat Commun* (2020) 11:1–10. doi: 10.1038/s41467-020-17736-x

93. Jang H, Arce FT, Mustata M, Ramachandran S, Capone R, Nussinov R, et al. Antimicrobial protegrin-1 forms amyloid-like fibrils with rapid kinetics suggesting a functional link. *Biophys J* (2011) 100:1775–83. doi: 10.1016/j.bpj.2011.01.072

94. Torrent M, Pulido D, Nogués MV, Boix E. Exploring new biological functions of amyloids: Bacteria cell agglutination mediated by host protein aggregation. *PLoS Pathog* (2012) 8:e1003005. doi: 10.1371/journal.ppat.1003005

95. Mahalka AK, Kinnunen PKJ. Binding of amphipathic α-helical antimicrobial peptides to lipid membranes: Lessons from temporins b and l. *Biochim Biophys Acta - Biomembr.* (2009) 1788:1600–9. doi: 10.1016/j.bbamem.2009.04.012

96. Zavascki AP, Nation RL. Nephrotoxicity of polymyxins: Is there any difference between colistimethate and polymyxin B? *Antimicrob Agents Chemother* (2017) 61:e02319-16. doi: 10.1128/AAC.02319-16

97. Zhu Y, Monsel A, Roberts JA, Pontikis K, Mimoz O, Rello J, et al. Nebulized colistin in ventilator-associated pneumonia and tracheobronchitis: Historical background, pharmacokinetics and perspectives. *Microorganisms* (2021) 9:1–25. doi: 10.3390/microorganisms9061154

98. Basabe-Burgos O, Zebialowicz J, Stichtenoth G, Curstedt T, Bergman P, Johansson J, et al. Natural derived surfactant preparation as a carrier of polymyxin e for treatment of pseudomonas aeruginosa pneumonia in a near-term rabbit model. *J Aerosol. Med Pulm. Drug Delivery* (2019) 32:110–8. doi: 10.1089/jamp.2018.1468

frontiers | Frontiers in Immunology

TYPE Original Research
PUBLISHED 13 September 2022
DOI 10.3389/fimmu.2022.945317

OPEN ACCESS

EDITED BY
Nicole Thielens,
UMR5075 Institut de Biologie Structurale (IBS), France

REVIEWED BY
Suprabhat Mukherjee,
Kazi Nazrul University, India
Chintan K Gandhi,
College of Medicine, The Pennsylvania State University, United States
Marco Marazzi,
University of Alcalá, Spain

*CORRESPONDENCE
Samarth Sandeep
samarth@iff.bio
Angela Haczku
haczku@ucdavis.edu

SPECIALTY SECTION
This article was submitted to Molecular Innate Immunity, a section of the journal Frontiers in Immunology

RECEIVED 16 May 2022
ACCEPTED 10 August 2022
PUBLISHED 13 September 2022

CITATION
Aramyan S, McGregor K, Sandeep S and Haczku A (2022) SP-A binding to the SARS-CoV-2 spike protein using a hybrid quantum and classical *in silico* modeling and molecular pruning by Quantum Approximate Optimization Algorithm (QAOA) based MaxCut with ZDOCK. *Front. Immunol.* 13:945317. doi: 10.3389/fimmu.2022.945317

SP-A binding to the SARS-CoV-2 spike protein using hybrid quantum and classical in silico modeling and molecular pruning by Quantum Approximate Optimization Algorithm (QAOA) Based MaxCut with ZDOCK

Sona Aramyan[1], Kirk McGregor[1], Samarth Sandeep[1*] and Angela Haczku[2*]

[1]If and Only If (Iff) Technologies, Pleasanton, CA, United States, [2]University of California (UC) Davis Lung Center Pulmonary, Critical Care and Sleep Division, Department of Medicine, School of Medicine, University of California, Davis, CA, United States

The pulmonary surfactant protein A (SP-A) is a constitutively expressed immune-protective collagenous lectin (collectin) in the lung. It binds to the cell membrane of immune cells and opsonizes infectious agents such as bacteria, fungi, and viruses through glycoprotein binding. SARS-CoV-2 enters airway epithelial cells by ligating the Angiotensin Converting Enzyme 2 (ACE2) receptor on the cell surface using its Spike glycoprotein (S protein). We hypothesized that SP-A binds to the SARS-CoV-2 S protein and this binding interferes with ACE2 ligation. To study this hypothesis, we used a hybrid quantum and classical *in silico* modeling technique that utilized protein graph pruning. This graph pruning technique determines the best binding sites between amino acid chains by utilizing the Quantum Approximate Optimization Algorithm (QAOA)-based MaxCut (QAOA-MaxCut) program on a Near Intermediate Scale Quantum (NISQ) device. In this, the angles between every neighboring three atoms were Fourier-transformed into microwave frequencies and sent to a quantum chip that identified the chemically irrelevant atoms to eliminate based on their chemical topology. We confirmed that the remaining residues contained all the potential binding sites in the molecules by the Universal Protein Resource (UniProt) database. QAOA-MaxCut was compared with GROMACS with T-REMD using AMBER, OPLS, and CHARMM force fields to determine the differences in preparing a protein structure docking, as well as with Goemans-Williamson, the best classical algorithm for MaxCut. The relative binding affinity of potential interactions between the pruned protein chain residues of SP-A and SARS-CoV-2 S proteins was assessed by the ZDOCK program. Our data indicate that SP-A could ligate the S protein with a similar affinity to the ACE2-Spike binding.

Interestingly, however, the results suggest that the most tightly-bound SP-A binding site is localized to the S2 chain, in the fusion region of the SARS-CoV-2 S protein, that is responsible for cell entry Based on these findings we speculate that SP-A may not directly compete with ACE2 for the binding site on the S protein, but interferes with viral entry to the cell by hindering necessary conformational changes or the fusion process.

KEYWORDS

SARS-CoV-2, SP-A, in silico, quantum computation (QC), glycosylation, immunoprotection, QAOA, MaxCut

Introduction

The main site of the viral entry of the Severe Acute Respiratory Syndrome Coronavirus 2 (SARS-CoV-2) is through lung epithelial cells involving interactions between the Angiotensin Converting Enzyme 2 (ACE2) and the Spike glycoprotein (S protein) (1). The majority of enveloped viruses bind to host cell surface receptors *via* their surface glycoproteins. This process induces a conformational change of these viral ligands resulting in fusion with the host cell membrane delivering the virus genome to the cytoplasm (2). ACE2 as the main functional receptor was already identified for the SARS-CoV in 2003 when it was also established that the binding site (Receptor Binding Domain, RBD) was localized between amino acid residues 303 and 537 of the virus S protein (3, 4). The SARS-CoV and SARS-CoV-2 S proteins are highly similar and their structure together with their glycosylation sites have been partly established (4–8). The S protein is a trimeric class I fusion protein (Figure 1) with two functional subunits: S1 and S2. S1 is responsible for binding to the ACE2 receptor and S2 is responsible for host membrane fusion (4, 9–12). The S1 subunit RBD can be in a closed or an opened conformation. The open position is required for ACE2 binding. As demonstrated by numerous theoretical and experimental approaches (13–15), a main focus of research has been to find ways to interfere with S1 subunit RBD-ACE2 binding.

The S protein is highly glycosylated and in addition to ACE2 binding, it is known to ligate pattern recognition receptors. Each monomer in the S protein trimer has 22 glycosylation sites (shown in Figure 1A) (8, 16, 17). Glycosylation is important in protein conformation, target binding, and host evasion (7, 8, 18). The soluble carbohydrate pattern recognition receptors of the innate immune system could hinder ACE2 - S protein ligation through several different pathways including potential direct competition, inducing conformational changes that prevent receptor recognition, or sequestering the virus through opsonization for clearance by macrophages (19–21). The most abundantly expressed lung collectin, surfactant protein A (SP-A), is a particularly relevant pattern recognition host defense molecule because it is mainly produced by type II alveolar epithelial cells in the distal air spaces that are also the main site of entry for respiratory viruses (22–24). Together with SP-D and mannose-binding lectin (MBL), SP-A was implicated in binding to and regulating SARS-CoV-2 function (19, 21, 25–32).

Here we aimed to give *in silico* insights into the binding between SARS-CoV-2 S protein and SP-A. Since the RBD is much smaller in size than the entire S protein, this domain would provide an attractive reduced size target to be studied for binding predictions. However, whether SP-A directly binds to RBD, or other S1 or S2 areas, remains unclear. In fact, the RBD might be protected from SP-A access by glycosylation shielding (7). Further, targeted binding to the S2 fusion region was recently shown to effectively inhibit SARS-CoV-2 function (33–36), suggesting that the RBD may not be an exclusive target for viral inhibition. Importantly, SP-A preferentially targets carbohydrate moieties such as glycosylation sites that can be found in either the S1 or the S2 regions. For these reasons, we chose to assess the entire S protein in this study (Figure 1A).

Identification of the most likely binding sites between proteins found in Protein Data Bank (PDB) formatted files means that for "n" number of potential bindings between all potential atoms, "n^3" or greater time in seconds is required for processing. While this could be straightforward when detailed binding kinetics data are available, it is difficult for proteins with no binding information, as chemical kinetics can require completion in non-deterministic, polynomial time. Such polynomial state computational problems can be infeasible or even impossible by classical computing (37, 38). Protein binding site analysis needs to be performed before docking assessment at the precision level of molecular dynamics, either by using third-degree polynomial topological algorithms (39) or quantum annealing devices that straddle the line between highly optimized classical computing and fully quantum computation within a first-degree polynomial complexity class (40, 41). Quantum Processing Units (QPUs) use the effects of quantum mechanics for methods of information transfer among bit-like devices (i.e., quantum bits, or "qubits"). Due to the qubits' ability to hold multiple states, QPUs could ideally solve molecular

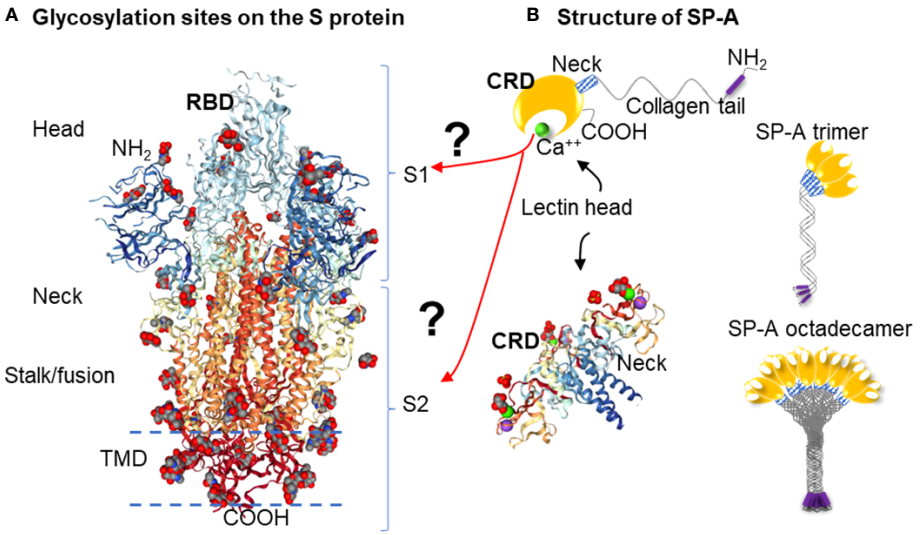

FIGURE 1
Hypothesis: SARS-CoV-2 Spike glycoprotein glycosylation sites are potential binding sites for SP-A **(A)**: Glycosylation sites on the SARS-CoV-2 spike glycoprotein trimer are denoted by NAG residues, shown in (O): red; (C): grey; (N): blue space fill balls. Structure of SARS-CoV-2 spike glycoprotein with a single receptor-binding domain up NGL Viewer (AS Rose et al. 2018) PDB: 6VSB DOI: 10.2210/pdb6VSB/pdb EM Map EMD-21375: EMDB EMDataResource **(B)**: Structure of monomer (top panel), trimeric and octadecameric SP-A and potential carbohydrate recognition sites on the S protein by the Carbohydrate Recognition Domain (CRD) of the lectin head of SP-A. The CRD binds carbohydrate residues with high affinity in a Ca^{++} dependent manner. The *X-ray Crystal Structure* depicts the rat Surfactant Protein A neck and carbohydrate recognition domain ligated with mannose. Atoms represented by the spacefill balls are: (O): red; (C): grey; (Ca): green; (Na): purple. PDB: 3PAK DOI: 10.2210/pdb3PAK/pdb 2010-11-03 Shang, F. et al. (X-RAY DIFFRACTION Resolution: 1.90 Å). (RBD, receptor binding domain; S1, Spike 1 region; S2, Spike 2 region; TMD, Transmembrane domain; CRD, Carbohydrate recognition domain).

kinetics calculations as they could represent every electron within a protein (42), given that QPUs can be treated as extra-large electrons due to their macroscopic quantum effects. Quantum processors provide superposition and entanglement features on their qubits and have the potential to take exponential scale problems and turn them into polynomial or even log scale problems. However, the largest QPUs that exist as per the writing of this paper are the Xanadu Borealis device with 216 qubits (43), the IBM Eagle with 127 qubits and the Google Bristlecone with 72 qubits (44). As one qubit simulates one extra-large electron (42), it would take many hundreds of qubits to model even the simplest proteins (45).

We, therefore, developed a model-simplification approach (QAOA-MaxCut) by systematically eliminating atoms within amino acids in the protein structure before processing for the selection of the most likely ones for binding. The QAOA-MaxCut protein pruning tool is based on the quantum approximate optimization algorithm (QAOA) (46) that includes further bioinformatics contextualization to aid the MaxCut algorithm. This hybrid approach combines the quantum computer's ability to effectively solve exponential problems with a classical cost function to determine the best cuts within a set of quantum bits. If designed to scale effectively with classical devices, QAOA provides benefits with few qubits.

In this study, we used a QAOA-MaxCut's protein pruning tool running on a (QPU) connected to a 1-node classical computer for investigating the potential binding sites of SP-A to the SARS-CoV-2 S protein. This method was previously used in SARS-CoV-2 Spike-ACE2 complex pruning in Autodock Vina, investigating potential binding when azithromycin and hydroxychloroquine were considered for COVID-19 treatment, and was compared with GROMACS on the JUWELS and BRIDGES supercomputers for preparing a relaxed structure for docking (47, 48). Here we hypothesized that SP-A binds to the SARS-CoV-2 S protein and this binding interferes with ACE2 ligation by targeting the Receptor Binding Domain (RBD, Figure 1A).

Materials and methods

SP-A and S protein structures

We obtained the protein sequences and initial configuration data for the S protein and SP-A from the Research Collaboratory for Structural Bioinformatics (RCSB) protein data bank (Figure 1). The crystallographic coordinates for the SP-A protein structure were determined by available UniProt

models. We selected 5FFR (49) as the most all-encompassing structural model of SP-A, covering 147 of its amino acids at a resolution of 2.20 Å. However, this model did include phosphocholine ligands, which could interfere with the direct probing of the amino acids that constitute the structure of SP-A (49). We therefore removed the phosphocholine ligands from the 5FFR model before binding site analysis. To investigate potential binding between the S protein and SP-A and to compare it with S protein-ACE2 binding in their respective sites and affinities, we completed a two-step analysis of the proteins' crystallographic data, and further UniProt analysis of the results. The Protein Data Bank structure 6VSB was used to represent the SARS-CoV-2 Spike, as it had 44 of its 66 N-Acetylglucosamine (NAG) identified in experimental cryoEM microscopy work, not through computational placement (12). We would like to remark that since the initial release of the 6VSB model (that we used for identification of the NAG sites), the original NAG sites and identification numbers have been changed. Our data reflect the original NAG labeling numbers on this molecule.

T-REMD with GROMACS

For the completion of the T-REMD analysis as a comparison to QAOA, GROMACS 5.0.4 was utilized to create a suitable solvent environment, along with a set of temperature and pressure controls, in order to most accurately determine the protein configuration in a binding environment. Being a molecular dynamics software, GROMACS completes sets of multi-axial nearest neighbor calculations for a set of forces for coordinate position and velocities across a number of time steps (50, 51). First, forces for each molecule within a solute and solvent are calculated using a prescribed set of forces unique to different solvation environments. To better understand a protein in a neutral solvent environment, we used three different force models: 1) the Assisted Model Building with Energy Refinement (AMBER) force field; 2) the Optimized Potentials for Liquid Simulations (OPLS) force field; and 3) the CHemistry At Harvard Macromolecular Mechanics (CHARMM) force field.

Being the oldest force field used, AMBER has the simplest form, with total potential energy for a macromolecule following a summation between bond energy as an ideal spring, geometrical energy from each angle within the covalent bonding between atoms, torsioning due to bond order, and intra-atomic forces represented as a van der Waals force added to an electrostatic force, wherein f_{ij} represents the Fourier transformation, E_{ij} represents the well depth of the atom's location, and other constants represent their respective parts. This study used AMBER99sb.

$$V(r^N) = \sum_{i \in bonds} k_{bi}(l_i - l_i^o)^2 + \sum_{i \in angles} k_{ai}(\theta_i - \theta_i^o)^2 \quad (1)$$

$$+ \sum_{i \in torsions} \sum_{n} \frac{1}{2} V_i^n [1 + \cos(nw_i - \Upsilon_i)] \quad (2)$$

$$+ \sum_{j=1}^{N-1} \sum_{i=j+1}^{N} f_{ij} \left\{ \in_{ij} \left[\frac{r_{ij}^{0\,12}}{r_{ij}} - 2\frac{r_{ij}^{0\,6}}{r_{ij}} \right] + \frac{q_i q_j}{4\pi \in_0 r_{ij}} \right\} \quad (3)$$

Equation 1. AMBER Force Field Formula (adapted from Case et al. AMBER9 Manual for Electrical Potential Across Protein.

OPLS (52) shares much of the same structure as AMBER. However, it aims to provide better analysis of the differences between bonded, nonbonded, and dihedral atoms, present on multiple energetic planes, through the use of torsional and electrostatic constants derived for each element and each organic functional group, represented as A and C. OPLS is also designed for use with the TIP3P water model, which is a 3-sided rigid water molecule with charges, as the default solvent for the force field.

$$E(r^N) = E_{bonds} + E_{angles} + E_{dihedrals} + E_{nonbonded} \quad (4)$$

$$E_{bonds} = \sum_{bonds} K_r(r - r_0)^2 \quad (5)$$

$$E_{angles} = \sum_{angles} K_\theta(\theta - \theta_0)^2 \quad (6)$$

$$E_{dihedrals} = \sum_{dihedrals} \left(\frac{V_1}{2}[1 + \cos(\phi - \phi_1)] + \right. \quad (7)$$

$$\frac{V_2}{2}[1 + \cos(2\phi - \phi_2)] + \frac{V_3}{2}[1 + \cos(3\phi - \phi_3)] + \frac{V_4}{2}[1 + \cos(4\phi - \phi_4)]) \quad (8)$$

$$E_{nonbonded} = \sum_{i>j} f_{ij}\left(\frac{A_{ij}}{r_{ij}^{1}2} - \frac{C_{ij}}{r_{ij}^{6}} + \frac{q_i q_j}{4\pi \in_0 r_{ij}}\right. \quad (9)$$

$$A_{ij} = \sqrt{A_{ij}A_{jj}} \quad (10$$

$$C_{ij} = \sqrt{C_{ii}C_{jj}} \quad (11)$$

Equation 2. OPLS Force Field Formula (adapted from Jorgensen et al.) for Electrical Field Across Protein (52).

CHARMM (53) is a force field (delete hyphen) model that aims to take OPLS further through the addition of an impropers and a Urey – Bradley term, which what both intend to improve upon the torsional modeling of the atomic interactions in OPLS through the accounting of bending and non-binding interactions between atoms in the 1,3 positions of an organic molecule due to proximity of electrostatic forces, respectively. This study used CHARMM36.

$$V = \sum_{bonds} K_b(b - b_0)^2 + \sum_{angles} K_\theta(\theta - \theta_0)^2 + \sum_{dihedrals} K_\phi(1 + \cos(n\phi - \delta)) \quad (12)$$

$$+ \sum_{impropers} k_\omega(\omega - \omega)^2 + \sum_{Urey-Bradley} k_u(u - u_0)^2 + \quad (13)$$

$$\sum_{nonbonded} \left(\in \left[\left(\frac{R_{\min_{ij}}}{r_{ij}} \right)^{12} - \left(\frac{R_{\min_{ij}}}{r_{ij}} \right)^{6} \right] + \frac{q_i q_j}{\in r_{ij}} \right) \quad (14)$$

Equation 3. CHARMM force field formula adapted from Mackerell et al. for electrical potential across protein (53).

GROMACS software testing involved SP-A protein in water bulk that consisted of ~62,000 atoms (number of water molecules ~20,000) in a 6.5×6.5×6.5 nm^3 cell. The test runs were done using the following parameters: 2fs timestep, PME electrostatics, and van der Waals forces truncated at 1.2 nm with corresponding pressure and temperature control. We performed benchmark runs typically for 10000 steps (20ps) with/without writing output any trajectory and coordinate files (Note that with no write trajectories and confout slightly increases the performance). For our tests, we used the "-pin on" and "-dlb yes" GROMACS flags, where "-pin on" stopped the kernel from moving processes between cores by locking the cores, and allowed dynamic load balancing to automatically run when the load imbalance was 5% or more, which is important for handling inhomogeneous systems. For optimal performance, we also tried mdrun −resethway and −maxh=0.05 options, which corrected the benching results. After these first test runs, the force fields for SP-A were taken into consideration for a total of 10 ns, or 5,000,000 time steps, in order to obtain reasonable interaction accuracy of SP-A within a water model.

T-REMD device: JUWELS supercomputer

The JUWELS multi-petaflop supercomputer (54) is located at the Julich Supercomputing Centre (JSC, Germany). This is one of the most powerful computing resources available in Europe. It consists 2567 compute nodes (2511 CPU-only partitions and 56 Nvidia V100 GPU nodes), where the nodes are interconnected through Mellanox Infiniband high performance network architecture. The CPU-nodes are equipped with two Intel Xeon Platinum 8168 processors (base frequency of 2.7GHz), while GPU-nodes are fitted with the two 2.4GHz Intel Xeon Gold 6148 processors. Each GPU node contains four Nvidia V100 cards with 5120 CUDA cores. Note that the peak performance of the mentioned cluster is ~4,15 TF/s based on the Linpack Benchmark.

T-REMD and classical graph cutting device: Bridges at the Pittsburgh Supercomputing center

The Bridges Supercomputer at the Pittsburgh Supercomputer Center has 752 Regular Shared Memory (RSM) nodes. Each of these nodes consist of 2 Intel Haskell CPUs with 14 cores per CPU, 9 AI-GPU nodes, each including 2 Intel Xeon Gold 6148 CPUs with 20 cores each and 8 NVIDIA Volta V100 GPUs. Because of GROMACS' capability to improve performance through the use of GPUs, the AI-GPU nodes were used for the completion of OPLS, CHARMM, and AMBER force field implementations in T-REMD analyses on SP-A. These nodes were also utilized for the completion of the Goemans-Williamson interpretation of the MaxCut problem.

Goemans-Williamson implementation

We applied the Goemans-Williamson algorithm by using the CVXGraph Algorithms Python package across the entire atom map of the protein. In this implementation of the algorithm, the atoms that were identified to be cut, were cut from the map, leaving the most energy-resilient atoms, and therefore the key binding sites on the protein.

$$E[W] = \sum_{i<j} \omega_{ij} \frac{\arccos(v_i * v_j)}{\pi} \quad (15)$$

Equation 4. Goemans-Williamson MaxCut algorithm (55): *E [W]* represents the expectation value of a node, *i* and *j* represent the two dimensions of node movement, *w* represent the weight of each node, and *v* represent the vector that the node produces itself.

We used the Bridges Supercomputing System to run this algorithm with PySpark used as the batching mechanism between nodes. Other than this addition, there were no additional changes made to the CVXGraph Goemans-Williamson algorithm used.

Protein pruning by QAOA-based MaxCut to feed into modular binding/docking algorithms

Quantum computational graph cutting was necessary to overcome the poor computational scaling of the docking algorithms that make large scale protein structures prohibitively time- and compute-expensive. Additionally, ZDOCK's web server does not allow for large protein structure

inputs. In this process, the weak potential bindings between atoms without polarized qualities ("topological minima or maxima" as described by Agarwal et al. (56) bound in low electronegative environments) were cut (Figure 2).

Using the QPUs as analogs for the atoms in the proteins, sets of three atoms each were mapped on qubits next to each other in placements topologically similar to the interaction space between the atoms themselves as identified by their PDB files. Then, either the Goemans-Williamson was implemented on the Bridges-AI cluster (https://www.psc.edu/resources/bridges-2/), or the QAOA-MaxCut package from Rigetti and Co. (https://grove-docs.readthedocs.io/en/latest/qaoa.html), were utilized to implement the MaxCut process on the 3-atom subgraph of those qubit positions on the Rigetti Aspen 8 QPU. The Rigetti Aspen 8 is a QPU device that operates using superconducting Josephson junctions to create a silicon based lattice structure of 31 qubits embedded onto a piece of gold and cooled to nearly 0°K through the use of helium based cooling chambers (https://patents.google.com/patent/US10050630B2/en).

In the case of using Goemans-Williamson, the algorithm was implemented on the Bridges-AI cluster. However, the input and output processes for handling (e.g., with a Python file handler) with Goemans-Williamson were the same as for QAOA-MaxCut, and, at the end of these processes, basis states representing different qubits were cut from the graph at different probability levels. These basis states were translated to binary numbers according to the qubit and the flip state of that qubit, and were contextualized to identify the qubit that needed to be cut from the graph: 1s were accepted into the new graph, and 0s were eliminated. To find the best binding site in the best configuration, the highest probability basis states was assessed, and the atoms with positions that had 0 values within the basis states calculated were taken out from the overall list of protein atom positions. Lastly, these atom positions were then cross-referenced to the atoms they originally referred to in order to verify which atoms need to be part of a new PDB file representing only the best binding sites. Finally, this conversion took place using the Biopython software package. Once completed, the atoms that remained were rewritten into a Protein Data Bank (PDB) file (Figure 3) (47, 57).

Measuring the effectiveness of SP-A models through docking using ZDOCK

In order to study the effectiveness of each model in determining tightest-bound binding sites, the models were

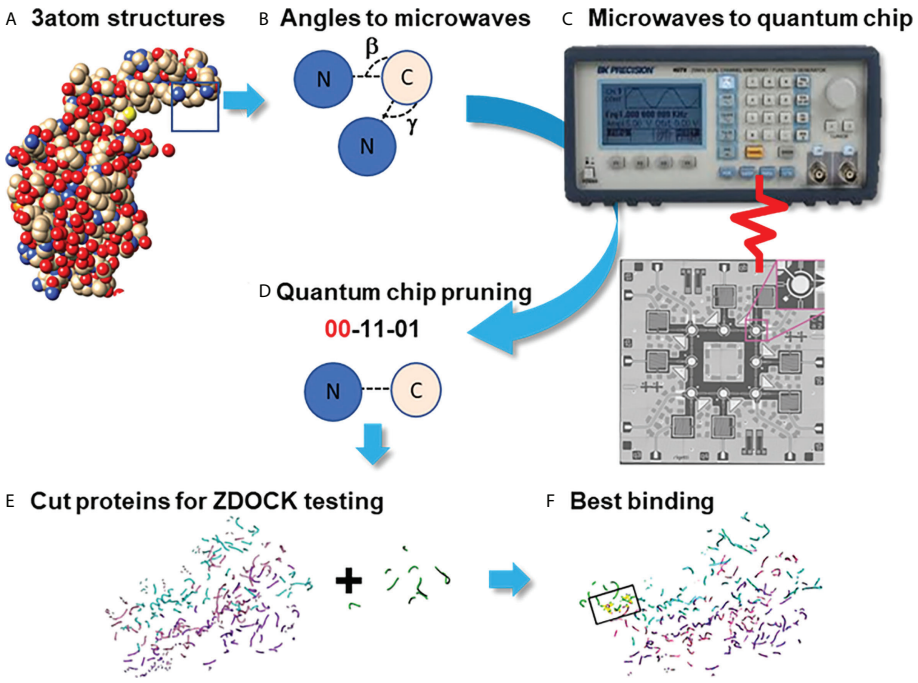

FIGURE 2
Pruning Program by utilizing the Quantum Approximate Optimization Algorithm (QAOA) on the Rigetti Quantum Processor. Process diagram for finding protein binding by Pruning. **(A)** Create graphs of 3 neighboring atoms each, with angles beta and gamma stored **(B)** Fourier-transform angles into frequencies to be placed on quantum chip by microwave. **(C)** Send microwaves to quantum chip. **(D)** Read results from quantum chip to determine which atoms to cut, with 00=Cut. **(E)** Summation of cut atom graphs to build reduced structures. **(F)** Binding studies between reduced structures with ZDOCK testing to identify the best binding sites.

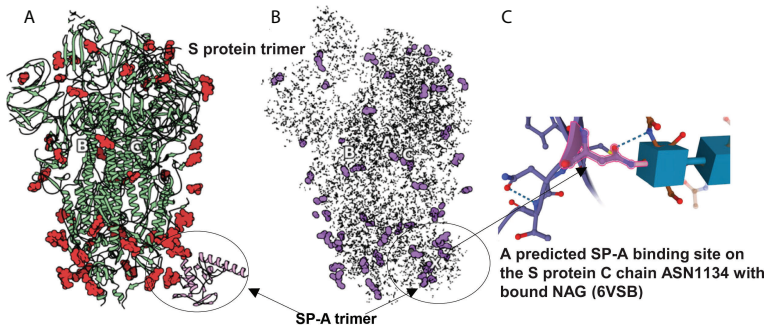

FIGURE 3
SARS-CoV-2 S protein (6VSB) modeling. **(A)**: The S protein trimer model (green ribbons representing chains A, B and C with red denoting glycan residues) and bound SP-A (pink). **(B)**: The final reduced S-protein-SP-A complex processed by our QAOA-based MaxCut protein pruning tool followed by ZDOCK docking (purple representing glycan residues and X marking the SP-A binding site. **(A, B)** were derived from the visualization software SAMSON. **(C)**: The amino acid ASN 1134 on the S protein C chain is identified as a likely candidate to mediate SP-A binding. ASN 1134 is outlined by dark pink and the blue cubes represent NAG glycosylation.

made to bind with the SARS-CoV-2 spike protein in its open conformation (PDB: 6VSB). The binding between the reduced (pruned) structures was completed by the use of the software ZDOCK (University of Massachusetts Medical Center) (58, 59). Within this software, tightest-bound binding sites are determined through the closeness of a summation of Fourier transform of topological and desolvation energetic parameter scalars, and electrostatic values from CHARMM, for each atom in 6 dimensions. We checked the potential binding presence, affinity and locations for two complexes: the Spike protein and ACE2, as well as Spike protein and SP-A. Binding locations, ZDOCK affinity scores, and Root Mean Square Deviation (RMSD) scores between the top 2000 conformations were collected, assessed, and compared to each other and other literature data.

Because the binding capability was reflected as a scalar score value, a higher $Score_{total}$ value represents stronger binding. We compared the top 2000 conformations produced by ZDOCK for the AMBER, OPLS, CHARMM, and QAOA-MaxCut models and the tightest-bound binding candidates were reviewed against other SP-A results. RMSD values across the top 2000 conformations were then calculated to determine which model produces the highest accuracy conformations by the use of ZDOCK.

Results

SARS-CoV-2 S protein (6VSB) and SP-A (5FFR) trimer molecular pruning

The comparison of full protein structure and the reduced molecules is shown in Figure 3. The left panel (Figure 3A) depicts the known structure of Spike protein (as published in 6VSB). The reduced structure (Figure 3B) is a result of processing initial all-atom structures with MaxCut's protein pruning. In this, the angles between every neighboring three atoms were Fourier-transformed into microwave frequencies and sent to a QPU that identified the chemically irrelevant atoms to eliminate based on their chemical topology (Figure 2). The structures produced by QAOA-MaxCut (Figure 3 not right panel) were identical to those produced by Goemans-Willamson. This reduced all-atom structure has approximately one-third of the original atoms, leaving only those groups of atoms that represent the best binding sites for the protein; these are electrostatically more actively "charged" and more likely to be involved in the binding process. We confirmed that the remaining residues contained all the potential binding sites in the molecules as verified by the Universal Protein Resource (UniProt) database. QAOA-MaxCut was also compared to GROMACS using T-REMD using AMBER, OPLS, and CHARMM force fields (47, 57).

SARS-CoV-2 S protein - SP-A complex formation

In order to prepare the SP-A protein for docking, we took the initial PDB file [model 5FFR (49)] from RCSB. Because 5FFR was designed for the assessment of SP-A lipid binding characteristics, it contained ions and phosphocholine to facilitate that binding. To avoid any unexpected influence from ions and phosphocholine, we removed them from the PDB. Then, we processed this SP-A's PDB with the aforementioned protein pruning tool and received the reduced structure. Again, there was a significant change in atom numbers

after using our QAOA-MaxCut based protein pruning tool: 5FFR (without ions and phosphocholine) has 1119 atoms and the reduced model has only 411 atoms. Figure 4 shows the S protein and SP-A complex after docking of corresponding reduced PDB structures by ZDOCK. Surprisingly, while each of the GROMACS based models predicted SP-A binding to the open RBD of SARS-CoV-2 S protein, each of the graph cutting based methods predicted binding to S2 instead.

The bound residues identify the known carbohydrate groove of the SP-A including an ASN cluster (at positions 151, 190 and 214) flanked by TYR 188 and GLU 171. The structure also shows the close proximity of NA+ and Ca++. Ca++ is required for functional carbohydrate recognition by SP-A (Figures 4B, C).

Characteristics of SARS-CoV-2 S protein-SP-A binding after QAOA-MaxCut pruning and root mean square deviation values

RMSD values indicate the average deviation between the corresponding atoms of two proteins evaluated for binding. Smaller RMSD values suggest greater similarity between the structures compared. The goal of designing improved algorithms has been to be able to find the best orientation between two structures that would result in the lowest possible RMSD. We calculated the RMSD values characterizing SARS-CoV-2 S protein-SP-A binding after QAOA-MaxCut pruning using ZDOCK scores.

Table 1 shows the top 16 ranked conformations (out of 2000). The higher ZDOCK scores predict greater binding affinity between docking sites. Each specific docking site/conformation is identified by a 3-dimensional topological assignment denoted by x, y, and z coordinates.

Table 2 shows the top 16 amino acids/ligands included in the binding between SARS-CoV-2 S protein and SP-A together with the atoms involved in the contact and the binding distance between these atoms. By studying the originally published 6VSB NAG glycosylated model of SARS-CoV-2 S protein, we found that many of the NAG residues located in the S2 fusion domain were predicted to be involved in SP-A binding. Notably, a group of NAGs (labeled in this model as 1301, 1302 and 1312) are identified as top candidates for binding. This is important because ASN molecules known to undergo post-translational glycosylation were also found in a cluster (at positions 1125, 1134, 1135) in the S2 fusion domain creating a "hot spot" for carbohydrate-lectin (add hyphen) binding. Indeed, from the SP-A side, the TYR at position 188 had the strongest potential binding with S protein NAGs, while ASN at position 151 also came up in multiple conformations. ASN 151, similarly to the SARS-CoV-2 S protein, forms a carbohydrate binding cluster with ASN 190 and 214 near to the Ca++ binding pore (Figure 4; Table 2).

The average RMSD value calculated from 2000 ZDOCK binding conformations was 43.5 Å for the S protein - SP-A complex. This value is markedly lower than what we found for the average S protein - ACE2 RMSD, which was 272 Å following the same pruning and docking procedure. Using our QAOA-MaxCut protocol, the RMSD value was also lower than what we found by OPLS, AMBER, and CHARMM; these were 133.9 Å,

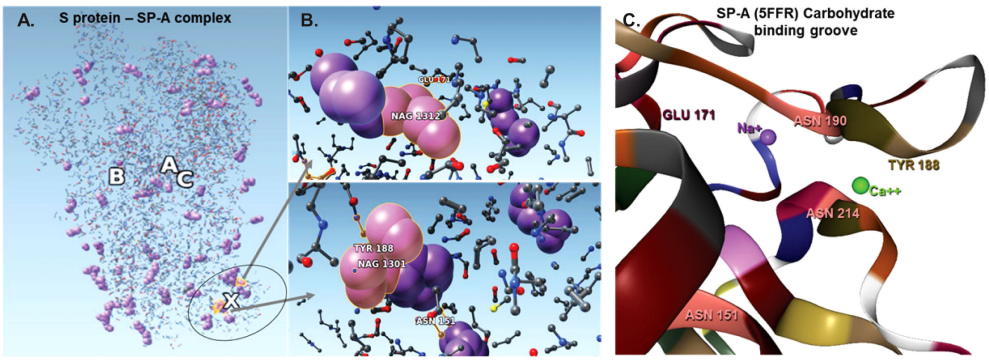

FIGURE 4
The complex resulting from docking of reduced structures of the S protein and SP-A with ZDOCK highlighting the top ranked binding sites on SP-A. **(A)**: Visualization by SAMSON after clashes/contacts with less than 2 Å distance were identified using the Chimera program. **(B)**: The top 5 binding sites are shown (ball and stick) highlighting bound NAG (purple space fill balls). SP-A and S protein amino acid residues are shown as a ball and stick. NAG1301 is bound to ASN1134 on the S protein and is shown in close proximity to ASN151 of SP-A. **(C)**: The SP-A carbohydrate binding grove showing the amino acids identified in the pruned complex including ASN 151 (pink) TYR 188 (khaki), GLU 171 (bordeaux) and Ca++ (green) and Na+ (purple). ASN 151 is clustered with ASN 214 and ASN 190 amplifying carbohydrate binding ability. The groove is flanked by TYR 188 and GLU 171 and harbors a Ca++ and a Na+ ligand. Presence of Ca++ is known to be required for carbohydrae binding. Atoms represented by the balls and stick are: (O): red; (C): grey; (Ca): green; (Na): purple; (S): yellow.

TABLE 1 Top 16 ZDOCK scores, representing the electrostatic and geometric fit between protein residues, out of 2000 potential conformations between SP-A and SARS-CoV-2 Spike.

Conformation rank (of 2000)	X Docking Grid coordinate	Y Docking Grid coordinate	Z Docking Grid coordinate	ZDOCK Score
1	140	38	30	448.202
2	173	21	60	405.703
3	5	27	55	390.222
4	163	48	44	386.713
5	140	38	28	386.160
6	178	31	65	376.122
7	139	40	31	373.924
8	147	49	26	372.902
9	5	25	53	372.588
10	145	39	27	371.860
11	139	43	29	365.741
12	173	22	60	364.003
13	138	34	22	359.788
14	8	30	55	352.675
15	140	46	31	349.967
16	151	55	27	342.542

The central atom position between each conformations of the bound SP-A and the S protein is determined by the X,Y,Z coordinates that reflect the spatial localization differences.

150.7 Å, and 173.1 Å, respectively, for assessment of SP-A- S protein binding. These results suggest that the S protein - SP-A complex forms with a high affinity, that it is likely a biochemically relevant configuration, and that the QAOA-MaxCut produced pruned structures are effective in predicting binding conformations.

Discussion

Using a novel *in silico* approach we discovered potential binding sites between the SARS-CoV-2 S protein and SP-A, an immunoprotective lung collectin. We originally hypothesized that SP-A competes with ACE2 for the same binding sites. Our

TABLE 2 Top 16 binding sites between SP-A and SARS-CoV-2.

S Protein Chain; Amino Acid/ Glycan residue; Contact Atom for Binding SP-A	Position of NAG or amino acid on the S protein (6VSB, published Feb 2020)	SP-A Amino Acid; Contact Atom for Binding the S Protein	Position of Amino acid on SP-A (5FFR)	Distance between both atoms (Å)
C; NAG; O	1301	TYR; C	188	1.308
C; NAG; O	1301	TYR; C	188	1.730
C; NAG; O	1301	TYR; C	188	1.905
C; NAG; C	1312	ASN; C	151	2.309
C; NAG; O	1312	ARG; C	197	2.079
C; NAG; O	1311	PRO; C	175	2.153
C; NAG; C	1312	GLU; C	171	2.455
C; NAG; C	1312	GLN; C	199	2.635
C; CYS; C	1126	SER; C	187	2.572
C; ILE; C	1130	SER; C	185	2.715
C; NAG; C	1302	TYR; C	188	2.620
C; NAG; C	1301	THR; C	189	2.653
C; NAG; C	1302	TYR; C	188	2.745
C; NAG; C	1302	TRP; C	213	2.749
C; NAG; C	1302	ASN; C	151	2.885
C; NAG; C	1311	PRO; C	175	2.809

The chain, the amino acid, and their respective atoms that are predicted to mediate binding between the S protein and SP-A according to the minimal distance that can be achieved between two atoms.

pruned molecular binding models indicated that SP-A is bound to the S protein with a similar affinity to that of ACE2 but in a different site in the S2 fusion segment. The amino acids involved in this interaction point to a highly glycosylated area of both molecules. Our hybrid quantum and classical computational study augments currently available structural and experimental results and highlights the importance of carbohydrate binding in the pathogenesis of SARS-CoV-2 infection.

The binding domain on the S2 segment we uncovered is not the most well-known of the S protein. Interference with this region, however, may affect viral fusion with the host cell membrane preventing viral entry and infection. Indeed, recent cryoEM, X-ray crystallography and membrane fusion assays show broad inhibition of the virus through areas other than the RBD (33–35, 60–62). Thus, binding by SP-A to the S2 region responsible for conformational destabilization of both the S1 and S2 segments may prevent viral entry to the host cell (9, 63). We found that SP-A would preferentially bind glycosylated sites on the S protein. Similarly to mannose binding lectin (MBL) and SP-D, carbohydrate binding by SP-A takes place in a specific pore in the carbohydrate recognition domain of the molecule in close proximity to a Ca+ ion. These collectin molecules have a high affinity to mannose (49). S protein is also a mannose-binding protein (20, 64). Interactions between SP-A, the S protein, and glycans may have functional significance in regulating protease access using glycan shields (8, 18).

Binding between the CRD of SP-A and carbohydrate residues on the S protein could also lead to opsonization and viral clearance by immune cells not bearing ACE2 receptors. SP-A binds to polysaccharides, phospholipids, and glycolipids on the surface of pathogens and also induces calcium-dependent aggregation of lipid vesicles (65). This binding is essential for the opsonization process resulting in the clearance and elimination of pathogens by phagocytes (22, 66, 67). SP-A-mediated phagocytosis is facilitated by collagen receptors such as calreticulin/CD91/LRP. In fact, SP-A can induce both anti- or proinflammatory immune cell responses by alternately ligating SIRP-α or calreticulin/CD91/LRP on the membrane of macrophages (68). Glycosylation alterations in SP-A can affect maturation, secretion, aggregation, and degradation of the molecule itself, although not usually through N-glycosylation sites (69). Thus, independent of ACE2 binding, SP-A recognition of carbohydrate moieties clustered on the surface of the S protein may drive pathogen clearance through opsonization (66) and protect from receptor-mediated internalization, increased inflammation, and systemic spread of infection (20).

Cell surface-bound lectin type receptors such as L-SIGN and DC-SIGN were also implicated in glycosylation-dependent S protein interactions with multiple cell types (70). Other cell surface receptors were also shown to facilitate alternative (ACE2-independent) viral entry to cells. Apart from the lectin receptors (that utilize carbohydrate moieties on the S protein), a group of integrin-type receptors also emerged as important players. Integrins can mediate viral internalization either through recognition of the arginin-glycine-aspartate (RGD) region of the RBD (arginin-glycine-aspartate) of the SARS-CoV-2 Spike protein (71–73), or independently of it (72). These alternative cell entry pathways are important in amplifying and spreading viral entry to structural cells. Thus, by binding to a highly glycosylated portion of the S2 region, SP-A may play an important protective role in ACE2-independent viral pathologies. It is notable that our investigation was based on utilizing a "fully glycosylated" model of the S protein (6VSB) to represent the SARS-CoV-2 S protein, as it had 44 of its 66 N-Acetylglucosamine (NAG) identified in experimental cryoEM microscopy work, not through computational placement (12). Since the initial release of the 6VSB model (that we used for identification of the NAG sites), the original NAG sites and identification numbers have been changed. It is important to bear in mind that most glycosylation sites on available models are arbitrarily added to proteins and may not always be an accurate reflection of reality. Our observations therefore warrant additional *in silico*, *in vitro* and *in vivo* investigations to verify and identify further mechanistic details and the specific clinical and pathological significance of carbohydrate-based SP-A – SARS-CoV-2 interactions.

Along the same line, the most naturally occurring configuration of SP-A is an octadecamer (22, 66) but our *in silico* predictions were performed using an available trimeric neck-CRD (5FFR) model of the molecule. SP-A (encoded by two genes SP-A1 and SP-A2 into largely identical 35-kD peptides) has a similar structure to MBL, SP-D, and C1q. Six of the SP-A homotrimers form an octadecamer "bouquet" of unidirectionally positioned molecules composed of a carboxy-terminal C-type lectin domain, a coiled-coil neck region, a collagen tail and an amino-terminal domain (19, 22, 26, 28). However, when complexed with SP-B, lipids or detergents (65) or under inflammatory conditions, SP-A loses its geometric and topological octadecamer features and structurally reforms into smaller oligomers (i.e., it falls apart) (74). Given that to date no experimentally determined SP-A structural model that includes all of its amino acids exists, *in silico* results using current truncated models should be carefully interpreted. Further studies will be necessary to determine how higher order oligomerization of SP-A is regulated and how it affects binding characteristics especially interactions between SP-A and the S protein.

Our computational approach used a shared logical model from the quantum chemistry of these proteins, including the modeling of their binding/docking after computationally

pruning targeted sites to reduce the size of the proteins and the number of conformations to be analyzed. We used a combination of an electronegativity mapping software that performs QAOA-MaxCut functions, followed by ZDOCK assessment of binding between the SARS-CoV-2 S protein and SP-A. This novel approach allowed to complete top binding site determination in a more rapid manner than the widely used GROMACS program, while providing similar binding sites that OPLS, QAOA-MaxCut, and AMBER did. Quantum algorithms can utilize superpositions of each state and entanglement between states to produce strong cut probabilities nearly instantaneously for multiple atoms, while classical processing devices must complete these tasks serially for each atom. This allows for a slimmer algorithmic approximation that does not require multi-axial force calculations or higher order functions. The steps completed by GROMACS to properly characterize the forces for each atom are additive amongst the atoms and then additive amongst each pair of atoms, creating a computational complexity of $O(n^2)$ for each atom (75). Goemans-Williamson, while it requires lower dimensionality, has a complexity of $O(n^2 logn)$ due to its arccos term (76). Thus, QAOA is naturally the fastest algorithmic implementation, with an expected performance in the $O(logn)$ regime.

Surprisingly, while each of the GROMACS based models predicted SP-A binding to the open RBD of SARS-CoV-2 spike, each of the graph cutting based methods predicted binding to S2 instead. This discrepancy prompted us to compare the programs we used. Regarding the accuracy of the configurational spaces, GROMACS was the only software that effectively captured the effects of simulation with a saline solution on the protein in the form of direct coordinate shifts, and initialization of a water model to ensure neutral solvency. However, this process, which leans heavily on atom-by-atom calculation of Coulombic forces, scaled up exponentially with squared time steps for each added atoms when it came to assessing protein-to protein interactions. To be able to feasibly perform our study, a cap at 5,000,0000 time steps, or 50 ns, had to be implemented on both the BRIDGES and JUWELS clusters limiting the ability to precisely simulate protein movement dynamics (57). Further, we compared the top docking score, docking pose (conformation and orientation), and Root Mean Square Deviation (RMSD) across OPLS, AMBER, CHARMM, and the QAOA-MaxCut-prepped SP-A models. We found that the docking values created with the new graph cut model had lower deviation across all final conformations than those found by GROMACS, and the top binding sites identified on SP-A were on the same residues by all the programs we studied. These results suggested that the S2 - SP-A complex forms with a high affinity, that it is likely a biochemically relevant configuration, and that the QAOA-MaxCut produced pruned structures are effective in predicting binding conformations.

Nonetheless, it is important to address the question whether the discrepancy in binding site prediction between the GROMACS and QAOA-MaxCut programs could be due to the elimination of some important amino acids by the latter. QAOA-MaxCut is a state-of-the-art method to approximating a solution to MaxCut, a problem-space characterized by the maximum size cut within a graph of nodes and edges that cannot be completed in polynomial time on a classical computer. Critically, QAOA-MaxCut studies atomic graphs of only three atoms in every instance of cutting one. The program finds maximum cut values based on the angles within the graph and evaluates the ability of the algorithm on quantum hardware to reach the lowest possible cost values, or combined bias values, for each potential cut. The graphs we fed the algorithm in this study had the bond angles of each atom within the 3-atom sets. As electronegativity and bond angles are directly proportional, the most electronegative atom with the largest bond angle within a set was cut. Important amino acids would not be eliminated in this atomic level modeling. Additionally, we confirmed that the remaining residues contained all the potential binding sites in the molecules as verified by the Universal Protein Resource (UniProt) database for both SP-A and the SARS-CoV-2 S protein. On SP-A, UniProt identified a glycosylation site at amino acid 207, which in our model would be amino acid 214 (5FFR), included in the ASN cluster we identified. As we discussed above, in our interpretations we need to carefully take into account the discrepancies in the amino acid and glycan ligand numbering due to structural file differences between available published structures.

Our computational model while, providing improved accuracy (low RMSD) and efficiency (reduced computational time) in assessing protein-protein binding sites between SP-A and the SARS-CoV-2 S protein similarly to other currently available algorithms, could not provide insights to the molecular dynamics of the bindings. Molecular dynamics simulation packages such as GROMACS are based on the application of classical mechanics models to study physical systems at the atomic level. Regardless of the software, they include force computation with van der Waals, electrostatic (Coulomb), and various bonded and non-bonded terms to provide a projection of laboratory experiments with potentially greater detail albeit still as an approximation [reviewed in detail by Khan et al.(77)]. Importantly, protein folding, the process necessary to assume biologically meaningful ligand-receptor interactions, is estimated to take at least a microsecond (77), making accurate modeling of these currently beyond the reach of available computational approches. How molecular dynamics simulation can be accelerated, however, is an exciting area of investigations in the computational field.

Data availability statement

The raw data supporting the conclusions of this article will be made available by the authors, without undue reservation.

Author contributions

SA performed the study and wrote the initial draft. KM and SS expanded the draft to include algorithmic details and binding sites on glycosylation and serine proteases. AH and SS conceived the idea for the study and directed the work. AH and KM edited the manuscript. All authors contributed to the article and approved the submitted version.

Funding

SS: Pittsburgh Supercomputer Center startup award from the Extreme Science and Engineering Discovery Environment (XSEDE). AH: Chester Robbins Endowment for pulmonary research, UC Davis; 27IR-0053C Tobacco Related Disease Research Program, UCOP

Acknowledgments

We would like to thank Vaibhav Gupta and the development team at Iff Technologies for building and improving upon the software; Rigetti and Co for providing credits to use their platform and their employees, Mark Skillbeck and Tom Lubowe, for providing software and hardware troubleshooting help. Angela Linderholm, Melissa Teuber, Pedro Hernandez, and Nikita Mohapatra of the Haczku Lab for weekly discussions on presentation and interpretation of the results, and Dr. Armen Poghosyan, Bioinformatics Group Leader at the International Scientific and Educational Center, the National Academy of Sciences of the Republic of Armenia (NAS RA) for fruitful discussions around accurate modeling of SP-A and modeling support.

Conflict of interest

SA was working for Iff Technologies developer of the graph pruning algorithm. KM and SS are current shareholders and employees of Iff Technologies.The remaining author declares that the research was conducted in the absence of any commercial or financial relationships that could be construed as a potential conflict of interest.

Publisher's note

References

1. Brini E, Simmerling C, Dill K. Protein storytelling through physics. *Science* (2020) 370(6520):1–8. doi: 10.1126/science.aaz3041

2. Watanabe Y, Bowden TA, Wilson IA, Crispin M. Exploitation of glycosylation in enveloped virus pathobiology. *Biochim Biophys Acta Gen Subj* (2019) 1863(10):1480–97. doi: 10.1016/j.bbagen.2019.05.012

3. Xiao X, Chakraborti S, Dimitrov AS, Gramatikoff K, Dimitrov DS. The SARS-CoV s glycoprotein: expression and functional characterization. *Biochem Biophys Res Commun* (2003) 312(4):1159–64. doi: 10.1016/j.bbrc.2003.11.054

4. Lan J, Ge J, Yu J, Shan S, Zhou H, Fan S, et al. Structure of the SARS-CoV-2 spike receptor-binding domain bound to the ACE2 receptor. *Nature* (2020) 581 (7807):215–20. doi: 10.1038/s41586-020-2180-5

5. Prabakaran P, Gan J, Feng Y, Zhu Z, Choudhry V, Xiao X, et al. Structure of severe acute respiratory syndrome coronavirus receptor-binding domain complexed with neutralizing antibody. *J Biol Chem* (2006) 281(23):15829–36. doi: 10.1074/jbc.M600697200

6. Walls AC, Park YJ, Tortorici MA, Wall A, McGuire AT, Veesler D. Structure, function, and antigenicity of the SARS-CoV-2 spike glycoprotein. *Cell* (2020) 181 (2):281–92e6. doi: 10.1016/j.cell.2020.02.058

7. Sztain T, Ahn SH, Bogetti AT, Casalino L, Goldsmith JA, Seitz E, et al. A glycan gate controls opening of the SARS-CoV-2 spike protein. *Nat Chem* (2021) 13(10):963–8. doi: 10.1038/s41557-021-00758-3

8. Casalino L, Gaieb Z, Goldsmith JA, Hjorth CK, Dommer AC, Harbison AM, et al. Beyond shielding: The roles of glycans in the SARS-CoV-2 spike protein. *ACS Cent Sci* (2020) 6(10):1722–34. doi: 10.1021/acscentsci.0c01056

9. Kirchdoerfer RN, Cottrell CA, Wang N, Pallesen J, Yassine HM, Turner HL, et al. Pre-fusion structure of a human coronavirus spike protein. *Nature* (2016) 531 (7592):118–21. doi: 10.1038/nature17200

10. Letko M, Marzi A, Munster V. Functional assessment of cell entry and receptor usage for SARS-CoV-2 and other lineage b betacoronaviruses. *Nat Microbiol* (2020) 5(4):562–9. doi: 10.1038/s41564-020-0688-y

11. Hoffmann M, Kleine-Weber H, Schroeder S, Kruger N, Herrler T, Erichsen S, et al. SARS-CoV-2 cell entry depends on ACE2 and TMPRSS2 and is blocked by a clinically proven protease inhibitor. *Cell* (2020) 181(2):271–80.e8. doi: 10.1016/j.cell.2020.02.052

12. Wrapp D, Wang N, Corbett KS, Goldsmith JA, Hsieh CL, Abiona O, et al. Cryo-EM structure of the 2019-nCoV spike in the prefusion conformation. *Science* (2020) 367(6483):1260–3. doi: 10.1126/science.abb2507

13. Lamers MM, Haagmans BL. SARS-CoV-2 pathogenesis. *Nat Rev Microbiol* (2022) 20(5):270–84. doi: 10.1038/s41579-022-00713-0

14. Frances-Monerris A, Hognon C, Miclot T, Garcia-Iriepa C, Iriepa I, Terenzi A, et al. Molecular basis of SARS-CoV-2 infection and rational design of potential antiviral agents: Modeling and simulation approaches. *J Proteome Res* (2020) 19 (11):4291–315. doi: 10.1021/acs.jproteome.0c00779

15. Hu B, Guo H, Zhou P, Shi ZL. Characteristics of SARS-CoV-2 and COVID-19. *Nat Rev Microbiol* (2021) 19(3):141–54. doi: 10.1038/s41579-020-00459-7

16. Watanabe Y, Allen JD, Wrapp D, McLellan JS, Crispin M. Site-specific glycan analysis of the SARS-CoV-2 spike. *Science* (2020) 369(6501):330–3. doi: 10.1126/science.abb9983

17. Zhou D, Tian X, Qi R, Peng C, Zhang W. Identification of 22 n-glycosites on spike glycoprotein of SARS-CoV-2 and accessible surface glycopeptide motifs: Implications for vaccination and antibody therapeutics. *Glycobiology* (2021) 31 (1):69–80. doi: 10.1093/glycob/cwaa052.

18. Chawla H, Fadda E, Crispin M. Principles of SARS-CoV-2 glycosylation. *Curr Opin Struct Biol* (2022) 75:102402. doi: 10.1016/j.sbi.2022.102402

19. Watson A, Madsen J, Clark HW. SP-a and SP-d: Dual functioning immune molecules with antiviral and immunomodulatory properties. *Front Immunol* (2020) 11:622598. doi: 10.3389/fimmu.2020.622598

20. Gadanec LK, McSweeney KR, Qaradakhi T, Ali B, Zulli A, Apostolopoulos V. Can SARS-CoV-2 virus use multiple receptors to enter host cells? *Int J Mol Sci* (2021) 22(3):1–36. doi: 10.3390/ijms22030992

21. Stravalaci M, Pagani I, Paraboschi EM, Pedotti M, Doni A, Scavello F, et al. Recognition and inhibition of SARS-CoV-2 by humoral innate immunity pattern recognition molecules. *Nat Immunol* (2022) 23(2):275–86. doi: 10.1038/s41590-021-01114-w

22. Haczku A. Protective role of the lung collectins surfactant protein a and surfactant protein d in airway inflammation. *J Allergy Clin Immunol* (2008) 122 (5):861–79. doi: 10.1016/j.jaci.2008.10.014

23. Haczku A. Role and regulation of lung collectins in allergic airway sensitization. *Pharmacol Ther* (2006) 110(1):14–34. doi: 10.1016/j.pharmthera.2005.08.008

24. Forbes LR, Haczku A. SP-d and regulation of the pulmonary innate immune system in allergic airway changes. *Clin Exp Allergy* (2010) 40(4):547–62. doi: 10.1111/j.1365-2222.2010.03483.x

25. Madan T, Biswas B, Varghese PM, Subedi R, Pandit H, Idicula-Thomas S, et al. A recombinant fragment of human surfactant protein d binds spike protein and inhibits infectivity and replication of SARS-CoV-2 in clinical samples. *Am J Respir Cell Mol Biol* (2021) 65(1):41–53. doi: 10.1165/rcmb.2021-0005OC

26. Labarrere CA, Kassab GS. Pattern recognition proteins: First line of defense against coronaviruses. *Front Immunol* (2021) 12:652252. doi: 10.3389/fimmu.2021.652252

27. Hsieh MH, Beirag N, Murugaiah V, Chou YC, Kuo WS, Kao HF, et al. Human surfactant protein d binds spike protein and acts as an entry inhibitor of SARS-CoV-2 pseudotyped viral particles. *Front Immunol* (2021) 12:641360. doi: 10.3389/fimmu.2021.641360

28. Ghati A, Dam P, Tasdemir D, Kati A, Sellami H, Sezgin GC, et al. Exogenous pulmonary surfactant: A review focused on adjunctive therapy for severe acute respiratory syndrome coronavirus 2 including SP-a and SP-d as added clinical marker. *Curr Opin Colloid Interface Sci* (2021) 51:101413. doi: 10.1016/j.cocis.2020.101413

29. Choreno-Parra JA, Jimenez-Alvarez LA, Ramirez-Martinez G, Cruz-Lagunas A, Thapa M, Fernandez-Lopez LA, et al. Expression of surfactant protein d distinguishes severe pandemic influenza A(H1N1) from coronavirus disease 2019. *J Infect Dis* (2021) 224(1):21–30. doi: 10.1093/infdis/jiab113

30. Arroyo R, Grant SN, Colombo M, Salvioni L, Corsi F, Truffi M, et al. Full-length recombinant hSP-d binds and inhibits SARS-CoV-2. *Biomolecules* (2021) 11 (8):1–14. doi: 10.3390/biom11081114

31. Almuntashiri S, James C, Wang X, Siddiqui B, Zhang D. The potential of lung epithelium specific proteins as biomarkers for COVID-19-Associated lung injury. *Diagn (Basel)* (2021) 11(9):1–13. doi: 10.3390/diagnostics11091643

32. Alay H, Laloglu E. The role of angiopoietin-2 and surfactant protein-d levels in SARS-CoV-2-related lung injury: A prospective, observational, cohort study. *J Med Virol* (2021) 93(10):6008–15. doi: 10.1002/jmv.27184

33. Sauer MM, Tortorici MA, Park YJ, Walls AC, Homad L, Acton OJ, et al. Structural basis for broad coronavirus neutralization. *Nat Struct Mol Biol* (2021) 28 (6):478–86. doi: 10.1038/s41594-021-00596-4

34. Lavie M, Dubuisson J, Belouzard S. SARS-CoV-2 spike furin cleavage site and S2' basic residues modulate the entry process in a host cell-dependent manner. *J Virol* (2022) 96(13):e0047422. doi: 10.1128/jvi.00474-22

35. Fraser BJ, Beldar S, Seitova A, Hutchinson A, Mannar D, Li Y, et al. Structure and activity of human TMPRSS2 protease implicated in SARS-CoV-2 activation. *Nat Chem Biol* (2022) 18:963–971. doi: 10.1038/s41589-022-01059-7

36. Farhadian S, Heidari-Soureshjani E, Hashemi-Shahraki F, Hasanpour-Dehkordi A, Uversky VN, Shirani M, et al. Identification of SARS-CoV-2 surface therapeutic targets and drugs using molecular modeling methods for inhibition of the virus entry. *J Mol Struct* (2022) 1256:132488. doi: 10.1016/j.molstruc.2022.132488

37. Lukac I, Abdelhakim H, Ward RA, St-Gallay SA, Madden JC, Leach AG. Predicting protein-ligand binding affinity and correcting crystal structures with quantum mechanical calculations: lactate dehydrogenase a. *Chem Sci* (2019) 10 (7):2218–27. doi: 10.1039/C8SC04564J

38. Barker C, Lukac I, Leach AG. Designing hydroxamates and reversed hydroxamates to inhibit zinc-containing proteases but not cytochrome P450s: Insights from quantum mechanics and protein-ligand crystal structures. *Mol Inform* (2015) 34(9):608–14. doi: 10.1002/minf.201400171

39. Wang Y, Agarwal PK, Brown P, Edelsbrunner H, Rudolph J. Coarse and reliable geometric alignment for protein docking. *Pac Symp Biocomput* (2005); 64–75. doi: 10.1142/9789812702456_0007

40. Leman JK, Weitzner BD, Lewis SM, Adolf-Bryfogle J, Alam N, Alford RF, et al. Macromolecular modeling and design in Rosetta: recent methods and frameworks. *Nat Methods* (2020) 17(7):665–80. doi: 10.1038/s41592-020-0848-2

41. Koehler Leman J, Weitzner BD, Renfrew PD, Lewis SM, Moretti R, Watkins AM, et al. Better together: Elements of successful scientific software development in a distributed collaborative community. *PloS Comput Biol* (2020) 16(5):e1007507. doi: 10.1371/journal.pcbi.1007507

42. Ollitrault PJ, Miessen A, Tavernelli I. Molecular quantum dynamics: A quantum computing perspective. *Acc. Chem Res* (2021) 54(23):4229–38. doi: 10.1021/acs.accounts.1c00514

43. Madsen LS, Laudenbach F, Askarani MF, Rortais F, Vincent T, Bulmer JFF, et al. Quantum computational advantage with a programmable photonic processor. *Nature* (2022) 606(7912):75–81. doi: 10.1038/s41586-022-04725-x

44. Arute F, Arya K, Babbush R, Bacon D, Bardin JC, Barends R, et al. Quantum supremacy using a programmable superconducting processor. *Nature* (2019) 574 (7779):505–10. doi: 10.1038/s41586-019-1666-5

45. Guerreschi GG, Matsuura AY. QAOA for max-cut requires hundreds of qubits for quantum speed-up. *Sci Rep* (2019) 9(1):6903. doi: 10.1038/s41598-019-43176-9

46. Graham TM, Song Y, Scott J, Poole C, Phuttitarn L, Jooya K, et al. Multi-qubit entanglement and algorithms on a neutral-atom quantum computer. *Nature* (2022) 604(7906):457–62. doi: 10.1038/s41586-022-04603-6

47. Sandeep S, McGregor K. Energetics based modeling of hydroxychloroquine and azithromycin binding to the SARS-CoV-2 spike (S) protein - ACE2 complex. *ChemRxiv* (2020) 2020:1–15. doi: 10.26434/chemrxiv.12015792.v2

48. Damle B, Vourvahis M, Wang E, Leaney J, Corrigan B. Clinical pharmacology perspectives on the antiviral activity of azithromycin and use in COVID-19. *Clin Pharmacol Ther* (2020) 108(2):201–11. doi: 10.1002/cpt.1857

49. Goh BC, Wu H, Rynkiewicz MJ, Schulten K, Seaton BA, McCormack FX. Elucidation of lipid binding sites on lung surfactant protein a using X-ray crystallography, mutagenesis, and molecular dynamics simulations. *Biochemistry* (2016) 55(26):3692–701. doi: 10.1021/acs.biochem.6b00048

50. Barnoud J, Monticelli L. Coarse-grained force fields for molecular simulations. *Methods Mol Biol* (2015) 1215:125–49. doi: 10.1007/978-1-4939-1465-4_7

51. Heinz H, Lin TJ, Mishra RK, Emami FS. Thermodynamically consistent force fields for the assembly of inorganic, organic, and biological nanostructures: the INTERFACE force field. *Langmuir* (2013) 29(6):1754–65. doi: 10.1021/la3038846

52. Jorgensen WL, Tirado-Rives J. The OPLS [optimized potentials for liquid simulations] potential functions for proteins, energy minimizations for crystals of cyclic peptides and crambin. *J Am Chem Soc* (1988) 110(6):1657–66. doi: 10.1021/ja00214a001

53. MacKerell AD, Bashford D, Bellott M, Dunbrack RL, Evanseck JD, Field MJ, et al. All-atom empirical potential for molecular modeling and dynamics studies of proteins. *J Phys Chem B* (1998) 102(18):3586–616. doi: 10.1021/jp973084f

54. Stephan M, Docter J. Juqueen: IBM blue Gene/Q® supercomputer system at the jülich supercomputing centre. *J Large-Scale Res facilities* (2015) 1(1):1–5. doi: 10.17815/jlsrf-1-18

55. Goemans MX, Williamson DP. (1994). 879-approximation algorithms for MAX CUT and max 2SAT Proceedings of the twenty-sixth annual ACM symposium on Theory of Computing , in: *Proceedings of the twenty-sixth Annual ACM Symposium on Theory of Computing*, (Association of Computing Machinery:Montreal, QC, Canada, Vol. 1994. pp. 422–31.

56. Agarwal P, Edelsbrunner H, Harer J, Wang Y. Extreme elevation on a 2-manifold. *Discrete Comput Geom* (2006) 36:553–72. doi: 10.1007/s00454-006-1265-8

57. Sandeep S, Aramyan S, Poghosyan AH, Gupta V. Quantum approximated graph cutting: A rapid replacement for T-REMD? *BioRxiv* (2020); 1–18. doi: 10.1101/2020.12.11.420968

58. Chen R, Weng Z. Docking unbound proteins using shape complementarity, desolvation, and electrostatics. *Proteins* (2002) 47(3):281–94. doi: 10.1002/prot.10092

59. Pierce BG, Wiehe K, Hwang H, Kim BH, Vreven T, Weng Z. ZDOCK server: interactive docking prediction of protein-protein complexes and symmetric multimers. *Bioinformatics* (2014) 30(12):1771–3. doi: 10.1093/bioinformatics/btu097

60. Yamamoto M, Gohda J, Kobayashi A, Tomita K, Hirayama Y, Koshikawa N, et al. Metalloproteinase-dependent and TMPRSS2-independent cell surface entry pathway of SARS-CoV-2 requires the furin cleavage site and the S2 domain of spike protein. *mBio* (2022) 13(4):e0051922. doi: 10.1128/mbio.00519-22

61. Shi W, Wang L, Zhou T, Sastry M, Yang ES, Zhang Y, et al. Vaccine-elicited murine antibody WS6 neutralizes diverse beta-coronaviruses by recognizing a helical stem supersite of vulnerability. *bioRxiv* (2022) 30:1–12. doi: 10.1101/2022.01.25.477770

62. Lin X, Guo L, Lin S, Chen Z, Yang F, Yang J, et al. An engineered 5-helix bundle derived from SARS-CoV-2 S2 pre-binds sarbecoviral spike at both serological- and endosomal-pH to inhibit virus entry. *Emerg Microbes Infect* (2022) 11(1):1–50. doi: 10.1080/22221751.2022.2095308

63. Kirchdoerfer RN, Wang N, Pallesen J, Wrapp D, Turner HL, Cottrell CA, et al. Stabilized coronavirus spikes are resistant to conformational changes induced by receptor recognition or proteolysis. *Sci Rep* (2018) 8(1):15701. doi: 10.1038/s41598-018-34171-7

64. Zhang S, Go EP, Ding H, Anang S, Kappes JC, Desaire H, et al. Analysis of glycosylation and disulfide bonding of wild-type SARS-CoV-2 spike glycoprotein. *J Virol* (2022) 96(3):e0162621. doi: 10.1128/jvi.01626-21

65. Sarker M, Jackman D, Booth V. Lung surfactant protein a (SP-a) interactions with model lung surfactant lipids and an SP-b fragment. *Biochemistry* (2011) 50(22):4867–76. doi: 10.1021/bi200167d

66. Wright JR. Immunoregulatory functions of surfactant proteins. *Nat Rev Immunol* (2005) 5(1):58–68. doi: 10.1038/nri1528

67. Gil M, McCormack FX, Levine AM. Surfactant protein a modulates cell surface expression of CR3 on alveolar macrophages and enhances CR3-mediated phagocytosis. *J Biol Chem* (2009) 284(12):7495–504. doi: 10.1074/jbc.M808643200

68. Gardai SJ, Xiao YQ, Dickinson M, Nick JA, Voelker DR, Greene KE, et al. By binding SIRPalpha or calreticulin/CD91, lung collectins act as dual function surveillance molecules to suppress or enhance inflammation. *Cell* (2003) 115 (1):13–23. doi: 10.1016/S0092-8674(03)00758-X

69. Yang W, Shen H, Fang G, Li H, Li L, Deng F, et al. Mutations of rat surfactant protein a have distinct effects on its glycosylation, secretion, aggregation and degradation. *Life Sci* (2014) 117(2):47–55. doi: 10.1016/j.lfs.2014.09.006

70. Lenza MP, Oyenarte I, Diercks T, Quintana JI, Gimeno A, Coelho H, et al. Structural characterization of n-linked glycans in the receptor binding domain of the SARS-CoV-2 spike protein and their interactions with human lectins. *Angew Chem Int Ed Engl* (2020) 59(52):23763–71. doi: 10.1002/anie.202011015

71. Liu J, Lu F, Chen Y, Plow E, Qin J. Integrin mediates cell entry of the SARS-CoV-2 virus independent of cellular receptor ACE2. *J Biol Chem* (2022) 298 (3):101710. doi: 10.1016/j.jbc.2022.101710

72. Beaudoin CA, Hamaia SW, Huang CL, Blundell TL, Jackson AP. Can the SARS-CoV-2 spike protein bind integrins independent of the RGD sequence? *Front Cell Infect Microbiol* (2021) 11:765300. doi: 10.3389/fcimb.2021.765300

73. Makowski L, Olson-Sidford W, W-Weisel J. Biological and clinical consequences of integrin binding *via* a rogue RGD motif in the SARS CoV-2 spike protein. *Viruses* (2021) 13(2):1–20. doi: 10.3390/v13020146

74. Atochina-Vasserman EN, Beers MF, Gow AJ. Review: Chemical and structural modifications of pulmonary collectins and their functional consequences. *Innate Immun* (2010) 16(3):175–82. doi: 10.1177/1753425910368871

75. Brooks BR, Brooks CL3rd, Mackerell ADJr., Nilsson L, Petrella RJ, Roux B, et al. CHARMM: the biomolecular simulation program. *J Comput Chem* (2009) 30 (10):1545–614. doi: 10.1002/jcc.21287

76. Bravyi S, Kliesch A, Koenig R, Tang E. Obstacles to variational quantum optimization from symmetry protection. *Phys Rev Lett* (2020) 125(26):260505. doi: 10.1103/PhysRevLett.125.260505

77. Khan MA, Chiu M, Herbordt MC. FPGA-accelerated molecular dynamics. In: W Vanderbauwhede and K Benkrid, editors. *High-performance computing using FPGAs*. New York, NY: Springer (2013). p. 105–35.

Glossary

ACE2	Angiotensin Converting Enzyme 2
ARG	Arginine
ASN	Asparagine
CHARMM	Chemistry at Harvard Macromolecular Mechanics
COVID-19	Coronavirus Disease Pandemic 2019
CRD	Carbohydrate Recognition Domain
Fc	Crystallizable Fragment
GLN	Glutamine
GLU	Glutamic acid
HAT	Human Airway Trypsin-like protease
HIS	Histidine
LEU	Leucine
MASP	Mannose Binding Lectin Associated Serine Protease
MBL	Mannose Binding Lectin
NET	Neutrophil Extracellular Traps
Extracellular Traps	
NHS	National Health Service United Kingdom
NISQ	Near Intermediate Scale Quantum
PAR4	Protease-activated Receptor 4;
PHE	Phenylalanine
PRO	Proline
QAOA	Quantum Approximate Optimization Algorithm
RMSD	Root Mean Square Deviation
RSV	Respiratory Syncytial Virus
S1	Subunit 1 of the SARS-CoV-2 Spike that is found at its tip
S2	Subunit 2 of the SARS-CoV-2 Spike that is bound to the rest of the virion
SARS CoV-2	Severe Acute Respiratory Syndrome Coronavirus 2
SER	Serine
SIRPa	Signal Regulatory Protein-alpha
SP-A	Surfactant Protein-A
SP-B	Surfactant Protein-B
SP-C	Surfactant Protein-C
SP-D	Surfactant Protein-D
S Protein	SARS-CoV-2 Spike Protein
THR	Threonine
TMPRSS2	Transmembrane Protease Serine 2
TRP	Tryptophan
TTSP	Type II Transmembrane Serine Proteases
TYR	Tyrosine
UNK	Unknown/Unlabeled
VAL	Valine
ZDOCK	Docking Program based on the Fast Fourier Transform algorithm developed by the Zheng Lab, at the University of Massachusetts, Amherst

Frontiers in Immunology

Explores novel approaches and diagnoses to treat immune disorders.

The official journal of the International Union of Immunological Societies (IUIS) and the most cited in its field, leading the way for research across basic, translational and clinical immunology.

Discover the latest Research Topics

See more →

Frontiers

Avenue du Tribunal-Fédéral 34
1005 Lausanne, Switzerland
frontiersin.org

Contact us

+41 (0)21 510 17 00
frontiersin.org/about/contact